UILU-ENG-98-2005

CIVIL ENGINEERING STUDIES
Structural Research Series No. 622
Illinois Cooperative Highway and Transportation
Series No. 264

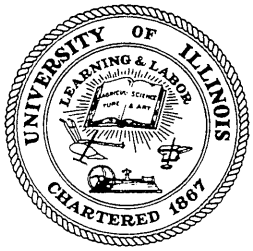

ISSN: 0069-4274

SEISMIC BEHAVIOR OF BRIDGE COLUMN NON-CONTACT LAP SPLICES

By

Yongqian Lin
William L. Gamble
and
Neil M. Hawkins

A Report to the Illinois Department of Transportation

on Project IHR-330

DEPARTMENT OF CIVIL AND ENVIRONMENTAL ENGINEERING
UNIVERSITY OF ILLINOIS AT URBANA-CHAMPAIGN
URBANA, ILLINOIS

June 1998

ABSTRACT

Inadequate shear strength, or inadequate flexural ductility, of concrete columns have caused severe damage to bridges in recent Californian and Japanese earthquakes. In general, those columns were constructed in the 1960's and prior to the implementation in the mid 1970's of improved seismic design methods for bridges. By contrast, columns designed in accordance with the improved methods, or columns strengthened by jacketing, performed well in those same earthquakes.

Much of southern Illinois can expect severe earthquakes and in that area many bridge columns were constructed in the 1960's. Those columns are vulnerable to seismic damage because of inadequate length lap splices at their bases. In 1993 and 1994 field tests conducted for the Illinois Department of Transportation confirmed that vulnerability and demonstrated several acceptable methods for strengthening such splices through jacketing. However, it was found that, in contrast to the details shown on the design drawings, the dowel bars were always located inside the column bars and that there were often large separations in the radial direction between those bars. This study examines the significance of the presence of those non-contact lap splices for the seismic performance of the as built columns. This work forms the first part of an on-going research program, sponsored by the Illinois Department of Transportation, to study seismic retrofit methods appropriate for the type of columns and conditions existing in Illinois.

From field and laboratory tests a simple analytical model was developed that can provide reasonable predictions of the strength, stiffness and ductility of circular concrete bridge columns with inadequate length lap splices at their bases. The field tests involved the reversed cyclic lateral loading to failure of four as-built 1.22 and 1.37 meter diameter columns reinforced with No. 11 longitudinal bars. Those columns contained 18, 24 or 28 bars lapped 30 bar diameters at the base with the same size dowel bars extending up from the footings. The laboratory tests involved the reversed cyclic lateral loading to failure of six 0.61 meter diameter columns, each reinforced with 6 No. 11 column bars and each containing lap splices of the same length as the lengths in the field columns. For the laboratory tests systematic variations were made in the concrete cover to the column bars, the circumferential spacing of the column bars and the separation in the radial direction between the column and dowel bars.

To calculate the stiffness and ductility of such columns account must be taken of the concentrated rotations occurring at the base due to bond slip of the reinforcing bars. For all 10 test specimens lap splice failure was caused by vertical splitting of the concrete covering the longitudinal column bars. The load for bond failure depended on two factors: the tensile force developed in the most highly stressed column bar and the intensity of the reversing forces. The ductility of the test columns was limited by either crushing of the concrete or bond failure of the lap splice. Thus, jacketing of columns for ductility improvements may be needed for any one of three reasons: prevention of lap splice failure; prevention of shear failure; and confinement of the compressed concrete. These tests demonstrated that the bond strength of the lap splice was controlled by the anchorage characteristics for the column bars while the flexural and rotational characteristics at the base were determined by the locations and confinement for the dowel bars. The strength of the lap splice increased as the cover to the column bars increased and as the circumferential separation of the column bars increased. An increase in the separation in the

radial direction between column and dowel bars did not alter the lap splice capacity and the resulting increased cover for the dowel bars allowed those bars to develop increased forces.

USER SIGNIFICANCE

Much of Illinois, and particularly Southern Illinois, is in an area of moderate to high seismic risk, necessitating that new bridge construction meet the seismic detailing requirements of Division IA of AASHTO's Standard Specification for Highway Bridges. However, many bridges in Illinois were constructed in the period between 1950 and the mid 1970's and prior to the introduction of any seismic design requirements into the AASHTO Specifications. Those bridges include most bridges on Illinois' Interstate System.

Two of the major hazards often found in bridge columns constructed prior to the mid-1970's are: (1) inadequate confinement reinforcement for the plastic hinge zones that can develop at the top and bottom of such columns during an earthquake; and (2) inadequate lap length for the splices connecting the longitudinal reinforcement of the column to dowel bars protruding from the pile cap and/or crash wall to which the column is connected. The current 16th Edition of the AASHTO Bridge Specification requires that lap splice lengths be the greater of 60 bar diameters or 406 mm (16 in.), and be located at mid-height of the column for columns located in zones of moderate and high seismic risk. However, in the older existing bridge columns in Illinois the lap length is typically only about 30 bar diameters and usually located in the potential plastic hinge regions of the column.

In California methods have been developed for mitigating inadequate confinement and inadequate lap splice length hazards by jacketing columns using either steel, external reinforcement or various composite wraps. Each strengthening method has advantages and disadvantages. However, for the soft soil conditions commonly encountered in Illinois it is important that the jacket not stiffen the column significantly. Otherwise the earthquake forces felt by the structure are increased and costs can increase because strengthening of the foundation may also become necessary. Thus in Illinois it is desirable that the wrap provide the minimum confinement necessary to ensure adequate plastic hinge and splice capacity.

The wrap design procedures developed in California assume contact lap splices in the plastic hinge region. However, when validation testing was undertaken for the different wraps being considered for use in Illinois, it was found that non-contact rather than contact lap splices were the norm in potential plastic hinge regions. Use of non-contact splices, where the dowel bars lay within a circle of smaller radius than the column bars, made for easier construction of columns. One aim of the research described in this document was to determine the significance of that non-contact condition for assessments of plastic hinge rotational capacities and bond strength of splices.

From this research it was found that, where there was a non-contact lap splice in the plastic hinge region, the flexural strength of the hinge was determined by the number, strength and cross sectional layout for the dowel bars because the internal lever arm between tension and compression forces for those bars was less than for the column bars. Further, the rotational characteristics for the hinge region were determined by bond slip associated with the anchorage of those dowel bars within the column, and the beam into which the column framed, rather than by yielding of those bars over a finite height of the column. For a non-contact splice with the dowel bars located within the column bars, the additional concrete cover to the dowel bars ensures that load-slip characteristics are determined by shearing of the concrete beneath the lugs of those bars rather than by splitting of the

cover over those bars. Slip of the dowel bars results in a concentrated rotation at the beam to column connection that takes the form of a crack that opens wide at that connection. Such concentrated rotations can provide a viable alternative to plastic hinging since the reliability of the anchorage for the dowel bars ensures reliable concentrated rotational capacity. Eq. 6.3b can be used to determine slip values and Eq. 6.2 can be used to determine the resulting concentrated rotation.

In both the field and the laboratory tests, failure of the lap splice was caused by splitting of the cover over the main longitudinal bars of the column. Splitting started from the end where those bars terminated at the face of the crash wall and failure occurred when that splitting extended the length of the splice. The load for bond failure of the splice depended on the tensile force acting on the most highly stressed longitudinal column bar at the end of the splice remote from the crash wall. The bar force for failure can be predicted using Eq. 6.9b multiplied by a factor that varies with the degree of reversal of force in that bar. If the force variation is from a maximum in tension to an equal value in compression that factor is 0.7. Values increase linearly from 0.7 to 1.0 as the compression force decreases from a value equal to the tension force to a value equal to half the tension force.

Equation 6.9b implies that the load for failure of the lap splice will decrease as the cover over the most highly stressed column bar decreases and as the circumferential spacing of the column bars decreases. However, the effect of the former is more important than the latter. The separation between the dowel and column bars has no effect on the splice capacity. Thus, accurate assessments of splice capacity require measurements of the cover over the column bars. Reliable values for cover can be obtained by non destructive assessment methods.

If the cover over the column bars is large, the dowel bars lie around the perimeter of a circle with a radius significantly smaller than the radius of the similar circle for the longitudinal column bars, and the column bars are relatively widely spaced, then such columns, even with lap splice lengths less than the current AASHTO provisions in their potential plastic hinge regions, may be able to develop deflection ductilities greater than the value of five required by the AASHTO provisions for multi-column bridge piers. That possibility should be assessed before an expensive column wrapping operation is undertaken. However, while the cover and circumferential spacing of the column longitudinal bars can be reliably measured using many readily available non destructive assessment methods, measurement of the location of the dowel bars is more challenging. The only non-destructive assessment method that has provide reliable information to date when there are two layers of reinforcement has been ground penetrating radar.

ACKNOWLEDGMENTS

The work reported here was conducted in the field in East St. Louis and in the Newmark Civil Engineering Laboratory of the University of Illinois at Urbana-Champaign. Funding for the study was provided by the Illinois Department of Transportation as part of the Illinois Cooperative Highway Research Program under contract IHR-330. The guidance provided for this study by Mr. Iraj Kaspar, Engineer of Bridge Design, Dr. M. Karshenas, Special Design and Evaluation Engineer, Mr. Ralph Anderson, Engineer of Bridge and Structures, and Mr. Eric Harm, Engineer of Physical Research, Illinois Department of Transportation, is gratefully acknowledged. The assistance of Mr. Fatjon P. Shkurti, Research Assistant in Civil Engineering, in conducting both field and laboratory experimental work and the assistance of Dr. Susumu Kono, former Research Assistant in Civil Engineering in conducting the field work, are also gratefully acknowledged. Dr. Grzegorez Banas and Mr. David Hines of the Newmark Civil Engineering Laboratory assisted with the strain gaging of the bars for the laboratory tests, with the instrumentation of the test specimens and with data collection during testing.

This report is based on a Ph.D. thesis prepared by Dr. Yongqian Lin working under the direction of Professor Neil M. Hawkins and William L. Gamble.

Opinions and findings expressed in this report do not necessarily reflect the opinions of the Illinois Department of Transportation.

TABLES OF CONTENTS

LIST OF TABLES

LIST OF FIGURES

Figure Page

CHAPTER 1

INTRODUCTION

1.1 Background

Inadequate flexural strength and ductility, or inadequate shear strength, of concrete bridge columns have resulted in collapse or severe damage to several California bridges in recent moderate earthquakes. In general, those bridges were designed prior to the AASHTO seismic design methods introduced in the mid-seventies. Bridges constructed in accordance with those methods have performed well in recent earthquakes. However, the large number of older bridges built in the 1950's to 1970's and still in service, particularly in freeway overpasses are now recognized as constituting a cause for major concern should a moderate earthquake occur at the bridge's location.

Due to the inadequate seismic resistance and also the deterioration of some of its bridges, the Illinois Department of Transportation (IDOT) decided in 1993 that the early 1960's designed main-line roadway bridges of I-70, approaching the Poplar Street Bridge over the Mississippi River in East St. Louis, should be replaced. However, to reduce costs, without compromising safety, IDOT also wished to continue to use the less deteriorated bridges of the fly-overs and reconnect them to the new roadway bridges. That decision required that IDOT take steps to reduce the seismic hazards associated with the continued use of the fly-overs.

The fly-over bridges were supported on piers similar to the piers that supported the main-line bridges. Those piers contain columns with their main reinforcement spliced at their connections to the foundation. That splice does not meet 1993 AASHTO seismic standards* and

*See List of References

posed a potential hazard in the event of a major earthquake. IDOT determined that it could reduce seismic hazards for the fly-over bridges by inserting isolators between the column tops and the bridge girders. However, during a severe earthquake, even with such isolators the rotational demands placed on the splices at the column bases could exceed the yield rotation. Therefore, IDOT decided that it was desirable to test several of those columns to determine their rotational capacities at their connections to the foundation, and to assess the effectiveness of external confinement reinforcement for improving those capacities.

The pier and column details for the fly-overs were similar to those of the main roadways. Therefore, the replacement of the main Roadways provided an opportunity to test such piers in place and assess their strength and ductility, prior to the demolition of those piers. The details of the piers that were tested are described in Chapter 2.

The design drawings showed the dowel bars that protruded up from the footing were to be in close contact with the main column reinforcement. However, this was not the situation observed in the field tests. The dowel bars were found to be located around the perimeter of a circle significantly smaller than the perimeter of the circle for the spliced-on column bars. There was little or not contact between the two sets of bars, and in some instances they were separated by as much as six inches in the columns where detailed measurements of the separations were made after testing (see Figs. 3.13 through 3.16).

The field test results, which are described in Chapter 3, differed from column to column for supposedly identical columns due to the column-dowel bar separation caused by the construction methods that were used. That dislocation resulted in irregular noncontact lap splices, instead of the regular contact lap splices as specified for each column and shown in design drawing Fig. 2.2b. The irregular noncontact lap splices were accompanied by irregular

bar cover, bar lap separation and spacing. The field test results suggested that those three variables were critical parameters affecting the likely seismic performance of such lap splices, and therefore, such bridge columns.

1.2 Relevant Previous Research

1.2.1 Factors Affecting the Behavior of Lapped Splices

It is customary in practice to specify contact lap splices and therefore most previous research has examined the behavior of contact lap splices. Only a few tests have been made to examine the behavior of noncontact lap splices and those tests have been for tensile loading only. From tests on contact splices it is known that the subject of lap splices is a general problem in bond and development length, and previous research has identified the following parameters as having significant influence on the behavior of lapped splices under monotonic loading; steel properties; concrete strength and cover; splice length; and transverse reinforcement. By contrast the noncontact splices at the base of the bridge columns would be subject effectively to fully reversed, (tension-compression), inelastic loadings. To date no systematic studies have been made of the behavior of noncontact lap splices under fully reversed inelastic cyclic loading.

1.2.1.1 Steel Properties

It is logical to expect bond strength to be affected by the level of forces to be transferred to the steel at the concrete-steel interface. For a given bar diameter and development length, the higher the yield strength of the reinforcing steel, the higher the forces that are generated at the concrete-steel interface. In most practical situations the yield strength of the steel is greater than the specified minimum value. Splices must be detailed with sufficient strength reserve to resist the actual forces in the reinforcement rather than forces based on nominal steel properties. This is particularly important for structures in earthquake zones since forces significantly greater than

the yield strength can be developed in reinforcing bars during a severe earthquake. Strain hardening during post-yielding deformation of steel can lead to stresses as much as 1.5 times the nominal yield strength of the reinforcing bars (Park and Pauley, 1975), whereas it is customary for codes such as ACI 318-89 and AASHTO 1993 to specify use of values only 1.25 times the nominal yield strength.

The load-deformation characteristics of the steel also influence bond slip and therefore the bond strength characteristics of reinforced concrete structures. The more highly a bar is strained into its inelastic range, the greater is the accompanying reduction in area. Such reduction increases the bearing stresses beneath the lugs, and increases the likelihood of splitting and shearing failures.

In addition to the load-deformation characteristics of the reinforcing steel, the size and geometry of the bars also influence the strength and ductility of lapped splices. The ratio of the cross-sectional area to the surface area of the bar is directly proportional to the bar diameter. Thus larger bond stress concentrations are to be expected for larger bars. In design this effect is partly offset by using longer splice lengths for larger bars. However, in spite of the use of longer splices for large bars, experimental investigations have shown that large bars generally give much weaker anchorage than smaller bars with the same total cross-sectional area (Tepfers, 1973). The larger the bars the larger and more numerous are the cracks that occur along the length of bar. Cracks are weak points that initiate splitting failure. Morita and Kaku (1979) have reported that for bar sizes greater than 50 mm it is almost impossible to avoid a splitting failure. The various forms of splitting and related failures are influenced by concrete strength and cover, splice length, and transverse reinforcement. Each of those effects are discussed in the next three sections.

1.2.1.2 Concrete Strength and Cover

As reported by Lutz and Gergely (1967) bond stresses generate longitudinal, radial and circumferential tensile stresses. When the resulting stresses exceed the tensile strength of the concrete cracks are formed in the concrete. Such cracks can occur even at relatively low load levels. Once formed these cracks widen and propagate, resulting in stiffness degradation, bond deterioration and ultimately failure of the force transfer mechanism between concrete and steel. There are three kinds of cracks in reinforced concrete influencing bond behavior: primary cracks, secondary cracks, and longitudinal cracks. Primary cracks transverse the total section of tension members and extend to about the neutral axis of flexural members. Secondary cracks are small internal cracks surrounding the bar and they form shortly after the formation of the primary cracks. Longitudinal cracks begin at existing primary cracks or secondary cracks and propagate along the reinforcement. During the formation of the internal cracks, the concrete around the reinforcement in the zone of stress transfer has the appearance of a comb as shown in Fig. 1.1. Since internal cracks are not at right angles to the bar, the deformation of the teeth of the comb-like concrete serves to tighten the concrete around the reinforcing bar. The reaction to such tightening also produces ring tensions in the concrete around the bar, and those ring tensions cause longitudinal splitting cracks. That is the main reason that longitudinal cracks form first on the line of the bar and at the face of primary cracks, and then extend along the bar with increasing tensile force on the section.

Cracking is dependent on the tensile strength of concrete. The tensile strength of concrete is approximately proportional to the square root of the concrete compressive strength. Thus from the standpoint of tensile strength alone, it is natural to expect better bond performance as the compressive strength of concrete increases. There is, however, no clear cut relationship

between concrete compressive strength and bond performance. The influence of concrete strength is often clouded by more significant factors such as load history, amount of confinement, etc. Ferguson and Breen (1965) found that up to a point increased concrete strength is beneficial for bond and hence splice strength. However, beyond that point increased strength provides excessive stiffness that hampers the process of stress redistribution caused by cracking, resulting in very high localized stresses and less effective bond performance.

Fig. 1.2 illustrates some of the basic splice failure patterns observed for reinforced concrete. If the clear cover to the bar from the bottom of the beam, c_b, exceeds the clear side cover, c_s, then splitting will occur in the plane of the bars and parallel to the bottom of the beam. In that case no longitudinal cracking is observed on the bottom of the beam. Conversely if the reverse is true and $c_s > c_b$, then shortly before failure longitudinal cracks will occur on the bottom of the beam. Final failure will then be in a v-notch or face and side split mode.

For spliced bars it is clear that the cover to the bars and their spacing play major roles in determining the mode of failure. Normally, there are three ways in which a lapped splice or an embedded bar can fail:

1) The spliced bars can yield and, with increased loading, fracture near their loaded ends within the splice. This is the ideal form of failure, as the bars have then developed their full potential strength before anchorage failure;

2) Failure can occur due to pull out of the embedded bar if inadequate splice length is used.

3) Splitting of the concrete cover can occur, resulting in loss of bond transfer and failure.

The longitudinal component of the bond stress tends to shear off or crush the concrete between deformations while the radial and circumferential tensile stresses tend to burst the

concrete cylinder surrounding the lapped bars. An increased cover means that there is a larger diameter concrete cylinder to resist the radial and circumferential tensions. Thus it is essential to provide adequate cover to prevent a premature splice failure due to splitting of the concrete cover. Chinn et al (1955) observed that for No. 6 bars, doubling the concrete width from 92 to 184 mm (3.62 to 7.25 in.) per splice (i.e. the distance c_s in Fig. 1.2) resulted in as much as a 15 to 40 percent increase in splice strength under monotonic loading. Similarly, doubling the bottom cover from 19 to 38 mm (0.75 to 1.5 in.) (i.e. the distance c_b in Fig. 1.2) resulted in a 7 to 15% rise in splice strength for short splices with178, 280 and 406 mm (7, 11 and 16 in.) lap lengths. The same effect, however, was very small for 610 mm (24 in.) lap splices.

1.2.1.3 Splice Length

For a given bar size, when the splice length is increased there are less splitting forces per unit length to be developed along the length of the splice and consequently there is greater potential for developing high forces in the spliced bars. For monotonic loading there is an upper limit above which further increase in splice lengths has little or no beneficial effect on the strength of the splice. The cracking that causes stress redistribution and increasing strength with increasing splice length occurs only at the outer regions of the splice where one of the bars is loaded. The middle third of the splice then remains relatively uncracked and under a small constant stress. Therefore that central region does little to improve the strength or performance of the splice.

1.2.1.4 Transverse Reinforcement

Of all the parameters that influence the strength and energy dissipation ability of lapped splices, the amount and distribution of confining steel is probably the most important one, particularly in the case of structures required to withstand earthquake induced forces. By controlling the

formation of cracks and their subsequent propagation, transverse bars greatly enhance lap strength and particularly ductility. Stirrups also enhance the integrity and the compressive strength of the concrete within the confined core, thus possibly delaying a crushing failure.

Lateral reinforcement can be provided in the following forms in rank order of decreasing effectiveness: spirals, stirrups, hoops, and straight transverse reinforcing bars as used in walls. The amount and distribution of transverse reinforcement is of paramount importance in the detailing of lapped splices. High stresses originate around the ends of a splice. Thus stirrups placed in this zone are more effective than those placed in the center of a splice (Tepfers, 1973) for increasing splice strength and toughness. The enhancement in the strength of a splice, caused by the presence of stirrups, increases as the size of the stirrup increases, or as the spacing decreases.

1.2.2 Contact Lapped Splices under Cyclic Loading

The behavior of lapped splices under cyclic loading is different from that for splices under monotonic loading or repeated unidirectional loading. For reinforced concrete structures subjected to monotonic loads the main concern is to provide structures with adequate strength. The displacements that can be achieved along with that strength are of less concern. However, in the case of structures built to resist seismic loads a satisfactory level of structural ductility must be provided in addition to ensuring sufficient strength. Thus, the displacements than can be achieved for repeated loadings in both tension and compression to stresses beyond those for bar yield become of more importance than the strength. The total energy that the splice can absorb and dissipate becomes the primary concern.

Some of the earliest research work, relevant to splice behavior under repeated and reversed cyclic loading, was carried out at Cornell University by Fagundo et al (1979). Their

work centered mainly on the influence of load history and the effects of varying levels of confinement on the strength and ductility of lapped splices in constant moment zones in beams. The subsequent series of investigations completed at Cornell University consisted of six phases. Five phases were for contact splices and only one for noncontact splices. In these investigations the ability of a specimen to withstand, without failure, a minimum of fifteen reversing load cycles beyond yield was considered indicative of satisfactory performance without any specific minimum strain or stress consideration.

For the first four phases of the work on contact splices, including the studies by Fagundo et al (1979), together with those by Tocci et al (1981) and Sivakumar et al (1982), a total of sixty-eight large beam and column-type specimens with lapped splices, subjected to high-level repeated or reversed cyclic flexural loads, were tested to failure. Splice lengths were initially based on the suggested provisions of ACI Committee 408 (1979), in which the effects of concrete strength, cover, and transverse reinforcement are all explicitly considered. The splice lengths ranged from 24 to 45 bar diameters. The amount of transverse reinforcement ranged generally from about one-third to twice the amount suggested by the ACI Committee 408 (1979) provisions.

The conclusions from those four phases of the investigation were summarized by Lukose et al (1982) as follows:

1). Repeated loading, and the number of load cycles, have little effect on the performance of lap splices if the load level is below about 75 percent of the monotonic capacity. On the other hand, the rate of bond deterioration increases rapidly, even after only a few cycles of repeated load, once loads exceed 95 percent of the yield load. Above yield, splice performance is determined predominantly by the total number of cycles of load application.

With yield penetration into the splice region, the force transfer capacity of the yielded portions can not increase until strain hardening begins in the main reinforcing bars;

2.) Multiple stirrups at splice ends are effective only for monotonic loading cases, where damage is confined to these locations. With cyclic inelastic loads, yield penetrates into the splice past the heavily reinforced ends and will proceed at an accelerated rate if internal confinement is poor. In these cases, uniformly spaced stirrups are needed for adequate splice resistance. The rate of increase of stirrup strain with main bar strain in repeated cyclic tests can be significantly reduced by adopting a larger total area of stirrups. That condition can be achieved either by using closer stirrup spacings, (preferable), or larger diameter stirrups;

3.) The effect of cover is important in determining the type of splitting pattern. Certain splitting patterns are more desirable than others, and in this respect, cover variations can result in differences in splice strength. For monotonic loads, bond resistance depends on concrete tensile strength and therefore on the cover. However, the influence of this factor is less for cyclic loads. In that case, the considerable amount of cover cracking evident before failure makes cover resistance an unreliable factor. The cover is an essential part of the load transfer mechanism in the splice region, and a minimum clear cover of at least 1.5 d_b was found to be sufficient to achieve the required load transfer characteristics;

4). For #6 and #8 reinforcing bars, under the action of high-intensity reversed cyclic loads, a clear spacing of at least 4 d_b between splices was found adequate to prevent a plane of splitting from developing across the plane of the splices;

5). The onset of splitting does not constitute failure. Loads can be carried beyond this point, through confinement afforded by the stirrups, up to the stage where splitting along two perpendicular faces results in a cover spalling mechanism; and

6). Splices can be made successfully in regions where flexural yielding or severe stress reversals are anticipated. Most codes for seismic areas do not permit lapped splices in these regions, suggesting that splices are unreliable in these situations.

In the fifth stage of the investigation, Panashahi et al (1987) studied the performance of compression lapped splices in columns and beams under inelastic cyclic loading. Five columns, (two concentrically loaded specimens and three eccentrically loaded specimens), and four beams were tested to failure. From that study on compression lap splices, it was concluded that:

1). Inelastic cyclic loading induces progressive deterioration of the force transfer mechanism. The existence of residual compression stresses in steel bars, combined with bond and end bearing deterioration, results in a large amount of yield penetration along the splice length. Thus, the effective length over which bond resistance can occur becomes less than the lap length;

2). As yielding penetrates along the spliced bars, the bond, (and the radial bursting), stresses over the central, elastic, portion of the splice increase. Consequently, the bond stress distribution along the elastic portion of the spliced bar approaches a uniform state;

3). Inelastic cycling of a compression splice strains the end bearing concrete significantly. This can have a detrimental effect on the contribution of the end bearing to the strength of a compression splice; and

4). The concrete outside the splice region is subjected to a high intensity cyclic loading in compression when the splice is loaded repeatedly into inelastic range. Therefore, for satisfactory performance of the concrete outside the splice region, adequate confining reinforcement is of vital importance for the seismic design of compression splices.

Paulay et al (1981) undertook a pilot experimental investigation of the behavior of contact lapped splices in the end region of reinforced concrete bridge piers and columns of multistory frames under reversed cyclic loads. Ten prototype units with different cross sections (octagonal and square sections) were tested to failure. Those columns were designed and constructed according to the requirements of the Draft New Zealand Code for the Design of Reinforced Concrete Structures, DZ 3101-1980. Splice lengths ranged from 22.5 to 32 bar diameters (5-30 d_b, 1-22.5 d_b, 1-17.5 d_b, 1-27.7 d_b, 1-25 d_b and 1-32 d_b). All the columns were subjected to reversed cyclic loads which resulted in both elastic and inelastic deformations in the zone where reinforcing bars were lap spliced.

The objective of this study was, first, to assess whether or not lapped splices can sustain a satisfactory number of cycles of high intensity reversing load in the elastic range of response and, second, to check whether the requirements of the Code (DZ 3101-1980) with respect to confinement along lapped splices in high moment regions were adequate to preserve splice strength under inelastic loadings. Both objectives were realized, demonstrating that lapped splices can be used in high moment regions of suitable designed columns, (upper story columns), likely to experience severe seismic loads. It was concluded that splice lengths determined by the requirements of the Draft New Zealand Code (DZ 3101-1980), which followed the recommendations of ACI Committee 408 (1979) very closely, were adequate. Recommendations were also made for design of transverse reinforcement to ensure satisfactory splice behavior. The columns behaved in a satisfactory fashion up to a displacement ductility factor of four. However, yielding of the longitudinal reinforcement was restricted to a very small length adjacent to the critical section, resulting in extremely high longitudinal steel strains in both tension and compression. With further increases in ductility demands buckling of the

longitudinal reinforcement occurred adjacent to the critical section, there was some stiffness and strength degradation, and after a few cycles at a ductility demand of 6, fracture of the longitudinal steel occurred as a result of alternate buckling and straightening of the bars under the cyclic displacements. The tests showed that there are different failure modes for differing bar layouts and demonstrated that splices should not be used in end regions, if the possibility of the formation of a plastic hinge exists.

1.2.3 Noncontact Tensile Lap Splices

The conclusion to be drawn from the noncontact splice research performed thus far is that there is little or no difference in strength and performance between spaced, (noncontact), and contact splices under monotonic loading. Researchers, such as Chamberlain (1952, 1958) and Chinn, et al (1955) used both pull out and full-scale beam specimens with contact and noncontact splices and found no significant differences in performance.

In order to explain the behavior of lap splices in general, and especially, noncontact lap splices, Goto and Otsuka (1979) showed (Fig. 1.3) that there is diagonal cracking of the concrete between two spaced splice bars. The lap length and spacing of the bars affects the angle of cracking.

In addition, in the final stage of the series of investigations at Cornell University, Sagan et al (1988) tested forty-seven full-scale flat plate tension specimens, subject to in-plane loadings, to determine the effects on strength and behavior of the noncontact spacing of the spliced bars, bar size, concrete strength, splice length, and transverse steel area and spacing. The specimens had splice bar spacings ranging from direct contact to 8 bar diameters clear spacing for both spliced #6 and #8 bars, concrete compressive strengths ranging from 21.4 to 42.1 MPa (3,100 to 6,100 psi), and splice lengths of 30 and 40 bar diameters. The typical tension specimen

contained two lap splices and modeled a half wall thickness. The major conclusions reached from that investigation were:

1). The spliced bar spacing affects the number of inelastic load cycles that can be attained before failure, but it does not affect the ultimate strength of a splice. The ultimate load that can be carried by a splice is independent of the spliced bar spacing for spacings of up to 152mm (6 inches) clear for monotonic loading. For repeated loading up to the yield strength of the splice bars, (which was a testing limitation and the ultimate load), the ultimate load was also independent of the spliced bar spacing for spacings of up to 8 bar diameters for both #6 and #8 bars; and

2). Noncontact lap splice design should consider the effects of the added confinement provided by the additional concrete between the spaced bars, the reduction in the tensile strength of the concrete because of the compression force transfer stresses in the concrete between the bars, and the reduction in the effective lap length of the splice (see Fig. 1.4). As a result of the development of diagonal cracks between spliced bars, the overall lap splice length, l_s, is determined by adding to the effective lap length l_{eff}, the splice bar clear spacing, s_p, multiplied by 0.75, that is

$$l_s = l_{eff} + 0.75 s_p \qquad \textbf{(1.1)}$$

1.2.4 Concluding Remarks

The foregoing review of the available literature on studies of the performance of lapped splices indicates that there is little information existing about the behavior of noncontact lap splice under reversed cyclic loading. However, it is also clear, from studies in California by Priestly et al for Caltrans and those performed in East St. Louis for IDOT, that there are many

examples of this type of splice at the base of columns of existing bridge piers constructed during the development of the interstate system in the 1950's and 1960's. Therefore, in order to define the characteristics needed for the design of retrofit methods for seismic loadings for such splices, quantitative information is needed on the specific influences of bar spacing, tangential and radial, and bar cover, on lap splice performance.

1.3 Objective and Scope

The principal objective of this study is to provide basic knowledge on the performance of circular columns with noncontact lap splices at their maximum moment sections. As part of that work the validity of existing equations, (Darwin et al, 1995), for calculating the maximum bond force (or bar stress) at failure along the splice length is examined. Then a simple model is used to provide reasonable predictions of the response to seismic loadings of bridge columns with inadequate length lap splices at the column to foundation connection.

This study involved both field and laboratory investigations. The field work involved the reversed cyclic lateral load testing to failure of four as-built large diameter circular columns which formed parts of existing bridge piers. Chapter 2 provides a description of the bridge piers, the as-designed reinforcement details of the piers, and the test setup and instrumentation for the field tests. The field test results are presented in Chapter 3. Those results suggested that bar cover, bar lap separation and bar spacing were critical parameters affecting the behavior of a column with noncontact lap splices at the maximum moment section at its base. However, due to the wide irregularities in the details of the field columns, it was not possible to determine the relative importance of the various parameters. Therefore, a laboratory investigation was undertaken to examine physically the effects that concrete cover, bar spacing and bar lap separation had on the behavior of columns with splices at the maximum moment region at their

bases. In order to be able to apply the laboratory test results directly to interpretation of the results of the tests on the field columns, the laboratory columns were designed to keep the flexural deformation characteristics and the longitudinal bar sizes (#11 or 35.8 mm diameter), as well as the bar lap length (1.09m or 43 in.), the same as those in the field columns. Six laboratory columns, with sizes half those of the field columns were made and tested to failure in the Newmark Civil Engineering Laboratory. The laboratory test specimens, their fabrication and instrumentation are described in Chapter 4. The results of the laboratory tests are discussed in Chapter 5 and in Chapter 6 a simple analytical model for predicting the results of both the laboratory and field tests is developed. Chapter 7 summarizes the study and draws conclusions.

CHAPTER 2

FIELD TEST COLUMNS, TEST SETUP AND INSTRUMENTATION

2.1 Introduction

As noted in Chapter 1, the bridge piers which were tested to failure in the field had, according to AASHTO seismic standards, deficient lap splice lengths at their bases. Further they also had other detailing and construction defects such as the details for the column hoops. While the test columns were to be removed and replaced as part of rehabilitation of the Poplar Street bridge interchange, a large number of other similar columns had to remain in service in the same interchange for the foreseeable future. Therefore, the columns in the remaining parts of the interchange and especially those supporting the fly-over ramps, had to be seismically strengthened in order to protect the two new mainline roadway bridges that were to be constructed and to preserve the integrity of the interchange in the case of a major seismic event.

To validate that the scheme developed for strengthening the fly-over columns was effective, tests were completed in the field for IDOT on nine full size columns, five of which were retrofitted with various schemes for increasing the strength and ductility of the lap splices at their bases, and four of which were tested as built. This Chapter describes the loading setup and instrumentation for those as-built column tests.

The pier and column details for the fly-overs were similar to those of the main roadways. Therefore, the replacement of the main roadways, in October 1993 and September 1994, provided an opportunity to test typical piers in place and assess their strength and ductility, prior to the demolition of those piers. The complex had been built in the early 1960's. Soon after construction some of the columns of the piers developed splitting cracks at their tops as a result of their having inadequate ties at that location to resist the forces exerted on them by the bearings

of steel bridge beams. In the interchange those splitting cracks had been arrested by confining the column tops with externally applied hoop reinforcement. With the demolition of the main-line bridges that hoop reinforcement was available for use as confinement reinforcement for the splices at the bases of the fly-over columns. Therefore, in the field test program, that use along with other procedures, was explored as one method for reinforcing inadequate strength splices.

2.2 Description of Test Piers

The test piers were very similar in geometry and reinforcing details. Therefore, details are described here for one typical pier only. The as-designed plan and elevation geometry for typical test pier B18 having 1.37 m (54 in.) diameter columns are shown in Fig. 2.1.

Each pile-supported concrete pier consisted of four components: (1) a pile cap, 915 mm (36 in.) thick; (2) a crash wall, 1,530 mm (60 in.) high and 102 mm (4 in.) wider than the column diameter; (3) two columns located at 9,754 mm (384 in.) on centers and with heights ranging from about 9,000 to 11,000 mm (360 to 432 in.) above the top of the crash wall. The heights of the columns for a given pier were not equal because of the superelevation necessary for the curved roadway supported by the columns; and (4) a 380 mm (15 in.) wide by 915 mm (36 in.) deep horizontal reinforced concrete tie beam connecting the tops of the columns and with its top located 305 mm (12 in.) below the top of the shorter of the two columns in a given pier. The lengths of the pile caps parallel to the roadway differed slightly, depending on the column size and the number of piles.

A construction joint was located in each column, 153 mm (6 in.) below the horizontal tie beam connecting the two columns in a pier. That joint was clearly visible in each pier where it showed up as a clean horizontal line apparently formed by means of a piece of molding placed in the formwork. Details of that construction joint were not available.

The plan view of Fig. 2.1 shows the locations of the 30 concrete piles under pier B18. Two thirds of those piles were battered parallel to the direction of the roadway. The design pile capacities were 275 to 311 kN (31 to 35 tons) at service load, and the estimated lengths varied between 12,000 and 15,000 mm (39 and 50 ft) for the several piers for which drawings were available. The actual installed lengths are not known. The piles were 305 mm (12 in.) diameter concrete-filled steel pipe. One seismic concern, additional to the inadequate length lap splices at the column bases, was the lack of positive tension connections between the piling and the pile cap.

The as-designed reinforcement details for pier B18 are shown in Figs. 2.2a and 2.2b. Those piers were designed originally using service load procedures and assuming the use of Intermediate Grade Steel with a yield strength of 275 N/mm^2 (40 ksi) and a concrete with a compressive strength, of 24 N/mm^2 (3,500 psi). For pier B18 each 1.37 m (54 inc.) diameter column contained 28-#11 (35.8 mm) bars as its main longitudinal reinforcement. All those bars were spliced at the base of the column with a 1,090 mm (43 in.) lap length to dowel bars of the same size and number anchored in the pile cap. The lap length was the equivalent of 30 bar diameters for a #11 bar. The lateral reinforcement over the height of the columns consisted of #4 (12.7 mm) hoops spaced at 305 mm (12 in.) centers. The hoop ends were neither shown as anchored into the core of the column nor as welded into closed circles as required by 1993 AASHTO provisions. A nominal 380 mm (15 in.) lap was shown in the original drawings for those hoops. By contrast typical field values were 300 mm (12 in) lap lengths. The concrete cover was specified as 50 mm (2 in.) clear to the hoop reinforcement. However, in the field it was clearly apparent that the actual cover was less on several of the existing columns. For several columns in the interchange the concrete cover to the hoop reinforcement had partially

spalled, exposing some of the bars of the columns and resulting in their rusting. The reinforcing bars of the tie beam were shown as extending horizontally to the mid-plane of the column. There were no hooks on those bars so that the two columns were not strongly connected to each other and obviously the tie beam would be ineffective in providing moment resisting frame action in the case of a severe seismic event.

2.3 Idealization of Piers for Testing

To develop a scheme for in-situ testing of the bridge piers the likely flexural strength of the pier for seismic loading was investigated by conducting a plastic analysis of a typical bent. As shown in Fig. 2.3a, horizontal forces, H, were applied at the column tops and any restraints provided by the bridge superstructure were ignored. Those horizontal forces were increased gradually and an examination made of the order in which plastic hinges formed at the ends of the tie beam and at the bases of the columns, while those columns were acted on by the dead load, P_D, of the roadway. The analysis showed that hinges formed almost simultaneously at both ends of the tie beam and at the bases of the columns. The analysis also showed that the point of contraflexure, (Fig. 2.3b), with the two columns and the tie beam acting as a frame, was about 6.71 m (22 ft) above the crash wall.

For that plastic analysis, the capacity reduction factor Φ, was taken as unity, and the computed nominal strengths and deformations of the columns were as given in Figs. 2.4, 2.5 and 2.6 for an assumed concrete compressive strength, of 27.6 N/mm^2 (4,000 psi), a steel yield stress of 275 N/mm^2 (40,000 psi) and the uniform distribution of bars around the circumference of each column, as shown in the design drawings. The moment, for a given curvature, for Figs. 2.4, 2.5 and 2.6 was not very sensitive to concrete strength, although the deformation capacity for a given moment was somewhat sensitive.

It can be seen from Fig. 2.4 that the nominal limiting moment capacities, in the absence of thrust, were about 2,440 and 4,200 kN-m (1,800 and 3,100 k-ft) for a 1.22 m (48 in.) diameter column containing 18-#11 bars and a 1.37 m (54 in.) column containing 28-#11 bars, respectively. Shown in Figs. 2.5 and 2.6 are moment-curvature relationships for three different axial compression values. While the addition of compression increases the moment capacity for a given curvature, and reduces the ultimate curvature, such changes are not large within the range from zero to 1780 kN (400 kips). The latter value was the maximum expected column service load thrust due to dead and live loads. Further, while the seismic overturning forces would add to the compressive thrust due to dead load for one column, those same forces would reduce that compressive thrust for the other column. Therefore, for test purposes it was concluded that axial force effects could be neglected and seismic effects simulated by testing each single columns instead of whole piers. However, to recognize the frame action that would occur in an actual pier the reversing horizontal force simulating seismic effects needed to be applied 6.71 m (22 ft) above the top of the crash wall.

The horizontal forces required to simulate seismic effects and cause yielding at the column bases when axial force effects were ignored were calculated to be 365 and 628 kN (82 and 141 kips) for 1.22 m (48 in.) and 1.37 m (54 in.) columns, respectively, for forces applied at 6.71 m (22 ft) above the crash wall. The value of the larger force was used to proportion the steel frame used for the field tests. Further, both the 365 and 628 kN (82 and 141 kips) forces were significantly less than 0.3 times the nominal shear strengths of the two column sizes for monotonic loadings to failure. Therefore, shear degradation of the test columns at high ductilities was not to be expected.

2.4 Field Test Columns

During 1993, three columns were tested in the field (Lin et al., 1994). Two columns were tested in the as-built condition and for one the splice at the base of the column was strengthened with steel bands. During 1994, six columns were tested in the field (Shkurti et al., 1995). Two columns were tested in the as-built condition and for four the splice was strengthened with steel bands, pre-stressing strands, and two types of fiberglass jackets, respectively. This report discusses the testing and performance of the as-built columns only.

Four as-built columns were tested. Those columns were designated as B18S, C17S, B14S and C15S and had the following characteristics:

B18S—a 1.37 m (54 in.) diameter column reinforced with 28 #11 bars;

C17S—a 1.37 m (54 in.) diameter column reinforced with 24 #11 bars; and

B14S and C15S—two 1.22 m (48 in.) diameter columns, each reinforced with 18 #11 bars.

2.5 Field Test Setup

Shown in Fig.2.7 is the test setup used to apply fully reversed horizontal cyclic loads to a single test column. First, the superstructure above the pier was removed along with the tie beam that connected the two columns of the pier. Next, a steel load frame was erected between the columns and its legs attached to the crash wall. A box-like structure was then fitted to the top of the load frame and used to support the loading jacks. The jacks in turn reacted against a loading head fitted around the column and supported from a frame placed over the top of the column.

Loads were applied in the plane of the pier at a point 6.71 m (22 ft) above the top of the base of the column. The steel reaction frame shown in Fig. 2.7 were designed to resist a

horizontal force of 890 kN (200 kips). That force was 40 percent greater than the nominal 628 kN (141 kips) capacity of the strongest column to be tested. Each leg of the frame was composed of a pair of channels, (as detailed in Fig. 2.8), with one channel positioned on each side of the crash wall connecting the base of the columns. Each channel was braced against the other in the weak-axis direction by batten plates, which were connected to the channel by 22 mm (7/8 in.) diameter high strength bolts (Fig. 2.9). The channels were attached to the crash wall and the pile cap with 22 and 25 mm (7/8 and 1 in.) diameter post-installed horizontal and vertical anchor bolts set into the concrete with epoxy resin. At the bottom end of each channel there was a base plate held in position with two vertical anchor bolts each of 305 mm (12 in.) anchorage length. Eight horizontal anchor bolts each of 178 mm (7 in.) anchorage length held each vertical channel to the crash wall and twelve horizontal bolts each of the same anchorage length held each inclined channel to the crash wall. The locations for horizontal bolts are not shown in the test setup of Fig. 2.7, because those locations depended on the exact positions of the reinforcing bars within the crash wall. In order that the bolts could be placed so that they avoided reinforcing bars twice as many holes as the number of bolts required were drilled in the bottom part of each channel. The locations of those holes are shown in Fig. 2.8. At their upper end the two legs of the steel frame were connected together, as shown in Fig. 2.10 by gusset plates and 25 mm (1 in.) diameter high strength bolts. The gusset plates formed the sides of a box-like structure that was used to support the test jacks. The channels were detailed so that they could be used with piers with columns of either 1.22 or 1.37 m (48 or 54 in.) diameter. However, separate box-like assemblies were required for the two different column sizes.

Shown in Figs. 2.11 are details of the frame that was positioned on top of the column (Fig. 2.7) and used with 19 mm (3/4 in.) diameter tie rods to support the loading heads. Shown

in Fig. 2.12 are details of the loading heads. As apparent from the plan view of the top of the test setup shown in Fig. 2.13 there were two loadings heads connected together with 35 mm (1 3/8 in.) diameter high strength bars and constituting a loading yoke that surrounded the column and allowed the application of reversing horizontal loads. Those loads were applied by two 890 kN (100-ton) hydraulic center-hole jacks whose forces were monitored by load cells positioned behind the jacks. The jacks and load cells were threaded over a 44.5 mm (1-3/4 in.) diameter high strength steel rod. That rod passed through the box-like structure, through the load cells and the two jacks, and was anchored at both ends with a nut.

2.6 Loading Method

The two 890 kN (200 kips) jacks in the test setup were operated so that they alternately pushed and pulled the column. For the left column in fig. 2.7 the operation of the jacks through a fully reversed load cycle was as follows:

To push the top of the column to the left, both jacks were retracted and the gap between the left jack and the column filled with spacers. Then the left jack was extended to produce the desired load or deflection;

To reverse the load, the left jack was retracted and the spacers were removed. The nut on the right end of the loading rod was tightened to bring it in contact with the right jack, and the right jack then extended to produced the desired load or deformation.

For small deformation cycles, both jacks were operated alternatively starting from the mid-range of their 254 mm (10 in.) strokes and no further adjustments of nuts or spacers were required. However, for large deformation cycles some additional adjustments were required. The maximum possible motion in a single uninterrupted cycle were less than the full jack stroke because of the flexibility of the steel reaction frame.

The loading system had greater deformation capacity in the pull direction than in the push direction. In the push direction, when the deflection exceeded about 200 mm (8 in.), the rotations of the loading head became large enough to pry on the piston of the jack and prevent the latter from moving smoothly. The loading system was much more compliant in the pull direction with the length of the tension rod leading from the jack to the loading head, preventing similar prying actions. The tension rod was continuously threaded, and very large deflections could be imposed by the process of pulling on the rod to the limit of the jack stroke, unloading the column, turning down the nut on the rod, and reloading. However, to be effective this process depended on significant residual deflections remaining each time the column was unloaded.

2.7 Test Instrumentation

The forces applied by the jacks, and the deformations of the column, were measured throughout each test. However, the number of locations at which deformation measurements could be made was limited because of the short time over which the structures were available for testing, security considerations at the site, weather conditions, and the time needed to obtain and install robust instrumentation.

The force in the jacks was determined using pre- and post-calibrated load cells positioned between the jacks and the nuts on the loading rod or between the loading yoke and the jack, (Fig. 2.13). The hydraulic pressure applied to the jacks was also monitored, but values were used primarily as an aid in controlling the jack.

Lateral deformations of the vertical centerline of the column on the line at which the loading was applied were measured using a theodolite. Vertical deflections for the crash wall on the centerlines of the column and at the middle of the crash wall were also measured in the first

Test in order to observe if any base rotations were induced. The theodolite was positioned approximately 6 m (20 Ft) from the base of the column being tested and on a line perpendicular to the longitudinal axis of the crash wall. Readings were taken on a horizontal scale attached to the column at the load point and a reference point attached to the crashwall. The scale was marked in mm, and readings were taken to the nearest 0.5 mm. No base rotations were observed in the first test and therefore, vertical deflections of the crash wall were not measured in the three remaining tests.

Rotations at the base of the columns were measured using six dial gages positioned as shown in Fig. 2.14. The displacements recorded by gages D_1 and D_2 effectively measured the opening of any crack at the base of the column. In combination the gages D_1 through D_6 recorded deformations over gage lengths of 127 mm, and then two subsequent gages lengths each equal to one half column diameter, either 610 or 686 mm (24 or 27 in.), as appropriate for the given column size. The gages were attached to rods set in holes drilled in the concrete, and they were moved from test column to test column as required.

CHAPTER 3

FIELD TEST RESULTS

3.1 Loading Procedure

The experimental testing of structures, to assess their performance and available ductility during severe earthquakes, requires decisions concerning the appropriate displacement history to be imposed to simulate seismic loading. There are three types of seismic load testing used in experimental studies, namely: shake table testing; pseudodynamic testing and quasi–static cyclic load testing.

In this study, quasi–static cyclic load testing was used, because available information shows that it usually gives conservative estimates of the real strength of the structure, since real earthquake loads are dynamic and an increase in the strain rate generally results in an increase in the strength of the materials without a change in the mode of failure. However, significant differences between the shapes of the hysteresis loops obtained from quasi–static and dynamic loading tests may result unless carefully controlled testing procedures are used (Park, 1989). In quasi–static load testing the displacement history does not follow in detail the complex response of a structure to an actual earthquake. Instead a simpler displacement history is applied to enable an assessment to be made as to whether the structure is tough enough to perform satisfactorily during a severe earthquake. Unfortunately, investigators in the past have used a range of displacement histories, and various definitions of yield and ultimate deformation, which have made the comparison of results of different investigations difficult. Consequently, values for ductility factors obtained from experimental tests have sometimes been misused in judging the likely performance of structures during severe earthquakes.

Care must be taken in defining the main parameters describing inelastic behavior for quasi–static load testing, so that performance obtained from the experimental investigations can be properly assessed and compared. In this study, a testing procedure similar to that one recommended by Park (1989) was used. That procedure consisted of two parts: 1) application of load controlled test

cycles until yield was achieved; 2) application of displacement controlled test cycles after yield was achieved. Obviously, the definition of yield is critical.

Shown in Fig. 3.1 is an idealized envelope for the reversed cyclic loading response of a concrete member. Points A and D represent the limiting theoretical lateral load capacities, $\pm P_u$, based on the specified material properties. Points B and C represent the measured linear response limits for a fully cracked column section. The line BOC extended to $\pm P_u$, and corresponding to points E and F, results in an effective deflection for yield, Δ_y, for the column idealized as having an elasto–plastic response. Therefore, an analysis was performed for each of the column sections, using a specially adapted analysis program, to obtain the limiting theoretical lateral load capacities P_u based on the specified material properties, a strength reduction factor of 1.0 and a uniform bar distribution around each column's circumference as shown in design drawings. The calculated values of P_u for the four field test columns are listed in the table in Fig. 3.1. Based on those values an appropriate loading pattern was established for each column. In the field tests, an "easy–to–work–with" load or deflection value was established for each column for loading applications. The resulting loading histories are shown in Figs. 3.2a–d. The initial fully reversed load cycle was applied under "load control", i.e., the preselected forces (integral numbers) were applied and the resulting deflections measured. Then the average Δ_{ave} of the resulting deflections for both loading directions was calculated. In all later load cycles, the tests were conducted under "stroke control", except for column B18S which was tested completely in a load control mode. Increments of lateral deflection were applied and the required forces were measured. The deflection steps were chosen as integral values, which are equal to or close to multiples of the average Δ_{ave}. For discussion purposes, (see Chapter 6), those values can be defined in terms of an effective ductility ratio derived from the test results according to the concept of Fig. 3.1. The ductility ratio for a given subsequent loading is defined as the ratio of the lateral deflection associated with that loading to the "effective" yield displacement.

3.2 Field Test Results

3.2.1 Hysteretic Performance

All as–built four columns were subjected to reversed cyclic loads of increasing magnitude and displacements. The lateral load versus lateral displacement at the loading level curves for all four tests are shown in Figs. 3.3a–d. The curves of Figs. 3.3a–d are shown to an enlarged scale in Figs. A1–A4 in Appendix A along with the corresponding ductility ratio for each load cycle. Columns B18S and B14S were tested in 1993, while columns C17S and C15S were tested in 1994. Also in every case, the first loading pulled the top of the column toward the center of its pier. Thus, with reference to Fig. 2.7, the column was pulled toward the reaction frame. This motion, and bending moment, tended to make the angle between the column and the crashwall smaller, and is referred to a "closing corner, or positive load, case". Pushing the column to force it away from the reaction frame produced an "opening corner, or negative load, case". The stiffness for the closing corner case was always slightly greater than that for the opening corner case.

All columns were closely observed for the cracks that developed during the different loading cycles. Cracks were marked and photographs taken for future reference. Some relevant photographs are shown in Fig. 3.4 through Fig. 3.12. Shown in Fig. 3.4 is the general complex of bridges of which the test piers were part. Shown in Figs. 3.5 and 3.6 are the top and bottom parts of the setup for testing the column B18S. The detailed performance of each column is described in the subsequent paragraphs.

3.2.1.1 Column B18S

The load–deflection curve for this column is shown in Fig. 3.3a and a photographic record of the cracking in Figs. 3.7 through 3.9. The 1.37 m (54 in.) diameter south column of pier B18 was loaded first to 356 kN (80 kips) laterally in the positive direction. That load was sufficient to crack the column at its base. The resulting displacement was about 15 mm (0.6 inch). The lateral force was then reversed and the column loaded to 356 kN (80 kips) in the negative loading direction. The resulting displacement was about 25 mm (1 inch). The difference in displacements for the two directions was due to the column cracking through its full depth with the reversal of the load, and to the

lateral load causing opening rather than closing of the connection between the column and the crash wall. The load was again reversed to 535 kN (120 kips) with the resulting displacement of 34 mm in the positive direction and to 508 kN (114 kips) with the resulting displacement of 50 mm in the negative direction. Flexural cracking over the height of the column increased, the width of the crack at the base of the column increased and the stiffness, especially for the loading in the negative direction, decreased. Clearly visible long horizontal and vertical cracks were observable on the south side, (tension face), of the column after the applied load had reached 535 kN (120 kips) for the positive loading direction. Those cracks are marked as 18 in Fig. 3.7. Also at the same load several short cracks were observed on the top of crash wall, (Fig.3.8). With the loading in the negative direction to 508 kN (114 kips), vertical cracks occurred on the tension face and the existing vertical crack on the compression face extended further. Those cracks are marked as 24 and 25 in Fig. 3.9. Also, several inclined cracks extended to the bottom of the crash wall on the tension side.

Finally the load in the positive direction was increased to 601 kN (135 kips) at 52.5 mm (2.1 inches) displacement and at the same displacement the load dropped abruptly to 396 kN (89 kips). At that displacement, cracking noises were heard, and splitting cracks, accompanied by inclined cracks, developed vertically along the lines of the bars on the bottom part of the tension side of the column. Those cracks are indicated by numerals greater than 25 in Figs. 3.8 and 3.9. The load was reduced and reversed. In the negative direction it was only possible to reach a peak load of 481 kN (108 kips) at 62 mm (2.4 inches) displacement. Then the load dropped abruptly to 378 kN (85 kips), and with increasing displacements to 83 mm (3.3 inches) the load decreased further to 303 kN (68 kips). This cyclic peak load was less than the maximum load of 508 kN (114 kips) reached in the prior load cycle. Splitting failure then also occurred along the bars on the tension side of the column. The maximum capacity for the final reversal of load in the positive direction was less than 267 kN (60 kips) and the deflection at that load was about the same as the deflection of 52.5 mm (2.1 inches) for the maximum load of 601 kN (135 kips). For lateral displacements greater than 52.5 mm (2.1 inches) the capacity decreased with increasing displacements.

3.2.1.2 Column B14S

The load–deflection curve for this column is plotted in Fig. 3.3b and the extent of cracking at the end of reversed cyclic loading is shown in Fig. 3.10. The 1.22 m (48 in.) diameter south column of pier B14 was initially subjected to two fully reversed cycles of lateral loading to 223 kN (50 kips) for both positive and negative loading directions. The resultant average displacement at peak load was about 22.5 mm (0.89 in.). As summarized in Fig. 3.2b subsequent loading consisted of displacement–controlled testing starting with two fully reversed cycles to displacements of $\pm$ 45 mm with the first cycle to those displacements peaking at loads of 360 and 304 kN (80.8 and 68.3 kips) for the positive and negative loading directions, respectively. Another four fully reversed cycles were then applied with limiting displacements of $\pm$ 67.5 mm for the first two cycles and $\pm$ 90 mm for the second two cycles. For the first cycle to $\pm$ 67.5 mm loads peaked at 396 and 313 kN (89.0 and 70.2 kips), and for the first cycle to $\pm$ 90 mm loads peaked at 412 and 322 kN (92.5 and 72.4 kips) for the positive and negative loading directions, respectively. Finally, one fully reversed cycle to $\pm$ 112.5 mm was applied with the loads peaking at 413 and 305 kN (92.8 and 68.5 kips), respectively.

Since 120 mm represented approximately the maximum displacement for which loads could be readily applied in the negative direction without using shims, all subsequent loading was in the positive direction only. A half cycle of load was applied to the column in the positive direction to a displacement of 131 mm with the load peaking at 415 kN (93.1 kips) and then a second half cycle was applied to 197.5 mm with the load peaking at 448 kN (100.5 kips). Because of the short time over which the column was available for testing, the column could not been tested to failure completely. However, from a seismic standpoint failure had been achieved in the sense that the load capacity had started to decrease with increasing deflections when the fully reversed cyclic loading portion of the test was ended at 90 mm maximum deflection. The maximum load achieved was 448 kN (100.5 kips) for loading in the positive direction and 322 kN (72.4 kips) for loading in the negative direction.

3.2.1.3 Column C17S

The load–deflection curve for this column is plotted in Fig. 3.3c. The 1.37 m (54 in.) diameter south column of pier C17 was loaded first to 362 kN (81 kips) laterally in the positive direction. The resulting displacement was about 22 mm (0.88 inch). The lateral force was then reversed and the column loaded to 362 kN (81 kips) in the negative direction. The resulting displacement was about 24 mm (almost 1 inch). At the maximum load there was a 2 mm opening of the crack at the base of the column. As summarized in Fig. 3.2c subsequent loading consisted of displacement–controlled testing starting with a fully reversed loading cycle to 40 mm deflection in each direction. The resulting loads were 554 kN (124 kips) in the positive direction and 520 kN (117kips) in the negative direction. Flexural cracking over the height of the column increased and reached a total of seven complete rings. The width of the crack at the base increased, and the stiffness, especially for the loading in the negative direction, decreased. At 554 kN load, some small vertical cracks appeared. At the 520 kN reversed load, some small, short cracks developed on each side of the crashwall.

Finally the load in the positive direction was increased to 579 kN (130 kips) at a deflection of 55 mm. At that load, cracking noises were heard, splitting cracks developed vertically along the lines of the bars on the bottom part of the tension side of the column and the load dropped. Inclined cracks, branching from the splitting cracks, also formed as shown in Fig. 3.11, indicating that the lap splices were failing on both sides of the column. The load was then reversed and applied in the negative direction. Shortly before the same peak load as for the positive direction was reached as for the negative direction, at 576 kN (129.5 kips) and 70 mm (2.75 in.) deflection, the load dropped abruptly by about 13–18 kN (3–4 kips). At this point the pressure valve on the pump was turned off. However, that action did not stop the continued development of vertical cracking. Those cracks kept growing without any increase in the lateral load, and the displacement also increased by 4 mm (about 0.15 in.) as the load fell. The width of the crack at the junction between the crashwall and the column base increased to about 6 mm as measured on the tension side of the column at the maximum load of 576 kN. As the column was pushed further in the negative direction there were increas-

ing deflections as the load kept decreasing. At 80 mm (3.15 in.) deflection, the load was only 437 kN (98 kips) and at 100 mm (about 4 in.) deflection the load dropped even further to 350 kN (78 kips). The column had failed.

3.2.1.4 Column C15S

The load–deflection curve for this column is plotted in Fig. 3.3d. The 1.22 m (48 in.) diameter south column of pier C15 was initially subjected to a fully reversed cycle of lateral loading to 270 kN (60 kips) in both positive and negative directions. The resultant average displacement was about 26 mm (1.02 in.). A small crack opened at the base of the column during this first cycle. As summarized in Fig. 3.2d subsequent loading consisted of displacement–controlled testing starting with a single cycle at $\pm$ 40 mm displacement and with the loads peaking at 376 and 352 kN (84 and 79 kips) for the positive and negative loading directions, respectively. Two fully reversed cycles were then applied to displacements of $\pm$ 80 mm and $\pm$ 120 mm, with the corresponding loads reaching maximums of 470 and 420 kN (105 and 94 kips) for the first 80 mm cycle, and increasing a little for the first cycle of the next pair, to 486 and 425 kN (109 and 95 kips) respectively. During these cycles several flexural cracks opened over the height of the column. At 470 kN load, the first vertical crack opened on the south side, and also the first crack opened in the crashwall. Subsequently the crack at the base of the column grew larger, as did the damage to the crashwall and the flexural cracks in the column. In addition, some crushing started on the north side of the column at its junction with the crashwall. In the last cycle, it was planned to pull the column to 160 mm (6.3 in.) displacement in the positive direction. However, before reaching this deflection, at 134 mm (5.3 in.) and 430 kN (96.7 kips), the load dropped with the vertical cracks growing significantly in size and length as the column failed in this direction. The column and crashwall suffered significant damage, but it was the splice failure that caused the vertical cracks to open and the column to fail. Shown in Fig. 3.12 is the vertical cracking, (marked as load steps No. 89 and 90), on the south side of the column immediately after the splitting failure occurred. The base crack at this stage was about 20 mm wide and the vertical cracks were 1.5–1.7 mm wide. The column was pushed to 160 mm (6.3 in.), but the load kept dropping and decreased to 345 kN (77 kips). The load was released and then the column

pushed in the negative direction. At 140 mm (5.5 in.) the load peaked at 398 kN (89 kips) and then fell slowly with increasing deflections. The column had failed with new vertical cracks opening on the tensile side of the column with a width slightly larger in size than for the reverse direction. Meanwhile the damage to the cover on the north side became significant. At 160 mm (6.3 in.) displacement, the load was 335 kN (75 kips), and at 180 mm (7.1 in.) displacement, the load fell to 281 kN (63 kips).

3.2.2 Reinforcing Bar Locations

After testing was completed, details of the reinforcing bars for each column at the maximum moment section were carefully measured. Locations in plan of the longitudinal bars are shown in Figs. 3.13 through 3.16, respectively, and their coordinates are listed in Appendix B. The bars extending up from the crash wall are cross–hatched in Figs. 3.13 through 3.16, while the bars extending down the column are shown as open circles. The design drawings showed the dowel bars and the column bars to be in contact, but in practice very few of them actually touched and some separations were as large as 150 mm (6 in.). The column bars always lay outside the crash wall dowel bars, and both dowel bars and column bars were not uniformly distributed.

The cover to the column reinforcement was found to be highly variable. For example, for the column B18S, the clear cover to the hoops ranged from a low of about 2.5 mm (0.1 in.) to a maximum of nearly 150 mm (6 in.). For the smaller columns B14S and C15S with 18 bars each, both bar locations and concrete cover were much more uniform than for the larger columns B18S and C17S with 28 and 24 bars respectively. In spite of the small cover, very little corrosion of the main bars was found in the test columns. Some other columns in the interchange had more severe corrosion and areas of spalled concrete. In the design plans the lap length for the hoop steel was shown to be 380 mm (15 in.). However, the actual lap length as measured in the field varied considerably from that value and in most cases were smaller than the specified lap length. Typical values ranged from 250 mm (10 in.) to 300 mm (12 in.).

3.2.3 Material Properties

The specified yield strength was 276 N/mm^2 (40,000 psi) for all steels and the specified concrete strength was 24 N/mm^2 (3,500 psi) for all concrete.

Samples of typical main column bars and hoop bars were taken from the specimens after failure along with samples of the concrete from each column. Typical measured stress–strain curves for the reinforcing bar samples are presented in Fig. 3.17, and the test values for the reinforcing bar samples are listed in Tables 3.1 and 3.2 for columns tested in years 1993 and 1994, respectively. In general the tests were conducted on 914 mm (3 ft) bar lengths removed from the mid–plane of the column after testing was complete. Strains were measured on a 254 mm (10 in.) gage length using an LVDT. The measured average yield and tensile strengths were 325 and 547 N/mm^2 (47,200 psi and 79,100 psi), respectively, for the #11 column main bars from the 1993 tests, and the corresponding values obtained from 1994 test specimens (see Table 3.3) were within 0.5% of those same strengths. Thus, the overall scatter in the values was small and average values of 325 and 550 N/mm^2 (47,000 psi and 79,600 psi) were used for the yield and tensile strengths, respectively, for analysis purposes (see Chapter 6).

The average yield and maximum strengths for the #4 column hoops for the 1993 tests were 290 and 490 N/mm^2 (41,500 psi and 71,000 psi), respectively. No additional column hoop test was made for the 1994 investigations.

For the 1993 tests, specimens to measure the concrete strength were at first carefully cut from concrete blocks removed from column B18S after the completion of the main tests. Specimen sizes were determined by the concrete pieces that could be readily recovered. The resultant cut sizes were either cubes 51 x 51 x 51 mm (2 x 2 x 2 in.) or prisms 51 x 51 x 102 mm (2 x 2 x 4 in.). The compressive test results are listed in Table 3.3a. Strengths varied from 34.5 N/mm^2 (5,000 psi) for a specimen for which one face was a weak layer of outer concrete in the column to over 62 N/mm^2 (9,000 psi) for a piece of concrete taken from the area where the column and dowel bars were widely separated. The strength of a prism or cylinder with a length twice the characteristic cross–sectioned dimension is approximately 85% of the strength of a cube with the same characteristic dimension, and the

strength of a prism with a characteristic dimension of 51 mm (2 in.) is approximately 108% of that of a prism with a characteristic dimension of 152 mm (6 in.). When those corrections are applied to the concrete strengths listed in Table 3.4, the average measured strength corresponds to a 153 x 305 mm (6 x 12 in.) cylinder strength of 43.5 N/mm^2 (6,350 psi). Later for the subsequent columns tested in 1993, concrete properties were obtained from 102 mm (4in.) diameter cores with the results listed in Table 3.3b. The average strength, excluding the result B18N–2, was 40.8 N/mm^2 (5,950 psi).

For the 1994 tests, a total of seven specimens for measurements of concrete strength were removed from the tops of the columns with a core drill after the completion of the main tests. Results are shown in Table 3.4. One specimen was taken per column except for two from column C15S. Specimens were trimmed from 102 mm (4in.) diameter cores to a final 203 mm (8 in.) height. Strengths varied from about 31 N/mm^2 (4,530 psi) for a specimen taken from column C17N, for which there was one small honeycomb near mid height, to over 43 N/mm^2 (6,200 psi) for a piece of concrete taken from C15N. The average measured strength and modulus for the concrete of the two non–retrofitted columns C15S and C17S were 37.6 N/mm^2 (5,560 psi) and 29.7 kN/mm^2 (4,300 ksi), respectively. Based on the results of all the 1993 and 1994 tests an average concrete compressive strength and modulus of 41 N/mm^2 (6,000 psi) and 29.7 kN/mm^2 (4,300 ksi), respectively, are used for analysis of the non–retrofitted column results (see Chapter 6).

3.2.4 Rotations of Column Base

Rotations at the base of each column were recorded for examination of distributions of curvature and curvature capacities. Rotation Θ over a given gage length L_g was calculated from:

$$\Theta = \frac{\Delta_p}{L_p} \tag{3.1}$$

where Δ_p = algebraic difference of readings between dial gage pairs, and L_p = center–to–center distance between dial gage pairs.

Lateral load vs. rotation hysteresis curves for the three gage lengths at the bottom of each column are plotted in Figs. 3.18 through 3.21. It is to be noted that for each column most of the rotation occurred at the lowermost gage length.

CHAPTER 4

LABORATORY SPECIMEN DESCRIPTION, FABRICATION, AND INSTRUMENTATION

4.1 Description of Specimens

The objective of the laboratory investigation was to examine what effects bar spacing, bar lap separation and concrete cover had on the behavior of columns spliced at maximum moment regions. Because of financial and time constraints, only six laboratory columns were made with varying combinations of longitudinal bar spacing, bar lap separation, and concrete cover. The overall dimensions of the test specimens including crash wall and column, the number and diameter of main longitudinal reinforcing bars in the column, and the number and diameter of the hoop reinforcement for the column were kept constant for all six columns. As shown in Fig. 4.1, a specimen consisted of two columns and one base beam (crash wall). Two columns were cast on top of a single base beam. The height of each column was 4.25 m (12 ft), and its diameter 0.61 m (2 ft). The reinforcing details of the specimens were as shown in Figs. 4.2a and 4.2b. Each column contained 6–#11 Grade 60 deformed bars. The lap length of every longitudinal bar at the base of each column was 1.09 m (43 in.), which was the same as the lap length for the full scale specimens tested in the field. The lateral reinforcement over the height of the columns consisted of #3 Grade 60 hoops spaced at 254 mm (10 in.) on center. A 305 mm (12 in.) lap length was used for those hoops. Shown in Fig. 4.3 are the geometric properties of the steel reinforcing bars used for each specimen, including the size, dimensions, number and shape of the different steels. Each specimen was designated by a letter and a numeral, as for example A–1. For each letter there were three columns with varying combinations of longitudinal bar lap separation, L, for the radial direction, and concrete cover, C. Between letters there was a variation in the bar's angular separation. Thus, the six columns were designated as A–1 (L = 0, and C = 12.7 mm (0.5 in.)); A–2 (L = 50.8 mm (2 in.), and C = 12.7 mm (0.5 in.)); and A–3 (L = C = 50.8 mm (2 in.)); and B–1 (L = 0, and C = 12.7 mm (0.5 in.)); B–2 (L = 50.8 mm (2 in.), and C = 12.7 mm (0.5 in.)) and B–3 (L = C = 50.8 mm (2 in.)).

The details of the cross section for each column are shown generically in Fig. 4.4a and by

specifics in Figs. 4.4b through 4.4g and Table 4.1. Two different angular spacings, S_d, were used for the dowel bars and on that basis the six columns were divided in two categories with those specimens with a dowel bar spacing of 1.4 d_b being designated by the letter A and those with a spacing of 2.9 d_b by the letter B.

4.2 Fabrication of Specimens

All specimens were cast in the Newmark Civil Engineering Laboratory of the University of Illinois at Urbana–Champaign. Ready mixed concrete was used for all specimens and was supplied in two batches by a local builders' supply company. The steel reinforcement was bought in two batches from a local reinforcing steel distribution company. A total of three specimens were cast. Each specimen consisted of two columns and one base beam, and was cast in two stages.

First the base beam (crash wall) was cast. Beams were cast in plywood forms consisting of 19 mm (3/4 in.) laminated plywood stiffened with 51 x 102 mm (2 x 4 in.) lumber elements and 6.4 mm (1/4 in.) tie rods (Fig. 4.5). Since only one form was available, the three base beams were cast in the waterproof laminated plywood forms at three different times, on January 5 and 19, and February 2, 1995, respectively. Nine 102 x 203 mm (4 x 8 in.) control cylinders were cast along with each base beam. Before beam casting, the steel cage for each base beam was assembled and placed in its proper position inside the formwork. Then the dowel bars for each column were placed in their proper positions with respect to the beam's steel cage.

In order to ensure consistency of the concrete for all columns, all six columns were cast in the same time, on April 4, 1995. Since the precise locations for the bars of each column were critical, all column bars were carefully positioned with respect to the dowel bars, and then all the hoops were tied in the correct positions. Finally each column form was carefully positioned with respect to the hoop reinforcement and fixed in location. The column form consisted of a 1/2 in. thick round cardboard. Before the casting of the column the bottom of each column form was temporarily fixed to the top of the base beam with four 51 mm (2 in.) long and 6.4 mm (1/4 in.) diameter bolts through four 51 x 51 x 3.2 mm (2 x 2 x 1/8 in.) triangles and then all the columns were placed side by side

and temporarily braced at their tops with a plywood floor reinforced by 51 x 51 x 6.4 mm (2 x 2 x 1/4 in.) triangles. Eighteen 102 x 203 mm (4 x 8 in.) control cylinders were cast along with the columns.

Due to the limited space of the laboratory, a pumper truck was used to place the ready mixed concrete into each column form. Great care was taken during the consolidation of the column concrete in the region of the lap splices, since there were many strain gages in that region. Each column was cast in three layers with the height of each layer being about 1.22 m (4 ft). Two loads of concrete were required. The first load was used to fill the lower two thirds of all column forms. Thus, the same batch of concrete was used in the critical sections of all six columns. The concrete inside the column forms was consolidated with two high frequency, 25 mm (1 in.) diameter, internal rod vibrators.

Bonded electrical resistance strain gages were applied to the column reinforcing bars for all six columns. The locations and designations of the gages for each column were the same and are shown in Fig. 4.6. A total of 26 gages were placed on each column. Twenty 0.5–inch (12.7 mm) length gages were placed on the central #11 bar for each side of the column and six 0.25–inch (6.4 mm) length gages were placed on the #3 hoops. Thus, there were five gages on the bottom of each central longitudinal bar of the column, five gages on the top of each central dowel bar and a gage on each side of each alternate hoop over the height of the splice.

To attach the strain gages the deformations were filed from the reinforcing bars in the areas where the gages were to be applied, and those areas polished with emery cloth. After the gages and the lead wires attached, the gages were water–proofed so that they would survive the casting of the concrete around them.

4.3 Material Properties

Typical measured stress–strain curves for the reinforcing bars of the laboratory test columns are presented in Fig. 4.7. Test values for the #11 column bars and the #3 hoop bars are listed in Table 4.2. In general the tests were conducted on 914 mm (3 ft) bar lengths. Strains were measured on

a 254 mm (10 in.) gage length using an LVDT. The measured average yield and maximum strengths were 456 and 733 N/mm^2 (66,000 psi and 106,000 psi), respectively, for the #11 bars. The average maximum strength for the #3 hoops was 788 N/mm^2 (114,000 psi). However, while there was no well defined yield strengths for those hoop bars, the stress of 518 N/mm^2 (75,000 psi) corresponded to the 0.5% strain for the typical measured stress–strain curve shown in Fig. 4.7.

The control cylinders used to determine the concrete properties were tested one day before, or one day after, each column test. The compressive strength test results for each column and each base, as recorded at the time of test along with the age at test, and the Young's modulus of the concrete are listed in Table 4.3.

The Young's modulus of concrete was evaluated according to ASTM specification C 469. A compressometer with a gage length of 125 mm (5 inches) was used to obtain the strains at the mid-height of each cylinder, and the Young's modulus E was calculated by the following formula

$$E = (S_2 - S_1) / (\varepsilon_2 - 0.000050) \qquad (4.1)$$

where

S_1 = stress corresponding to a longitudinal strain, ε_1, of 50 millionths;

S_2 = stress corresponding to 40% of ultimate load; and

ε_2 = longitudinal strain produced by stress S_2.

4.4 Laboratory Test Setup

Shown in Fig. 4.8 is the laboratory test setup for applying the reversing horizontal loads to a single column at a point 3.3 m (11 ft) above the top of the base beam. The specimen was tension–anchored to the 0.61 m (2 ft) thick laboratory strong floor using four 38 mm (1.5 in.) diameter high strength bolts. The lateral load was applied by a 445 kN (100 kips) capacity servo–controlled hydraulic actuator that reacted against a steel frame also bolted to the laboratory floor. The steel reaction frame consisted of a 2.74 m (9 ft) long reaction beam consisting of a square tube with a cross section of 356 x 356 x 12.7 mm (14 x 14 x 1/2 in.), two 4.57 m (15 ft) tall reaction columns with

W12 x 65 sections and two 4.57 m (15 ft) long braces consisting of 127 x 127 x 6.4 mm (5 x 5 x 1/4 in.) tubes. A 25 mm (1 in.) thick steel bearing plate was welded on each end of the braces. The member sizes of the steel frame were designed to resist a total horizontal force of 356 kN (80 kips). That capacity was considerably greater than the nominal 184kN (41.4 kips) capacity of the strongest of the six columns and resulted in the reaction frame having a stiffness considerably greater than the stiffness of the strongest column.

The test setup was developed by first placing the test specimen in its proper position on the laboratory floor and then erecting the steel reaction frame adjacent to that specimen. The steel reaction frame was erected according to the following procedure: first, the two reaction columns were erected 1.80 m (6 ft.) apart with each bottom fixed by a 38 mm (1.8 in.) diameter high strength bolt to the 0.61 m (2 ft.) thick laboratory strong floor; second, the upper end of each bracing member was attached to the flange on one side of each column using four 25 mm (1 in.) diameter bolts placed through its end plate, and the lower end of each bracing was anchored down to the laboratory strong floor using two 38 mm (1.5 in.) bolts through its end plate; third, the reaction beam was seated on the two 4.11 m (13 ft. and 6 in.) tall triangles and attached to the specimen side flange of each column using four 25 mm (1 in.) diameter bolts, and then each end of the reaction beam was clamped to the column flanges using four 25 mm (1 in.) diameter bolts. Finally, one end of the actuator assembly was connected to the center point of the reaction beam using four 25 mm (1 in.) diameter bolts, and the other end was connected by four 25 mm (1 in.) diameter bolts to a 51 mm (2 in.) thick plate, that was clamped to the test column by a 31.8 mm (1–1/4 in.) diameter high strength bolt through two aluminum spacers, one positioned on each face of the column. Those spacers had been machined so that the curvature of their inner faces were the same as that of the column.

4.5 Instrumentation

Column lateral deflections, rotations, strains on the main bars and hoops, the applied force and the circumferential elongations over the lap splice height were monitored as follows:

4.5.1 Deflections

Shown in Fig. 4.9 is the arrangement of the LVDTs (Linear Variable Differential Transduc-

ers) used to measure the lateral deflections at three locations over the column height. Those LVDTs were positioned 1.2 m (4 ft), 2.4 m (8 ft) and 3.3 m (11 ft) respectively above the top of the base beam. All LVDTs were fixed to a rigid reference frame secured to the laboratory floor and separate from the reaction frame for the loading setup.

4.5.2 Rotations

Shown in Fig. 4.10 is the arrangement of the three pairs of LVDTs, positioned vertically, located on opposite column faces, and used to measure the rotations of the bottom of the column over three sequential gage lengths. Those lengths are termed the lowermost gage length (127 mm (5 in.)), the intermediate gage length (305 mm (12 in.)) and the uppermost gage length (305 mm (12 in.)), respectively, in later discussions of the results. The LVDTs were attached to horizontal mounting rods cast in the column concrete, and they were moved from column to column as required during testing.

4.5.3 Steel Strains

Shown in Fig. 4.6 are the locations and numbers of the electrical resistance strain gages, which were used to measure both longitudinal bar strains and hoop strains. The electrical resistance strain gages used in this study were EA–Series gages. They were of open–faced construction with a 1 mil (0.03 mm) tough, flexible polyimide film backing and belonged to a general purpose family of constantan strain gages widely used in experimental stress analysis. For gage lengths 3.2 mm (1/8 in.) and larger, they can be used at temperature ranges from –75 to 175 °C (–100 to 350 °F) within an approximate range of 5% strain. Two kinds of gages with different gage lengths were used in this study. The gages attached to the #11 bars had a 12.7 mm (half inch) gage length whereas those attached to the #3 hoops had a gage length of 6.4 mm (quarter inch). Both gages had a resistance of 120 ± 0.15% ohms at 24 °C. The 12.7 mm gages had a gage factor of 2.085 ± 0.5% and the 6.4 mm gages had a factor of 2.075 ± 0.5% at 24 °C.

4.5.4 Load

The lateral force applied to the column was monitored using a load cell built into the ±250 mm (± 10 in.) long stroke MTS hydraulic actuator. The actuator had a capacity of 445 kN (100 kips)

and could work equally well in both tension and compression.

4.5.5 Circumferential Elongations

Optical fibers with 160 μm diameter were used to measure the circumferential elongations at three locations over the lap splice height. Those fibers were epoxied around column's circumference at positions of 25 mm (1 in.), 530 mm (21 in.) and 1,100 mm (44 in.) respectively above the top of the base beam (see the brown strips as shown in Fig. 5.27 through 5.31).

4.5.6 Data Acquisition

During the active period of the test the output voltages of all the instruments, except the one for fiber–optic reading, were recorded using a multifunction I/O board data acquisition system that used the software Labview on a Macintosh Quadra 650 operating at a frequency of 0.5 Hertz (a point every 2 seconds). The maximum recording time was 10,000 seconds per data file. The fiber–optic readings were recorded using data acquisition system termed OTDR (Optical Time Domain Reflectometer). Additional details on the system used are contained in the paper by Signore et al (1996). The instrument used in this research was a system that could detect elongations or compressions as small as 0.1 mm.

During each test, the lateral load measured by the load cell within the horizontal actuator and the deflection measured on the column at 3.3 m (11 ft) height above the top of the base beam were plotted versus one another on the computer screen. That plot provided a means for controlling the test program for each column by providing immediate feedback on the behavior of each column during testing. Before the actual test, all the instruments were set to zero at their balance points and care was taken to ensure that all were working properly by giving them a small displacement and checking results.

Chapter 5

LABORATORY TEST RESULTS

5.1 Test Procedure

As described previously in Section 3.1 for the field tests, in this laboratory study quasi–static fully reversed cyclic load testing was again used. The procedure used initially load controlled cycling to 80 % of the calculated yield strength and then displacement controlled cycling beyond that load and until failure. The loading histories for the six test columns are shown diagrammatically in Fig. 5.1.

1) Load controlled test cycles to 80% of the calculated yield strength:

The lateral loads required to cause first yield of a dowel bar and the maximum load capacities for each column were calculated using a moment curvature analysis procedure for each column section. Resultant capacities are listed in Table 5.1. In that analysis, a strength reduction factor of 1.0 was used, and only the dowel bars for each column taken into consideration. The material properties used were a concrete compressive strength of 27.6 N/mm^2 (4,000 psi), a modulus of elasticity of 24.9 kN/mm^2 (3,600 ksi) and a steel yield stress of 454 N/mm^2 (66,000 psi). It should be recognized that while the properties of the steel were known in advance, those of the concrete were not, and values for the concrete's compressive strength and modulus had to be assumed. Thus, the values of Table 5.1 differ slightly from those of Table 6.1 because of the use of different concrete strengths in the calculation.

In the first part of the test, the lateral load was increased in step–wise cycles. First, two cycles to 20% of the calculated yielding strength were applied, followed by two cycles to 40% of that yield strength, two cycles to 60% of that yield strength, and finally two cycles to 80% of that calculated yield strength.

2) Displacement controlled test cycles starting from the 'calculated' yield displacement:

Before starting the second phase of the test, the mean value of the resulting displacements in both loading directions for the first loading cycle to 80% of the calculated yield strength load was

computed. Then 1.25 times that mean value was define as the 'calculated' yield displacement, Δ_{cy}, of the column.

In the second phase of the test, a column displacement multiplication factor, f, was imposed. That factor was increased step–wise in subsequent cycles. The column displacement multiplication factor, f, equalled $\Delta_{max} / \Delta_{cy}$ where Δ_{max} was the maximum displacement imposed in the loading excursion. First, two cycles to f equal to ± 1 were applied, followed by two cycles to f equal to ± 1.5 and two cycles to f equal to ± 2, etc., up to the f factor at which the lateral load that could be sustained by the column had dropped to 80% of the maximum lateral load applied during the test.

The loading rate was either 35 kN per minute for load controlled test cycles or 18 mm per minute for displacement controlled test cycles. In order to allow for fiber–optic measurements, the marking of cracks and the taking of photos at each load or displacement level, the first cycle of each load or displacement to a new peak load or peak displacement for both directions was held constant for about 5 to 6 minutes. Labview software installed in a Macintosh Quadra 650 computer was used to record data at a rate of a point every two seconds, i.e., a frequency of 0.5 Hertz. That data were processed to filter out noise so that each output value used in the following discussion is the average of ten successive recorded data points.

The steel reaction frame was designed to be very stiff and its computed deflection at maximum load was only about 1.4 mm. Since that displacement was small relative to the maximum anticipated displacement for the test columns, displacements for the first test column B–1 were controlled by the internal stroke measurement of the actuator. However, after the test, it was found that, due to slippage of joints within the frame and slip between the frame and the laboratory floor, the maximum movement of the steel reaction frame was actually about 17 mm. Because of that flexibility, the remainder of the tests were controlled by an external LVDT attached to a separate reference frame.

5.2 Experimental Results

5.2.1 Hysteretic Performance

All six columns were subjected to reversed cyclic loads of increasing magnitude and displacement. For all six columns lateral load versus lateral deflection relationships for the load point, (3.3 m above the base), and for the two lower recording points are shown in Figs 5.2 through 5.7. The curves of Figs. 5.2a through 5.7a are shown to an enlarged scale in Figs. C1 through C6 in Appendix C along with the corresponding ductility ratio for each load cycle. The detailed performance of each column is described in the following paragraphs.

5.2.1.1 Column A–1

As apparent from Fig. 5.2a, the initial response of this column was essentially elastic up to the 140 kN load level. At the 35, 70, 105 and 140 kN load levels, the resulting displacements were, respectively, 2.16, 7.19, 14.93 and 23.78 mm in the positive direction, and –3.35, –7.64, –14.73 and –20.61 mm in the negative direction. Based on extrapolation of those values to the calculated yield strength of the column of 175 kN the 'calculated' yield displacement Δ_{cy} of the column was 28 mm.

With subsequent loading, for the positive direction, there was a significant reduction in the rate at which the capacity increased with increasing displacement, so that at 36.64 mm displacement, the lateral load capacity was only 174.4 kN. At that point, the load was held constant for about 5 minutes so that cracking could be recorded and the data recording instruments adjusted. Load was then begun in the negative direction and at –28.27 mm displacement the load had again reached –174.4 kN ($-P_{max}$). The load was then held constant for about 2 or 3 minutes at which time the column failed abruptly. The capacity decreased rapidly with increasing displacements so that at –49.63 mm displacement, the load was only –144.6 kN, a value equal to 83% of $-P_{max}$.

5.2.1.2 Column A–2

The load–displacement relationship for this column is shown in Fig. 5.3a. The initial, essentially elastic, response terminated at the 118 kN load level for which the resulting displacements were 21.4 mm and –20.0 mm for the positive and negative loading directions, respectively. Thus,

the 'calculated' average yield displacement, Δ_{cy}, for this column corresponding to the calculated yield strength of 148 kN was 26 mm.

With subsequent loading, the stiffness decreased with increasing displacements. For the positive loading direction, the peak load achieved in the next cycle was 123.5 kN at a displacement of 26 mm, and there was essentially no deterioration in that capacity for the second cycle to the same displacement. However, for subsequent cycles to greater displacements, the capacity corresponding to the peak displacement decreased with cycling. In the next cycle to the peak displacement of 39 mm, the load corresponding to that displacement was 157.1 kN and that load was less than the maximum load of 160.5 kN (P_{max}) which occurred at 37.7 mm displacement. Further for the second cycle to the displacement of 39 mm the maximum load was only 143 kN. With increasing peak displacement, the peak load achieved in the first cycle continued to deteriorate. For a 52 mm peak displacement, the peak load achieved in the first cycle was 144.7 kN (0.9 P_{max}) and that value had decreased from a maximum for that cycle of 155.6 kN at a displacement of 45.7 mm. For the second cycle to the displacement of 52 mm the maximum load was only 119 kN. For a 65 mm peak displacement, the load was only 109.1 kN (0.68 P_{max}) for the first cycle and that value had decreased from a maximum for that cycle of 123.8 kN at a displacement of 55.21 mm. After that cycle further loading was discontinued because of the loss in column capacity.

The behavior for the negative loading direction was similar to that for the positive loading direction. At the peak displacement of –26 mm, the load was –140.5 kN. In the subsequent cycle to a peak displacement of –39 mm, the maximum load achieved was –152.2 kN ($-P_{max}$) at a displacement of–33.6 mm and by the displacement of –39 mm the load had dropped to –145.3 kN. In the second cycle to the same limiting displacement the load decreased further and reached a maximum value of only –121 kN. In the subsequent two cycles to a peak displacement of –52 mm, the maximum load achieved in the first cycle was –129.9 kN at a displacement of –48.73 mm and the load at peak displacement was –125.7 kN (–0.83 P_{max}). For the second cycle the maximum load achieved was only –99 kN at the peak displacement of –52 mm. In the final cycle to –65 mm displacement,

the peak load achieved was –103.0 kN at a displacement of –61.3 mm, and the load at the peak displacement of –65 mm was –98.3 kN (–0.65 P_{max}).

5.2.1.3 Column A–3

The load–displacement relationship for this column is shown in Fig. 5.4a. The initial, essentially elastic, response terminated at the 104 kN load level for which the resulting displacements were 21.9 mm and –21.4 mm for the positive and negative loading directions, respectively. Thus, the 'calculated' average yield displacement, $\Delta_{cy,}$ for this column corresponding to the calculated yield strength of 128 kN was 26 mm.

With subsequent loading, the stiffness decreased with increasing displacements. For the positive loading direction, the peak loads achieved in the next cycles were 109.1 kN at a displacement of 26 mm and 147.6 kN at a displacement of 39 mm, respectively, and there was essentially no deterioration in those capacities for the second cycle to the same displacement. With further increase in peak displacements, the peak load achieved in the first cycle began to deteriorate. For a 52 mm peak displacement, the peak load achieved in the first cycle was 158.9 kN and that value had decreased slightly from a maximum for that cycle of 160.6 kN (P_{max}) at a displacement of 50.8 mm. For the second cycle to the displacement of 52 mm the maximum load was only 145 kN. For a 65 mm peak displacement, the load achieved in the first cycle was the cycle peak load of 159.8 kN (0.995 P_{max}) at 65 mm; the peak load in the second cycle was again only 145 kN. For a 78 mm peak displacement, the peak load achieved in the first cycle was 155.4 kN (0.97 P_{max}) and that value had decreased slightly from a maximum for that cycle of 155.6 kN at a displacement of 72.8 mm. For the second cycle to the peak displacement of 78 mm the maximum load was only 132 kN. In the final two cycles to 91 mm displacement, the peak load achieved in the first cycle was 127.9 kN (0.80 P_{max}) and that value had decreased from a maximum for that cycle of 131.5 kN at a displacement of 85.0 mm. For the second cycle to the displacement of 91 mm the maximum load was only 98 kN.

The behavior for the negative loading direction was similar to that for the positive loading direction. At the peak displacements of –26 mm and –39 mm, the loads were –117.6 kN and –149.1

kN, respectively. In the subsequent two cycles to a peak displacement of –52 mm, the peak load corresponding to that displacement was –154.0 kN for the first cycle and –143 kN for the second cycle, respectively. In the subsequent two cycles to a peak displacement of –65 mm, the maximum load achieved was –155.3 kN ($-P_{max}$) at a displacement of–63.2 mm and by the displacement of –65 mm the load had dropped to –152.4 kN. In the second cycle to the same limiting displacement the load decreased further and reached a maximum value of only –146 kN. In the subsequent two cycles to a peak displacement of –78 mm, the maximum load achieved in the first cycle was –148.4 kN at a displacement of –72.6 mm and the load at peak displacement was –147.0 kN ($-0.95\ P_{max}$). For the second cycle the maximum load achieved was only –128 kN at the peak displacement of –78 mm. In the final two cycles to –91 mm displacement, the peak load achieved in the first cycle was –122.2 kN at a displacement of –84.9 mm, and the load at the peak displacement of –91 mm was –116.2 kN ($-0.75\ P_{max}$). For the second cycle the maximum load achieved was only –81 kN at the peak displacement of –91 mm.

5.2.1.4 Column B–1

Column B–1 was the first specimen tested, and that testing took place before the flexibility of the load reaction frame was fully known. Due to the flexibility of the steel reaction frame, the reading from the Instron machine, which controlled the stroke movement of the actuator, included both the real column displacement and the movement of the steel reaction frame, so that all load readings from the Instron machine were used to control loading even under displacement–controlled loading cycles. The numbers in parentheses in the following paragraphs are real column displacement.

Shown in Fig. 5.5a is the lateral load versus real column displacement relationship for this column. The initial, essentially elastic, response terminated at the 120 kN load level for which the resulting displacements from the Instron machine reading were 27.6 and –22.8 mm (19.5 and –18.0 mm) for the positive and negative loading directions, respectively. Thus, the 'calculated' average yield displacement, Δ_{cy}, for this column corresponding to the calculated yield strength of 157 kN was 25 mm.

With subsequent loading, for the positive direction, at 42.24 mm displacement from the Instron machine reading (27.6 mm column displacement) the load was 150 kN. On the next cycle the load dropped from 174.6 kN at 53.68 mm displacement from the Instron machine reading (37.58 mm displacement), to 172.3 kN at 53.89 mm (37.73 mm) displacement. Considerable noise was heard from the test specimen and therefore unloading was started.

In the negative direction, at –32.03 mm displacement, as recorded by the Instron machine reading (–24.73 mm column displacement) the load was –150 kN. On the next cycle the load dropped from –172.3 kN at –38.22 mm displacement from the Instron machine reading to –169.1 kN at –38.71 mm displacement. However, unfortunately the computer did not record all the data because of the limited recording time to which it had been set. More noise was heard from the column and therefore it was unloaded. Finally the load in the positive direction was increased to 182.9 kN (P_{max}) at 65.00 mm displacement from the Instron machine reading (48.79 mm column displacement), and then, with increasing displacements, the maximum load dropped to 123.9 kN at 100 mm displacement from the Instron machine reading (84.37 mm column displacement). The column was considered to have failed when the load dropped to 0.80 P_{max} (146.3 kN) at 71.13 mm column displacement.

5.2.1.5 Column B–2

The load–displacement relationship for this column is shown in Fig. 5.6a. The initial, essentially elastic, response terminated at the 104 kN load level for which the resulting displacements were 19.2 mm and –18.67 mm for the positive and negative loading directions, respectively. Thus, the 'calculated' average yield displacement, $\Delta_{cy,}$ for this column corresponding to the calculated yield strength of 130 kN was 24 mm.

With subsequent loading, the stiffness decreased with increasing displacements. For the positive loading direction, the peak loads achieved in the next two cycles were 110 kN at displacements of 24 mm, so that there was essentially no deterioration in capacity for the second cycle to the same displacement. With increasing peak displacements, the capacity for the second cycle to the same displacement began to deteriorate. For a 36 mm peak displacement, the load achieved in the first

cycle was the cycle peak load of 151 kN. For the second cycle to the same displacement of 36 mm the maximum load was only 142 kN. In the next cycle to the peak displacement of 48 mm, the load corresponding to that displacement was 159.7 kN and that load was less than the maximum load of 164.4 kN (P_{max}) which occurred at 46.1 mm displacement. Further for the second cycle to the displacement of 48 mm the maximum load was only 145 kN. For a 60 mm peak displacement, the peak load achieved in the first cycle was 155.4 kN (0.95 P_{max}) and that value had decreased slightly from a maximum for that cycle of 160.6 kN at a displacement of 57.12 mm. For the second cycle to the displacement of 60 mm the maximum load was only 131 kN. For a 72 mm peak displacement, the peak load achieved in the first cycle was 136.6 kN (0.83 P_{max}) and that value had decreased slightly from a maximum for that cycle of 142.2 kN at a displacement of 66.32 mm. For the second cycle to the displacement of 72 mm the maximum load was only 116 kN. In the final cycle to 84 mm displacement, the peak load achieved was 114.6 kN (0.70 P_{max}) and that value had decreased from a maximum for that cycle of 118.9 kN at a displacement of 77.48 mm.

The behavior for the negative loading direction was similar to that for the positive loading direction. At the peak displacements of –24 mm, the load was –122 kN. In the subsequent two cycles to a peak displacement of –36 mm, the peak load corresponding to that displacement was –157.5 kN (maximum load, $-P_{max}$) for the first cycle and –147 kN for the second cycle, respectively. In the subsequent two cycles to a peak displacement of –48 mm, the maximum load achieved in the first cycle was –154.8 kN at a displacement of –47.08 mm and the load at peak displacement was –153.7 kN (–0.97 P_{max}). For the second cycle the maximum load achieved was only –137 kN at the peak displacement of –48 mm. In the subsequent two cycles to a peak displacement of –60 mm, the maximum load achieved in the first cycle was –138.4 kN at a displacement of –54.13 mm and the load at peak displacement was only –131.6 kN (–0.84 P_{max}). For the second cycle the maximum load achieved was only –106 kN at the peak displacement of –60 mm. In the final cycle to –72 mm displacement, the peak load achieved was –110.8 kN at a displacement of –69.38 mm, and the load at the peak displacement of –72 mm was –105.8 kN (–0.67 P_{max}).

5.2.1.6 Column B–3

The load–displacement relationship for this column is shown in Fig. 5.7a. The initial, essentially elastic, response terminated at the 88 kN load level for which the resulting displacements were 20.04 mm and –19.89 mm for the positive and negative loading directions, respectively. Thus, the 'calculated' average yield displacement, Δ_{cy}, for this column corresponding to the calculated yield strength of 111 kN was 24 mm.

With subsequent loading, the stiffness decreased with increasing displacements. For the positive loading direction, the peak loads achieved in the next cycles were 93.9 kN at a displacement of 24 mm and 121 kN at a displacement of 36 mm, respectively, and there was essentially no deterioration in those capacities for the second cycle to the same displacement. With increasing peak displacement, the capacity for the second cycle to the same displacement began to deteriorate. For a 48 mm peak displacement, the load achieved in the first cycle was the cycle peak load of 143.2 kN. For the second cycle to the displacement of 48 mm the maximum load was only 132 kN. In the next cycle to the peak displacement of 60 mm, the load corresponding to that displacement was 149.4 kN and that load was less than the maximum load of 152.2 kN (P_{max}) which occurred at 58.2 mm displacement. Further for the second cycle to the displacement of 60 mm the maximum load was only 136 kN. For a 72 mm peak displacement, the load achieved in the first cycle was the cycle peak load of 150.2 kN (0.99 P_{max}). For the second cycle to the displacement of 72 mm the maximum load was only 136 kN. For a 84 mm peak displacement, the peak load achieved in the first cycle was 144 kN (0.95 P_{max}) and that value had decreased slightly from a maximum for that cycle of 146.4 kN at a displacement of 81.77 mm. For the second cycle to the displacement of 84 mm the maximum load was only 129 kN. For a 96 mm peak displacement, the peak load achieved in the first cycle was 126.9 kN (0.83 P_{max}) and that value had decreased slightly from a maximum for that cycle of 131.8 kN at a displacement of 92.65 mm. For the second cycle to the displacement of 96 mm the maximum load was only 100 kN. In the final cycle to 108 mm displacement, the peak load achieved was 111.2 kN (0.73 P_{max}) and that value had decreased from a maximum for that cycle of 113.8 kN at a displacement of 106.69 mm.

The behavior for the negative loading direction was similar to that for the positive loading direction. At the peak displacements of –24 mm and –36 mm, the loads were –99.7 kN and –134.3 kN, respectively. In the subsequent two cycles to a peak displacement of –48 mm, the peak load corresponding to that displacement was –151.1 kN for the first cycle and –140 kN for the second cycle, respectively. In the subsequent two cycles to a peak displacement of –60 mm, the maximum load achieved in the first cycle was –155.2 kN ($-P_{max}$) at a displacement of –59.5 mm and the load at peak displacement was –152.2 kN. For the second cycle the maximum load achieved was only –144 kN at the peak displacement of –60 mm. In the subsequent two cycles to a peak displacement of –72 mm, the maximum load achieved in the first cycle was –152.9 kN (–0.99 P_{max}) at a displacement of –69.25 mm and the load at peak displacement was –151.7 kN (–0.98 P_{max}). For the second cycle the maximum load achieved was only –135 kN at the peak displacement of –72 mm. In the subsequent two cycles to a peak displacement of –84 mm, the load achieved in the first cycle was the cycle peak load of –145 kN (–0.93 P_{max}) at the peak displacement of –84 mm. For the second cycle the maximum load achieved was only –126 kN at the peak displacement of –84 mm. In the subsequent two cycles to a peak displacement of –96 mm, the maximum load achieved in the first cycle was –127.9 kN at a displacement of –94.82 mm and the load at peak displacement was –123.8 kN (–0.80 P_{max}). For the second cycle the maximum load achieved was only –109 kN at the peak displacement of –96 mm. In the final cycle to –108 mm displacement, the peak load achieved was –110.3 kN at a displacement of –106.75 mm, and the load at the peak displacement of –108 mm was –106.8 kN (–0.69 P_{max}).

5.2.2 Displacement Profile

The displacement profile over the column height for each laboratory test column is shown in Figs. 5.8 through 5.13. In each figure, the displacement distribution is that corresponding to the peak displacement for the first cycle of each new load or displacement level. Profile are straight lines connecting the displacements measured at three locations over the height of the column except for

column B–3 where displacements measured at the lower third point were not used because those values were not stable.

5.2.3 Rotations

Rotations Θ over a given gage length L_g were calculated from the relationship:

$$\Theta = \frac{\Delta_p}{L_p} \tag{5.1}$$

where Δ_p is the algebraic difference of the readings for a pair of LVDTs for a given gage length, and L_p equals the center–to–center distance between those LVDT pairs.

Lateral load versus rotation hysteresis curves for the three gage lengths at the bottom of each column are plotted in Figs. 5.14 through 5.19. It is obvious that for each column most of the total rotation occurred within the lowermost gage length. The lowermost gage length was 127 mm (5 in.) long, while the intermediate and uppermost gage lengths were both 305 mm (12 in.), or half the column diameter.

5.2.4 Strain Measurements

Strains were measured using electrical resistance strain gages attached to the longitudinal bars, including both column bars and dowel bars, as well as the lateral hoops. The two different gage types that were used, and their locations, have already been discussed in Chapter 4 and depicted in Fig. 4.6. However, it should be pointed out that when the specimens were finally prepared for testing and the necessary arrangements made for acquiring data from the gages, certain gages did not work satisfactorily. Some did not respond at all to the loads on the specimens due to short–circuits or damage during specimen construction. Strain value results for each gage at different loads during the tests are described in the following paragraphs for each column. Only strains for gages beyond yield strain are discussed below. In the following the sign convention for strain is positive for tension and negative for compression.

5.2.4.1 Column A–1

For column A–1, gage 6 on the dowel bar was damaged and no strains were recorded by it. Strain values from the remaining 25 gages have been plotted against the lateral load applied to the

column in Figs. D1a through D26a in Appendix D. Blank spaces indicate missing data. Distributions of strain over the length of the bars, plotted to scale, for increasing values of peak loads and peak deflections are shown in Fig. 5.20.

In the positive loading direction, for the maximum load reached in the test of 174.4 kN, at 36.64 mm displacement, the maximum dowel bar strain was 2018 με. That value was close to, but less than, the yield strain. That value occurred at gage 4 located at the column–base interface. Further, at that load strains were almost constant over the 500 mm (20 in.) bar length centered on gage 4. The maximum hoop strain at gage 21 at that load was only 1203 με, a value well below the hoop yield strain.

In the negative loading direction, for the maximum load reached in the test of –174.4 kN ($-P_{max}$), at –28.27 mm displacement, the maximum dowel bar strain was at gage 9 and was 2123 με, a value close to but less than the bar yield strain of about 0.22% (Fig. 4.7a). The hoop strain recorded by gage 22 at maximum load was 2672 με. That value was below the hoop yield strain of about 0.50%, but considerably greater than the elastic limit strain of about 0.20%. As the load dropped from its maximum value of –174.4 kN to –144.6 kN ($-0.83\ P_{max}$) and the test ended, the strains in the hoops at all three levels, and on the tension side of the column increased markedly. However, only the strains in the lower two hoops ended up exceeding the hoop yield strain of about 0.50%. The hoop strain for gage 22 increased from 2672 με to 9939με, the hoop strain for gage 24 increased from 285 με to 9863 με, and the hoop strain for gage 26 increased from 98 με to 2303 με.

5.2.4.2 Column A–2

For column A–2, gages 17 and 20 on the column bars were damaged, and the data acquired from gages 11 and 25 fluctuated markedly during the test and were not stable. Therefore, only the strain values from the remaining 22 gages have been plotted against the load in Figs. D1b through D26b. The strain distributions for increasing values of peak loads and peak deflections are shown in Fig. 5.21.

In the positive loading direction, for the maximum load of 160.5 kN, at 37.7 mm displacement, the bar strain at gage 4 on the dowel bar was 2193 με, about equal to the strain for bar yield,

and the hoop strain at gage 21 was 1202 με. At the first 52 mm peak displacement, when the load was 144.7 kN and had already dropped from its peak value of 155.6 kN at 45.69 mm displacement, the hoop strains recorded by gages 21 and 23 had increased greatly and both had reached values well beyond the yield strain of 0.50%. For gage 21 the strain values were, respectively, 4009 με at the peak load of 155.6 kN, and 6377 με at the 144.7 kN load. For gage 23 the corresponding strain values were 2213 με at the peak load, and 6485 με at the 144.7 kN load, respectively. At the first 65 mm displacement cycle, the hoop strains for gages 21 and 23 increased further to 7637 με and greater than 10,000 με, respectively. The latter value was the maximum strain that the strain gage indicator could record.

In the negative loading direction, for the maximum load of –152.2 kN, at –33.6 mm displacement, the dowel bar strain for gage 9 was 1968 με close to, but not equal to, the yield strain, and the hoop strain for gage 24 was only 549 με. From its maximum value of –152.2 kN the load dropped to –145.3 kN as the displacement increased to the maximum of –39 mm for the next cycle. The hoop strain for gage 24 increased markedly to 2112 με. The hoop strain for gage 24 continued to increase with increasing displacements reaching 7884 με at the first –52 mm peak displacement cycle, and to 10,000 με at the first –65 mm peak displacement cycle.

5.2.4.3 Column A–3

For column A–3, all gages were good. Therefore, strain values from all 26 gages have been plotted against the load in Figs. D1c through D26c. Strain distributions over the length of the bars for increasing values of peak loads or peak deflections are shown in Fig. 5.22.

In the positive loading direction, for the maximum load of 160.6 kN, at 50.8 mm displacement, the dowel bar strains for gages 3 and 4 were 2218 με, about bar yield, and 5568 με, well beyond bar yield, respectively. The hoop strain at gage 21 for that load was 836 με. Bar first yield occurred at gage 4 at 152.7 kN load and 43.16 mm displacement. At the load of 159.8 kN, corresponding to the peak for the first 65 mm displacement cycle, the strain for gage 5 was 2235 με and, in addition, the bar strain for gage 4 increased markedly to 6331 με and the bar strain for gage 3 increased slightly to 2266 με. The hoop strain for gage 23 was 1950 με. At the first 78 mm displacement cycle, the

hoop strain for gage 21 increased from 2008 με to 3599 με. Further, for the second 78 mm displacement cycle, hoop strains for both gages 21 and 23 increased to more than 10,000 με.

In the negative loading direction, bar yielding occurred first at gage 9, 2214 με, at a load of –142.3 kN, –34.72 mm displacement, and in advance of the peak load of –149.1 kN which occurred at the first –39 mm displacement cycle. By the peak load of –149.1 kN, strains for both gages 8, (2227 με), and 9, (3600 με), were greater than the bar yield strain. By the maximum load of –155.3 kN and –63.2 mm displacement, the strains for gages 8 and 9 had increased markedly and had reached 4025 με, and 8763 με, respectively. The strain on the hoop gage 22 was 3257 με, and by the first cycle to the peak displacement of –78 mm the strain in that gage had increased to more than 10,000 με. The strain for gage 24 had increased to 8552 με by the second cycle to a peak displacement of –78 mm, and the hoop strains for both gages 22 and 24 had exceeded the maximum recordable strain by the first cycle to a peak displacement of –91 mm.

5.2.4.4 Column B–1

For column B–1, gage 15 on the column bar was damaged. Strain values from the remaining 25 gages are plotted against the applied load in Figs. D1d through D26d. The strain distributions for different peak loads and deflections are shown in Fig. 5.23.

In the positive loading direction, dowel bar first yield occurred at gage 4 at 156 kN load and 30.44 mm displacement. That yield occurred before the peak load of 174.6 kN and displacement of 37.58 mm were reached. At the peak load of 174.6 kN, the strains for gages 3 and 4 were 2272 με and 3821 με, respectively, with both values in excess of the yield strain. At the maximum load of 182.9 kN, 48.79 mm displacement, the strains for gages 3 and 4 were 2346 με and 7434 με, respectively. The strains in hoop gages 21, 23 and 25, on tension side, were 3715 με, 2069 με and 516 με, respectively, showing clearly a decrease in hoop strain with increasing height above the top of the base beam. As the load dropped from the maximum of 182.9 kN to 179 kN, the strain for gage 21 increased to 9501 με, and as the load fell further to 176.4 kN the strain for gage 23 increased to 9642 με. At the failure load of 146.3 kN the strain for gage 25 had increased to 1999 με, but had not reached yield.

In the negative loading direction, at the peak load of –172.3 kN and –38.22 displacement, only the strain at gage 9 was beyond yield. The hoop strain at the same load for gage 22 was more than 2500 με. However, the exact load for first bar yielding was not recorded. Unfortunately the data acquisition equipment failed because its capacity was exceeded.

5.2.4.5 Column B–2

For column B–2, gages 11 and 16 on the column bars were damaged, and gage 22 on the hoop steel was bad. Strain values from the remaining 23 gages are plotted against the load in Figs. D1e through D26e. Strain distributions for increasing peak loads and deflections are shown in Fig. 5.24.

In the positive loading direction, at the maximum load of 164.4 kN, 46.1 mm displacement, the dowel bar strains for gages 3 and 4 were 2635 με and 7800 με, respectively. Both values were well in excess of the bar yield strain. The corresponding strain for gage 21 on the hoop bar was 1734 με for the same peak load. Bar yielding occurred first at gage 3 (2204 με) at 136.3 kN load, 29.29 mm displacement, and before the peak load of 151.0 kN for the first 36 mm displacement cycle. The strain for gage 21 was 2012 με at the peak load of 160.6 kN at the corresponding displacement of 60 mm. For the first 72 mm peak displacement cycle and corresponding load of 142.0 kN, the strain for gage 21 increased to 7128 με, and that for gage 23 increased to 2439 με. For the first 84 mm displacement cycle, the strain for gage 23 increased further to 4150 με while that stain for gage 21 decreased to 6278 με.

For the negative loading direction, bar yielding was first recorded by gage 8 (2207 με) at –142.5 kN load, –30.19 mm displacement, and before the maximum load of –157.5 kN was reached for the first –36 mm displacement cycle. At the maximum load of –157.5 kN, the strains for gages 8 and 9 on the dowel bar were 2296 με, and 2588 με, respectively, both well beyond the bar yield strain. For the first 48 mm displacement cycle, the strain for gage 8 decreased to 2112 με, while the strain for gage 9 increased to 4088 με. The strain for gage 24 on the hoop bars was 3004 με for the first –60 mm displacement cycle, and had increased to 3988 με by the first –72 mm displacement cycle.

5.2.4.6 Column B–3

For column B–3, gages 6 and 16 on the column bars were damaged, and gage 25 on the hoop steel was bad. Strain values for the other 23 gages are plotted against the applied load in Figs. D1f through D26f. The strain distributions for increasing peak loads and deflections are shown in Fig. 5.25.

In the positive loading direction, at the maximum load of 152.2 kN, 58.2 mm displacement, the strains for gages 3 and 4 on the dowel bar were 2447 με and 7821 με, respectively, both values well beyond the bar yield strain. The strain for gage 5 was close to the bar yield strain at 2174 με. The strain for hoop bar gage 21 was 2231 με. Bar yielding was first recorded by gage 4 at 129.3 kN load, 40.44 mm displacement, before the peak load of 143.2 kN for the first 48 mm displacement cycle was reached. At that peak load, strains for both gages 3, (2324 με), and 4, (4296 με), were already well beyond the bar yield strain. For the first 72 mm displacement cycle, the strains for gages 3, 4 and 5 increased to 2466 με, more than 10,000 με and 2271 με, respectively, all values well beyond the bar yield strain, and the strain for gage 21 had increased to 7010 με. a value also greater than the hoop bar's yield strain. For the second 72 mm displacement cycle, the strain for gage 21 increased further to 9177 με. For the first 84 mm displacement cycle, both strains at gages 3 and 5 increased further to 2506 με and 2341 με, respectively, and the strain at gage 21 increased to more than 10,000 με. The strain for gage 23 was 1733 με for the first 96 mm displacement cycle, and increased to 2051 με for the first 108 mm displacement cycle.

In the negative loading direction, bar yielding first occurred at gage 8 (2200 με) at –124.5 kN load, –32.11 mm displacement, and before the peak load of –134.3 kN was reached for the first –36 mm displacement cycle. At that peak load, strains for both gages 8, (2389 με), and 9, (2275 με), were well beyond the bar yield strain. For the first –48 mm displacement cycle, the strain for gage 9 increased markedly to 6538 με. At the maximum load of –155.2 kN, –59.5 mm displacement, the bar strains for gages 8 and 9 were 2934 με, and 8629 με, respectively, and the strain for gage 10 was 1907 με. At the first –72 mm displacement cycle, the dowel bar strains increased greatly to 5379 με for gage 8 and to 9389 με for gage 9, and the hoop bar strain for gage 22 was 2094 με.

At the first –84 mm displacement cycle, the hoop bar strain for gage 22 increased to 2608 με and that for gage 24 to 3916 με. At the first –96 mm displacement cycle, the hoop bar strain for gage 24 increased to 8488 με, and that for gage 22 increased slightly to 3489 με. At the first –108 mm displacement cycle, those hoop bar strains became 3704 με and 8753 με for gages 22 and 24, respectively.

5.2.5 Visual Observations

All columns were closely observed for the cracks that developed during different loading cycles. Cracks were marked and photographs taken for future reference. Some relevant photographs of the specimens after they were loaded to failure are shown in Fig. 5.26 through Fig. 5.31. The cracks for each column are described in the following paragraphs.

5.2.5.1 Column A–1

Photographic records of the cracking on the tension face for both positive and negative loading are shown in Fig. 5.26. On the tension face for positive loading, the numbers marked in Fig. 5.26a were load values. For the first cycle to 70 kN load, one small vertical crack, about 100 mm in height, occurred near the bottom, and along the line, of the central column bar. At the first cycle to 105 kN load, that crack extended vertically to about 150 mm in height and two vertical cracks occurred from the bottom to about 100 mm in height for the two outside column bars, also six horizontal cracks occurred along the height of the lower part of the column. The horizontal cracks were at about 250 mm spacing and nearly coincident with the location of a transverse hoop. The first crack coincided with the third hoop location at 600 mm from the bottom of the column. In addition two inclined cracks occurred on both sides of the top surface of the base beam. On the first cycle to 140 kN load, the central vertical cracking extended to about 250 mm in height, while one of the side vertical cracks extended to about 350 mm in height. The lower two horizontal cracks became longer, and three more horizontal cracks occurred in between previous cracks and roughly at heights of 350 mm, 1,000 mm and 1,475 mm above the top of the base beam. At the peak load of 174.4 kN, at 36.64 mm displacement, the central vertical crack extended to about 600 mm in height, (marked as 175 in Fig. 5.26a), and one discontinuous inclined crack occurred around the bottom of the column, also

four inclined cracks occurred near the location of the top of both side lap splices. Two previous inclined cracks extended from the top surface to 50 to 100 mm down both sides of the base beam.

On the tension face for negative loading, as apparent in Fig. 5.26b, the vertical crack patterns ware similar to those for positive load at the first cycle to 70, 105 and 140 kN load. At the first cycle to 105 kN load, six horizontal cracks also occurred along the lower part of the column height. On the first cycle to 140 kN load, five more horizontal cracks occurred in between previous horizontal cracks and roughly at 350 mm, 475 mm, 725 mm, 975 mm and 1,225 mm above the top of the base beam. Finally, after the peak load of –174.4 kN load, –28.27 mm displacement, had been held fixed for about 2 or 3 minutes the column failed abruptly. As apparent in Fig. 5.26b the three vertical cracks along the column bars became pronounced, the cover over those bars fell off, exposing them for about the first 350 mm of their length.

5.2.5.2 Column A–2

Photographic records of the cracking for this column are shown in Fig. 5.27. As apparent in Fig. 5.27a, on the tension face for positive loading, at the first cycle to 89 kN peak load, two horizontal cracks happened at heights of about 350 mm and 600 mm. One small vertical crack, about 100 mm in height, occurred along the bottom part of the central column bar along with two other small cracks on either side of that crack but not on the side lap bar positions. At the first cycle to 118 kN load, a total of seven horizontal cracks occurred together with two inclined cracks about 350 mm in length, one centered around the central vertical crack, the other to one side of the bottom of the column. Inclined cracks also occurred on the top surface of base beam and extended to about the one third of the depth of the sides of that beam.

For subsequent cycles the column was loaded using displacement control. Again as apparent in Fig. 5.27a, on the tension face for positive loading, for the first cycle to 26 mm displacement, no new cracks occurred. For the first cycle to 39 mm peak displacement, the central vertical crack extended to about 225 mm in height, and short vertical cracks, about 150 mm in length, developed along the two outermost bars to different column heights (marked as 1.5Δ in Fig. 5.27a). The previously existing inclined cracks in the base beam extended further to about two thirds of the depth

of that beam. With the second cycle to a 39 mm peak displacement, those three vertical cracks extended higher, marked as 1.5Δ–2 in Fig. 5.27a. For the first cycle to 52 mm peak displacement, those three vertical cracks became continuous and extended to a height close to the lap length, (marked as 2Δ in Fig. 5.27a), together with many more inclined cracks around them. The existing cracks became bigger, and concrete crushing occurred near the very base of the column on the compression face. A final cycle to a 65 mm peak displacement caused complete failure of the column, with spalling of the concrete cover to the height of the first hoop from the bottom on the compression face of the column.

As apparent in Fig. 5.27b, on the tension face for negative loading, at the first cycle to 59 kN peak load, a small horizontal crack occurred at about 350 mm height above the base. For the first cycle to 89 kN peak load, two more horizontal cracks developed at about 600 mm and 850 mm heights above the base of the column. A vertical crack, about 325 mm in length, occurred along the bottom of the central column bar and a second vertical crack, about 100 mm in height, occurred to one side of the central bar but not on the line of an outermost bar. For the first cycle to 118 kN peak load, eight horizontal cracks developed extending up to the column to about 2,100 mm in height.

For subsequent cycles the column was loaded using displacement control. As apparent in Fig. 5.27b, on the tension face for negative loading, for the first cycle to 26 mm peak displacement, 140.5 kN load, the existing central vertical crack extended to about 650 mm in height, marked as 140 in Fig. 5.27b. For the first cycle to 39 mm peak displacement, marked as 1.5Δ in Fig. 5.27b, the three vertical cracks extended to, about the full lap length of 1,090 mm, on the lines of all three column bars and were accompanied by more inclined cracks. For the first cycle to 52 mm peak displacement, more inclined cracks occurred around those three vertical ones, marked as 2Δ in Fig. 5.27b. One previously existing inclined crack on the tension face at the bottom of the column developed an offset of about 4 to 5 mm, and minor concrete crushing occurred near the base of the compression side.

5.2.5.3 Column A–3

Photographic records of the cracking for both tension faces of this column are shown in Fig.

5.28. As apparent in Fig. 5.28a, on the tension face for positive loading, at the first cycle to a 52 kN peak load, two short horizontal cracks developed at heights of about 350 mm and 600 mm above the base of the column. At the first cycle to 78 kN load, three more horizontal cracks developed along the middle of the column at heights of roughly 1,100, 1,350 and 1,600 mm above the base. Two vertical cracks also occurred at the bottom of the column, not on the column bar locations, but on two different sides, with one crack about 100 mm in length and the other about 175 mm in length with an inclined upper end. At the first cycle to 104 kN load, four more horizontal cracks developed in between the previously existing horizontal cracks, making the crack spacing about 125 mm, instead of 250 mm, and one more horizontal crack occurred towards the top of the column. Inclined cracks also occurred on the top surface of base beam and extended down the sides of that base beam to about half its height.

Subsequent cycles of loading were conducted in displacement control. As apparent from Fig. 5.28a, on the tension face for positive loading, for the first cycle to 26 mm displacement, a central vertical crack occurred at the bottom of the column and extended to about 200 mm in height. For the first cycle to 39 mm peak displacement, marked as 1.5Δ in Fig. 5.28a, the central vertical crack extended up to about 300 mm in height and also down from the near top of the lap length, about 100 mm in length. For the first cycle to 52 mm peak displacement, marked as 2Δ in Fig. 5.28a, the central vertical crack became continuous, and a second vertical crack occurred to one side of the central bar, extending up to a height of 300 mm. Many cracking noises were heard. For the first cycle to 65 mm peak displacement, the horizontal crack near the top of the splice widened, more inclined cracks occurred around the bottom of the central vertical crack, marked as 2.5Δ in Fig. 5.28a, and the two vertical cracks along the outside bars extended higher. Minor concrete crushing occurred on both faces. For the first cycle to 78 mm peak displacement, the width of the central vertical crack became larger and accompanied by the development of more inclined cracks along its length, marked as 3Δ in Fig. 5.28a. Further the vertical crack along one of the outside bars extended much higher to about 800 mm in height. The width of the crack between the column and the top of the base beam grew to about 11 mm, and crushing of the concrete spread slightly across

the width of the bottom of the column. A final cycle to a 91 mm peak displacement, marked as 3.5Δ in Fig. 5.28a, caused complete failure of the column with more inclined cracks occurring around the three vertical splitting cracks on both faces of the column. One of the inclined cracks at the bottom of the column developed an offset of about 2 mm, and the width of the crack at the base of the column grew to about 15 mm. Also as can be seen from Fig. 5.28a, about 500 mm height of crushed concrete fell off the face of the column under the final cycle to a negative peak displacement of –91 mm.

As apparent in Fig. 5.28b, on the tension face for negative loading, at the first cycle to a 52 kN peak load, two short horizontal cracks happened at heights of about 350 mm and 600 mm above the base of the column. At the first cycle to 78 kN load, the two previously existing horizontal cracks grew longer, four more horizontal cracks developed along the middle height of the column, roughly at 1,100, 1,350, 1,600 and 1,850 mm in height above the base, and a side vertical crack, about 100 mm in length, occurred at the bottom of the column and not on the line of the outside column bar. At the first cycle to 104 kN load, two more horizontal cracks developed in between the previously existing horizontal cracks, the existing vertical side crack extended up to about 250 mm in length, another side vertical crack, about 250 mm in length with an inclined upper end, occurred at the bottom of the column along the line of the other outside column bar, and one more horizontal crack occurred towards to the top of the column.

Subsequent cycles of loading were conducted in displacement control. Again on the tension face for negative loading, for the first cycle to 26 mm displacement, marked as Δ in Fig. 5.28b, a central vertical crack occurred on the bottom of the column, about 150 mm in height. For the first cycle to 39 mm peak displacement, marked as 1.5Δ in Fig. 5.28b, the central vertical crack extended up to about 500 mm in height. For the first cycle to 52 mm peak displacement, marked as 2Δ in Fig. 5.28b, two more vertical cracks occurred at midheight of the lap for one of the outermost column bars, and minor crushing occurred for the bottom concrete on the compression side. With the second cycle to 52 mm peak displacement, marked as 2Δ–2 in Fig. 5.28b, one more vertical crack occurred at midheight of the lap for the other outside column bars. For the first cycle to 65 mm peak displacement, marked as 2.5Δ in Fig. 5.28b, the two vertical side cracks extended higher, and about an 8 mm

opening developed at the interface between the column and the top of the base beam. For the first cycle to 78 mm peak displacement, marked as 3Δ in Fig. 5.28a, the width of the central vertical crack became larger and that widening accompanied by the development of more inclined cracks along that crack's length. Two vertical cracks developed on either side of the central crack and at the bottom of the outside bars. One crack was about 100 mm in length with an inclined upper end and the other about 250 mm in height. The width of the crack between the column and the top of the base beam grew to about 13 mm. At the final cycle to a 91 mm peak displacement, marked as 3.5Δ in Fig. 5.28b, those two vertical side cracks extended much higher to about 1,250 mm in height above the column base. Two of the inclined cracks at the bottom of the column developed offsets of about 2 to 3 mm.

5.2.5.4 Column B–1

A photographic record of the cracking on the tension face of this column for positive loading is shown in Fig. 5.29. The numbers marked in Fig. 5.29 were load values. At the first cycle to 60 kN peak load, a small vertical crack, about 75 mm in length, occurred on the line of the central bar and at the bottom of the column for both tension faces. At the first cycle to 90 kN peak load, seven horizontal cracks occurred over the height of the lower part of the column for both tension faces. Each crack was located at the position of a transverse hoop, (250 mm spacing). The first crack from the bottom was located at the position of the second hoop from the bottom, 350 mm above the top of the base beam. Also on the tension face for positive loading, one vertical crack developed along the line of an outside bar extending from the bottom to about 150 mm in height. On the tension face for negative loading, similar vertical cracks occurred for both outside bars with one extending to about 175 mm in height and the other to about 100 mm in height. On the first cycle to 120 kN peak load, on the tension face for positive loading, the central vertical crack extended to about 250 mm in height, the previously existing vertical side crack extended to about 200 mm in height, and on the line of the other outside bar a vertical crack extended from the bottom to a height of about 350 mm. On the tension face for negative loading, the central vertical crack extended to about 500 mm in height, and one of the vertical side cracks extended to about 350 mm in height.

Subsequent loading was performed using displacement control. At the first cycle to 150 kN peak load, (still reading load because of the flexibility of loading frame), on the tension face for positive loading, two inclined cracks occurred at the bottom of each outside column bar and extended to about 350 mm in length. Several more small inclined cracks also occurred around the middle of the lap length for the central vertical crack. A large crack opening developed at the bottom of the column at its connection to the base beam. Inclined cracks occurred on both sides of the top surface of the base beam. On the tension face for negative loading, the outside vertical cracks extended to about 500 mm in height, and some of the horizontal cracks became noticeably longer. For the positive loading direction, the load dropped from 174.6 kN at 37.58 mm displacement to 172.3 kN at 37.73 mm displacement. The central vertical crack extended higher, marked cracking noises were heard, and therefore unloading was commenced. For the negative loading direction, the load dropped rapidly from –172.3 kN at –38.22 mm peak displacement to –169.1 kN at –38.71 mm peak displacement. At that time the data acquisition equipment stopped functioning because its maximum recording time was exceeded. Since noises continued to be heard the column was unloaded. The central vertical crack had extended to the full length of the lap, (1,090 mm), and two vertical cracks had extended up the lap length of the two outside bars. Finally, when the load in the positive direction was increased to 182.9 kN at 48.79 mm column displacement, three vertical cracks extended along the line of the column bars to about a height of 1,250 mm. Those cracks were surrounded by numerous inclined cracks, marked as 184 in Fig. 5.29. Over the height of the lap length of 1,090 mm, the width of the central vertical crack was between 2 and 3 mm and the width of some of the inclined cracks was even larger. The column was considered to have failed when the maximum load dropped to 146.3 kN at 71.13 mm column deflection.

5.2.5.5 Column B–2

A photographic record of the cracking on the tension face for positive loading is shown in Fig. 5.30. At the first cycle to 52 kN peak load, a small horizontal crack occurred at about 350 mm in height above the column base for the tension face for positive loading, (marked as 52 in Fig. 5.30), and two small horizontal cracks occurred at about 350 mm and 600 mm in height above the column

base for the tension face for negative loading. At the first cycle to 78 kN peak load, six more horizontal cracks developed along the height of the lower part of the column for the tension face for positive loading. On the tension face for negative loading, three more horizontal cracks occurred along with one small vertical crack, about 100 mm in length that occurred along the bottom part of the central bar's position. At the first cycle to 104 kN peak load, on the tension face for positive loading, one small vertical crack, about 100 mm in length, occurred near the bottom of the line of the central bar, and the lowest horizontal crack became longer. Inclined cracks also developed on the top surface of the base beam and extended down about one third of the height of sides of that beam. On the tension face for negative loading, the central vertical crack extended to about 350 mm in length, and four previous horizontal cracks extended around the circumference of the column.

Subsequent cycles were applied using displacement controlled loading. At the first cycle to 24 mm peak displacement, 110 kN load, for the tension face for positive loading, the second and third horizontal cracks extended almost completely around the circumference of the column, marked as 110 in Fig. 5.30. On the tension face for negative loading, vertical cracks occurred along the lines of each outside bar and were accompanied by several inclined cracks. At the first cycle to 36 mm peak displacement, on both tension faces, the central vertical crack extended to about the length of the lap height of 1,090 mm, and was accompanied by more inclined cracks, marked as 1.5Δ in Fig. 5.30. Cracking noises were plainly heard, and the inclined cracks in the base beam extended further through to about 80 percent of the depth of that beam. With the second cycle to 36 mm peak displacement, 142 kN load, several inclined cracks developed around the central vertical crack, marked as 142–2 in Fig. 5.30. At the first cycle to 48 mm displacement, on the tension face for the positive maximum load of 164.4 kN, the two vertical cracks along the outside bars grew higher, (marked as 165 in Fig. 5.30), the lowest horizontal crack linked together, and noises were heard. On the tension face for negative loading, two more horizontal cracks developed at about middle height of the column, and both vertical cracks along the outside bars became longer. Several more inclined cracks occurred around the central vertical crack, and more noises were heard. At the first cycle to 60 mm peak displacement, on the tension face for positive loading, the two vertical cracks along the outside

bars became continuous and elongated to about 1,000 mm in length, marked as 2.5Δ, 2.5 and 152 in Fig. 5.30, and more inclined cracks developed around the vertical cracks. Also on the opposite column face, the compression side for positive loading, a small area of concrete at the bottom of the column started to crush. On the tension face for negative loading, the three vertical cracks became much wider and several more inclined cracks developed near the bottom part of the column. At the first cycle to 72 mm peak displacement, the width of the cracks on both faces of the column became larger, minor concrete crushing occurred at the bottom of the column on the compression side for positive loading, and some irregular cracks happened. Finally, a half–cycle in the positive loading direction to 84 mm peak displacement caused complete failure of the column. Concrete spalled up to the level of the first hoop from the bottom on the compression side of the column.

5.2.5.6 Column B–3

A photographic record of the cracking on the tension face for positive loading for this column is shown in Fig. 5.31. At the first cycle to 44 kN peak load, three small horizontal cracks occurred on each of the tension faces, at about 350 mm, 600 mm and 850 mm heights, respectively, on the tension face for positive loading, and at about 600 mm, 850 mm and 1,100 mm heights, respectively, on the tension face for negative loading. At the first cycle to 66 kN peak load, on the tension face for positive loading, four more horizontal cracks happened along the middle height of the column, roughly at 1,350, 1,500, 1,750 and 1,850 mm heights, (i.e., not all at hoop locations), and in addition the three previously existing horizontal cracks grew longer. On the tension face for negative loading, the three previously existing horizontal cracks grew longer too. Some linked up with similar cracks on the other face, and two more horizontal cracks occurred, at approximately 350 mm and 1,850 mm heights, and one vertical crack occurred along the line of an outside bar to about 100 mm in length above the base of the column. At the first cycle to 88 kN peak load, on the tension face for positive loading, the central vertical crack occurred, extending to about 100 mm in length, and one more horizontal crack, roughly at 1,200 mm in height, occurred in between previously existing horizontal cracks. In addition an inclined crack developed on the top surface of the base beam, (see Fig. 5.31). On the tension face for negative loading, three more horizontal cracks occurred in between the pre-

viously existing horizontal cracks, the previously existing vertical crack along the outside bar became longer, extending from about 100 mm to 150 mm, and a central vertical crack occurred, extending to about 100 mm in height from the bottom.

For the subsequent cycles, loading was in displacement control. At the first cycle to 24 mm peak displacement, on the tension face for positive loading, the central vertical crack extended to about 200 mm in height, marked as Δ in Fig. 5.31. On the tension face for negative loading, the central vertical crack extended to about 350 mm in length, and the existing vertical side crack extended to about 250 mm in length. At the first cycle to 36 mm peak displacement, marked as 1.5Δ in Fig. 5.31, on the tension face for positive loading, an inclined crack developed extending from the upper end of the central vertical crack to about 350 mm in height, two more horizontal cracks occurred in between the existing ones, and a vertical crack about 100 mm in length occurred at the top of one of the outermost lap splice bars. On the tension face for negative loading, an inclined crack occurred around the central vertical crack, and the existing vertical side cracks extended further to about 350 mm in length. At the first cycle to 48 mm peak displacement, marked as 2Δ in Fig. 5.31, on both tension faces, vertical cracking occurred near the top of the central lap splice extending down the line of the bar about 400 mm. Also on the tension face for positive loading, a vertical crack developed along the line of the second outermost bar extending from the bottom of the column to about 150 mm in height. On the tension face for negative loading, the central vertical crack became wider at its bottom, and the crack at the connection between the column and the base beam opened to about 5 mm in width. At the first cycle to 60 mm peak displacement, minor concrete crushing occurred at the junction of the beam and column and the width of the crack at that junction opened to about 8 mm for both loading directions. At the positive maximum load of 152.2 kN, and the negative maximum load of –155.2 kN, marked as 2.5Δ in Fig. 5.31, the central vertical crack became continuous along the splice length, and on each face a vertical side crack occurred around the top of one side of the lap splice. For the tension face for positive loading that crack was about 250 mm in length, while on the tension face for negative loading the length of that crack was about 125 mm. Two more inclined cracks occurred on the top surface of the base beam and the existing ones extended down

the sides of that beam to almost its full height. At the first cycle to 72 mm peak displacement, marked as 3Δ in Fig. 5.31, on the tension face for positive loading, two more inclined cracks occurred around the midheight of the central vertical crack, a vertical crack, about 100 mm in length, occurred along one of the outside bars near the top of the lap splice, and crushing of the concrete occurred slightly at the bottom of the column at its junction with the base beam. On the tension face for negative loading, three more inclined cracks occurred around the bottom of the central vertical crack, a vertical crack, about 250 mm in length, occurred around the top of the second outside bar lap splice, and spalling of a patch of about 12 mm thick by 100 mm high concrete occurred at the bottom of the column. From it can be seen in Fig. 5.31 that patch dropped off. At the first cycle to 84 mm peak displacement, marked as 3.5Δ in Fig. 5.31, on the tension face for positive loading, one more inclined crack occurred around the midheight of the central vertical crack, one of the vertical side cracks extended from the bottom to about 350 mm in height, the width of the crack at the junction of the column and base beam opened to 11 mm. On the tension face for negative loading, the two vertical side cracks extended from the top of the lap splice down the bars for about 500 mm, and the width of the crack at the connection of the column and the base beam opened to 12 mm. At the first cycle to 96 mm peak displacement, both vertical side cracks became continuous over the height of the lap splice for both tension faces with more inclined cracks developing around them, marked as 4Δ in Fig. 5.31. The bottom part of the central vertical crack became much larger, increasing to 3 mm in width on the tension face for positive loading, and to 7 mm in width on the tension face for negative loading. Finally, one cycle to 108 mm peak displacement caused complete failure of the column. More inclined cracks occurred around the three vertical cracks on both tension faces, and crushed concrete about 25 mm thick by 150 mm high, located centrally at the bottom of the column, fell off from both sides of the column. Also, on the tension face for positive loading, the width of the crack at the base of the column opened to about 15 mm, and one of the vertical side cracks extended to about 1,250 mm in length, marked as 4.5Δ in Fig. 5.31.

5.2.6 Circumferential Elongations

The circumferential elongations as determined from the optical fiber instrumentation for the three different locations over the lap splice height for each laboratory test column, except column A–1, are shown in Figs. 5.32 through 5.36. In each figure, the elongation is that corresponding to the peak displacement for the first cycle of each new load or displacement level. Straight lines connect the elongations measured at the three locations. The sign convention for elongation is positive for positive loading and negative for negative loading. For each column, the largest circumferential elongation occurred at the bottom of the lap splice for both loading directions.

Comparisons of the circumferential elongations, as measured by the optical sensors, with the hoop strains, as measured by the electrical resistance strain gages, yield no useful information. For a given lateral deflection the measured circumferential elongations correspond to strains much larger than the measured hoop strains, this result suggests that either the strain gages did not record the maximum strains or that the inadequate anchorage for the lap splices in the hoop prevented those bars from functioning properly.

5.2.7 Concluding Remarks

The displacement distribution over the height of the column at each load level and in both directions is generally flexural in shape (Figs. 5.8 through 5.13). This response was determined primarily by the column height to diameter ratio. For all columns that ratio was 5.5, a value is greater than the value of 4 where shear deformations generally become important. However, it can also be seen that as the applied load increases particularly to values greater than those for first yield, a concentrated rotation occurs at the column base that increases significantly the tip displacement.

Strain distributions for increasing peak loads and deflections for all six columns were shown in Figs. 5.20 through 5.25. The measured first yielding loads, maximum loads and the corresponding main bar strains in both directions are summarized in Table 5.2. From the values shown in Figures and the Table, the following general observations can be made:

1). None of column bars, as opposed to the dowel bars, yielded before failure occurred. It can be seen that none of the strain values from gages located on the column bars at the level of, or above, the top of the dowel bars, (gages 11, 12, 16 and 17), exceeded the bar yield strain of about 0.22%. The maximum strain reached was in column B–3 and that value, (1850 με), was equal to only about 84% of the yield strain for the bar. From the gages located at the bottom of the column bars, (gages 15 and 20), it can be seen that the compression forces at nearly all load and displacement levels were much greater than the tensile forces. It can also be seen that it was not until the level of the next gage up the column bar, (gages 14 and 19), that the compression forces became somewhat less than the tension forces, as would be anticipated for a symmetrical reinforced member.

2). The dowel bars in columns A–1 and A–2 developed strains almost equal to those for yield; while the dowel bars in columns A–3, B–1, B–2 and B–3 all developed strains greater than yield. The yielding lengths of the dowel bars for columns A–3 and B–3 were longer, especially, in the positive loading direction, than the yielding lengths for columns B–1 and B–2. For column B–3, the yielding extended well into the base beam (see strain from gage 5). The maximum yielding length was around 508 mm (20 in.), from gage 3 to gage 5; and the maximum bar strain was greater than 10,000 με. While for columns B–1 and B–2, the yielding length was less and was around 254 mm (10 in.), from gage 3 to gage 4 only.

3).The hoop bars yielded in all columns, but at different locations for different columns. Based on the stress–strain curve for the #3 hoop bar, (Fig. 4.7b) a strain of about 0.50% was taken as the hoop yield strain. Hoop bars yielded only after displacements considerably greater than those for the maximum loads. At maximum lateral load for each column, no hoop bar yielded. The strains from gages 25 and 26 for all six columns were considerably less than the hoop yield strain.

From the failure mode for all six columns, it appears that opening of the vertical splitting cracks initiated failure of the splices, causing the capacity to drop, rather than crushing of the concrete on the compression face. For all laboratory test columns at failure, three clearly visible splitting cracks developed vertically along the lines of the spliced bars on the bottom part of both sides of

each column. The vertical splitting crack on the central bar was always much wider than the cracks on the other two bars. For all columns, by the first loading level (20% of the calculated column yield strength), only one tiny crack had occurred at the connection between column and base beam. For columns A–1, (S_d = 1.4 d_b, C = 12.7 mm and L = 0), and B–1, (S_d = 2.9 d_b, C = 12.7 mm and L = 0), as compared to the other four columns, the central vertical crack occurred at the bottom of the column earlier and, at failure, there were more inclined cracks around the three vertical ones, (Figs. 5.26 and 5.29). For columns A–2, (S_d = 1.4 d_b, C = 12.5 mm and L = 51 mm), A–3, (S_d = 1.4 d_b, C = L = 51 mm), B–2, (S_d = 2.9 d_b, C = 12.5 mm and L = 51 mm), and B–3, (S_d = 2.9 d_b, C = L = 51 mm), the horizontal flexural cracks appeared before those vertical cracks. Further at failure more inclined cracks developed around those three vertical ones on the faces for smaller spacing columns A–2 and A–3, (Figs. 5.27 and 5.28), than on the faces for larger spacing columns B–2 and B–3, (Figs. 5.30 and 5.31).

CHAPTER 6

DISCUSSION AND PREDICTION OF EXPERIMENTAL RESULTS

6.1 Introduction

In this Chapter the prediction of the test results, particularly the laboratory test results, is discussed. Section 6.2 describes the anticipated behavior in flexure for specimens with the proportions of the laboratory test columns. Section 6.3 describes how bond slip and splice failure can be expected to modify the flexural behavior. Section 6.4 compares the relative performance of the test columns. Section 6.5 discusses prediction of the measured load–deflection relationships, including prediction of the flexural behavior, and bond slip and lap splice failure behavior. In Section 6.6 a comparison is made between predicted and measured load–deflection relationships.

6.2 Idealized Flexural Behavior

Shown in Fig. 6.1a is the load–deflection response that can be expected, for a column with the proportions of the laboratory test columns, when that response is essentially flexural and there are no bond slip or shear effects. The load is the lateral force applied at the top of the column and the deflection is the lateral displacement at the point of application of that load. When the column is subjected to reversed cyclic lateral displacements of increasing peak values, a loading history similar to that applied to the test specimens, the envelope to the hysteretic response will be a relationship of the form of the solid curve OABCDE. There will be differences in the curves for positive and negative loadings because of the differing anchorage conditions for the dowel bars for corner opening and corner closing, respectively. However, for interpretation of the test results it is appropriate to neglect those differences and represent the response by a single relationship such as the solid curve OABCDE.

For Fig. 6.1 there are four different stages of response OA, AB, BD and DE. At A the load causes cracking at the connection between the column and the base. That location was also a construction joint for test columns. Therefore, test columns were effectively cracked at that location from the start of testing. Consequently, for practical purposes stage OA was often suppressed.

At B the load, P_y, causes first yield in the dowel bar having the greatest internal lever arm. Between A and B, or between O and B if the base connection is precracked, the response is essentially linearly elastic with horizontal cracks developing to increasingly greater heights up the column with increasing load.

Load stage C corresponds to the nominal flexural capacity, P_n, of the connection and is a theoretical quantity only. At that load all the dowel bars on the tension side of the column are assumed to have reached their yield stress and the concrete on the compression face to have reached its limiting capacity.

At D, the probable flexural strength, P_{pr}, of the laterally loaded column is reached. Crushing develops at the extreme compression face. The reinforcing bars in the tension face are stressed into their strain hardening range and plastic hinging spreads up the height of the column, causing increasingly greater deflections for increasing loads in the BD stage.

In the DE stage, the spread of crushing and spalling on the compression face results in a decreasing capacity for increasing deflections. In line with the recommendations of the Reference (Park, 1989), the useful capacity of the column is said to be reached at E when the lateral load capacity has decreased to 80 percent of the peak lateral load capacity.

The foregoing idealization assumes that the reinforcement is continuous out of the base beam and up the height of the column, and ignores the problems introduced by the presence of the lap splice and by differences between the locations for the dowel bars and for the column's longitudinal bars. The significance of those differences is examined in Section 6.5 when prediction of the measured responses is examined.

For earthquake response calculations it is customary to define an initial stiffness, a yield capacity, and a ductility demand "μ". The measured response of Fig. 6.1a is idealized as shown in Fig. 6.1b to obtain those characteristics. Extrapolation of the initial stiffness, as represented by the slope OI, to the nominal capacity, P_n, establishes the 'effective' yield displacement, Δ_y. The ratio of the displacement at any point along the load–deflection envelope to Δ_y establishes the ductility

ratio μ. That concept is used in Section 6.4 to define the test result of each column in terms of an effective ductility ratio μ.

6.3 Bond Slip and Splice Failure

The idealized flexural response of Fig. 6.1 will not be achieved if there is a bond failure. The average response for positive and negative loading, when there is a bond failure, can be idealized as the broken curve FG, in Fig. 6.1a. Initially, the response for a flexural or a bond failure are similar. However, at some point, F, the spread of splitting cracks up the longitudinal column bars and between column and dowel bars causes increased slips of the dowel bars relative to the surrounding concrete sufficient to cause the response for a flexural and a bond failure to deviate. As those splitting cracks continue to spread the response becomes increasingly softer and finally failure in bond, due to failure of the lap splice, occurs at the load corresponding to G. Thus, prediction of the response of the laboratory test specimens requires identification of the deflections, additional to those caused by flexure, resulting from bond slip and the limiting capacity for a splice failure. Calculation of those effects is discussed in Section 6.5.

6.4 Comparison of the Relative Performance of the Test Columns

6.4.1 Measured Load–Deflection Curves

For all four field test columns, the lateral load versus lateral displacement curves of Figs. 3.3a through 3.3d are shown to an enlarged scale in Figs. A1 through A4 in Appendix A. In Appendix A the corresponding ductility ratio μ, defined as discussed in Section 6.2, is shown for each load cycle. For all six laboratory test columns, curves of lateral load versus lateral displacement at the load point, (Figs. 5.2a through 5.7a), are shown to an enlarged scale in Figs. C1 through C6 in Appendix C along with the corresponding ductility ratio μ for each load cycle. For the first cycle to a new peak displacement value, the load, the displacement and the corresponding ductility ratio for each load or displacement level, are listed in Table 6.1 for each of the field test columns, and in Table 6.2 for each of the laboratory test columns, respectively. The ductility ratios of Tables 6.1 and 6.2 are calculated according to the concept of Fig. 6.1b.

Before the peak load was reached the reduction in capacity between the first and second

cycles to a given peak deflection was small. However, after the peak load and particularly for large displacements, the peak load attained in the second cycle to a given peak displacement became significantly less than the peak load for the first cycle. Those peak loads for the second cycle are shown in parentheses in Tables 6.1 and 6.2. The decrease in load during the second cycle to a prior peak displacement for each displacement–controlled loading cycle is quite noticeable in Figs. A1 through A4 and Figs. C1 through C6.

The measured envelope to the peak capacities for both positive and negative loading directions and for both the first and the second loading cycles to a given peak displacement is shown in Figs. 6.2 through 6.5 for each of the field test columns, and in Figs. 6.6 through 6.11 for each of the laboratory test columns, respectively.

6.4.2 Comparison

For comparison purposes, Park (1989) has suggested a failure standard, which includes both the failure load and the corresponding displacement determined from the measured load–displacement curve. The failure load is defined as the final load corresponding to 80% of the maximum applied lateral load measured during a test involving increasing fully reversed cyclic displacements. In accordance with that definition, the failure displacements, maximum loads and accompanying deflections for both positive and negative loading directions are listed in Table 6.3 for the field test columns, and in Table 6.4 for the laboratory test columns, respectively. For seismic loading, in addition to strength, the displacement is also critical. By considering the failure ductility ratios of Tables 6.3 and 6.4, the overall relative performance of each column was ranked.

For the field test columns, from consideration of the failure ductility ratios of Table 6.3, the overall performance (OP) can be ranked in order from the best to the worst as:

$$OP_{C15S} > OP_{B14S} > OP_{C17S} > OP_{B18S}$$

For the laboratory test columns, by considering the failure ductility ratios of Table 6.4, the overall performance (OP) can be ranked in order from the best to the worst as:

$$OP_{B-3} > OP_{A-3} > OP_{B-2} > OP_{B-1} > OP_{A-2} > OP_{A-1}$$

It should be noted the failure ductility ratios for columns A–1 and A–2 were still greater than one even though the longitudinal column bars did not yield prior to column failure. While this result contradicts the definition of ductility ratio for a column with continuous bars, for these columns with spliced bars, that result is due to the flexural behavior being controlled by the dowel bars and not the column bars. The strains in the dowel bars, at maximum load, were close to yield, and deflections were increased above those for continuous bars by relative slip between the dowel and column bars.

6.5 Prediction of Load–Deflection Curves

6.5.1 General

As described previously, the overall performance of any column under simulated seismic loading is determined both by its load capacity and its failure displacement as derived from the measured load–displacement curve. A cantilever column with splices at its maximum moment section can lose its lateral load resistance due to bond failure of the splice in the plastic hinge region. The subsequent response is characterized by rapid strength degradation and very narrow energy dissipation loops, (Fig 3.3 and Figs. 5.2 through 5.7). Further, as discussed in Section 6.3, before failure of the splice, slip of the dowel bars causes a decreasing stiffness, and also an increasing S–shape for the hysteresis loops.

The test results document that the bar locations are very critical for the performance of each column. However, to accurately predict the global behavior of this type of column with inadequate splices at its base, two fundamental analytical tools need to be available. The first is a three–dimensional nonlinear finite element program that can be used to determine stress transfer conditions in and around the bars of the splice. The second is a bond stress–slip relationship applicable to the anchorage of the dowel bars in the column. A three–dimensional nonlinear finite element analysis program using Finite Fiber Elements was developed in parallel with an experimental program at the University of California, Berkeley, by Mari (1984) and in the University of California, San Diego, by Sun et al (1992). With the limited amount of information available from the tests reported here,

such detailed modeling to predict behavior is neither appropriate nor warranted. In the following a simpler approach is developed. That approach consists of three parts: (1) a method for predicting flexural response; (2) a method for predicting the additional rotation that occurs at the base of the column due to dowel bar slip; and (3) a method for predicting the axial force in the extreme tension bar that causes a lap splice failure. Such an approach, while it can predict the maximum load and associated deflection, can not predict the additional post peak deflections caused by relative movement between dowel and column bars.

6.5.2 Prediction of Theoretical Flexural Response

In this document it is assumed, for simplicity, that the theoretical flexural response can be computed by calculating loads and deflections corresponding to points B and D in Fig. 6.1a, and joining those values by straight lines. Limiting load values for B and D can be computed from customary procedures using locations of the dowel bars at the base of the column. Calculation of the lateral deflections is more complex.

Shown in Fig. 6.12a is an idealized representation of the geometry of the column and its connection to the base beam. In Fig. 6.12a, AA is the location of the beam to column base connection. The curvatures at that section are controlled by the locations of the dowel bars. By contrast, at BB curvatures are controlled by the locations of the column bars. Between AA and BB it is not clear what controls curvatures. The number of bars is double that at either AA or BB but the effectiveness of any bar at any location depends on the stress that can be developed in the bar at that location. The measured load–rotation relationships of Figs. 5.14 through 5.19 show, for the intermediate and uppermost gage lengths, relatively little rotation. By contrast the displacement profiles of Figs. 5.8 through 5.12 show substantial rotation above the splice length. Thus, test observations suggest that rotations were severely restrained in the splice length.

For simplicity, for calculation of deflections, curvatures at and prior to yield are assumed to be as shown in Fig. 6.12c. The deflection for first yield, δ_y, due to flexural effects only, may then be estimated as

$$\delta_y = \frac{\phi_B\ (l - l_d)^2}{3} + \phi_y l_p(1 - 0.5 l_p) \tag{6.1a}$$

where ϕ_B is the curvature at BB for a section having bars at the locations of the column bars. Its value is computed using the section moment, M_B, shown in Fig. 6.12b; ϕ_y is the curvature at AA for a section having bars at the locations of the dowel bars. Its value is computed using the section moment, M_A, as shown in Fig. 6.12b. M_A is the yield moment for a section having bars at the locations of the dowel bars; and l_p is taken as 225 mm (9 in.). The flexural cracks that developed in the columns had a spacing very close to the vertical spacing of the hoop steel. That spacing was 250 mm (10 in.) except at the base of the column where the first hoop was located 100 mm (4 in.) above that base. Thus, l_p is taken as the distance between the base and the mid point between the first and second hoops. From Fig. 6.12 it can be seen that there was assumed to be zero curvature over the length $(l_d - l_p)$ between the location where the dowel bars terminated and the concentrated rotation at AA. That length is 864 mm (34 in.). That assumption is consistent with the measured rotation results for the intermediate and uppermost gage lengths shown in Figs. 5.14 through 5.19. The rotations measured at those locations are very small until the maximum load is reached or exceeded. Further, some of the measured rotations for the intermediate gage length, although small, are of opposite sign to those expected for the given direction of loading.

Once yielding develops at AA, curvatures, for a column with continuous bars, would spread up the column, extending at the ultimate flexural capacity, over a plastic hinge length that is between 0.5 and 1.0 times the member depth. However, for the test columns the rotation results of Figs. 5.14 though 5.19 clearly show that did not occur. Therefore, the assumptions for the curvature distributions of Fig. 6.12c were retained for the post–yield range also, becoming as shown in Fig. 6.12d. The tip displacement at the maximum flexural capacity, Δ_{pr}, as shown in Fig. 6.12e, is then given by:

$$\Delta_{pr} = \delta_y + \delta_p \tag{6.1b}$$

where δ_y is given by Eq. (6.1a) and δ_p is taken as

$$\delta_p = (\phi_{pr} - \phi_y) l_p (l - 0.5 l_p) + (\phi_B' - \phi_B) \frac{(l - l_d)^2}{3} \quad (6.1c)$$

where ϕ_{pr} is the curvature at AA corresponding to the predicted strength for a section having bars at the locations of the dowel bars, and ϕ_B' is the curvature at BB for the moment M_B acting at that section when the moment at AA is the maximum moment M_M. Again M_M and ϕ_{pr} are computed using properties of the section based on the dowel bar locations and M_B and ϕ_B are computed using properties for the section based on the column bar locations.

6.5.2.1 Prediction of Measured Load Capacities

For field test columns, the mechanical properties of the reinforcing steel and of the concrete differed markedly from the nominal properties used in their original design. Further the locations of the dowel bars also differed markedly from those shown on the design plans. For the laboratory test columns, while the mechanical properties of the reinforcing steel were known in advance, the measured concrete strengths were greater than those assumed in the design of the columns. To discuss the significance of the test results, a precise prediction of the first bar yield, nominal and probable strength capacities for each column, for cross–sections based on the locations of the dowel bars, and of first bar yield for cross–sections based on the locations of the column bars, was performed using a specially adapted analysis program termed CIRCLE.

The program CIRCLE was developed by Professor William L. Gamble to obtain the moment–curvature response of a circular reinforced concrete column under combined axial and lateral loads. The following assumptions are made in that program: 1) plane sections remain plane due to bending; and 2) there is no bond slip between the longitudinal reinforcing steel and the surrounding concrete. The program requires the user to input the stress–strain relationships for both steel and concrete, the ultimate strain of the concrete, and the location of each steel bar.

For the columns tested in this study, an ultimate concrete strain of 0.004 was used in the analysis because the confinement provided by the poorly anchored hoop steel would be minimal and applicable only to the core concrete located within the hoop. The stress–strain curve for concrete suggested by Hognestad (1951), as shown in Fig. 6.13, was used.

Computations for the strengths of the field test columns were based on the measured steel stress–strain curve for the steel in those columns, as shown in Fig. 3.17, (f_y equal to 325 N/mm^2 (47,000 psi)), a concrete strength, f'$_c$, of 41 N/mm^2 (6,000 psi), a concrete modulus of 29.7 N/mm^2 (4,300 ksi) and the dowel bar locations shown in Figs. 3.13 through 3.16. The corresponding calculated yield, nominal, and maximum probable lateral loads and the associated curvatures are listed in Table 6.5a. Also listed are the curvatures, ϕ_B and ϕ_B', for section BB having bars at the locations of the column bars. The moment curvature relationships for each of the field test columns, for the dowel bar locations, are plotted in Appendix E.

For computations of the strengths of the laboratory test columns, the measured steel stress–strain curve of Fig. 4.7a, (f_y equal to 456 N/mm^2 (66,000 psi)), a concrete strength, f'$_c$, of 41 N/mm^2 (6,000 psi), a concrete modulus of 29.9 N/mm^2 (4,340 ksi) and the dowel bar locations shown in Figs. 4.4b through 4.4g were used. The resultant calculated yield, nominal, and maximum probable lateral loads, as well as associated curvatures, are listed in Table 6.6a. Also listed are the curvatures, ϕ_B and ϕ_B', for section BB having bars at the locations of the column bars. The moment curvature relationships for each of the laboratory test columns, for the dowel bar locations, are also plotted in Appendix E.

6.5.2.2 Predicted Deflections for Flexural Behavior

The calculated curvature values in Tables 6.5a and 6.6a were used in combination with Eqs. (6.1a), (6.1b) and (6.1c) to calculate the first yield and maximum displacements for each column for flexural behavior. The resultant displacement values are listed in Table 6.5b for each of the field test columns and in Table 6.6b for each of the laboratory test columns, respectively. The resultant predicted load–deflection relationships for a "flexural result" are shown by short broken lines for each column in Figs. 6.2 through 6.11. Also shown on each "flexural result" are the loads corresponding to the predicted nominal capacity, P_n, and the predicted probable flexural strength, P_{pr}.

6.5.3 Additional Deflection Caused by Bond Slip

The additional deflection caused by bond slip was computed as shown in Fig. 6.14. The original undeformed position of the column is represented by broken lines. Under the applied loading

bond slip of the reinforcement at the base of the column results in a concentrated rotation θ at the base of the column that increases the lateral deflection by an amount of Δ_1. Fig. 6.15 illustrates how the rotation θ can be computed once a bar force–loaded end displacement relationship is established for the dowel bars. In Fig. 6.15, AA and A'A' represent column longitudinal bars that terminate at the column–base beam interface, BB, CC, B'B' and C'C' represent dowel bars that cross that interface and have locations as shown in Fig. 6.16. Based on the known stress–strain relationships for the concrete and steel, and strain compatibility considerations, the distance d_t from the neutral axis depth xx to the center of the extreme tensile bar B and the force in that bar can be computed for a given lateral force, P. For the test specimens extreme tensile bar stress values and neutral axis depth values, kd, were computed, as described previously, using the program CIRCLE. Thus, those values were controlled by flexural considerations only and also ignored deformation changes caused by the fully reversed cyclic loading. Values for the neutral axis depth at yield and at the probable flexural strength are listed in Table 6.7a for each of the field test columns and in Table 6.7b for each of the laboratory test columns, respectively. From Table 6.7 it can be seen that the neutral axis depth decreases markedly between the yield and probable flexural strength.

Application of a force to a bar embedded in concrete causes a displacement of the bar at its loaded end. The amount of that displacement depends on the bar's stress–strain properties and its bond stress–slip properties. The rotation θ in Fig. 6.15 was assumed to be controlled by the loaded end displacement–bar force relationship for bar B. If the loaded end displacement for bar B for a given bar force is δ then θ is given by

$$\theta = \frac{2\delta}{d_t} \tag{6.2}$$

The displacement for bar B across the interface between the base beam and the column is 2δ because that bar must anchor itself both in the column and the base beam.

Likely bar force–loaded end displacement relationships for a typical dowel were computed using the bond stress–slip relationships reported by Hawkins and Lin (1979), Ueda et al (1986) and Hawkins et al (1987). Based on the results of reversed cyclic laboratory tests on No. 10, No. 8 and

No. 6 bars anchored in well confined concrete, Hawkins and Lin (1979) proposed that for a bar force, F, less than yield, the loaded end displacement, δ, could be computed approximately by the following empirical expression:

$$\delta = \frac{F}{K} \tag{6.3a}$$

where $$K = (1,250 d_b^{\,2} + 1,900)\sqrt{\frac{f_c'}{3,200}} \quad \text{(kips / in)}$$

When the bar force exceeded its yield force, K decreased to K_s, and

$$\frac{K}{K_s} = \frac{E_s}{E_{sr}}$$

where E_s is the modulus of elasticity of the steel in the bar and E_{sr} is its strain hardening modulus. Thus, for a bar force F greater than the bar force F_y for yield, the loaded end displacement δ is given by:

$$\delta = \frac{F_y}{K} + \frac{(F - F_y)}{K_s} \tag{6.3b}$$

A more comprehensive treatment of the loaded end displacement–bar force relationship has been provided by Ueda et al (1986) and Hawkins et al (1987). For a bar subjected to high intensity reversed cyclic loading, as is the case for the dowel bars in the test specimens, the appropriate bond stress–slip relationship can be idealized, based on their findings, as shown in Fig. 6.17. For monotonic loading to failure γ is unity and τ_{max}, τ_y, S_o and S_y are given by the following expressions

$$\tau_{max} = \left(\frac{f_c'-2,300}{300}\right)^{\frac{2}{3}} \times 10^3 \nearrow 5,000 \quad \text{psi} \tag{6.4a}$$

$$\tau_y = 0.1 f_c' \text{ or } 400 \text{ psi, whichever is smaller} \tag{6.4b}$$

$$S_o = 0.002\left(\frac{f_c'}{d_b}\right)^{\frac{1}{3}} + \frac{70}{f_c' d_b} \tag{6.4c}$$

$$S_y = 0.5 \times \text{lug spacing} \tag{6.4d}$$

For the properties of the concrete used in the test columns, (f_c' of 6,000 psi), and the characteristics of the No. 11 bars used for the dowel bars; the following values apply

τ_{max} = 5,338 psi $\not>$ 5,000 psi, use 5,000 psi

τ_y = 400 psi

S_o = 0.04 in.

S_y = 0.5 in.

Under reversals that stress the bar inelastically both in tension and compression, a lower bound to the bond stress slip relationship becomes that represented by the broken lines OBDE and OCFE in Fig. 6.17. Relationship OBDE is the response for a non–yielding bar and OCFE is the response for a bar that starts to yield at C. The maximum bond stress that can be developed, τ_{max}, is a function of the intensity of the reversed loading, and the range of that loading. The intensity and range have no effect until the maximum loading results in a shear stress exceeding 0.75 τ_{max}. Then, the range in the loading, zero to a maximum, maximum to fully reversed minimum, etc. has a major effect. For the former, there is no decrease in τ_{max}. However, for the latter there is a major decrease in τ_{max}, with the maximum bond stress decreasing to 0.75 τ_{max}. Further, once the bar yields the maximum bond stress, may never reach even 0.75 τ_{max}, and, as represented by point C in Fig. 6.17, can decrease from whatever its value is before yielding to τ_y. Thus, the portion BD of the response in Fig. 6.17 can be completely suppressed if the bar yields before B is reached.

For the No. 11 bars of the laboratory test specimens, the relationship between bar force and loaded end displacement can be determined as follows: when, as shown in Fig. 6.18a, a force, P, is applied to the attack end of a bar, bond stresses are created along the embedded length of the bar. Unknowns can be described as the magnitude of the bond stress at the attack end, the shape of the stress distribution and the length over which bond stresses are created within the specimen. Shown in Fig. 6.18b is a free body diagram of a typical bar element of length dx. Bond stresses are assumed to be uniformly distributed over the surface of this element. Axial equilibrium gives:

$$\tau = \frac{A_b}{\pi d_b}\frac{d\sigma}{dx} \tag{6.5}$$

where:

τ = bond stress;

σ = steel stress;

A_b = bar cross–sectional area;

d_b = bar diameter.

The bond stress, τ, is dependent on the local slip, δ, and that relationship can be formulated as

$$\tau = f(\delta) = k_1\delta \quad \text{for} \quad \delta \leq S_o \tag{6.6a}$$

and

$$\tau = f(\delta) = 400 \text{ psi for } \delta \geq S_o \text{ or } \delta \text{ for bar yield} \tag{6.6b}$$

where:

$$\delta = \int_0^x \epsilon(\xi)d\xi \quad \text{if bond stress has not penetrated to the tail end} \tag{6.7}$$

and the force, P, is computed as

$$P = \int_0^x \tau \ \pi d_b d\xi \tag{6.8}$$

By substituting δ from Eq. (6.7) into Eq. (6.6) and then equating Eqs. (6.5) and (6.6), and substituting τ into Eq. (6.8), a set of linear second–order differential equations can be obtained. The bond stress distribution, the steel stress distribution, and the load–displacement relationship at the attack end of the bar can be determined by solving those differential equations.

A detailed analysis using the foregoing approach is not utilized here, because it adds little to an understanding of the problem examined in this document. However, the basic result, from the information presented by Hawkins et al (1987) and Harajli (1994) namely that there is a reduction in capacity that depends on the magnitude of the maximum bond stress, and the range of the reversing stresses, is utilized in the next section.

Shown in Table 6.8 are bar force–loaded end displacement values calculated from Eq. (6.3b). Column 1 lists the bar stress, column 2 lists the bar force corresponding to that stress, and column 3 lists the ratio of that stress to the yield stress for the bar. Column 4 lists the loaded end displacements. Displacements increase rapidly once the bar yields. The values of Tables 6.8a and 6.8b differ because bar yield stresses, strain hardening and concrete strength characteristics differ.

Based on the previous discussion, additional deflections caused by bond slip for each column are computed and listed in Table 6.9. In Figs. 6.2 through 6.11, the resultant idealized load–deflection results are termed "flexural and slip result" and are shown as broken lines of long length.

6.5.4 Prediction of Lap Splice Capacity

For lap splices arranged as those in the test columns, lap splice failure can occur in two ways: a splitting crack can develop along the length of the outermost bar and cause it to fail in bond or cracks can propagate between the lap spliced bars, causing a loss of load transfer between them. The failure mode that controls depends on the details of the variables in the cross–section as discussed in this section.

A detailed study of bond failure has recently been completed by Darwin et al (1995a). Based on the dummy variables analysis of 166 specimens in which the bars were confined by transverse reinforcement, the following equation was developed for calculations of the maximum force for bond failure in a spliced bar in a member with a rectangular cross section, (Fig. 1.2), and subject to monotonic loading to failure:

$$\frac{T_b}{(f'_c)^{\frac{1}{4}}} = \underbrace{[63l_d(c + 0.5d_b) + 2130A_b](0.1\frac{c_M}{c_m} + 0.9)}_{\text{Concrete Contribution}} + \underbrace{2226t_r t_d \frac{N_{tr}A_{tr}}{n_b}}_{\text{Steel Contribution}} + 66 \qquad (6.9a)$$

Eq. (6.9a) is based on a model in which the maximum bond force in a developed or spliced bar, T_b, is expressed as a "concrete contribution", T_c, and a "steel contribution", T_s. The "steel contribu-

tion" depends on the characteristics of the confining steel, A_{tr}, placed transverse to the developed or spliced steel, A_b.

$$T_b = T_c + T_s = A_b f_s \tag{6.9b}$$

The notations in Eq. (6.9a) and Eq. (6.9b) that follows later are:

A_b = longitudinal bar area (in^2);

f_s = steel stress in longitudinal bar at splice failure (psi);

f'_c = concrete compressive strength (psi);

d_b = nominal longitudinal bar diameter (in);

l_d = splice length (in);

c_M, (c_m) = maximum (minimum) value of c_s or c_b, ($c_M/c_m \leq 3.5$), (in);

c_s = minimum of (c_{si} + 0.25 in., c_{so}) or minimum of (c_{si}, c_{so}), (in.);

c_{si} = one–half of clear spacing between spliced bars, (in.);

c_b = bottom cover for spliced bars, (in.);

c_{so} = side cover of reinforcing bars, (in.);

N_{tr} = number of transverse reinforcing bars (stirrups or ties) crossing l_d;

A_{tr} = area of each stirrup or tie crossing the potential plane of splitting (in^2);

The terms t_r and t_d introduce the effects of the relative rib area, R_r, and the bar size, d_b, respectively. Their values are 0.927 and 1.295 for No. 11 (35.8 mm) bar, and are calculated by the following Eqs. (6.10) and (6.11)

$$t_r = 9.6R_r + 0.28 \tag{6.10}$$

$$t_d = 0.72d_b + 0.28 \tag{6.11}$$

Eqs. (6.10) and (6.11) were based on an analysis of test results for 70 splice specimens containing No. 5, No. 8 and No. 11 (15.9, 25.4 and 35.8 mm) bars confined by transverse reinforcement with

relative rib areas, R_r, ranging from 0.065 to 0.14. Details of the development of Eqs. (6.10) and (6.11) are given in Darwin et al (1995b).

The notation for c_{si}, c_b and c_{so} is illustrated in Fig. 6.19. Values used in Eq. (6.9a) depend on the mode of bond failure. n_b is the number of longitudinal bars being spliced along the plane of splitting. The value of n_b is determined by the smaller of c_b or c_s. If c_b controls, the plane of splitting passes through the cover and n_b equals unity. That situation is shown in Fig. 6.19a. If c_s controls, the plane of splitting intersects all of the bars and n_b equals the total number of bars spliced at one location. That situation is shown in Fig. 6.19b where n equals two.

Eq. (6.9a) was derived from the results of tests on beams of rectangular cross–section loaded monotonically to failure, and for about 17 percent of the specimens the bars yielded before failure occurred. For a rectangular beam with bars located in a manner analogous to those of the bars in the test columns. Eq. (6.9a) clearly covers, as illustrated in Fig. 6.20, both the possibility of a splice plane shearing failure mode and a cover splitting failure mode. To adapt Eq.(6.9a) to the field and laboratory column test specimens, it is necessary to modify the c_{si}, c_m, c_M, c_b, etc., terms in a manner consistent with the properties of those specimens. Shown in Fig. 6.21 are the splice plane shearing and cover splitting failure modes for the test specimens, analogous to the same modes for a rectangular beam. Clearly the critical dimensions relate to the properties of the column bars, (open circles), and not the properties of the dowel bars, (shaded circles), and the following transformations apply

$$c_m = c \text{ and } c_M = 0.5\ S_c + 0.25 \text{ in.}$$

where:

c = cover over extreme tension bar, (in.);

S_c = clear spacing in circumferential direction between columns bars, (in.).

For the test specimens Eq.(6.9a) then becomes

$$\frac{T_b}{(f'_c)^{\frac{1}{4}}} = \underbrace{[63l_d(c + 0.5d_b) + 2130A_b]}_{\text{Splice Length and Cover Term}}\underbrace{(0.1\frac{(0.5S_c + 0.25)}{c} + 0.9)}_{\text{Bar Spacing Term}} + \underbrace{2226t_r t_d \frac{N_{tr}A_{tr}}{n_b}}_{\text{Transverse Steel Term}} \quad (6.9b)$$

None of the specimens used to derive Eq. (6.9a) were reversed cyclically loaded to failure whereas all the test columns were subjected to such loading. For the test columns, therefore, a reduction in bar capacity, beyond that given by Eq. (6.9b), was to be expected as discussed in Section 6.5.3. Eq. (6.9b) applies to the column longitudinal bars and the critical location will be where its stress is a maximum, namely at the location in the column where the dowel bars terminate. A reduction in the maximum bond stress that can be developed by the column longitudinal bars develops once the peak reversing stress exceeds 75 percent of the maximum stress for bond failure for monotonic loading. Based on the information presented by Hawkins et al (1987) and Harajli (1994), for test columns, the reduction factor, γ, on the maximum stress is taken

For $\tau > 0.75\ \tau_{max}$,

$$\gamma = 0.9 - 5\ (\delta - 0.75\ S_o) \geq 0.65 \quad (6.12)$$

The term $5\ (\delta - 0.75\ S_o)$ does not start to apply until δ exceeds $0.75\ S_o$ for both positive and negative loading.

Eq. (6.9b) was used to calculate the total bond force, and the corresponding maximum stress for the critical column bar in each circular column. The resultant calculated maximum bar stresses are listed in Tables 6.10 and 6.11a for each of the four field columns, and each of the laboratory columns, respectively. In each of those tables the relative contributions of the concrete, A times B, and the transverse steel C, can be seen from the quantities for A, B and C listed in columns 2, 3 and 4, respectively. For all columns it can be seen that the strength of the columns is dependent primarily on the contribution of concrete because of the paucity of transverse reinforcement. Further, it should be appreciated that the transverse reinforcement in both the field and laboratory columns was inadequately anchored whereas the use of Eq. (6.9b) assumes that steel to be adequately anchored. How-

ever, whether that transverse steel is adequately anchored, or not, the relative values for A times B, and C in Tables 6.10 and 6.11a show that the predicted strengths would not be markedly affected.

From the values in Tables 6.10 and 6.11a, the column bar stresses for failure, f_s, can be ranked from largest to smallest as:

for field columns

$$f_{sC15S} > f_{sB14S} > f_{sC17S} > f_{sB18S}$$

and

for laboratory columns

$$f_{sB-3} > f_{sA-3} > f_{sB-2} > f_{sB-1} > f_{sA-2} > f_{sA-1}$$

Those orders are the same as the ranking for the order of performance as measured in the tests and discussed in Section 6.4. This result verifies that use of Eq. (6.9), or a derivative, is reasonable for prediction of the strength of the test column.

For the field tests, the lack of time and the operating conditions prevented attachment of strain gages to either the column or dowel bars. Therefore, no comparisons can be made between predicted and measured failure stress. For all six laboratory columns, the measured maximum bar stresses, including column bar and dowel bar, were calculated based on the measured maximum strain values reported in Table 5.2 and the stress–strain curve of Fig. 4.7a. The resultant values are listed in Table 6.11b along with the gage number and the load to which that strain corresponds. The predicted column bar stress values of Table 6.11a are compared with the measured stresses of Table 6.11b in Table 6.12. The measured column bar stresses are always smaller than the predicted stresses with the difference increasing as the the intensity of the reversed cyclic loading increased.

Columns A–1 and B–1 were subject to the least numbers of cycles prior to their failure and the maximum bar stress predicted exceeds 75 percent of the yield stress. Consistent with Eq. (6.12), the capacities could be expected to decrease to 90 percent of the predicted strengths. Similarly for A–3 and B–3, with the greatest intensity of reversed cyclic loading and bar stresses predicted to exceed the yield stress, strengths approach the lower limit of 0.65 predicted by Eq. (6.12).

From the moment curvature analyses made previously using the program CIRCLE and the computed column capacities, the associated bar stresses for each of the laboratory test columns for the yield load, P_y, and the probable flexural strength, P_{pr}, were computed. Results are listed in Table 6.13 with the columns in set 1 showing conditions for the dowel bars and those in set 2 showing conditions for the column bars. In the latter case load and stress values are listed for yield only for the laboratory column. Those results are also shown in the form of relationships plotted in Fig. 6.22. Fig. 6.22a shows clearly that for the field columns the column bars are anticipated to reach yield before the dowel bars reach their probable flexural strength. Fig. 6.22b shows clearly that for the laboratory columns the column bars are never anticipated to reach yield before the dowel bars reach their probable flexural strength.

Based on the results of Table 6.13, for the action of the maximum measured load for each laboratory column, the corresponding column and dowel bar stresses were computed. Results are listed in Table 6.14. Comparison of the stress values of Tables 6.11b and 6.14 shows that the computed column bar stresses for each column are considerably smaller than the measured stresses. Ratios of measured to computed column bar stresses, listed in column 5 of Table 6.14, range from 1.05 to 1.21 and average 1.12. Further, the agreement between measured and computed values is much better for columns B–1 through B–3, for which the average is 1.07, compared to columns A–1 through A–3 for which the average is 1.16. By contrast the agreement between measured and computed dowel bar stress values is much better than the agreement for column bar stresses. Ratios of measured to computed dowel bar stresses, listed in column 8 of Table 6.14, average 0.98 and there is no significant difference between the results for the A and B columns. The higher measured stresses for the column bars, than those computed, suggest some internal redistribution of stresses between reinforcing bars and concrete that is not been identified by assuming that plane sections remain plane.

The predicted column bar stresses in Tables 6.10 and 6.11a, for a bond failure, together with the results from moment curvature analysis for column bar locations in Table 6.13, were used to predict maximum lateral load values for each test column. Those loads are listed in column 5 of Table

6.15. In Table 6.15 the maximum load measured in each test is listed in column 2 and the load for yield of the column bars at location B, at the end of the dowel bars, is listed in column 3. The column bar stress for failure, based on the modified Darwin Eq. (6.9b), is listed in column 4. From Eq. (6.12), the reduction in bond stress due to fully reversed cyclic loading is about 0.7. If that value is applied to the computed bar stresses of column 4, a value can be computed for the maximum lateral load by proportion and is listed in column 5. Column 6 lists the maximum computed load for a flexural failure. That load is based on the capacity of the dowel bars and is taken from column 5 of Table 6.7b. Listed in column 7 are ratios of maximum measured to computed capacities where the latter is taken as the lesser of the values in columns 5 and 6. Ratios in column 7 range from 0.945 to 1.085 and average 1.003 for laboratory columns. For the field columns, the ratios range from 0.964 to 1.126 and average 1.0475. The lesser of the values from columns 5 and 6 is shown as a horizontal line, representing the predicted ultimate capacity, in Figs. 6.2 through 6.11.

The field tests involved columns with much more complex layouts of the bars within the cross–section than the laboratory columns. Therefore, more approximations had to be made in idealizing those bar positions for input into program CIRCLE. The result that the simple model proposed in this section also predicts the behavior and strength of the field columns, validates the appropriateness of that model for predicting overall behavior of bridge columns with inadequate length splices at the column to foundation connection.

The flexural capacity of each column is controlled by the dowel bar's locations, and the bond strength of the lap splice (column bar stress) is governed by the column bar's locations. There is no simple mechanism currently to model the transfer of force or stress from column bar to dowel bar. Some type of 3–dimensional model based on rotating truss type element, such as that proposed by Xiao et al (1995), might be appropriate.

6.6 Comparisons between Predicted and Measured Load–Deflection Curves

For the field test columns, as apparent in Figs. 6.2 through 6.5, the measured maximum loads for columns B18S, B14S and C17S never reached the calculated nominal flexural capacities for those columns. For column C15S the nominal flexural capacity was reached, and the measured max-

imum load was close to the calculated probable flexural strength. The predicted initial stiffnesses for all four columns matched reasonably well with the measured stiffnesses and the additional deflections are 20 percent or less of the deflections caused by flexure.

For each of the field test columns, the predicted and the measured maximum loads were in good agreement, (see Table 6.15a). By contrast, the predicted deflection at maximum load was smaller than the measured deflection at maximum load because all failures were in bond. For columns, B18S, and C17S, the measured maximum displacements, are less than the measured maximum displacements for the other two columns, B14S and C15S. It is significant that B18S and C17S were 1.37 m (54 in.) diameter columns with 1.81 percent and 1.55 percent column longitudinal reinforcement, while B14S and C15S were 1.22 m (48 in.) diameter columns with only 1.47 percent axial reinforcement. Clearly the responses for the latter were controlled more by flexural than bond considerations. For columns B18S and C17S the reverse is true.

For the laboratory test columns, as apparent in Figs. 6.6 through 6.11, the measured maximum loads for columns A–1 and A–2 never reached the predicted nominal capacities, and none of the columns reached their predicted probable flexural capacity. The predicted and the measured maximum loads for each of the laboratory columns were in good agreement (see Table 5.15b).

For columns A–1 and B–1 with only 12.7 mm (one half inch) cover and no separation between column and dowel bars, both the predicted response, including slip effects, and the measured curves matched reasonably well until about 40% of the calculated first yield load, P_y. However, for applied loads greater than $0.40P_y$, and until column failure, the measured displacements were all greater than the calculated values. Because both failures were in bond and the circumferential spacing of the column bars for B–1 was larger than that for column A–1, the measured ultimate capacity of column B–1 is larger than that of A–1. For column A–1 the predicted ultimate deflection, corresponding to the intersection of the predicted load–deflection response curve (broken line) and the predicted ultimate capacity line, is only 52 percent of the measured ultimate deflection even though both measured and predicted ultimate strengths agree closely. By contrast for column B–1 the predicted ultimate deflection at maximum load, 40 mm, agrees more closely with the measured deflec-

tion at maximum load of 48.8 mm.

For columns A–2, B–2 with the same small cover of only 12.7 mm (one half inch) and deeper dowel bars, the circumferential spacing of the bars for column B–2 was larger than that for column A–2, and therefore, the measured ultimate capacity for column B–2 was larger than that for A–2 because both had bond failures. For B–2 the initial stiffness was in good agreement with the predicted stiffness and the measured ultimate deflection at maximum load was in good agreement with the predicted ultimate deflection. The agreement is also reasonable for A–2 although the predicted ultimate deflection is only 81 percent of the measured deflection at maximum load.

For columns A–3 and B–3, with 51 mm (2 inch) cover and the maximum separation between column and dowel bars, the agreement between measured and predicted deflections for the complete range of behavior is good and the best of all three specimen pairs. That result is reasonable since the behavior of those two specimens is dominated by flexural effects (see Table 6.15b).

6.7 Concluding Remarks

In this Chapter a simple model has been developed for predicting the maximum load and associated deflection of each test column. That model provides a good prediction of maximum loads for all columns (see Tables 6.15a and 6.15b); also that model provides a conservative prediction of deflections at given loads for all columns failing in bond and a realistic prediction of deflections at given loads for all columns failing in flexure.

CHAPTER 7

SUMMARY AND CONCLUSIONS

7.1 Summary

In the early 1960's bridge columns were constructed with the longitudinal column steel spliced with 30 bar diameter or less lap lengths to dowel bars protruding out of the column's footings. Experience and testing since that date have demonstrated the inadequacy of such lap lengths for intense seismic loadings. In 1993 and 1994 field tests conducted for the Illinois Department of Transportation verified that finding and examined alternatives for strengthening such splices. However, after those tests were complete it was discovered that, in contrast to the details shown on the design drawings, there were often large separations between column and dowel bars in the lap region. The effect of those separations on the measured responses was not obvious. Therefore, a laboratory study was undertaken to determine the effects of bar spacing, bar lap separation and concrete cover on the behavior and strength for fully reversed cyclic loading of columns having non-contact lap splices at their maximum moment sections.

A literature review found that there was little existing information on the behavior of non-contact lap splices subject to reversed cyclic loading. While Darwin et al. (1995a) had developed a formula, Equation (6.9a), for calculating the maximum bar stress, or bond force, that could be developed by a spliced bar under monotonic loading, no corresponding formula existed for lapped bars subject to reversed cyclic loading. The most relevant available information was that developed by Hawkins et al. (1988) for bond slip movements of well anchored bars. A combination of those two results is used in Chapter 6 to develop a procedure for predicting the likely overall performance of bridge columns with inadequate length lap splices at their base.

The field work that resulted in this study involved lateral load testing of four as-built large circular columns which were parts of existing bridge piers. The results of those tests were reported in Chapter 3. The field test results suggested that bar cover, bar lap separation and spacing were critical parameters affecting the behavior of columns with non-contact lap splices at their maximum moment sections. However, due to irregularities in reinforcement details for the field columns, it was not obvious which parameter was important. Therefore, the laboratory investigation reported in Chapter 5 was undertaken to examine the effects of concrete cover, bar spacing and bar lap separation on the behavior of non-contact lap splices. To be able to correlate the laboratory test results directly with the field column results, the laboratory columns were designed to have their characteristics dominated by flexural deformations and to have longitudinal bar sizes, ((#11 (35.8 mm diameter), as well as the lap splice lengths, (1.09 m (43 in.)), the same as those in the field columns. A total of six half-scale columns were made and tested to failure in the Newmark Civil Engineering Laboratory.

7.2 Conclusions

(1) The simple model described in Chapter 6 can be used to provide reasonable predictions of the response to fully reversed cyclic loadings of bridge columns with inadequate length lap splices at the column to foundation connection. For such predictions account must be taken of the concentrated rotation occurring at the connection due to bond slip of the reinforcing bars. For a well anchored bar with cover exceeding 625 mm (2.5 inches), Eq. 6.3 can be used to provide reasonable predictions of that slip. For bars with lesser cover, greater slips can be expected than those predicted by Eq. 6.3;

(2) For both the laboratory and field tests, lap splice failure was caused by vertical splitting along the line of the main longitudinal reinforcing bars of the column. In the literature

splice failures have also been reported as caused by a splitting crack that separates dowel and column bars. A similar crack was observed in the laboratory test columns, but did not seem to be the cause of failure;

(3) The load or bond failure depended on two factors: the tensile force developed in the most high stressed bar and the degree of reversal of the applied forces. The bar force for failure could be predicted using Eq. 6.9b, a derivative of Darwin et al.'s Eq. 6.9a, multiplied by a reduction factor of 0.7 to account for the fully reversed loading ($-T_b$ to $+T_b$) applied to the most highly stressed bar. For less than fully reversed loadings, i.e. ($-0.5\ T_b$ to $+T_b$), the reduction factor should be varied as documented in Ueda et al. (1986).

(4) Comparisons of the measured and predicted load-deflection responses showed that the ductilities of the test columns were limited either by crushing of the concrete covering the main column bars at the base of the column or by bond failure of the lap splice. Hence, jacketing of columns subject to seismic forces may be necessary for any one of three reasons: inadequate lap splice strength; inadequate confinement of the compressed concrete in the maximum moment region, or inadequate column shear capacity;

(5) From this study the following conclusions can be drawn concerning the behavior of bridge columns with reinforcing bar layouts similar to those of the columns tested in the field and in the laboratory:

a) The bond strength of the lap splices for seismic loading is controlled by the anchorage characteristics of the column bars:

b) The locations and confinement for the dowel bars determine the flexural capacity of the column and the rotational characteristics of the column to foundation connection up to the maximum load;

c) The thicker the cover the better is lap splice performance:

d) The greater the circumferential spacing of the column bars the better is the lap splice performance;

e) An increase in cover thickness improves the performance faster than an increase in circumferential spacing of bars;

f) Increased separation between dowel and column bars does not change the lap splice capacity. The smaller internal moment arm for the dowel bars decreases the flexural capacity of the column to foundation connection, but the increased cover to the dowel bars allows them to develop a force greater than would be the case if the dowel and column bars were in contact.

(6) The ductility ratio for as built column C15S was close to four because the cover to the column bars was larger and those bars were more widely spaced than in columns B18S, B14S and C17S. Therefore, even when the lap length and transverse hoop spacing do not meet 1993 AASHTO seismic specifications, the ductility ratio for a given column may still be able to reach the value of five required by the AASHTO specification for multi-column piers.

7.3 Future Research

This research is the first to provide information about the behavior of non-contact lap splices at the maximum moment section of a cantilever member subjected to reversed cyclic loading. The present conclusions are based on a limited number of test results (four field tests

and six laboratory tests), that considered the effects on the behavior of non-contact lap splices of three parameters only. For a more comprehensive understanding of the behavior of such non-contact lap splices, the following additional parameters need study:

1) the effect of the transverse steel spacing;

2) the effect of bar size;

3) the effects of the cover and spacing when the cover does not control the plane of splitting;

and

4) the effect of lap length.

LIST OF REFERENCES

AASHTO Highway Sub-Committee on Bridges and Structures, "Standard Specifications for Highway Bridges," American Association of State Highway and Transportation Officials, Washington, DC, 1993.

ACI Committee 318, "Building Code Requirements for Reinforced Concrete (ACI 31X-89))," American Concrete Institute, Detroit, MI 1989.

ACI Committee 408, "Suggested Development, Splice, and Standard Hook Provisions for Deformed Bars in Tension," Concrete International, July 1979, p. 44-61.

ASTM Specification C 469 "Standard Test Method for Static Modulus of Elasticity and Poisson's Ratio of Concrete in Compression", Annual Book of ASTM Standards, Vol. 04.02, 1994, p. 238-241.

Chamberlin, S.J., "Spacing of Spliced Bars in Tension Pull-Out Specimens," ACI Journal, Proceedings Vol. 49, No. 4, Dec. 1952, p. 261-274.

Chamberlin, S.J., "Spacing of Spliced Bars in Beams," ACI Journal, Proceedings Vol. 54, No. 8, Feb. 1958, p. 689-697.

Chinn, J., Ferguson, P. M. and Thompson, J.M., "Lapped Splices in Reinforced Concrete Beams," ACI Journal, Vol. 52, Oct. 1955.

Darwin, D., Tholen, M. L., Idun, E. K. and Zuo, J., "Splice Strength of High Relative Rib Area Reinforcing Bars," SL Report No. 95-3, Structural Engineering and Engineering Materials, The University of Kansas Center for Research, Inc., Lawrence, Kansas, May, 1995.

Darwin, D., Zuo, J., Tholen, M. L. and Idun, E. K., "Development Length Criteria for Conventional and High Relative Rib Area Reinforcing Bars," SL Report No. 95-4, Structural Engineering and Engineering Materials, The University of Kansas Center for Research, inc., Lawrence, Kansas, May 1995.

Draft New Zealand Code of Practice for Reinforced Concrete Structures, DZ3101-1980, Part I, Chapter 5.

Fagundo, F., Gergely, P. and White, R. N., "The Behavior of Lapped Splices in R/C Beams Subjected to Repeated Loads," Report No. 79-7, Department of Structural Engineering, Cornell University, Ithaca, NY 1979.

Ferguson, P.M. and Breen, J.E., "Lapped Splices for High Strength Reinforcing Bars", ACI Journal, Vol. 62, No. 9, Sept. 1965, p. 1063-1078.

Goto, Y. and Otsuka, K., "Experimental Studies on Cracks Formed in Concrete around Deformed Tension Bars," The Technology Reports of the Tohoku University, Vol. 44, No. 1, June 1979, p. 49-83.

Harajli, M.H., "Development / Splice Strength of Reinforcing Bars Embedded in Plain and Fiber Reinforced Concrete", ACI Structural Journal, Vol. 91, No. 5, Sept-Oct. 1994, p. 511-520.

Hassan, F.M. and Hawkins, N.M., "Anchorage of Reinforcing Bars for Seismic Forces", SP-35, Reinforced Concrete in Seismic Zones, American Concrete Institute, Detroit, MI, p. 387-416.

Hawkins, N.M. and Lin, I., "Bond Characteristics of Reinforcing Bars for Seismic Loadings", Proceedings, Third Canadian Conference on Earthquake Engineering, Vol. 2, Montreal, Canada, June, 1979, p. 1225-1234.

Hawkins, N., Lin, I. and Ueda, T., "Anchorage of Reinforcing Bars for Seismic Forces", ACI Structural Journal, Vol. 84, No.5, Sept./Oct. 1987, p. 407-418.

Hawkins, N.M., Lin, I. and Jeang, F.L., "Local Bond Strength of Concrete for Cyclic Reversed Loadings", Bond in Concrete, P. Bartos, Editor, Applied Science, London, 1982, p. 151-161.

Hognestad, E., "A Study of Combined Bending and Axial Load in Reinforced Concrete Members", University of Illinois Engineering Experiment Station, Bulletin Series No. 399, Vol. 49, Nov.1951.

Lin, Y., Gamble, W.L. and Hawkins, N.M., "Testing of Bridge Piers, Poplar Street Bridge Approaches, East St. Louis, IL", Report to ILLDOT, Department of Civil Engineering, University of Illinois at Urbana-Champaign, Feb. 1994.

Lukose, K., Gergely, P. and White, R.N., "Behavior of Reinforced Concrete Lapped Splices for Inelastic Cyclic Loading," ACI Journal, Proceedings, V. 79, No. 5, Sept.-Oct. 1982, pp. 355-365.

Lutz, L.A. and Gergely, P., "Mechanics of Bond Slip of Deformed Bars in Concrete", ACI Journal, Vol. 64, No. 11, Nov. 1967.

Morita, S. and Kaku, T., "Splitting Bond Failures of Large Deformed Reinforcing Bars", ACI Journal, Vol. 76, No. 1, Jan. 1979, p. 93-110.

Panahshahi, N., White, R. N. and Gergely, P., "Compression and Tension Lap Splices in Reinforced Concrete Members Subjected to Inelastic Cyclic Loading," Report No.87-2, Department of Structural Engineering, Cornell University, Ithaca, NY 1987.

Park, R. and Pauley, T., "Reinforced Concrete Structures", John Wiley & Sons, New York, NY 1975, p. 396.

Park, R., "Evaluation of Ductility of Structures and Structural Assemblages from Laboratory Testing," Bulletin of the New Zealand National Society for Earthquake Engineering, Vol. 22, No. 3, Sept. 1989, p. 155-166.

Paulay T., Zanza, T.M. and Scarpas, A., "Lapped Splices in Bridge Piers and in Columns of Earthquake Resisting Reinforced Concrete Frames," Research Report 81-6, Department of Civil Engineering, University of Canterbury, Christchurch, New Zealand.

Sagan, V.E., Gergely, P. and White, R.N., "Behavior and Design of Non-Contact Lap Splices Subjected to Repeated Inelastic Tensile Loading," Technical Report NCEER-88-0033, National Center for Earthquake Engineering Research, State University of New York at Buffalo, Dec. 1988.

Shkurti, F.J., Lin, Y., Gamble, W.L. and Hawkins, N.M., "Testing of Bridge Piers, Poplar Street Bridge Approach, East St. Louis, IL," Report to IDOT on Project IHR-330, Department of Civil Engineering, University of Illinois at Urbana-Champaign, June 1995.

Signore, J.M., Abdel-Maksoud, M.G. and Dempsey, B.J., "Fiber Optic Sensing Technology in Rail Buckling Detection", TRB Conference, Washington, D.C., Jan. 1996, 20p.

Sivakamar, B., Gergely, P. and White, R. N., "Behavior and Design of R/C 'Column-Type' Lapped Splices under Inelastic Cyclic Loading," Report No. 82-11, Department of Structural Engineering, Cornell University, Ithaca, NY 1982.

Tepfers, R., "A Theory of Bond Applied to Overlapped Tensile Reinforcement Splices for Deformed Bars", Publication 73:2. Division of Concrete Structures, Chalmers University of Technology, Sweden, 1973.

Tocci, A. D., Gergely, P. and White, R. N., "The Behavior and Strength of Lapped Splices in R/C Beams Subjected to Cyclic Loading," Report No. 81-1, Department of Structural Engineering, Cornell University, Ithaca, NY 1981.

Ueda, T., Lin, I. and Hawkins, N.M, "Beam Bar Anchorage in Exterior Column-Beam Connections", ACI Journal, Vol. 83, No. 3, May-June 1986, p. 412-431.

Xiao, Y., Martin, G.R., Yin, Z. and Ma, R., "Bridge Column Retrofit Using SNAP-TITE Composite Jacketing for Improved Seismic Performance", Structural Engineering Research Report, No. USC-SERR95/02, University of Southern California, June, 1995.

TABLES

Table 3.1 Stress Values of Reinforcing Bars for Columns Tested in 1993

Sample	Bar Size	Yield Load (kN / kips)	Yield Stress (MPa / ksi)	Max. Load (kN / kips)	Max. Stress (MPa / ksi)	Column
1	#11	335 / 75.3	333 / 48.2	561 / 126.0	556 / 80.5	
2	#11	328 / 73.8	327 / 47.3	559 / 125.7	556 / 80.5	
3	#11	327 / 73.5	325 / 47.1	545 / 122.5	543 / 78.6	B18S
4	#11	323 / 72.5	321 / 46.5	543 / 122.0	540 / 78.2	B18S
5	#11	330 / 74.3	329 / 47.6	544 / 122.3	542 / 78.5	B18N
6	#11	329 / 74.0	328 / 47.4	544 / 122.3	542 / 78.5	B18N
7	#11	327 / 73.5	325 / 47.1	549 / 123.3	546 / 79.0	B14S
8	#11	323 / 72.5	321 / 46.5	546 / 122.8	544 / 78.7	B14S
Average		328 / 73.7	326 / 47.2	549 / 123.3	547 / 79.1	
9	#4	37.8 / 8.5	294 / 42.5	62.7 / 14.1	487 / 70.5	
10	#4	36.5 / 8.2	281 / 40.6	63.6 / 14.3	494 / 71.5	
11	#4	36.9 / 8.3	287 / 41.5	63.2 / 14.2	491 / 71.0	
Average		36.9 / 8.3	287 / 41.5	63.2 / 14.2	491 / 71.0	

Table 3.2 Stress Values of Reinforcing Bars for Columns Tested in 1994

Sample	Bar Size	Yield Load (kN / kips)	Yield Stress (MPa / ksi)	Max. Load (kN / kips)	Max. Stress (MPa / ksi)	Column
1	#11	325 / 73.1	323 / 46.8	536 / 120.5	533 / 77.2	C14S–1
2	#11	323 / 72.5	321 / 46.5	537 / 120.7	535 / 77.4	C14S–2
3	#11	331 / 74.4	330 / 47.7	526 / 118.2	524 / 75.8	C14N–1
4	#11	313 / 70.4	312 / 45.1	563 / 126.5	560 / 81.1	C14N–2
5	#11	338 / 76.0	337 / 48.7	545 / 122.6	543 / 78.6	C15S–1
6	#11	311 / 70.0	310 / 44.9	570 / 128.1	567 / 82.1	C15S–2
7	#11	335 / 75.4	334 / 48.3	535 / 120.2	533 / 77.1	C15N–1
8	#11	311 / 69.8	309 / 44.7	563 / 126.5	560 / 81.1	C15N–2
9	#11	327 / 73.5	325 / 47.1	553 / 124.3	551 / 79.7	C17S–1
10	#11	328 / 73.8	327 / 47.3	526 / 118.1	523 / 75.7	C17S–2
11	#11	333 / 74.8	331 / 47.9	557 / 125.2	555 / 80.3	C17N–1
12	#11	325 / 73.0	323 / 46.8	555 / 124.8	553 / 80.0	C17N–2
Average		325 / 73.1	323 / 46.8	547 / 123.0	545 / 78.8	

Table 3.3a Concrete Compressive Strength for Columns Tested in 1993

Concrete Location	Specimen Size (mm / in.)	Compressive Stress (MPa / ksi)
Layer with An Outside Face	51 x 51 x 102 / 2 x 2 x 4	34.9 / 5.05
Layer with An Outside Face	51 x 51 x 102 / 2 x 2 x 4	49.2 / 7.12
Layer Outside Main Bars	51 x 51 x 51 / 2 x 2 x 2	49.5 / 7.16
Layer Outside Main Bars	51 x 51 x 51 / 2 x 2 x 2	50.0 / 7.24
Layer Outside Main Bars	51 x 51 x 102 / 2 x 2 x 4	52.4 / 7.58
Inter Layer*	51 x 51 x 102 / 2 x 2 x 4	63.4 / 9.18

*layer between column and dowel bars

Table 3.3b Concrete Properties for Columns Tested in 1993

Sample	Cylinder Size (mm / in.)	f_c' (MPa / psi)	E (GPa / ksi)	Remark
B14S–1	102 x 203 / 4 x 8	44.7 / 6470	23.9 / 3460	
B14S–2	102 x 203 / 4 x 8	40.8 / 5900	23.9 / 3460	2 big honeycomb in top height
B18S–1	102 x 203 / 4 x 8	38.1 / 5510	20.2 / 2920	
B18S–2	102x171 / 4x6.75	40.8 / 5900		shorter cylinder
B18N–1	102 x 203 / 4 x 8	41.3 / 5980	26.0 / 3760	
B18N–2	102 x 203 / 4 x 8	32.6 / 4720	23.6 / 3420	2 big honeycomb at mid–height

Table 3.4 Concrete Properties for Columns Tested in 1994

Sample	Cylinder Size (mm / in.)	f_c' (MPa / psi)	E (GPa / ksi)	Remark
C14S	102 x 203 / 4 x 8	31.6 / 4580	23.1 / 3340	1 small honey-comb near 1 end
C14N	102 x 203 / 4 x 8	32.1 / 4640	27.4 / 3960	
C15S–1	102 x 203 / 4 x 8	41.5 / 6000	29.4 / 4250	1 cross crack in one end
C15S–2	102 x 203 / 4 x 8	40.4 / 5850	32.4 / 4690	
C15N	102 x 203 / 4 x 8	43.0 / 6220	33.0 / 4780	
C17S	102 x 203 / 4 x 8	33.4 / 4830	27.2 / 3940	
C17N	102 x 203 / 4 x 8	31.3 / 4530	22.3 / 3230	1 small honeycomb at mid ht.

Table 4.1 Parameters for Laboratory Columns

Column	S_c (d_b)	S_d (d_b)	L (mm / in.)	C (mm / in.)	α (Degree)
A–1	1.82	1.44	0 / 0	12.7 / 0.5	22
A–2	2.58	1.41	51 / 2	12.7 / 0.5	28
A–3	2.91	1.42	51 / 2	51 / 2	36
B–1	3.57	2.95	0 / 0	12.7 / 0.5	36
B–2	4.78	2.89	51 / 2	12.7 / 0.5	46
B–3	5.33	2.91	51 / 2	51 / 2	60

Where:
d_b——Main bar diameter;
S_c——Clear spacing between column bars;
S_d——Clear spacing between dowel bars;
L——Lap separation;
C——Concrete cover;
α——Angle of segment relevant to one pair of lapped bars.

Table 4.2 Stress Values of Reinforcing Bars for Laboratory Test Columns

Sample	Bar Size	Yield Load (kN / kips)	Yield Stress (MPa / ksi)	Max. Load (kN / kips)	Max. Stress (MPa / ksi)	Remark
1	#11	452 / 101.6	450 / 65.1	731 / 164.3	728 / 105.3	2rd batch
2	#11	450 / 101.2	448 / 64.9	727 / 163.5	724 / 104.8	2rd batch
3	#11	449 / 100.9	447 / 64.7	730 / 164.1	727 / 105.2	2rd batch
4	#11	456 / 102.5	454 / 65.7	735 / 165.2	732 / 105.9	1st batch
5	#11	460 / 103.3	457 / 66.2	735 / 165.2	732 / 105.9	1st batch
6	#11	452 / 101.6	450 / 65.1	734 / 165.0	731 / 105.8	1st batch
7	#11	452 / 101.7	451 / 65.2	733 / 164.7	730 / 105.6	1st batch
8	#11	447 / 100.5	456 / 66.0	733 / 164.8	730 / 105.6	1st batch
9	#3			56.5 / 12.7	798 / 115.5	1st batch
10	#3			56.1 / 12.6	791 / 114.5	1st batch
11	#3			57.4 / 12.9	811 / 117.3	1st batch
12	#3			55.2 / 12.4	779 / 112.7	1st batch
13	#3			54.3 / 12.2	766 / 110.9	2rd batch
14	#3			56.1 / 12.6	791 / 114.5	2rd batch
15	#3			54.7 / 12.3	773 / 111.8	2rd batch

Table 4.3a Concrete Properties for Category A Columns

Specimen Part	Cylinder No.	f_c' (MPa / psi)	E (GPa / ksi)	Age (Days)
Column A–1	1	43.7 / 6329	29.7 / 4300	78
	2	41.6 / 6023	29.0 / 4190	78
	3	38.8 / 5612	30.4 / 4400	78
	Average	41.4 / 5988	29.7 / 4297	78
Column A–1 Base	1	40.5 / 5865	30.7 / 4450	168
	2	41.3 / 5979	32.3 / 4670	168
	3	43.9 / 6359	32.0 / 4630	168
	4	43.8 / 6336	32.5 / 4700	168
	Average	43.9 / 6135	31.9 / 4613	168
Column A–2	1	42.3 / 6115	28.8 / 4170	94
	2	41.7 / 6037	28.5 / 4130	94
	3	37.2 / 5385	30.1 / 4350	94
	Average	40.4 / 5847	29.1 / 4217	94
Column A–2 Base	1	43.2 / 6254	29.5 / 4270	171
	2	39.2 / 5680	30.1 / 4360	171
	3	40.4 / 5848	30.3 / 4390	171
	4	45.3 / 6562	32.8 / 4750	171
	5	42.7 / 6186	32.5 / 4710	171
	Average	42.2 / 6106	31.1 / 4496	171
Column A–3	1	39.2 / 5672	28.5 / 4130	99
	2	44.7 / 6462	31.2 / 4510	99
	3	38.9 / 5628	29.2 / 4220	99
	Average	40.9 / 5921	29.6 / 4287	99
Column A–3 Base	1	31.0 / 4487	34.4 / 4980	162
	2	38.4 / 5562	31.5 / 4560	162
	3	32.9 / 4764	34.1 / 4930	162
	4	30.7 / 4447	34.8 / 5030	162
	5	34.0 / 4927	33.2 / 4810	162
	Average	33.4 / 4837	33.6 / 4862	162

Table 4.3b Concrete Properties for Category B Columns

Specimen Part	Cylinder No.	f_c' (MPa / psi)	E (GPa / ksi)	Age (Days)
Column B–1	1	43.8 / 6336	31.9 / 4620	62
	2	38.4 / 5558	30.2 / 4370	62
	3	40.8 / 5903	28.9 / 4180	62
	Average	41.0 / 5932	30.3 / 4390	62
Column B–1 Base	1	38.1 / 5516	29.9 / 4330	152
	2	43.6 / 6312	32.2 / 4660	152
	3	45.2 / 6543	32.5 / 4710	152
	4	42.5 / 6153	28.7 / 4160	152
	Average	42.4 / 6131	30.9 / 4465	152
Column B–2	1	45.7 / 6617	30.7 / 4450	86
	2	42.3 / 6115	30.5 / 4420	86
	3	43.1 / 6240	32.0 / 4630	86
	Average	43.7 / 6324	31.1 / 4500	86
Column B–2 Base	1	45.2 / 6544	32.1 / 4640	163
	2	36.3 / 5247	29.5 / 4270	163
	3	43.8 / 6341	31.3 / 4530	163
	4	44.1 / 6381	32.3 / 4680	163
	Average	42.3 / 6128	31.3 / 4530	163
Column B–3	1	43.0 / 6216	30.3 / 4380	106
	2	42.1 / 6092	29.2 / 4230	106
	3	43.9 / 6350	30.8 / 4460	106
	Average	43.0 / 6219	30.1 / 4357	106
Column B–3 Base	1	35.7 / 5170	33.7 / 4880	169
	2	38.9 / 5626	34.3 / 4960	169
	3	39.4 / 5705	32.5 / 4710	169
	4	33.6 / 4856	34.8 / 5040	169
	Average	36.9 / 5339	33.8 / 4898	169

Table 5.1 Calculated Results for the First Yield and Maximum Loads

Column	Yielding Load (kN)	Maximum Load (kN)
A–1	175.0	184.5
A–2	148.0	155.4
A–3	128.0	137.8
B–1	157.0	175.3
B–2	130.0	147.2
B–3	111.0	130.7

Note: Calculation based on assumed properties:

f_y = 456 N/mm^2 (66 ksi), f_c' = 27.6 N/mm^2 (4 ksi) and E_c = 24.9 kN/mm^2 (3600 ksi).

Table 5.2 Summary of the Laboratory Test Results for First Yield and Maximum Load and Strain

Column	Positive Direction				Negative Direction			
	About or At Yield		Maximum		About or At Yield		Maximum	
	Strain (με)	Load (kN)	Strain (με)	Load (kN)	Strain (με)	Load (kN)	Strain (με)	Load (kN)
A–1	2018	174.4	2018	174.4	2123	–174.4	2123	–174.4
A–2	2193	160.5	2193	160.5	1968	–152.2	1968	–152.2
A–3	2217	152.7	6331	160.6	2214	–142.3	8763	–155.3
B–1	2200	156.0	7134	182.9				
B–2	2204	136.3	7280	164.4	2207	–142.5	4088	–157.5
B–3	2200	129.3	>10,000	152.2	2200	–124.5	9389	–155.2

Table 6.1 Load, Displacement and the Corresponding Ductility Ratio at Different Load Levels

a) for Column B18S (Δ_y = 40 mm)

Positive Direction			Negative Direction		
Load (kN)	Displacement (mm)	Ductility Ratio	Load (kN)	Displacement (mm)	Ductility Ratio
356	15	0.4	–356	–25	–0.6
535	34	0.9	–508	–50	–1.3
601	52.5	1.3	–481	–62	–1.6
			–303	–83	–2.1

b) for Column B14S (Δ_y = 42 mm)

Positive Direction			Negative Direction		
Load (kN)	Displacement (mm)	Ductility Ratio	Load (kN)	Displacement (mm)	Ductility Ratio
223	21	0.5	–223	–24	–0.6
360 (345)	45	1.1	–304 (–291)	–45	–1.1
396 (356)	67.5	1.6	–313 (–296)	–67.5	–1.6
412 (373)	90	2.1	–322 (–301)	–90	–2.1
413	112.5	2.7	–305	–112.5	–2.7
415	131	3.1			
448	197.5	4.7			

Note: numbers in parentheses were loads during the second cycle to a prior peak displacement

Table 6.1 Load, Displacement and the Corresponding Ductility Ratio at Different Load Levels (cont.)

c) for Column C17S (Δ_y = 39 mm)

Positive Direction			Negative Direction		
Load (kN)	Displacement (mm)	Ductility Ratio	Load (kN)	Displacement (mm)	Ductility Ratio
362	22	0.6	–362	–24	–0.6
554	40	1.0	–520	–40	–1.0
579	55	1.4	–576	–70	–1.8
			–437	–80	–2.1
			–350	–100	–2.6

d) for Column C15S (Δ_y = 40 mm)

Positive Direction			Negative Direction		
Load (kN)	Displacement (mm)	Ductility Ratio	Load (kN)	Displacement (mm)	Ductility Ratio
270	25	0.6	–270	–27	–0.7
376	40	1.0	–352	–40	–1.0
470 (425)	80	2.0	–420 (–386)	–80	–2.0
486 (442)	120	3.0	–425 (–394)	–120	–3.0
430	134	3.4	–398	–140	–3.5
345	160	4.0	–335	–160	–4.0
			–281	–180	–4.5

Note: numbers in parentheses were loads during the second cycle to a prior peak displacement

Table 6.2 Load, Displacement and the Corresponding Ductility Ratio at Different Load Levels

a) for Column A–1 (Δ_y = 30 mm)

Positive Direction			Negative Direction		
Load (kN)	Displacement (mm)	Ductility Ratio	Load (kN)	Displacement (mm)	Ductility Ratio
140	23.78	0.8	–140	–20.61	–0.7
174.4	36.6	1.2	–174.4	–28.27	–0.9
			–144.6	–49.63	–1.7

b) for Column A–2 (Δ_y = 29 mm)

Positive Direction			Negative Direction		
Load (kN)	Displacement (mm)	Ductility Ratio	Load (kN)	Displacement (mm)	Ductility Ratio
118	21.4	0.7	–118	–20	–0.7
123.5	26	0.9	–140.5	–26	–0.9
157.1 (143)	39	1.3	–145.3 (–121)	–39	–1.3
144.7 (119)	52	1.8	–125.7 (–99)	–52	–1.8
109.1	65	2.2	–98.3	–65	–2.2

c) for Column A–3 (Δ_y = 32 mm)

Positive Direction			Negative Direction		
Load (kN)	Displacement (mm)	Ductility Ratio	Load (kN)	Displacement (mm)	Ductility Ratio
104	21.85	0.7	–104	–21.44	–0.7
109.1	26	0.8	–117.6	–26	–0.8
147.6	39	1.2	–149.1	–39	–1.2
158.9 (145)	52	1.6	–154 (–143)	–52	–1.6
159.8 (145)	65	2.0	–152.4 (–146)	–65	–2.0
155.4 (132)	78	2.4	–147 (–128)	–78	–2.4
127.9 (98)	91	2.8	–116.2 (–81)	–91	–2.8

Note: numbers in parentheses were loads during the second cycle to a prior peak displacement

Table 6.2 Load, Displacement and the Corresponding Ductility Ratio at Different Load Levels (cont.)

d) for Column B–1 (Δ_y = 28 mm)

Positive Direction			Negative Direction		
Load (kN)	Displacement (mm)	Ductility Ratio	Load (kN)	Displacement (mm)	Ductility Ratio
120	19.54	0.7	–120	–17.97	–0.6
150	27.61	1.0	–150	–24.73	–0.9
174.6	37.58	1.3			
146.3	71.13	2.5			

e) for Column B–2 (Δ_y = 29 mm)

Positive Direction			Negative Direction		
Load (kN)	Displacement (mm)	Ductility Ratio	Load (kN)	Displacement (mm)	Ductility Ratio
104	19.2	0.7	–104	–18.67	–0.6
110	24	0.8	–122	–24	–0.8
151 (142)	36	1.2	–157.5 (–147)	–36	–1.2
159.7 (145)	48	1.7	–153.7 (–137)	–48	–1.7
155.4 (131)	60	2.1	–131.6 (–106)	–60	–2.1
136.6 (116)	72	2.5	–105.8 (–84)	–72	–2.5
114.6	84	2.9			

f) for Column B–3 (Δ_y = 34 mm)

Positive Direction			Negative Direction		
Load (kN)	Displacement (mm)	Ductility Ratio	Load (kN)	Displacement (mm)	Ductility Ratio
88	20.04	0.6	–88	–19.89	–0.6
93.9	24	0.7	–99.7	–24	–0.7
121	36	1.1	–134.3	–36	–1.1
143.2 (132)	48	1.4	–151.1 (–140)	–48	–1.4
149.4 (136)	60	1.8	–152.2 (–144)	–60	–1.8
150.2 (136)	72	2.1	–151.7 (–135)	–72	–2.1
144.0 (129)	84	2.5	–145 (–126)	–84	–2.5
126.9 (100)	96	2.8	–123.8 (–109)	–96	–2.8
111.2	108	3.2	–106.8	–108	–3.2

Note: numbers in parentheses were loads during the second cycle to a prior peak displacement

Table 6.3 Summary of Field Test Results

a) for Maximum Load and Displacement as well as Failure Displacement

Column	Positive Direction			Negative Direction		
	Max. Load (kN)	Displace–ment for Max. Load (mm)	Failure Dis-placement (mm)+	Max. Load (kN)	Displace–ment for Max. Load (mm)	Failure Dis-placement (mm)+
Results of 1993 Tests						
B18S	601	52.5		–508	–50	–63
B14S	448	197.5	>197.5	–322	–90	>–112.5
Results of 1994 Tests						
C17S	579	55		–576	–70	–78
C15S	486	120	147	–425	–120	–155

+Failure displacement is the displacement corresponding to the 80% of the maximum load.

b) for Maximum Load and Ductility Ratio as well as Failure Ductility Ratio

Column	Positive Direction			Negative Direction		
	Max. Load (kN)	Ductility Ratio for Max. Load	Failure Ductility Ratio+	Max. Load (kN)	Ductility Ratio for Max. Load	Failure Ductility Ratio+
Results of 1993 Tests						
B18S	601	1.3		–508	–1.3	–1.6
B14S	448	4.7	>4.7	–322	–2.1	>–2.7
Results of 1994 Tests						
C17S	579	1.4		–576	–1.8	–2.0
C15S	486	3.0	3.7	–425	–3.0	–3.9

Table 6.4 Summary of Laboratory Test Results

a) for Maximum Load and Displacement as well as Failure Displacement

Column	Positive Direction			Negative Direction		
	Max. Load (kN)	Displacement for Max. Load (mm)	Failure Displacement (mm)+	Max. Load (kN)	Displacement for Max. Load (mm)	Failure Displacement (mm)+
A–1*	174.4	36.6		–174.4	–28.3	–50.1
A–2	160.5	37.7	58.9	–152.2	–33.6	–54.0
A–3	160.6	50.8	91.0	–155.3	–63.2	–84.0
B–1*	182.9	48.8	71.1			
B–2	164.4	46.1	74.0	–157.5	–36.0	–63.0
B–3	152.2	58.2	101.0	–155.2	–59.5	–96.0

*less test cycles

+Failure displacement is the displacement corresponding to the 80% of the maximum load.

b) for Maximum Load and Ductility Ratio as well as Failure Ductility Ratio

Column	Positive Direction			Negative Direction		
	Max. Load (kN)	Ductility Ratio for Max. Load	Failure Ductility Ratio	Max. Load (kN)	Ductility Ratio for Max. Load	Failure Ductility Ratio
A–1	174.4	1.2		–174.4	–0.9	–1.7
A–2	160.5	1.0	2.0	–152.2	–1.2	–1.9
A–3	160.6	1.6	2.8	–155.3	–2.0	–2.6
B–1	182.9	1.7	2.5			
B–2	164.4	1.6	2.6	–157.5	–1.2	–2.2
B–3	152.2	1.7	2.9	–155.2	–1.8	–2.8

Table 6.5a Calculated First Yield, Nominal and Probable Strengths and Associated Curvatures for Field Test Columns

Positive Direction							
Column	First Yield Strength P_y (kN)	First Yield Curvature ϕ_y x 10^{-6} (rad/mm)	Nominal Strength P_n (kN)	Probable Strength P_{pr} (kN)	Maximum Curvature ϕ_{pr} x 10^{-5} (rad/mm)	Curvature at BB ϕ_B x 10^{-6} (rad/mm)	Curvature at BB ϕ_B' x 10^{-6} (rad/mm)
B18S	523	1.909	764	797	1.420	1.427	2.175
B14S	311	2.102	450	475	1.781	1.602	2.447
C17S	409	1.917	612	641	1.556	1.215	1.904
C15S	302	2.134	436	462	.1821	1.595	2.440
Negative Direction							
B18S	–445	–1.929	–670	–703	–1.591	–1.306	–2.063
B14S	–265	–2.130	–391	–420	–1.939	–1.441	–2.284
C17S	–422	–1.953	–621	–649	–1.545	–1.407	–2.164
C15S	–274	–2.091	–403	–429	–1.883	–1.410	–2.208

Table 6.5b Calculated First Yield and Maximum Displacements for Field Test Columns (Eq. (6.1))

Positive Direction					
Column	First Yield Strength P_y (kN)	First Yield Displacement δ_y (mm)	Probable Strength P_{pr} (kN)	Plastic Part Displacement δ_p (mm)	Maximum Displacement Δ_{pr} (mm)
B18S	523	18.49	797	22.55	41.04
B14S	311	20.69	475	28.82	49.51
C17S	409	16.28	641	25.03	41.31
C15S	302	20.67	462	29.49	50.16
Negative Direction					
B18S	–445	–17.26	–703	–25.65	–42.91
B14S	–265	–19.05	–420	–31.67	–50.72
C17S	–422	–18.36	–649	–24.76	–43.12
C15S	–274	–18.65	–429	–30.71	–49.36

Table 6.6a Calculated First Yield, Nominal and Probable Strengths and Associated Curvatures for Laboratory Test Columns

Column	First Yield Strength P_y (kN)	First Yield Curvature ϕ_y x 10^{-6} (rad/mm)	Nominal Strength P_n (kN)	Probable Strength P_{pr} (kN)	Maximum Curvature ϕ_{pr} x 10^{-5} (rad/mm)	Curvature at BB ϕ_B x 10^{-6} (rad/mm)	Curvature at BB ϕ_B' x 10^{-6} (rad/mm)
A–1	175	6.201	189	215	3.592	3.284	4.035
A–2	149	7.303	165	174	2.835	2.915	3.404
A–3	133	8.433	154	166	3.577	3.333	4.160
B–1	159	6.201	182	200	3.269	3.323	4.180
B–2	132	7.303	161	165	2.637	3.034	3.793
B–3	116	8.433	153	159	3.856	3.595	4.928

Table 6.6b Calculated First Yield and Maximum Displacements for Laboratory Test Columns (Eq. (6.1))

Column	First Yield Strength P_y (kN)	First Yield Displacement δ_y (mm)	Probable Strength P_{pr} (kN)	Plastic Part Displacement δ_p (mm)	Maximum Displacement Δ_{pr} (mm)
A–1	175	10.20	215	22.04	32.24
A–2	149	10.39	174	15.75	26.14
A–3	133	11.94	166	20.27	32.21
B–1	159	10.26	200	19.64	29.90
B–2	132	10.59	165	14.14	24.73
B–3	116	12.39	159	22.34	34.73

Table 6.7a Extreme Tensile Bar Stress and Neutral Axis Depth for Field Test Columns for Dowel Bars

Column	Positive Direction						
	Yield			Probable Flexural Strength			
	Column Strength P_y (kN)	Bar Stress f_y (MPa / ksi)	N.A. kd (mm / in.)	Column Strength P_{pr} (kN)	Bar Strain ε (%)	Bar Stress f_y (MPa / ksi)	N.A. kd (mm / in.)
B18S	523	324 / 47	406/15.97	797	1.37	331 / 48	282/11.09
B14S	311	324 / 47	340/13.38	475	1.56	345 / 50	225/10.12
C17S	409	324 / 47	373/14.68	641	1.48	338 / 49	257/10.12
C15S	302	324 / 47	333/13.11	462	1.57	345 / 50	220/8.65
	Negative Direction						
B18S	–445	324 / 47	374/14.74	–703	1.51	338 / 49	251/9.90
B14S	–265	324 / 47	314/12.38	–420	1.67	352 / 51	206/8.12
C17S	–422	324 / 47	375/14.78	–649	1.45	338 / 49	259/10.19
C15S	–274	324 / 47	322/12.66	–429	1.63	352 / 51	214/8.43

Table 6.7b Extreme Tensile Bar Stress and Neutral Axis Depth for Laboratory Test Columns for Dowel Bars

Column	Yield			Probable Flexural Strength			
	Column Strength P_y (kN)	Bar Stress f_y (MPa / ksi)	N.A. kd (mm / in.)	Column Strength P_{pr} (kN)	Bar Strain ε (%)	Bar Stress f_{pr} (MPa / ksi)	N.A. kd (mm / in.)
A–1	175	455 / 66	181 / 7.11	215	1.52	524 / 76	112 / 4.39
A–2	149	455 / 66	182 / 7.17	174	0.97	483 / 70	141 / 5.56
A–3	133	455 / 66	184 / 7.24	166	1.01	483 / 70	163 / 6.40
B–1	159	455 / 66	181 / 7.11	200	1.34	511 / 74	122 / 4.82
B–2	132	455 / 66	182 / 7.17	165	0.87	483 / 70	152 / 5.97
B–3	116	455 / 66	184 / 7.24	159	1.04	483 / 70	182 / 7.15

Table 6.8a Bar Force and Loaded End Displacement Values for Field Test Columns

Bar Stress f_s (MPa / ksi)	Bar Force $F = f_s A_b$ (kN / kips)	Bar Force / Bar Yield Force	Loaded End Displacement δ (mm / in.)
324 / 47	327 / 73.3	1.0	0.3099 / 0.0122
331 / 48	334 / 74.9	1.021	0.5077 / 0.0199
338 / 49	340 / 76.4	1.043	0.7059 / 0.0278
345 / 50	347 / 78.0	1.064	0.9037 / 0.0356
352 / 51	354 / 79.6	1.085	1.1016 / 0.0434
359 / 52	361 / 81.1	1.106	1.2997 / 0.0512

Table 6.8b Bar Force and Loaded End Displacement Values for Laboratory Test Columns

Bar Stress f_s (MPa / ksi)	Bar Force $F = f_s A_b$ (kN / kips)	Bar Force / Bar Yield Force	Loaded End Displacement δ (mm / in.)
228 / 33	229 / 51.5	0.5	0.216 / 0.0085
455 / 66	459 / 103.0	1.0	0.432 / 0.017
476 / 69	479 / 107.6	1.045	0.966 / 0.038
483 / 70	486 / 109.2	1.061	1.143 / 0.045
511 / 74	514 / 115.4	1.121	1.857 / 0.073
524 / 76	528 / 118.6	1.152	2.210 / 0.087
559 / 81	563 / 126.4	1.227	3.104 / 0.1222
593 / 86	598 / 134.2	1.303	4.000 / 0.1573

Table 6.9a Additional Deflections for Field Test Columns

Positive Direction								
Column	Yield				Probable Flexural Strength			
	P_y (kN)	d_t (mm)	δ (mm)	Δ_1 (mm)	P_{pr} (kN)	d_t (mm)	δ (mm)	Δ_1 (mm)
B18S	523	845	0.3099	4.92	797	969	0.5077	7.03
B14S	311	725	0.3099	5.73	475	840	0.9037	14.43
C17S	409	829	0.3099	5.01	641	945	0.7059	10.02
C15S	302	724	0.3099	5.74	462	837	0.9037	14.48
Negative Direction								
B18S	–445	832	0.3099	5.00	–703	955	0.7059	9.91
B14S	–265	768	0.3099	5.41	–420	876	1.1016	16.87
C17S	–422	831	0.3099	5.00	–649	947	0.7059	10.00
C15S	–274	747	0.3099	5.56	–429	855	1.1016	17.28

Table 6.9b Additional Deflections for Labotoatory Test Columns

Column	Yield				Probable Flexural Strength			
	P_y (kN)	d_t (mm)	δ (mm)	Δ_1 (mm)	P_{pr} (kN)	d_t (mm)	δ (mm)	Δ_1 (mm)
A–1	175	353	0.432	8.21	215	422	2.21	35.12
A–2	149	301	0.432	9.62	174	342	1.143	22.41
A–3	133	261	0.432	11.10	166	282	1.143	27.18
B–1	159	353	0.432	8.21	200	412	1.857	30.22
B–2	132	301	0.432	9.62	165	331	1.143	23.16
B–3	116	261	0.432	11.10	159	263	1.143	29.14

Note: $\Delta_1 = \theta l$ and $\theta = (2\delta) / d_t$

Table 6.10 Predicted Column Bar Stresses for Field Columns (Eq. (6.9b))

Positive Direction					
Column	A	B	C	Bar Stress f_s (ksi)	Bar Stress f_s (N/mm^2)
B18S	9838	1.04	713	61.6	425
B14S	12710	1.01	1069	73.9	510
C17S	8755	1.09	713	61.8	426
C15S	10922	1.02	2138	74.7	515
Negative Direction					
Column	A	B	C	Bar Stress f_s (ksi)	Bar Stress f_s (N/mm^2)
B18S	10009	1.01	713	56.5	390
B14S	10922	1.01	1069	63.1	435
C17S	13089	1.01	713	68.6	473
C15S	11464	1.02	1069	71.7	494

Note: A——cover and lap length term

B——spacing term

C——transverse steel term

see Eq. (6.9b).

Table 6.11a Predicted Column Bar Stresses for Laboratory Columns (Eq. (6.9b))

Column	A	B	C	Bar Stress f_s (ksi)	Bar Stress f_s (N/mm^2)
A–1	7,603	1.075	1,470	54.8	380
A–2	7,603	1.137	1,470	57.4	398
A–3	11,469	1.003	1,470	73.6	512
B–1	7,603	1.216	1,470	60.8	422
B–2	7,603	1.314	1,470	65.0	451
B–3	11,667	1.069	1,470	79.0	548

Note: A——cover and lap length term

B——spacing term

C——transverse steel term

see Eq. (6.9b).

Table 6.11b Measured Maximum Bar Strains and Stresses for Laboratory Columns

Col.	Column Bar					Dowel Bar				
	Max. Bar Strain (με)	Gage No.	Load (kN) or Defln	Bar Stress f_s (N/mm^2)	Bar Stress f_s (ksi)	Max. Bar Strain (με)	Gage No.	Load (kN) or Defln	Bar Stress f_s (N/mm^2)	Bar Stress f_s (ksi)
A–1	1,603	12	174.4	334	48.1	2,123	9	174.4	442	63.7
A–2	1,413	12	39 mm	295	42.4	2,193	4	39 mm	457	65.8
A–3	1,703	17	65 mm	355	51.1	8,763	9	65 mm	479	69
B–1	1,680	12	182.9	350	50.4	7,434	4	182.9	472	68
B–2	1,632	17	36 mm	340	49.0	7,800	4	60 mm	472	68
B–3	1,850	12	72 mm	385	55.5	≃10,000	4	72 mm	≃493	≃71

Table 6.12 Comparison between Predicted and Measured Column Bar Stresses for Laboratory Columns

Column	Measured Bar Stress f_{sm}		Predicted Bar Stress f_{sp}		f_{sm} / f_{sp}
	(N/mm^2)	(ksi)	(N/mm^2)	(ksi)	
A–1	334	48.1	380	54.8	0.88
A–2	295	42.2	398	57.4	0.74
A–3	355	51.1	512	73.6	0.69
B–1	350	50.4	422	60.8	0.83
B–2	340	49.0	451	65.0	0.75
B–3	385	55.5	548	79.0	0.70

Table 6.13a Computed Column Capacities and the Associated Bar Stresses for Field Test Columns

Positive Direction								
Column	1				2			
	P_{yA} (kN)	f_{yA} (MPa / ksi)	P_{prA} (kN)	f_{prA} (MPa / ksi)	P_{yB} (kN)	f_{yB} (MPa / ksi)	P_{prB} (kN)	f_{prB} (MPa / ksi)
B18S	523	324 / 47	797	345 / 50	624	324 / 47	921	366 / 53
B14S	311	324 / 47	475	352 / 51	372	324 / 47	537	400 / 58
C17S	409	324 / 47	641	352 / 51	558	324 / 47	809	393 / 57
C15S	302	324 / 47	462	359 / 52	362	324 / 47	526	400 / 58
Negative Direction								
B18S	–445	324 / 47	–703	352 / 51	–590	324 / 47	–885	373 / 54
B14S	–265	324 / 47	–420	359 / 52	–355	324 / 47	–517	400 / 58
C17S	–422	324 / 47	–649	352 / 51	–520	324 / 47	–763	400 / 58
C15S	–274	324 / 47	–429	359 / 52	–368	324 / 47	–534	400 / 58

Table 6.13b Computed Column Capacities and the Associated Bar Stresses for Laboratory Test Columns

Column	1				2	
	P_{yA} (kN)	f_{yA} (MPa / ksi)	P_{prA} (kN)	f_{prA} (MPa / ksi)	P_{yB} (kN)	f_{yB} (MPa / ksi)
A–1	175	455 / 66	215	524 / 76	290	455 / 66
A–2	149	455 / 66	174	483 / 70	279	455 / 66
A–3	133	455 / 66	166	483 / 70	240	455 / 66
B–1	159	455 / 66	200	511 / 74	261	455 / 66
B–2	132	455 / 66	165	483 / 70	237	455 / 66
B–3	116	455 / 66	159	483 / 70	194	455 / 66

Note:
Column 1 = using properties of section based on the dowel bar locations;
Column 2 = using properties of section based on the column bar locations.

Table 6.14 Bar Stresses under Maximum Measured Column Loads for Laboratory Test Columns

Column	Maximum Measured Load (kN)	Column Bar Stress			Dowel Bar Stress		
		Computed f_{sc} (MPa / ksi)	Measured f_{sm} (MPa / ksi)	f_{sm} / f_{sc}	Computed f_{sc} (MPa / ksi)	Measured f_{sm} (MPa / ksi)	f_{sm} / f_{sc}
A–1	174.4	274 / 39.7	338 / 48.1	1.21	454 / 65.8	442 / 63.7	0.97
A–2	160.5	262 / 38.0	295 / 42.4	1.12	468 / 67.8	457 / 65.8	0.97
A–3	160.6	305 / 44.2	355 / 51.1	1.16	479 / 69.4	479 / 69.0	0.99
B–1	182.9	319 / 46.3	350 / 50.4	1.09	488 / 70.7	472 / 68.0	0.96
B–2	164.4	316 / 45.8	340 / 49.0	1.07	483 / 70.0	472 / 68.0	0.97
B–3	155.2	365 / 52.9	385 / 55.5	1.05	481 / 69.7	493 / 71.0	1.02

Table 6.15a Maximum Computed Lateral Loads for Field Columns Based on Predicted Column Bar Stresses

Column	Maximum Measured Load (kN)	P_{yB} (kN)	f_s (N/mm^2 / ksi)	Maximum Computed Bond Capacity (kN)	Maximum Computed Flexural Capacity (kN)	Maximum Measured / Computed Load	Failure Feature
Positive Direction							
B18S	601	624	425 / 61.6	573	797	1.049	Bond
B14S	448	372	510 / 73.9	434	475	1.032	Bond
C17S	579	558	426 / 61.8	514	641	1.126	Bond
C15S	486	362	515 / 74.7	441	462	1.102	Bond
Negative Direction							
B18S	–508	–590	390 / 56.5	–497	–703	1.022	Bond
B14S	–322	–355	435 / 63.1	–334	–420	0.964	Bond
C17S	–576	–520	473 / 68.6	–542	–649	1.063	Bond
C15S	–425	–368	494 / 71.7	–416	–429	1.022	Bond

Table 6.15b Maximum Computed Lateral Loads for Laboratory Columns Based on Predicted Column Bar Stresses

Column	Maximum Measured Load (kN)	P_{yB} (kN)	f_s (N/mm^2 / ksi)	Maximum Computed Bond Capacity (kN)	Maximum Computed Flexural Capacity (kN)	Maximum Measured / Computed Load	Failure Feature
A–1	174.4	290	380 / 54.8	168.5	215	1.035	Bond
A–2	160.5	279	398 / 57.4	169.7	174	0.945	Bond
A–3	160.6	240	512 / 73.6	187.1	166	0.967	Flexure
B–1	182.9	261	422 / 60.8	168.5	200	1.085	Bond
B–2	164.4	237	451 / 65.0	163.1	165	1.008	Bond
B–3	155.2	194	548 / 79.0	162.5	159	0.976	Flexure

Note:
Column 3 = Computed column yield load based on section having bars on column bar locations;
Column 4 = Column bar stress computed by modified Darwin's expression;
Column 5 = Maximum computed load, which equals $0.7f_s$ / f_yP_{yB}.

FIGURES

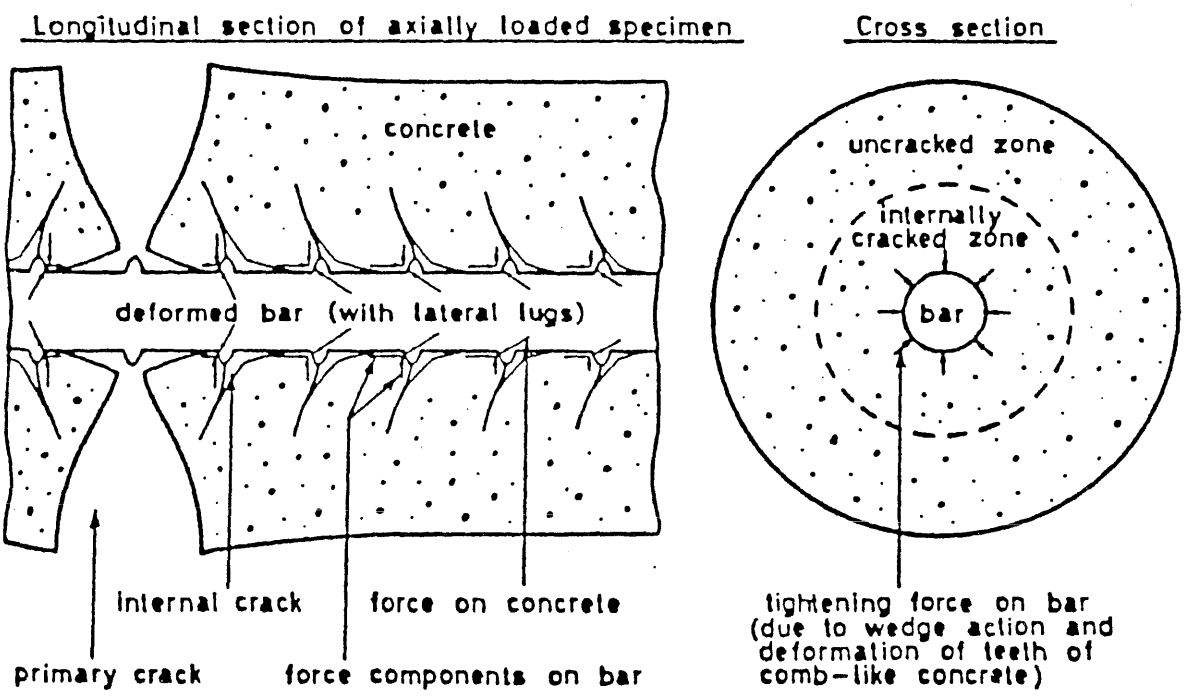

Fig. 1.1 Deformation of Concrete around Reinforcing Steel after Formation of Internal Cracks

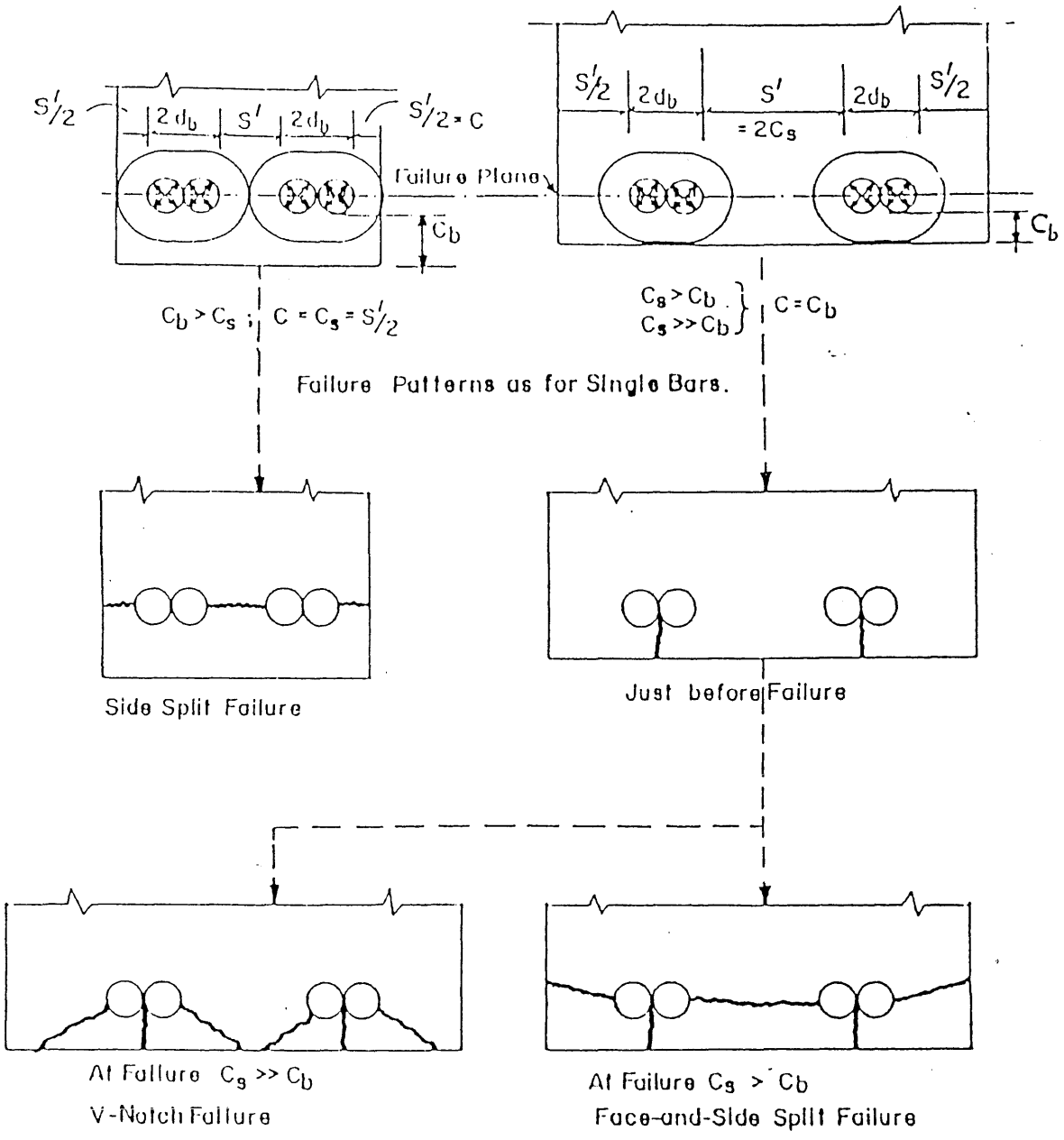

Fig. 1.2 Failure Patterns in Lap Splices

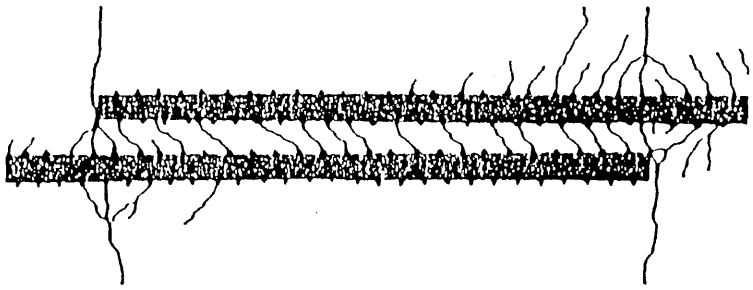

Fig. 1.3 Lap Splice Internal Cracking

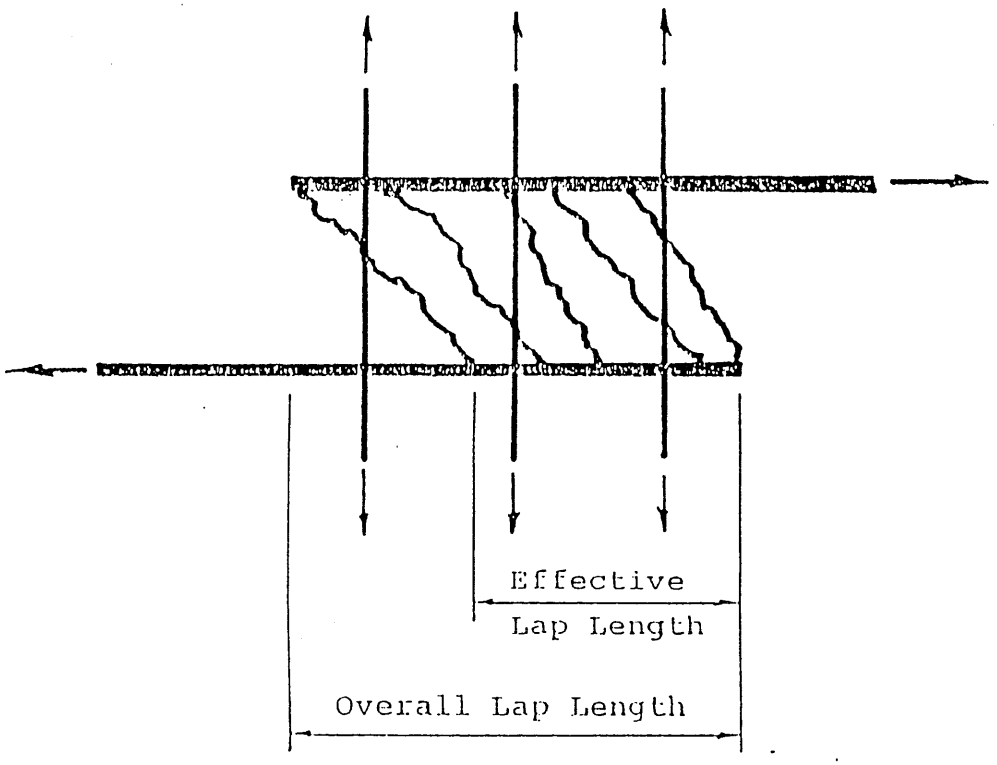

Fig. 1.4 Overall and Effective Lap Length

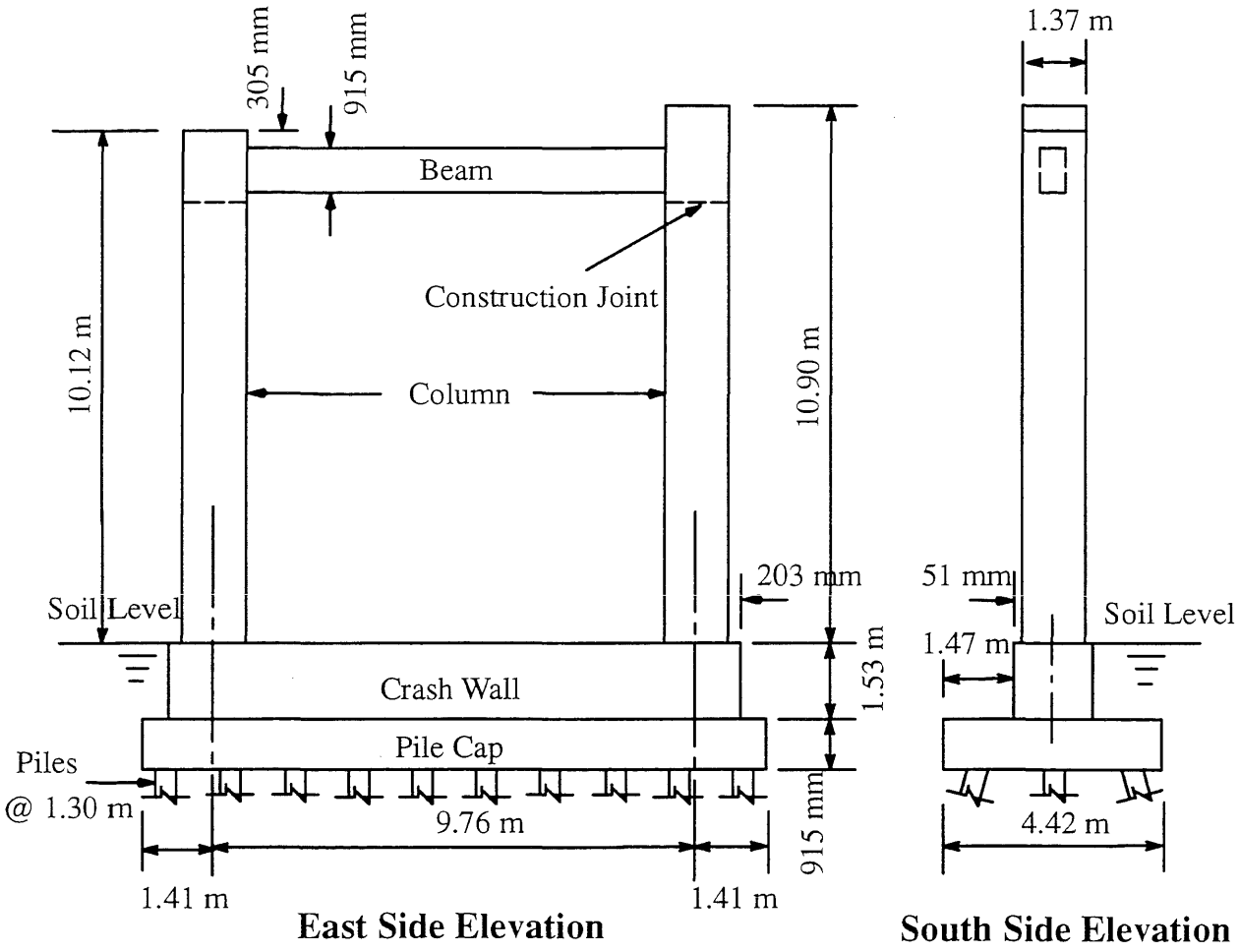

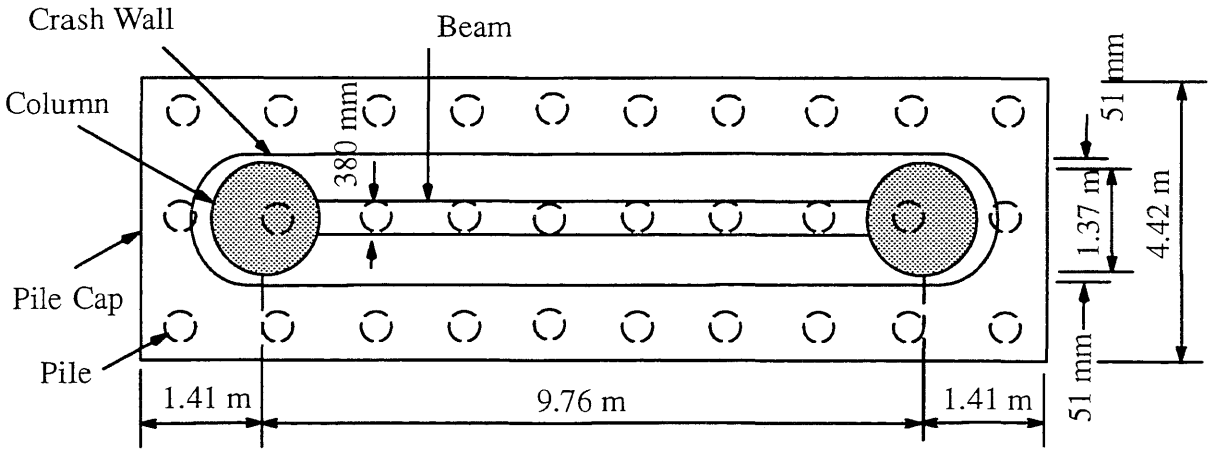

Plan View

Fig. 2.1 Characteristic Bridge Pier for 1.37 m (54 in.) Columns

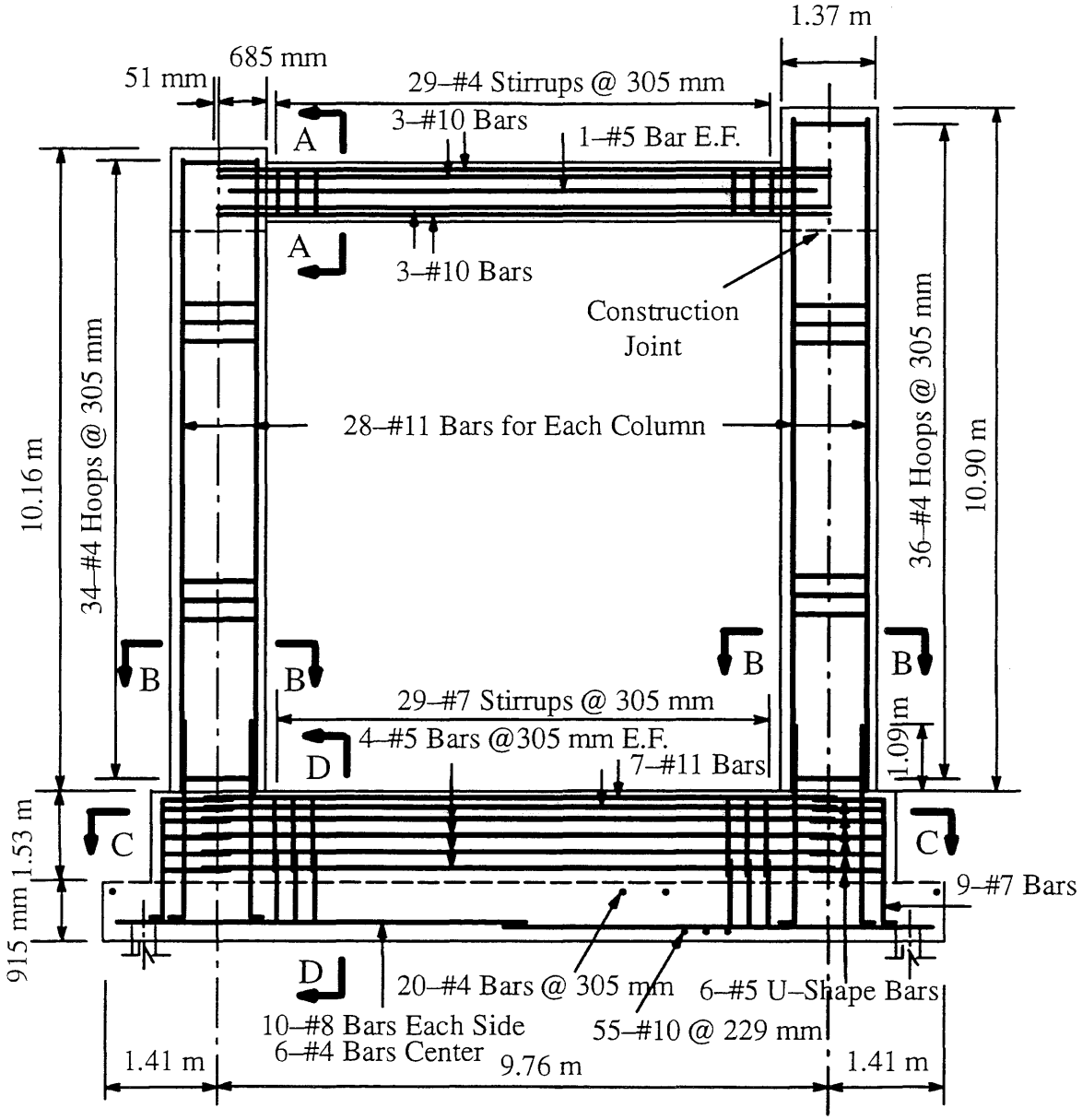

Fig. 2.2a Reinforcement Details for Characteristic Pier with 1.37 m (54 in.) Columns

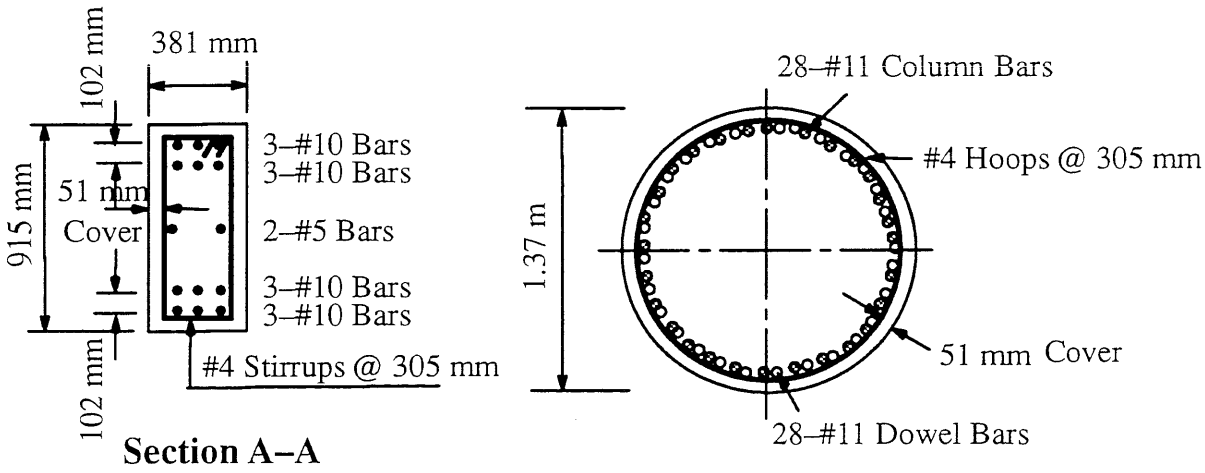

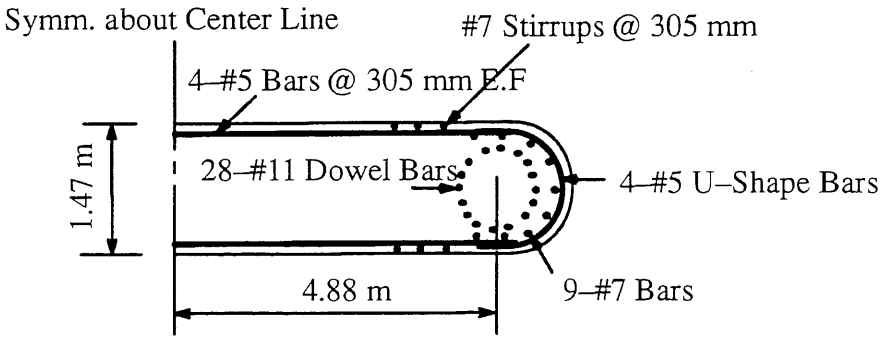

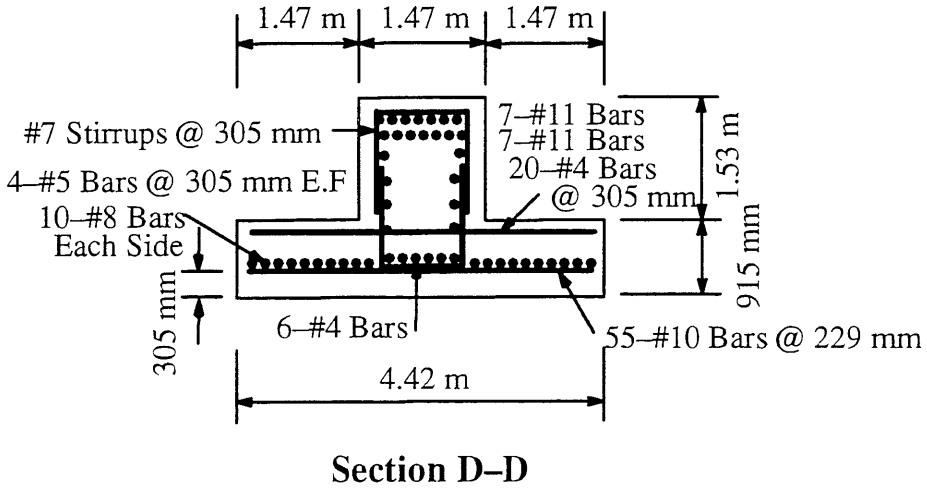

Fig. 2.2b Reinforcing Details for Characteristic Pier with 1.37 m (54 in.) Columns

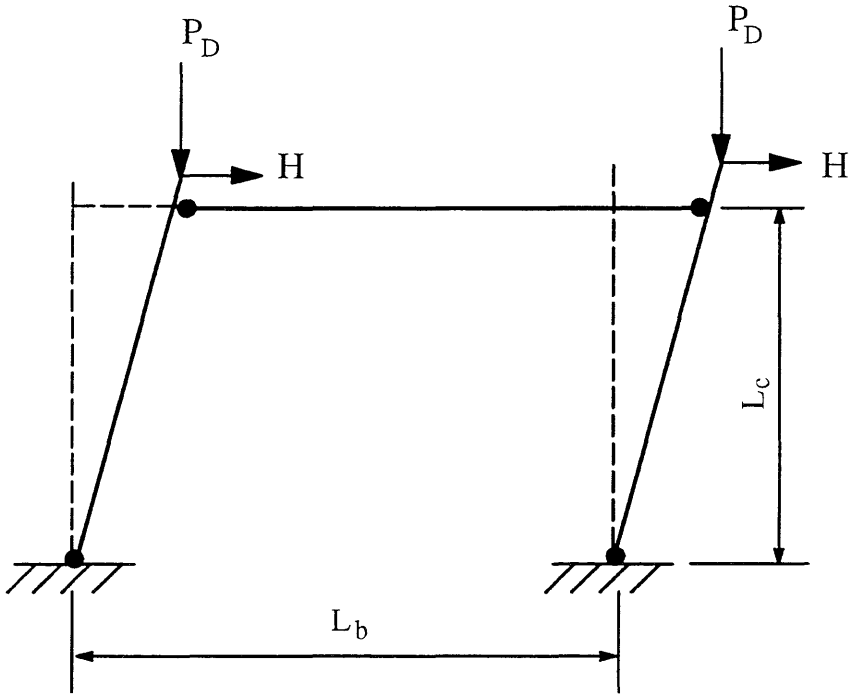

Fig. 2.3a Plastic Collapse Mechanism

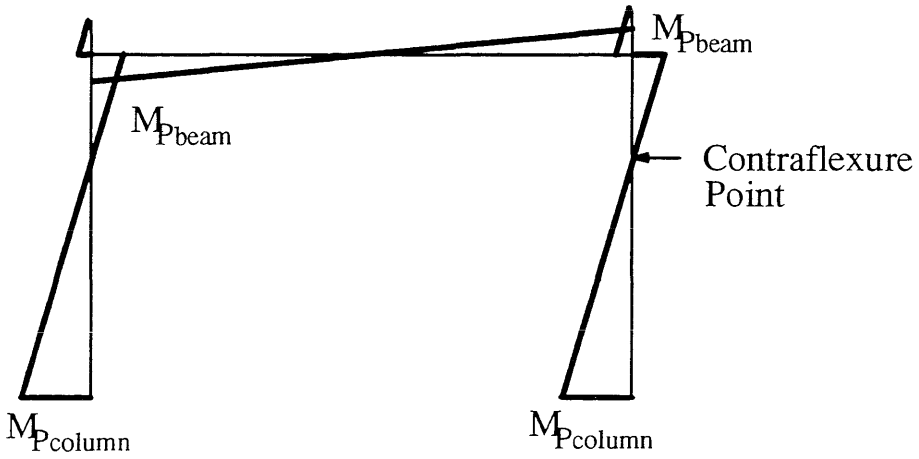

Fig. 2.3b Moment Diagram

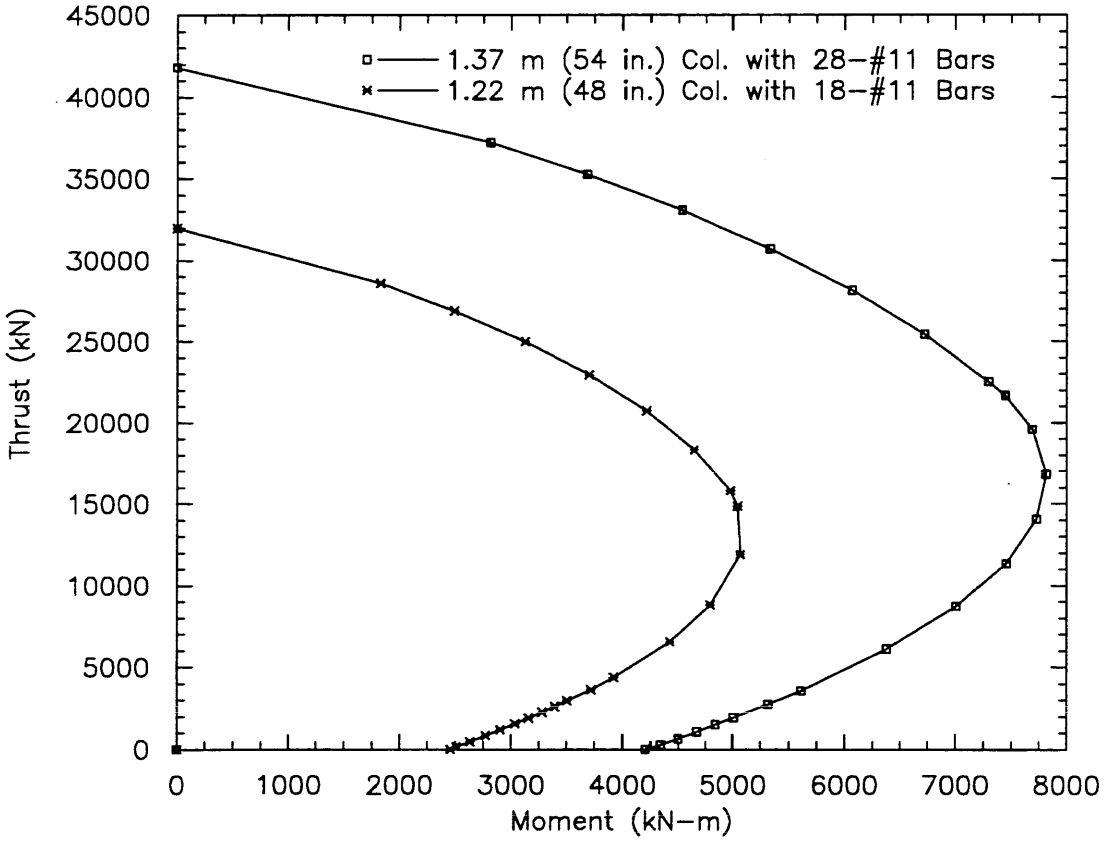

Fig. 2.4 Moment Thrust Interaction Diagram

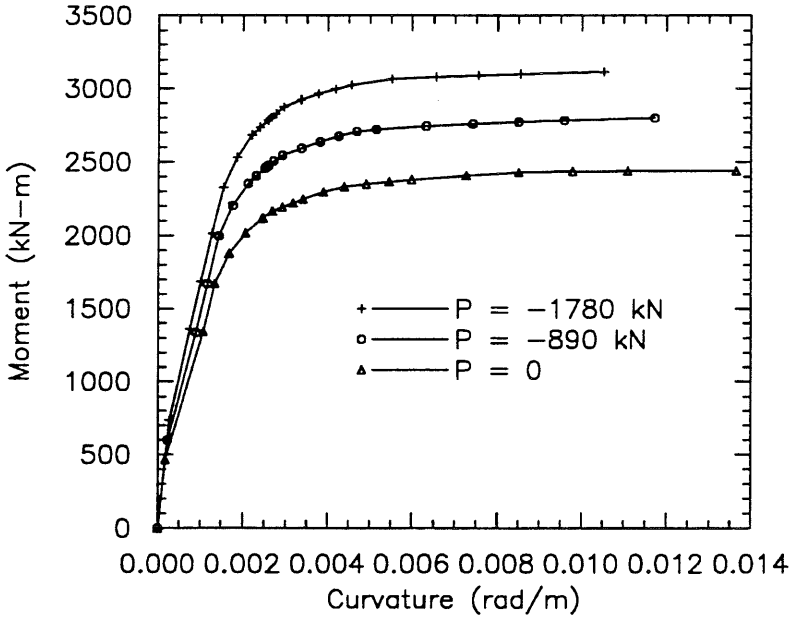

Fig. 2.5 Moment Curvature Relationship for 1.22 m (48 in.) Column

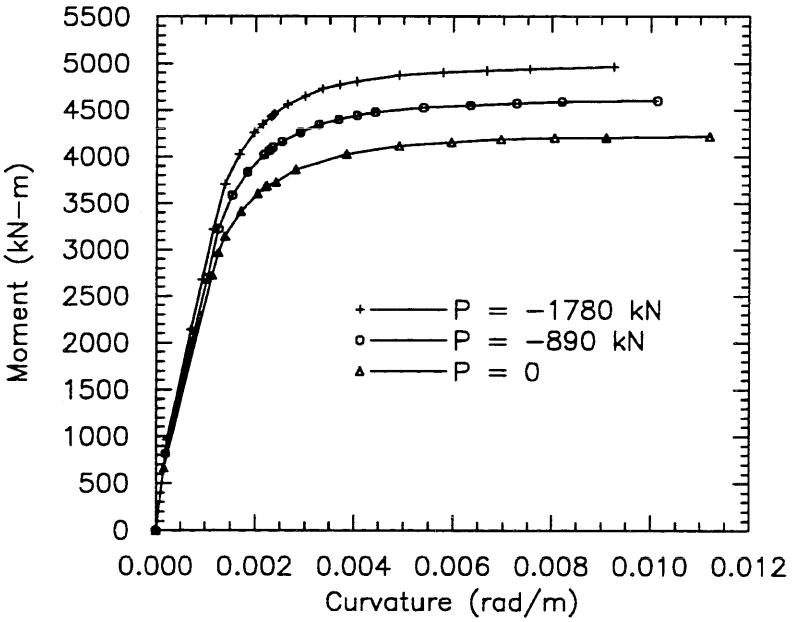

Fig. 2.6 Moment Curvature Relationship for 1.37 m (54 in.) Column

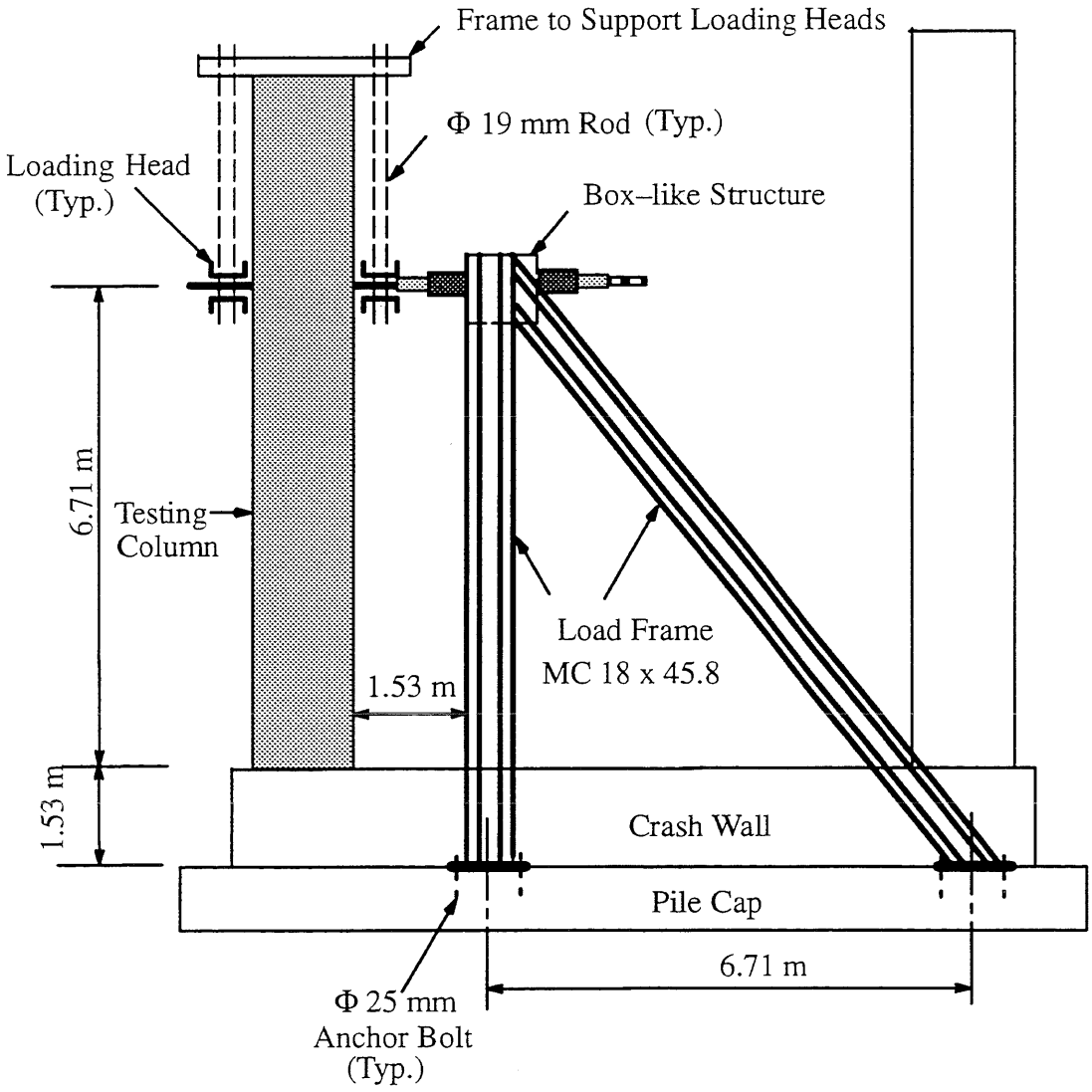

Fig. 2.7 Field Test Setup

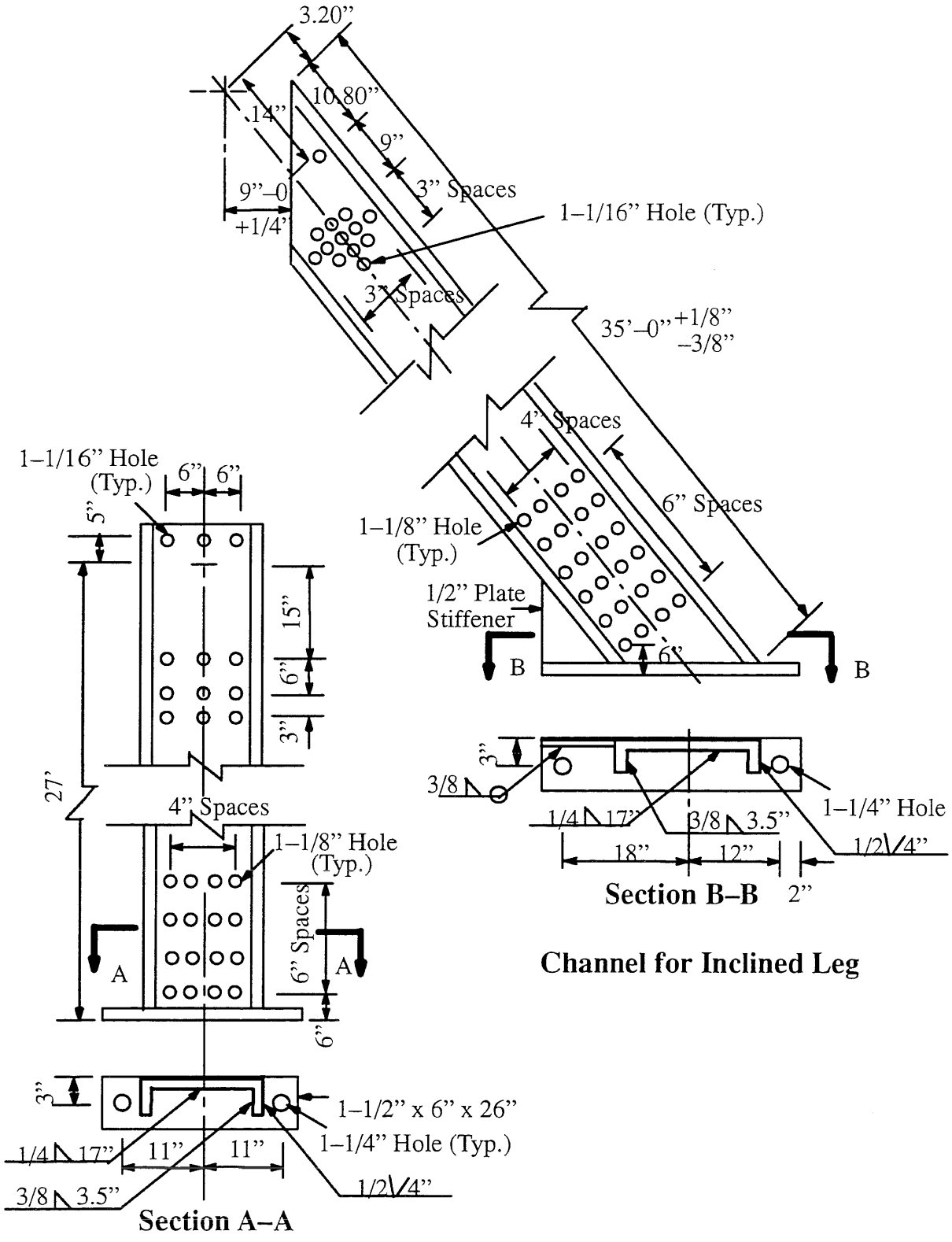

Fig. 2.8 Details of Channels for Frame Legs

(1 in. = 25.4 mm)

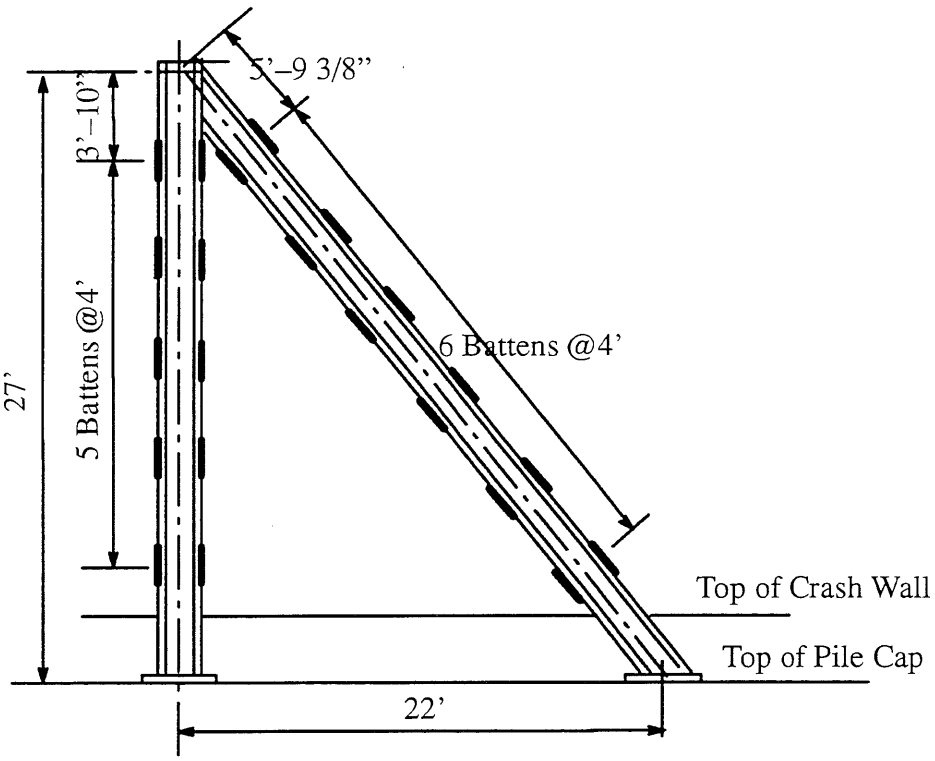

Location of Batten

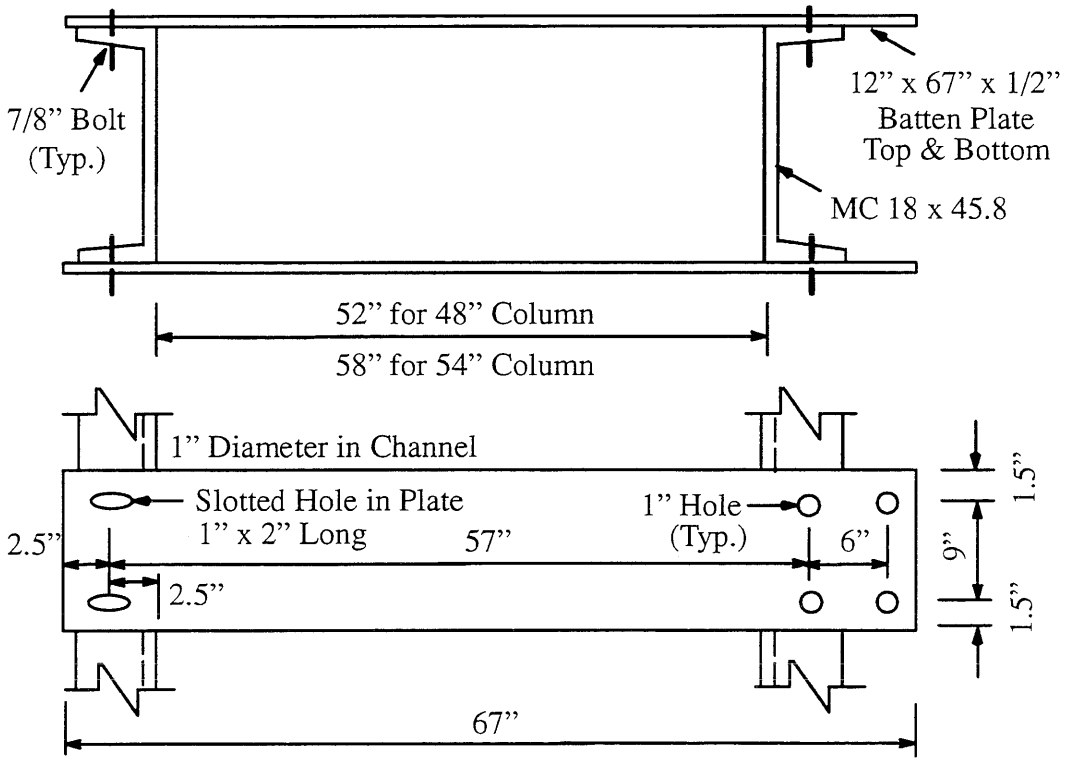

Batten Details

Fig. 2.9 Location and Details of Battens

(1 in. = 25.4 mm)

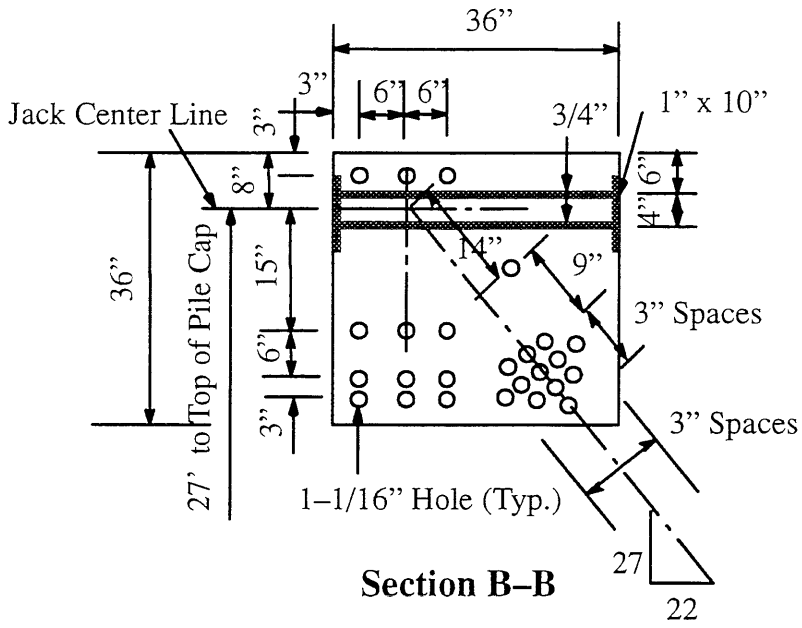

Section B–B

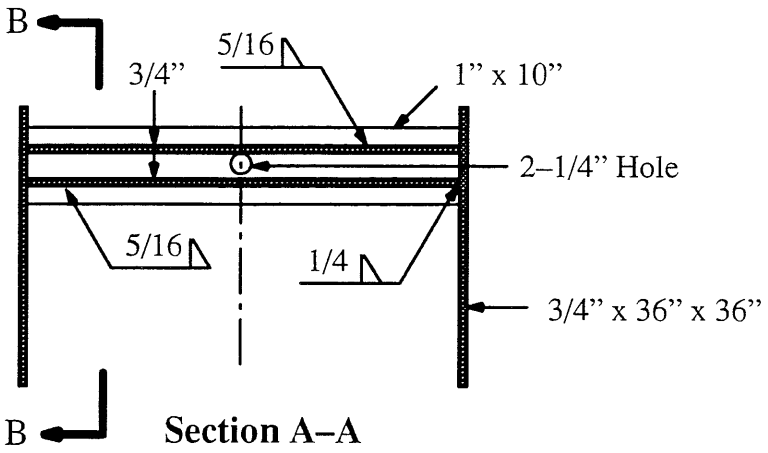

Section A–A

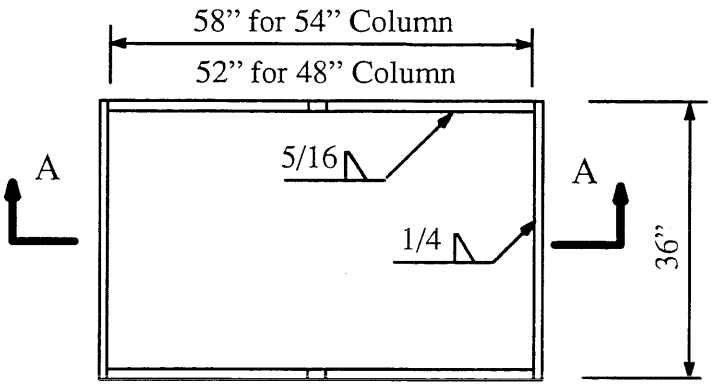

Top View of Box

Fig. 2.10 Details of Box–like Structure

(1 in. = 25.4 mm)

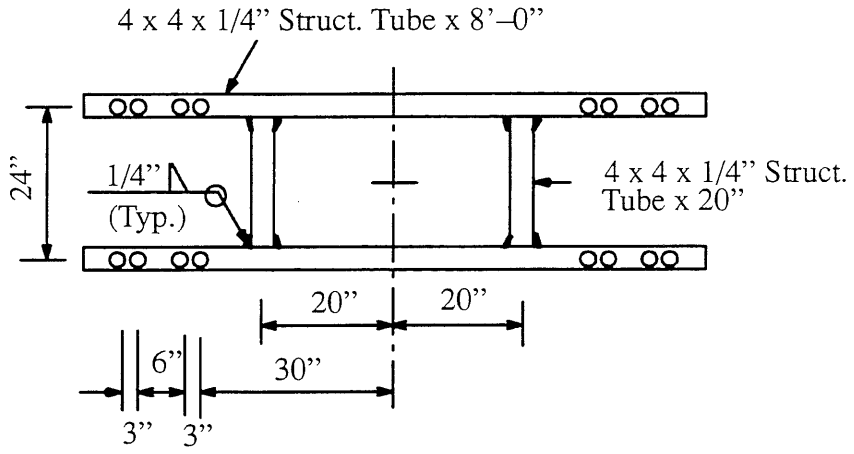

Fig. 2.11 Plan View of Frame to Support Loading Heads
(1 in. = 25.4 mm)

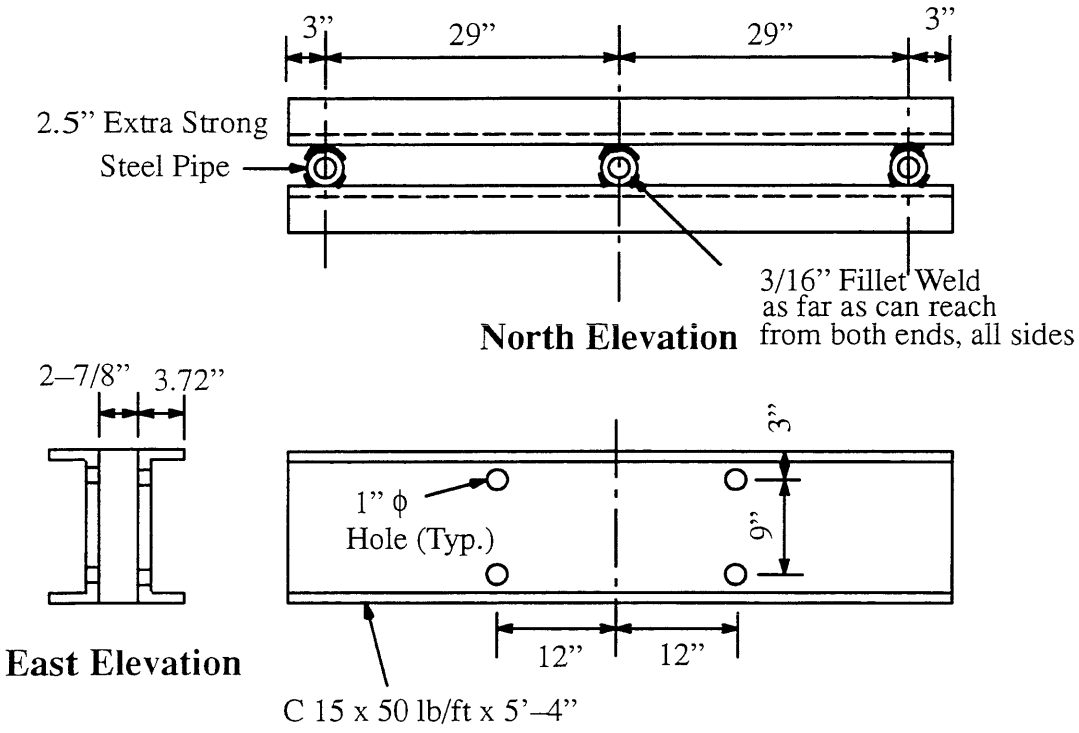

Fig. 2.12 Details of Loading Heads
(1 in. = 25.4 mm)

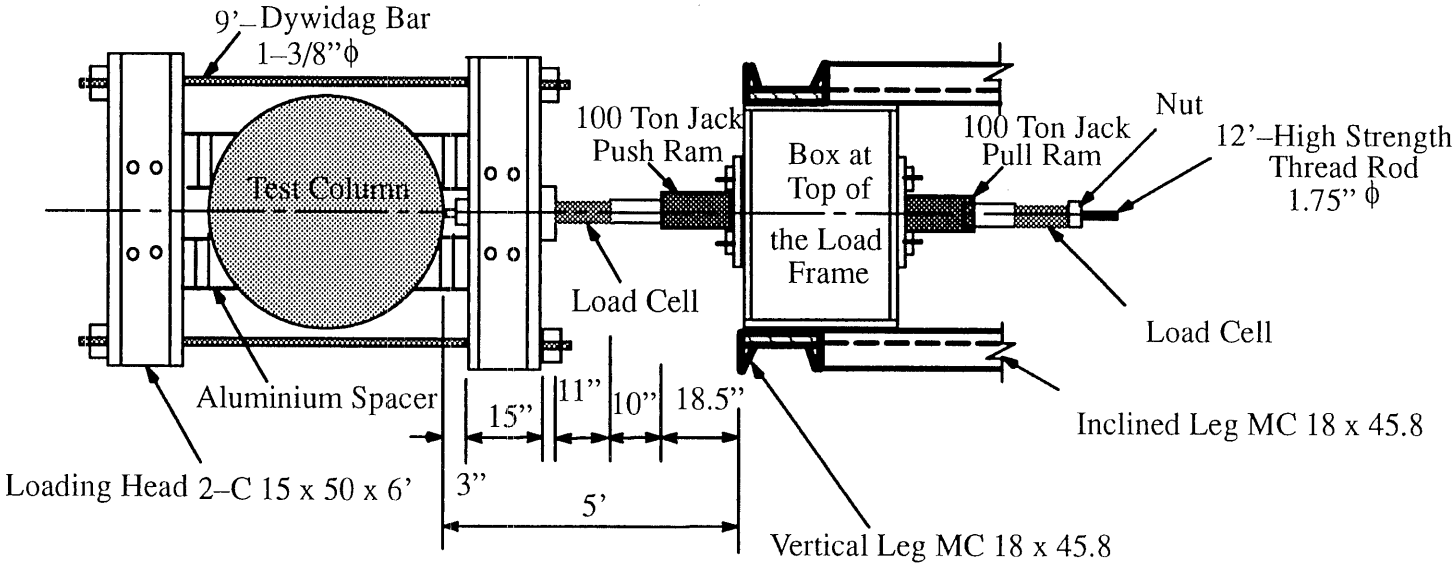

Fig. 2.13 Plan View of Loading Apparatus

(1 in. = 25.4 mm)

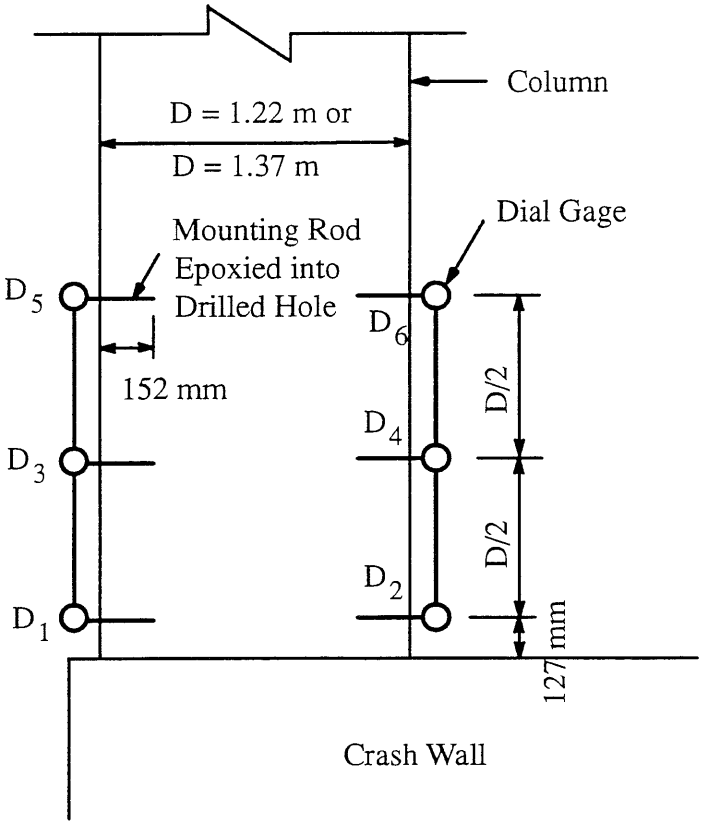

Fig. 2.14 Rotation Measurements

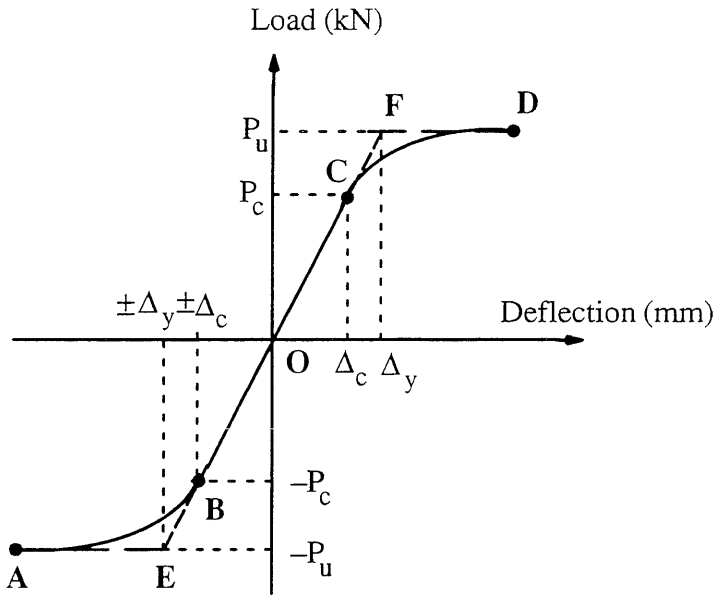

Column	Diameter (m)	No. of #11 Bar	P_u (kN)
B14S & C15S	1.22	18	365
B18S	1.37	28	628
C17S	1.37	24	538

Fig. 3.1 An Idealized Envelope to the Reversed Cyclic Response and the Corresponding Data for the Field Test Columns

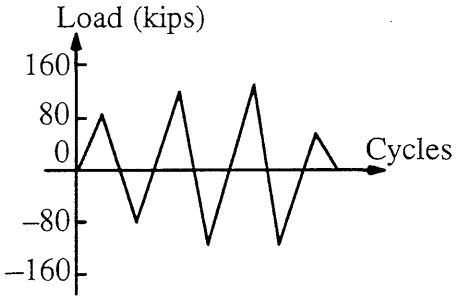

a) for the Column B18S

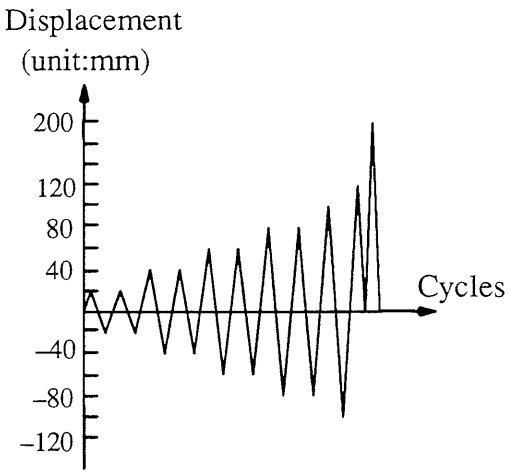

b) for the Column B14S

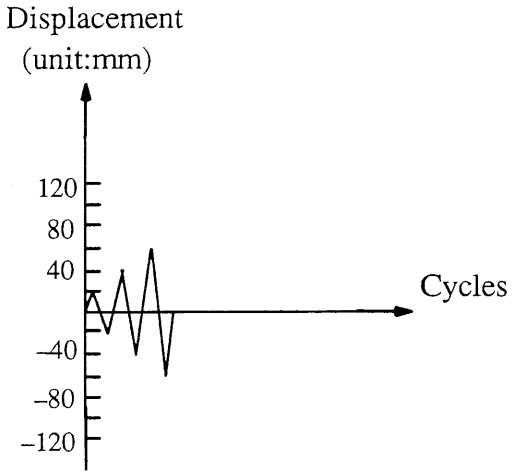

c) for the Column C17S

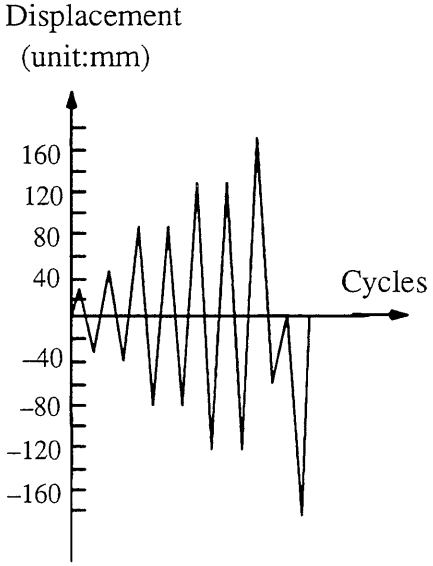

d) for the Column C15S

Fig. 3.2 Load History Used for Column Test in Field

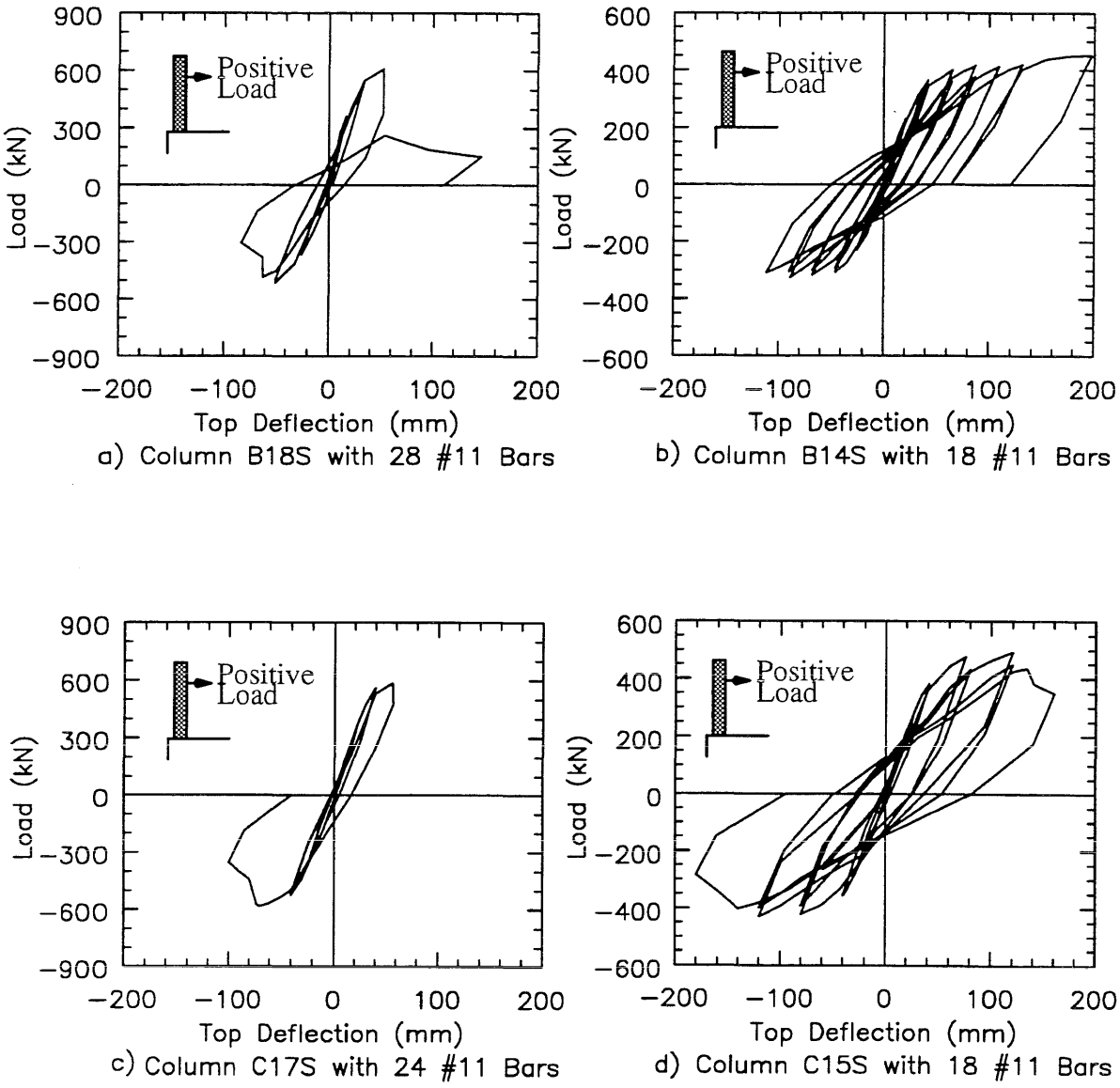

Fig. 3.3 Load vs. Deflection Curves for Field Test Columns

Fig. 3.4 The General Complex of Bridges

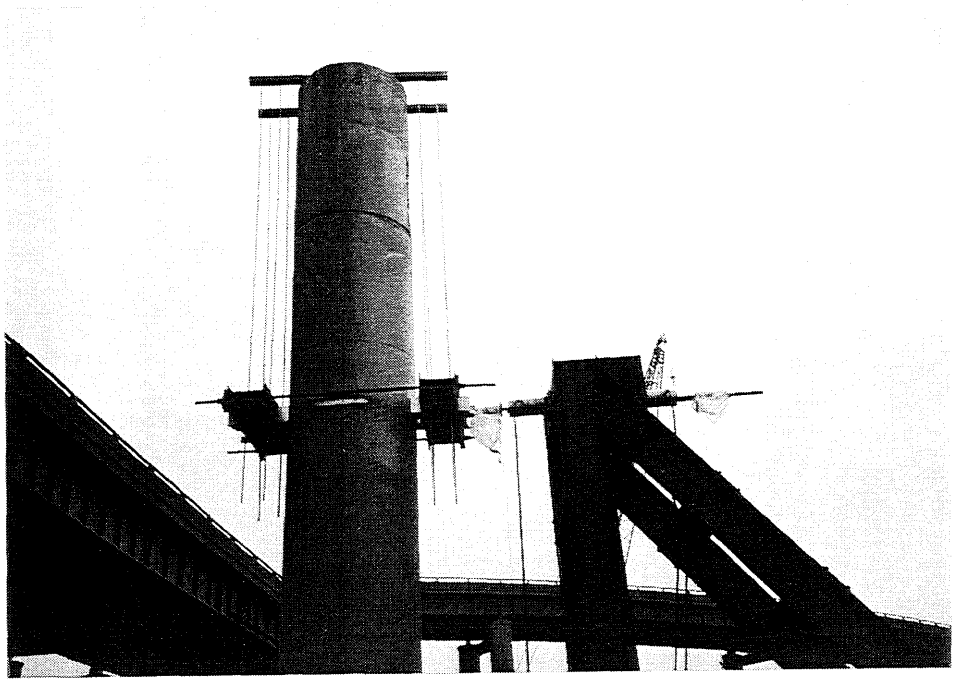

Fig. 3.5 The Top Part of the Test Setup

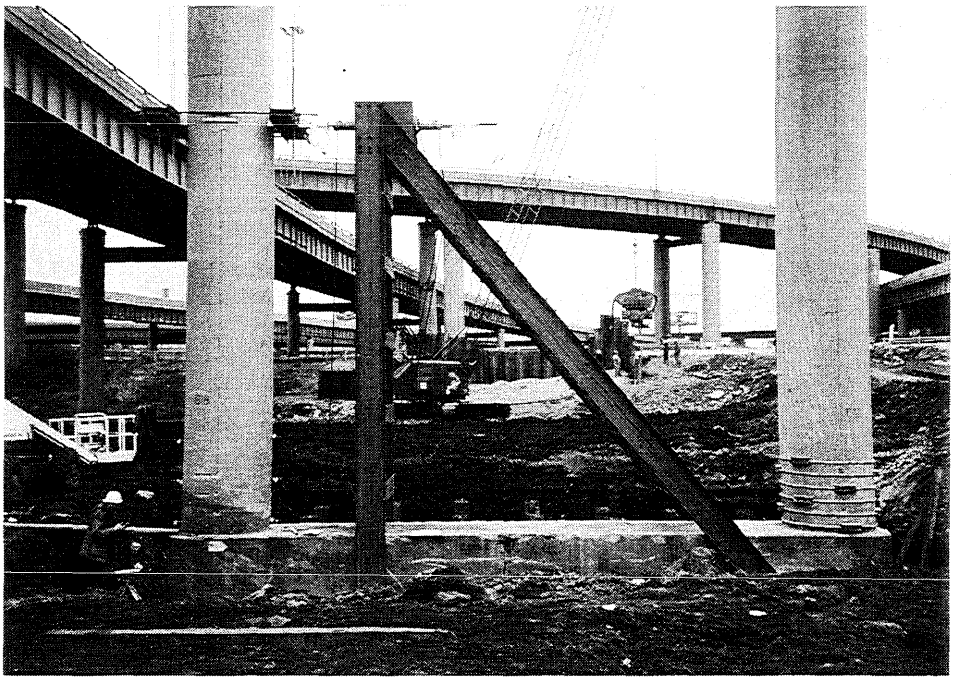

Fig. 3.6 The Bottom Part of the Test Setup

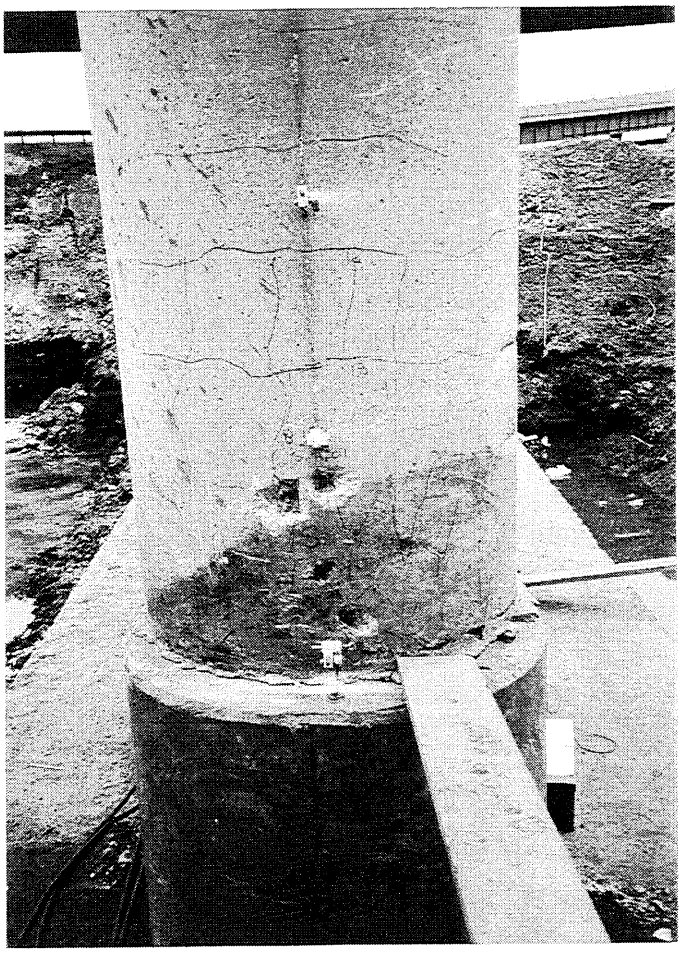

Fig. 3.7 Vertical and Horizontal Cracks on the Column Bottom Part

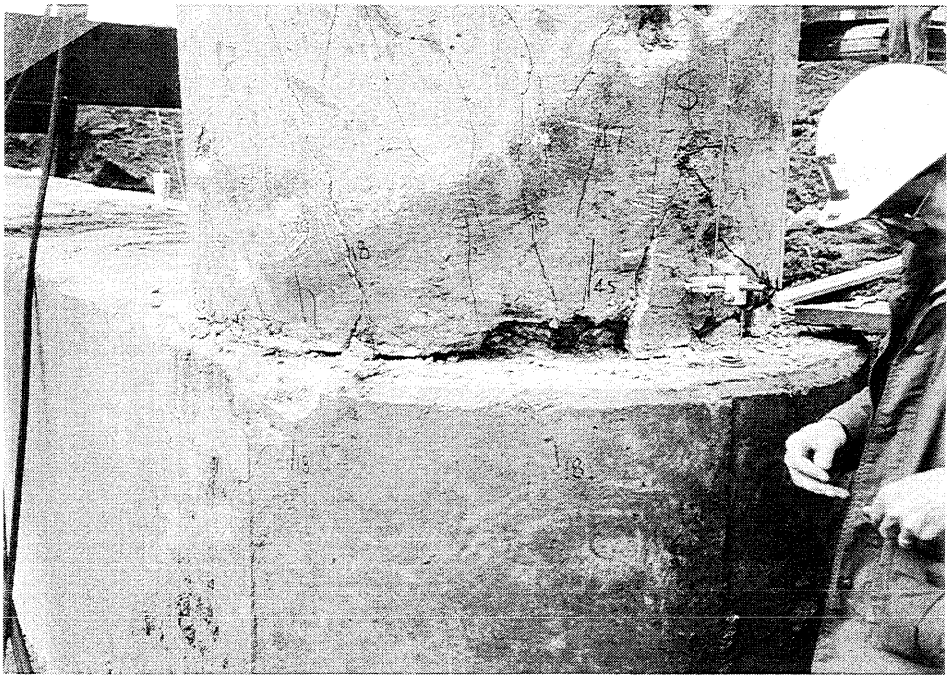

Fig. 3.8 Short Cracks on the Top of Crash Wall

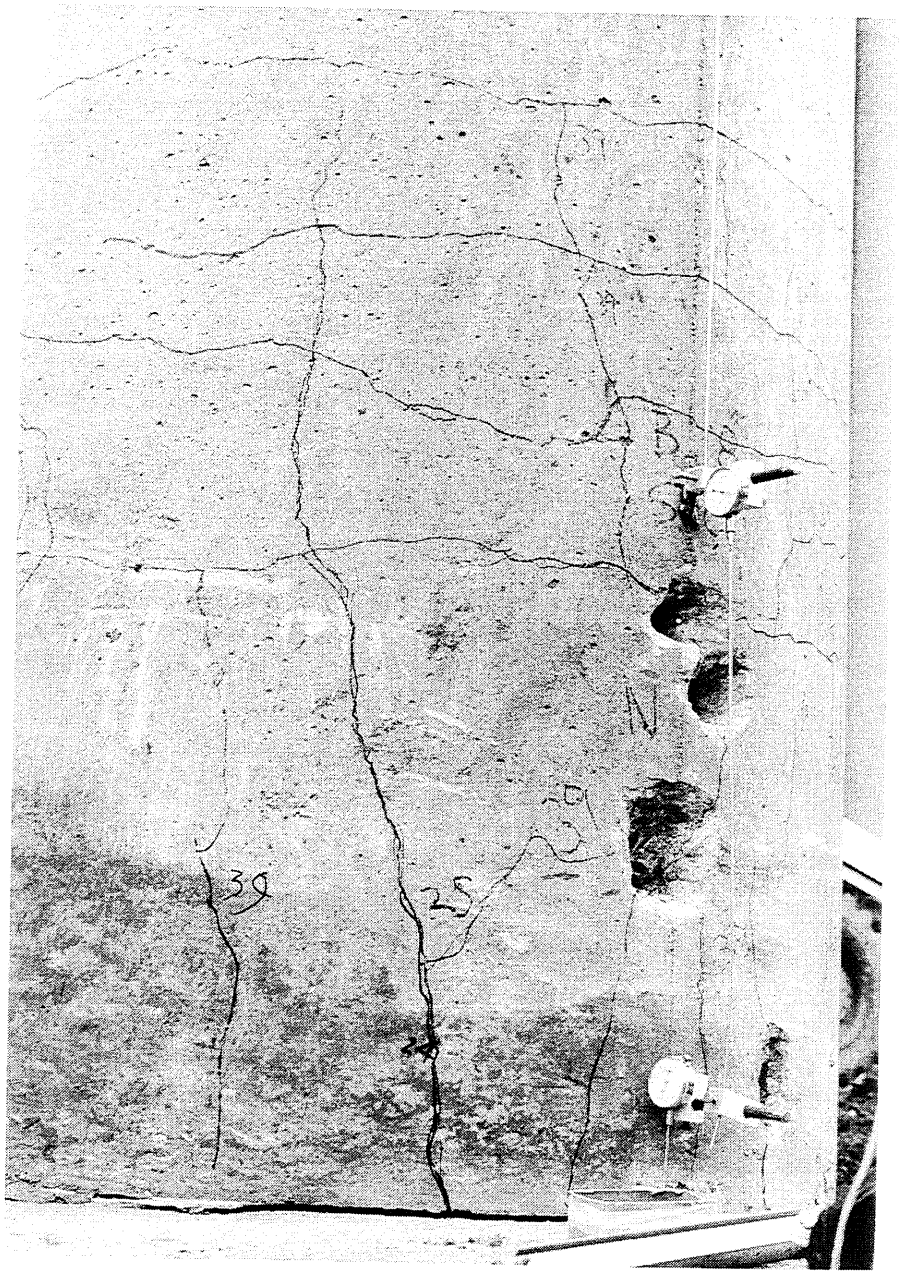

Fig. 3.9 More Vertical Cracks on the Column Bottom Part

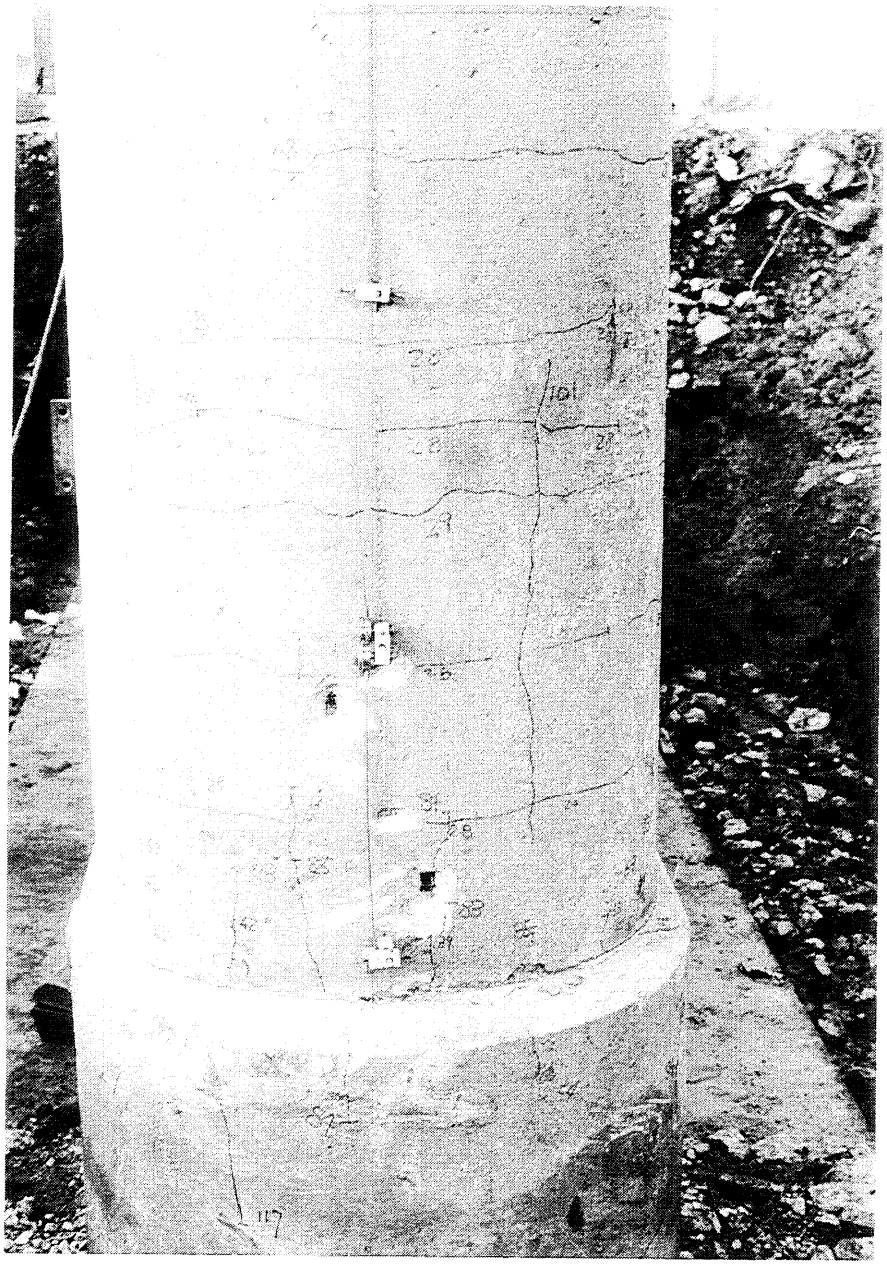

Fig. 3.10 The Last Stage of Cracking for the South Column of Pier B14

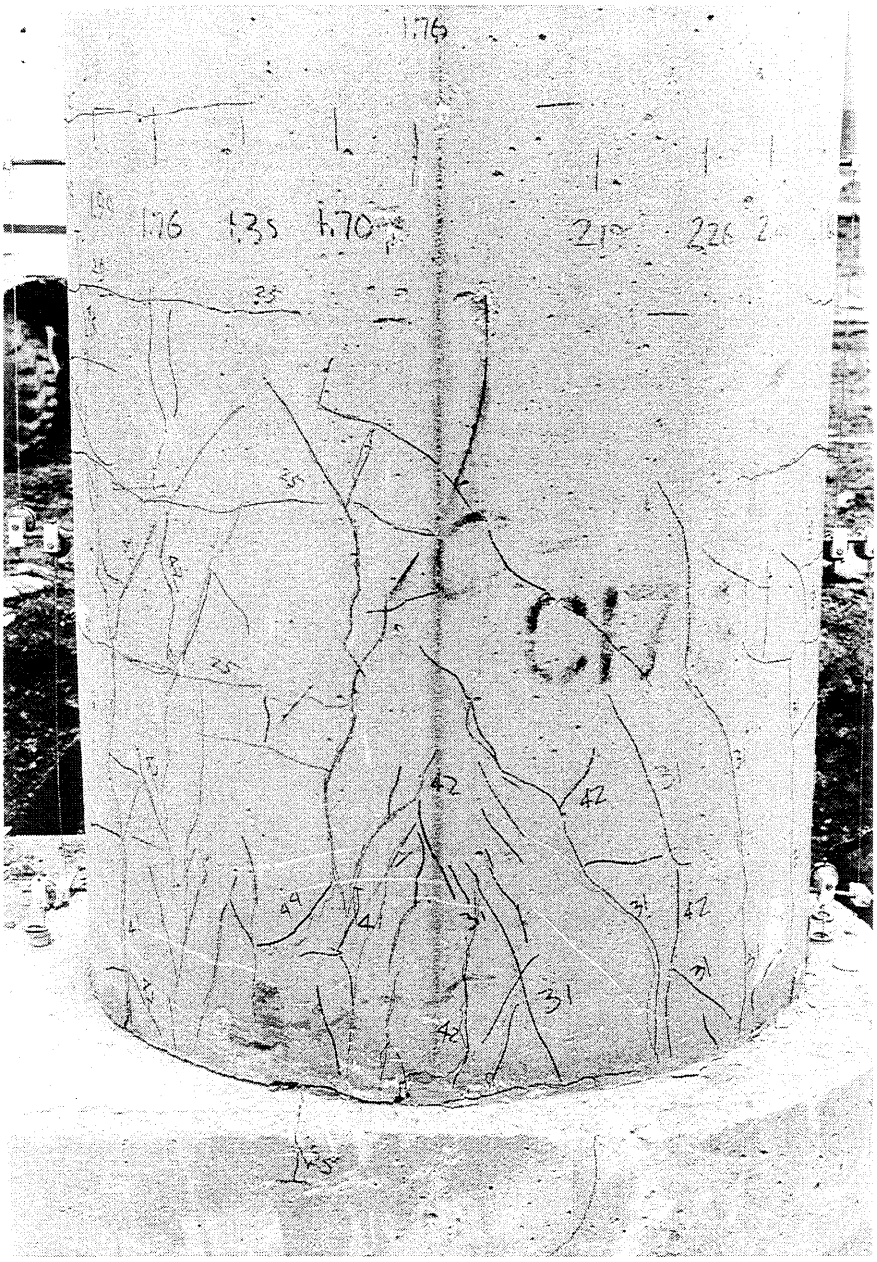

Fig. 3.11 Cracked As–Built Column C17S

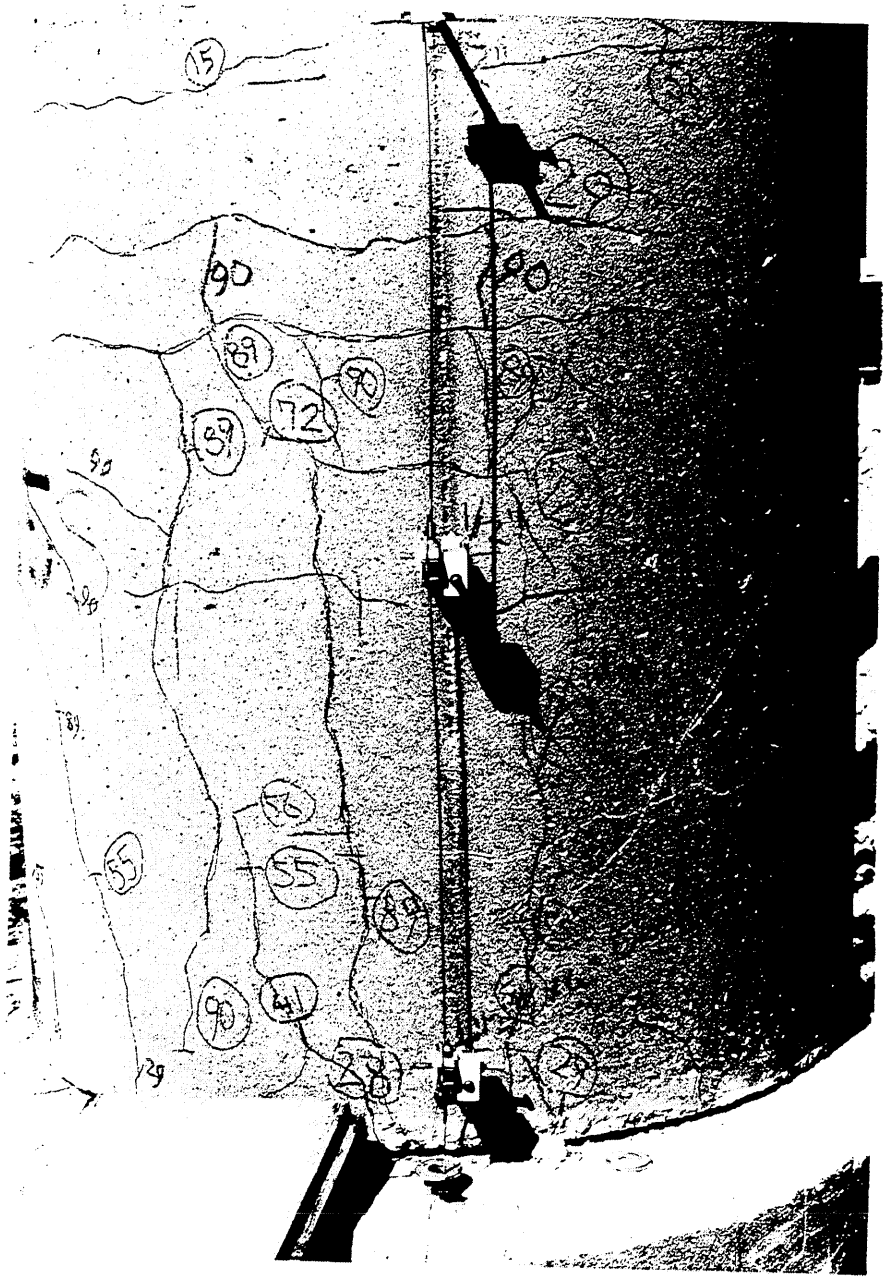

Fig. 3.12 As–Built Column C15S Damaged to Failure

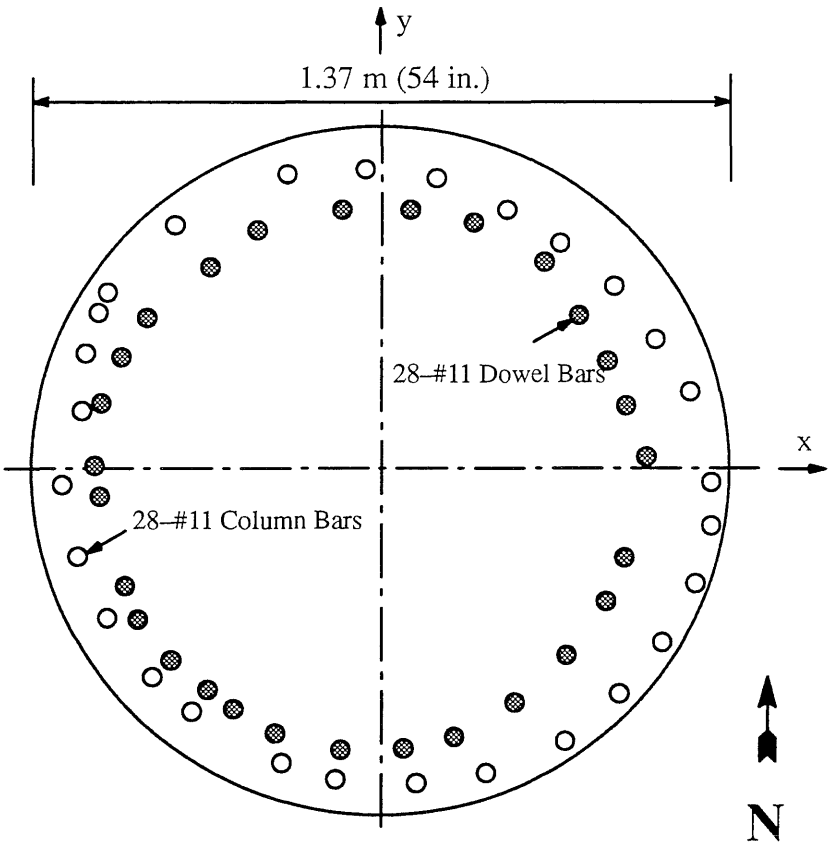

Fig. 3.13 Bar Locations in 1.37 m (54 in.) Diameter Column B18S

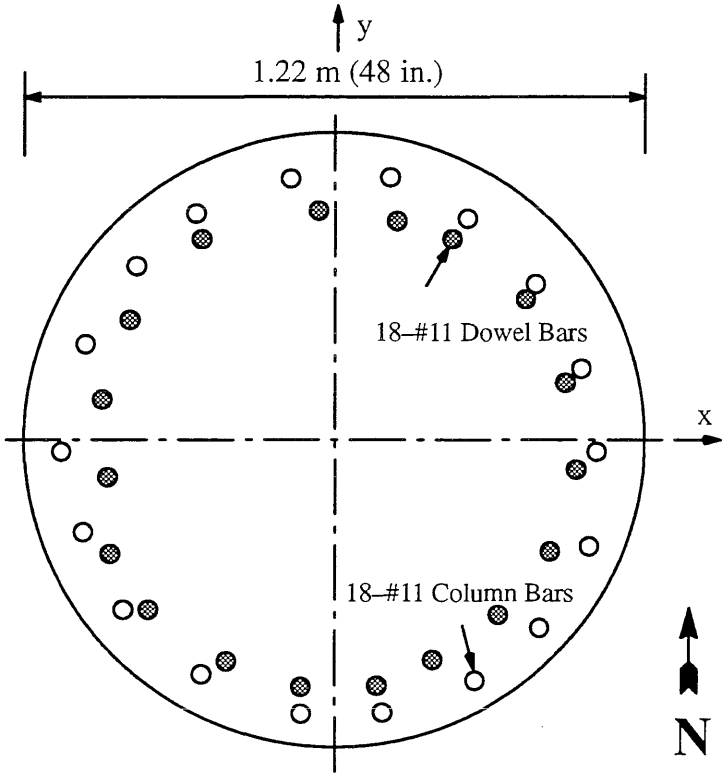

Fig. 3.14 Bar Locations in 1.22 m (48 in.) Diameter Column B14S

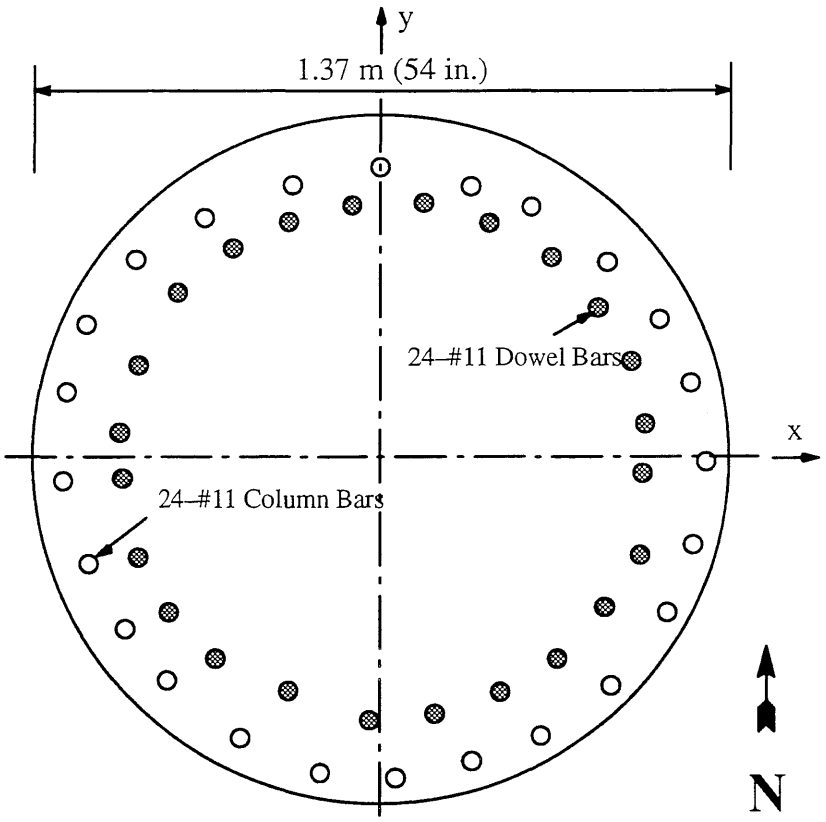

Fig. 3.15 Bar Locations in 1.37 m (54 in.) Diameter Column C17S

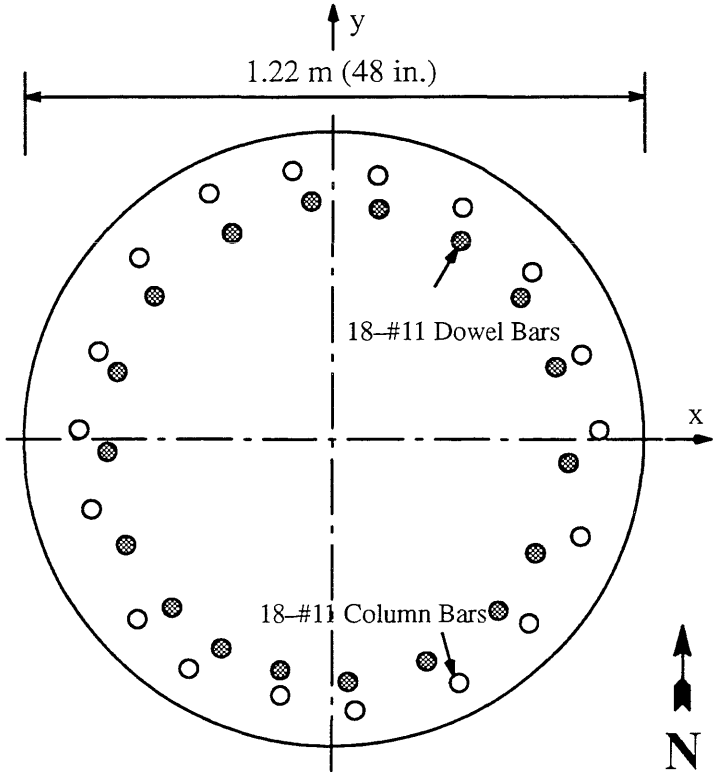

Fig. 3.16 Bar Locations in 1.22 m (48 in.) Diameter Column C15S

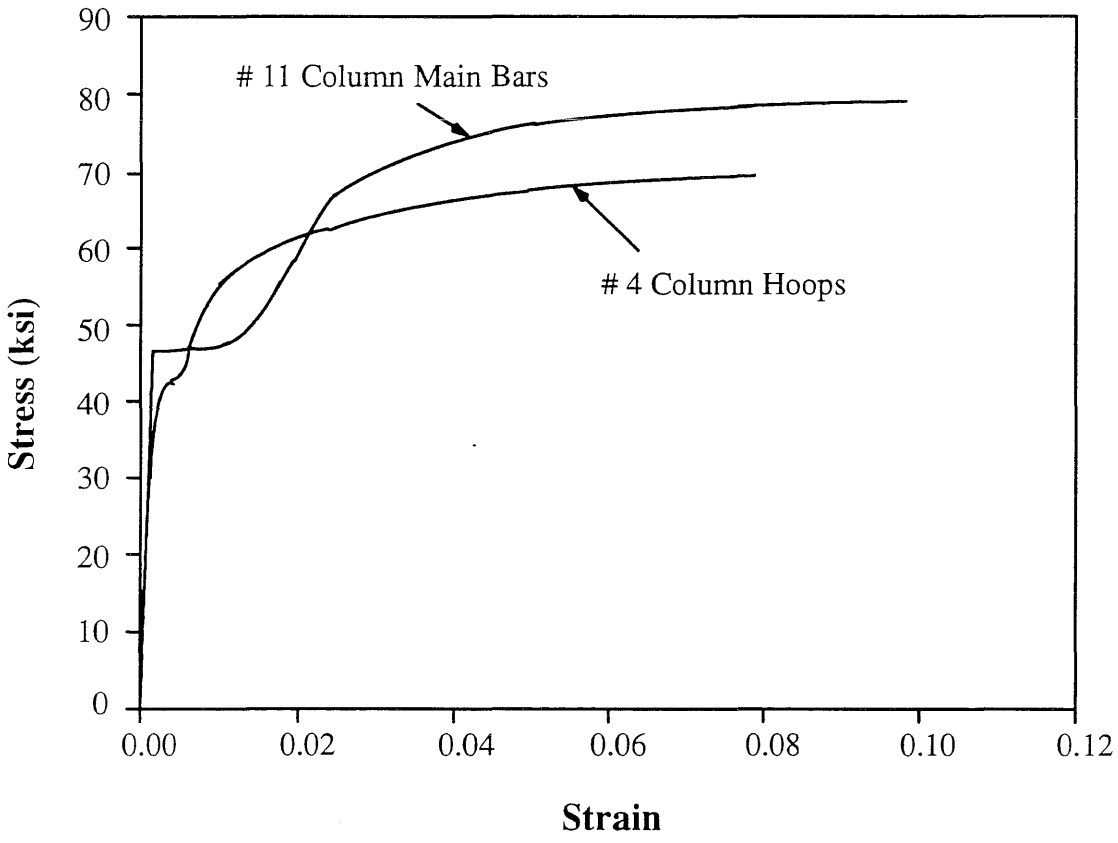

Fig. 3.17 Measured Stress vs. Strain Curve of Reinforcement for Columns

(1 ksi = 6.9 MPa)

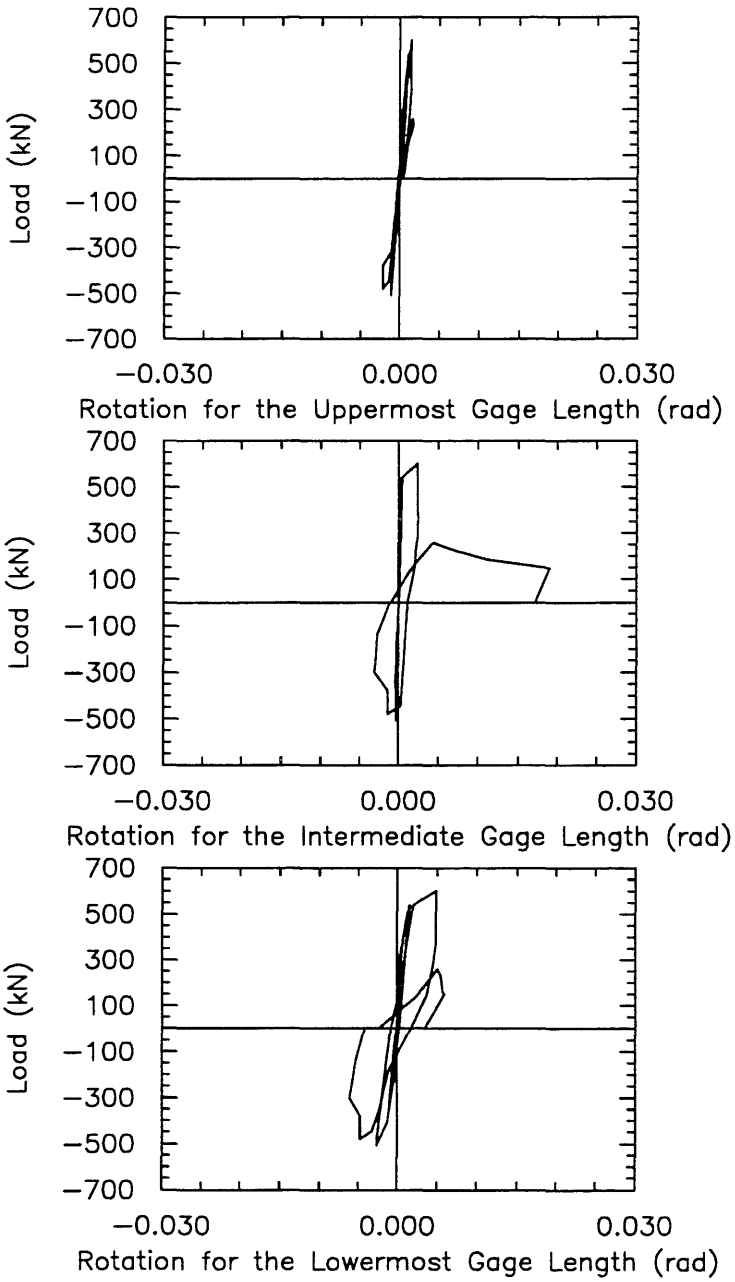

Fig. 3.18 Load vs. Rotation Curve for Column B18S

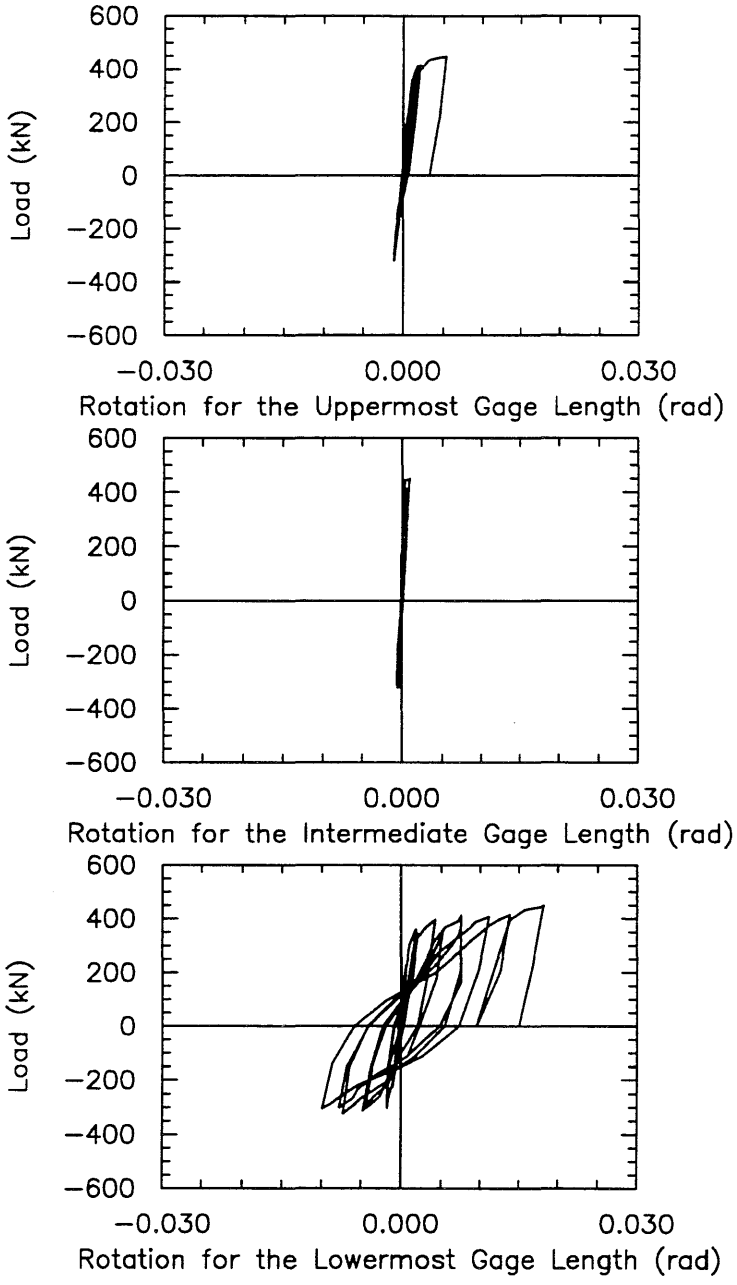

Fig. 3.19 Load vs. Rotation Curve for Column B14S

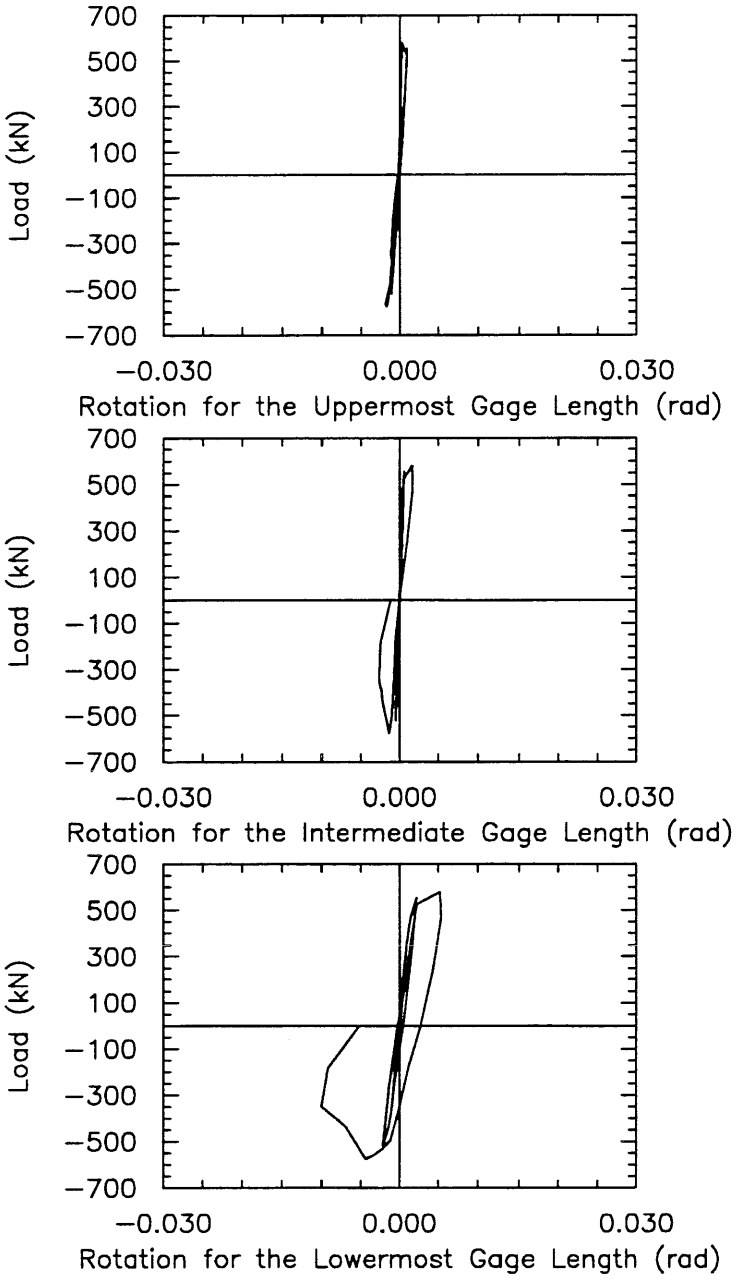

Fig. 3.20 Load vs. Rotation Curve for Column C17S

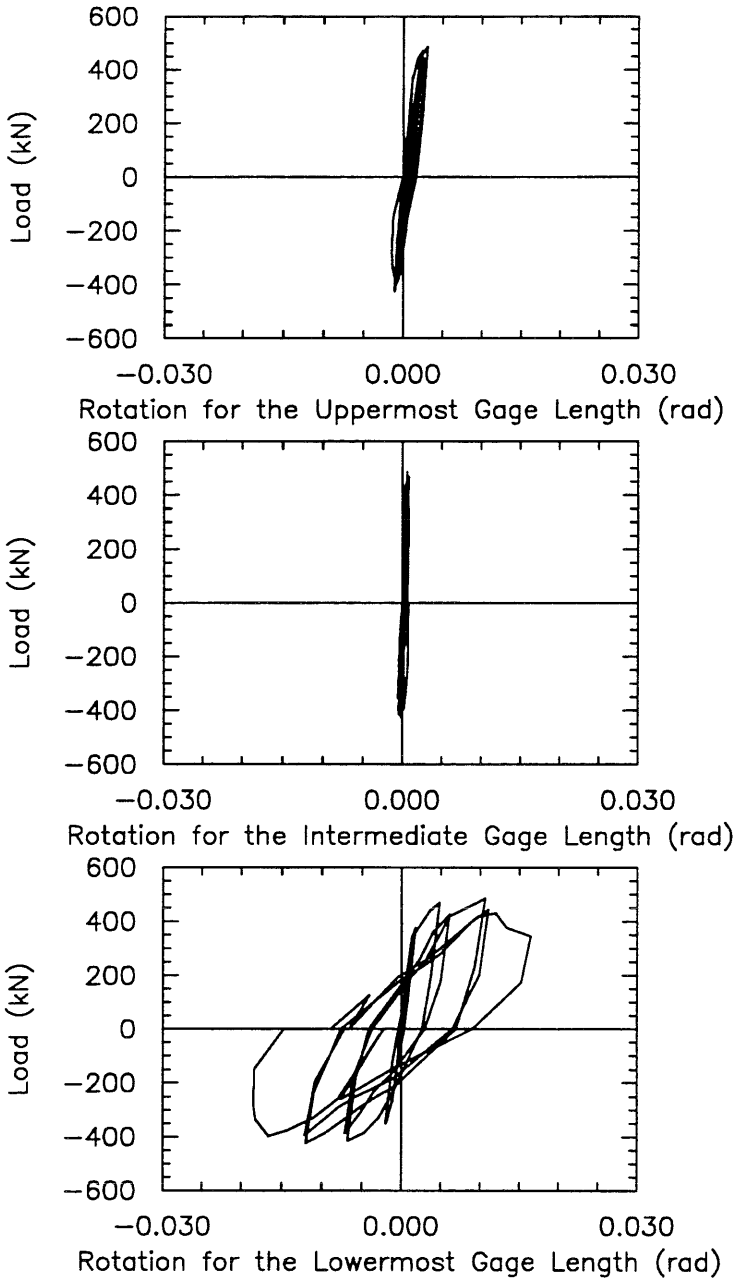

Fig. 3.21 Load vs. Rotation Curve for Column C15S

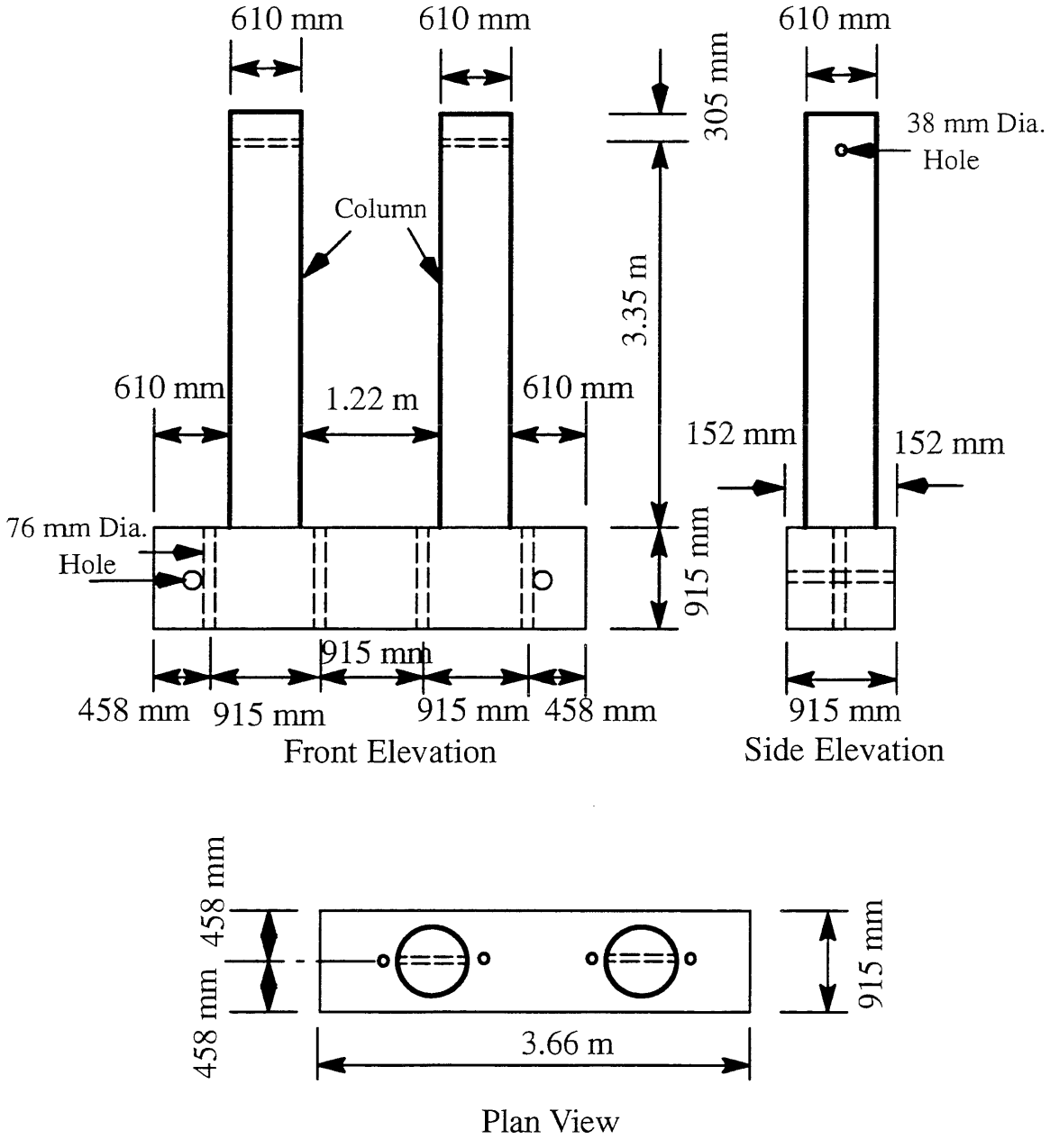

Fig. 4.1 Test Specimen

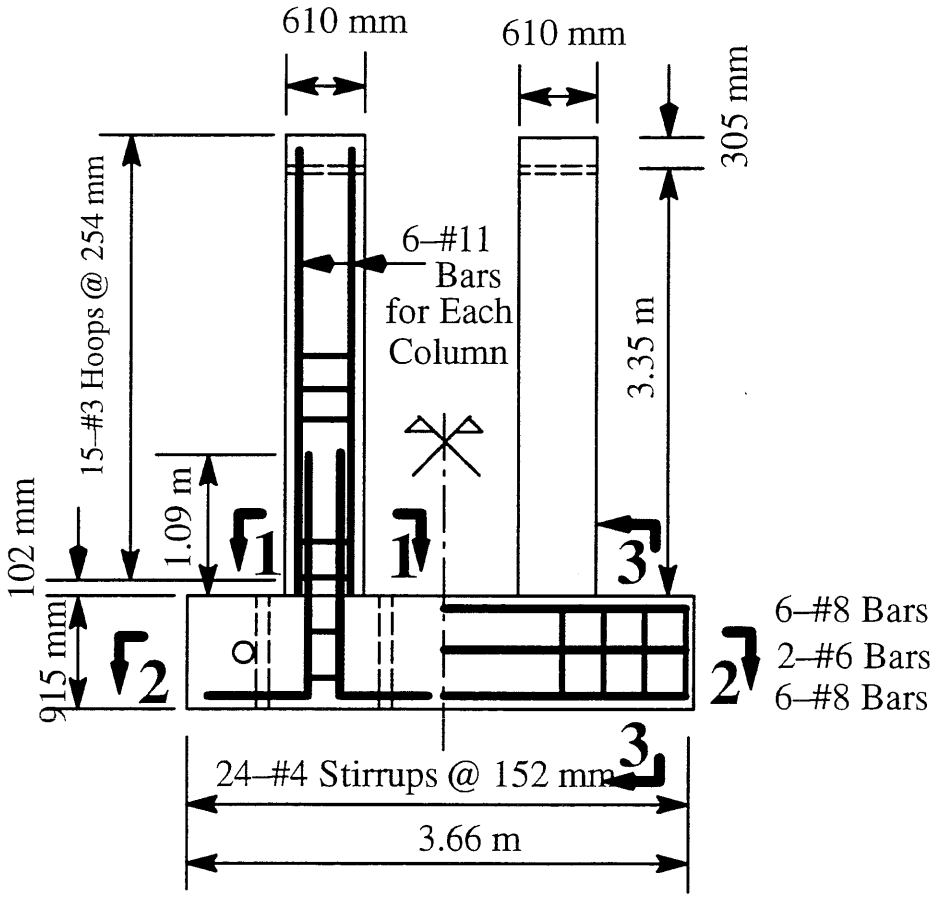

Fig. 4.2a Reinforcing Details for Specimen

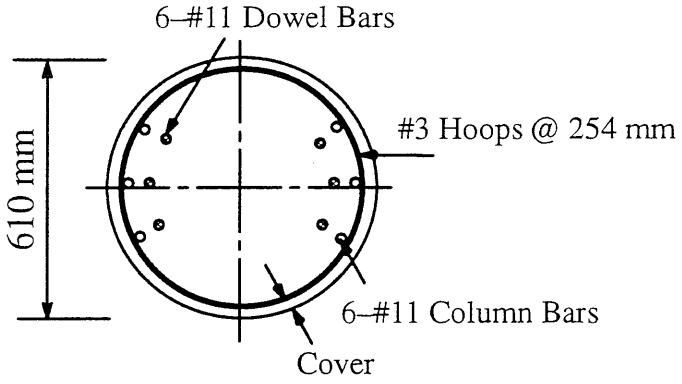

Section 1–1

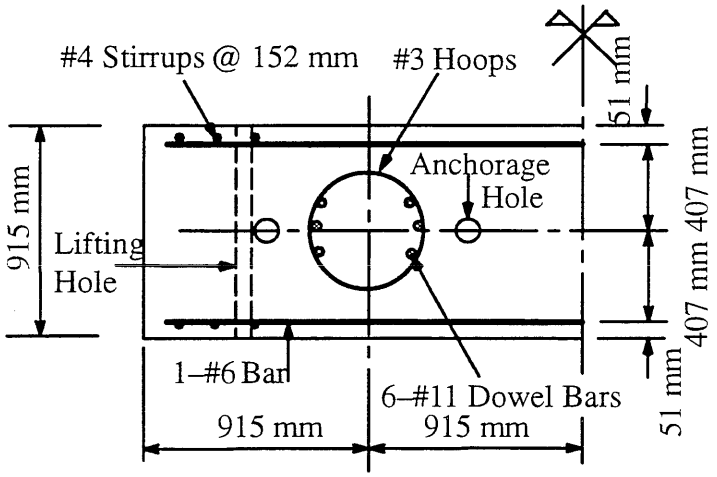

Section 2–2

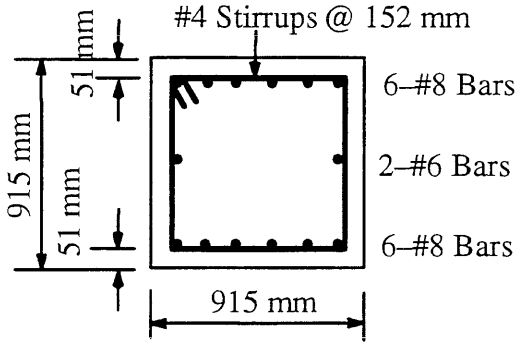

Section 3–3

Fig. 4.2b Reinforcing Details of Specimen Members

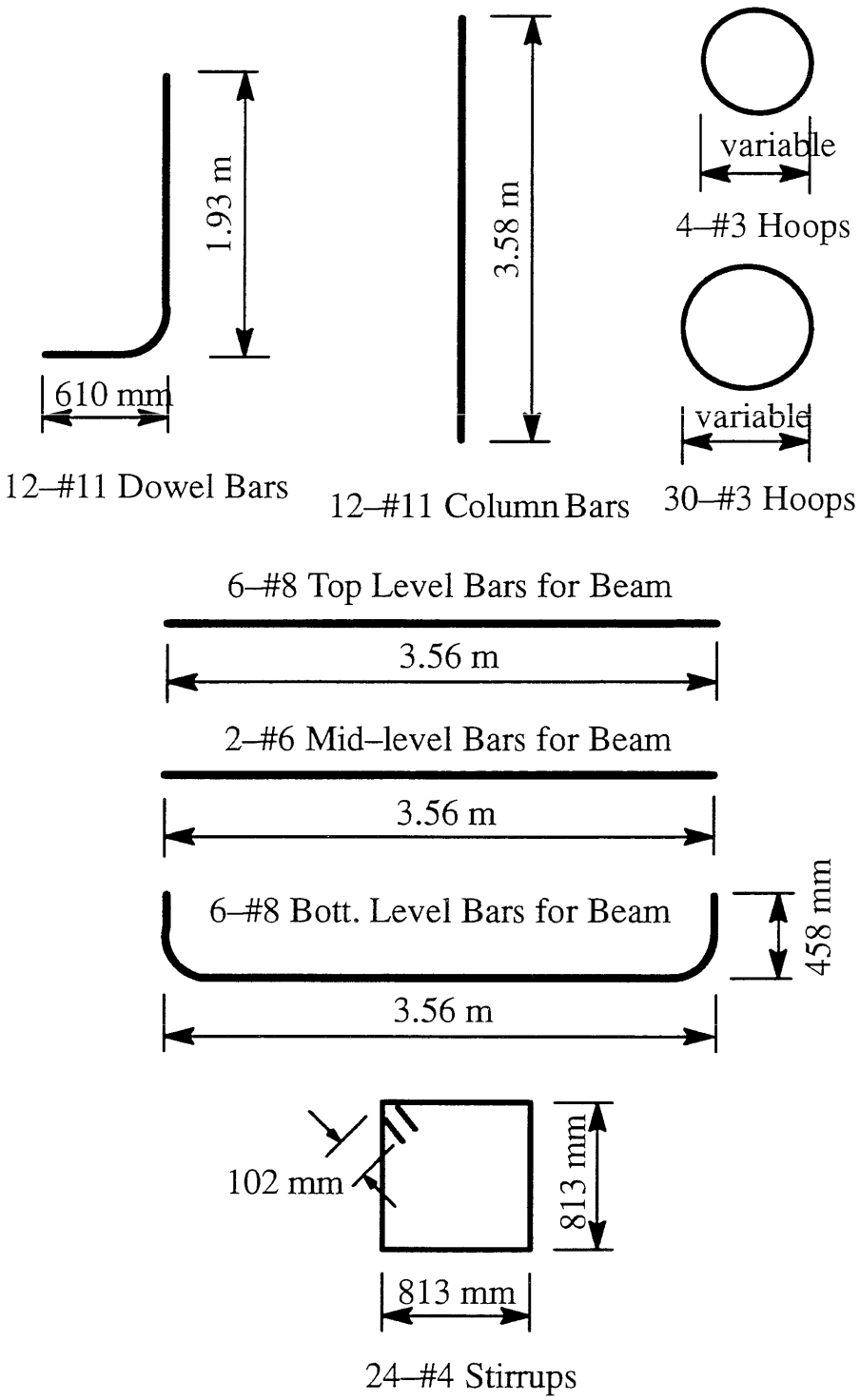

Fig. 4.3 Steel Material for Each Specimen

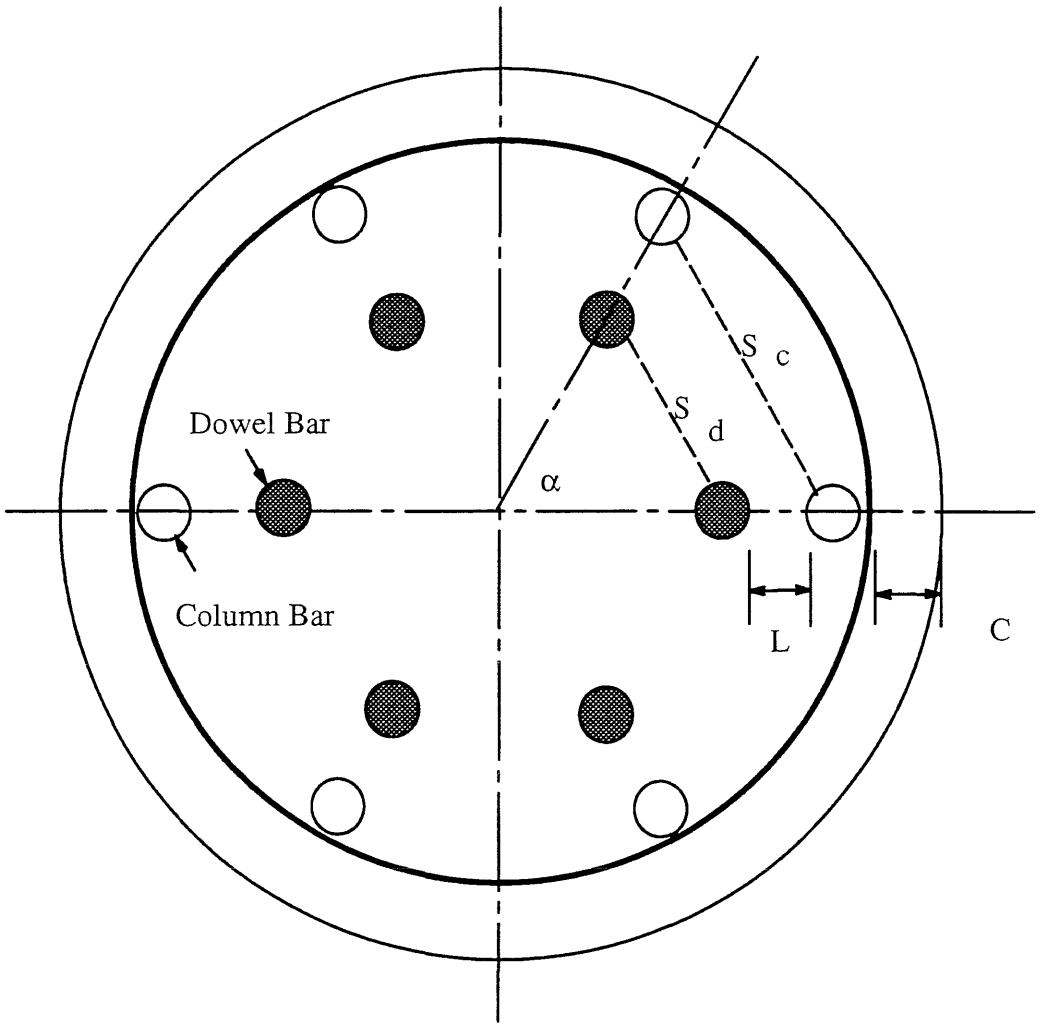

Fig. 4.4a Cross Section for Laboratory Column

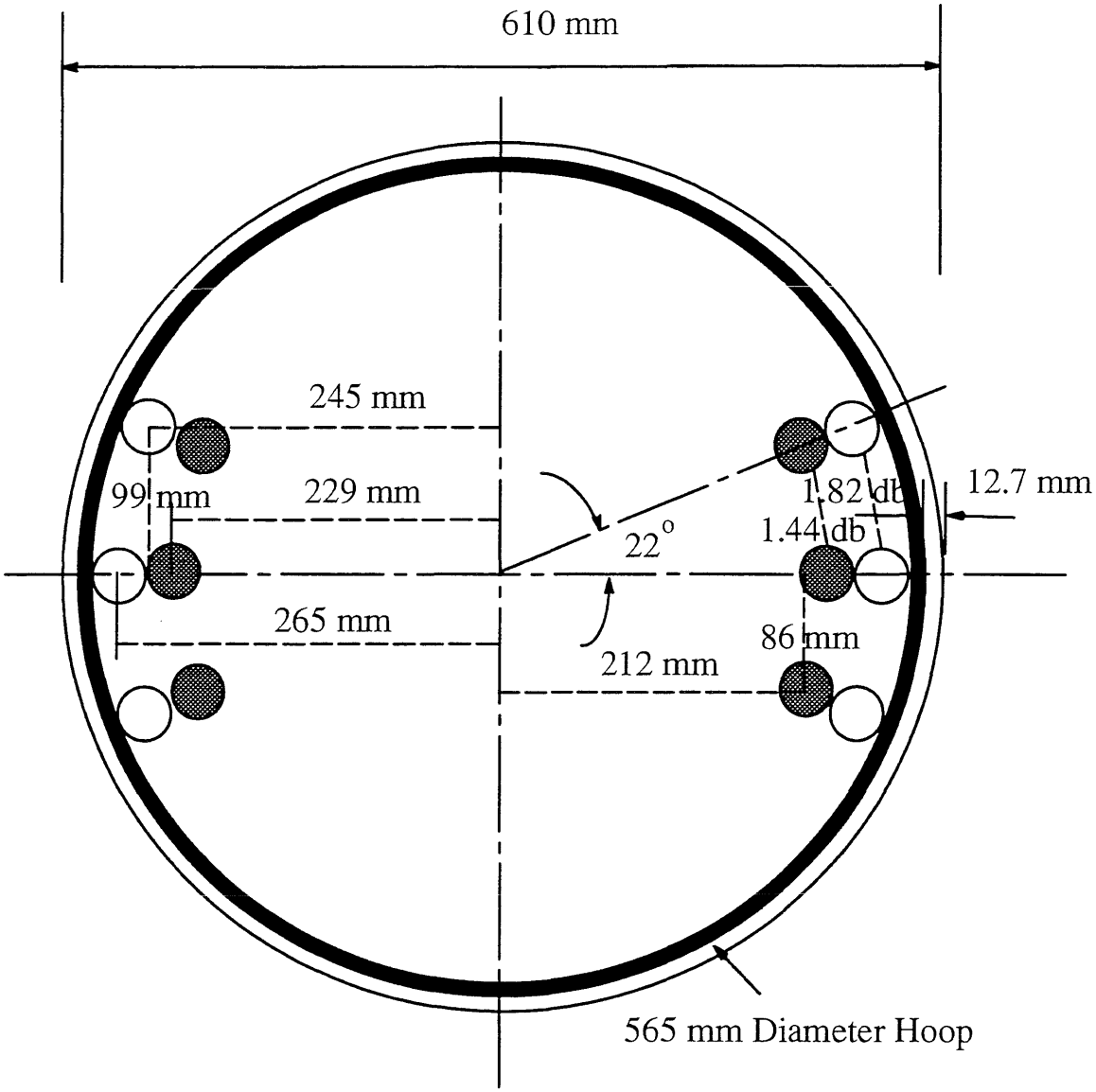

Fig. 4.4b Cross Section for Column A–1 (L=0, C=12.7 mm)

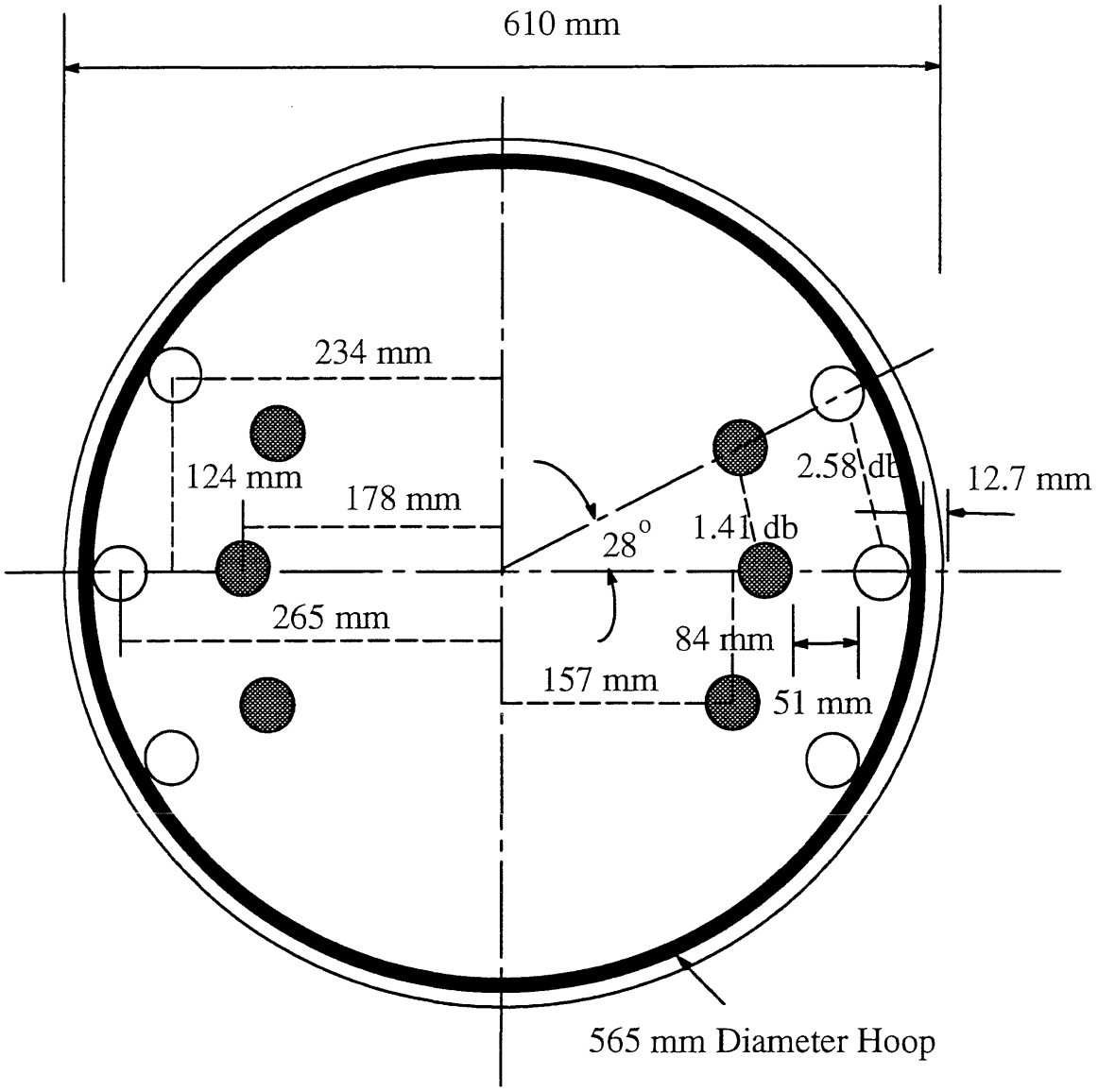

Fig. 4.4c Cross Section for Column A–2 (L=51 mm, C=12.7 mm)

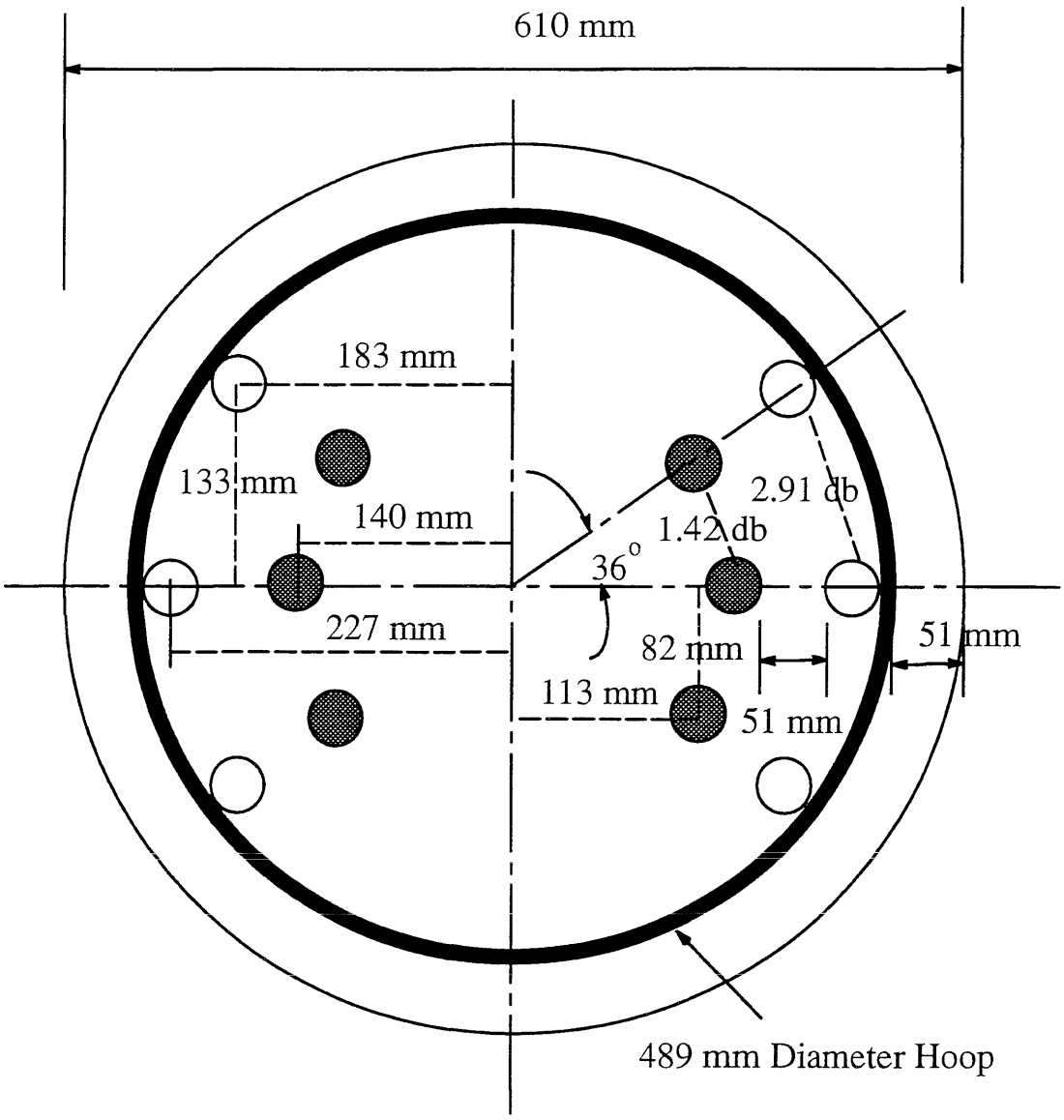

Fig. 4.4d Cross Section for Column A–3 (L=C=51 mm)

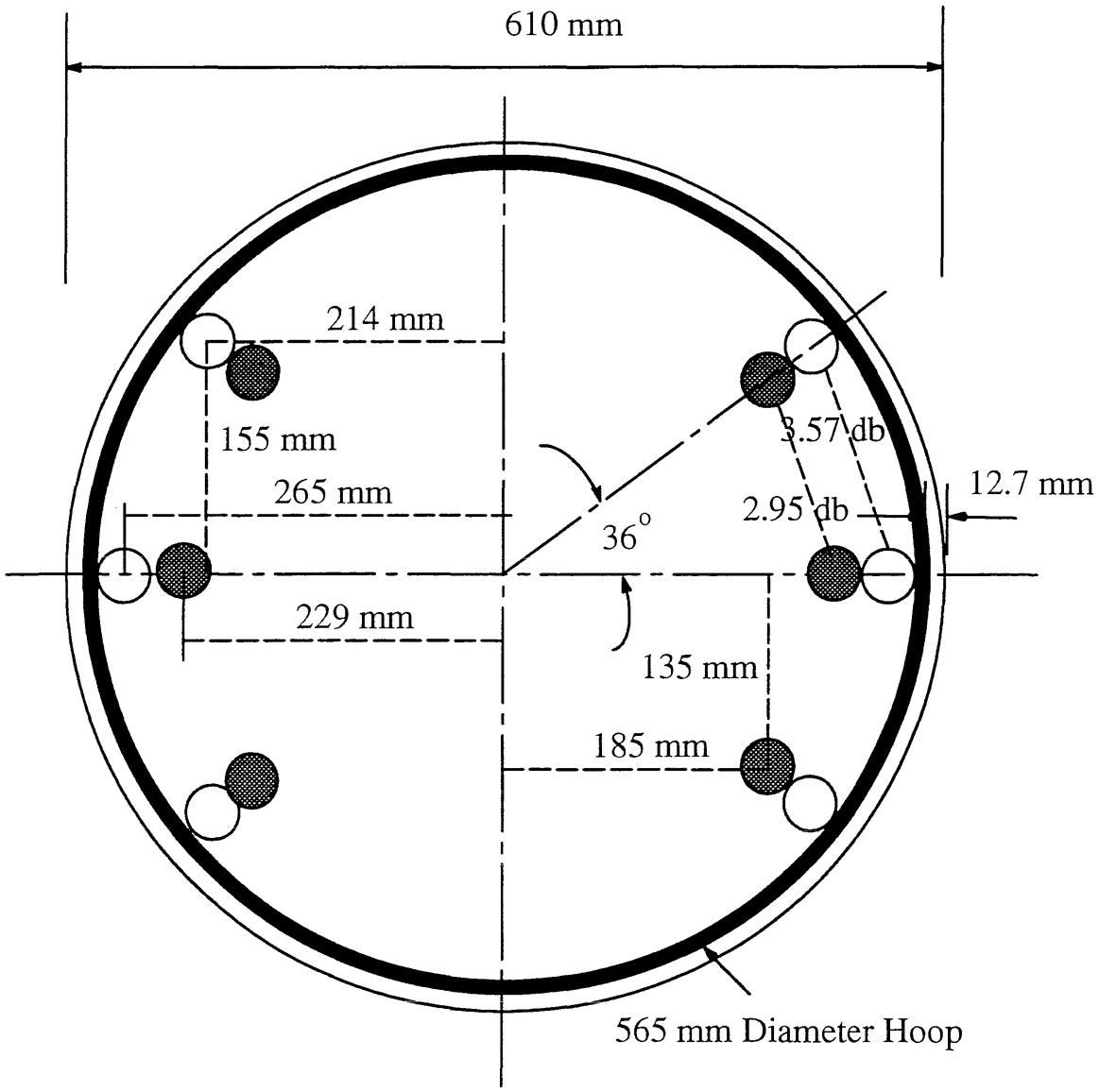

Fig. 4.4e Cross Section for Column B–1 (L=0, C=12.7 mm)

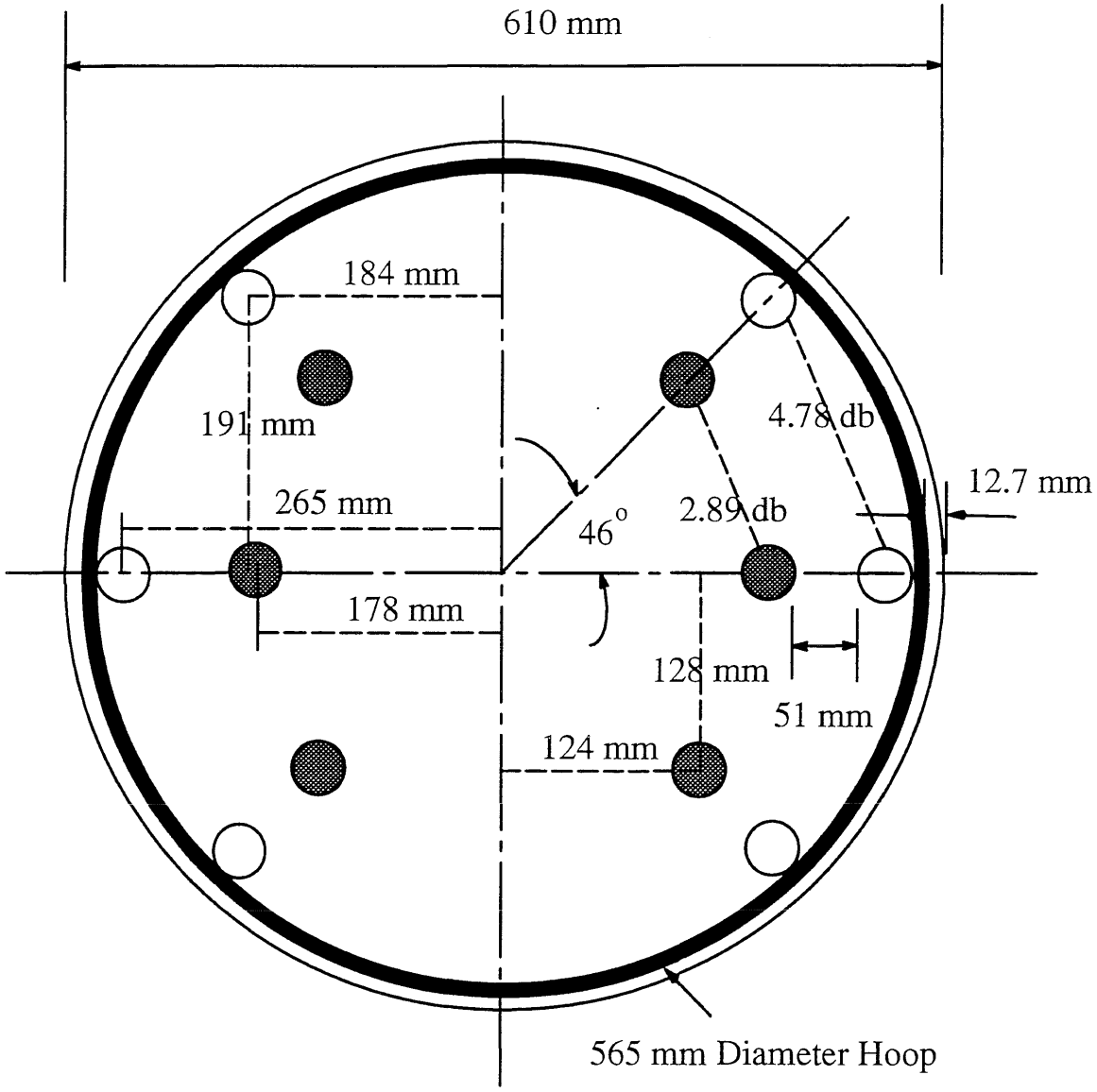

Fig. 4.4f Cross Section for Column B–2 (L=51 mm, C=12.7 mm)

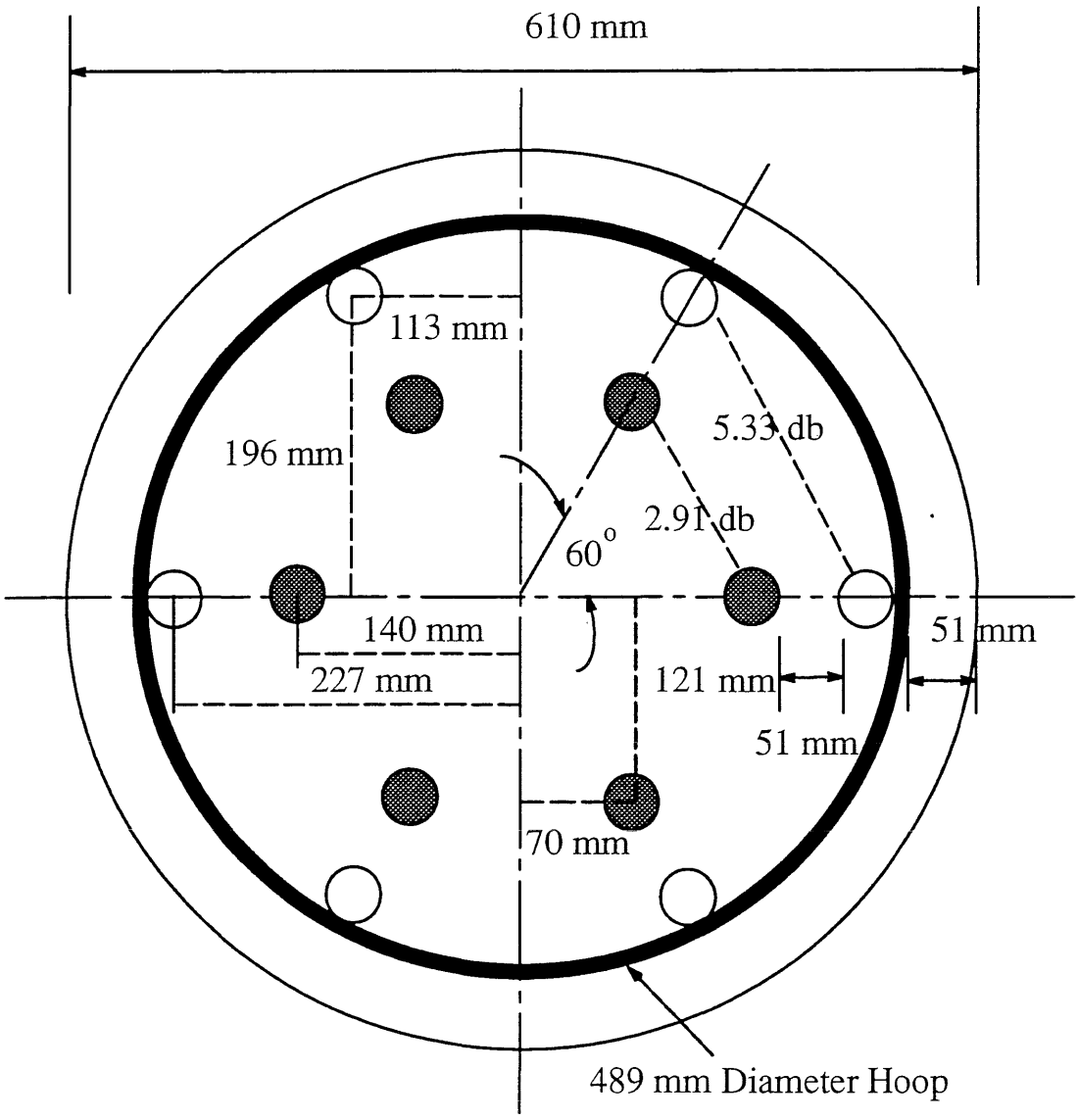

Fig. 4.4g Cross Section for Column B–3 (L=C=51 mm)

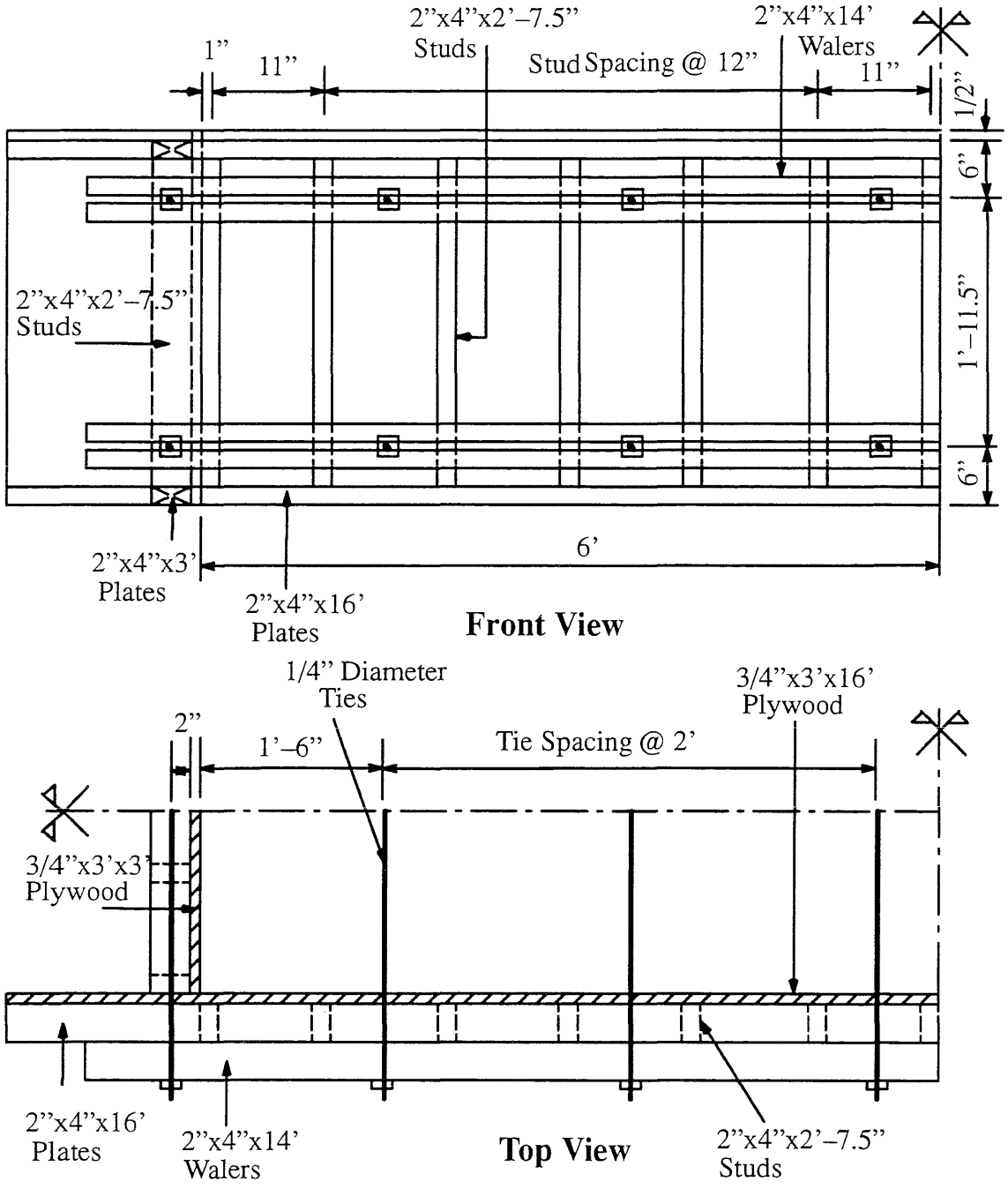

Fig. 4.5 Formwork for Base Beam
(1 in. = 25.4 mm)

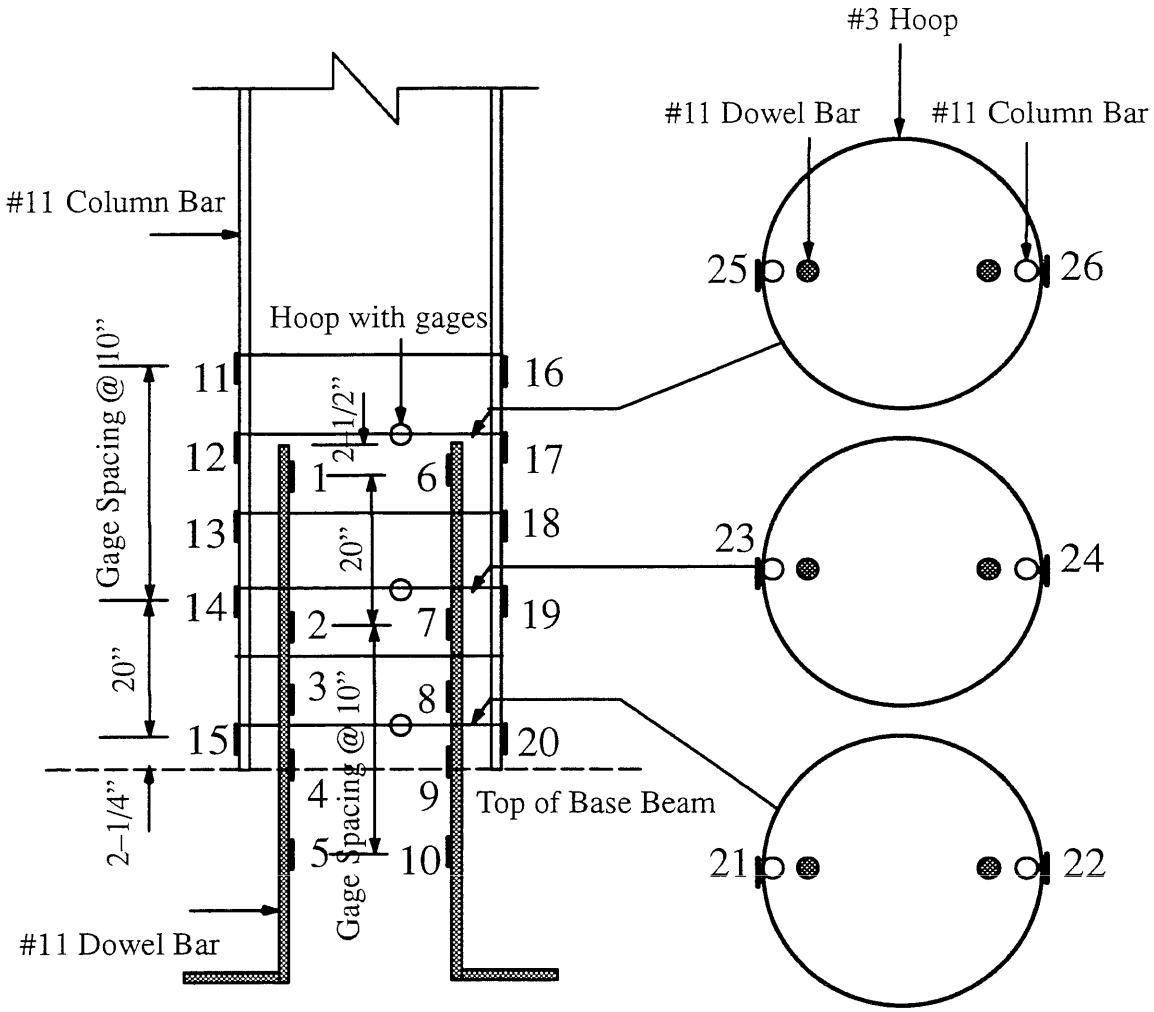

Fig. 4.6 Locations and Numbers of Strain Gages

(1 in. = 25.4 mm)

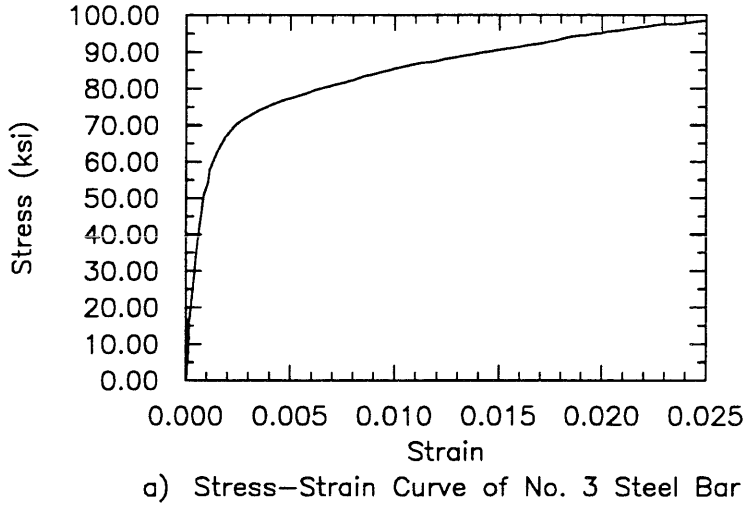

a) Stress–Strain Curve of No. 3 Steel Bar

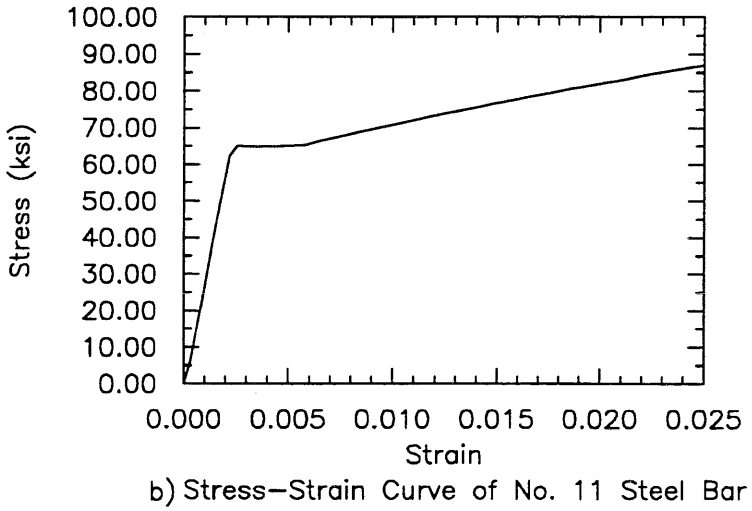

b) Stress–Strain Curve of No. 11 Steel Bar

Fig. 4.7 Measured Stress vs. Strain Curve of Reinforcement for Columns

(1 ksi = 6.9 MPa)

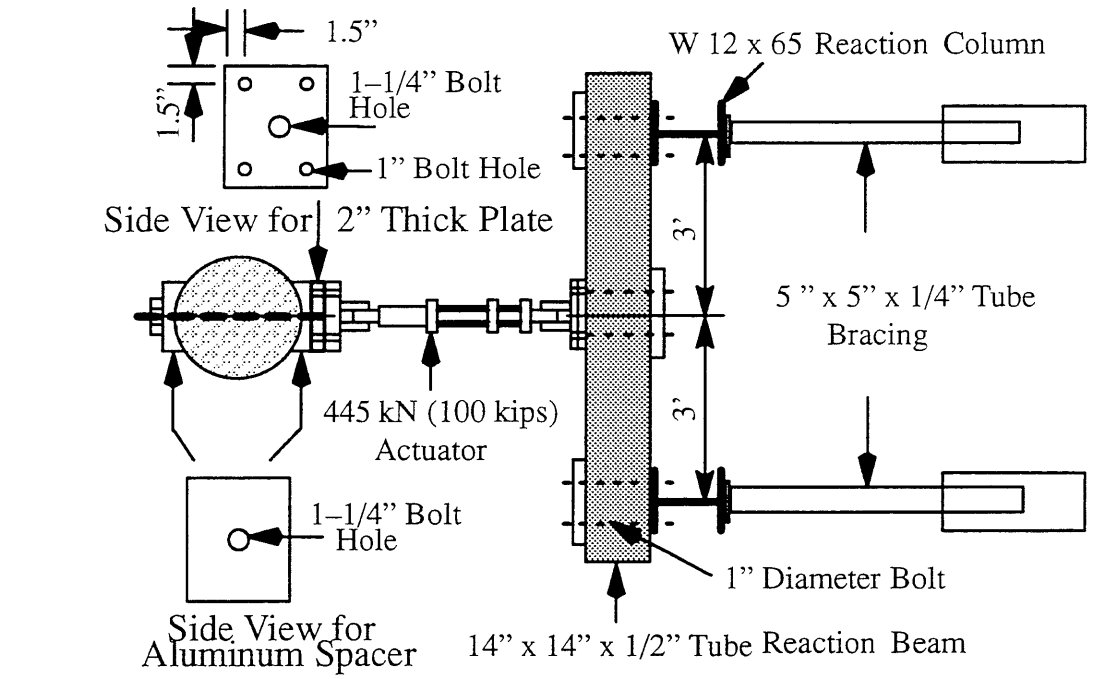

a) Top View

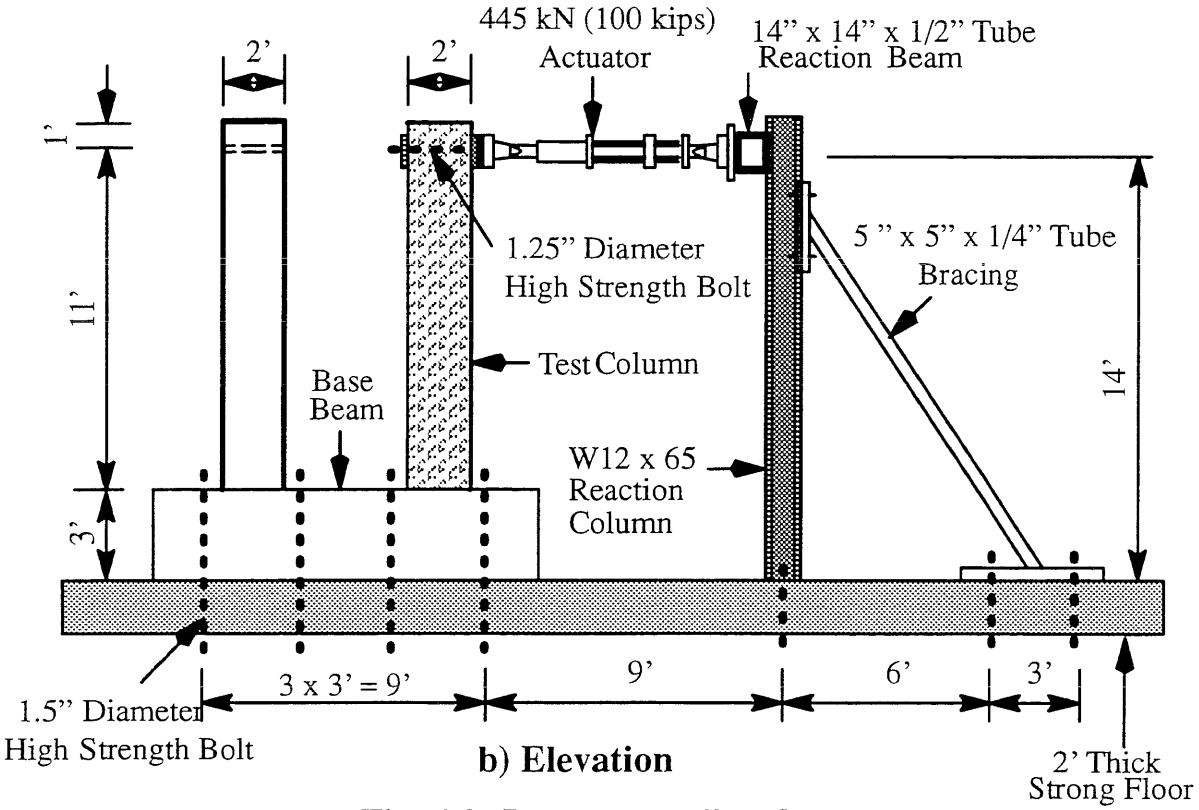

b) Elevation

Fig. 4.8 Laboratory Test Setup
(1 in. = 25.4 mm)

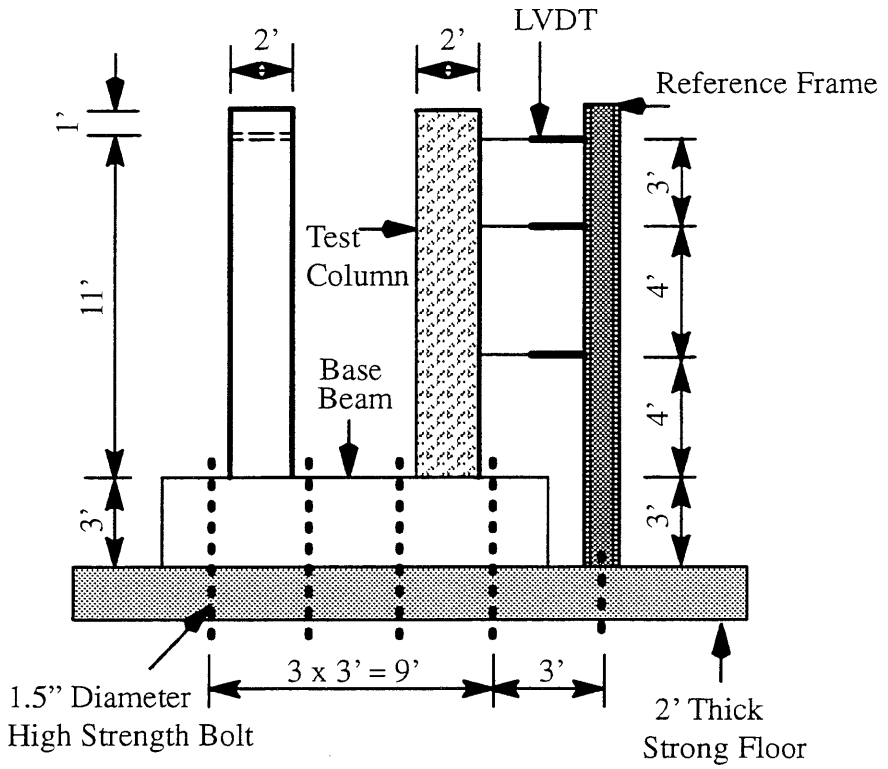

Fig. 4.9 LVDT Locations for Column Deflections
(1 in. = 25.4 mm)

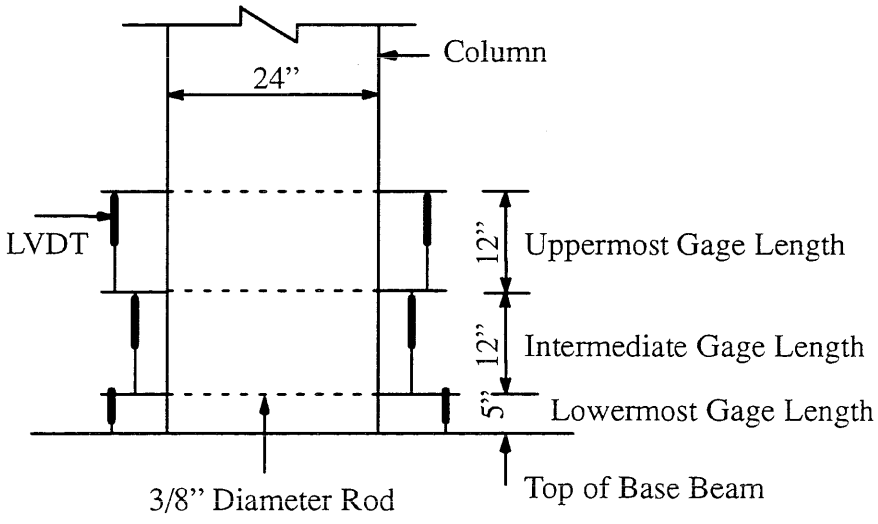

Fig. 4.10 Rotation Measurements
(1 in. = 25.4 mm)

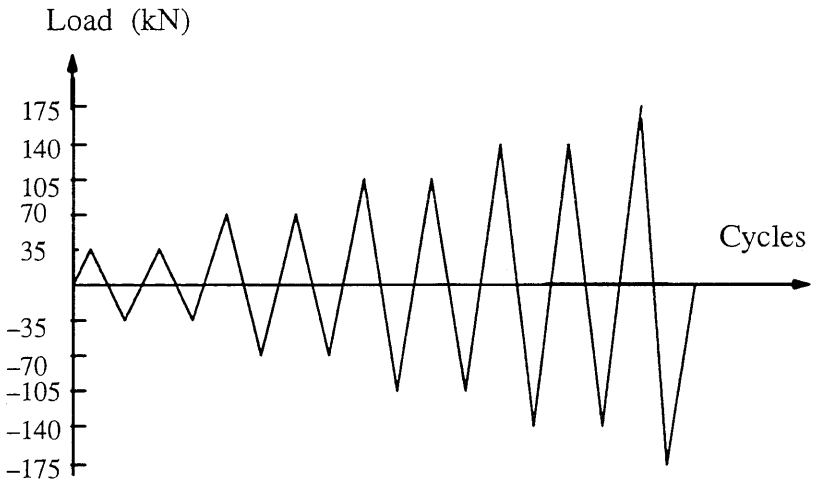

a) Stage 1–Load Control

Fig. 5.1a Loading History for Column A–1

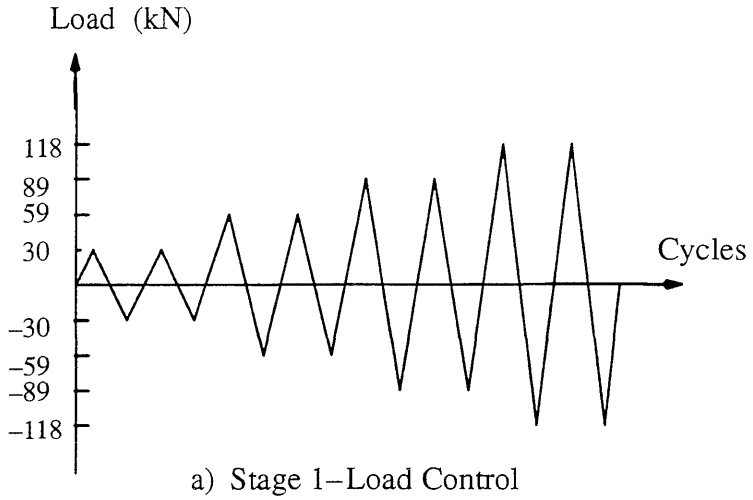

a) Stage 1–Load Control

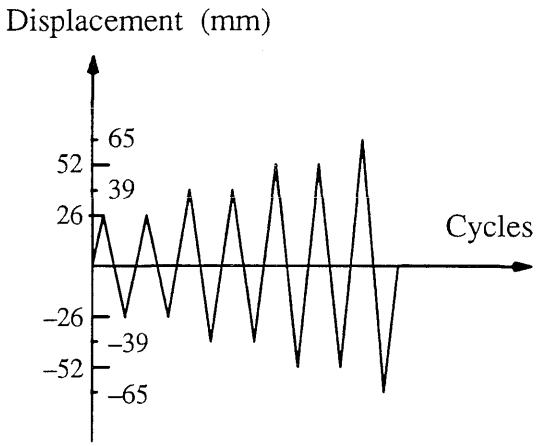

b) Stage 2–Displacement Control

Fig. 5.1b Loading History for Column A–2

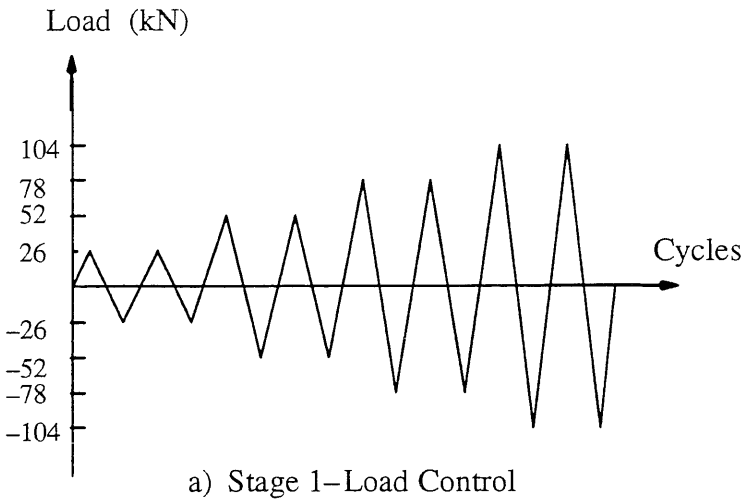

a) Stage 1–Load Control

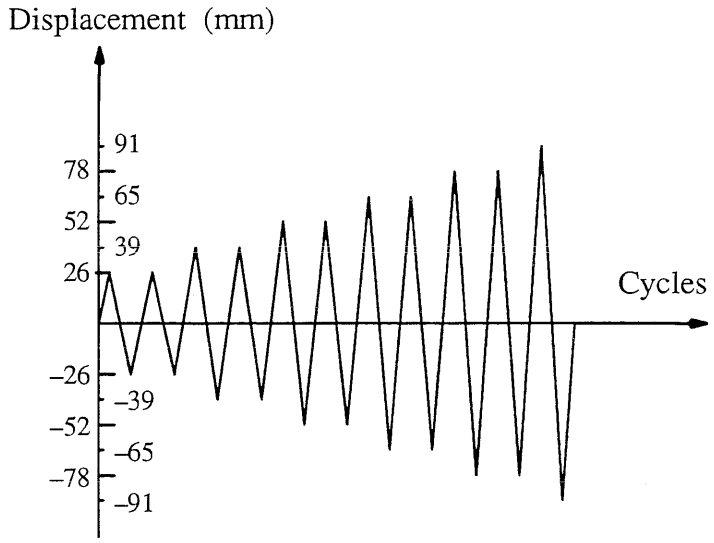

b) Stage 2–Displacement Control

Fig. 5.1c Loading History for Column A–3

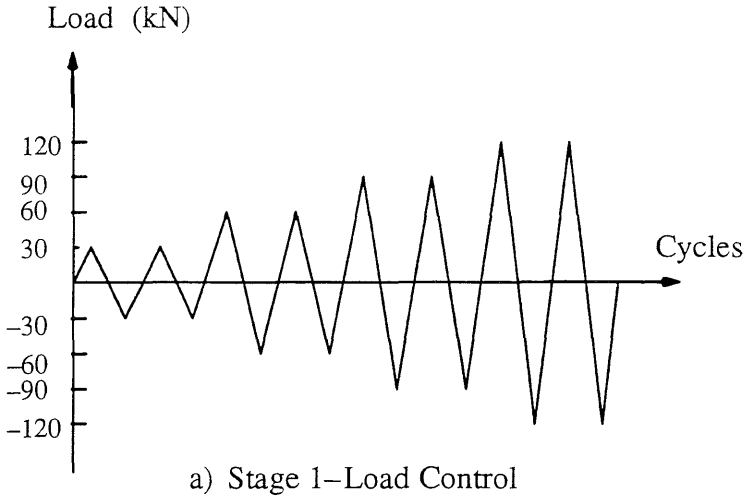

a) Stage 1–Load Control

(still reading load due to the flexible loading frame)

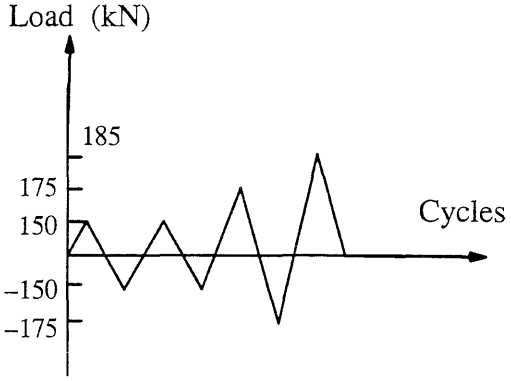

b) Stage 2–Displacement Control

Fig. 5.1d Loading History for Column B–1

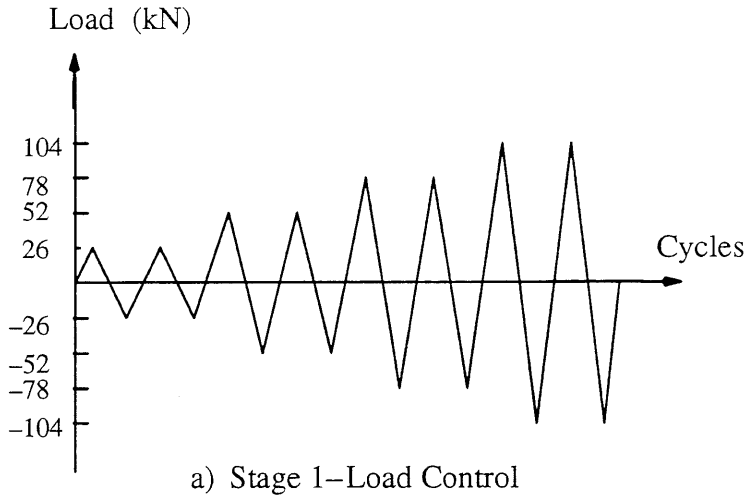

a) Stage 1–Load Control

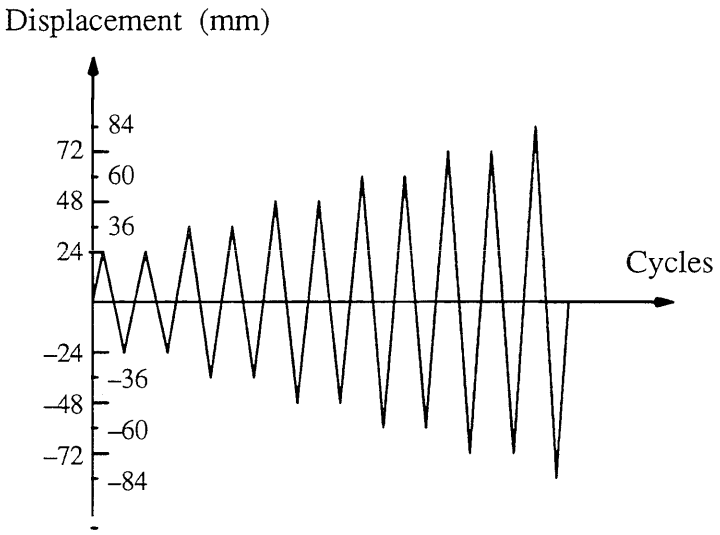

b) Stage 2–Displacement Control

Fig. 5.1e Loading History for Column B–2

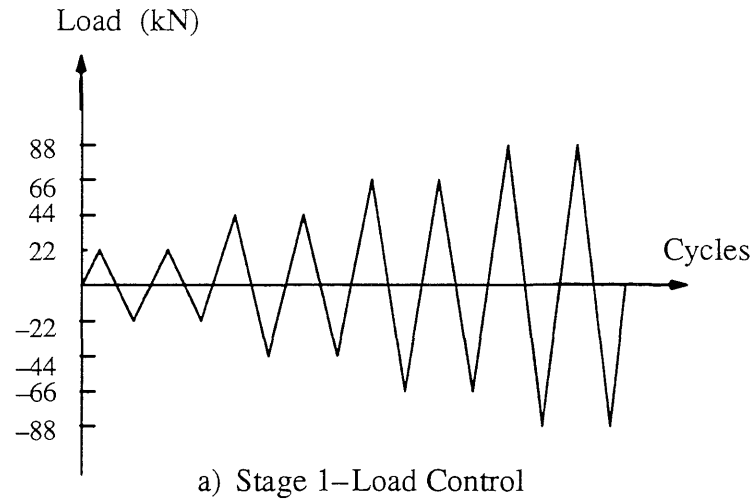

a) Stage 1–Load Control

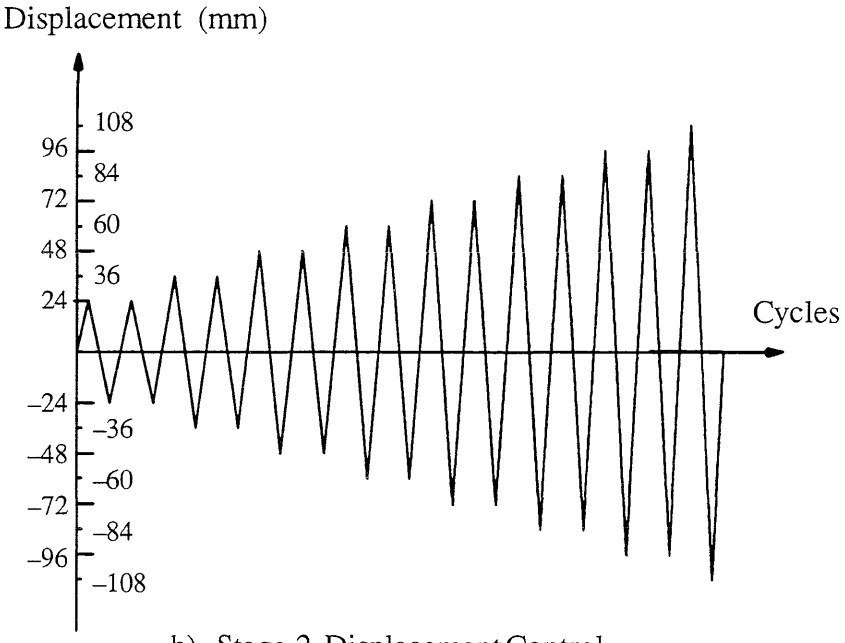

b) Stage 2–Displacement Control

Fig. 5.1f Loading History for Column B–3

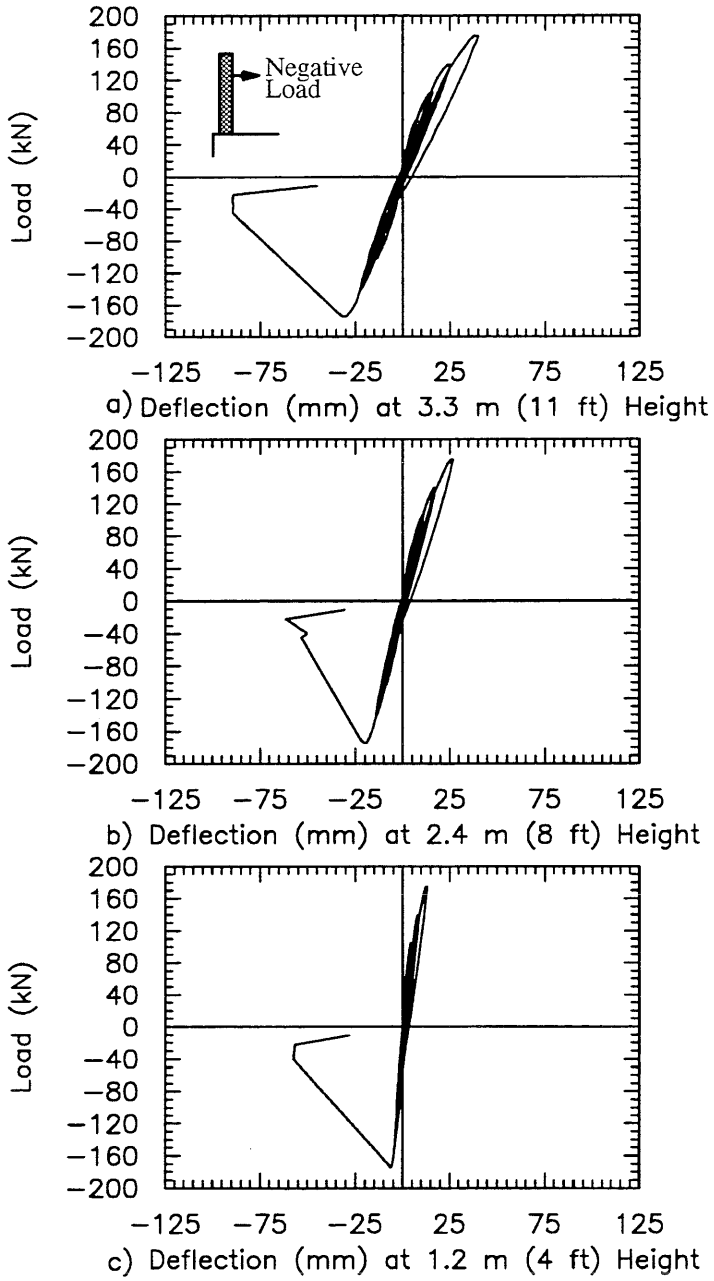

Fig. 5.2 Load vs. Deflection Curve for Column A–1

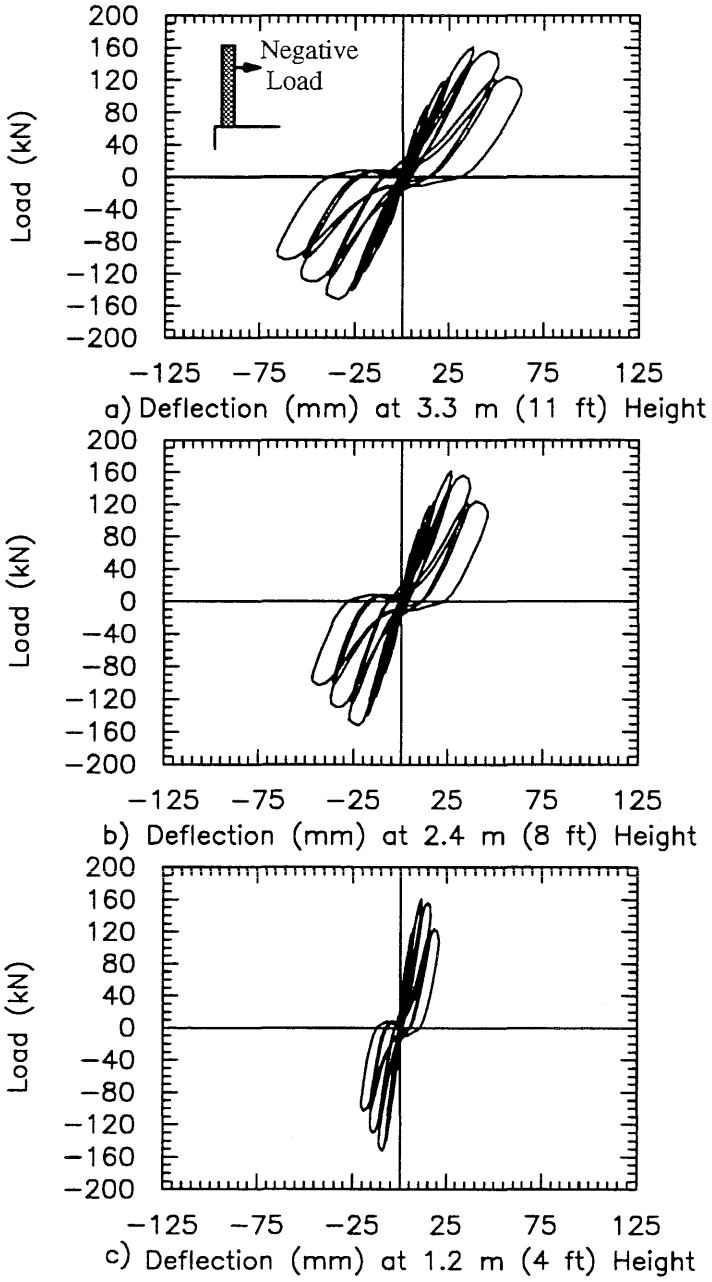

Fig. 5.3 Load vs. Deflection Curve for Column A–2

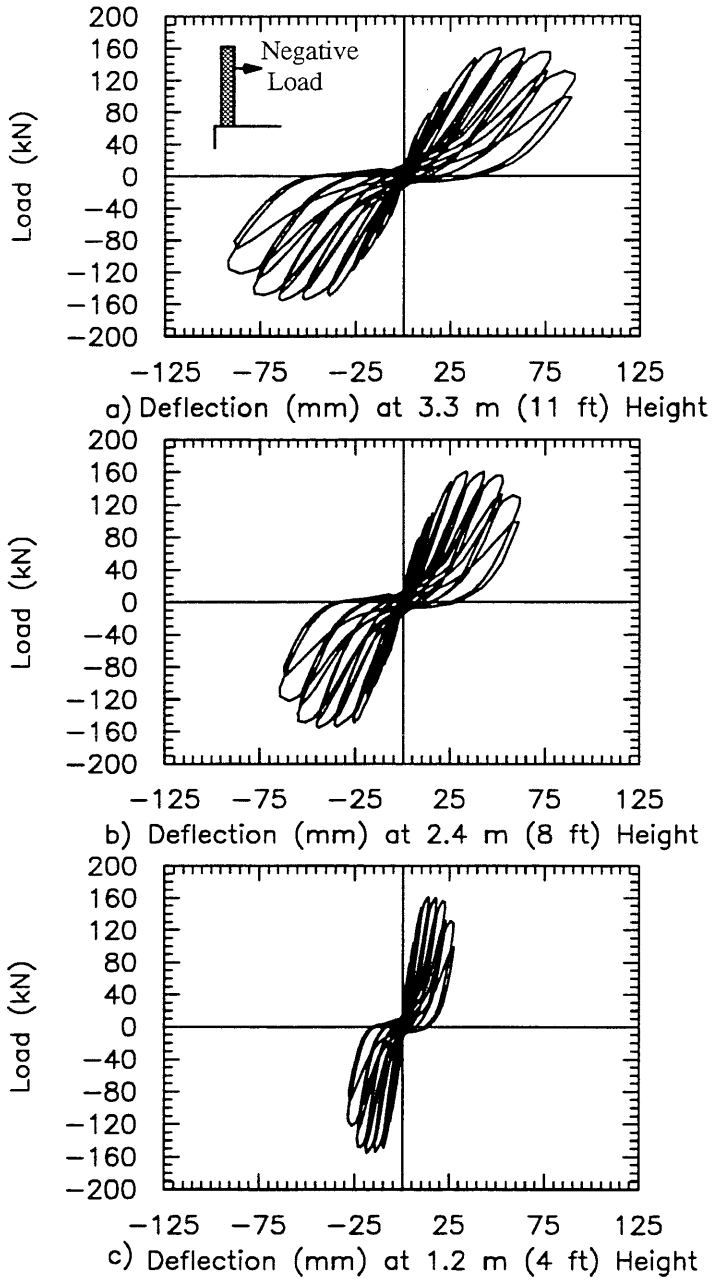

Fig. 5.4 Load vs. Deflection Curve for Column A–3

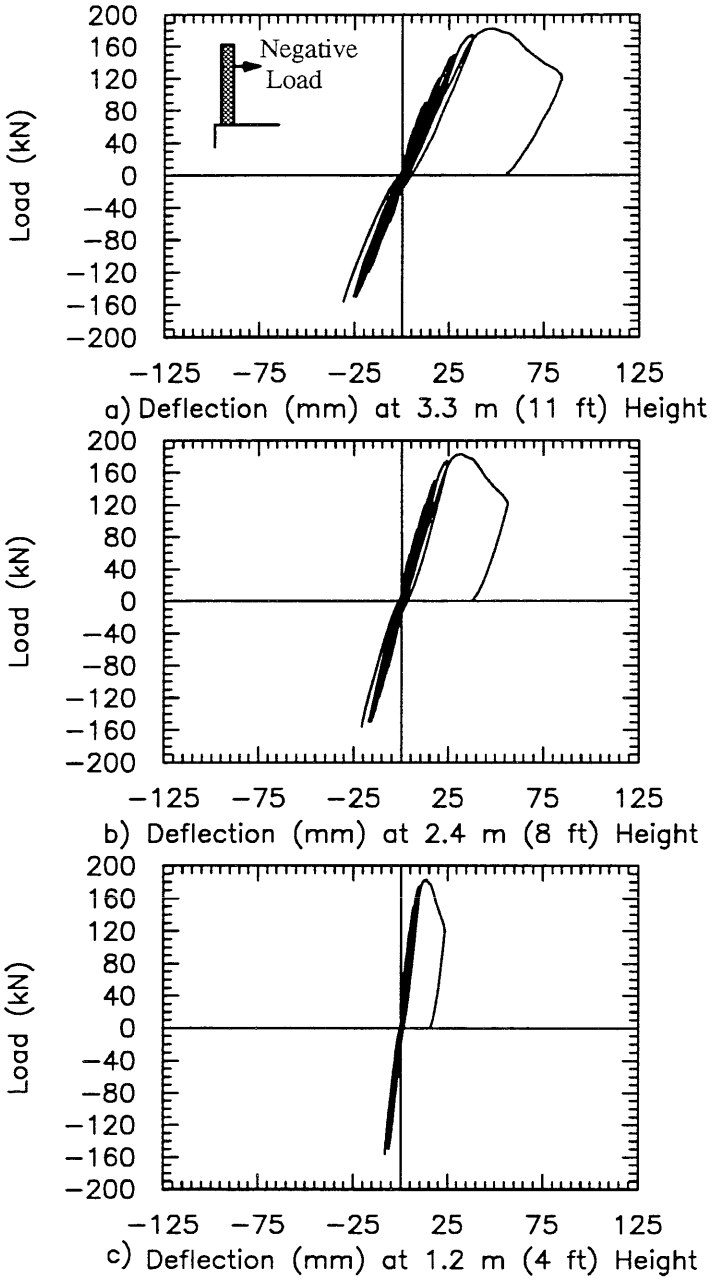

Fig. 5.5 Load vs. Deflection Curve for Column B–1

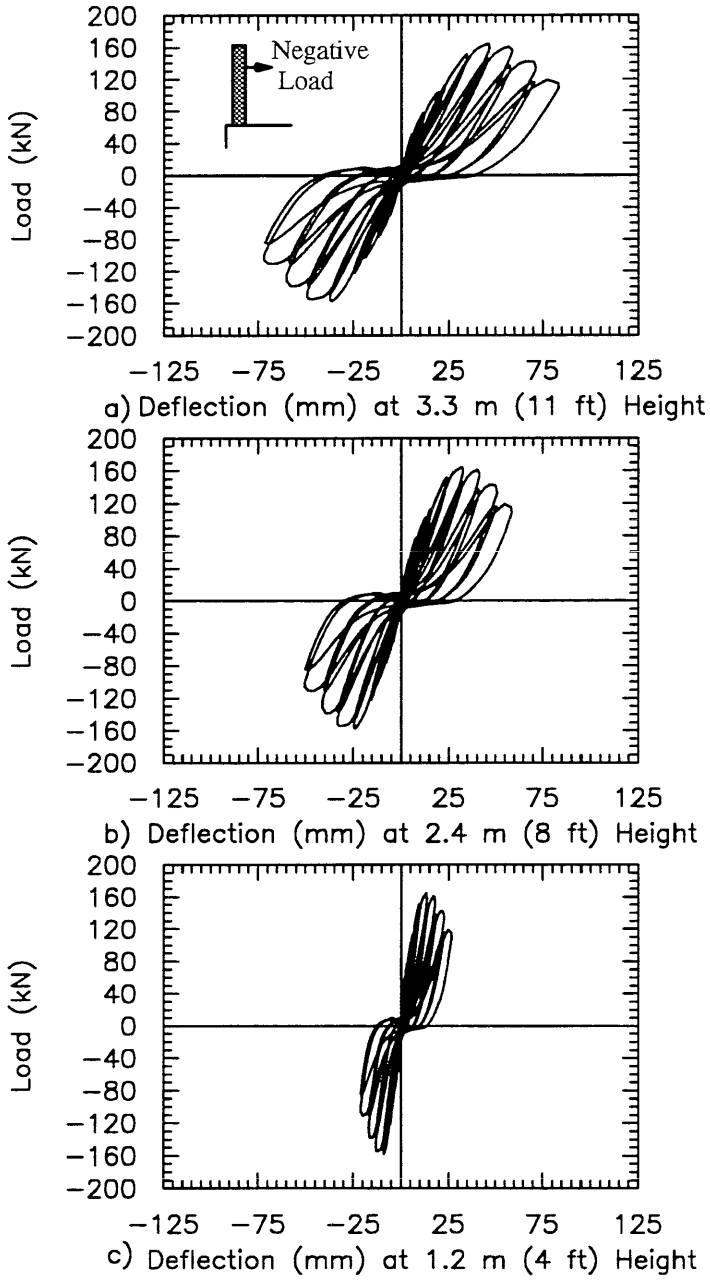

Fig. 5.6 Load vs. Deflection Curve for Column B–2

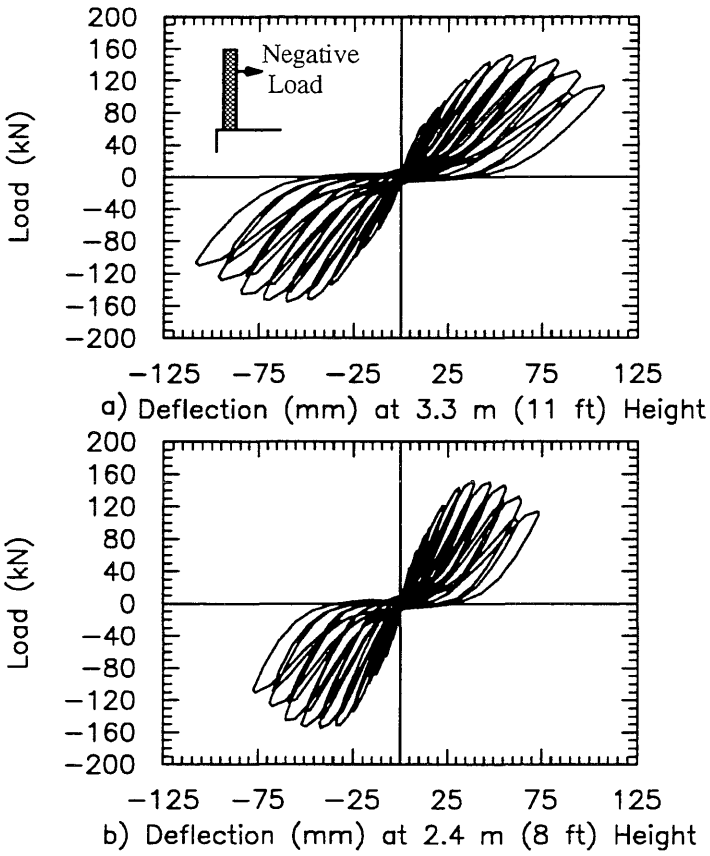

Fig. 5.7 Load vs. Deflection Curve for Column B–3

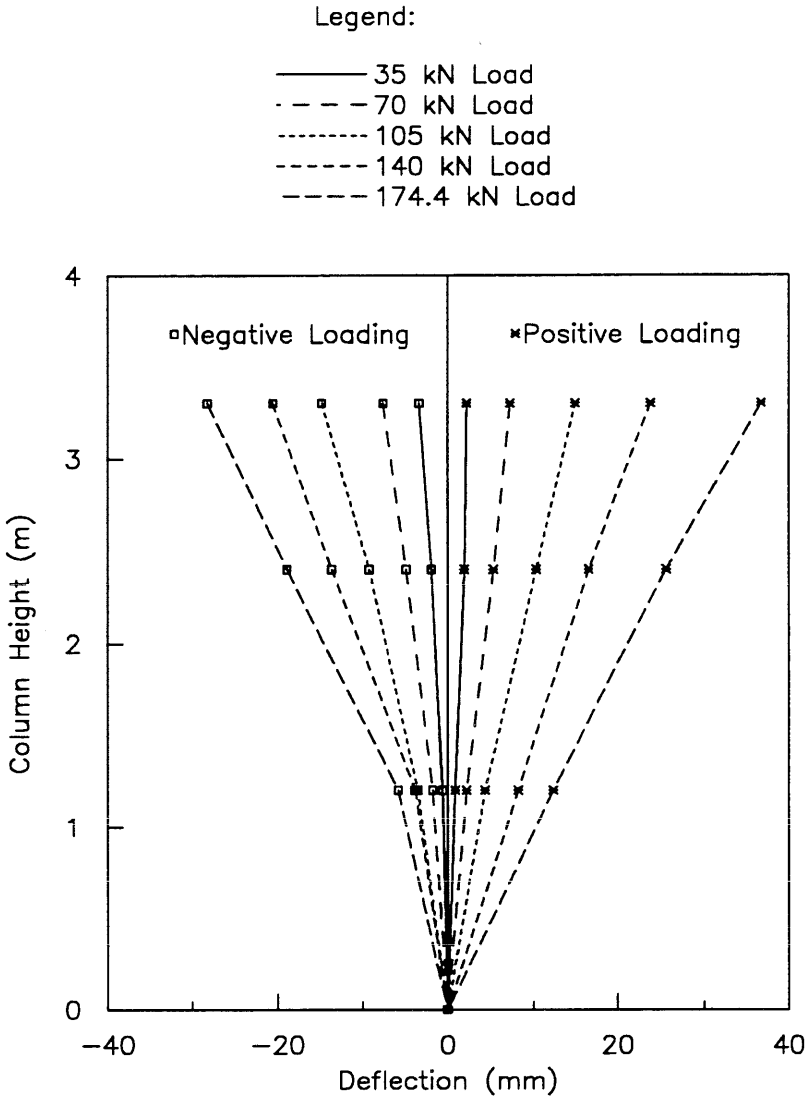

Fig. 5.8 Displacement Profile for Column A–1

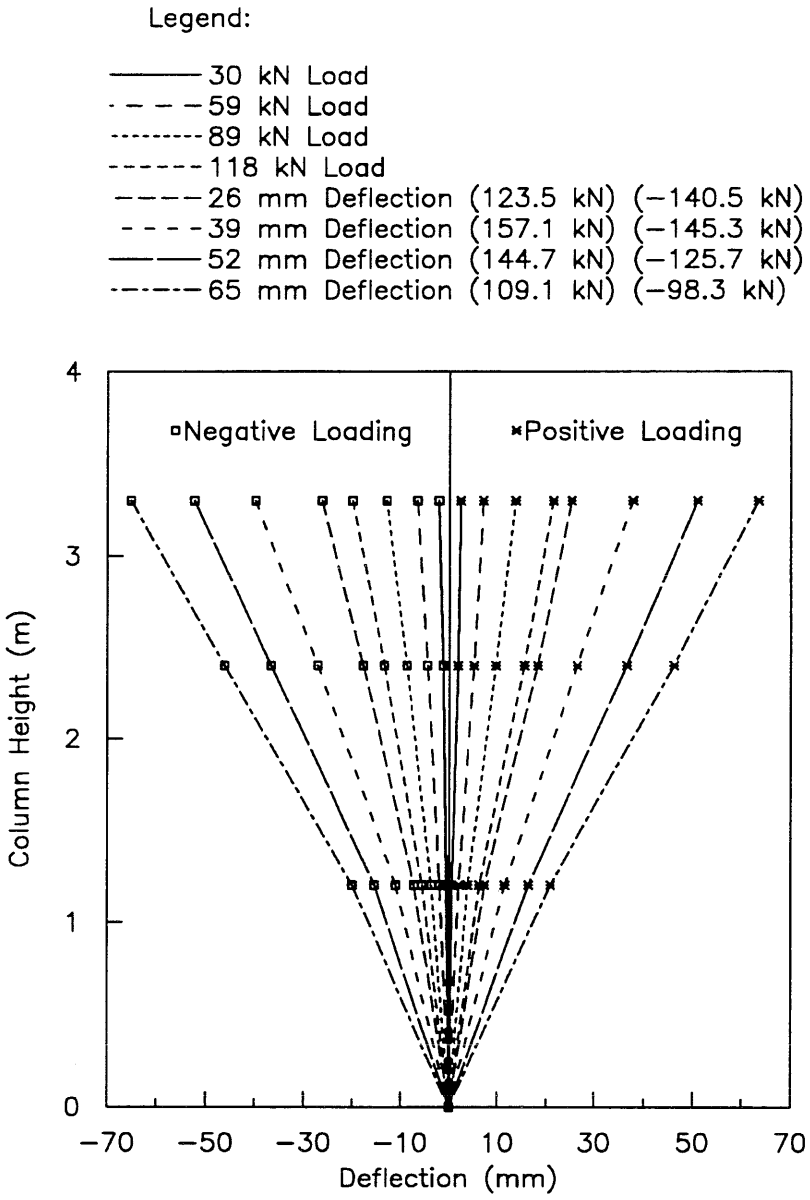

Fig. 5.9 Displacement Profile for Column A–2

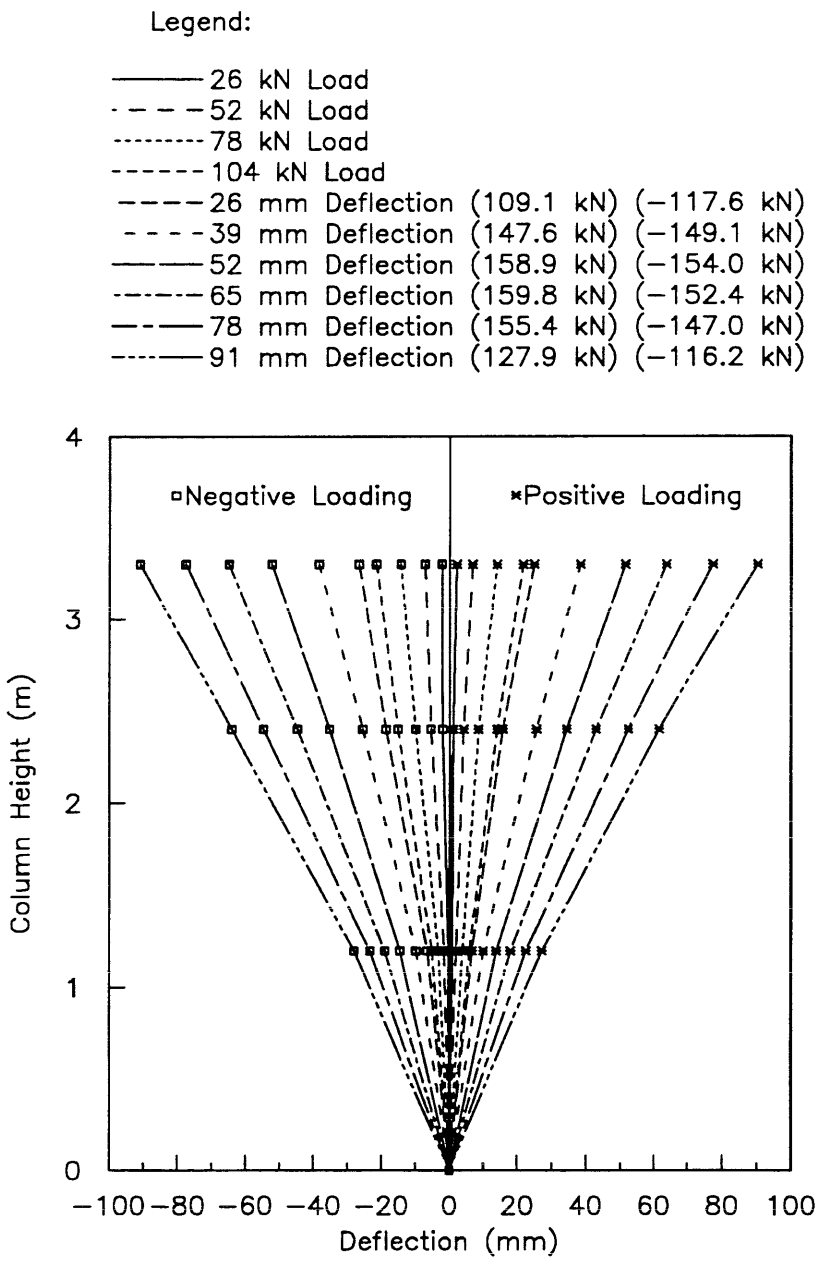

Fig. 5.10 Displacement Profile for Column A–3

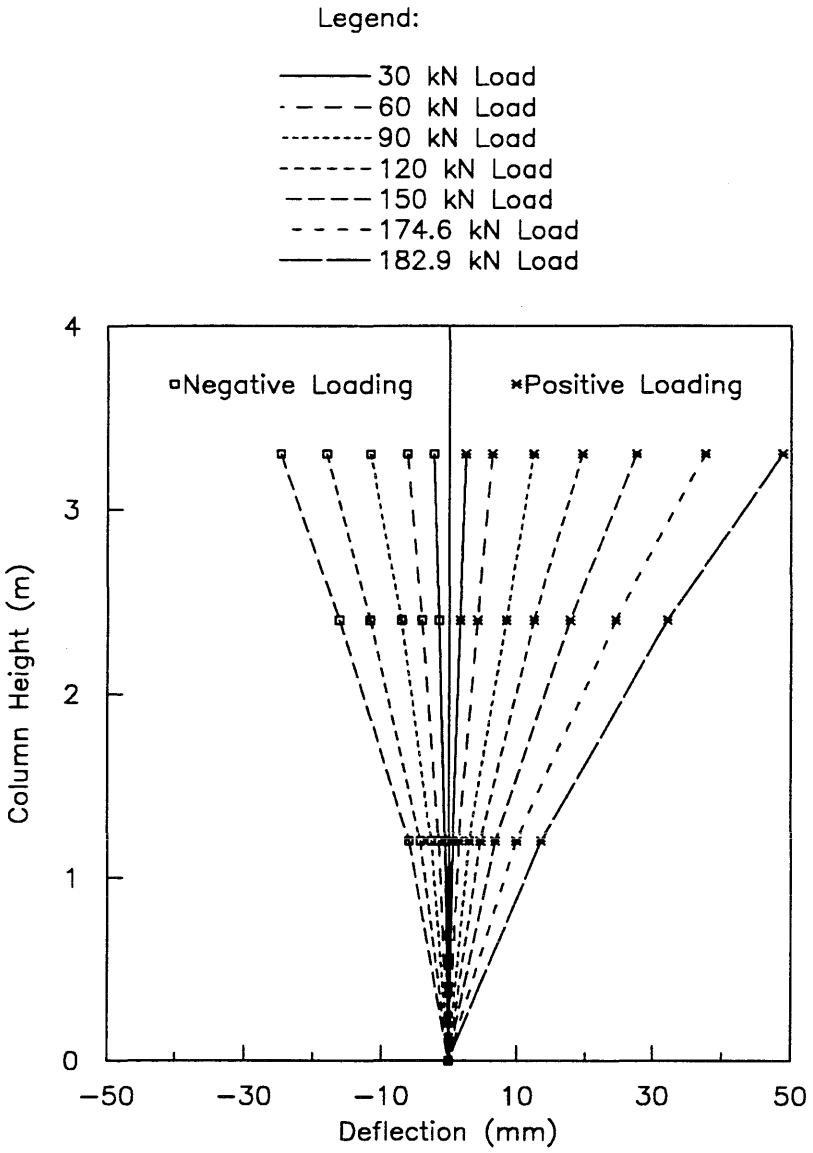

Fig. 5.11 Displacement Profile for Column B–1

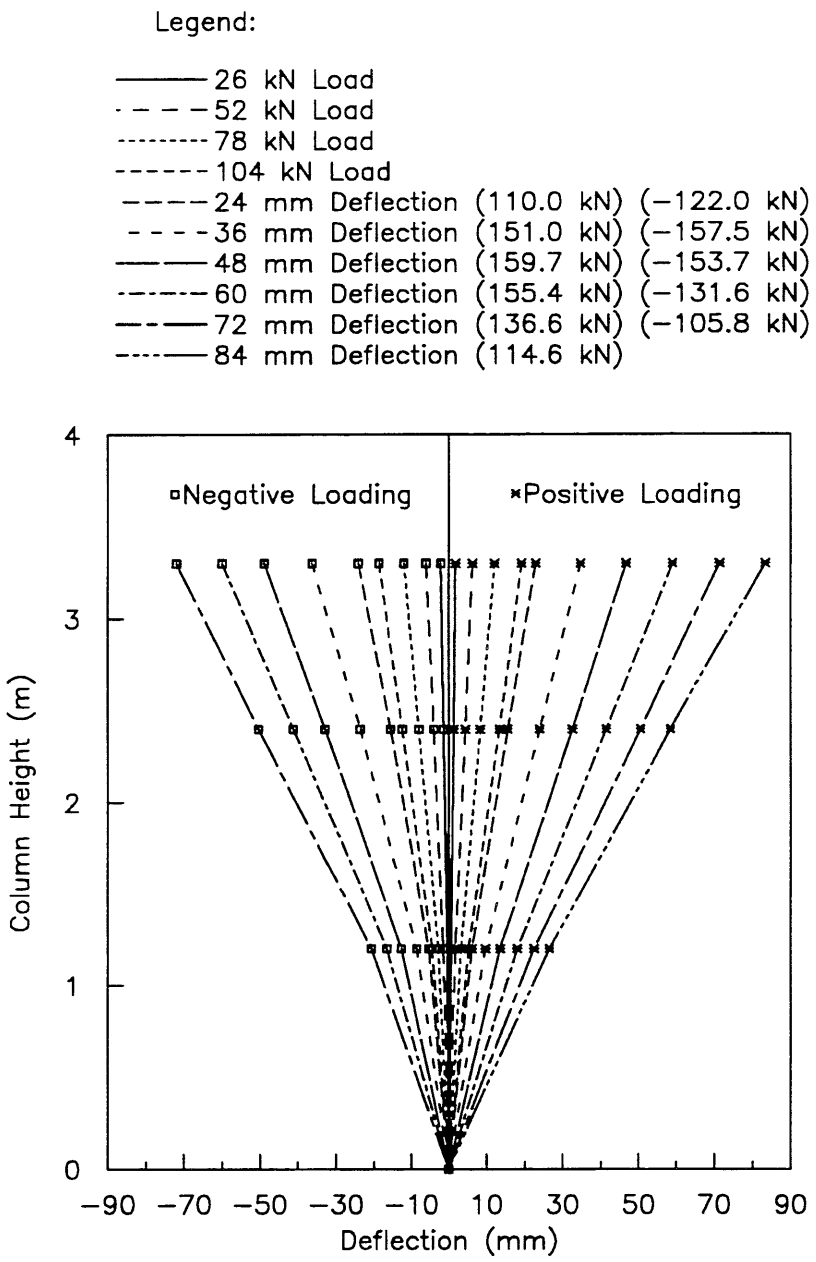

Fig. 5.12 Displacement Profile for Column B–2

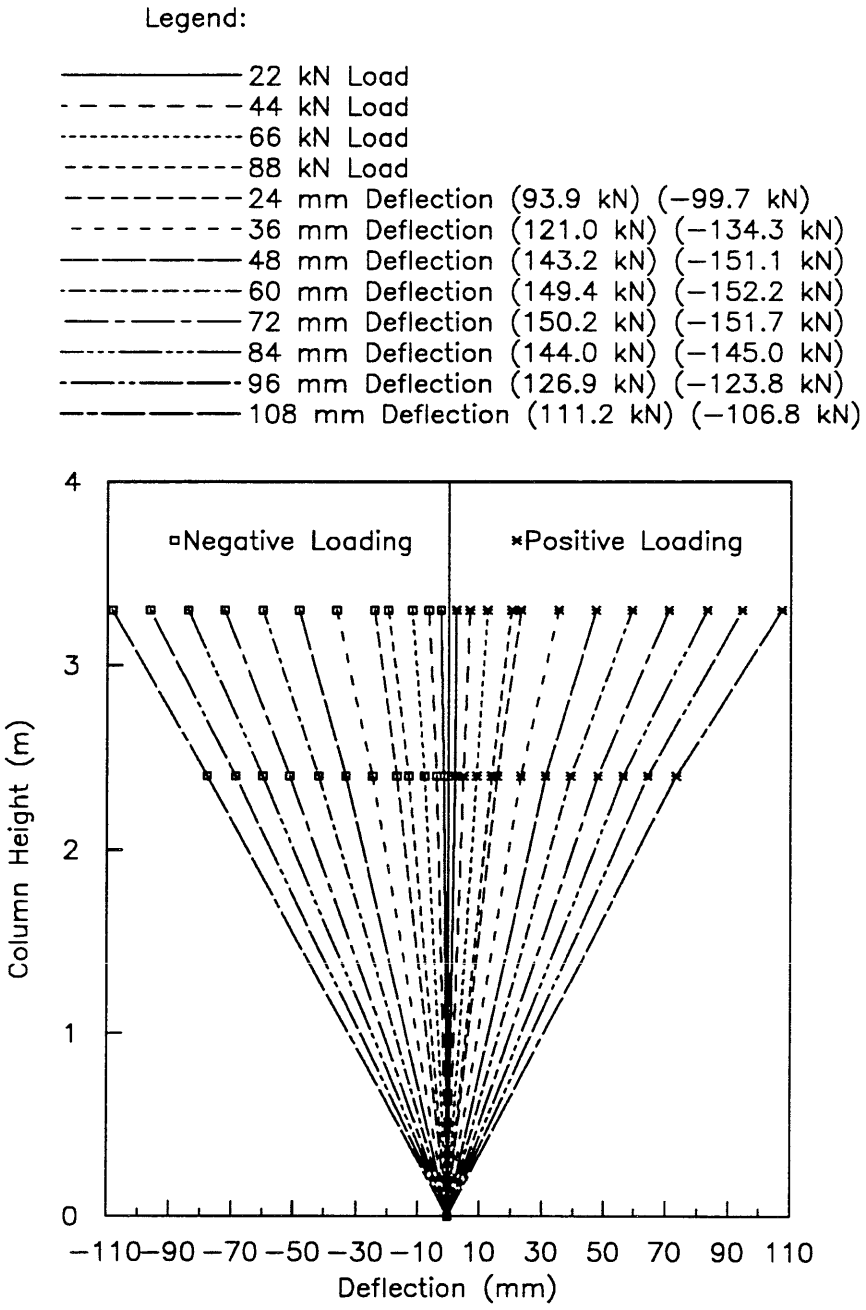

Fig. 5.13 Displacement Profile for Column B–3

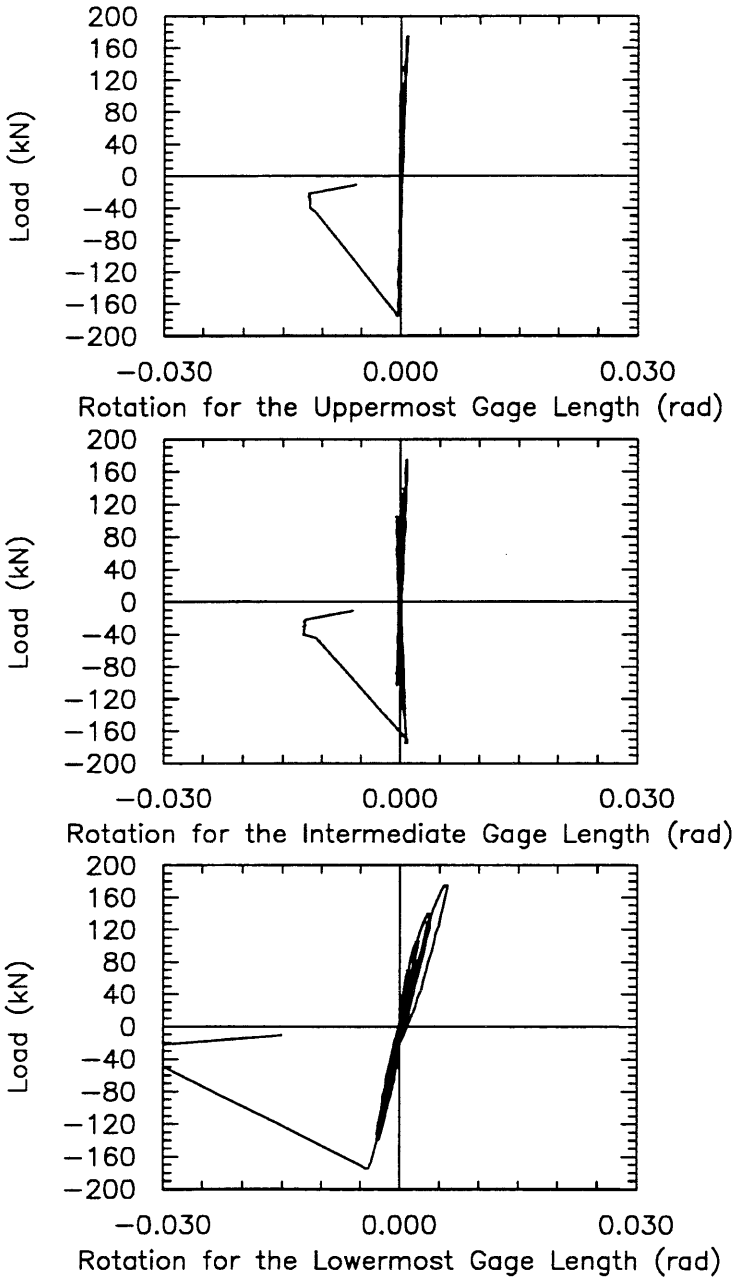

Fig. 5.14 Load vs. Rotation Curve for Column A–1

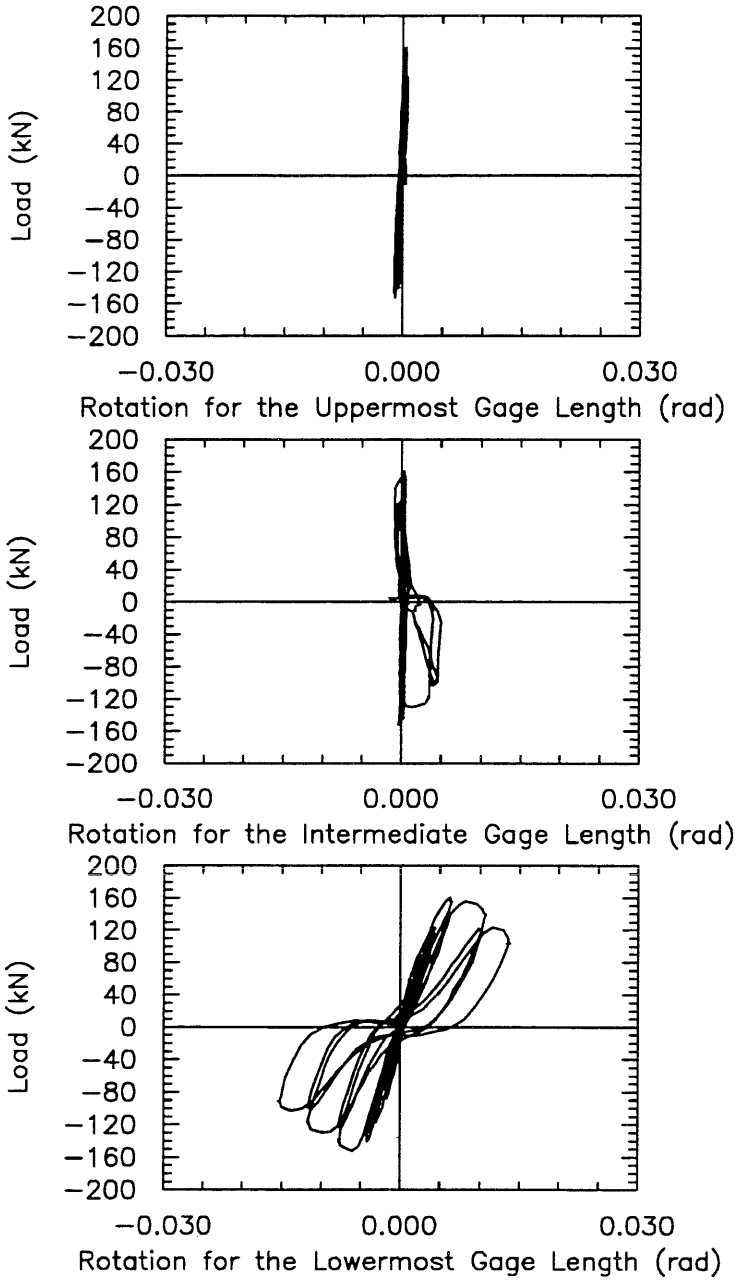

Fig. 5.15 Load vs. Rotation Curve for Column A–2

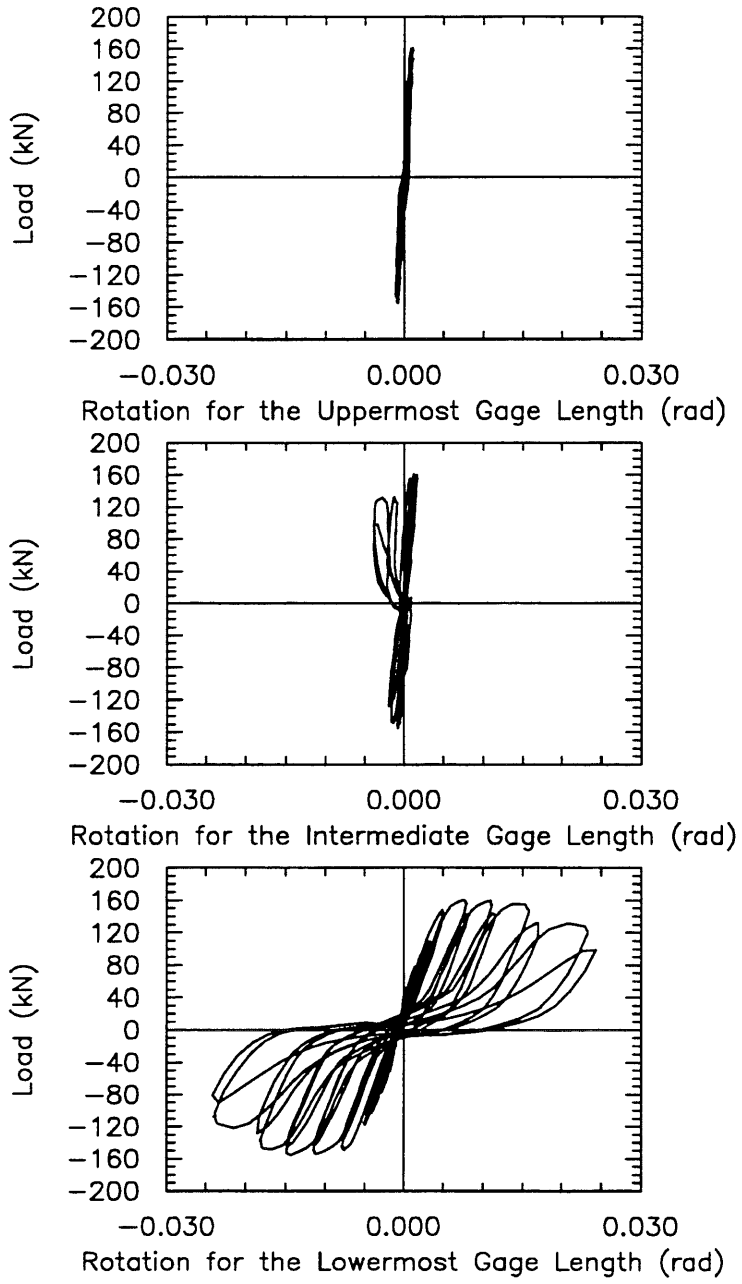

Fig. 5.16 Load vs. Rotation Curve for Column A–3

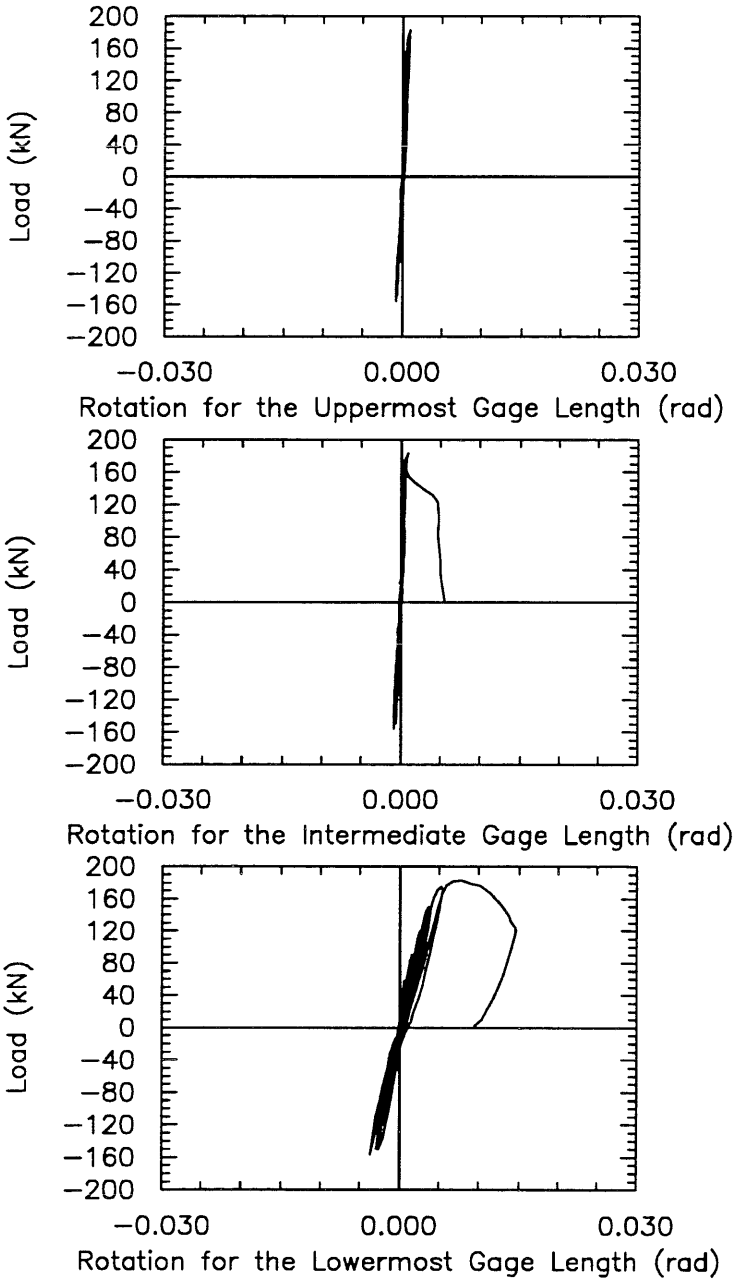

Fig. 5.17 Load vs. Rotation Curve for Column B–1

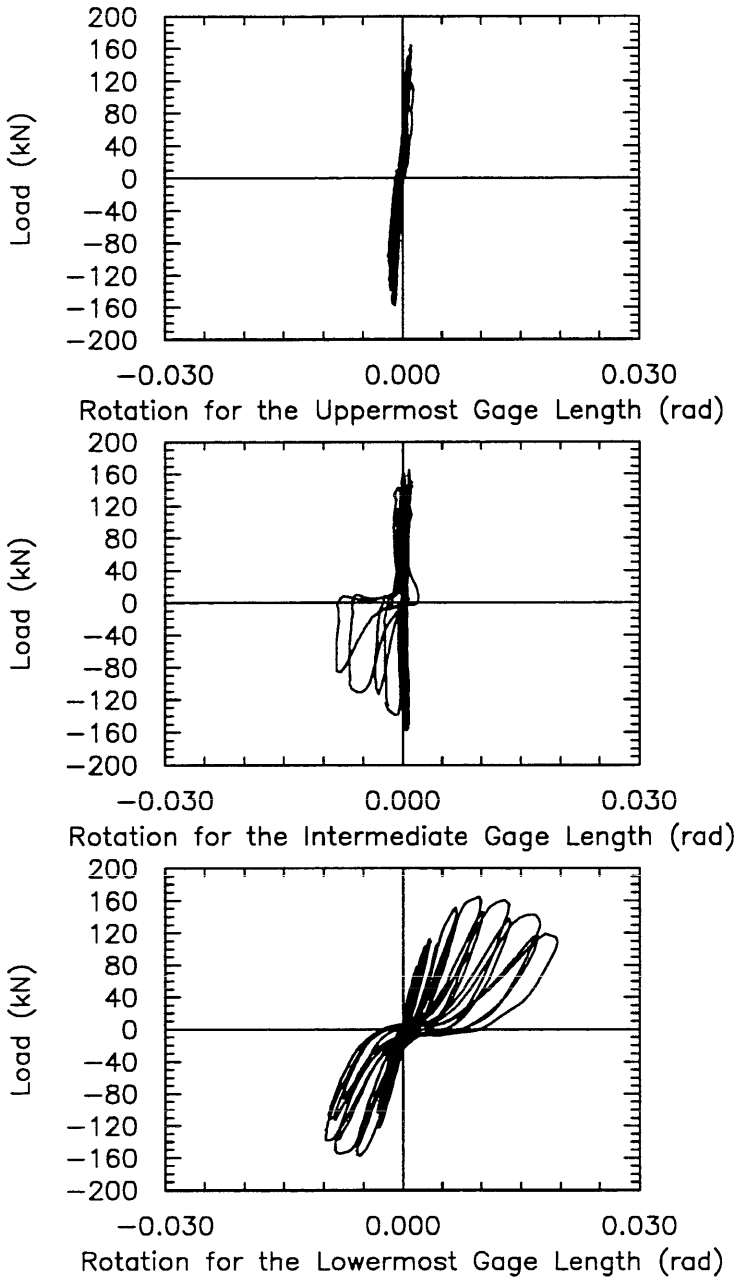

Fig. 5.18 Load vs. Rotation Curve for Column B–2

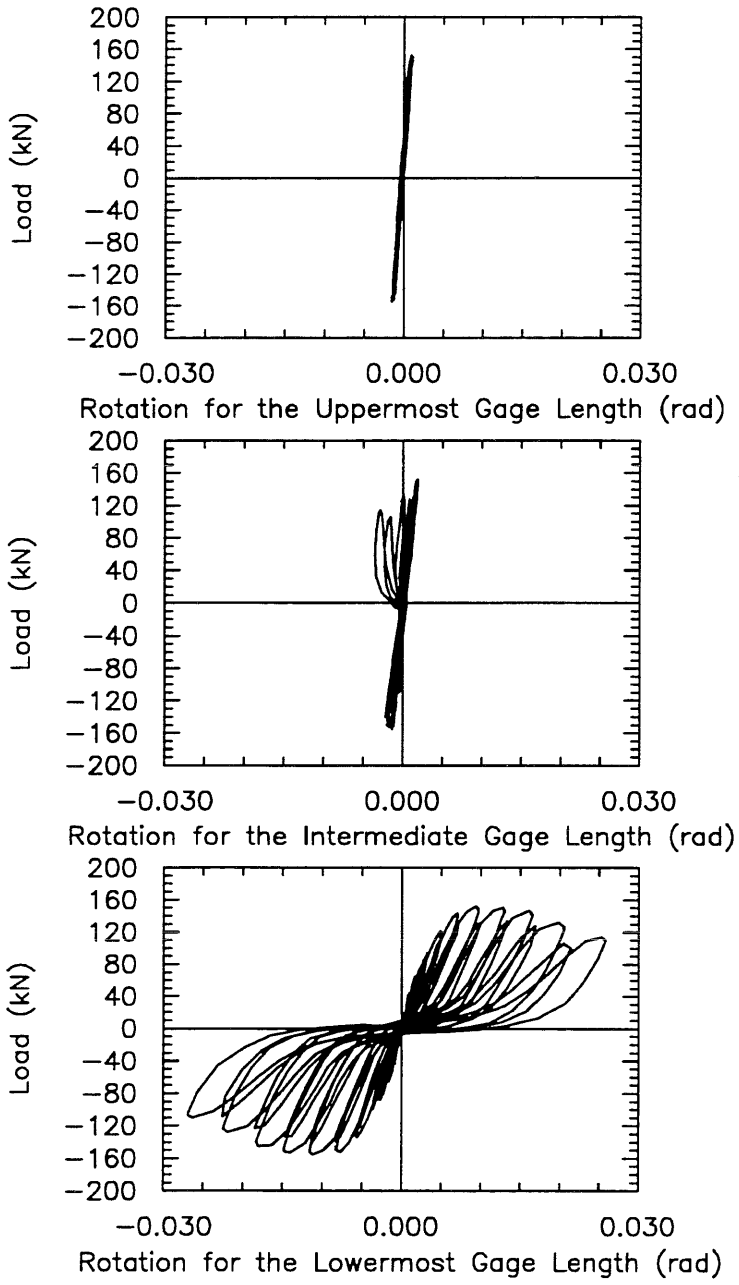

Fig. 5.19 Load vs. Rotation Curve for Column B–3

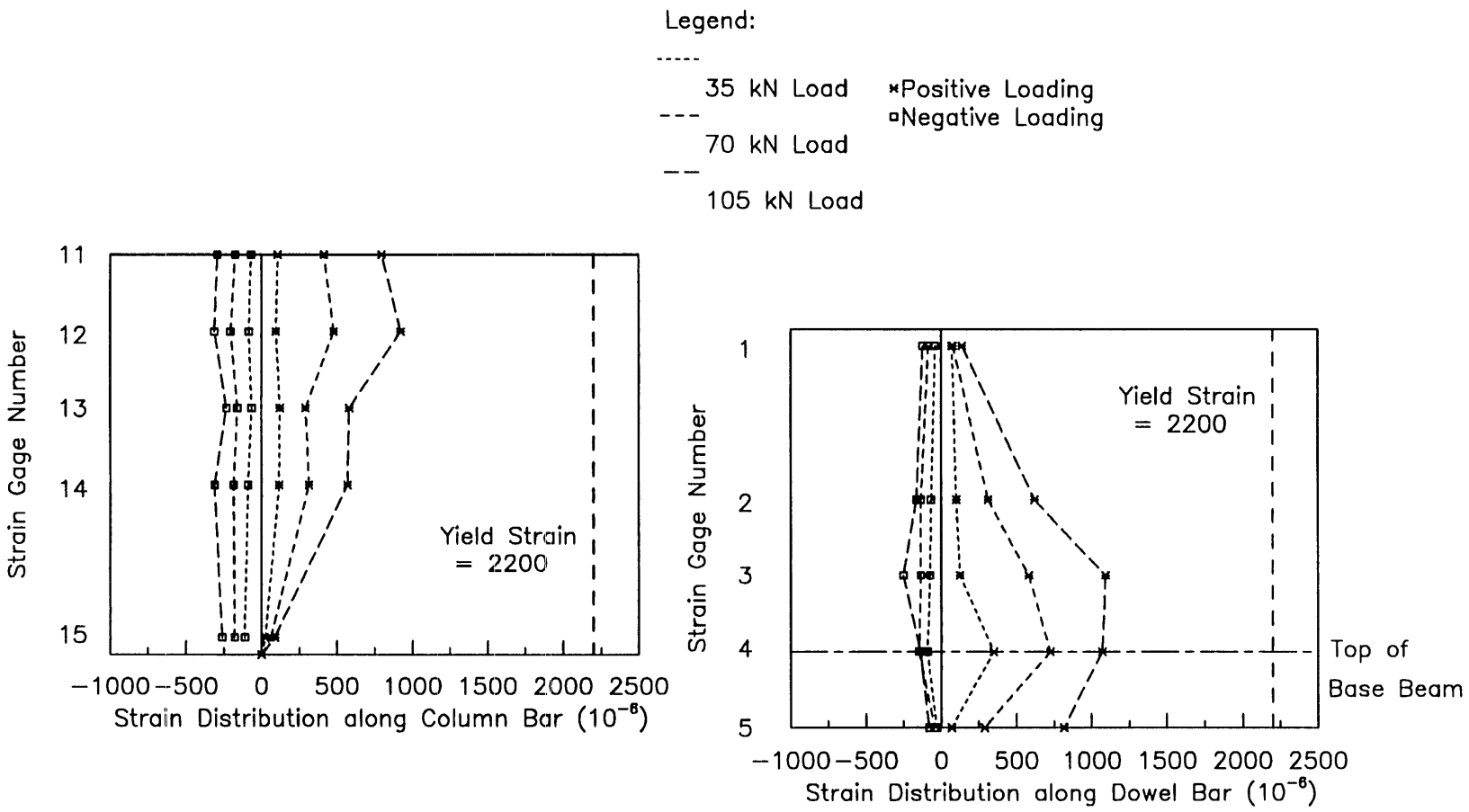

Fig. 5.20 Strain Distributions at Different Peak Loads or Deflections along Bars in Column A–1

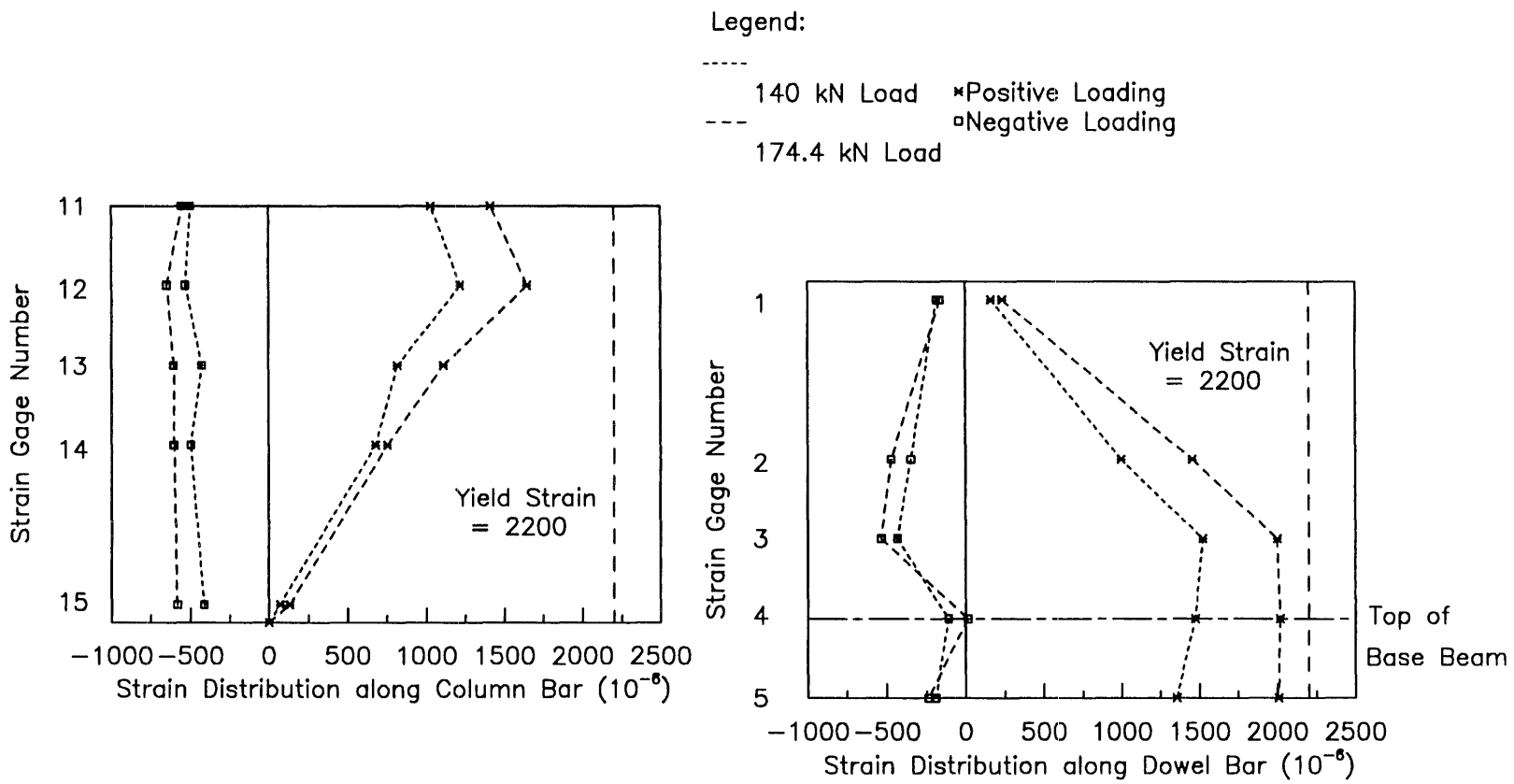

Fig. 5.20 Strain Distributions at Different Peak Loads or Deflections along Bars in Column A–1 (cont.)

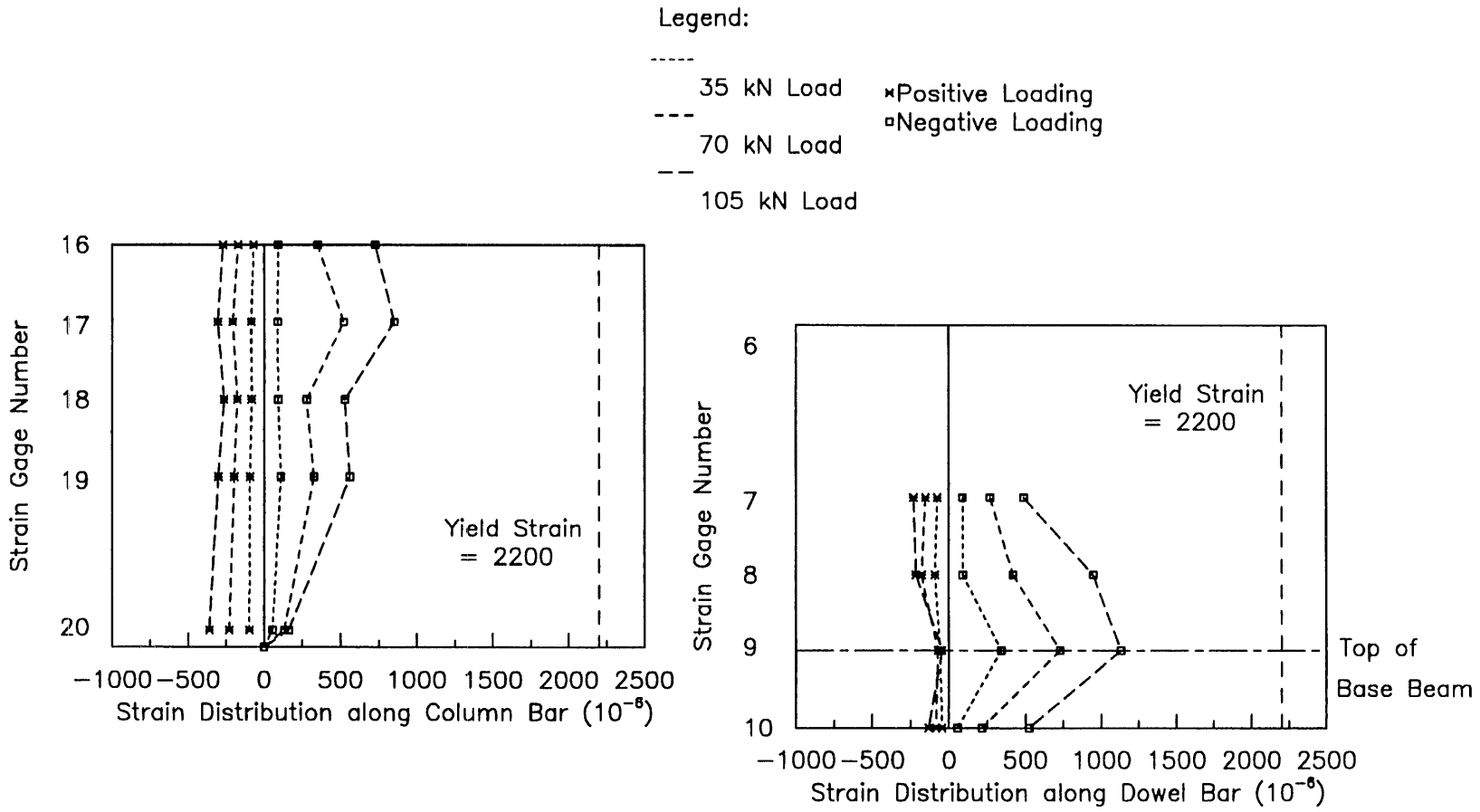

Fig. 5.20 Strain Distributions at Different Peak Loads or Deflections along Bars in Column A–1 (cont.)

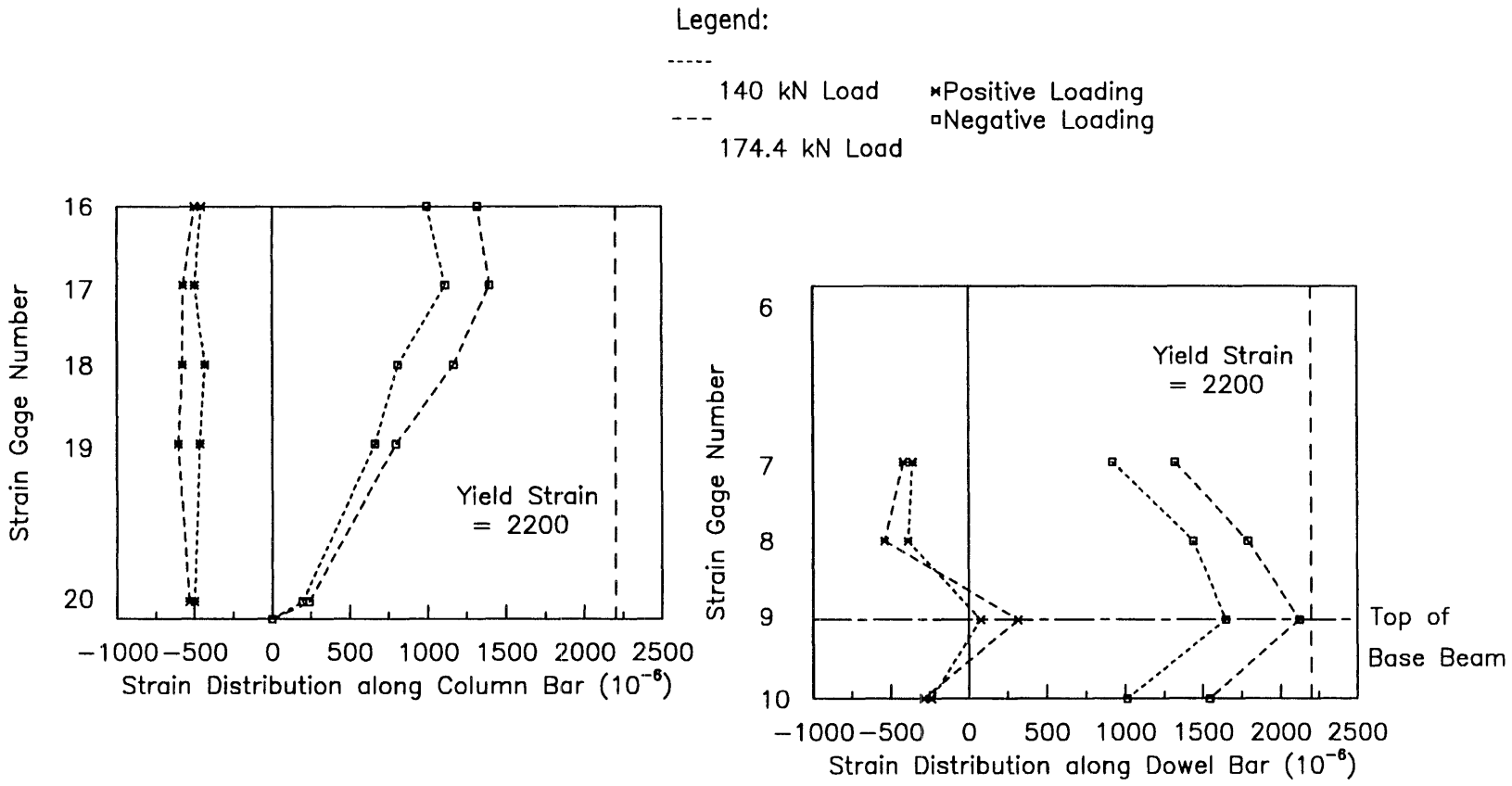

Fig. 5.20 Strain Distributions at Different Peak Loads or Deflections along Bars in Column A–1 (cont.)

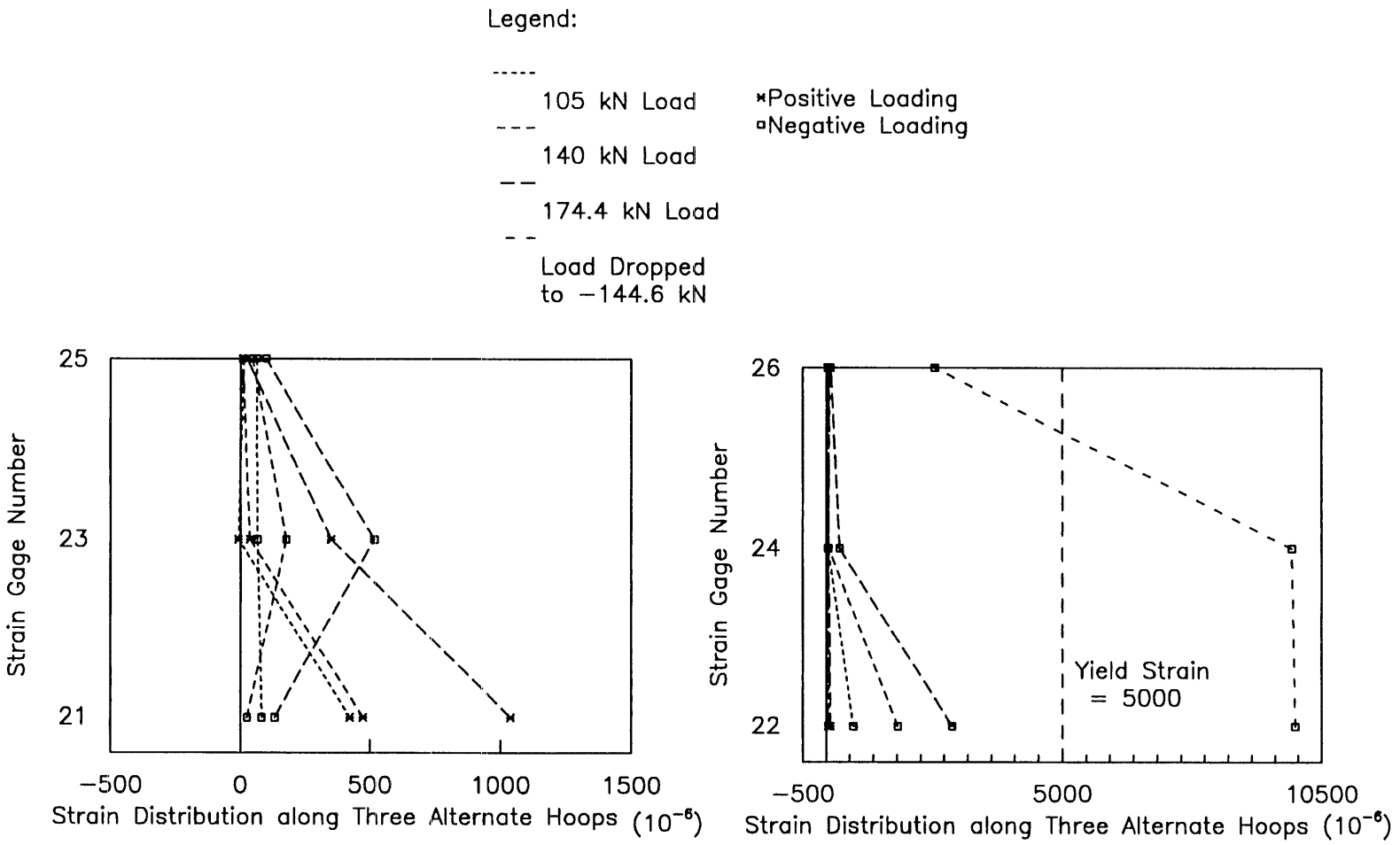

Fig. 5.20 Strain Distributions at Different Peak Loads or Deflections along Bars in Column A–1 (cont.)

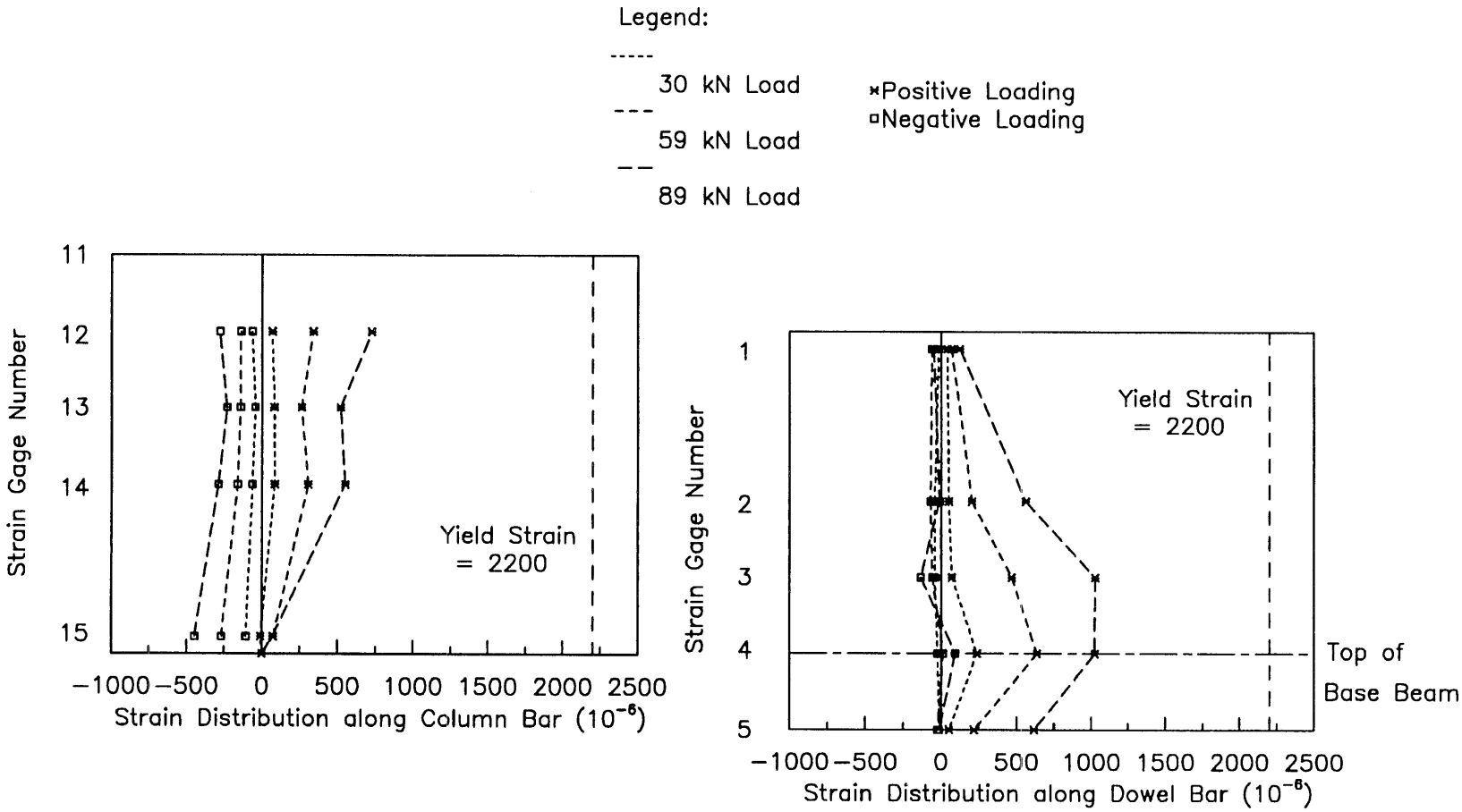

Fig. 5.21 Strain Distributions at Different Peak Loads or Deflections along Bars in Column A–2

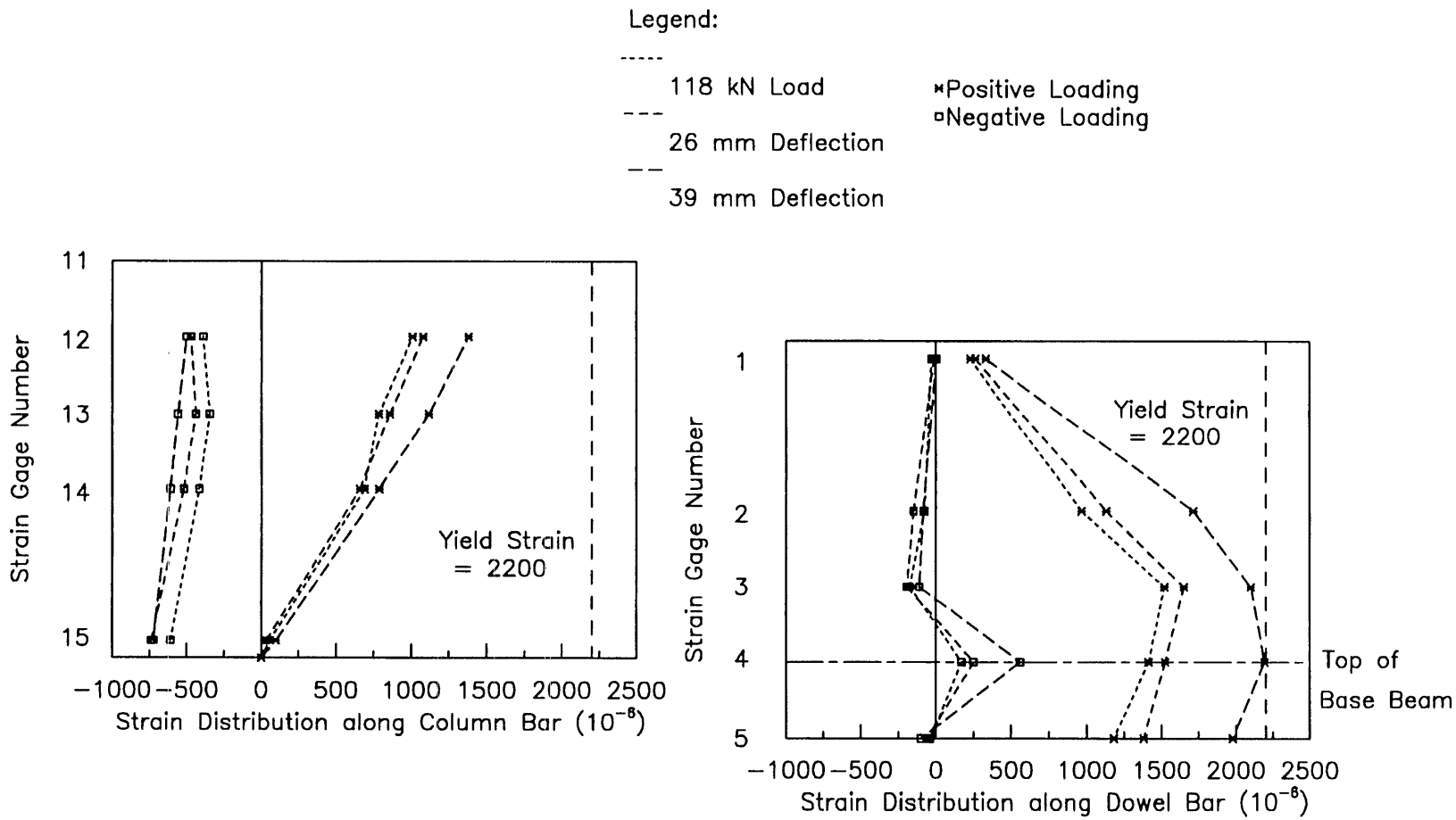

Fig. 5.21 Strain Distributions at Different Peak Loads or Deflections along Bars in Column A–2 (cont.)

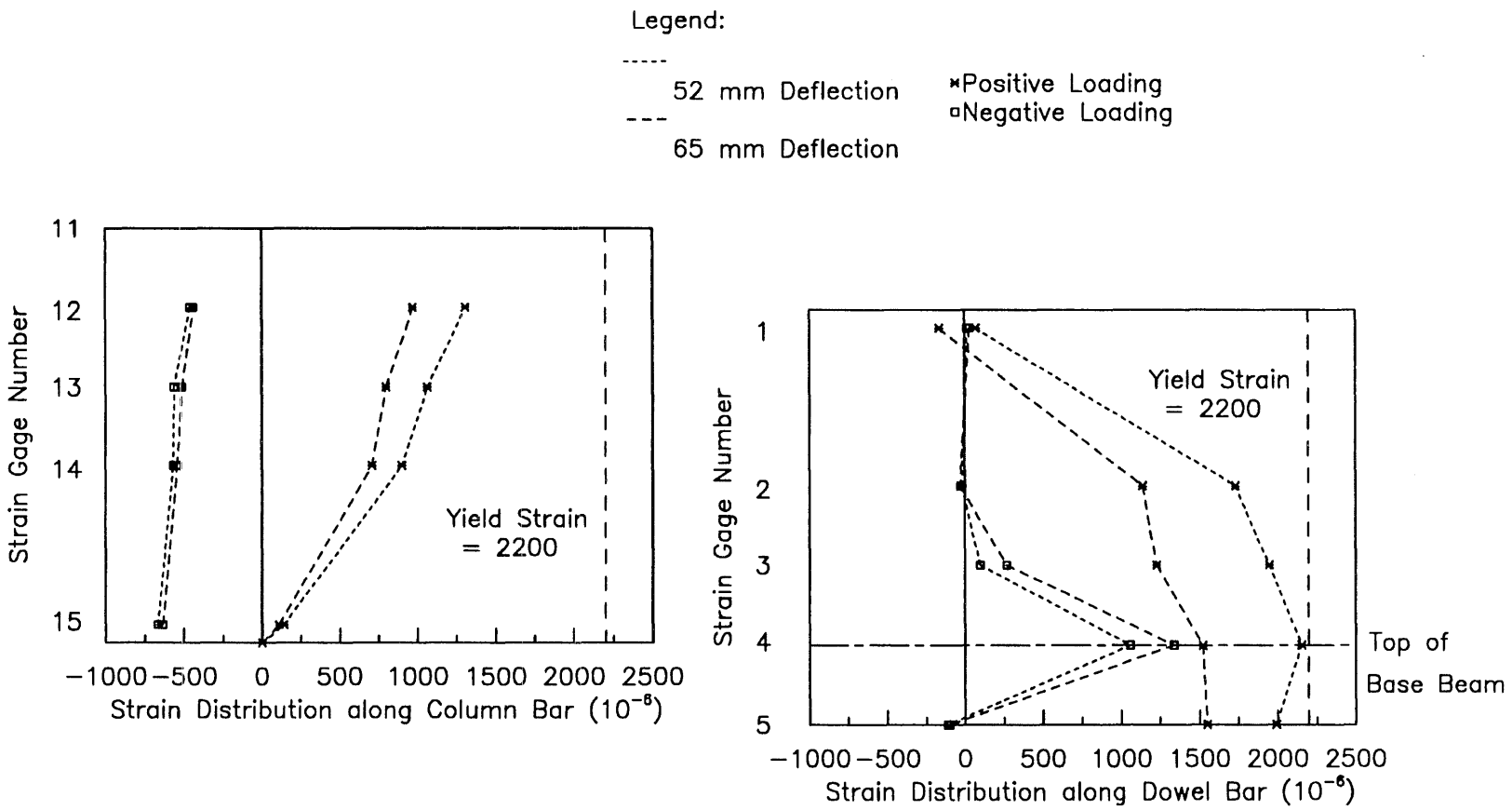

Fig. 5.21 Strain Distributions at Different Peak Loads or Deflections along Bars in Column A–2 (cont.)

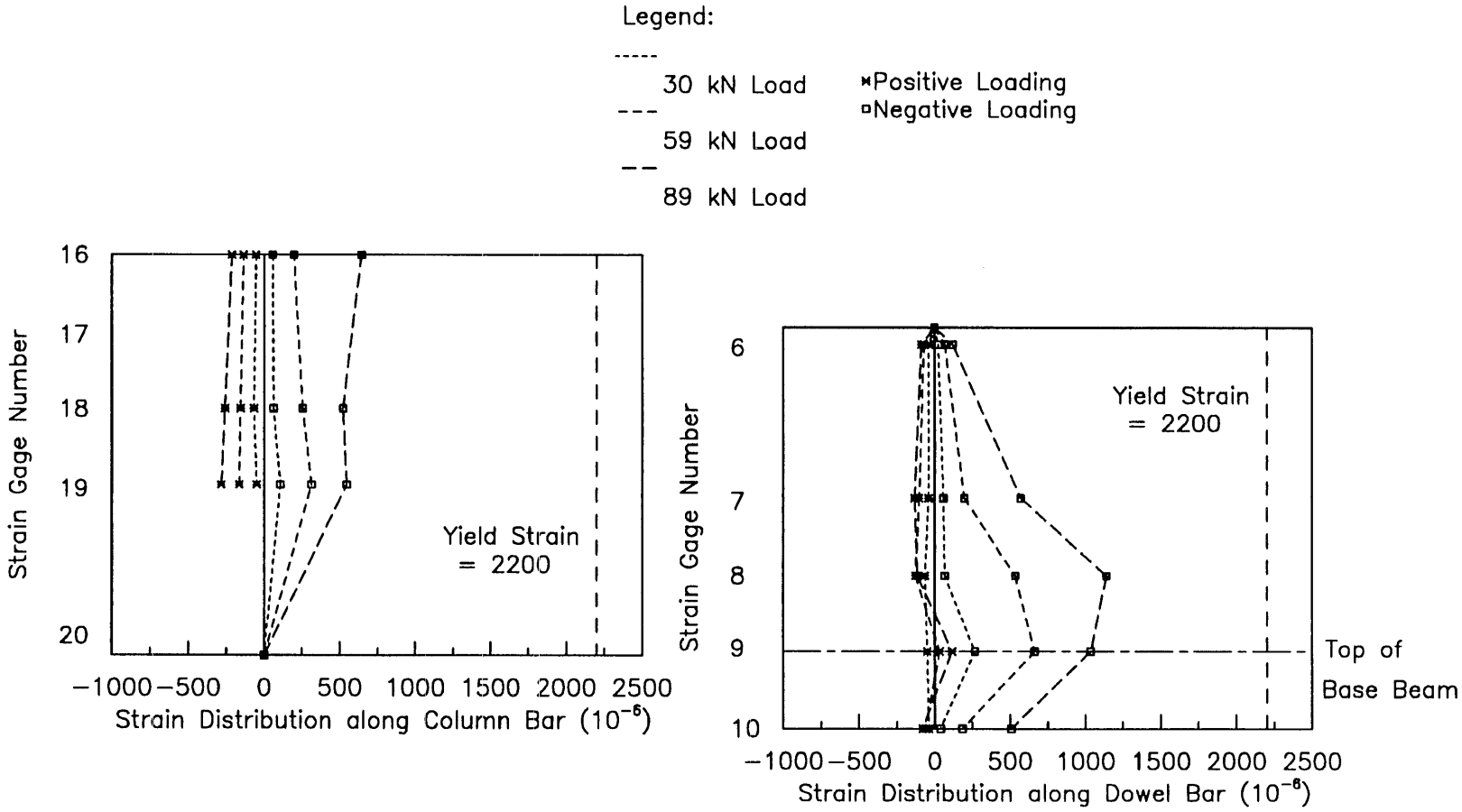

Fig. 5.21 Strain Distributions at Different Peak Loads or Deflections along Bars in Column A–2 (cont.)

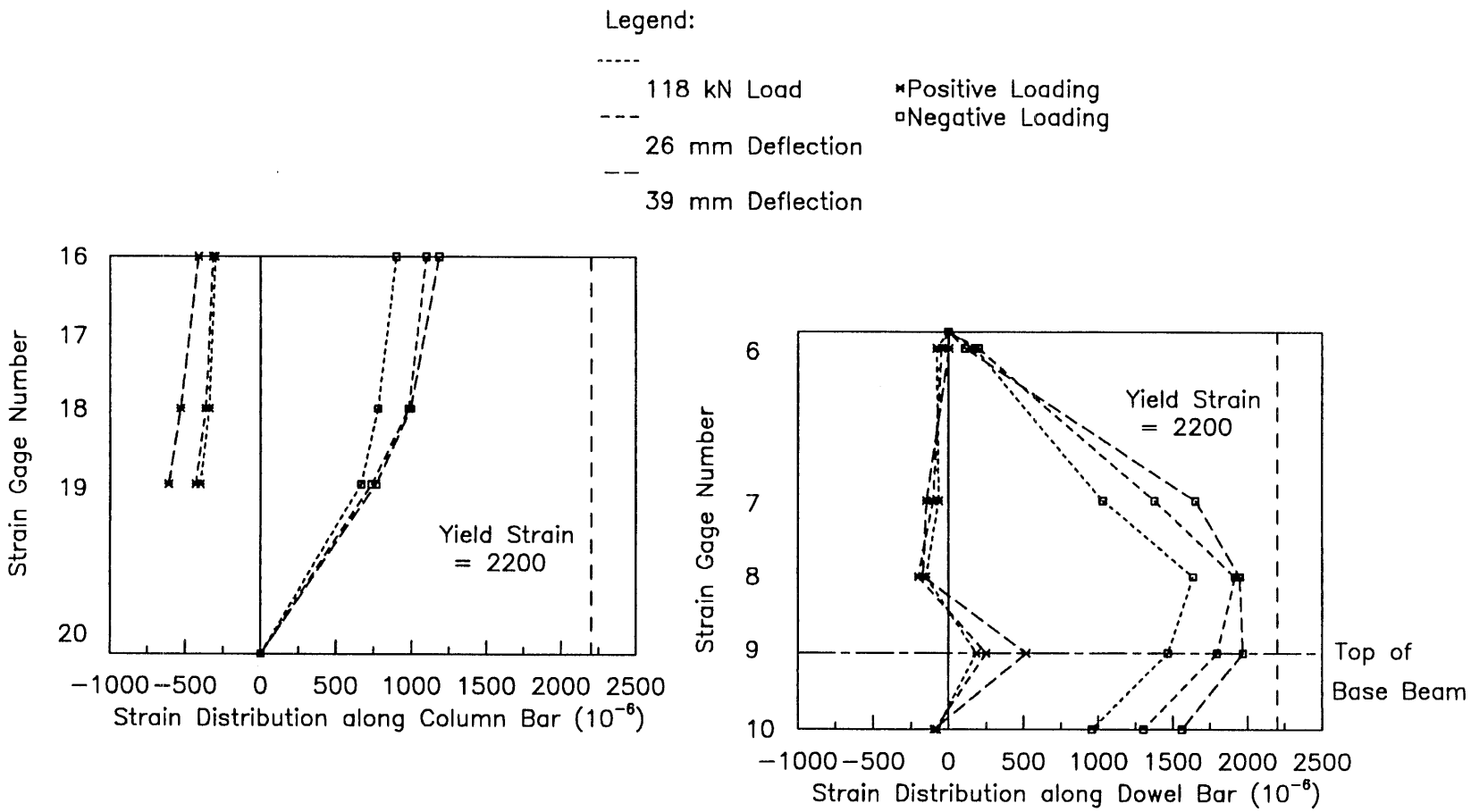

Fig. 5.21 Strain Distributions at Different Peak Loads or Deflections along Bars in Column A–2 (cont.)

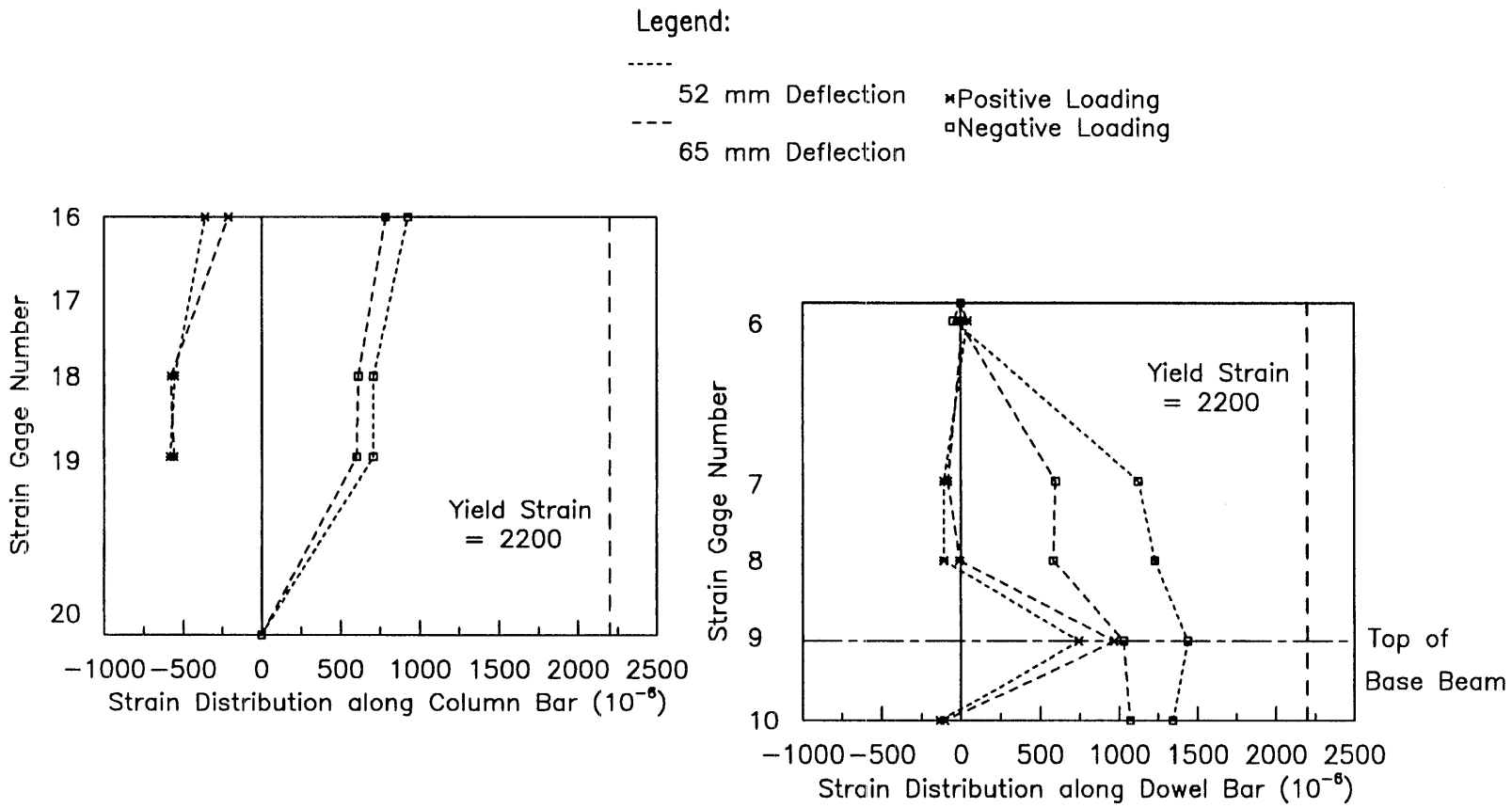

Fig. 5.21 Strain Distributions at Different Peak Loads or Deflections along Bars in Column A–2 (cont.)

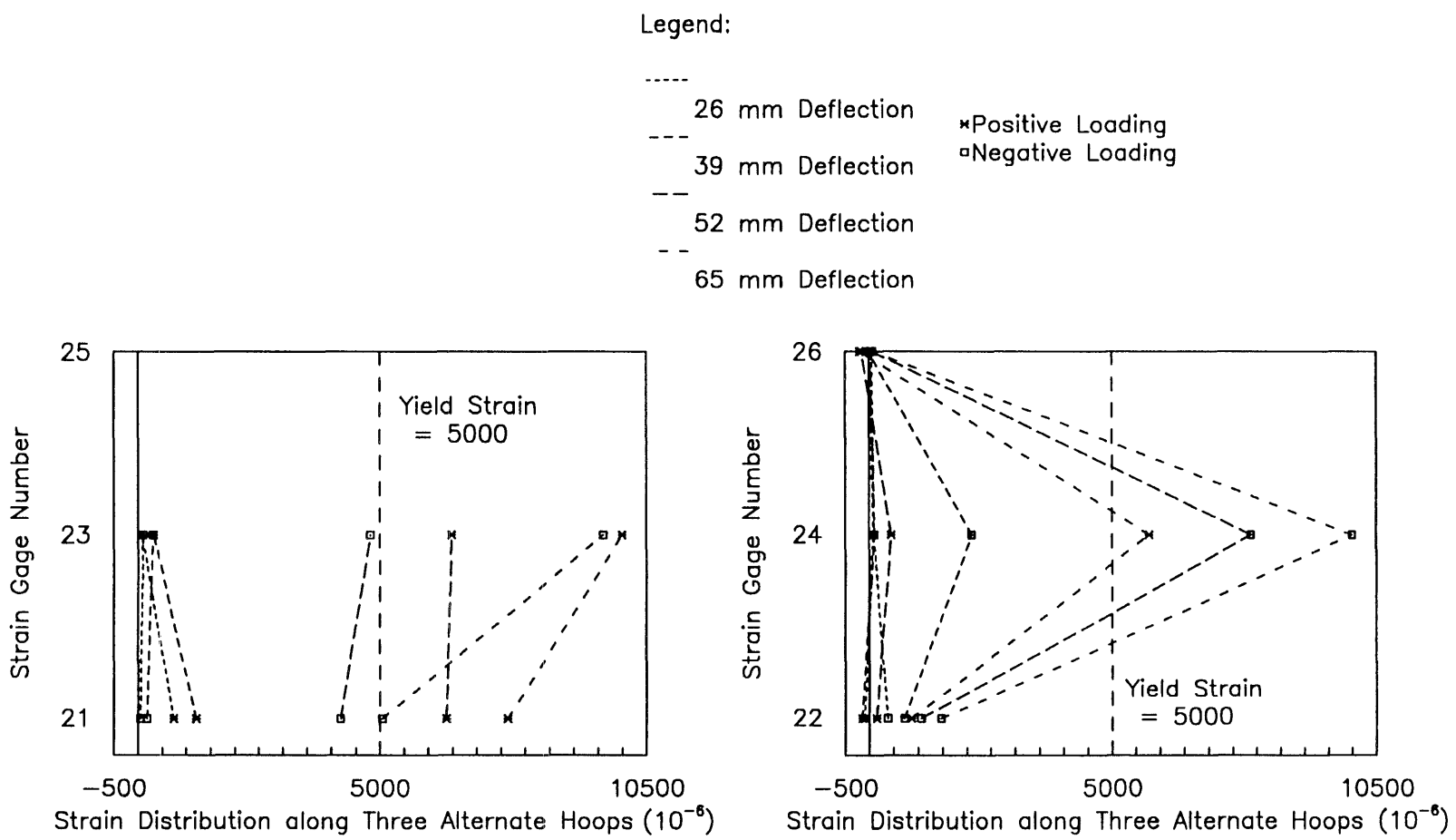

Fig. 5.21 Strain Distributions at Different Peak Loads or Deflections along Bars in Column A–2 (cont.)

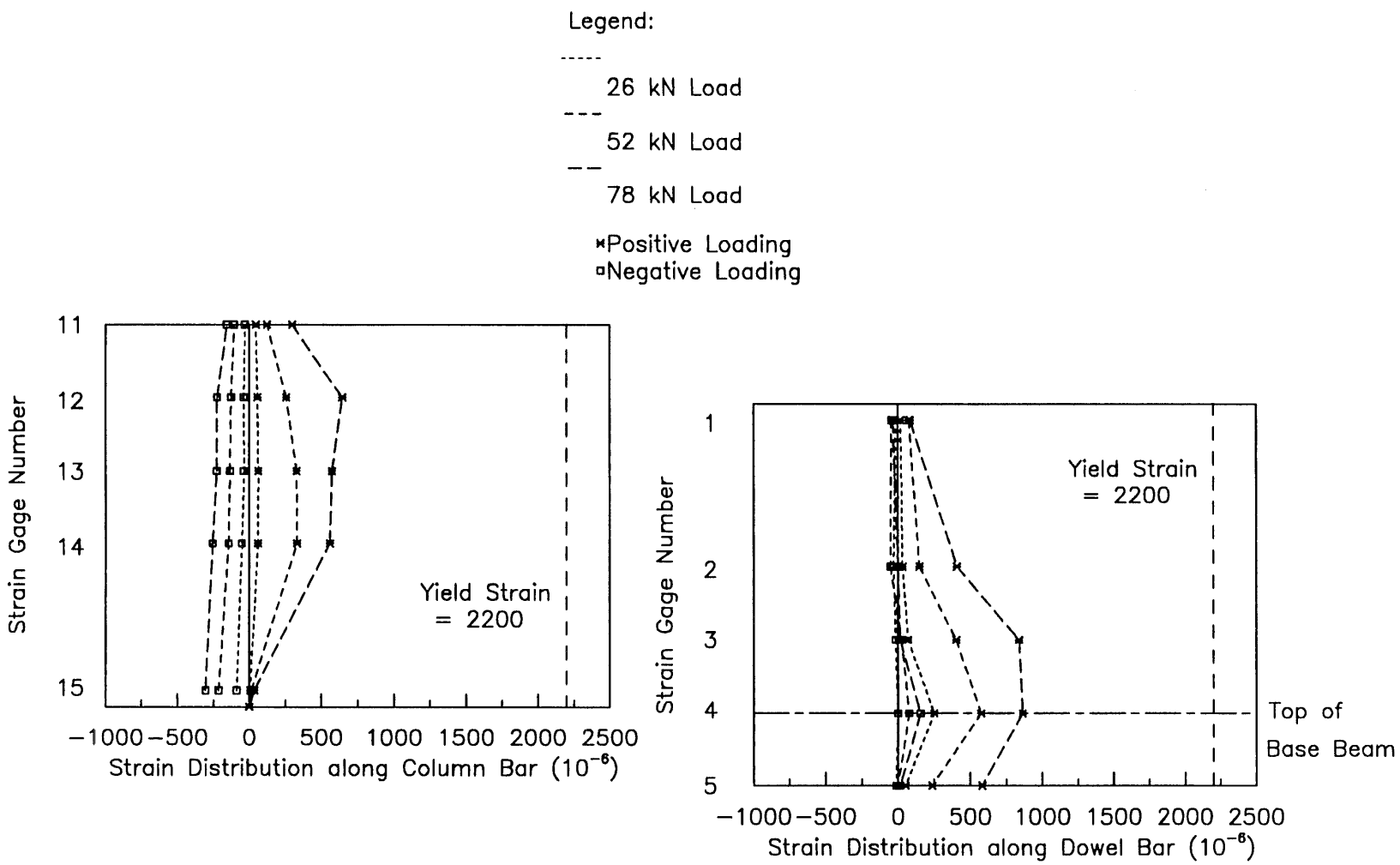

Fig. 5.22 Strain Distributions at Different Peak Loads or Deflections along Bars in Column A–3

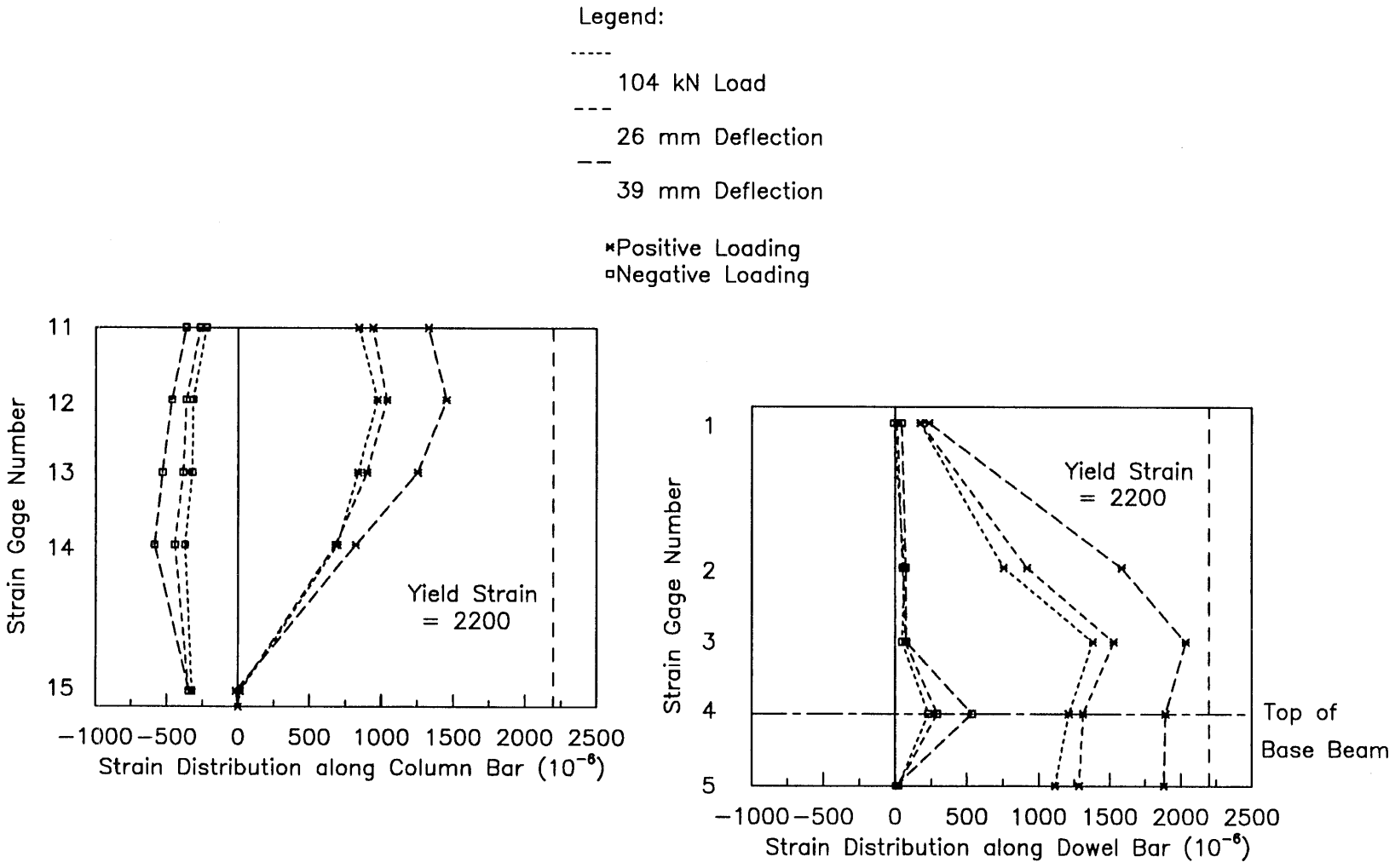

Fig. 5.22 Strain Distributions at Different Peak Loads or Deflections along Bars in Column A–3 (cont.)

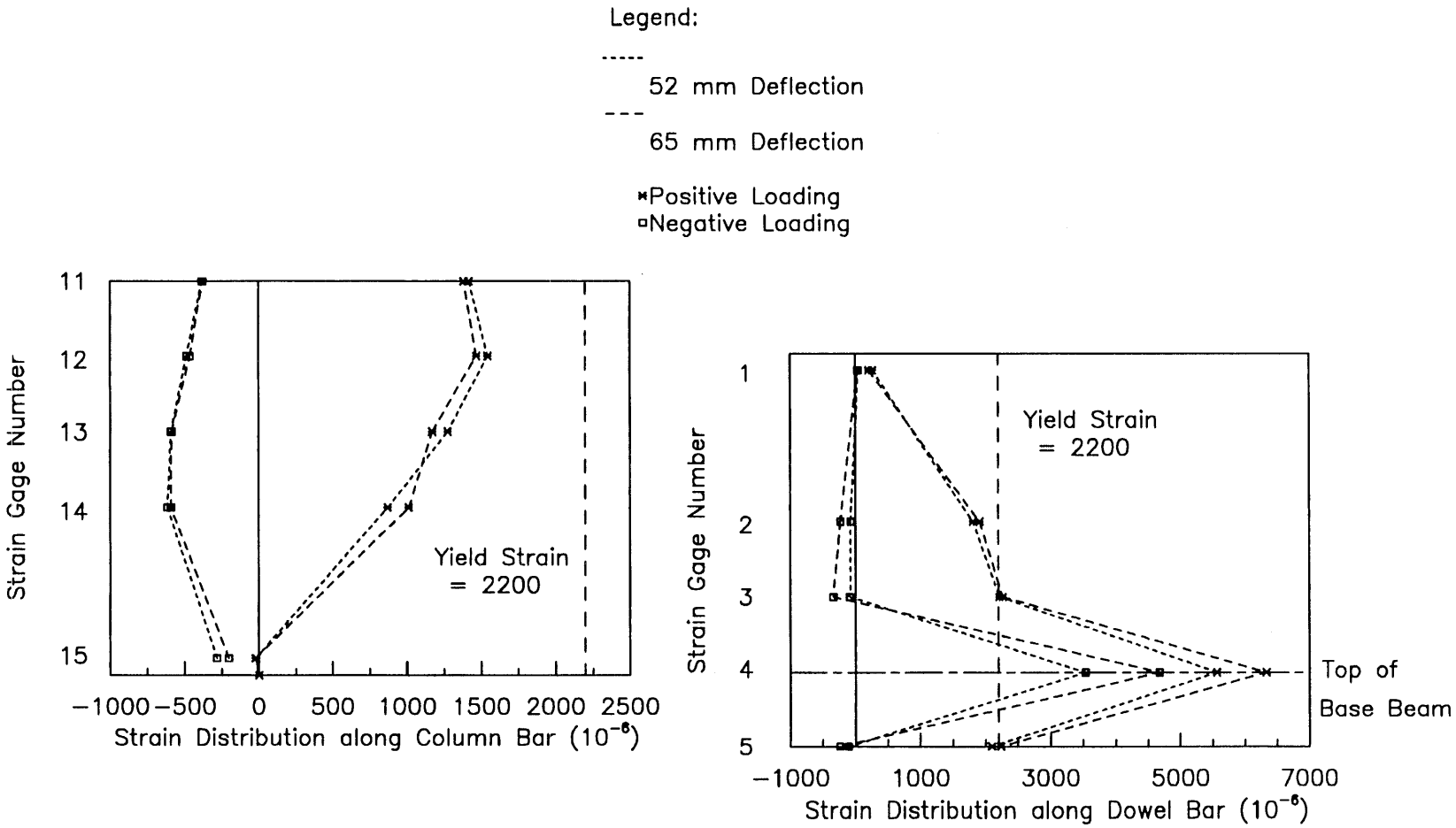

Fig. 5.22 Strain Distributions at Different Peak Loads or Deflections along Bars in Column A–3 (cont.)

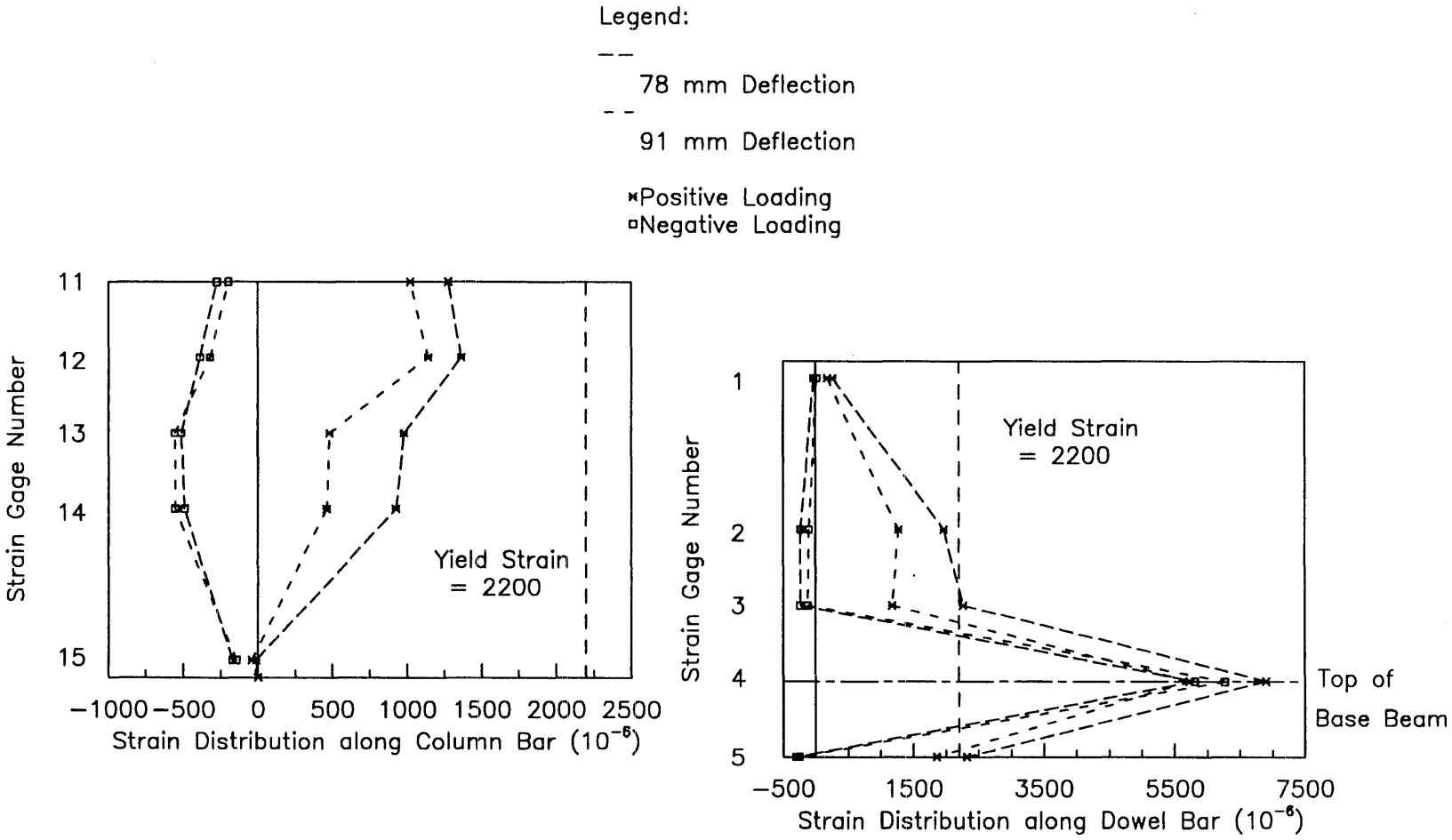

Fig. 5.22 Strain Distributions at Different Peak Loads or Deflections along Bars in Column A–3 (cont.)

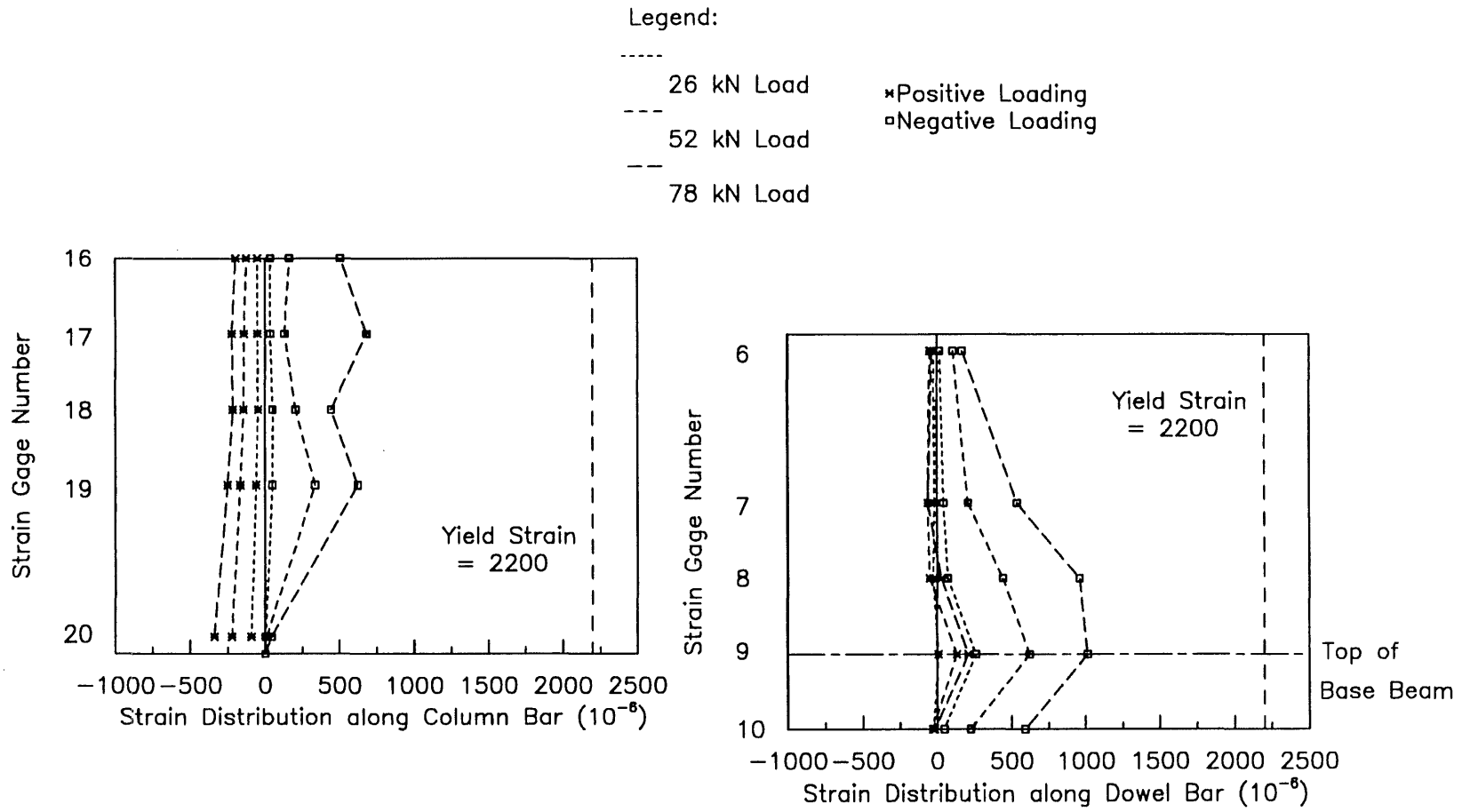

Fig. 5.22 Strain Distributions at Different Peak Loads or Deflections along Bars in Column A–3 (cont.)

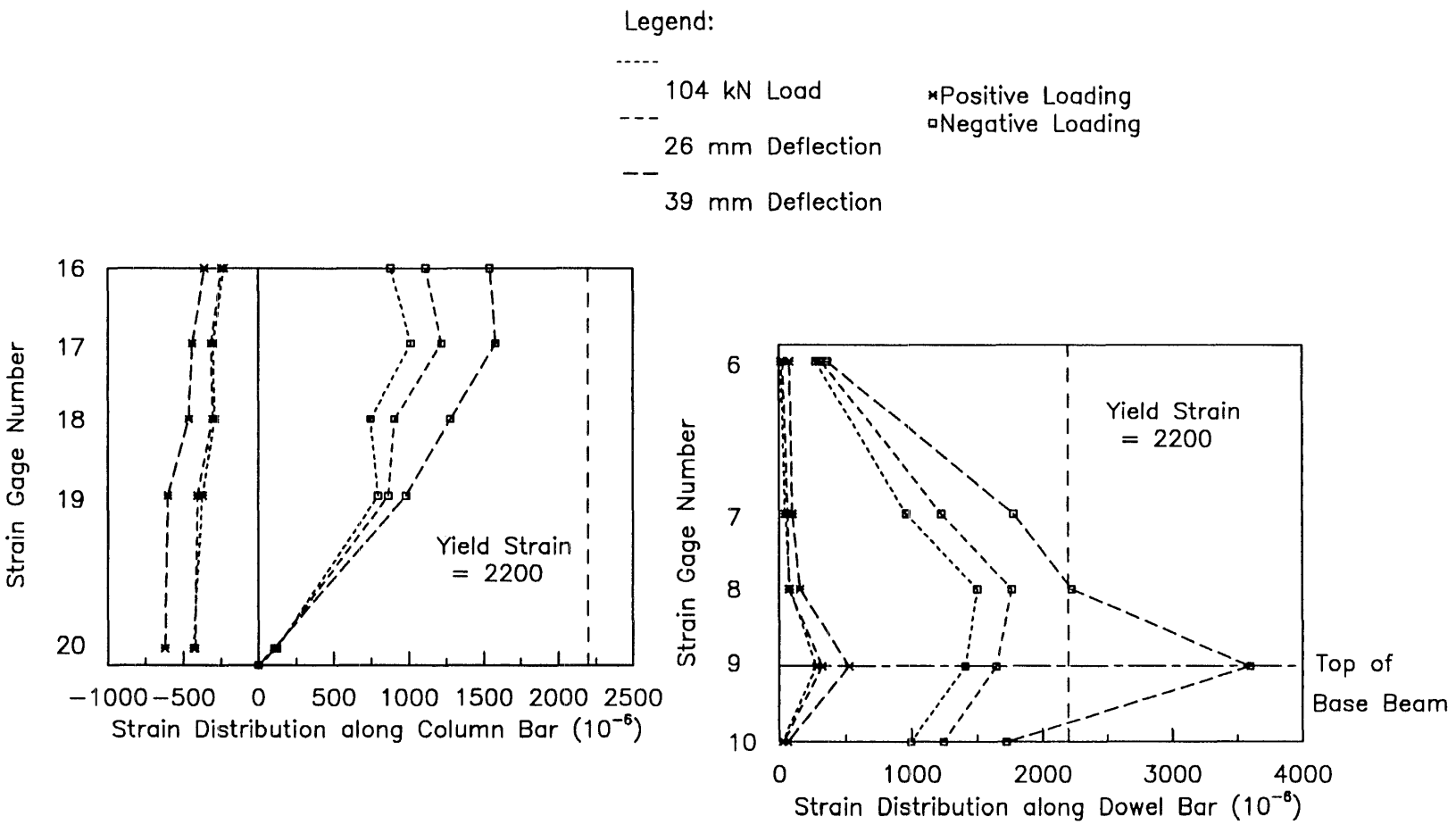

Fig. 5.22 Strain Distributions at Different Peak Loads or Deflections along Bars in Column A–3 (cont.)

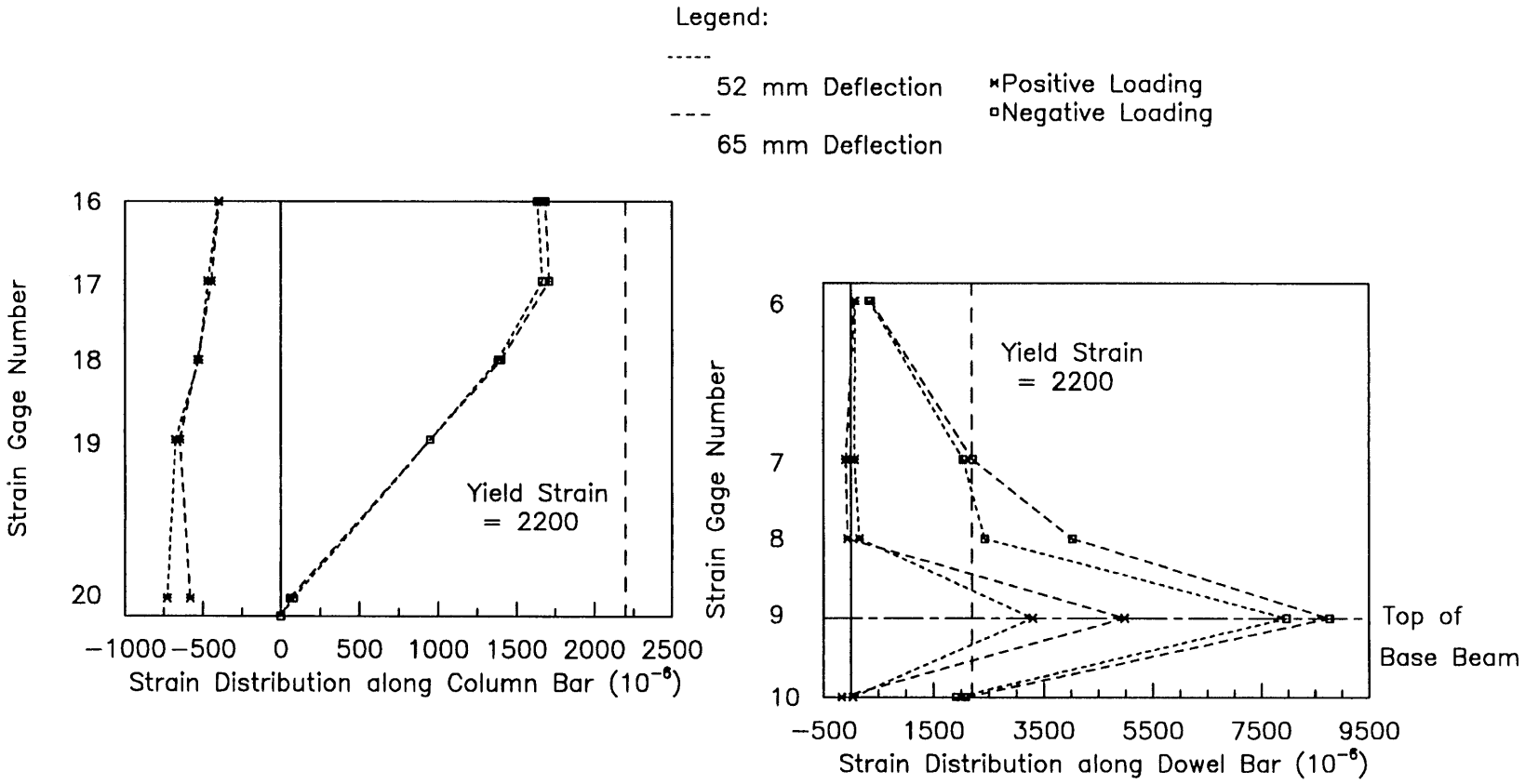

Fig. 5.22 Strain Distributions at Different Peak Loads or Deflections along Bars in Column A–3 (cont.)

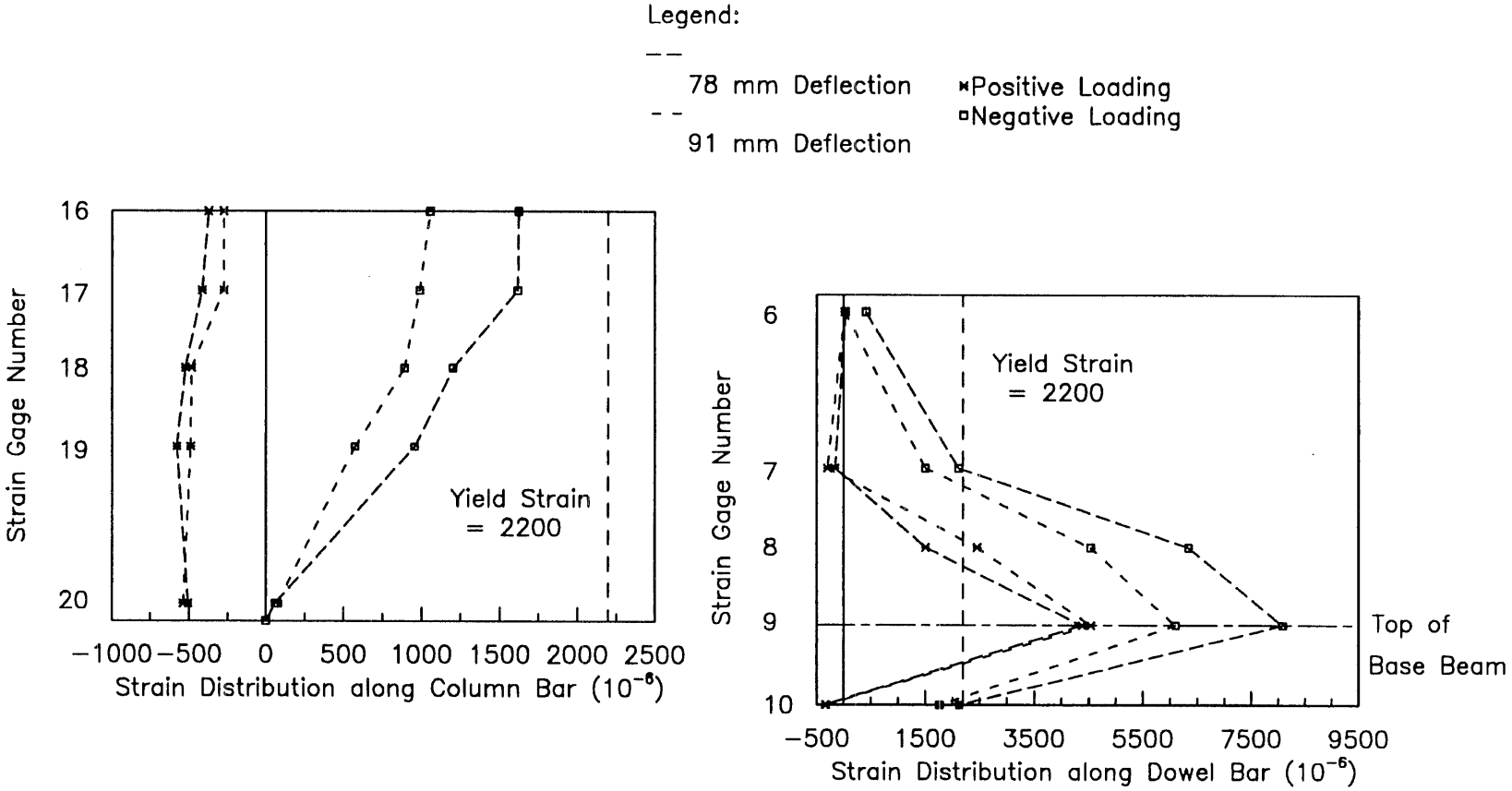

Fig. 5.22 Strain Distributions at Different Peak Loads or Deflections along Bars in Column A–3 (cont.)

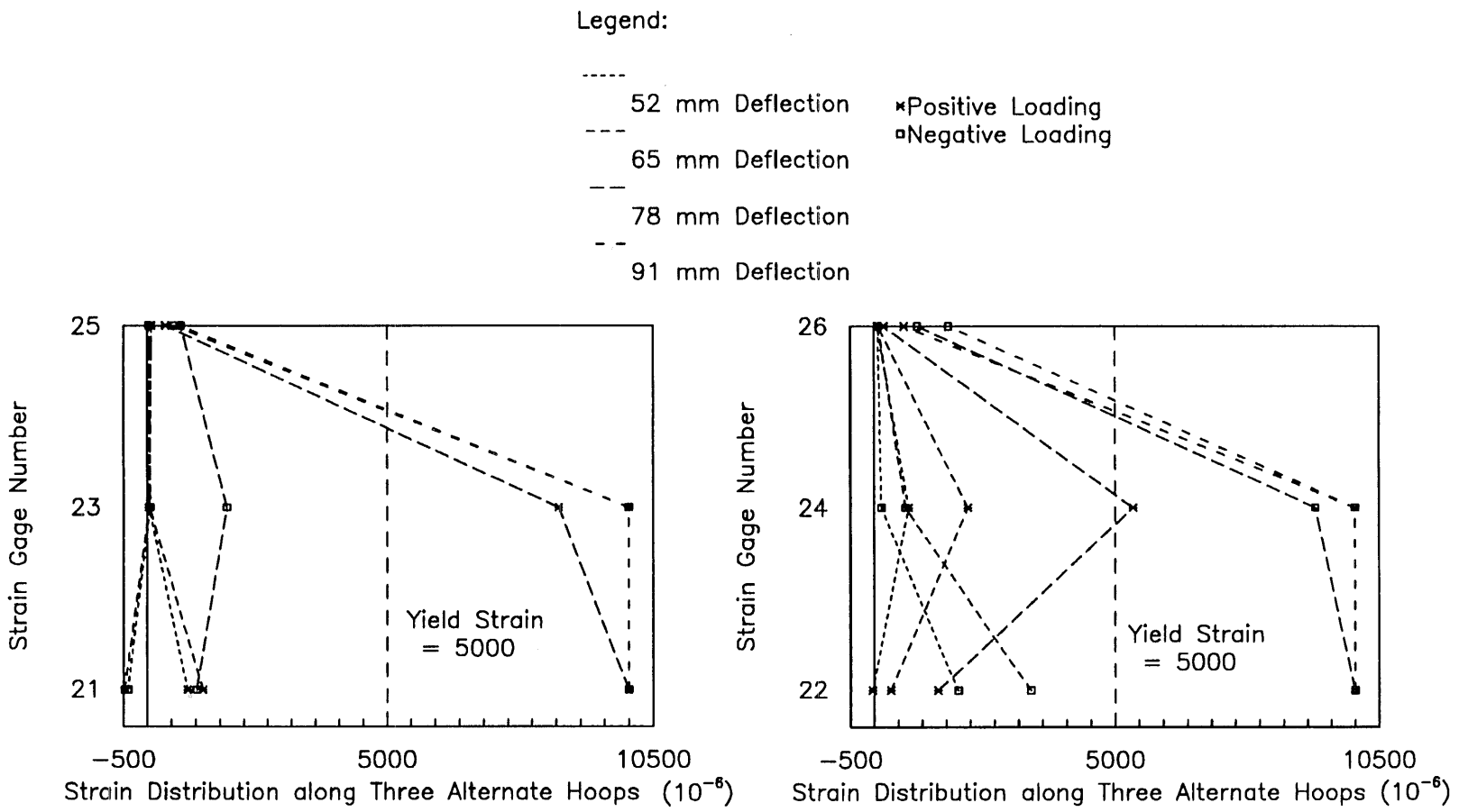

Fig. 5.22 Strain Distributions at Different Peak Loads or Deflections along Bars in Column A–3 (cont.)

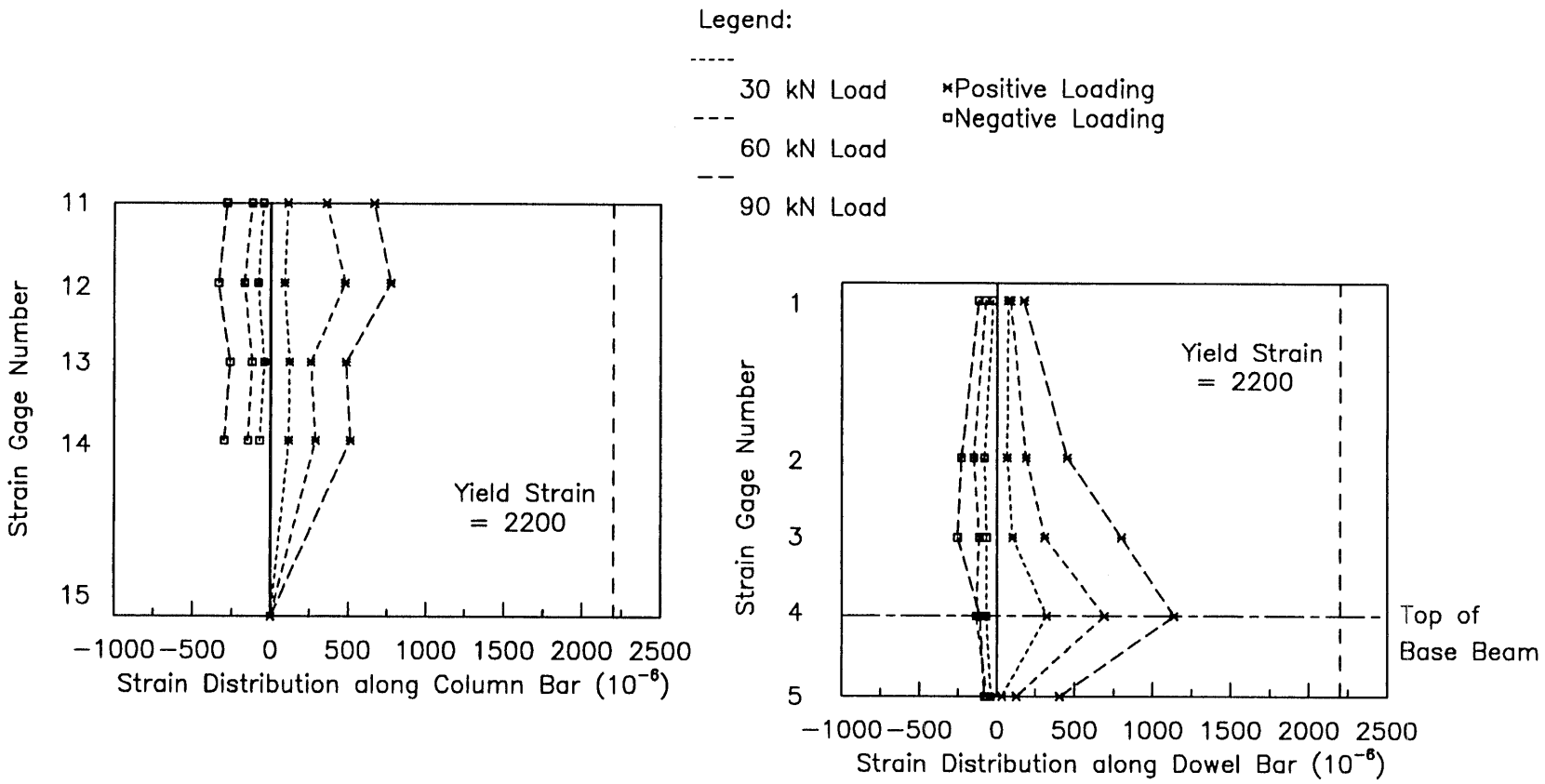

Fig. 5.23 Strain Distributions at Different Peak Loads or Deflections along Bars in Column B–1

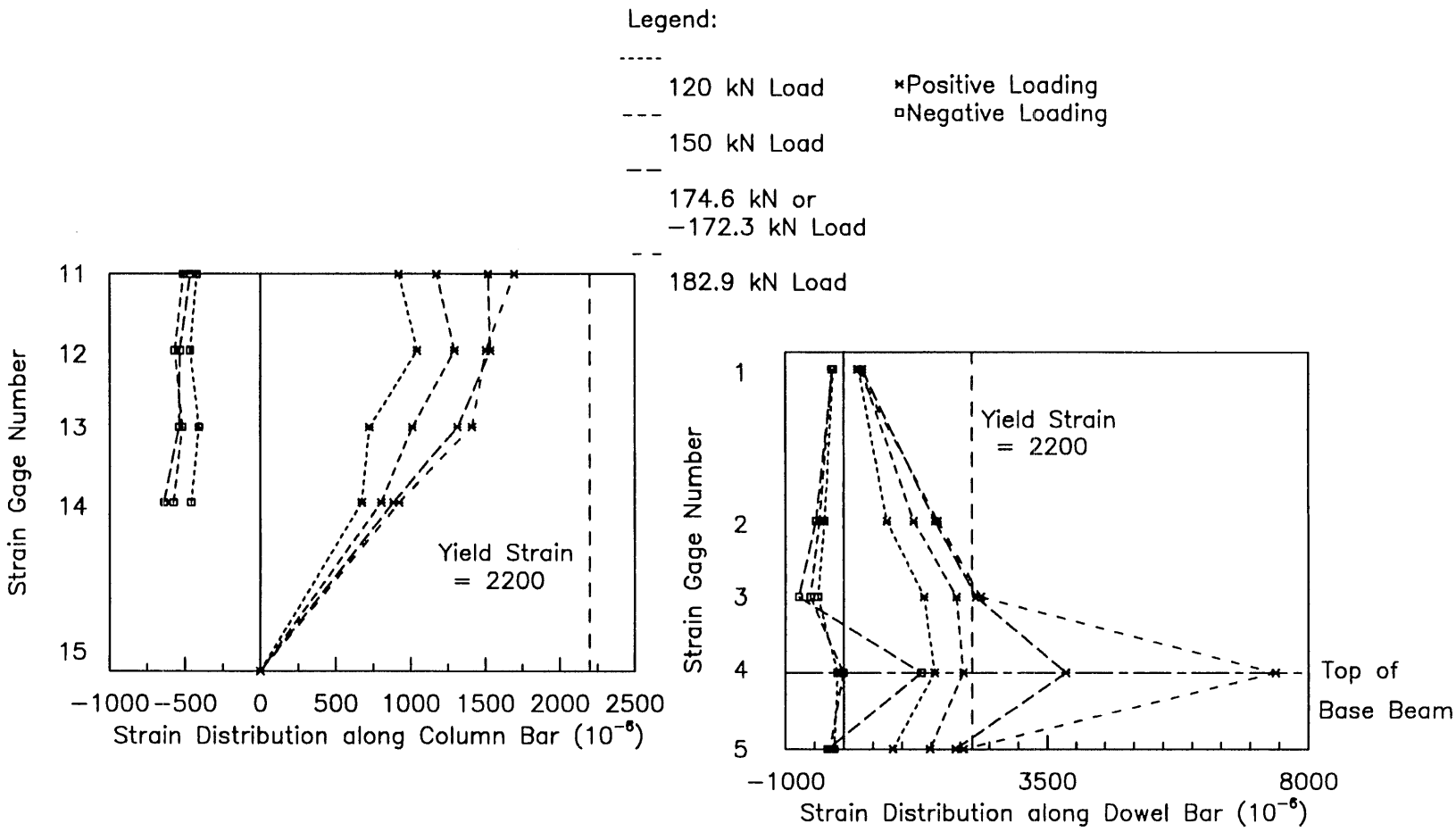

Fig. 5.23 Strain Distributions at Different Peak Loads or Deflections along Bars in Column B–1 (cont.)

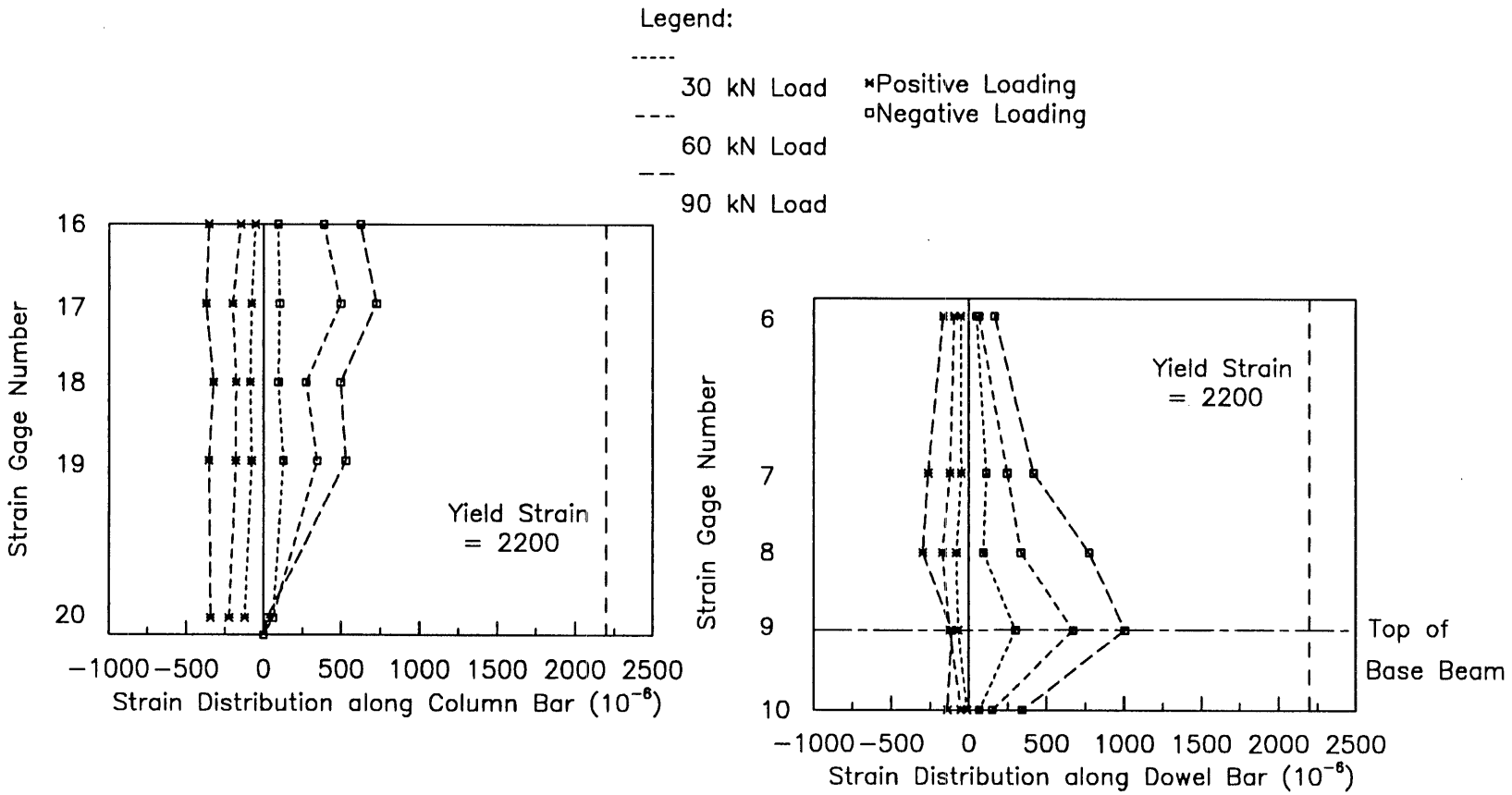

Fig. 5.23 Strain Distributions at Different Peak Loads or Deflections along Bars in Column B–1 (cont.)

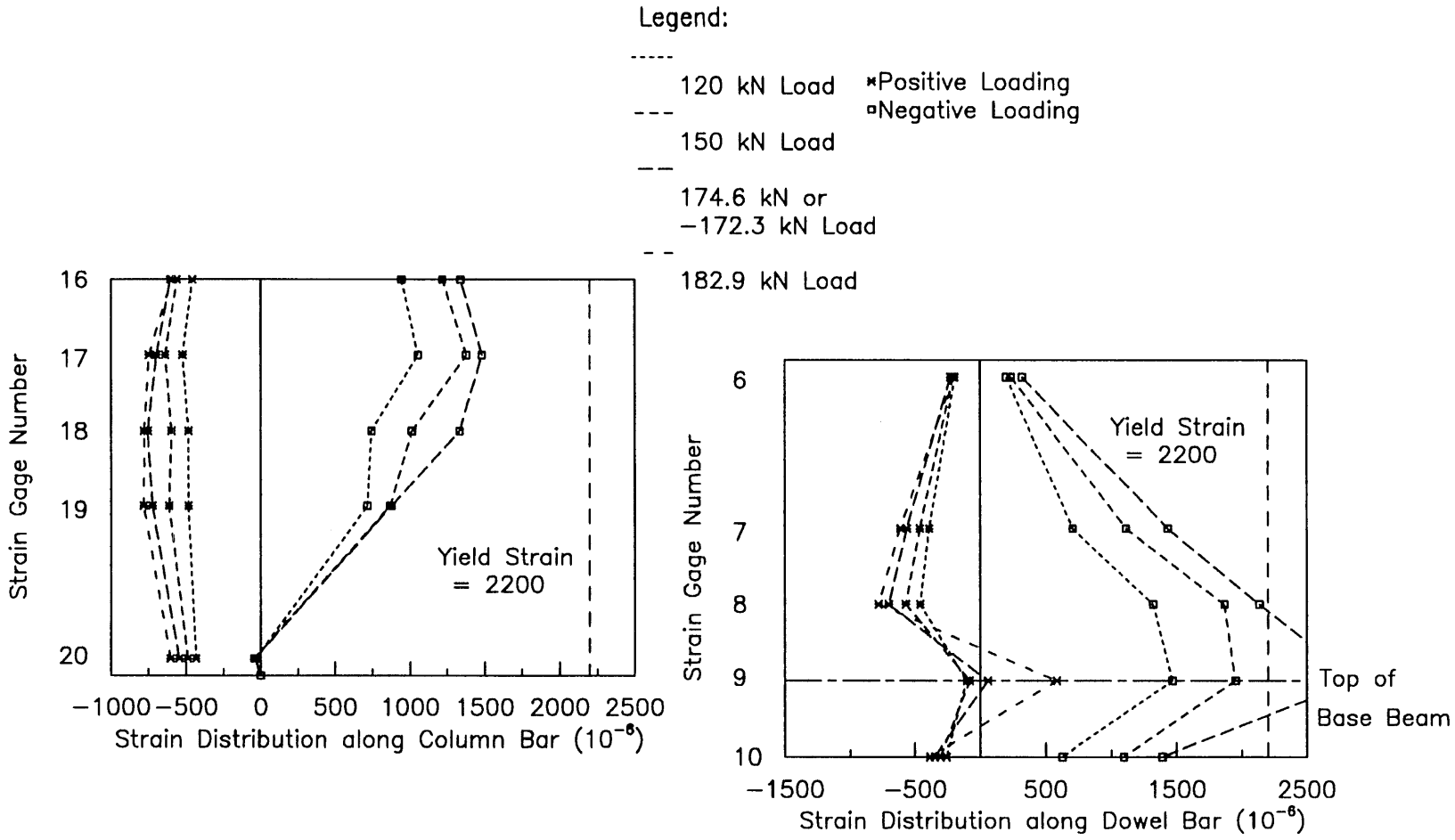

Fig. 5.23 Strain Distributions at Different Peak Loads or Deflections along Bars in Column B–1 (cont.)

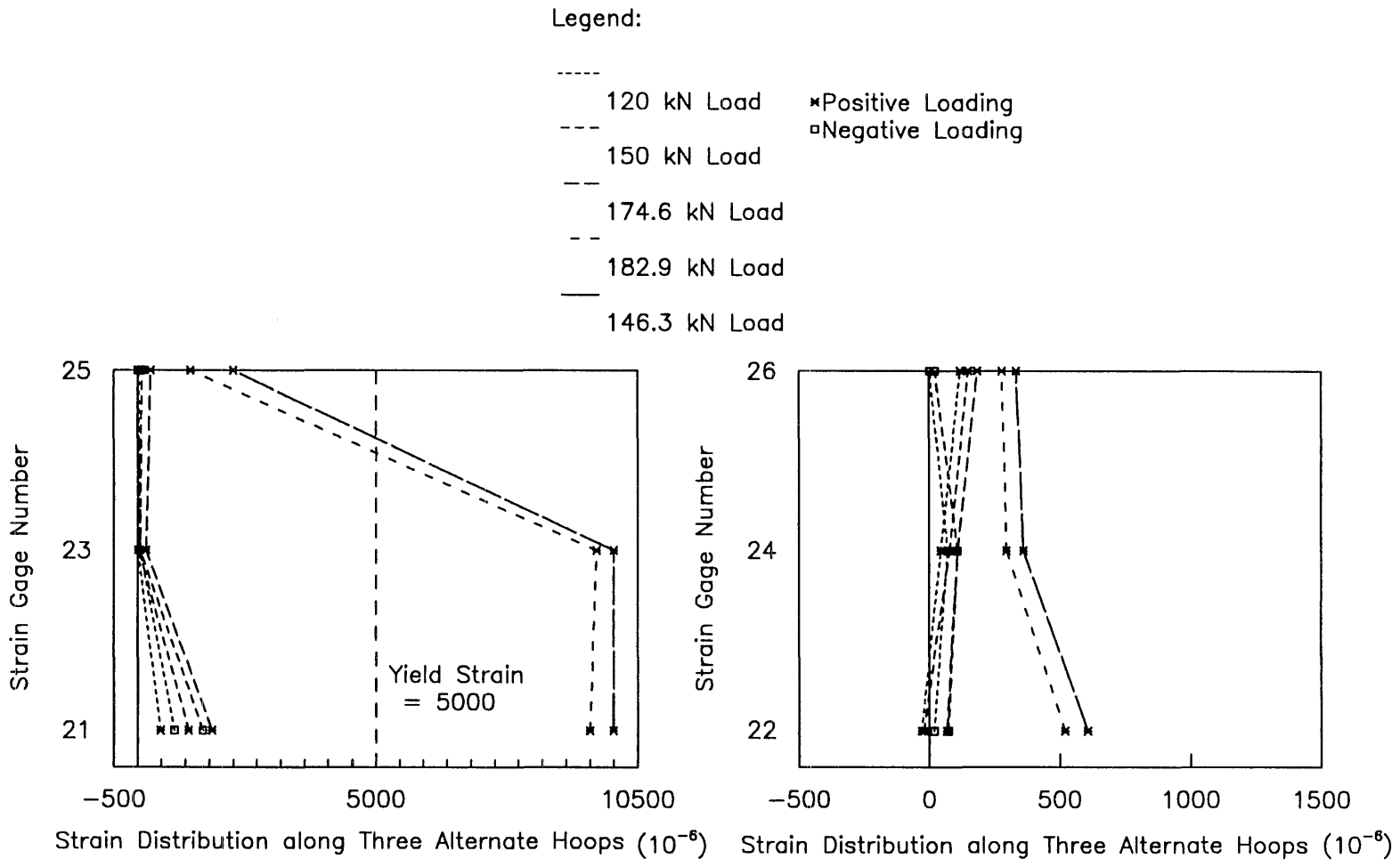

Fig. 5.23 Strain Distributions at Different Peak Loads or Deflections along Bars in Column B–1 (cont.)

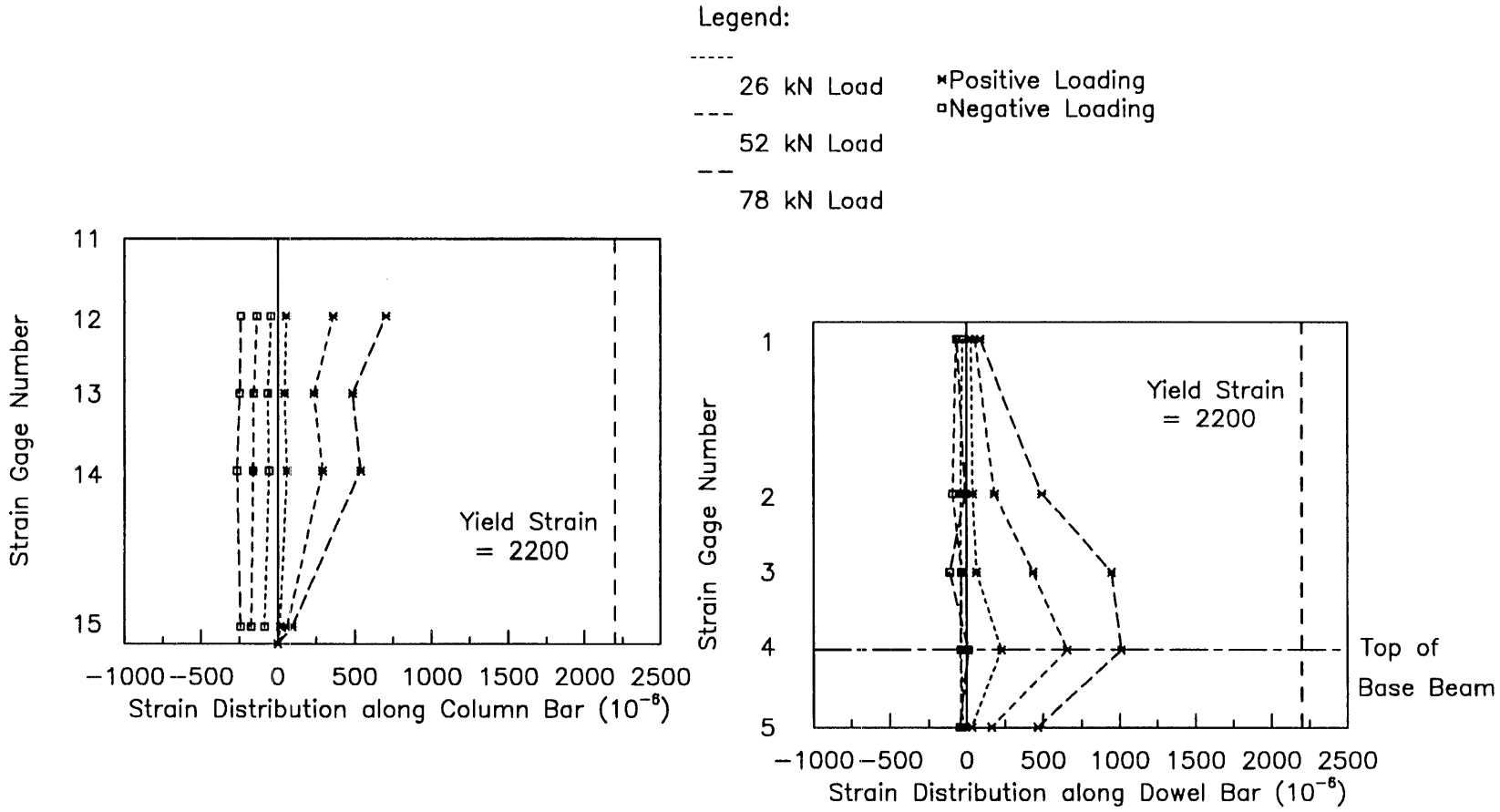

Fig. 5.24 Strain Distributions at Different Peak Loads or Deflections along Bars in Column B–2

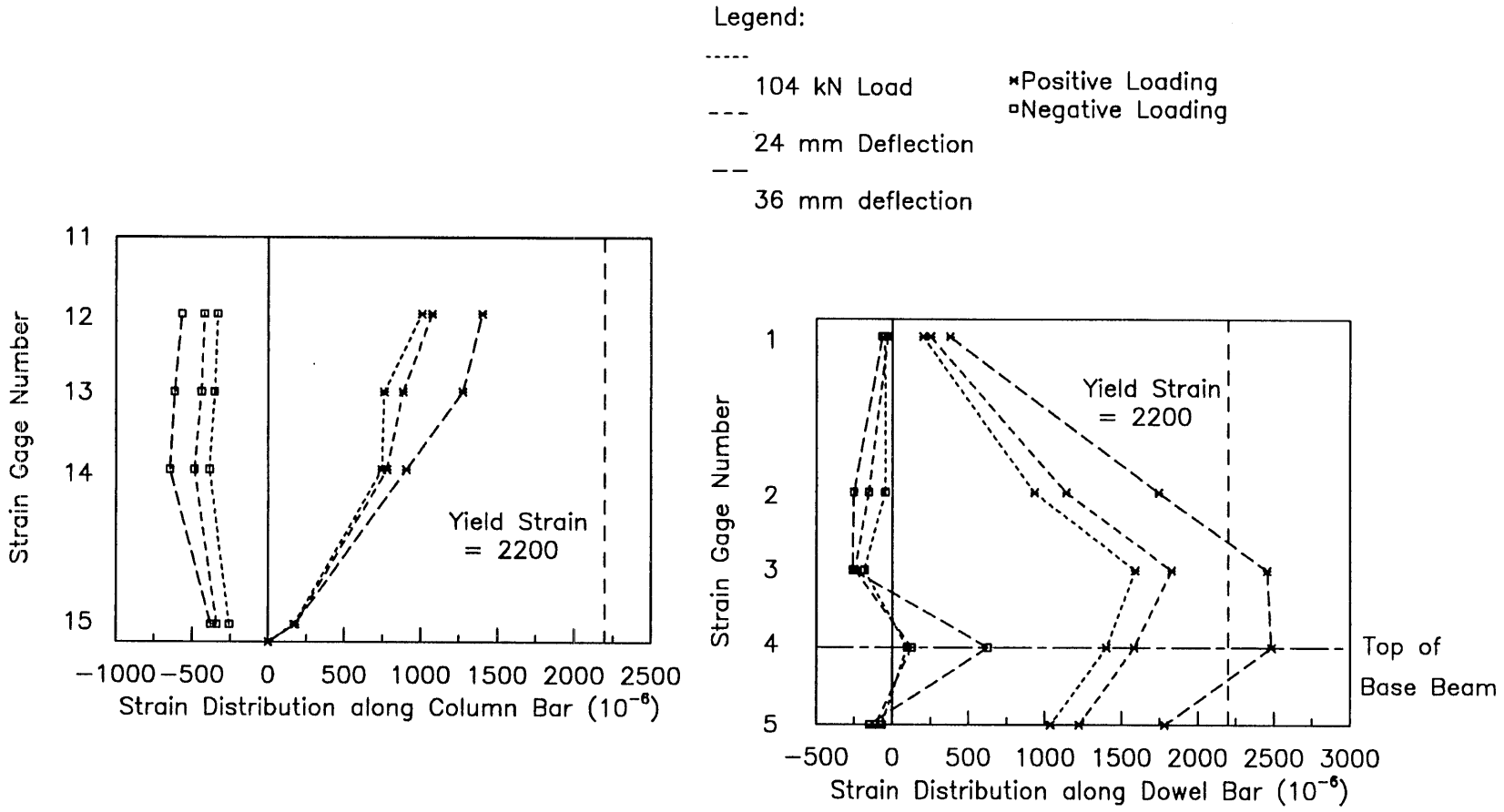

Fig. 5.24 Strain Distributions at Different Peak Loads or Deflections along Bars in Column B–2 (cont.)

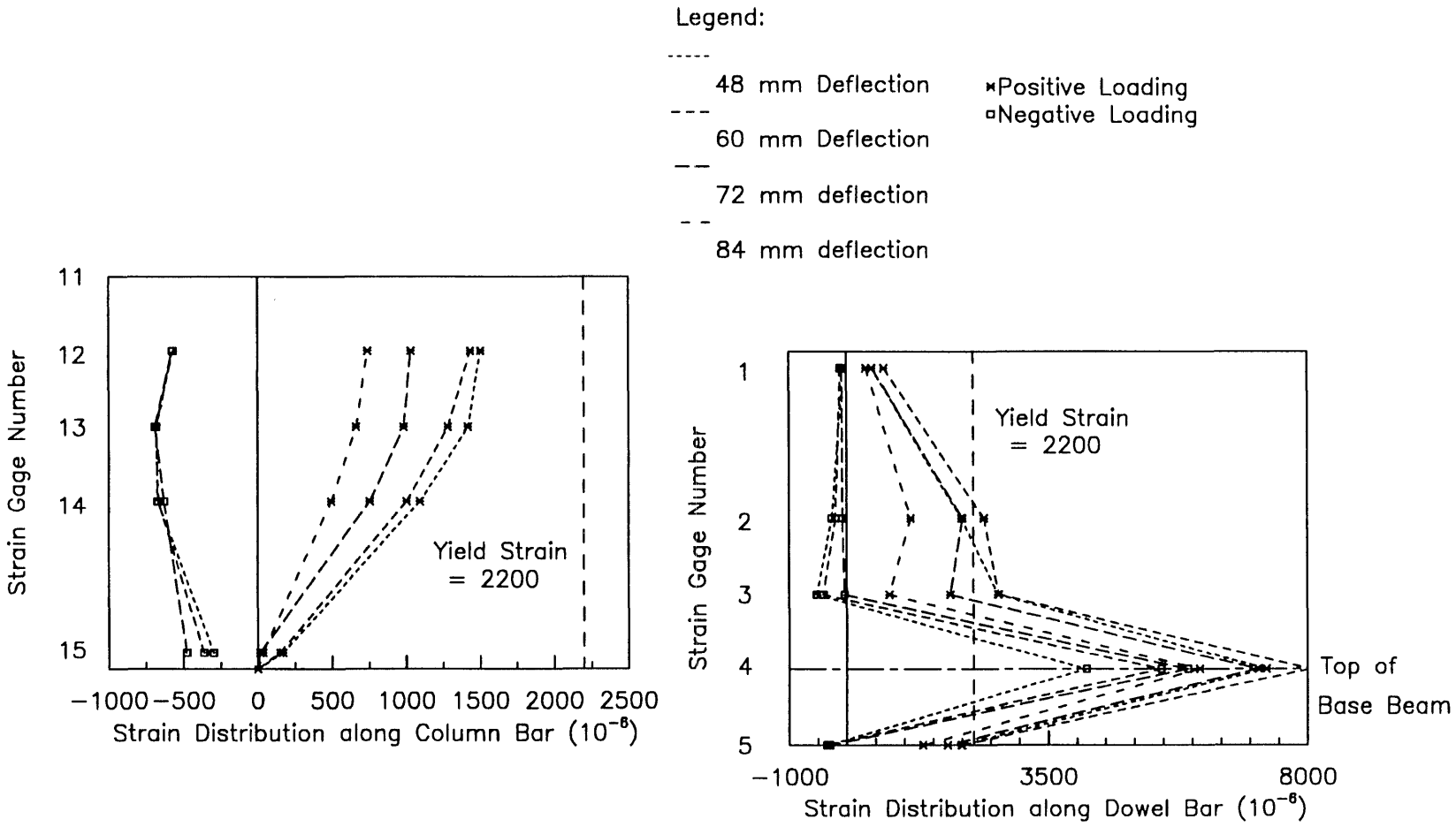

Fig. 5.24 Strain Distributions at Different Peak Loads or Deflections along Bars in Column B–2 (cont.)

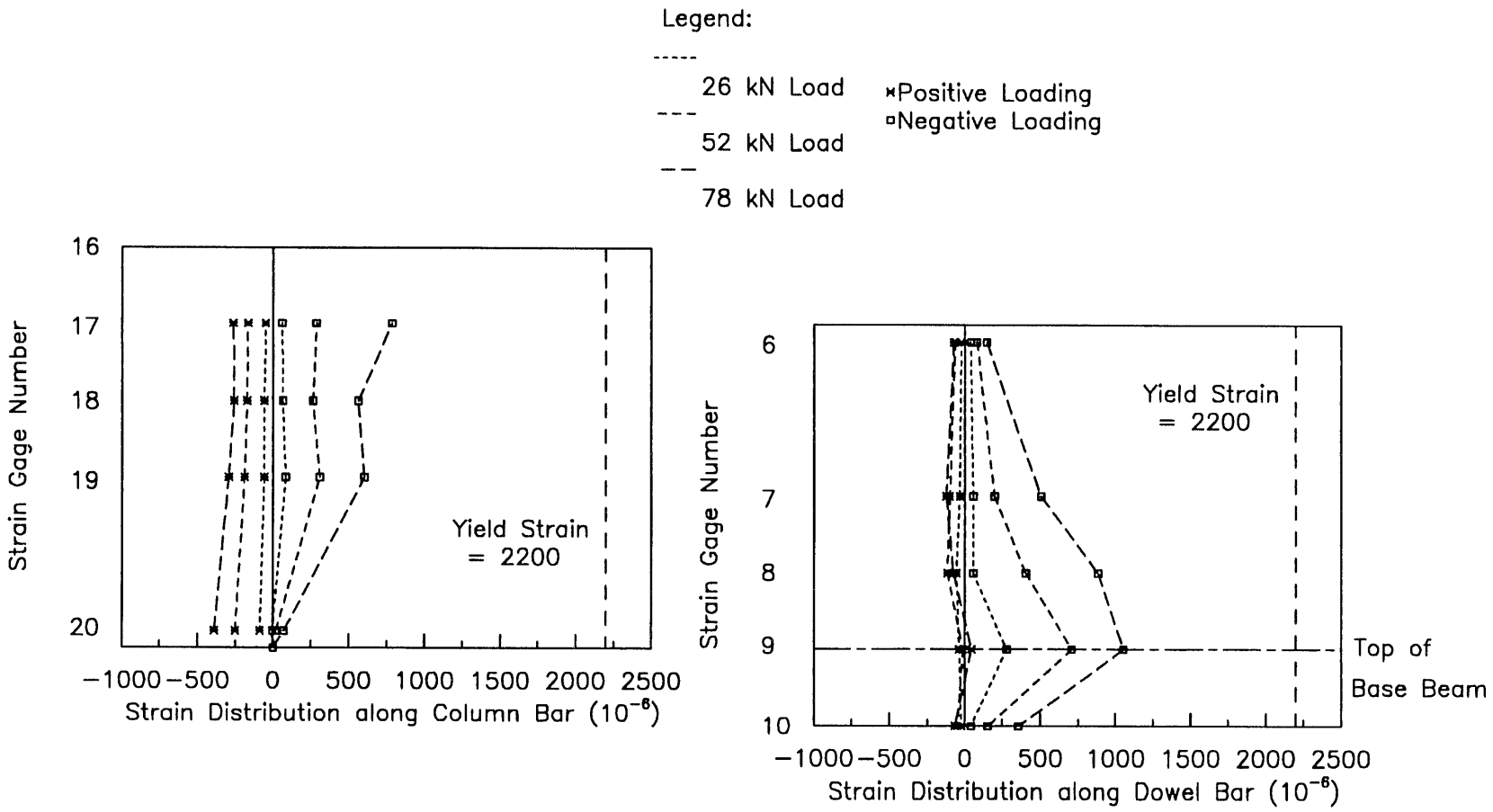

Fig. 5.24 Strain Distributions at Different Peak Loads or Deflections along Bars in Column B–2 (cont.)

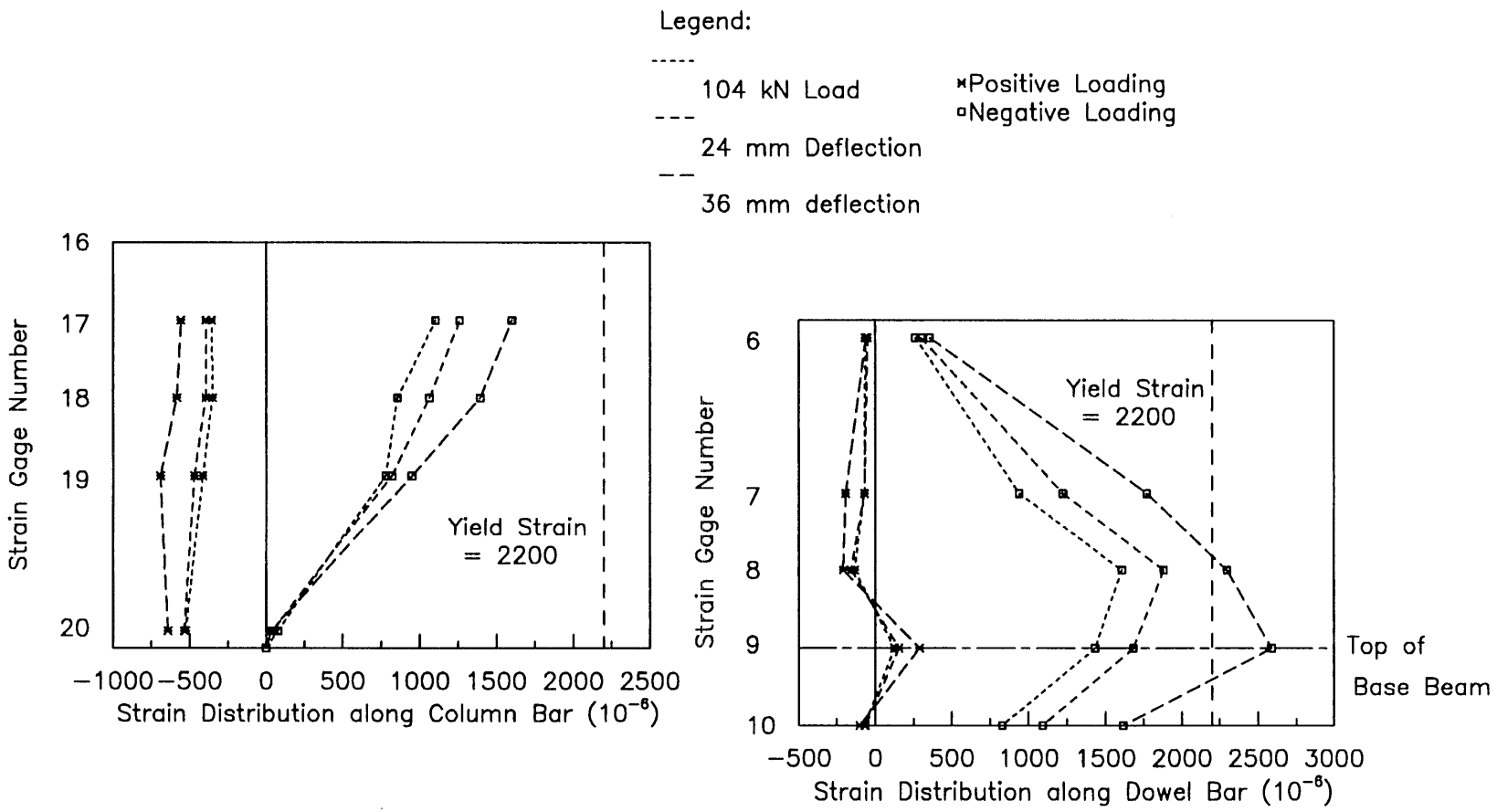

Fig. 5.24 Strain Distributions at Different Peak Loads or Deflections along Bars in Column B–2 (cont.)

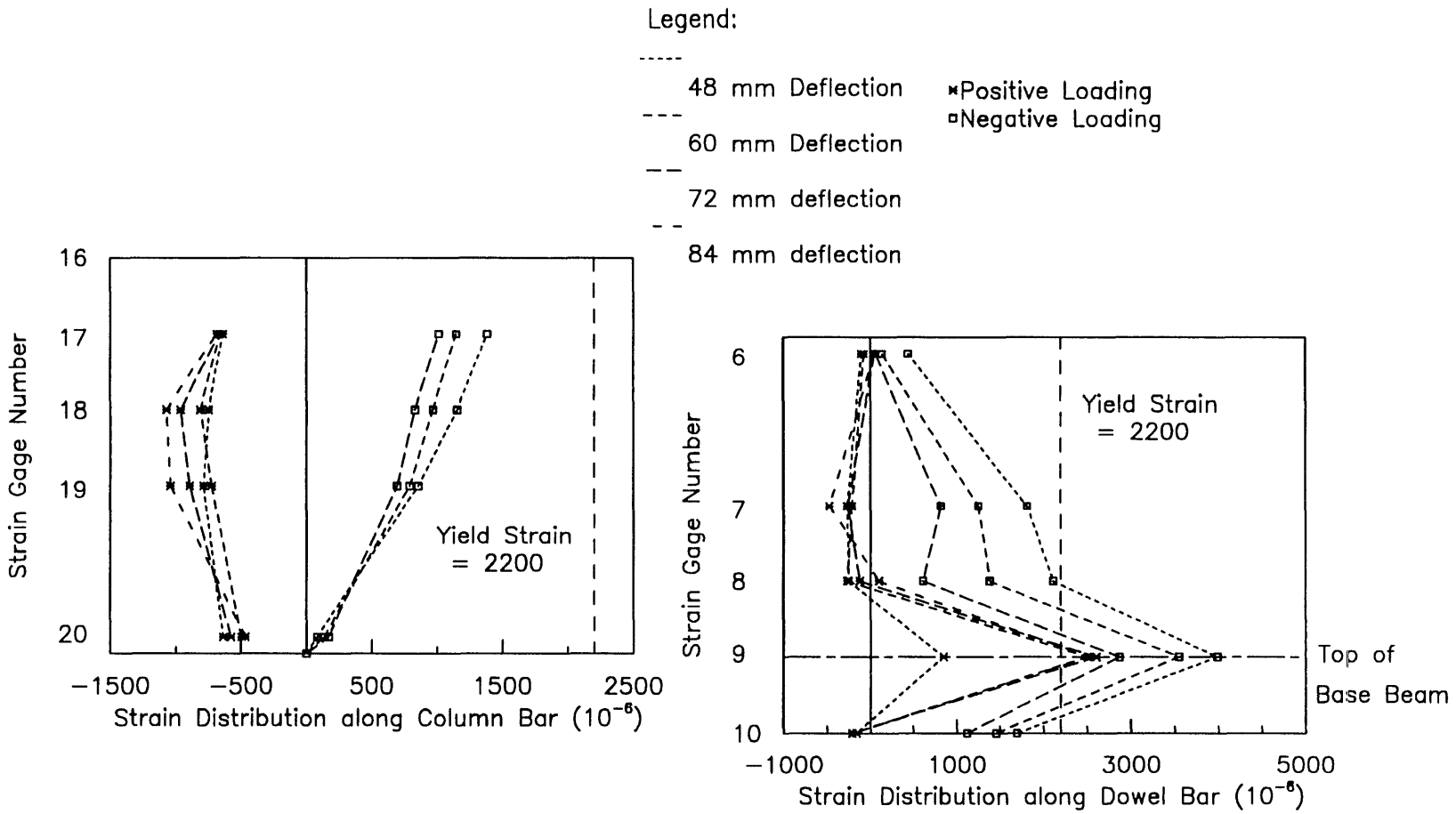

Fig. 5.24 Strain Distributions at Different Peak Loads or Deflections along Bars in Column B–2 (cont.)

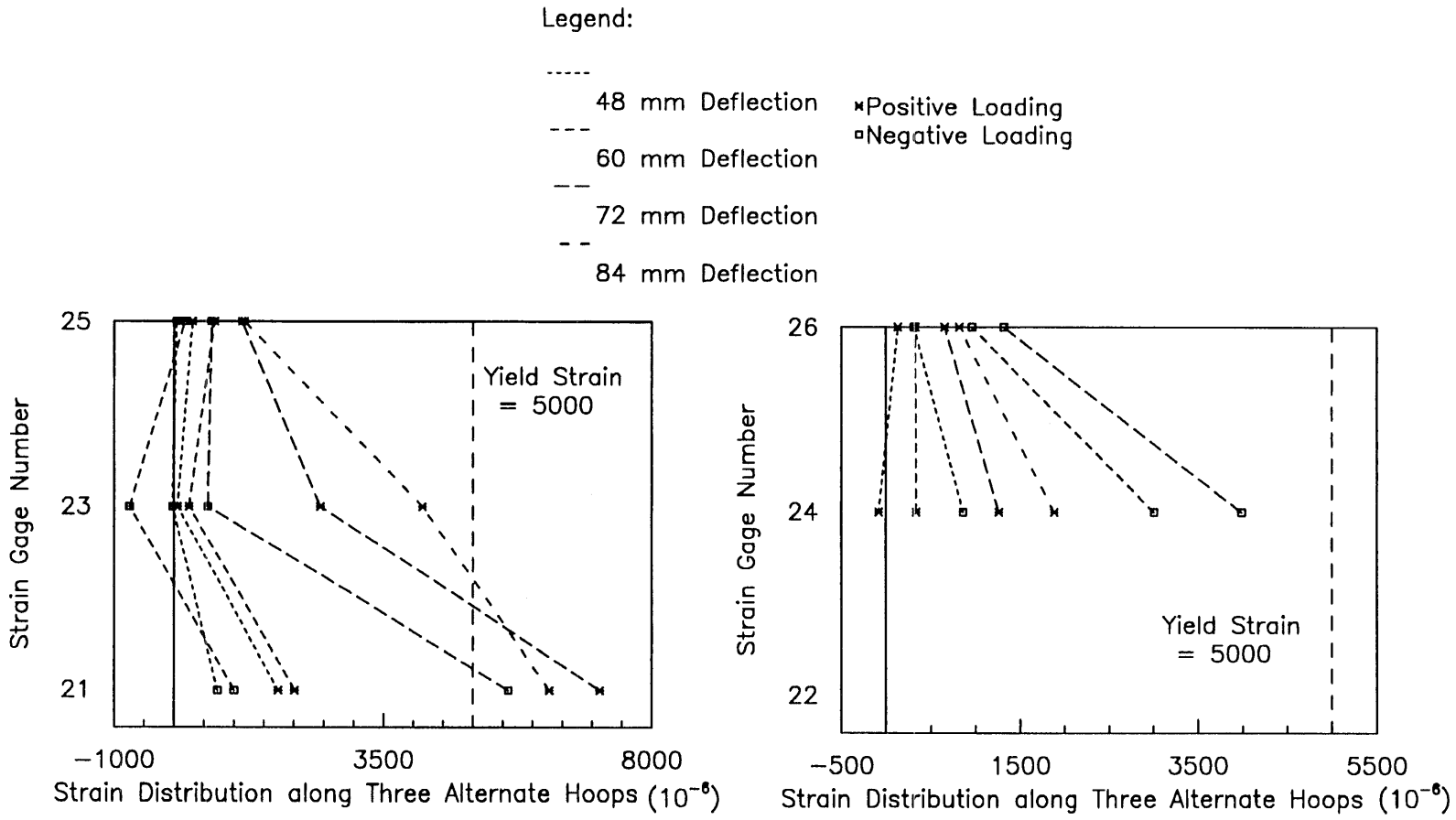

Fig. 5.24 Strain Distributions at Different Peak Loads or Deflections along Bars in Column B–2 (cont.)

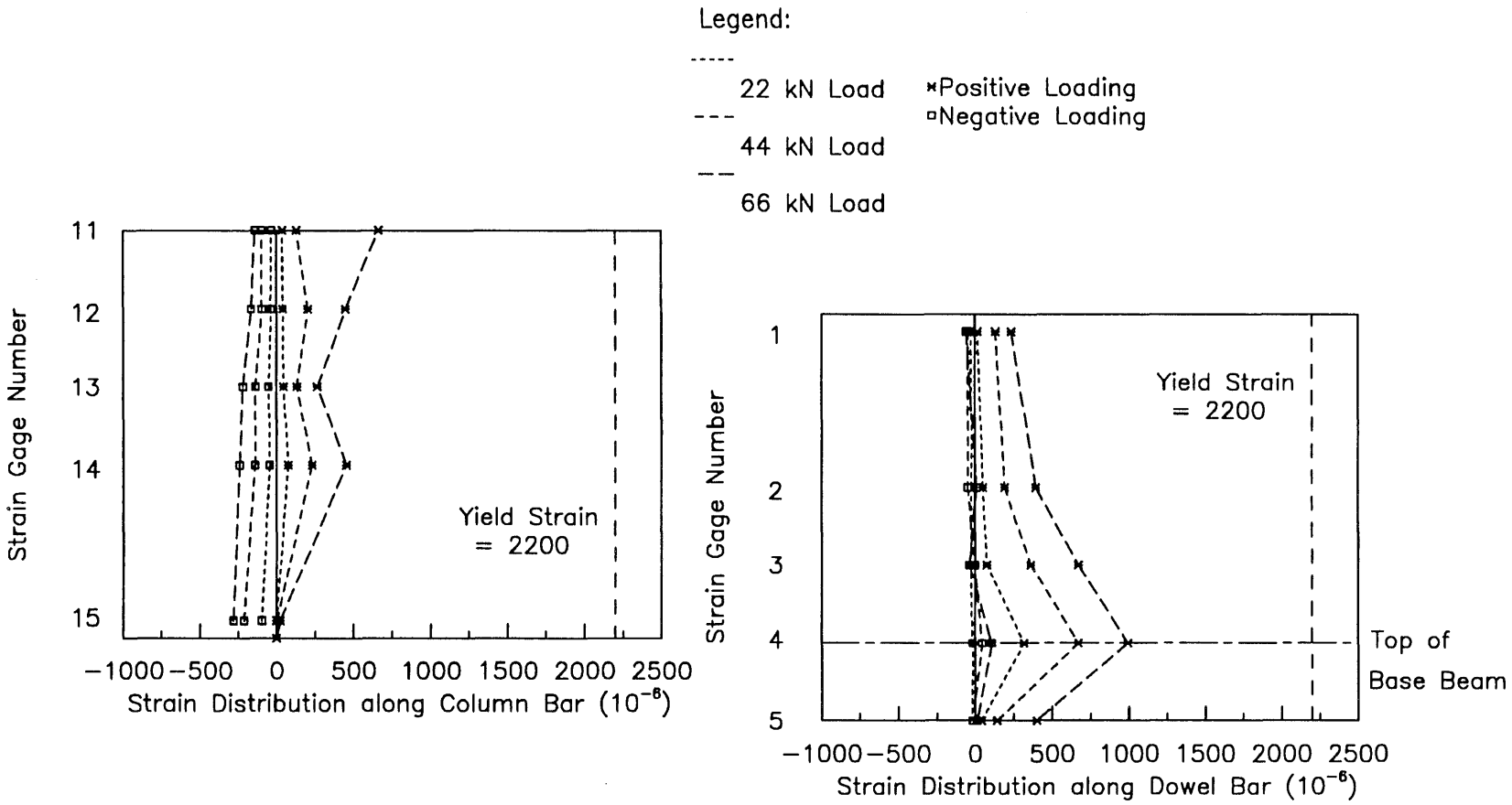

Fig. 5.25 Strain Distributions at Different Peak Loads or Deflections along Bars in Column B–3

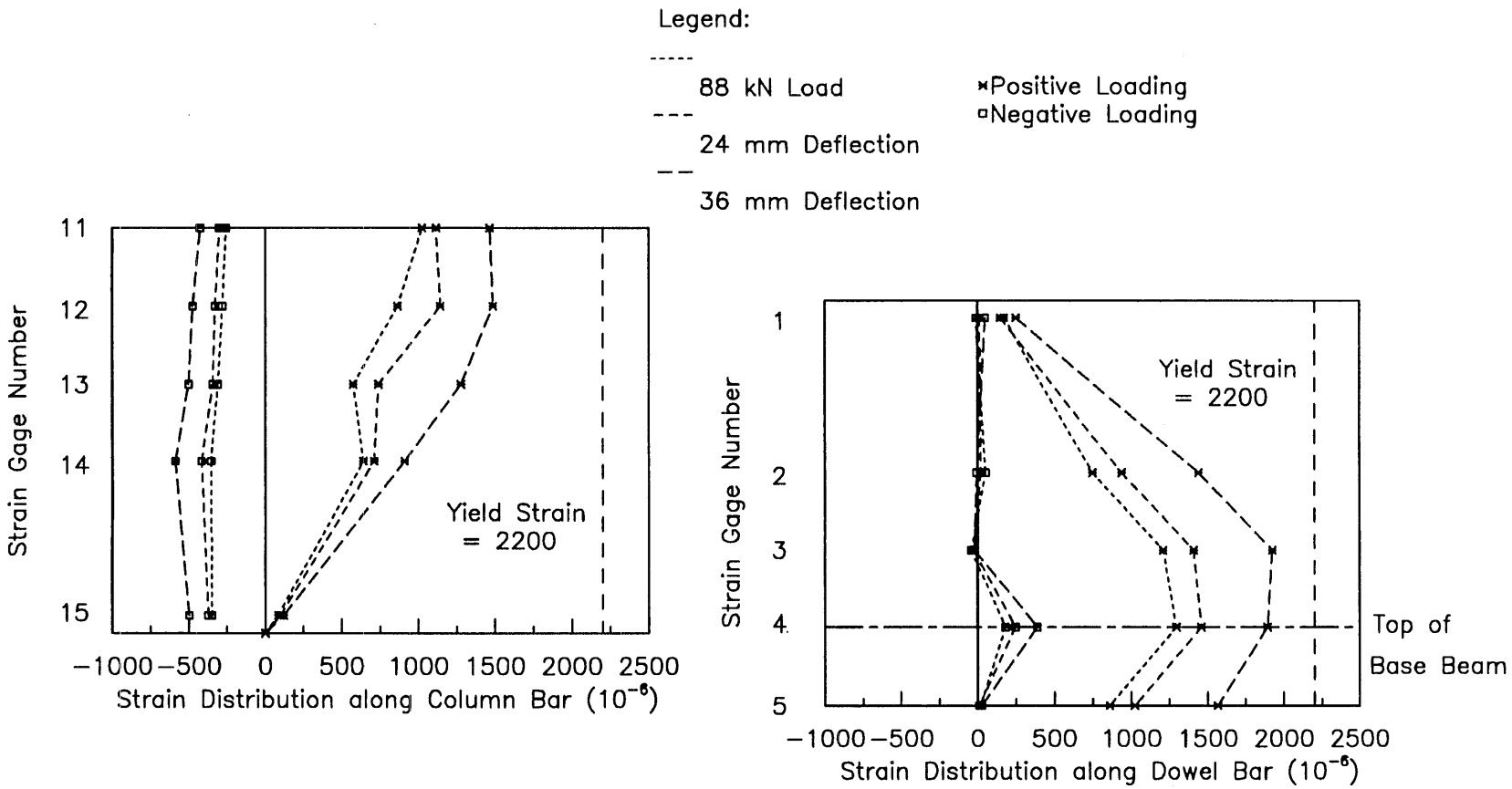

Fig. 5.25 Strain Distributions at Different Peak Loads or Deflections along Bars in Column B–3 (cont.)

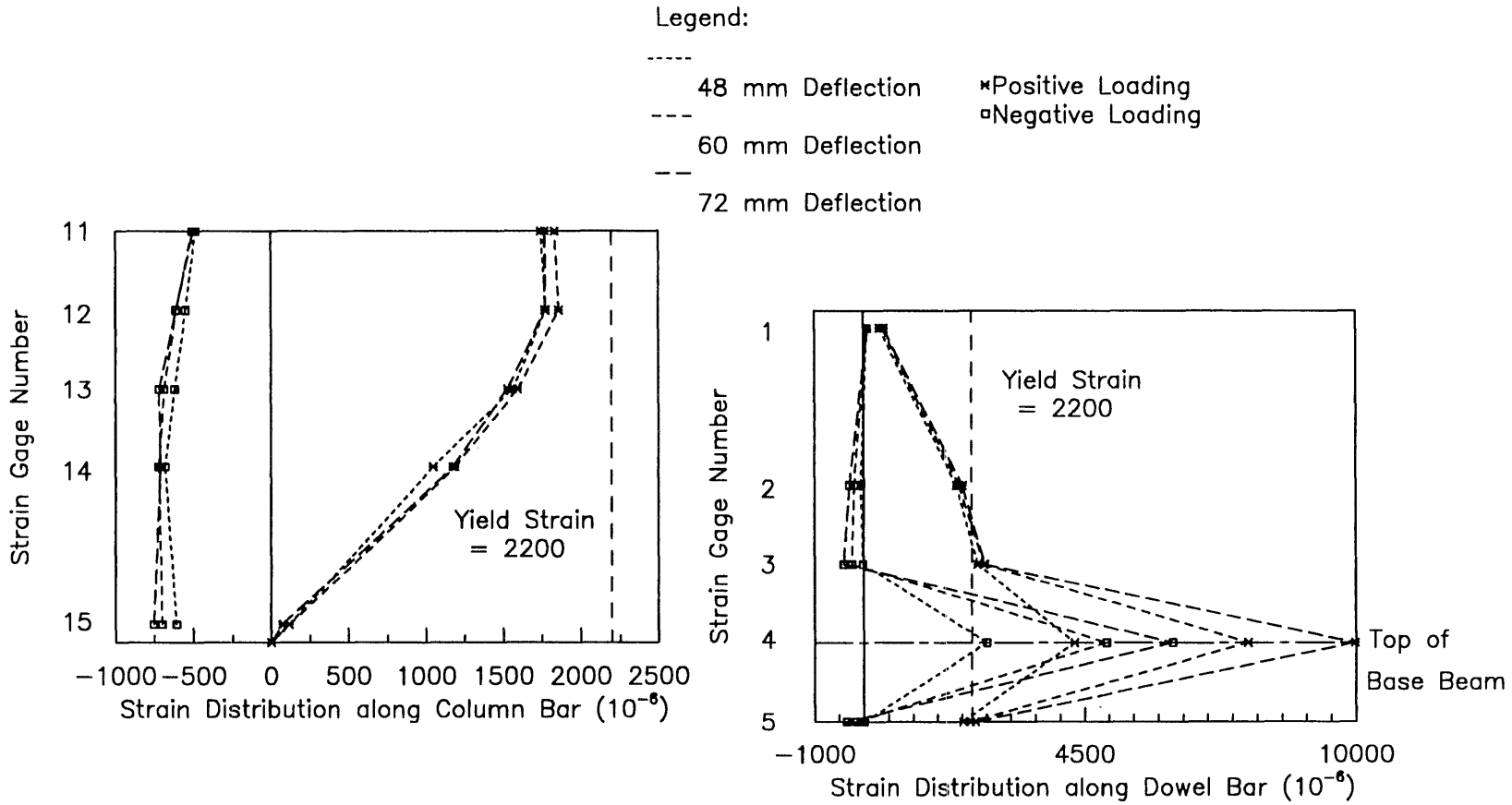

Fig. 5.25 Strain Distributions at Different Peak Loads or Deflections along Bars in Column B–3 (cont.)

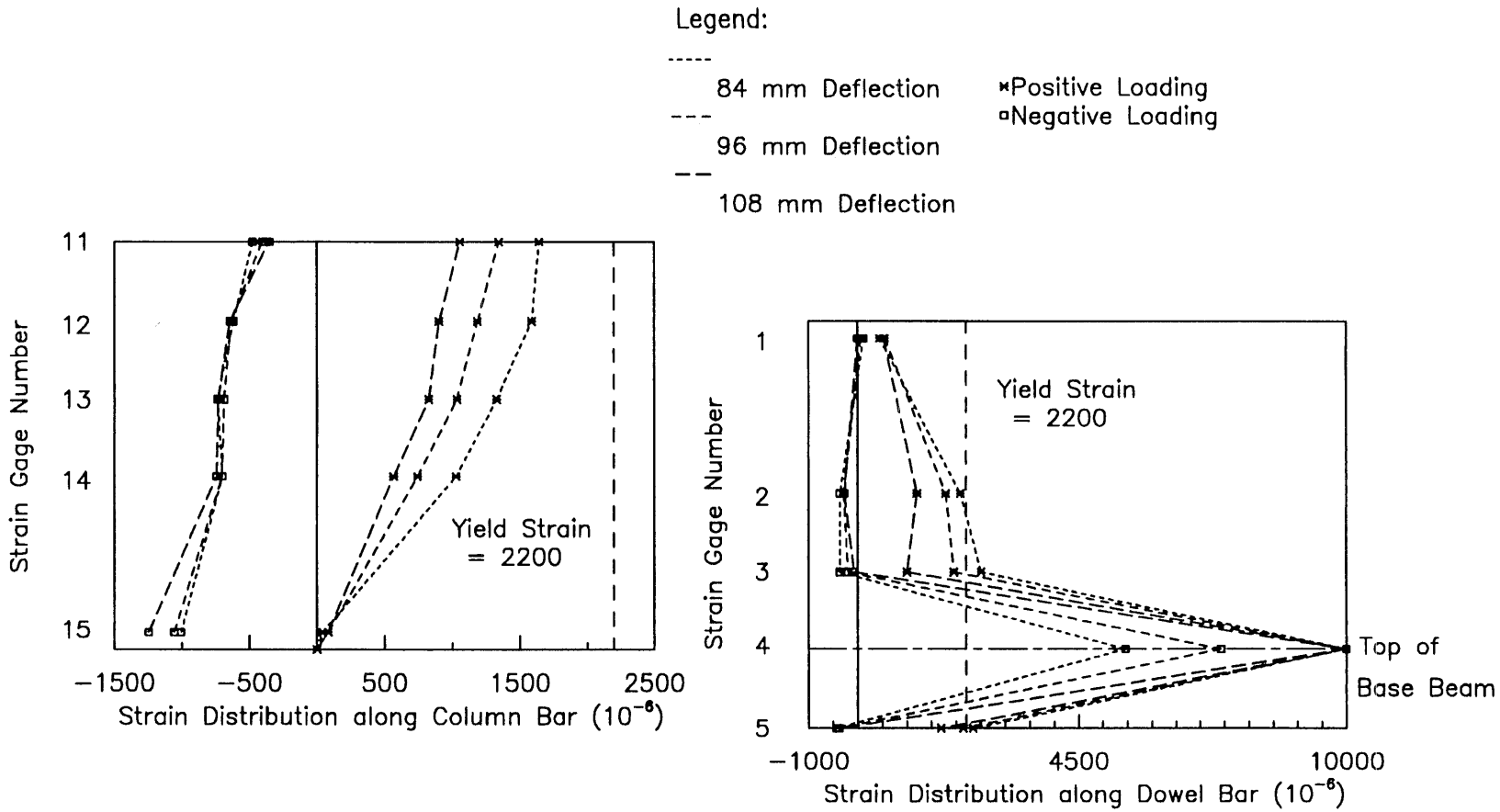

Fig. 5.25 Strain Distributions at Different Peak Loads or Deflections along Bars in Column B–3 (cont.)

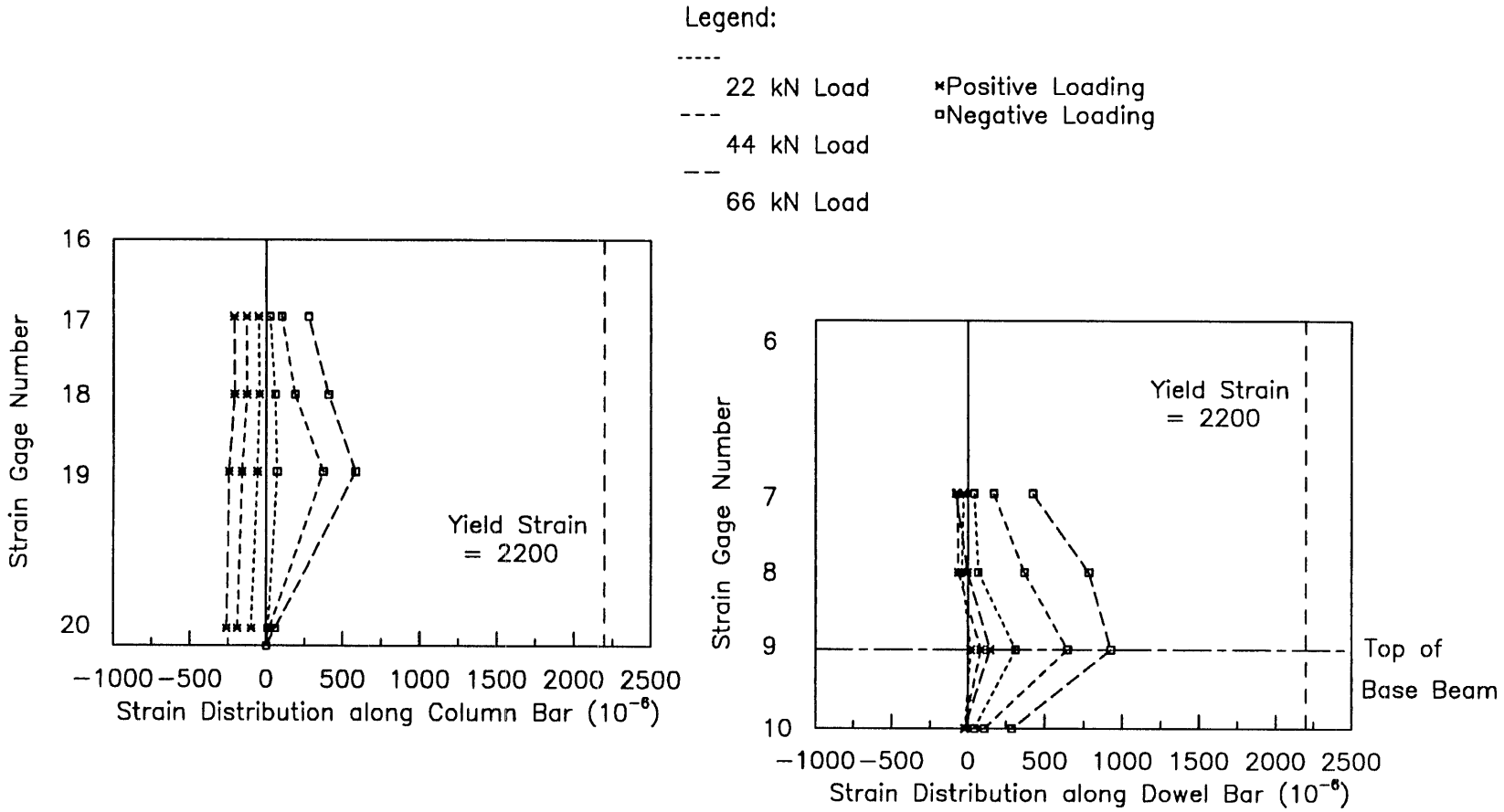

Fig. 5.25 Strain Distributions at Different Peak Loads or Deflections along Bars in Column B–3 (cont.)

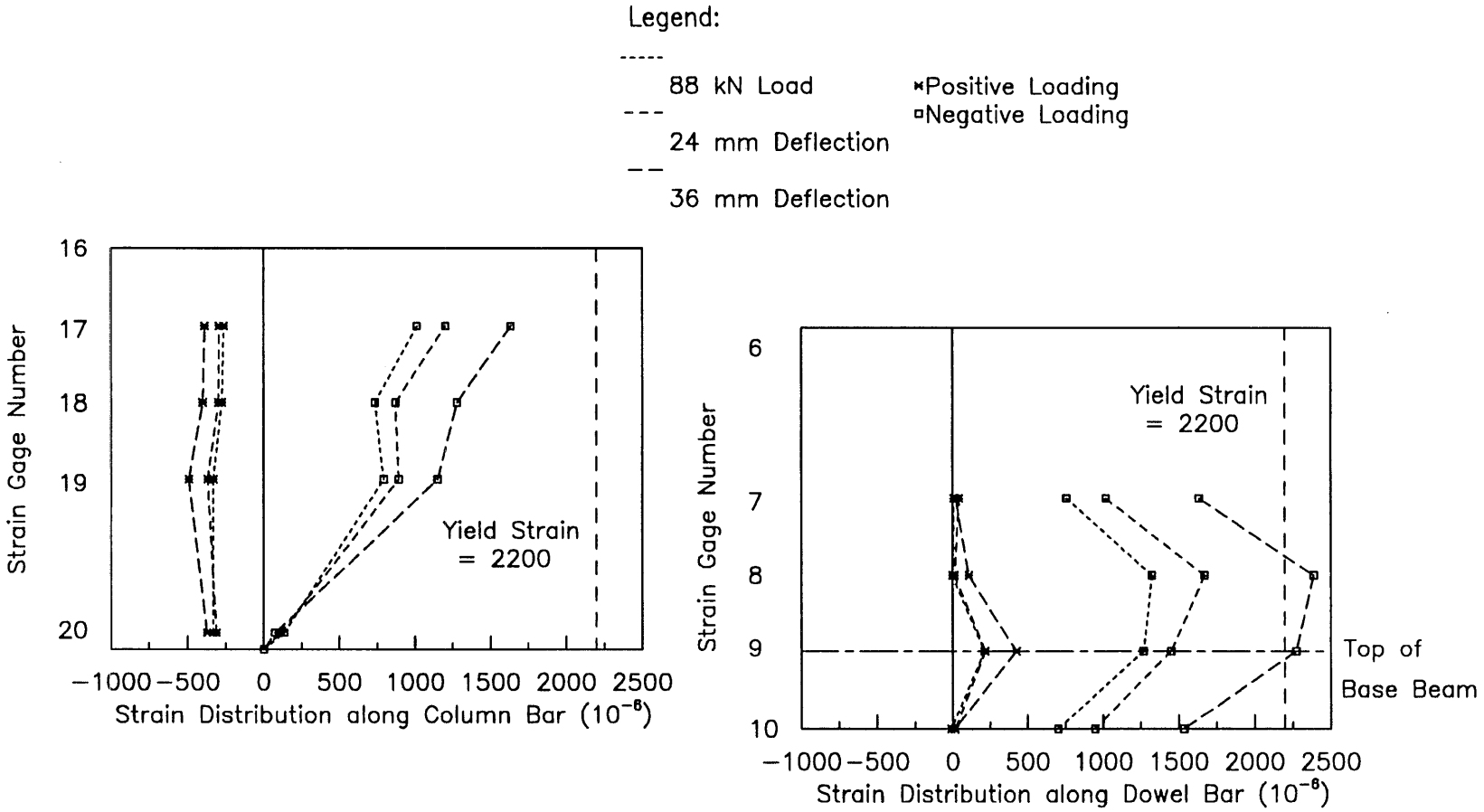

Fig. 5.25 Strain Distributions at Different Peak Loads or Deflections along Bars in Column B–3 (cont.)

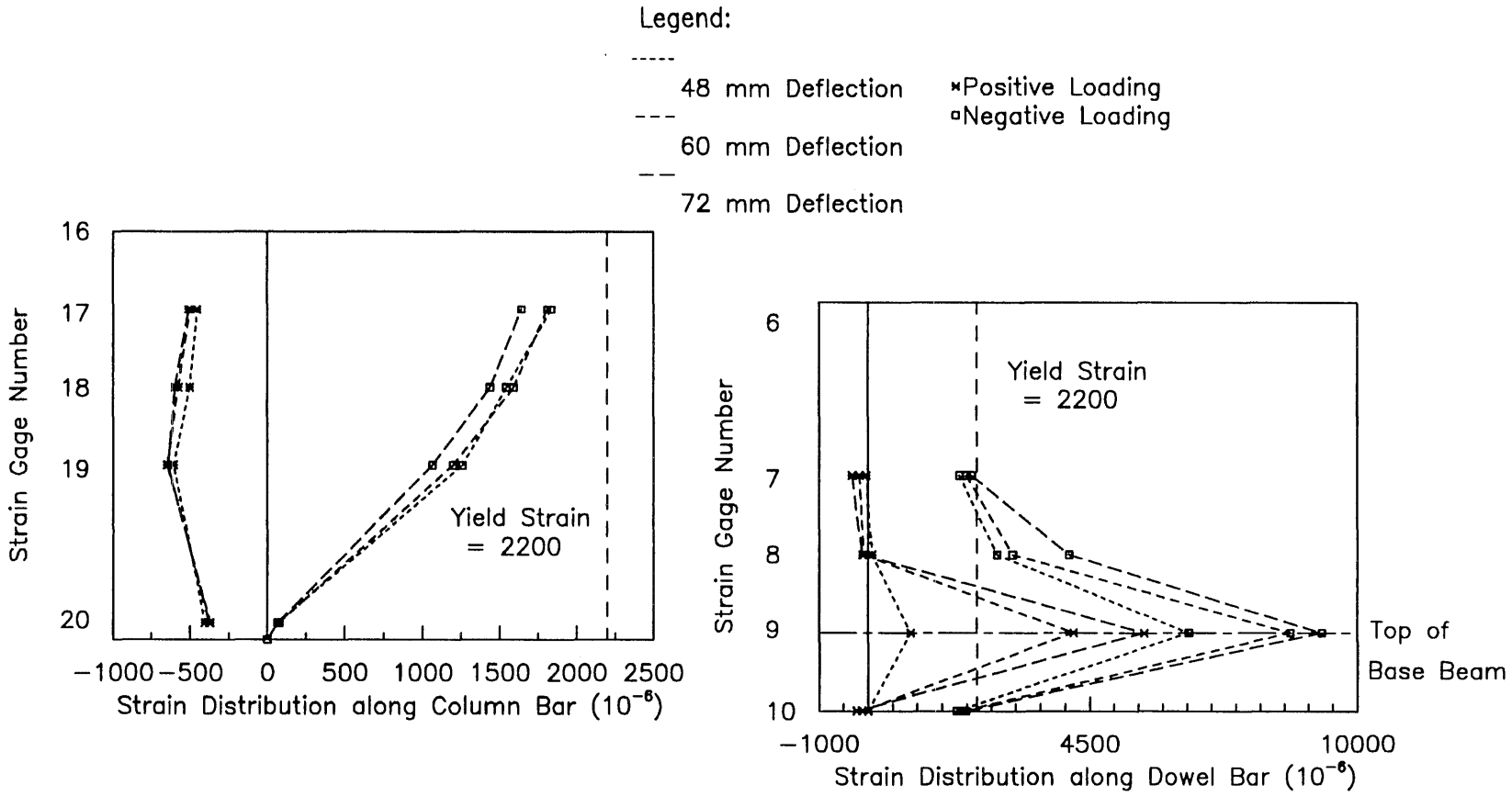

Fig. 5.25 Strain Distributions at Different Peak Loads or Deflections along Bars in Column B–3 (cont.)

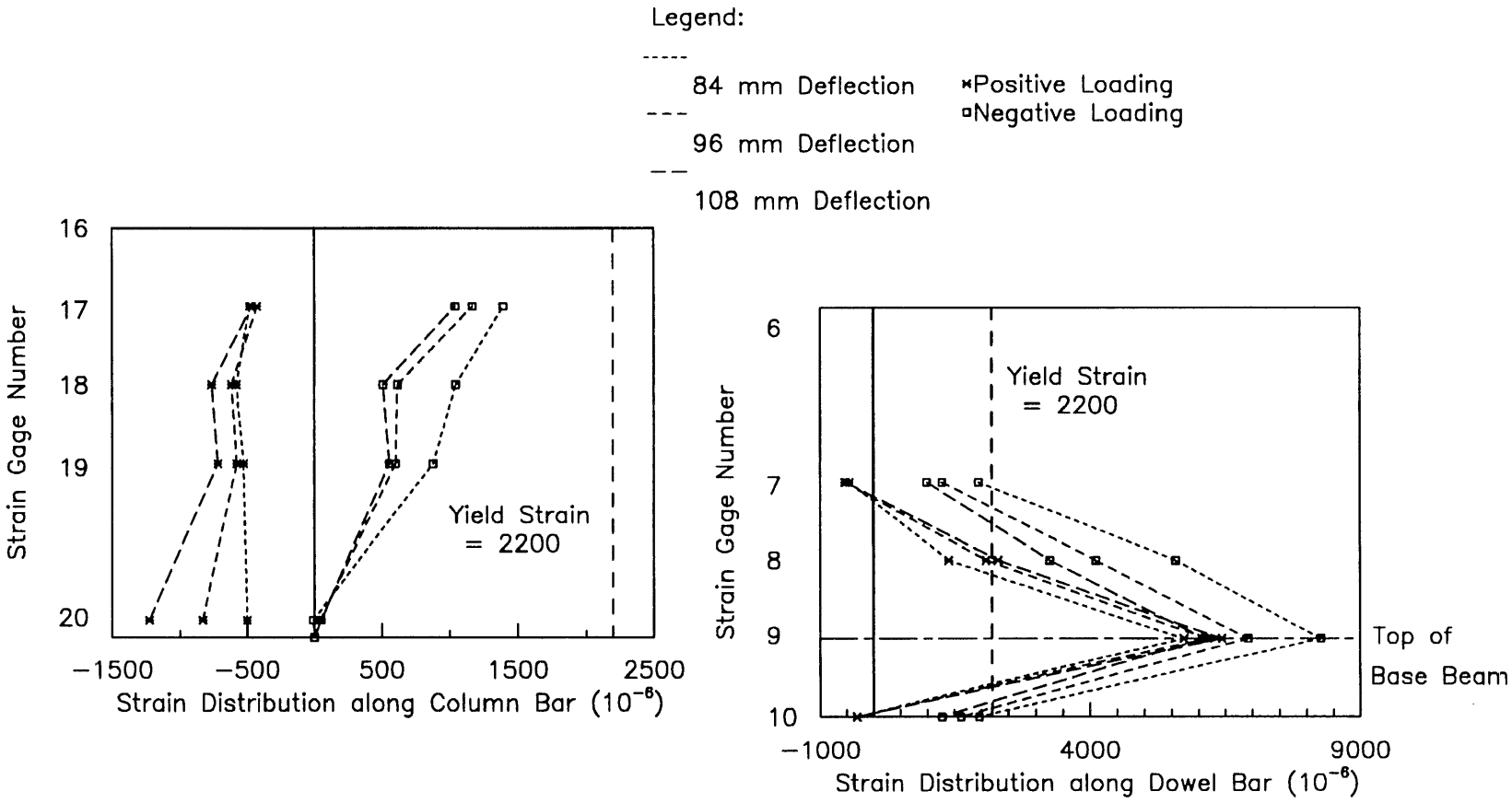

Fig. 5.25 Strain Distributions at Different Peak Loads or Deflections along Bars in Column B–3 (cont.)

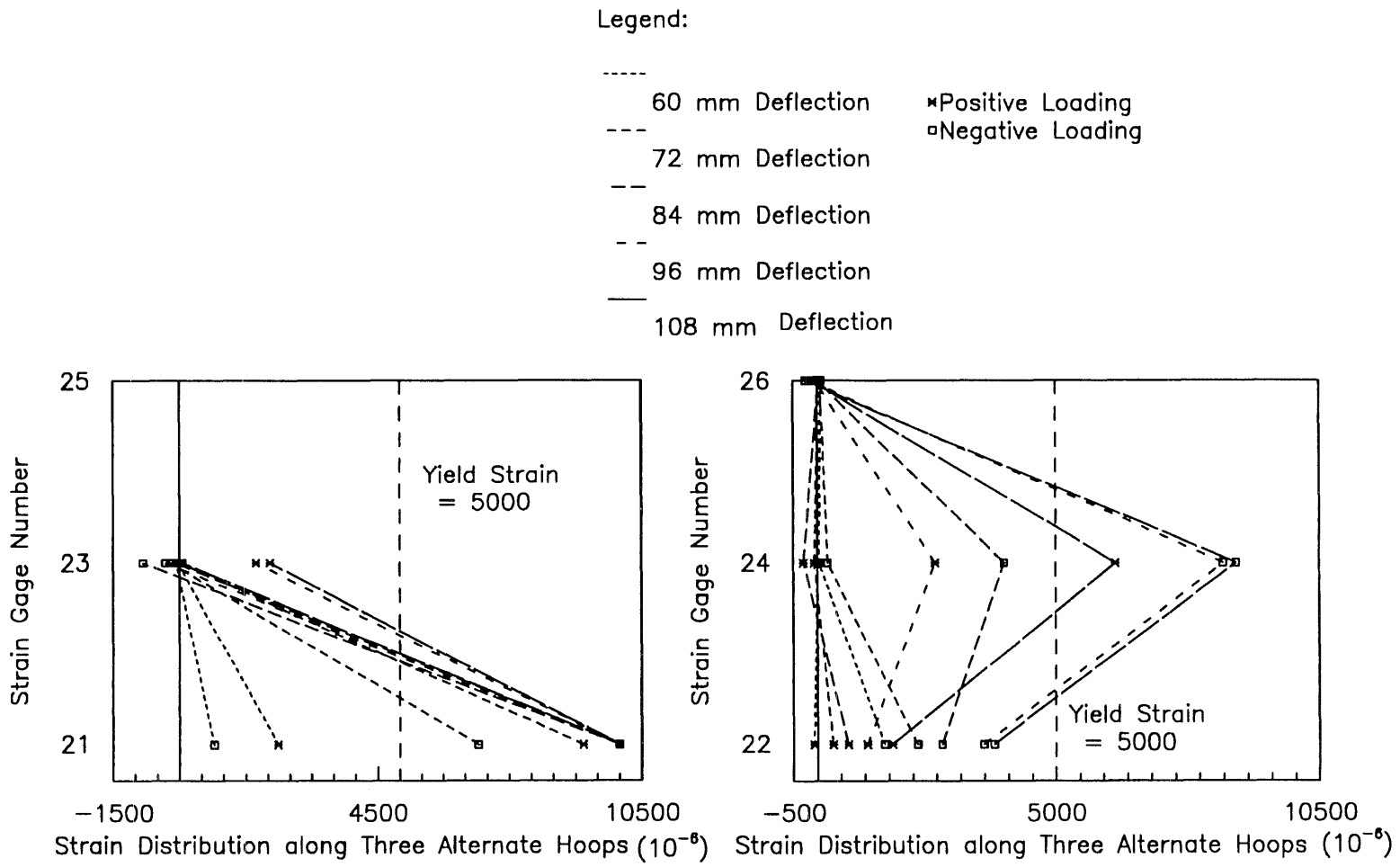

Fig. 5.25 Strain Distributions at Different Peak Loads or Deflections along Bars in Column B–3 (cont.)

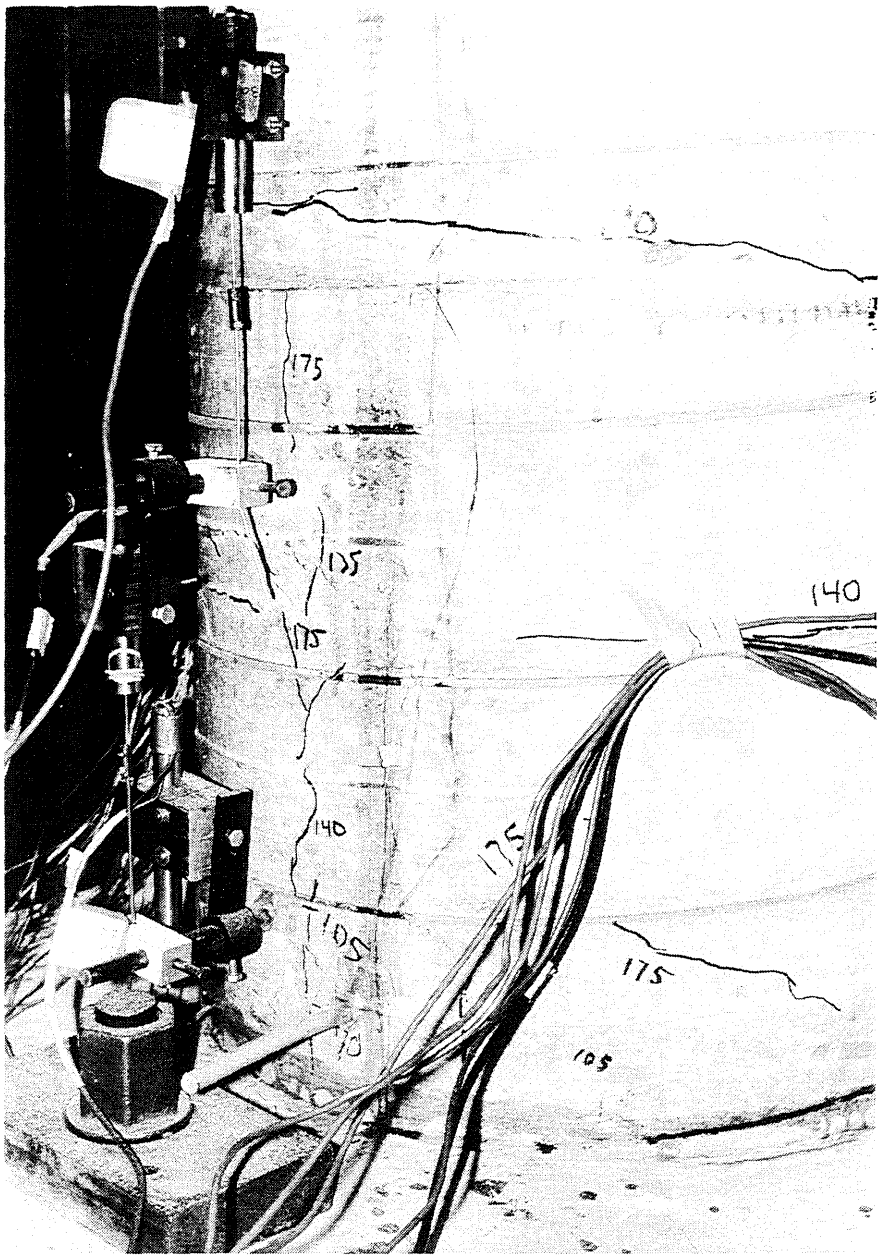

Fig. 5.26a Cracks on Tension Face for Positive Loading for Column A–1

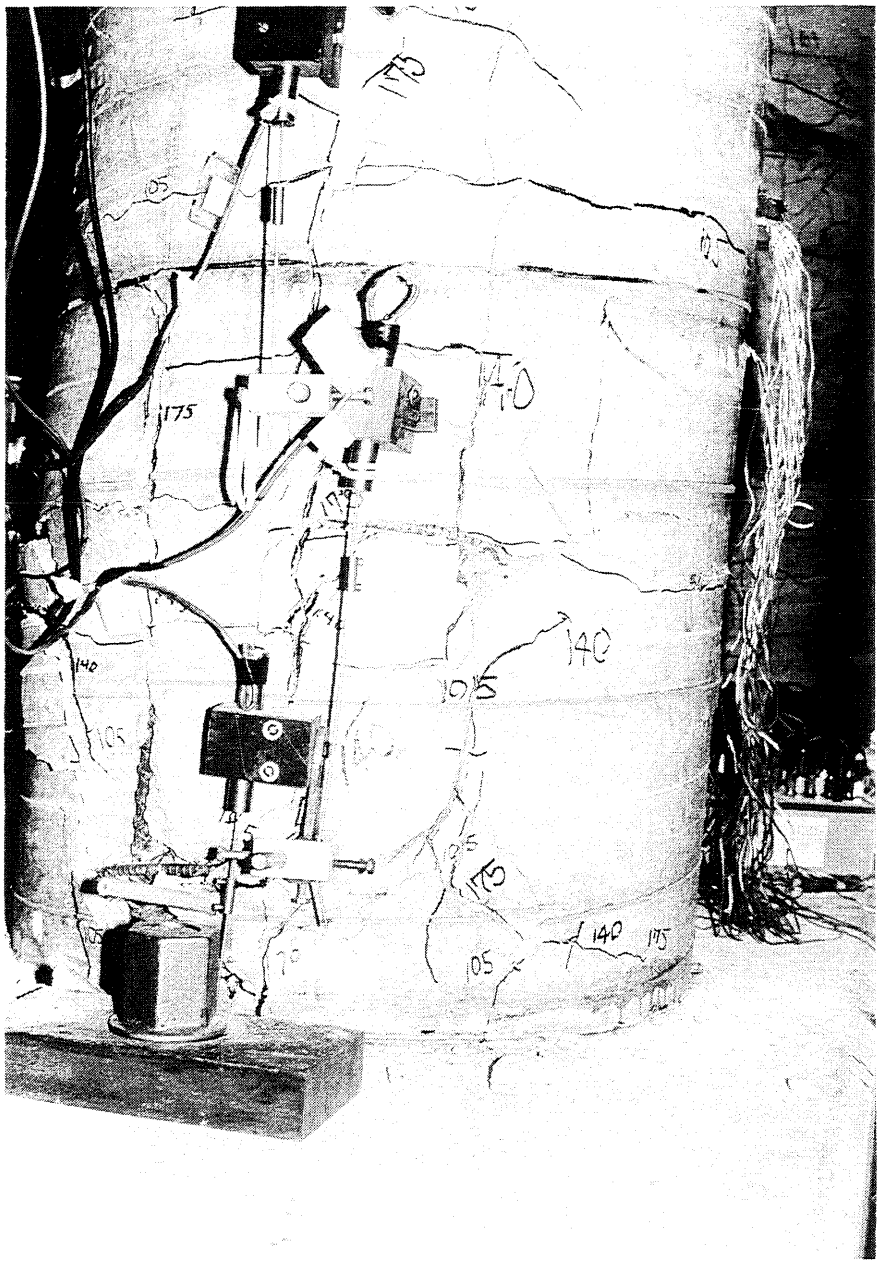

Fig. 5.26b Cracks on Tension Face for Negative Loading for Column A–1

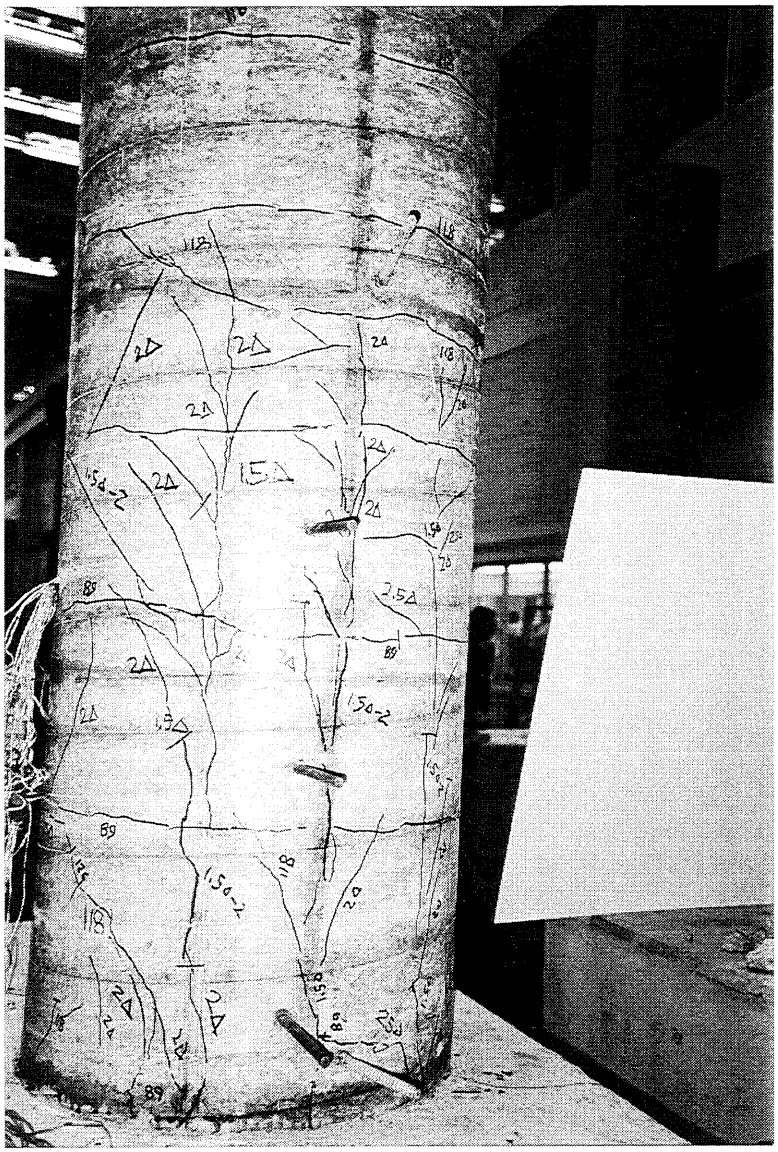

Fig. 5.27a Cracks on Tension Face for Positive Loading for Column A–2

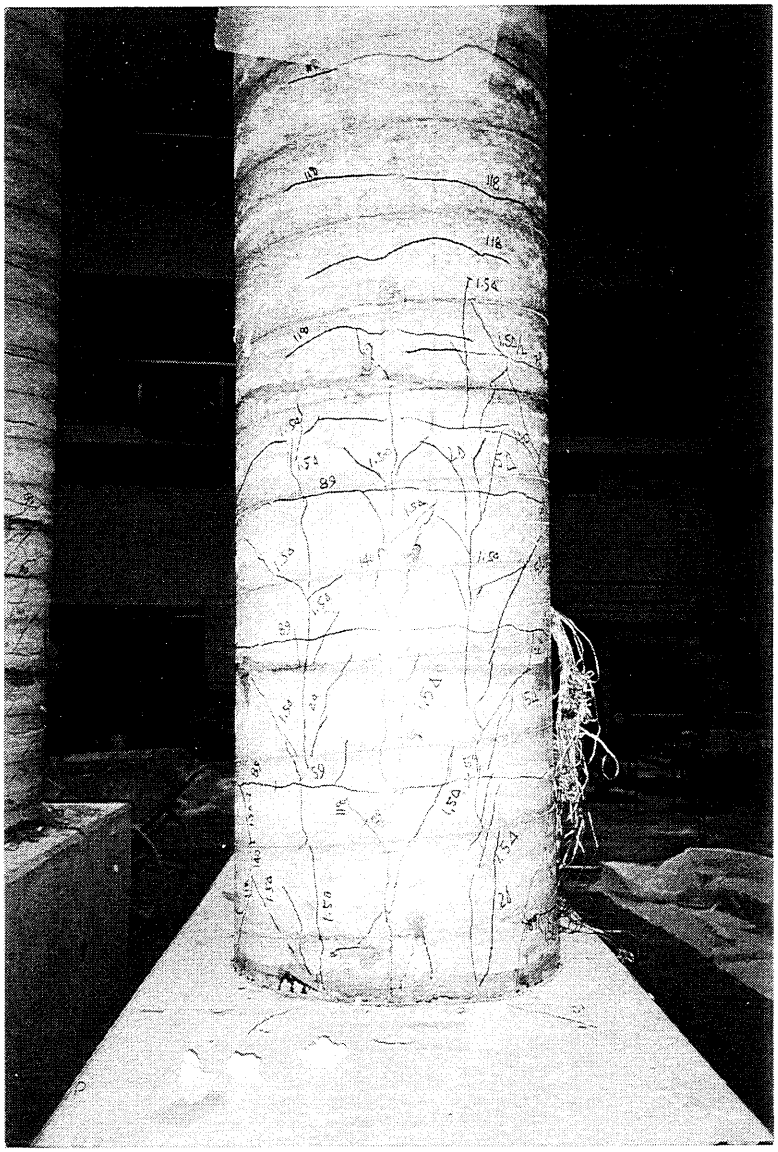

Fig. 5.27b Cracks on Tension Face for Negative Loading for Column A–2

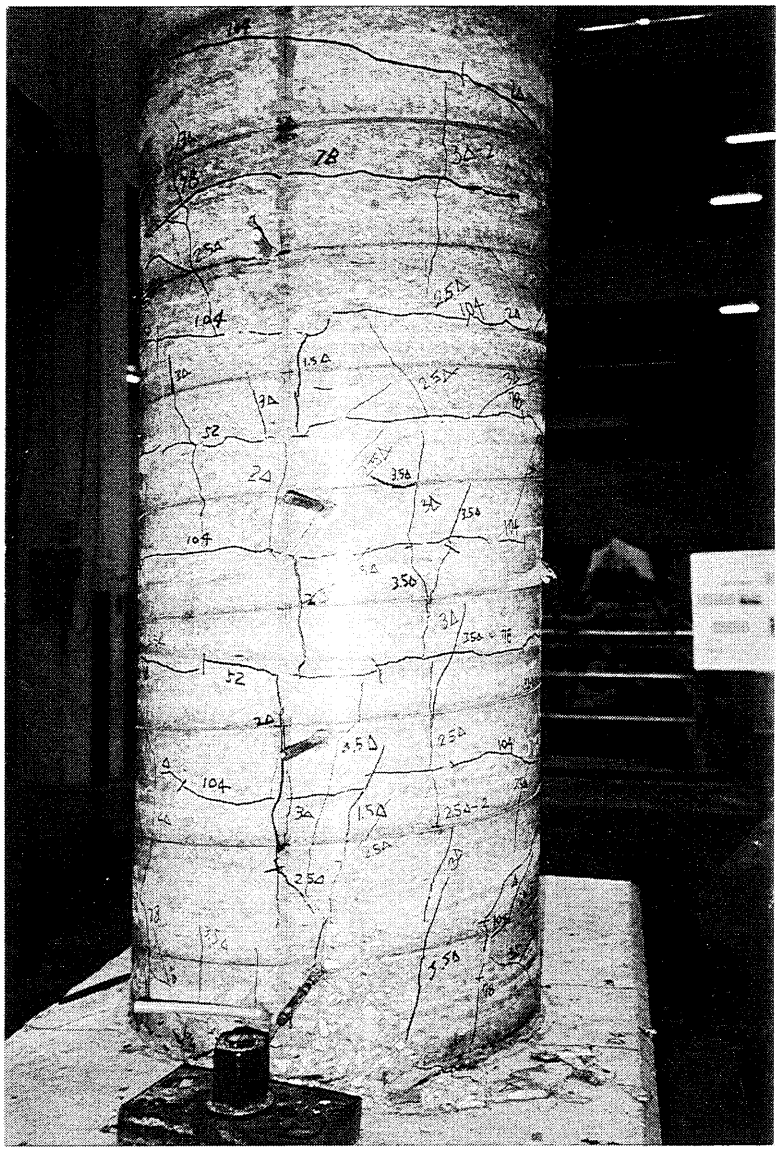

Fig. 5.28a Cracks on Tension Face for Positive Loading for Column A–3

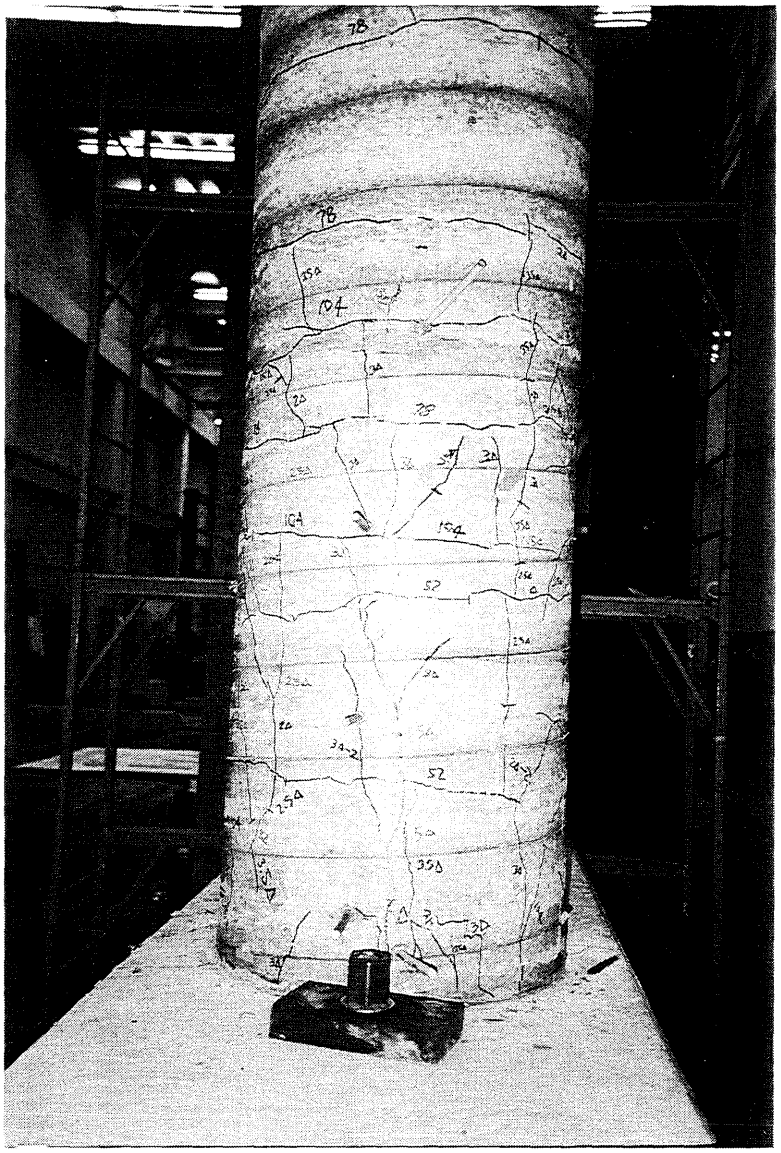

Fig. 5.28b Cracks on Tension Face for Negative Loading for Column A–3

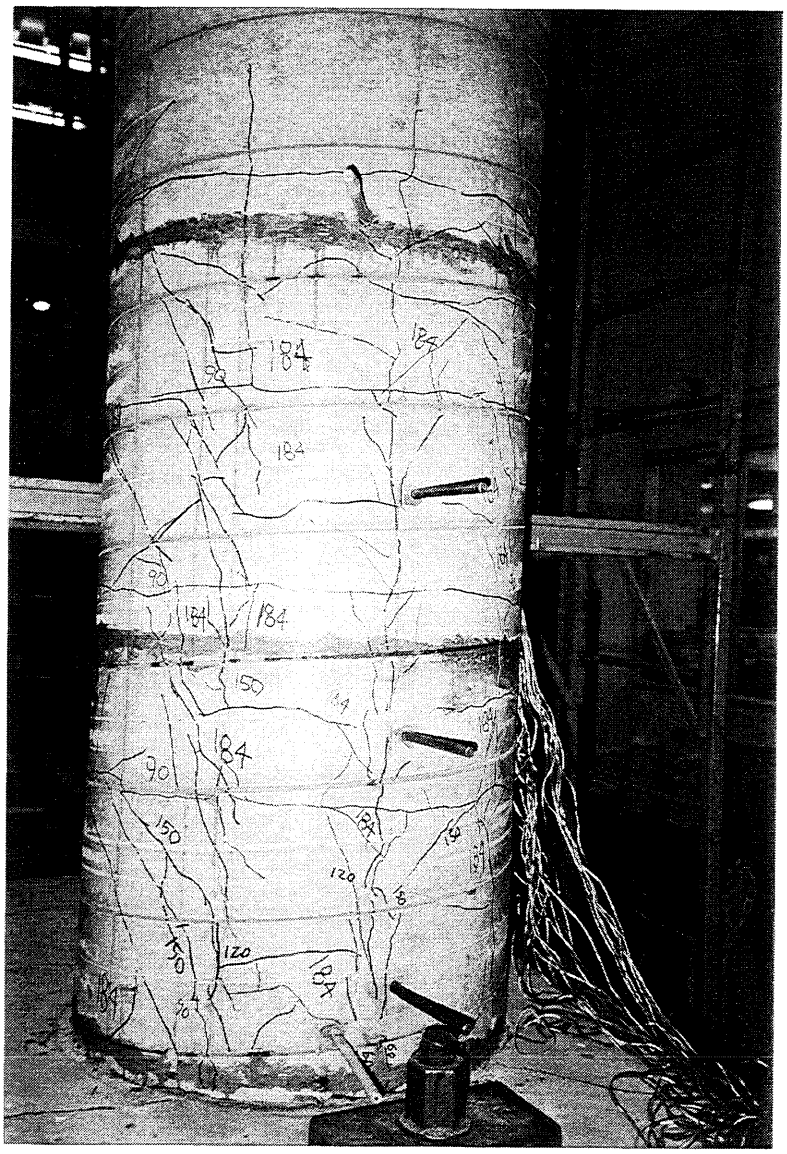

Fig. 5.29 Cracks on Tension Face for Positive Loading for Column B–1

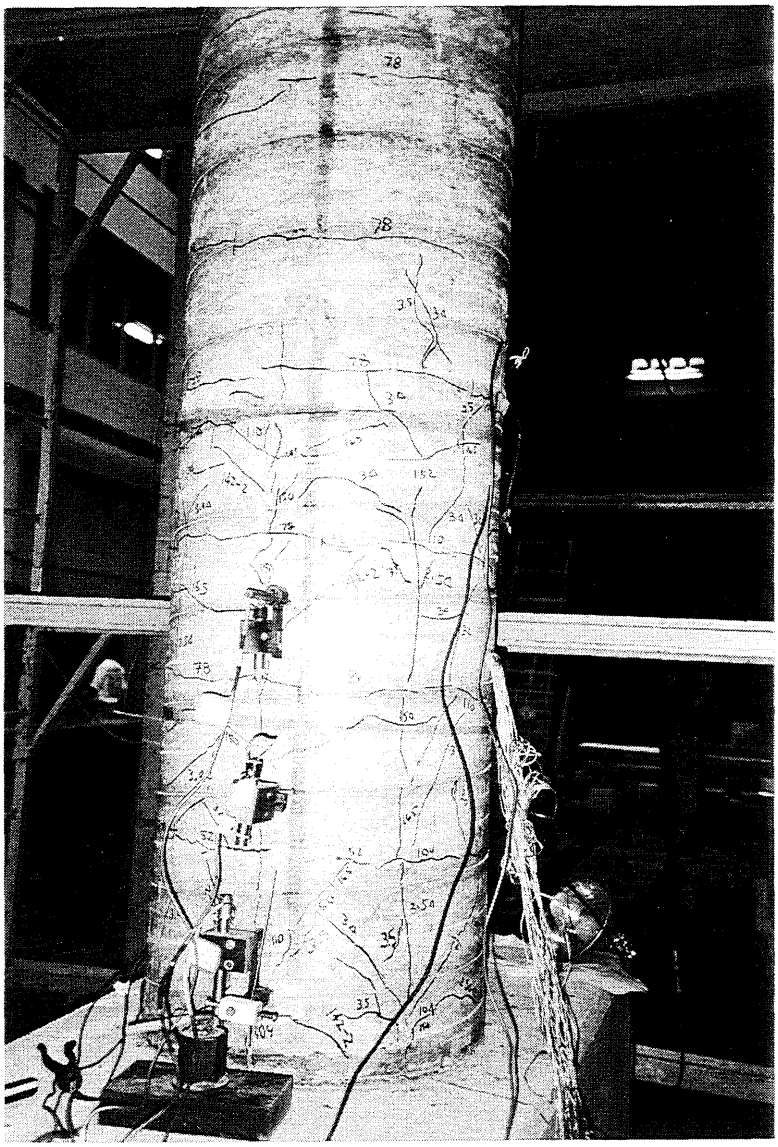

Fig. 5.30 Cracks on Tension Face for Positive Loading for Column B–2

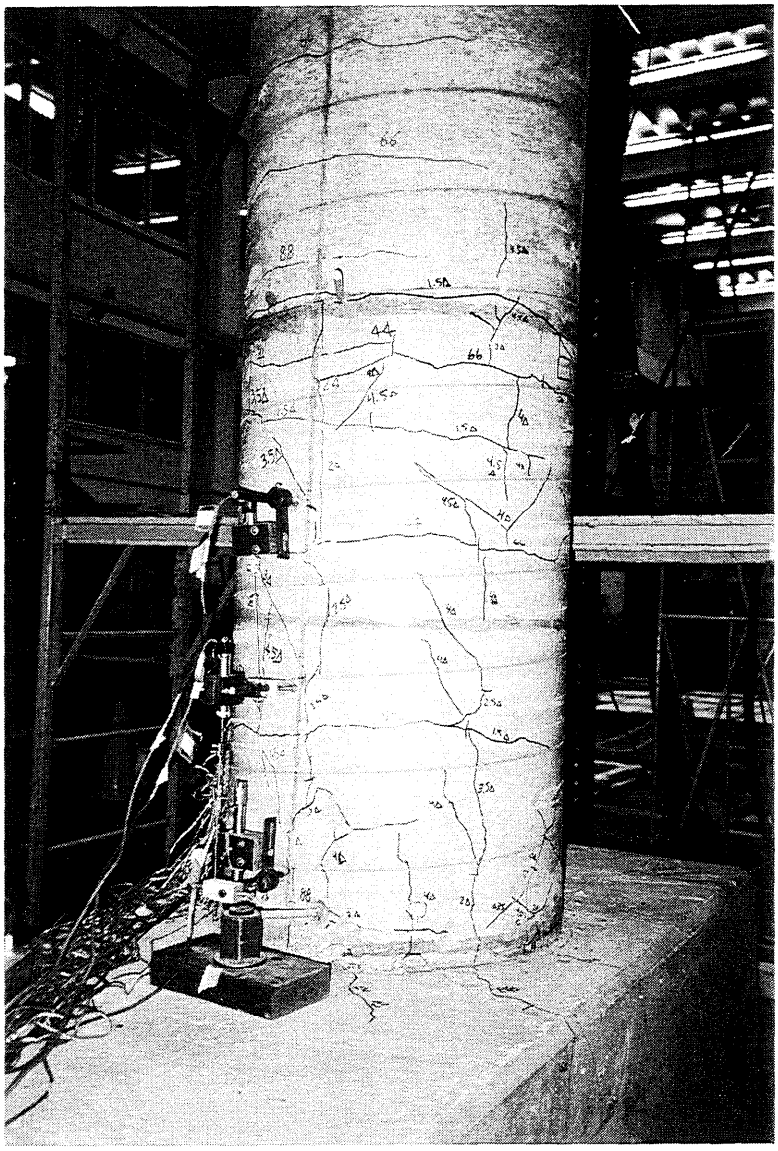

Fig. 5.31 Cracks on Tension Face for Positive Loading for Column B–3

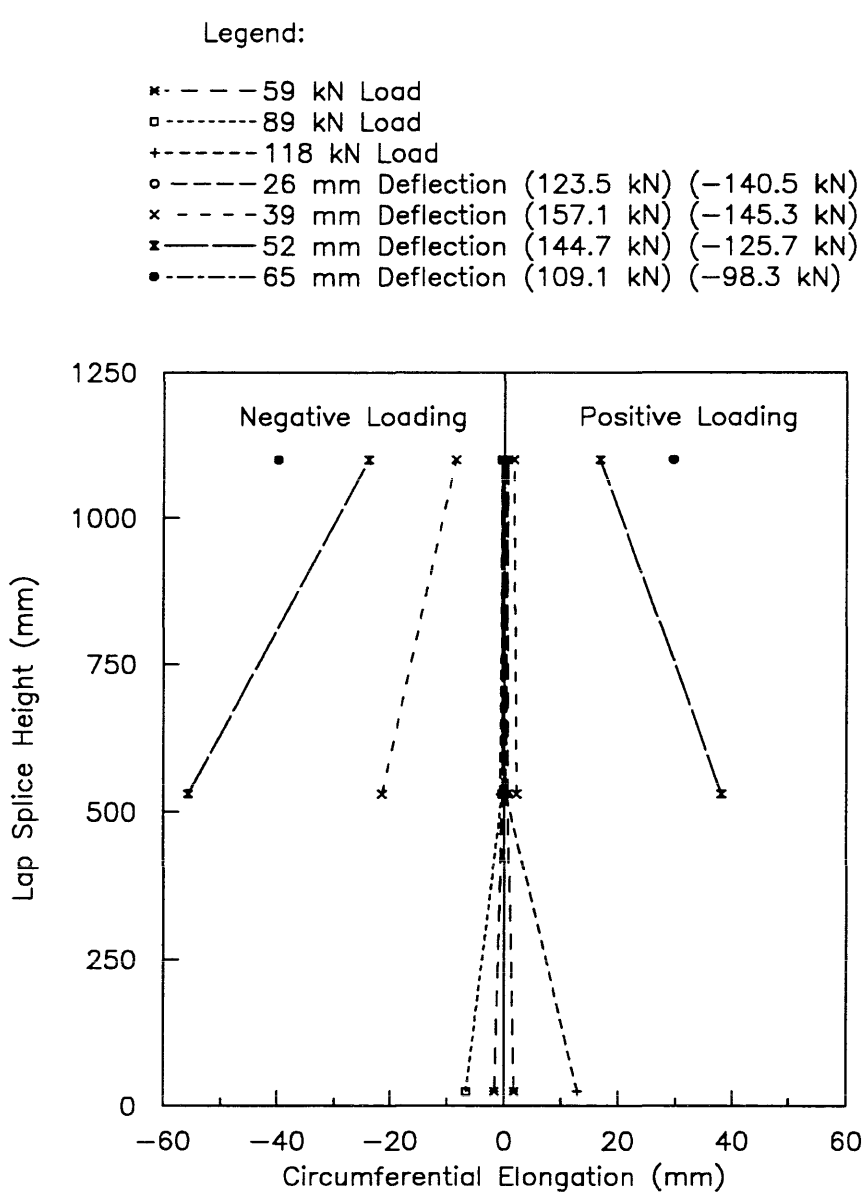

Fig. 5.32 Circumferential Elongations over the Lap Splice Height of Column A–2

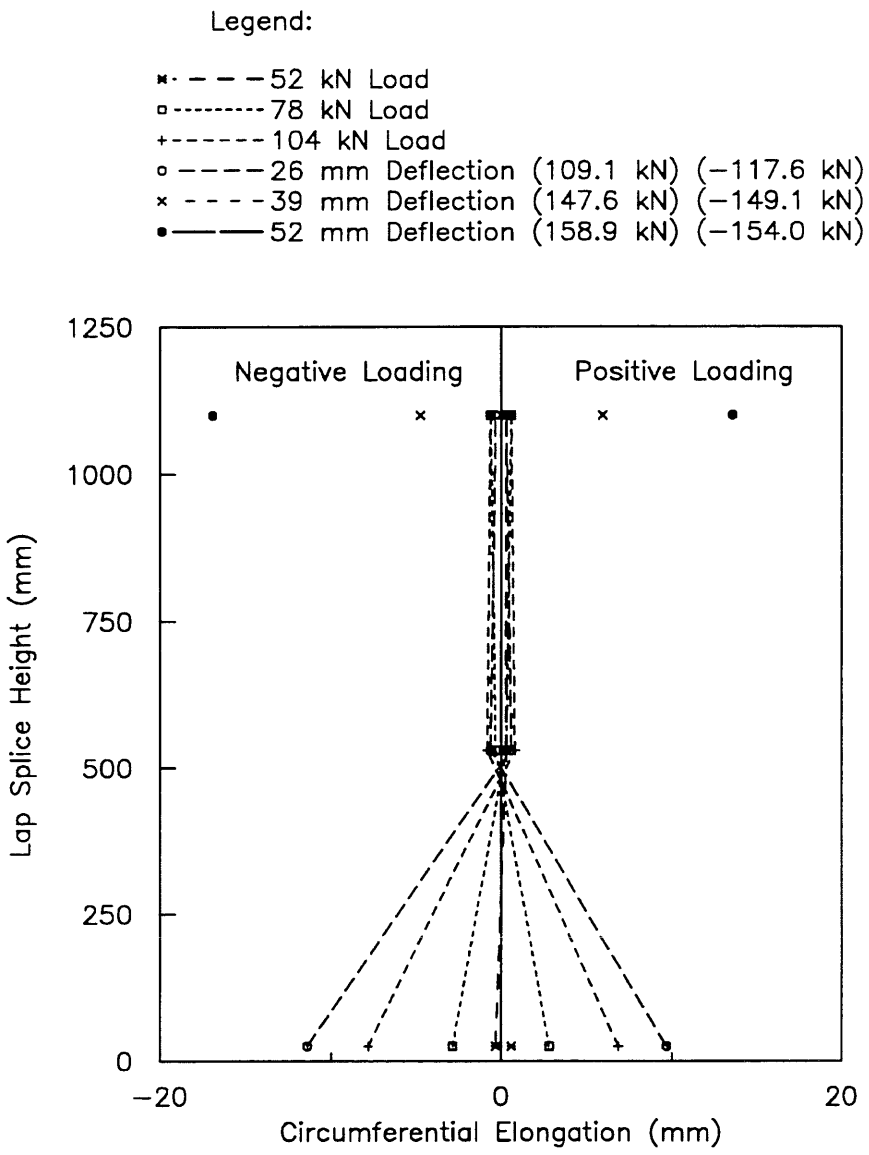

Fig. 5.33 Circumferential Elongations over the Lap Splice Height of Column A–3

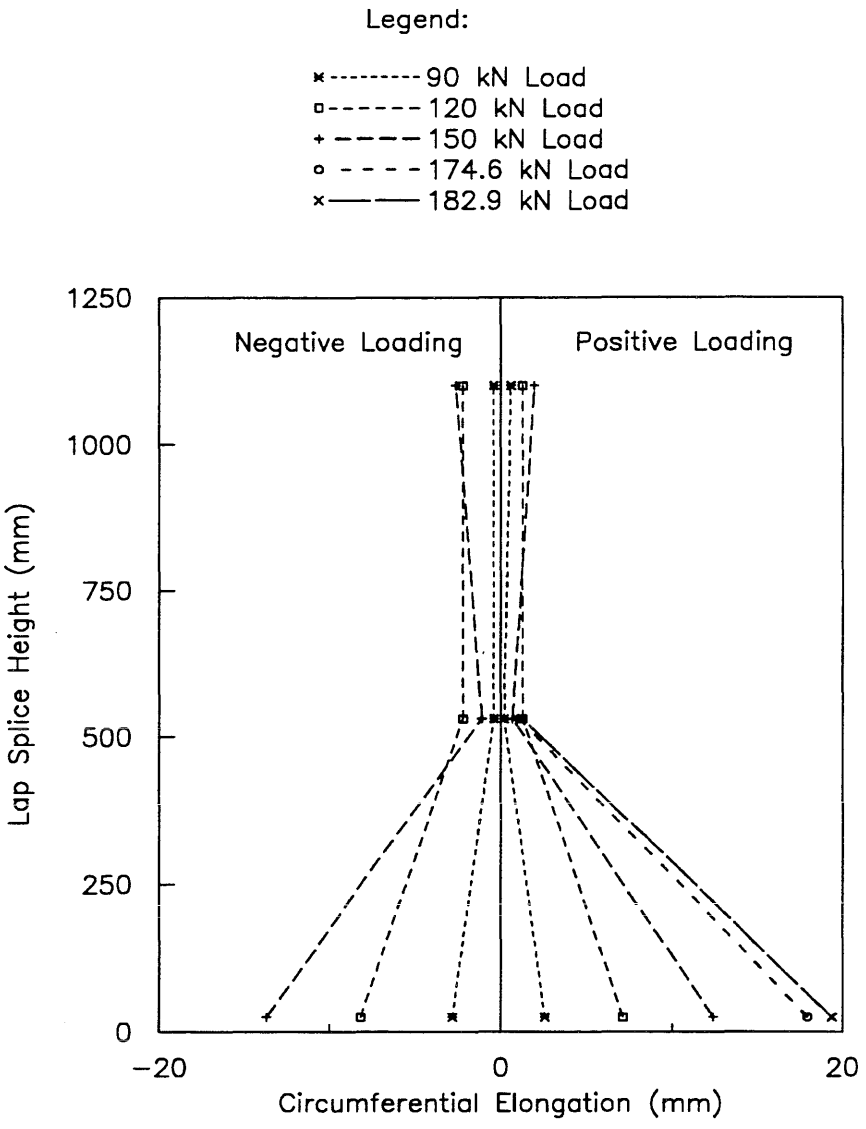

Fig. 5.34 Circumferential Elongations over the Lap Splice Height of Column B–1

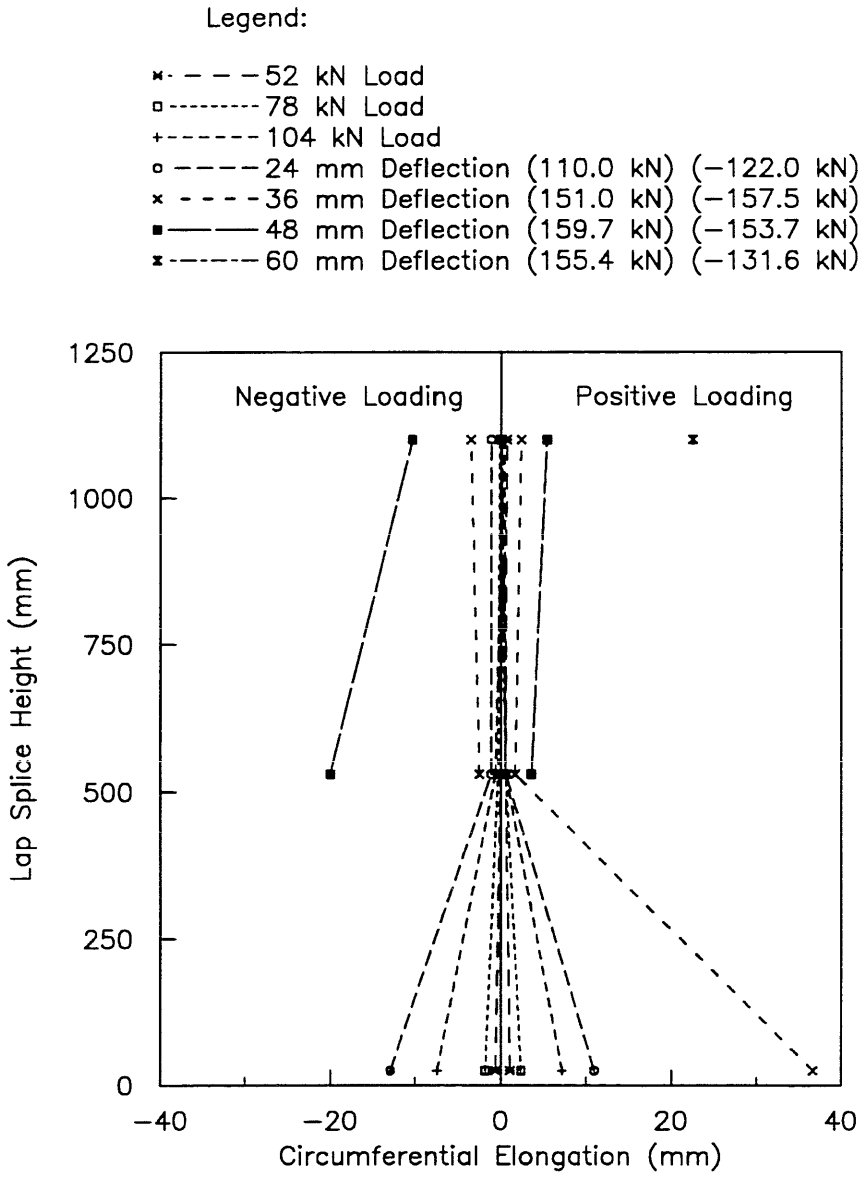

Fig. 5.35 Circumferential Elongations over the Lap Splice Height of Column B–2

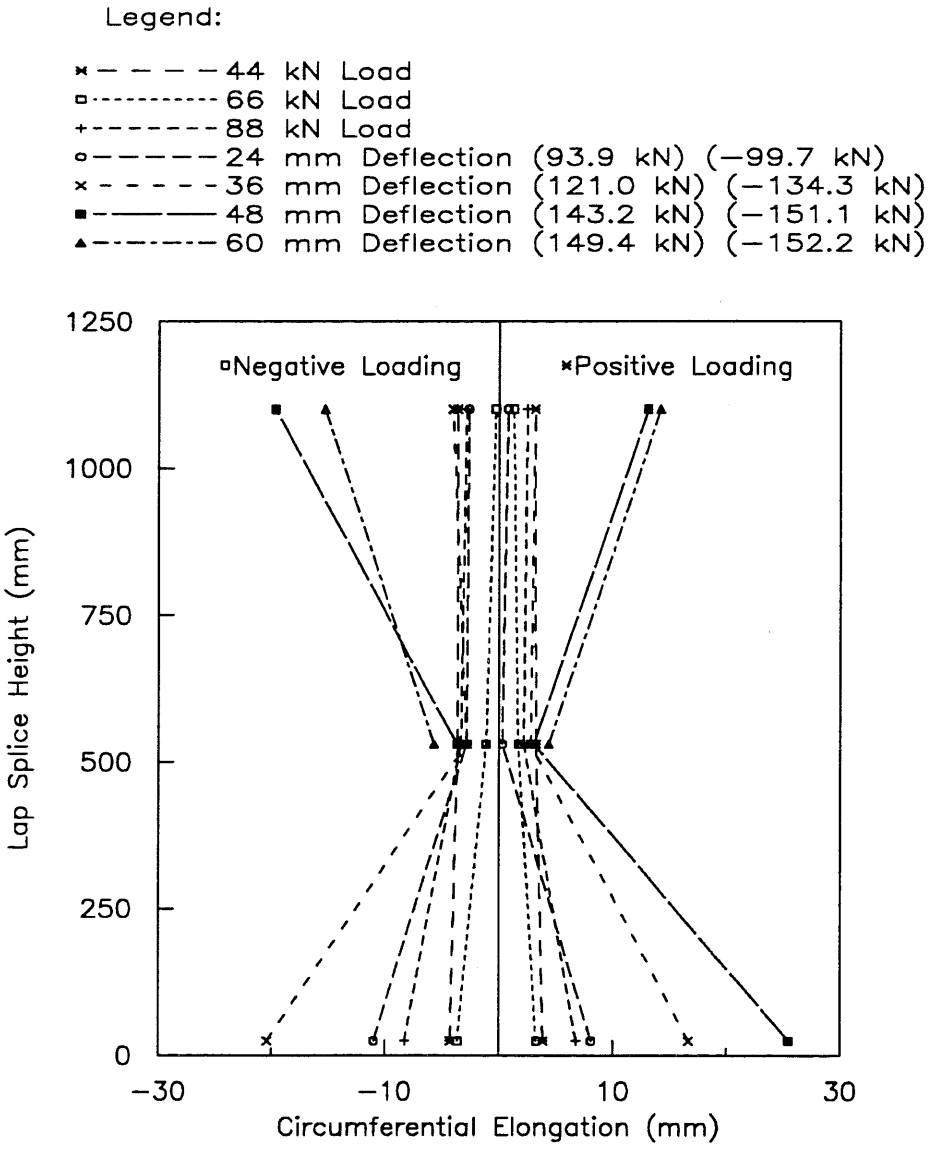

Fig. 5.36 Circumferential Elongations over the Lap Splice Height of Column B–3

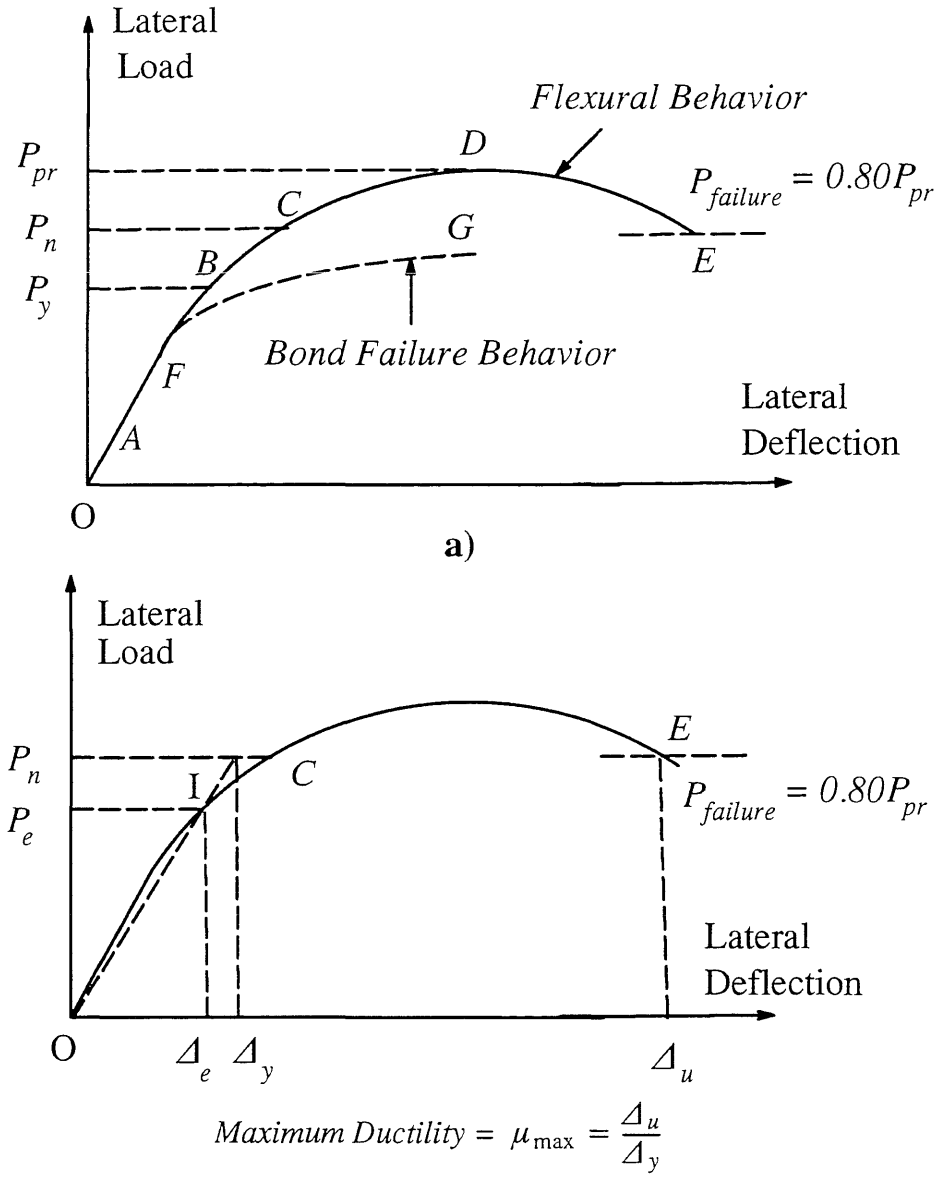

Fig. 6.1 Idealized Load–Deflection Response

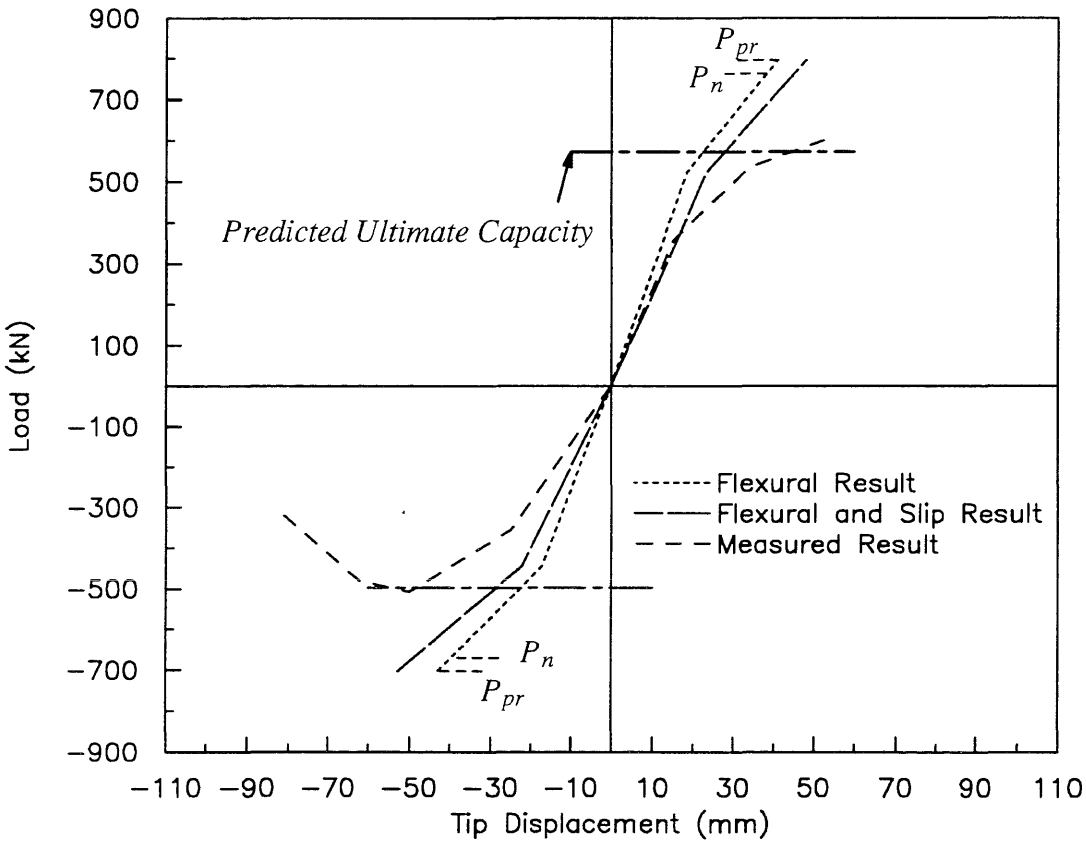

Fig. 6.2 Load–Deflection Relationship for Column B18S

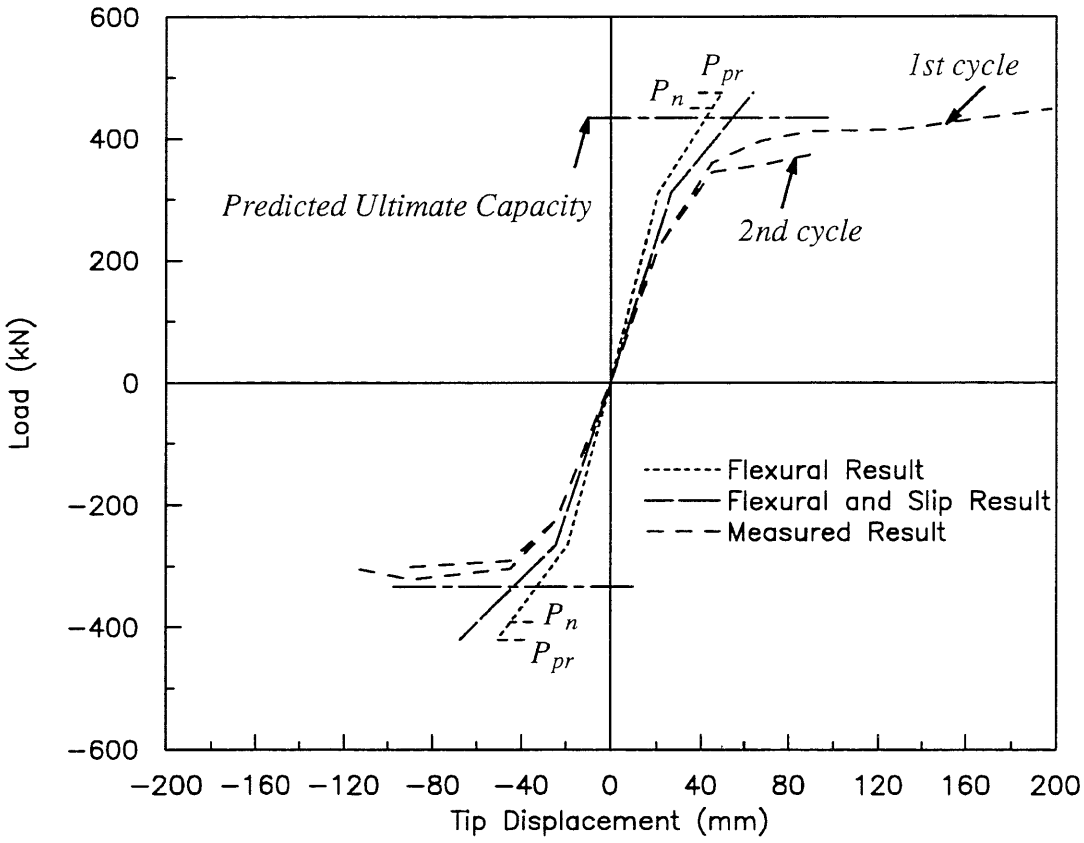

Fig. 6.3 Load–Deflection Relationship for Column B14S

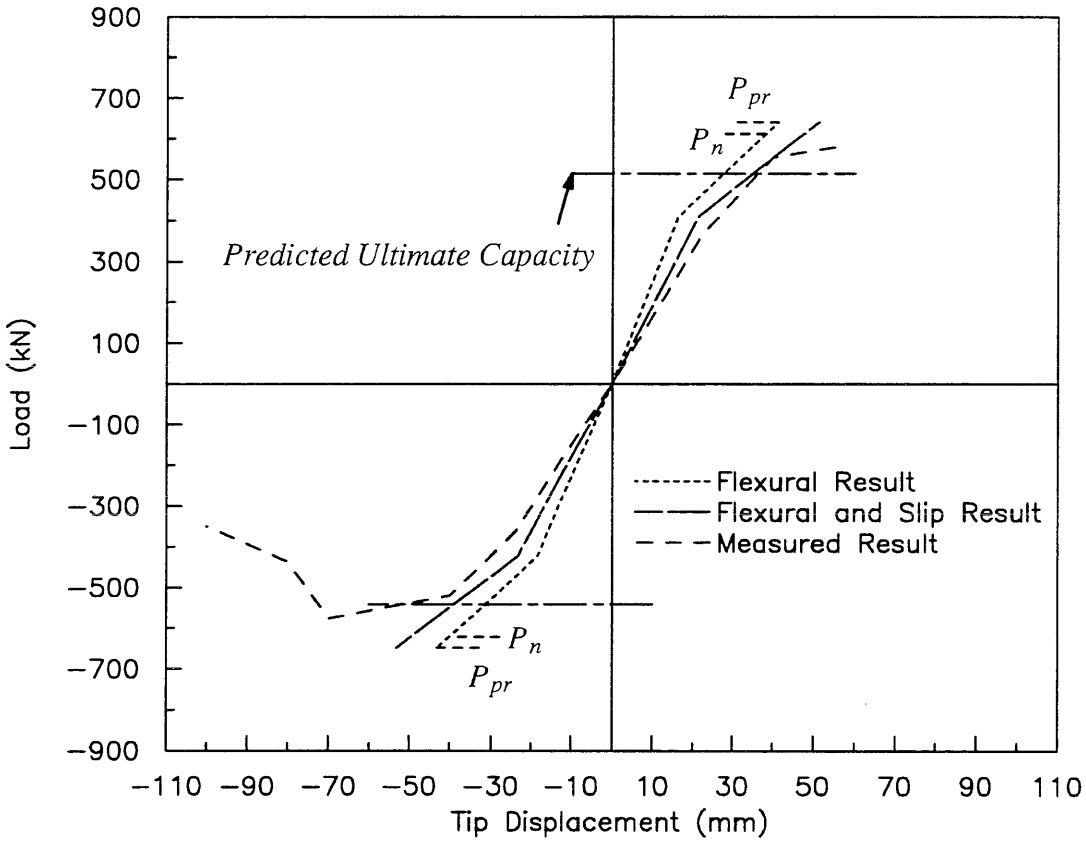

Fig. 6.4 Load–Deflection Relationship for Column C17S

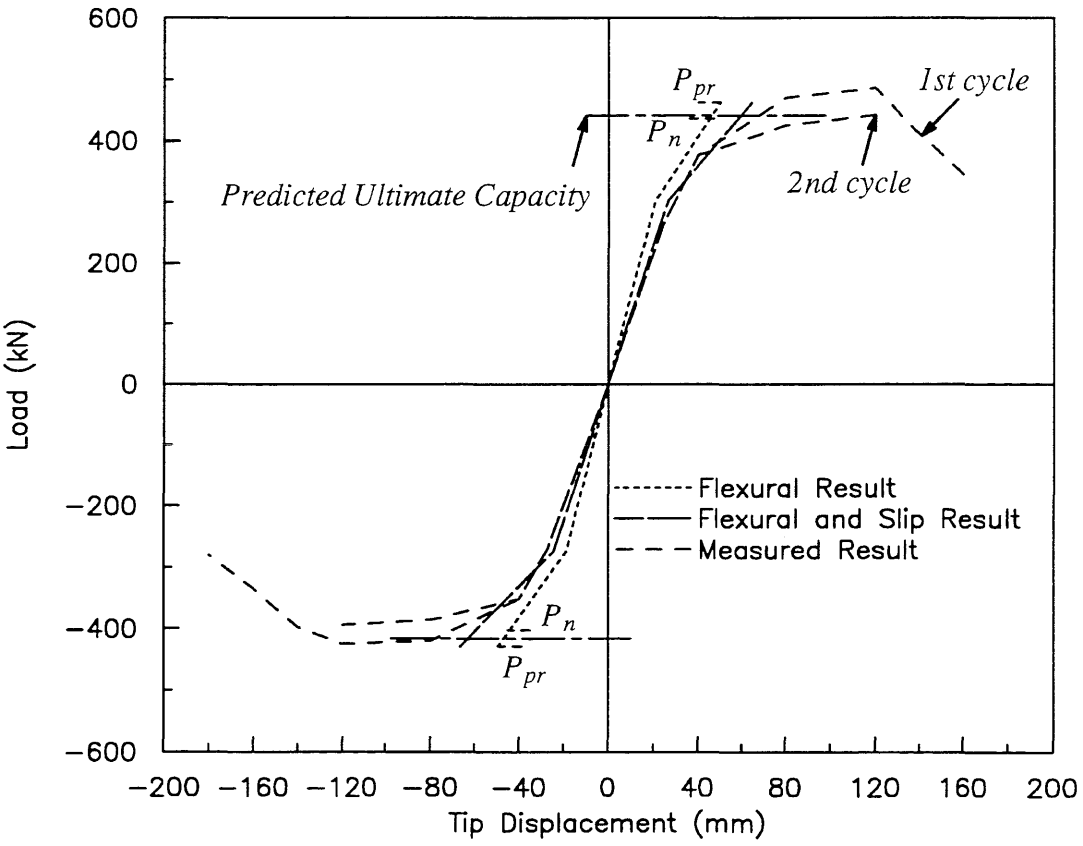

Fig. 6.5 Load–Deflection Relationship for Column C15S

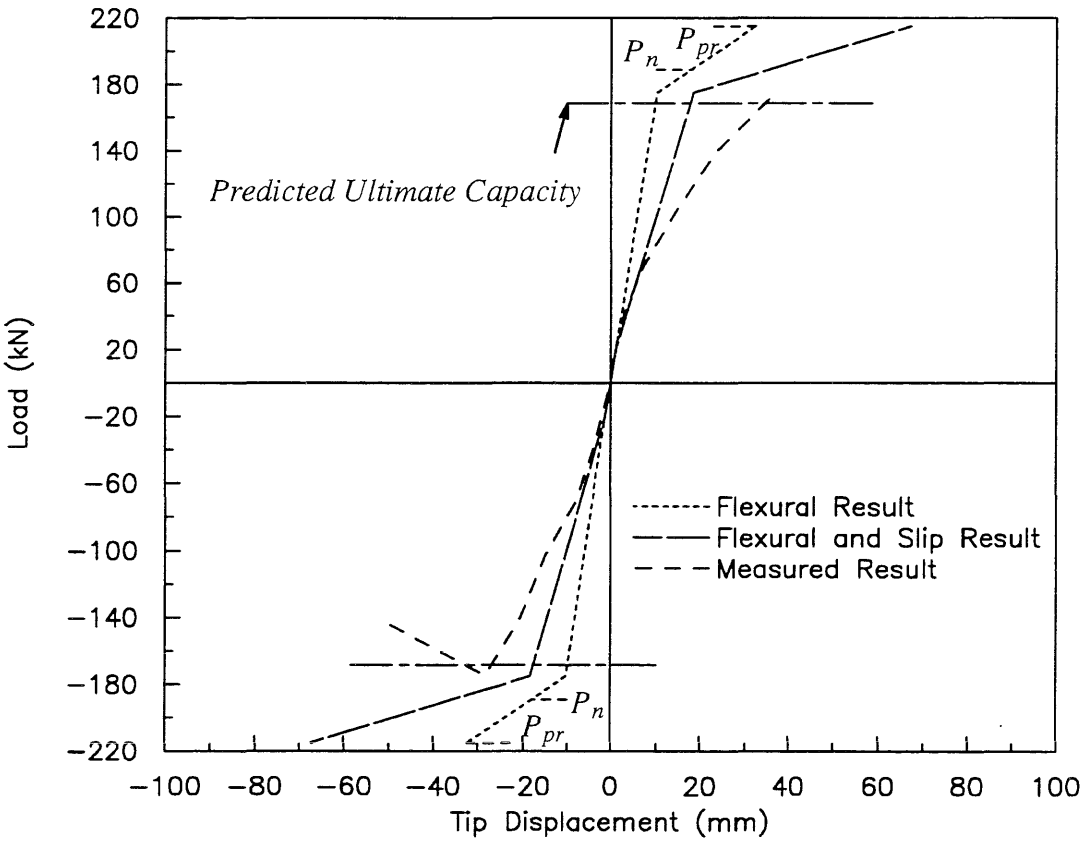

Fig. 6.6 Load–Deflection Relationship for Column A–1

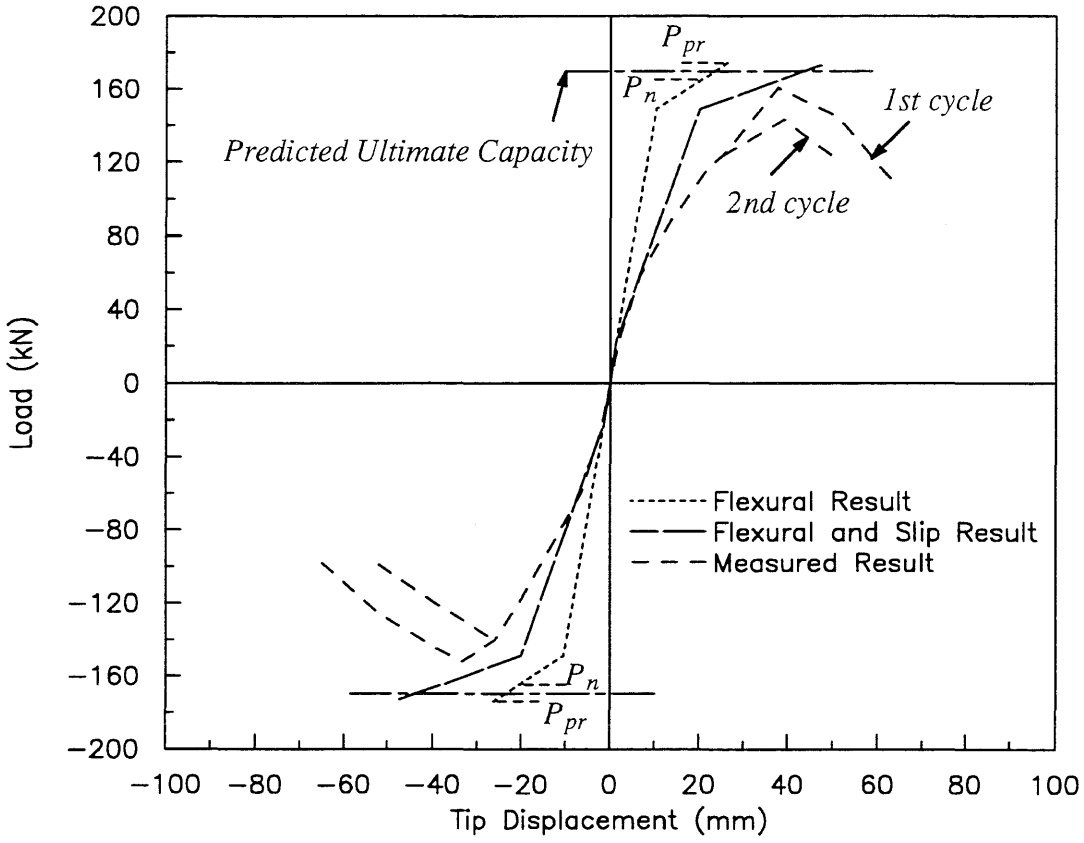

Fig. 6.7 Load–Deflection Relationship for Column A–2

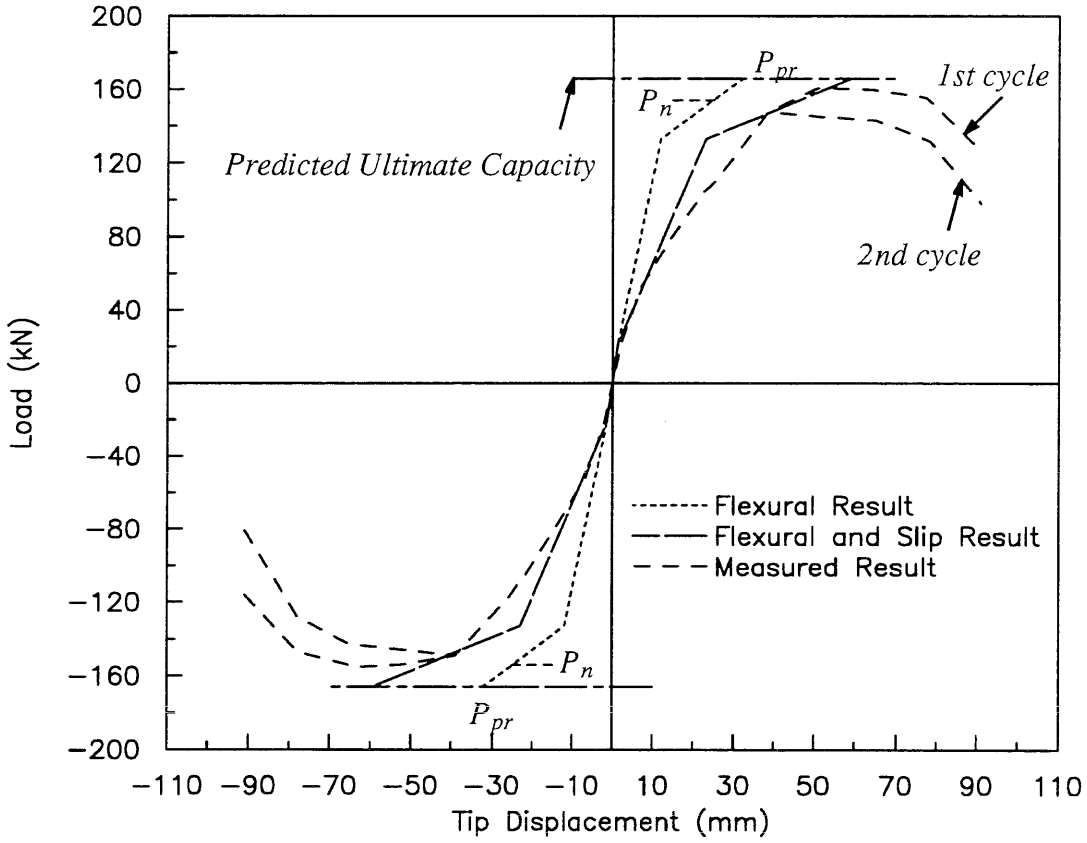

Fig. 6.8 Load–Deflection Relationship for Column A–3

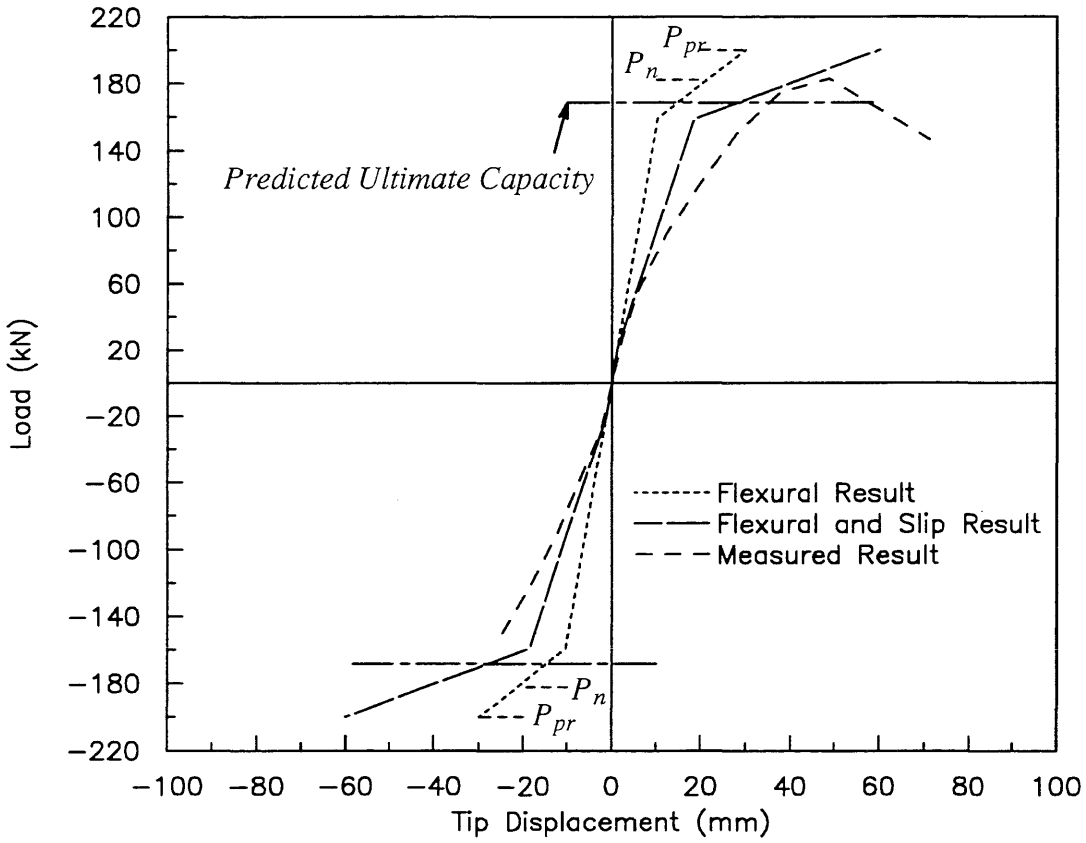

Fig. 6.9 Load–Deflection Relationship for Column B–1

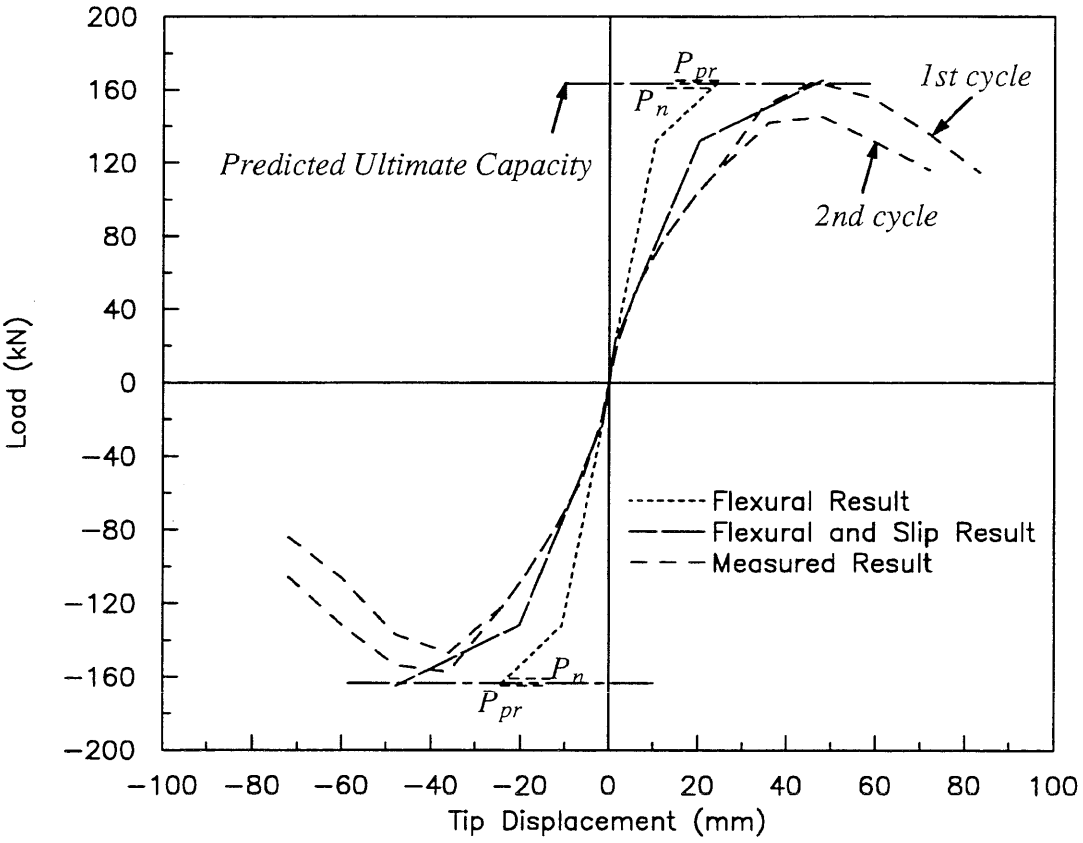

Fig. 6.10 Load–Deflection Relationship for Column B–2

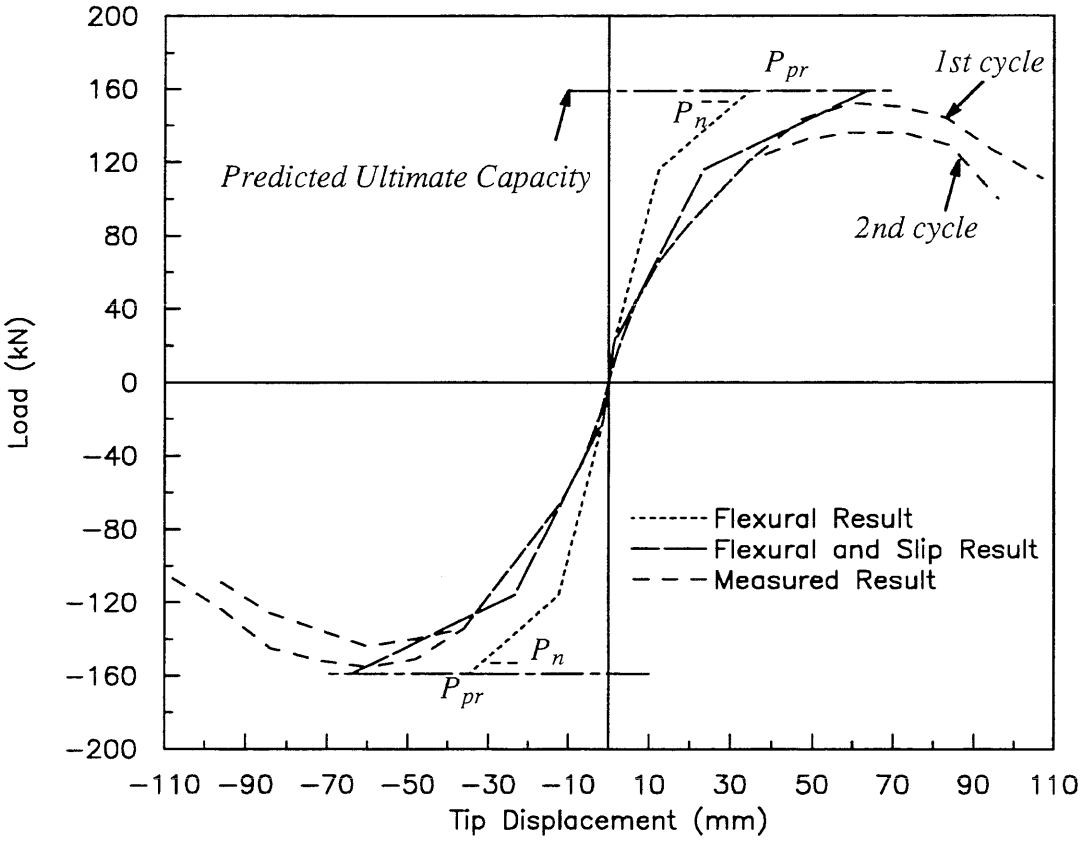

Fig. 6.11 Load–Deflection Relationship for Column B–3

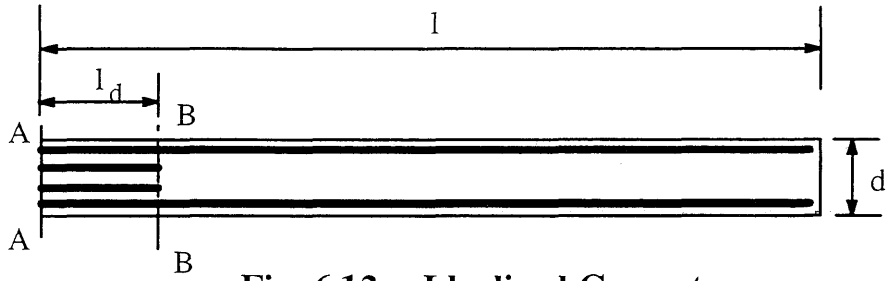

Fig. 6.12a Idealized Geometry

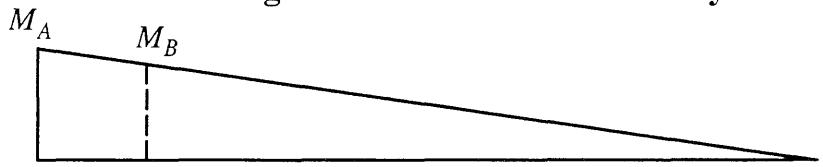

Fig. 6.12b Moment

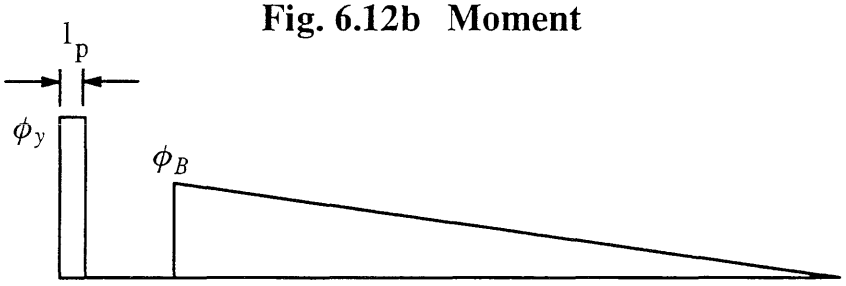

Fig. 6.12c Assumed Yield Curvatures

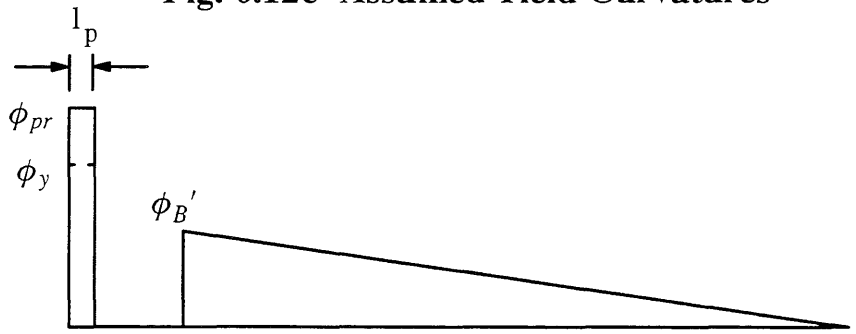

Fig. 6.12d Assumed Curvatures at Max. Response

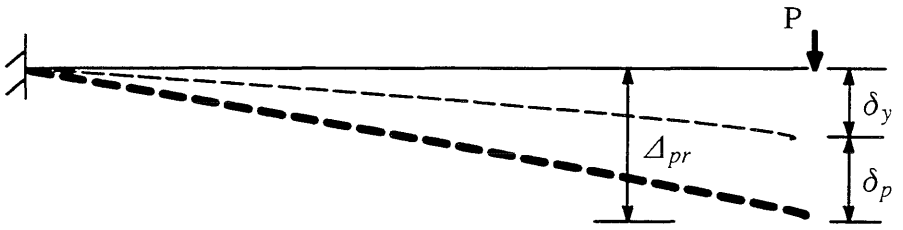

Fig. 6.12e Flexural Deflections

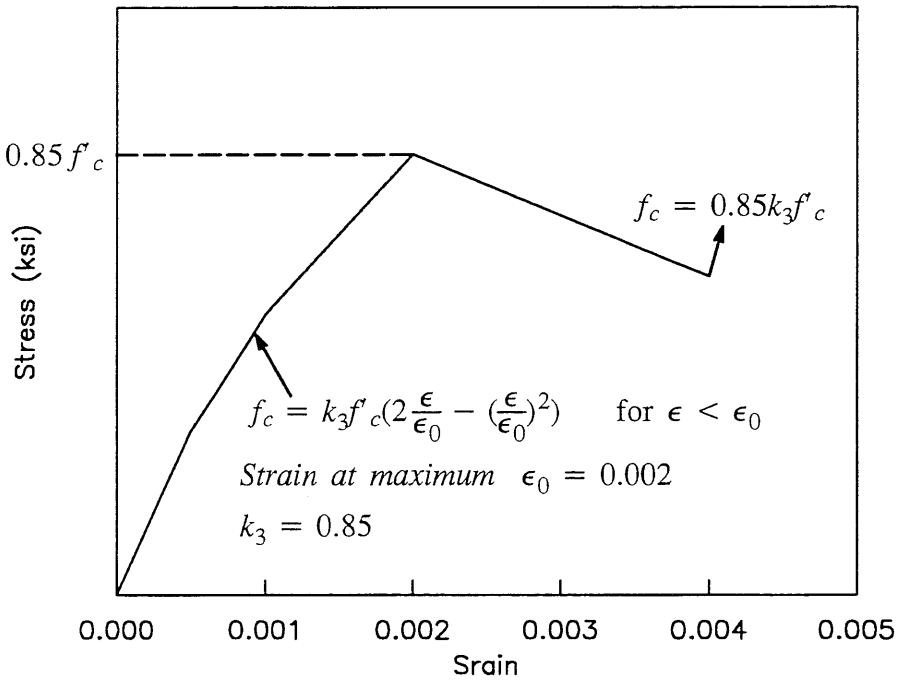

Fig. 6.13 Stress–Strain Curve of Concrete Suggested by Hognestad

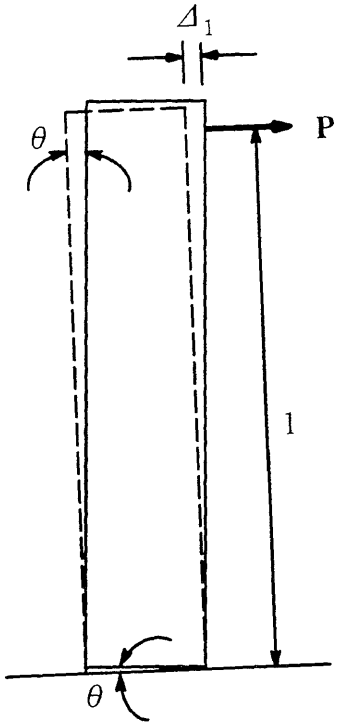

Deformed and Undeformed Column

Fig. 6.14

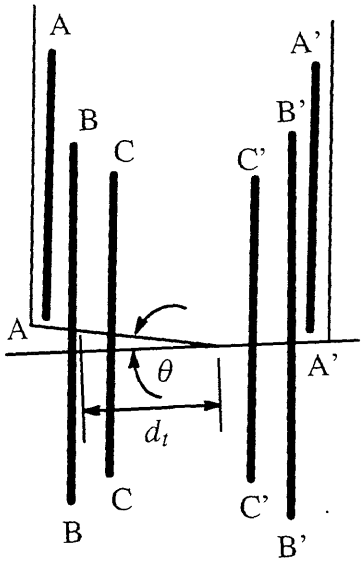

Dowel Bars cross Interface

Fig. 6.15

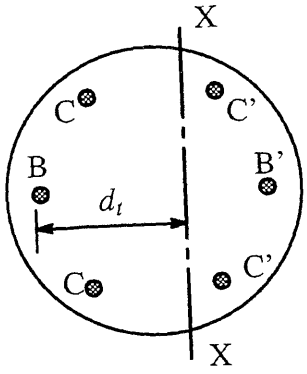

Fig. 6.16 Cross Section

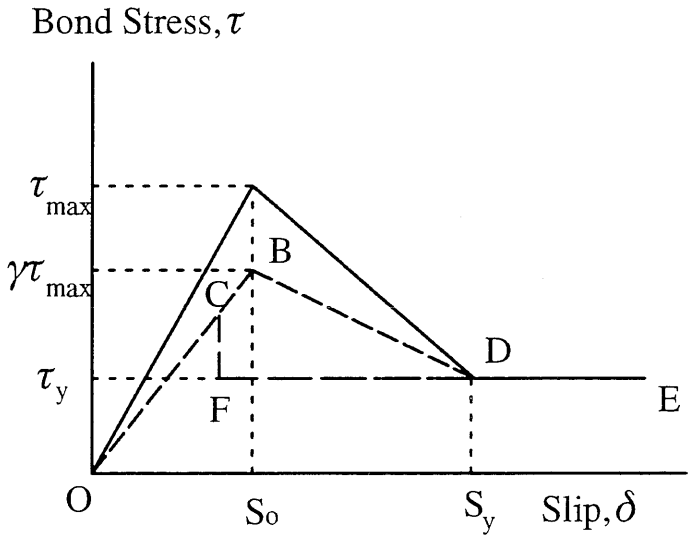

Fig. 6.17 Idealized Bond Stress–Slip Relationship

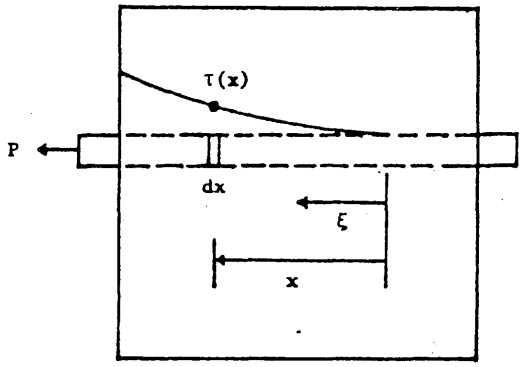

(a) Specimen

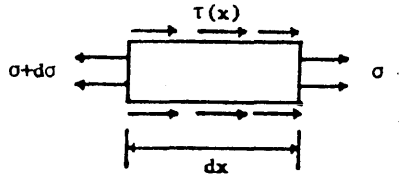

(b) Free body diagram of a bar element

Fig. 6.18 Diagrams for Derivation of Equilibrium Equation

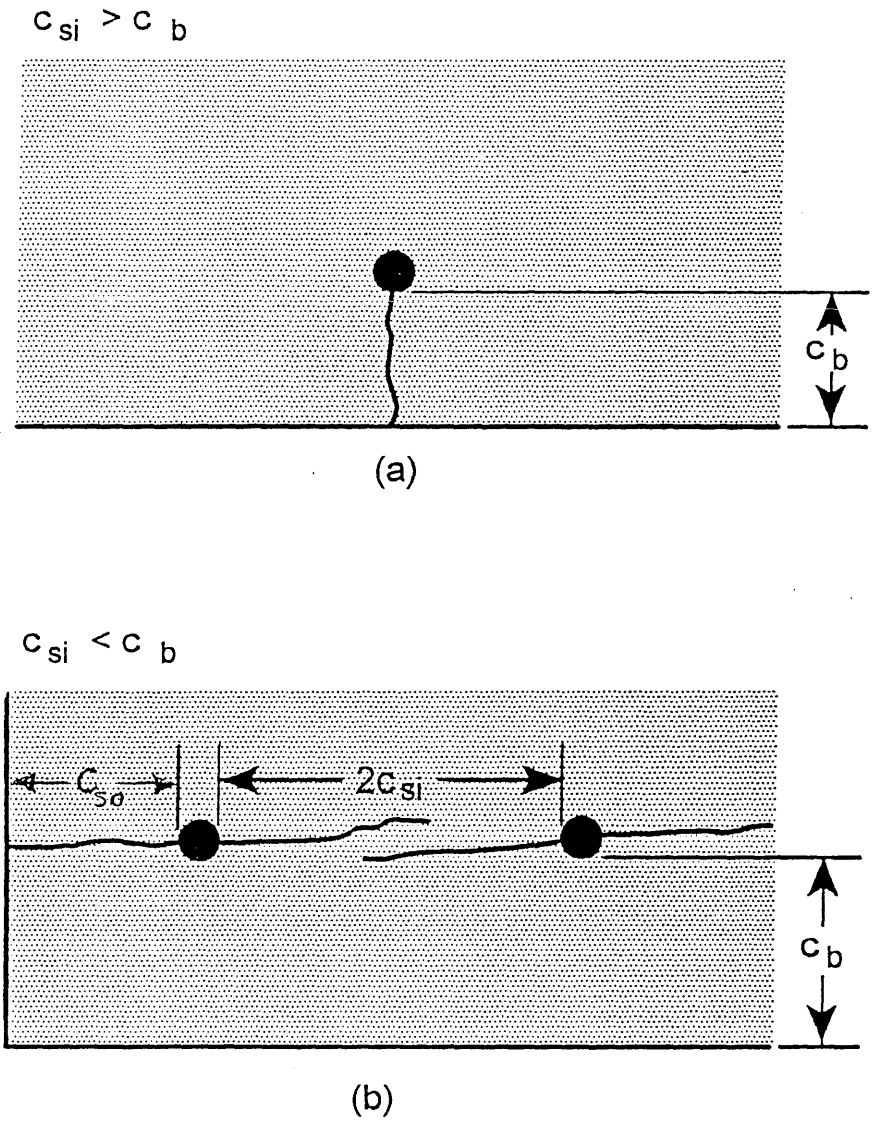

Fig. 6.19 Bond Cracks and Notations for Eq. (6.9a)

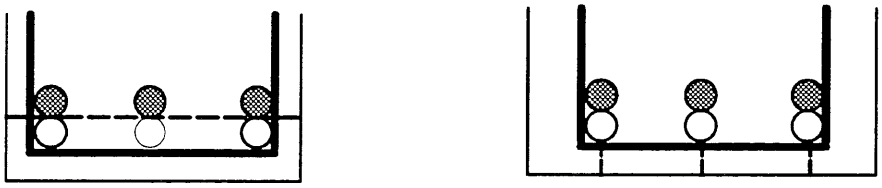

Side Split Failure
Splice Plane Shearing

Cover Splitting Failure

Fig. 6.20 Splice Failure Modes Covered by Eq. (6.9a)

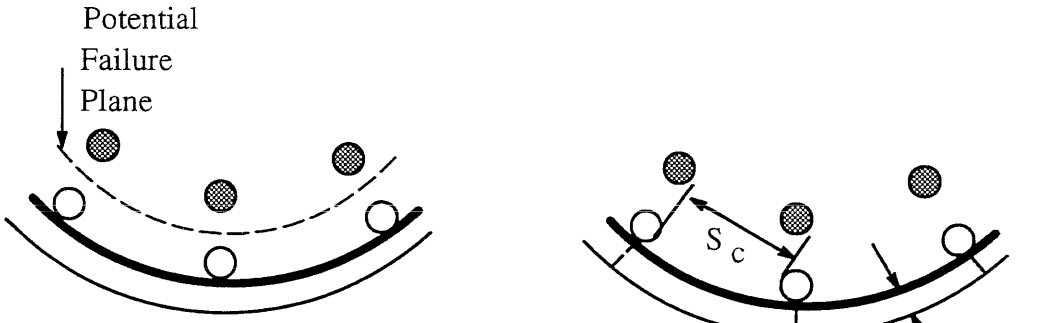

Splice Plane Shearing

Cover Splitting Failure

Fig. 6.21 Splice Failure Modes Possible for Test Columns

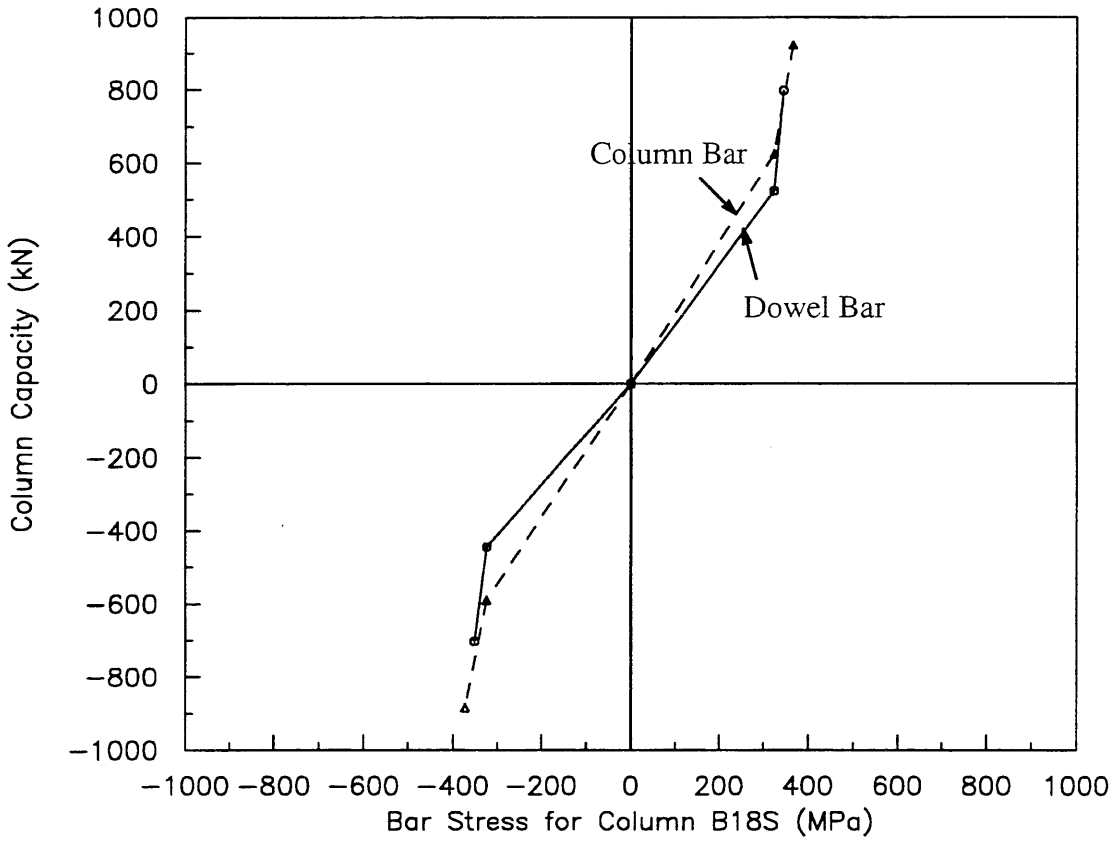

Fig. 6.22a Column Capacity–Bar Stress Relationships for Field Test Columns

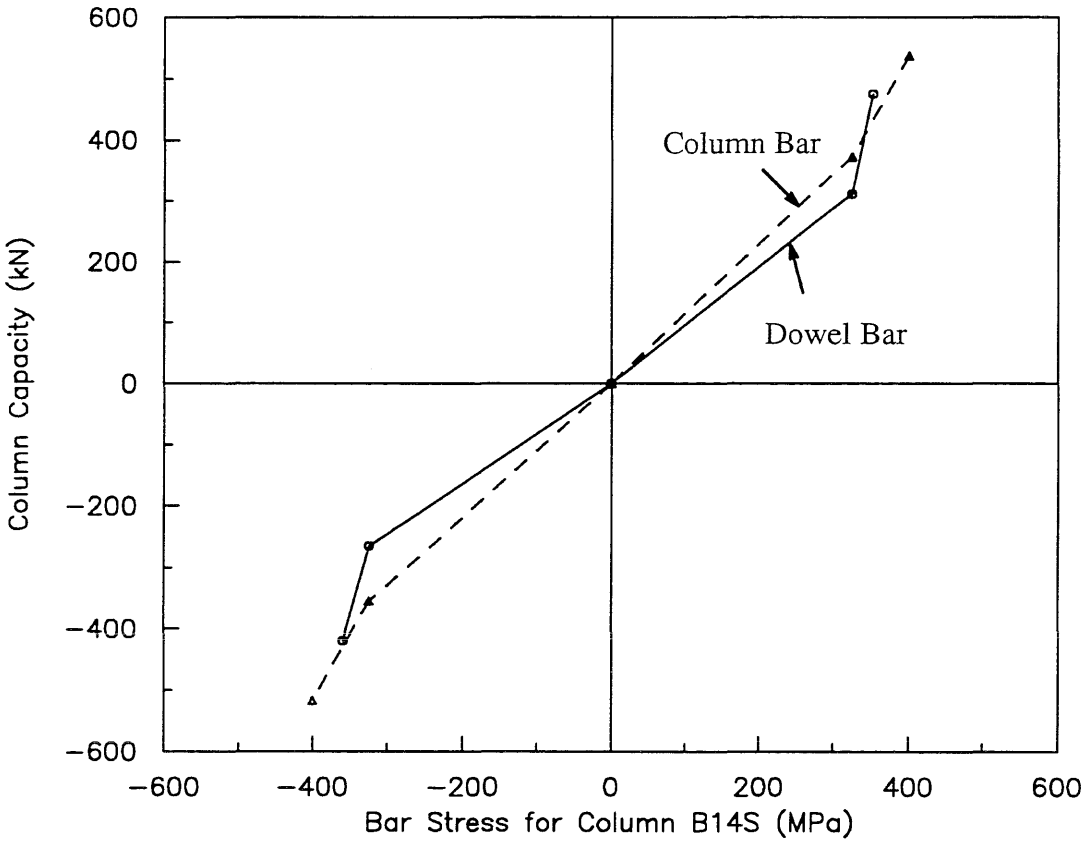

Fig. 6.22a Column Capacity–Bar Stress Relationships for Field Test Columns (cont.)

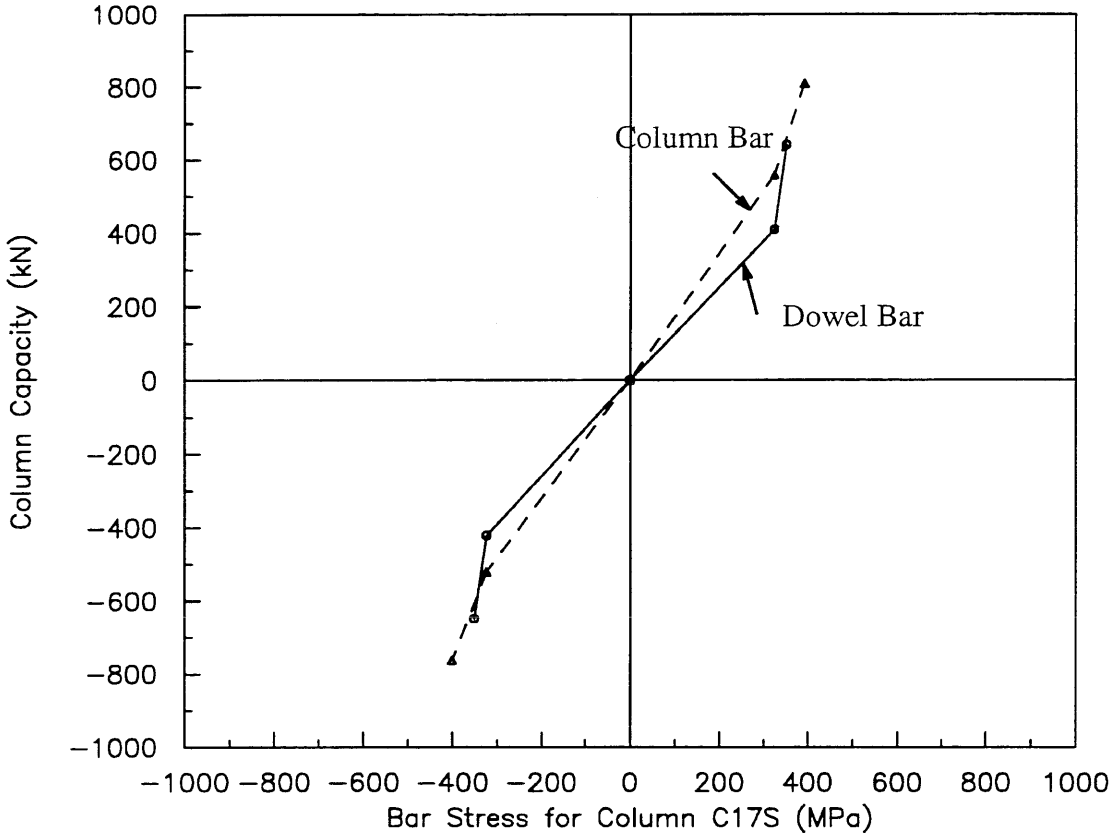

Fig. 6.22a Column Capacity–Bar Stress Relationships for Field Test Columns (cont.)

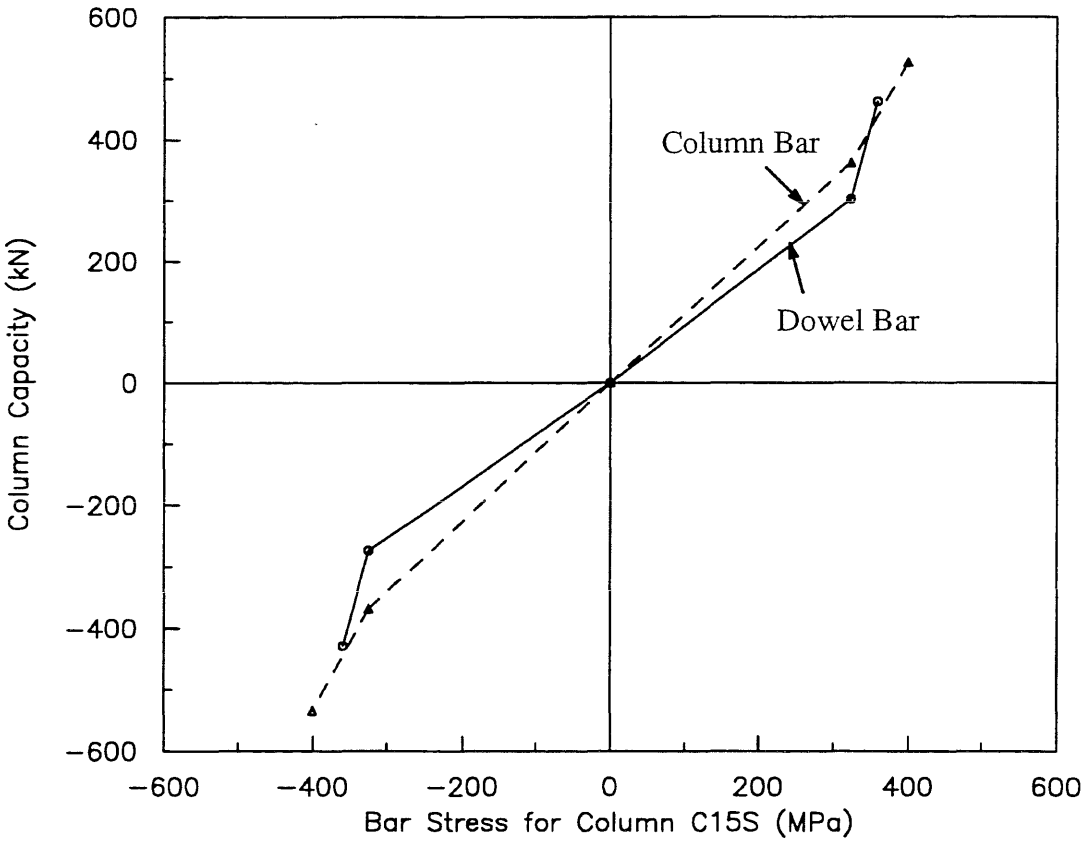

Fig. 6.22a Column Capacity–Bar Stress Relationships for Field Test Columns (cont.)

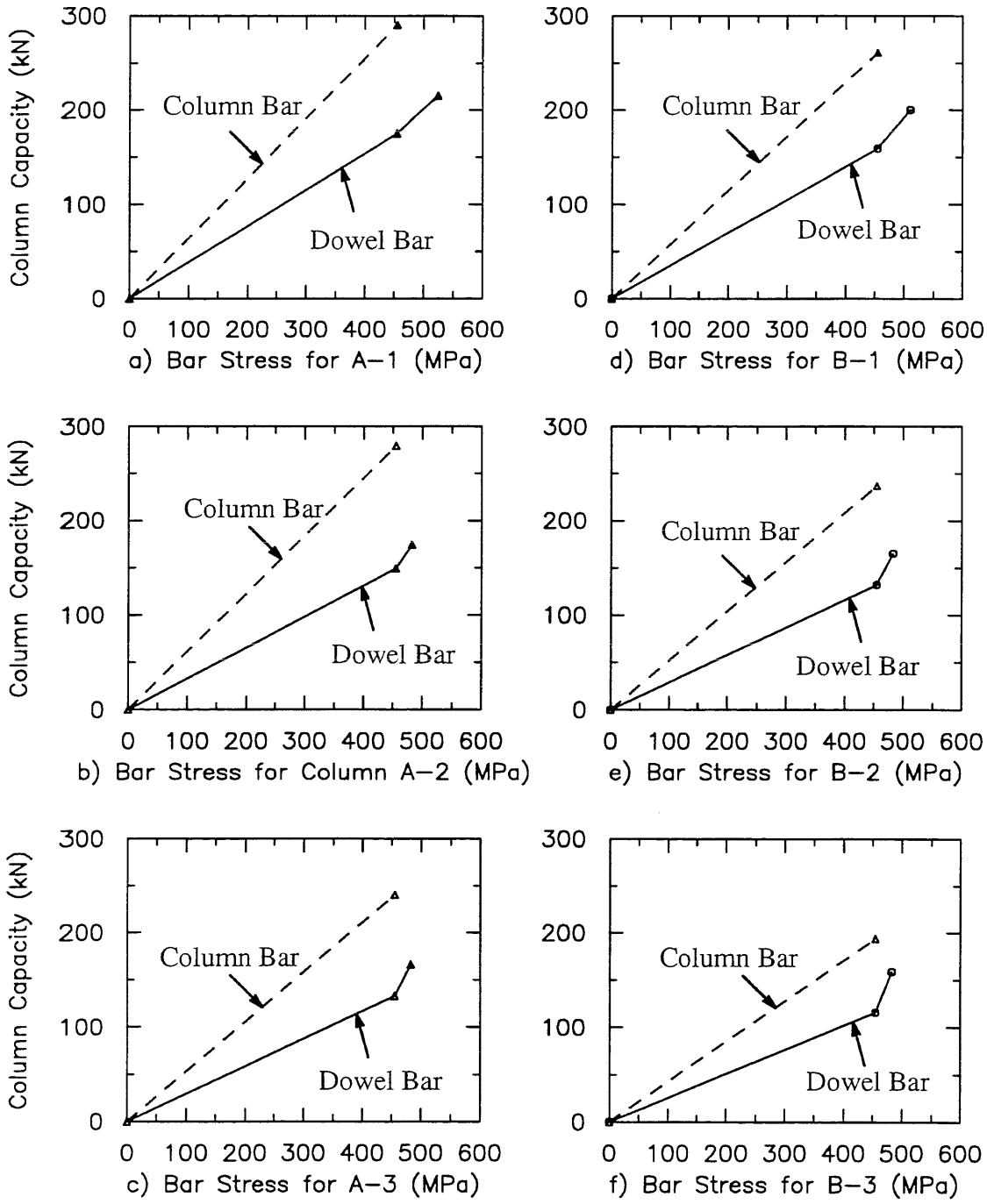

Fig. 6.22b Column Capacity–Bar Stress Relationships for Laboratory Test Columns

Appendix A

Enlarged Load vs. Deflection Curves with Ductility Ratio in Them for Field Test Columns

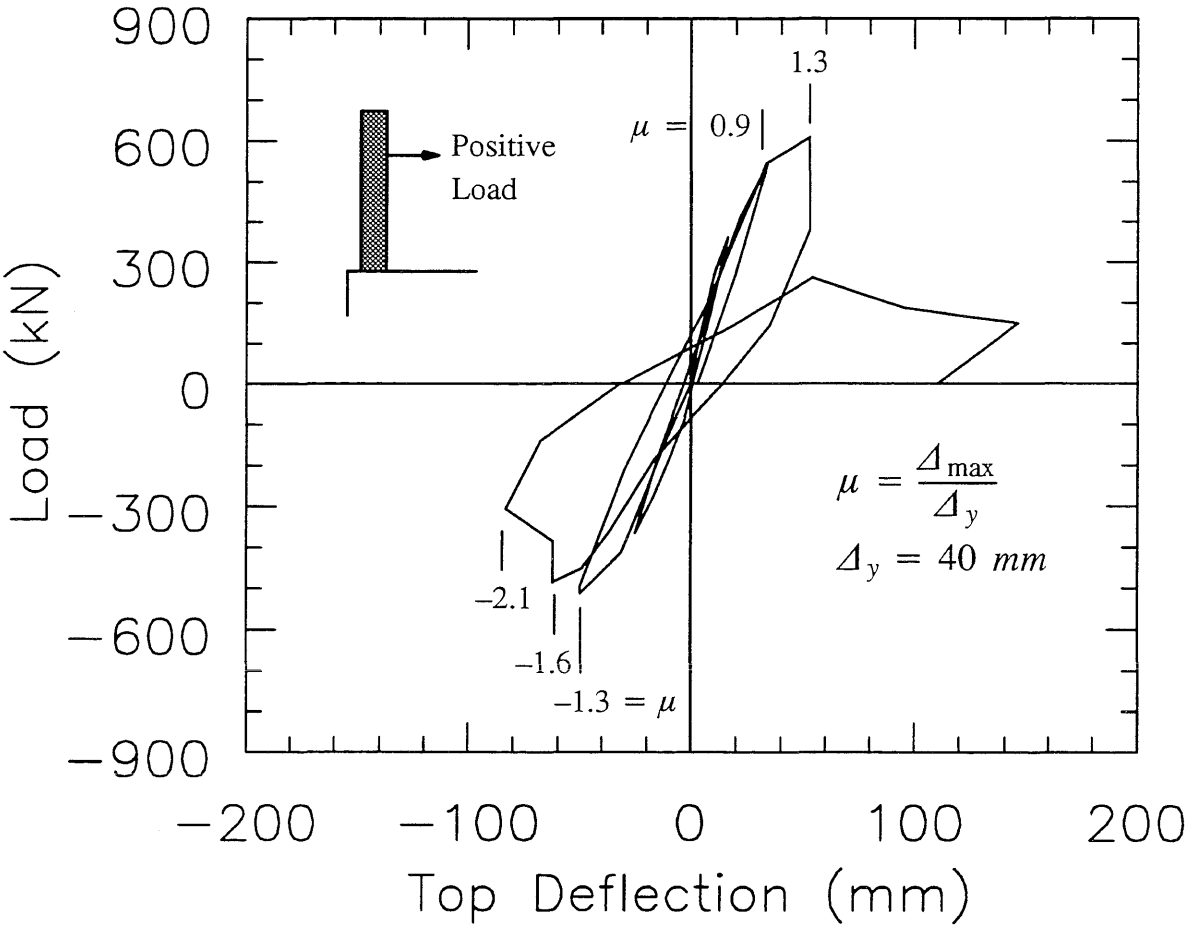

Fig. A1 Load vs. Deflection Curve for Column B18S with 28 #11 Bars

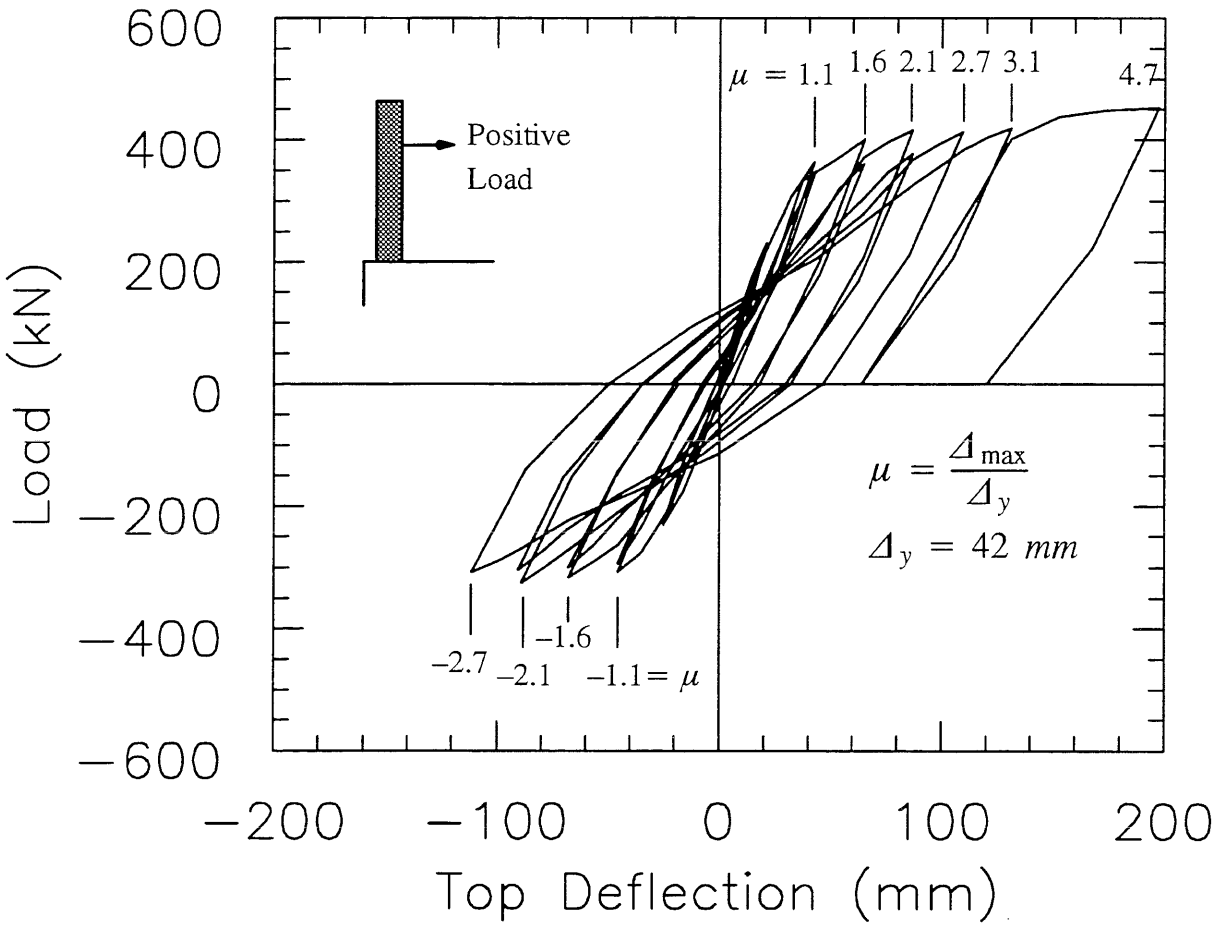

Fig. A2 Load vs. Deflection Curve for Column B14S with 18 #11 Bars

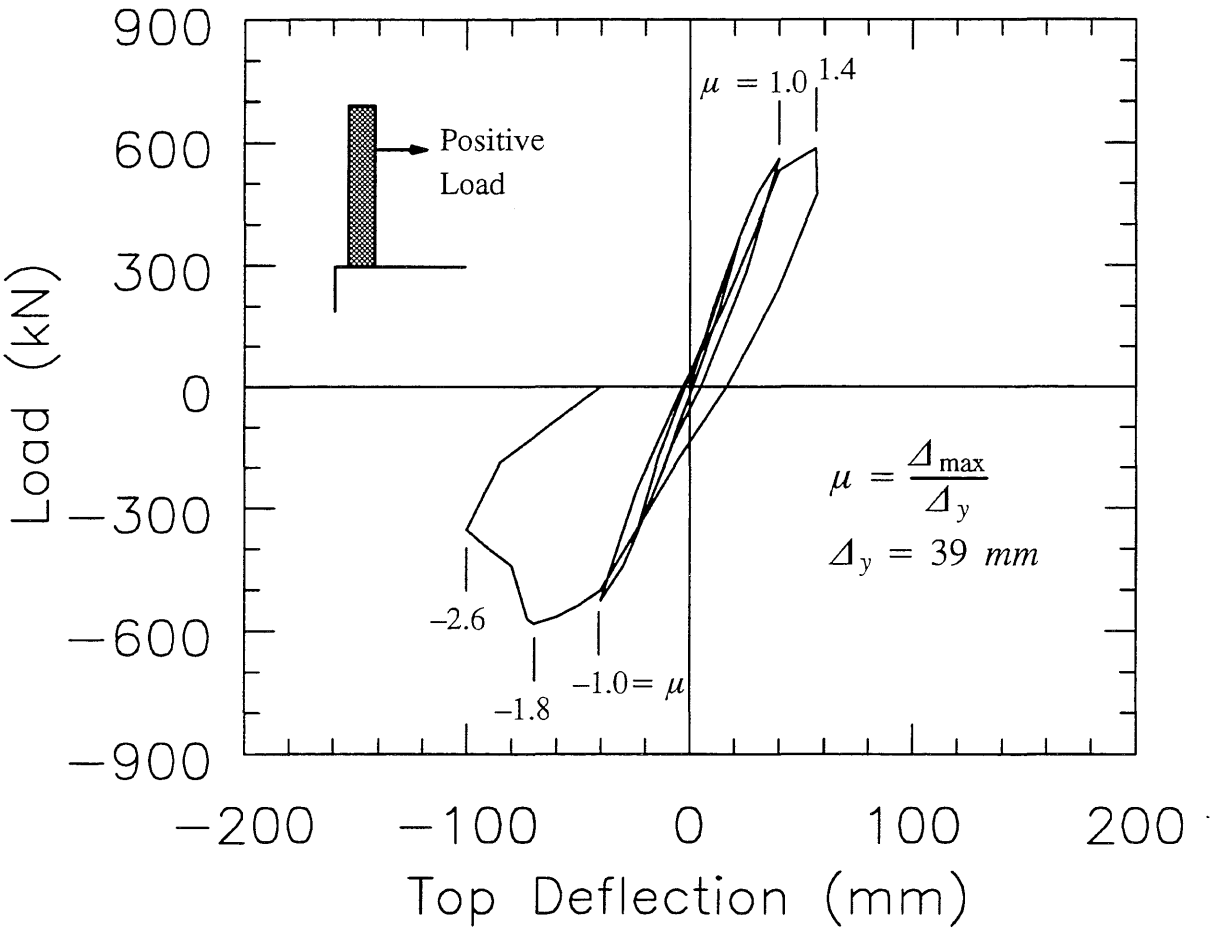

Fig. A3 Load vs. Deflection Curve for Column C17S with 24 #11 Bars

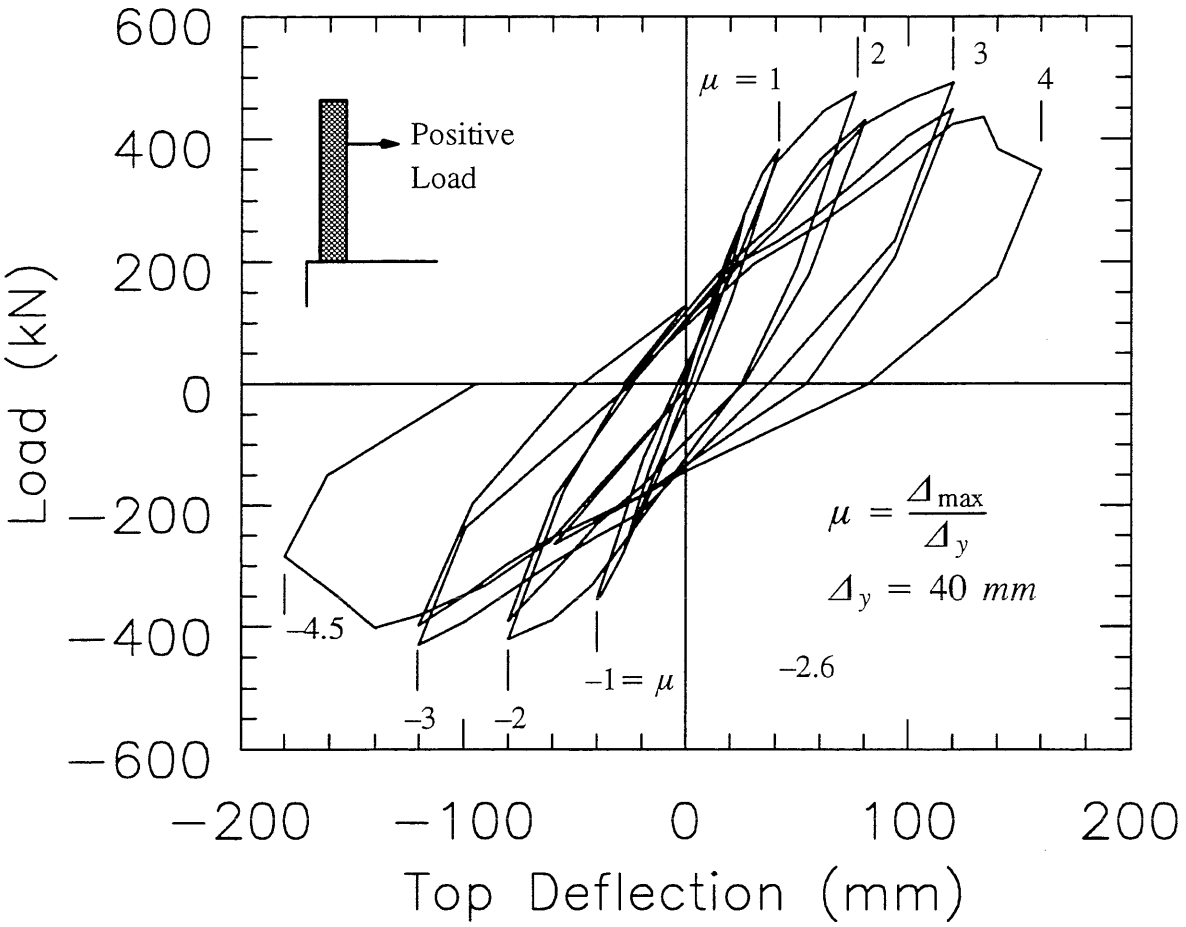

Fig. A4 Load vs. Deflection Curve for Column C15S with 18 #11 Bars

Appendix B

Table B1 Bar Coordinates for Field Test Columns

In the following tables, bar numbers were assigned clockwise from the north side of each column.

a) Bar Coordinates for Column B18S

Bar Number	Column Bar Coordinates		Dowel Bar Coordinates	
	x–coordinate (mm)	y–coordinate (mm)	x–coordinate (mm)	y–coordinate (mm)
1	106	568	57	518
2	244	517	178	489
3	351	451	320	411
4	458	363	388	308
5	538	260	446	216
6	604	153	480	122
7	647	–30	520	24
8	647	–114	476	–178
9	616	–231	441	–265
10	549	–344	363	–373
11	469	–446	263	–465
12	361	–542	141	–534
13	207	–602	41	–558
14	69	–626	–83	–559
15	–91	–616	–215	–530
16	–200	–584	–293	–476
17	–375	–481	–343	–441
18	–449	–413	–415	–382
19	–539	–298	–478	–300
20	–597	–175	–502	–231
21	–628	29	–556	–56
22	–591	116	–565	5
23	–581	230	–551	129
24	–556	308	–512	225
25	–538	351	–457	299
26	–408	487	–339	404
27	–189	586	–245	474
28	–33	596	–76	515

b) Bar Coordinates for Column B14S

Bar Number	Column Bar Coordinates		Dowel Bar Coordinates	
	x–coordinate (mm)	y–coordinate (mm)	x–coordinate (mm)	y–coordinate (mm)
1	109	522	121	440
2	261	439	229	403
3	395	308	376	281
4	484	144	455	115
5	517	–21	472	–59
6	498	–207	423	–218
7	404	–372	318	–345
8	273	–480	191	–436
9	90	–538	82	–488
10	–67	–538	–71	–490
11	–263	–464	–215	–439
12	–416	–338	–369	–340
13	–495	–181	–440	–227
14	–536	–22	–444	–74
15	–488	190	–455	86
16	–390	344	–403	240
17	–269	452	–260	399
18	–87	519	–28	456

c) Bar Coordinates for Column C17S

Bar Number	Column Bar Coordinates		Dowel Bar Coordinates	
	x–coordinate (mm)	y–coordinate (mm)	x–coordinate (mm)	y–coordinate (mm)
1	0	577	85	509
2	175	540	212	470
3	295	499	336	398
4	445	392	426	299
5	548	274	488	191
6	609	151	520	69
7	637	–10	515	–30
8	613	–176	500	–195
9	561	–314	437	–295
10	454	–455	346	–396
11	315	–555	232	–467
12	178	–607	104	–508
13	29	–637	–19	–521
14	–122	–623	–183	–461
15	–277	–558	–326	–401
16	–422	–448	–419	–306
17	–507	–342	–482	–198
18	–577	–213	–511	–40
19	–625	–48	–516	50
20	–622	130	–481	188
21	–583	265	–401	328
22	–484	396	–293	420
23	–347	480	–183	474
24	–176	542	–56	506

d) Bar Coordinates for Column C15S

Bar Number	Column Bar Coordinates		Dowel Bar Coordinates	
	x–coordinate (mm)	y–coordinate (mm)	x–coordinate (mm)	y–coordinate (mm)
1	89	529	88	463
2	252	463	251	399
3	388	339	368	283
4	486	175	435	146
5	520	26	459	–44
6	485	–185	396	–222
7	384	–358	325	–336
8	246	–475	181	–435
9	45	–535	29	–473
10	–106	–528	–106	–456
11	–289	–449	–222	–408
12	–384	–350	–318	–328
13	–479	–139	–410	–208
14	–501	25	–447	–14
15	–467	178	–427	143
16	–383	364	–354	285
17	–243	494	–205	416
18	–79	539	–40	477

Appendix C

Enlarged Load vs. Deflection Curves with Ductility Ratio in Them for Laboratory Test Columns

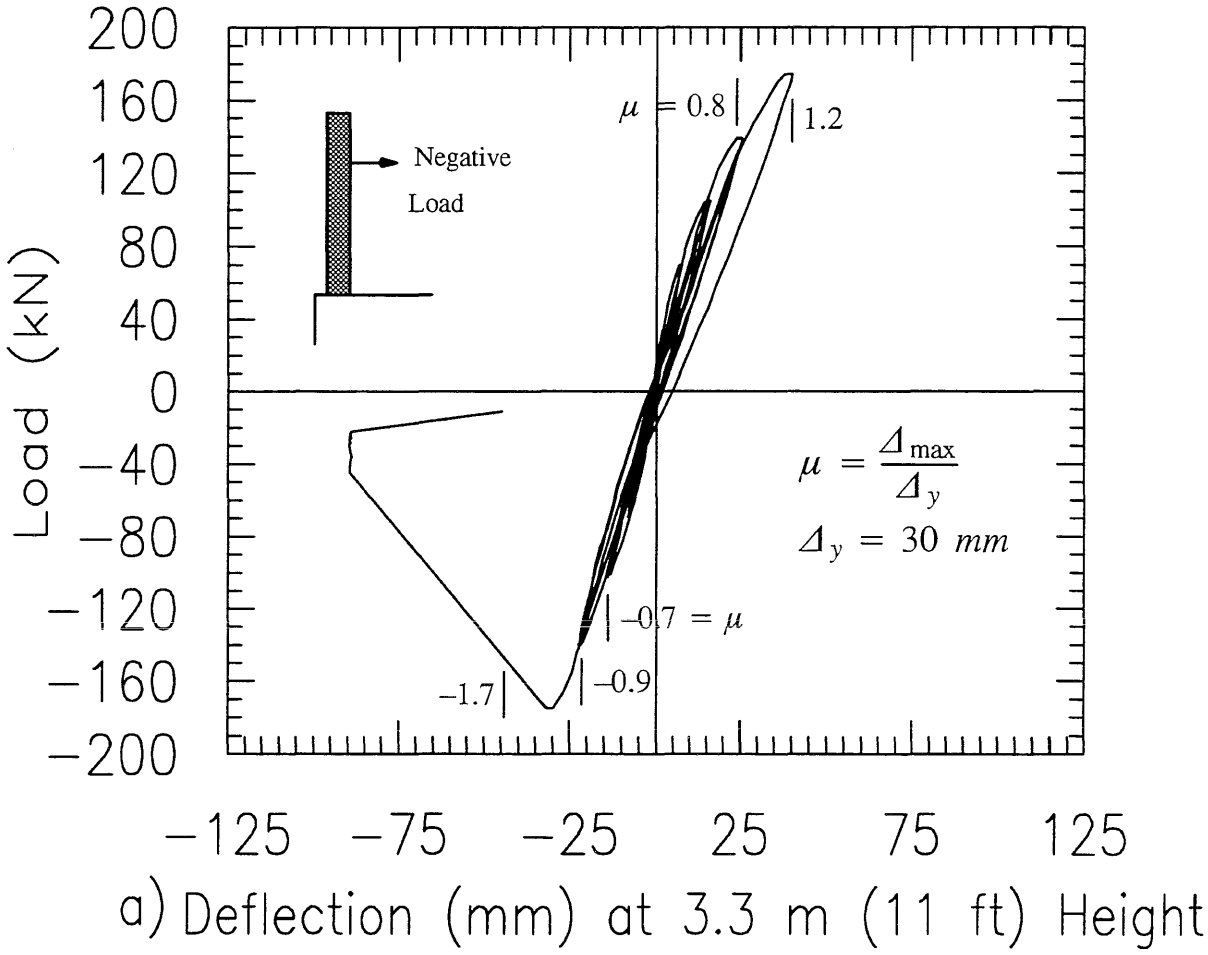

Fig. C1 Load vs. Deflection Curve for Column A–1

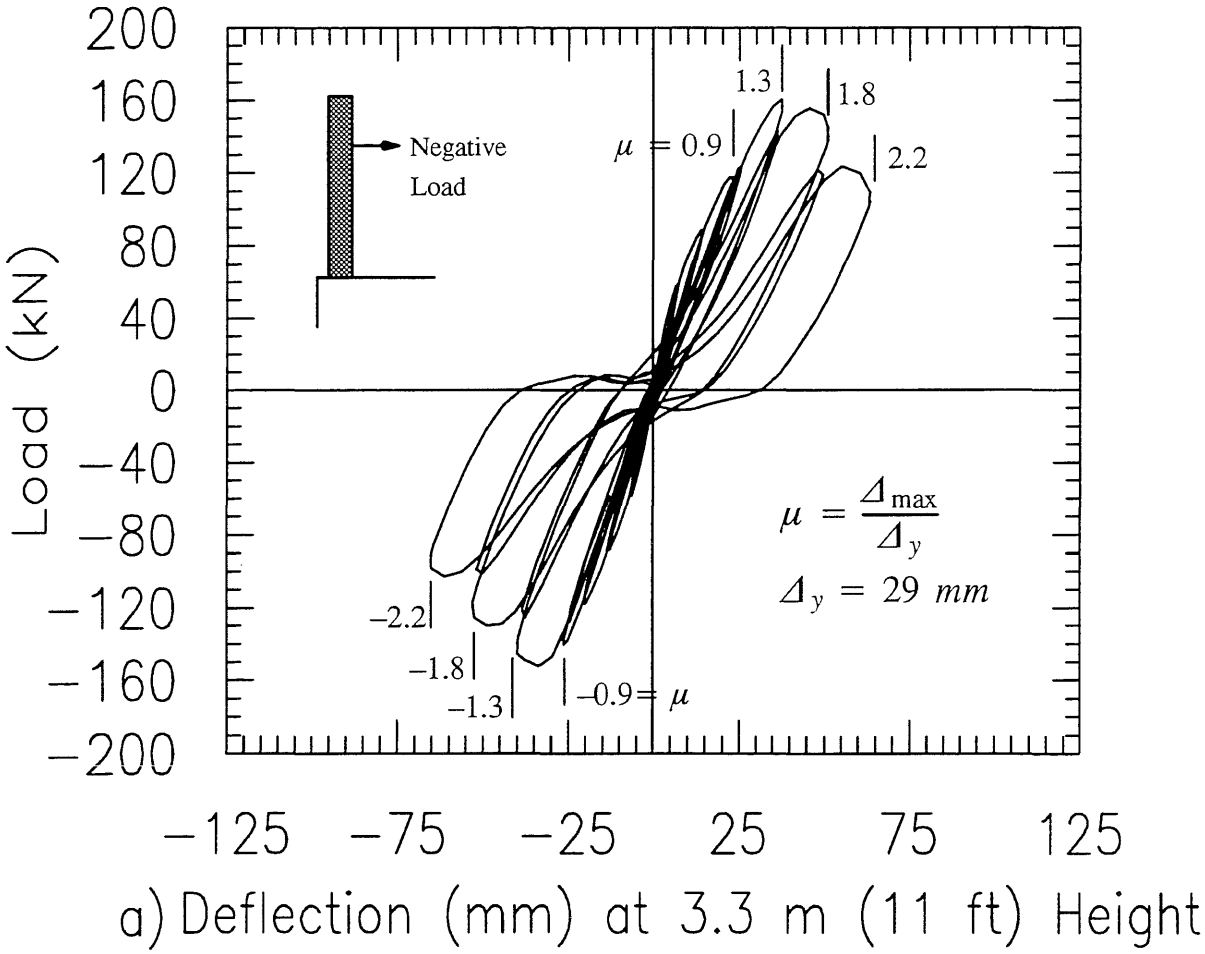

Fig. C2 Load vs. Deflection Curve for Column A–2

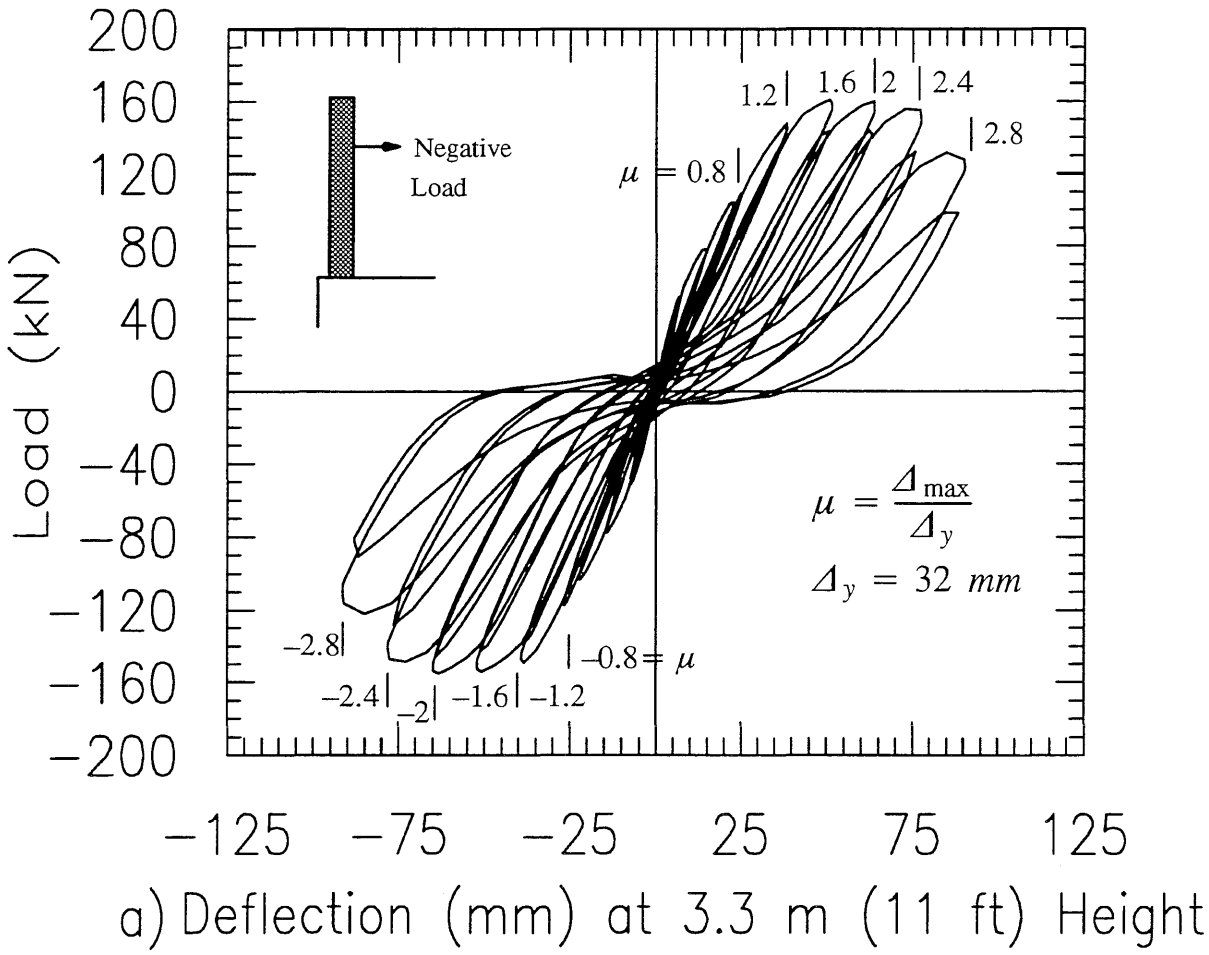

Fig. C3 Load vs. Deflection Curve for Column A–3

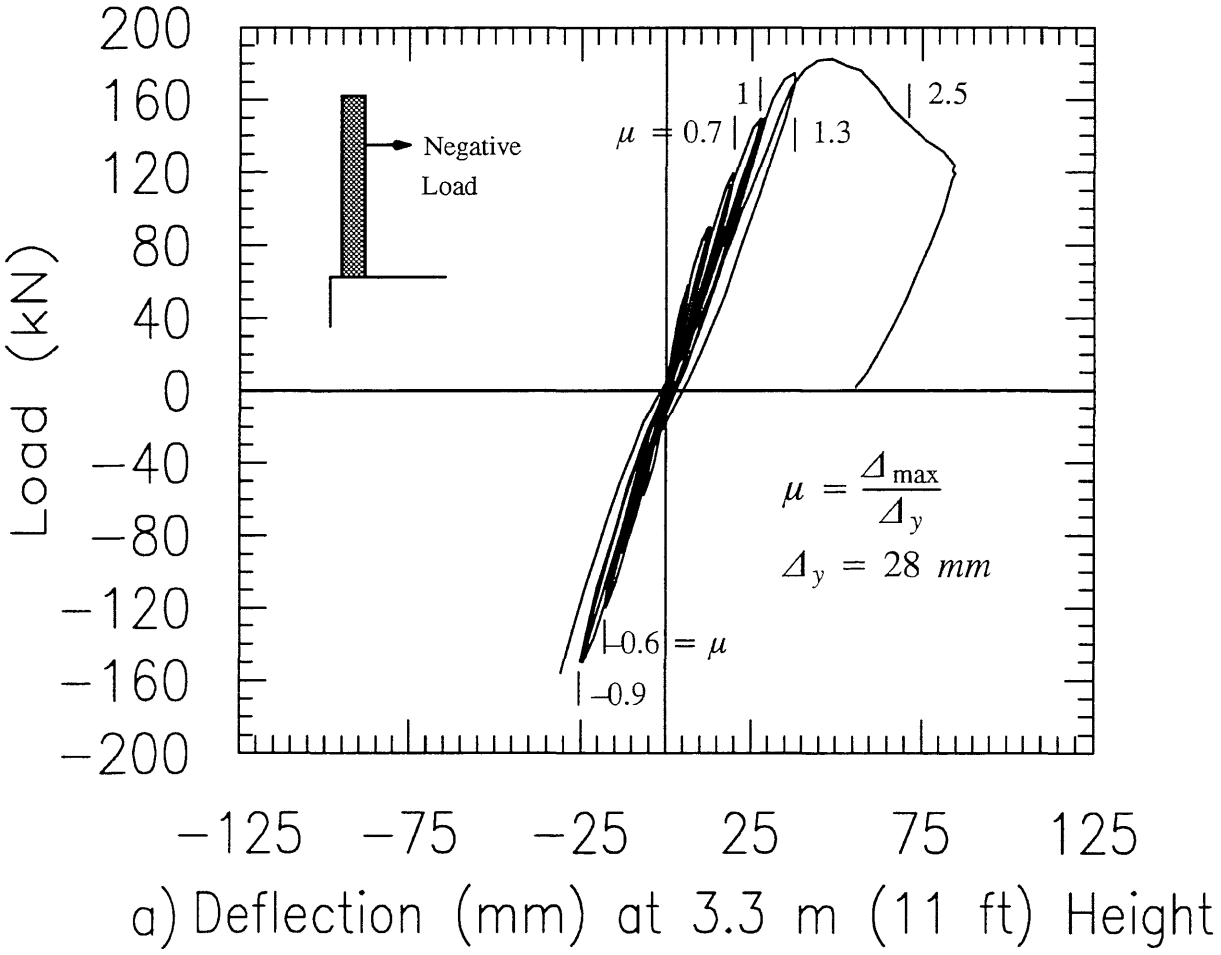

Fig. C4 Load vs. Deflection Curve for Column B–1

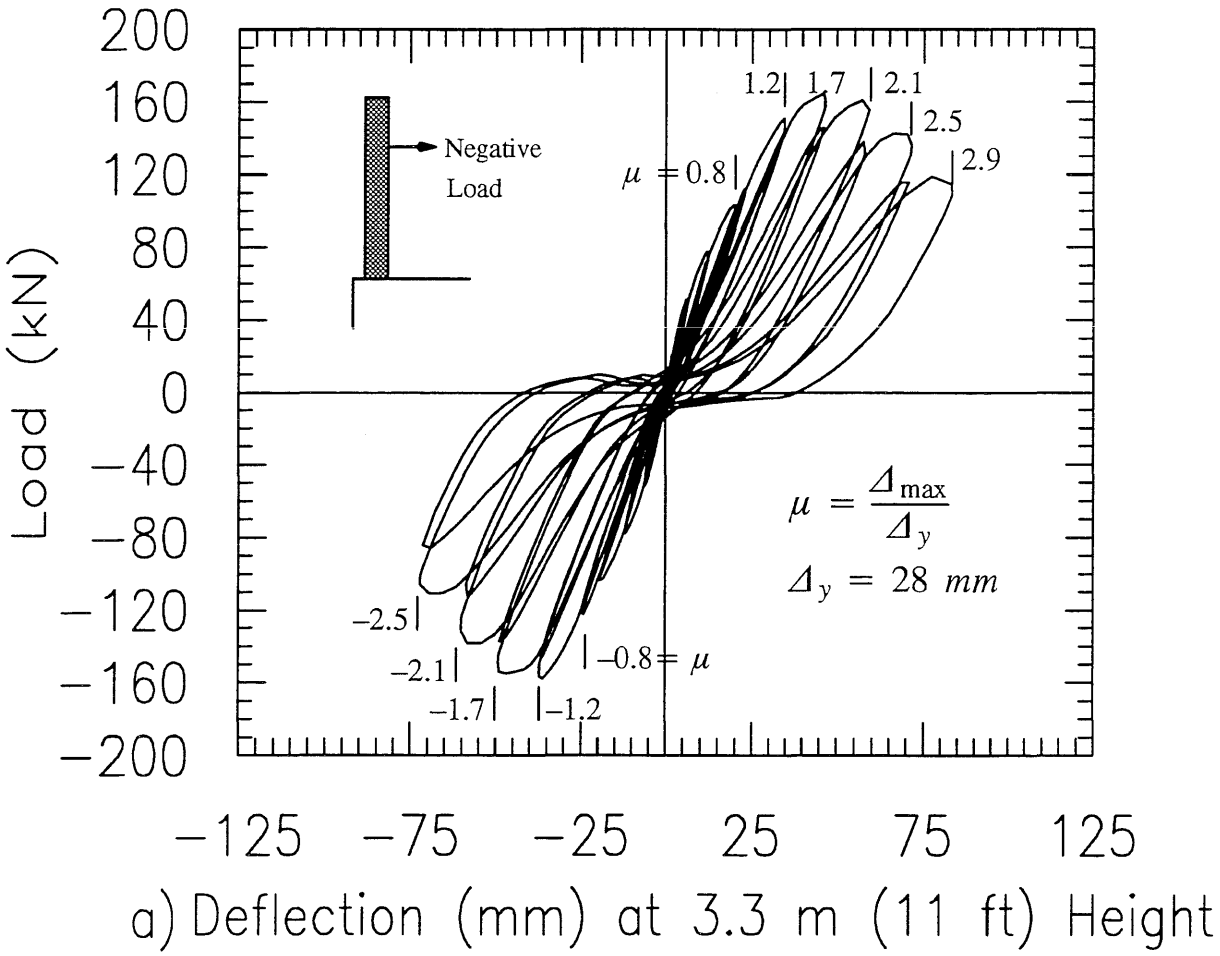

Fig. C5 Load vs. Deflection Curve for Column B–2

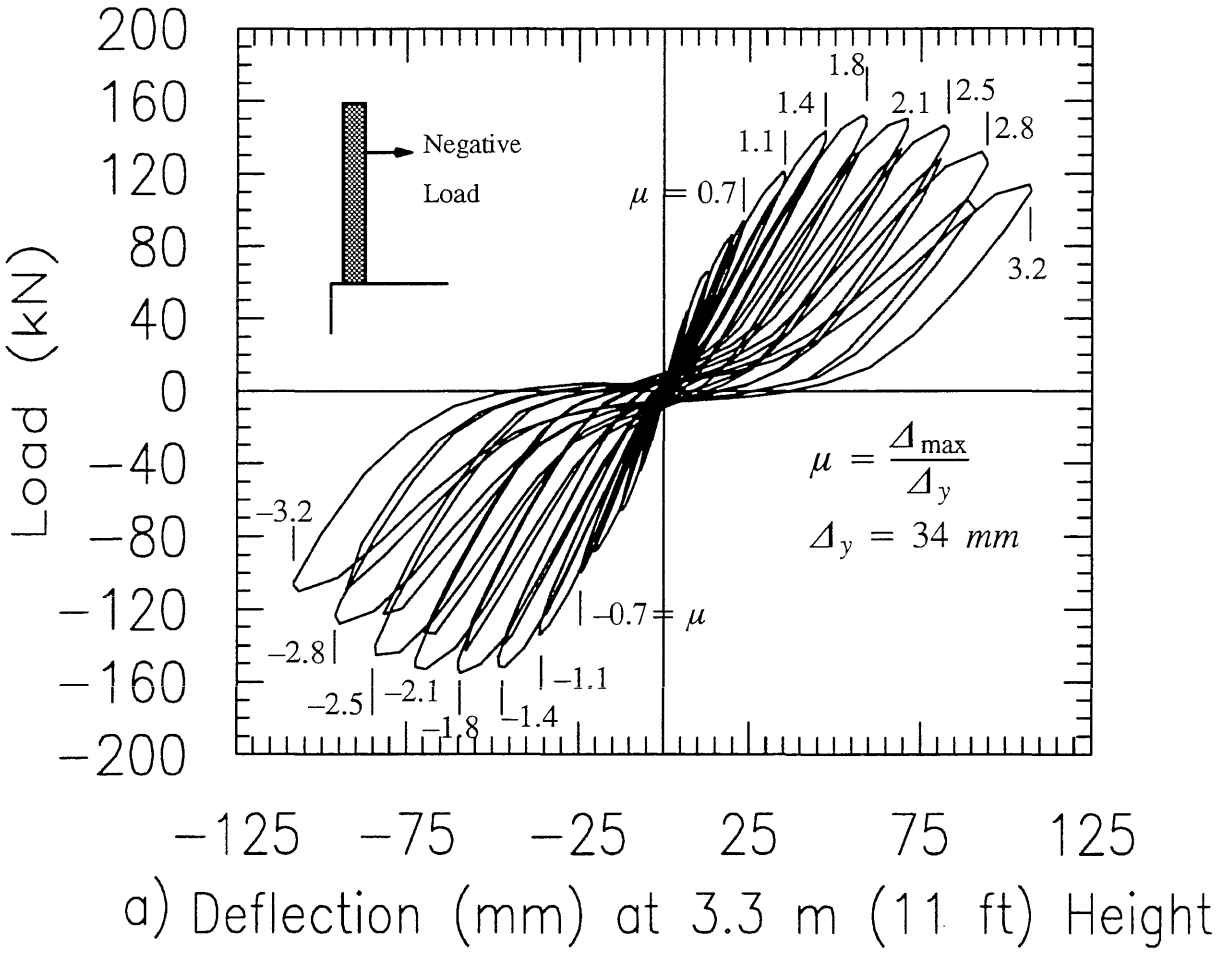

Fig. C6 Load vs. Deflection Curve for Column B–3

Appendix D

Load vs. Strain Curves for All Laboratory Test Columns

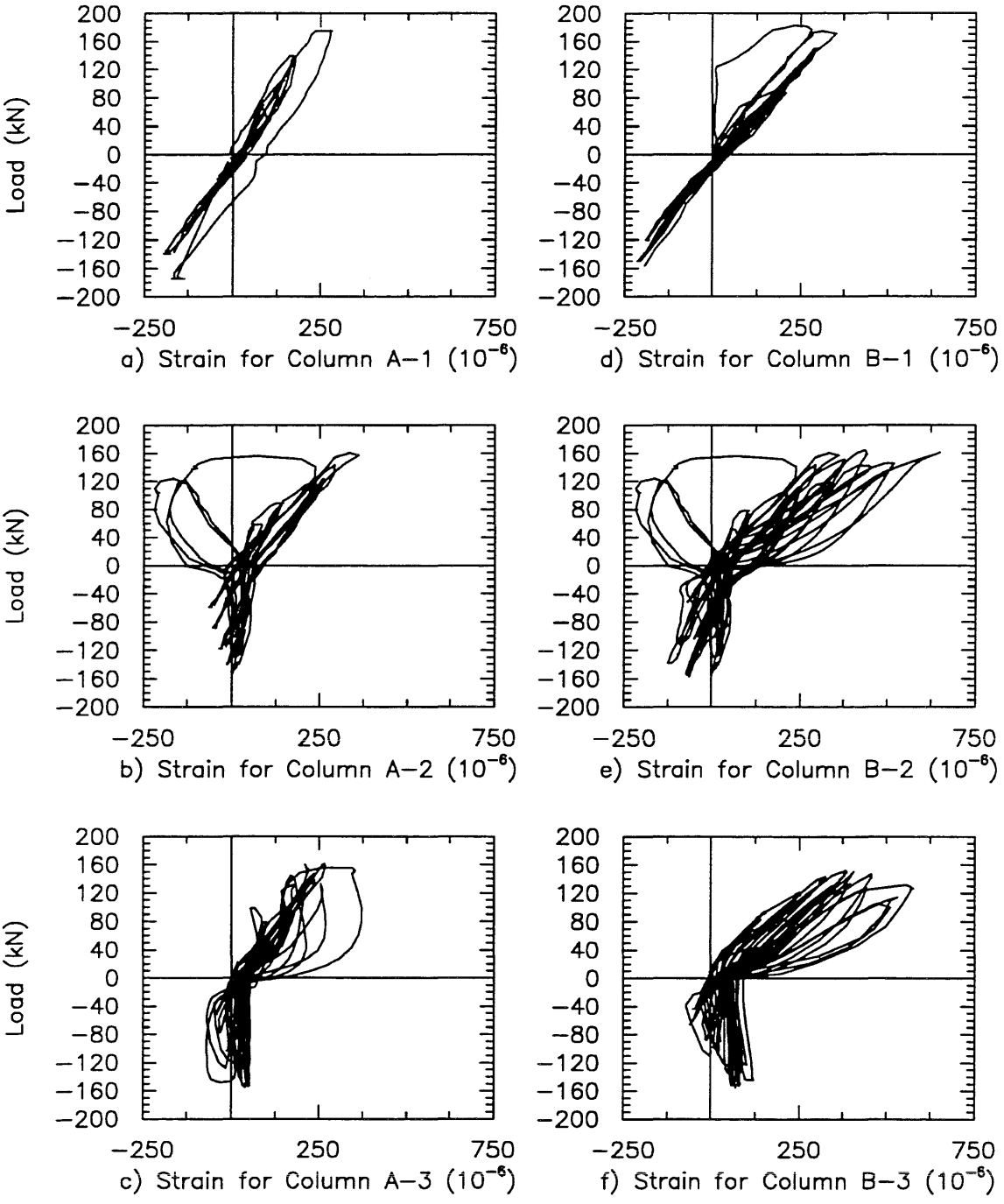

Fig. D1 Load vs. Strain Curve for Gage 1 on Dowel Bar

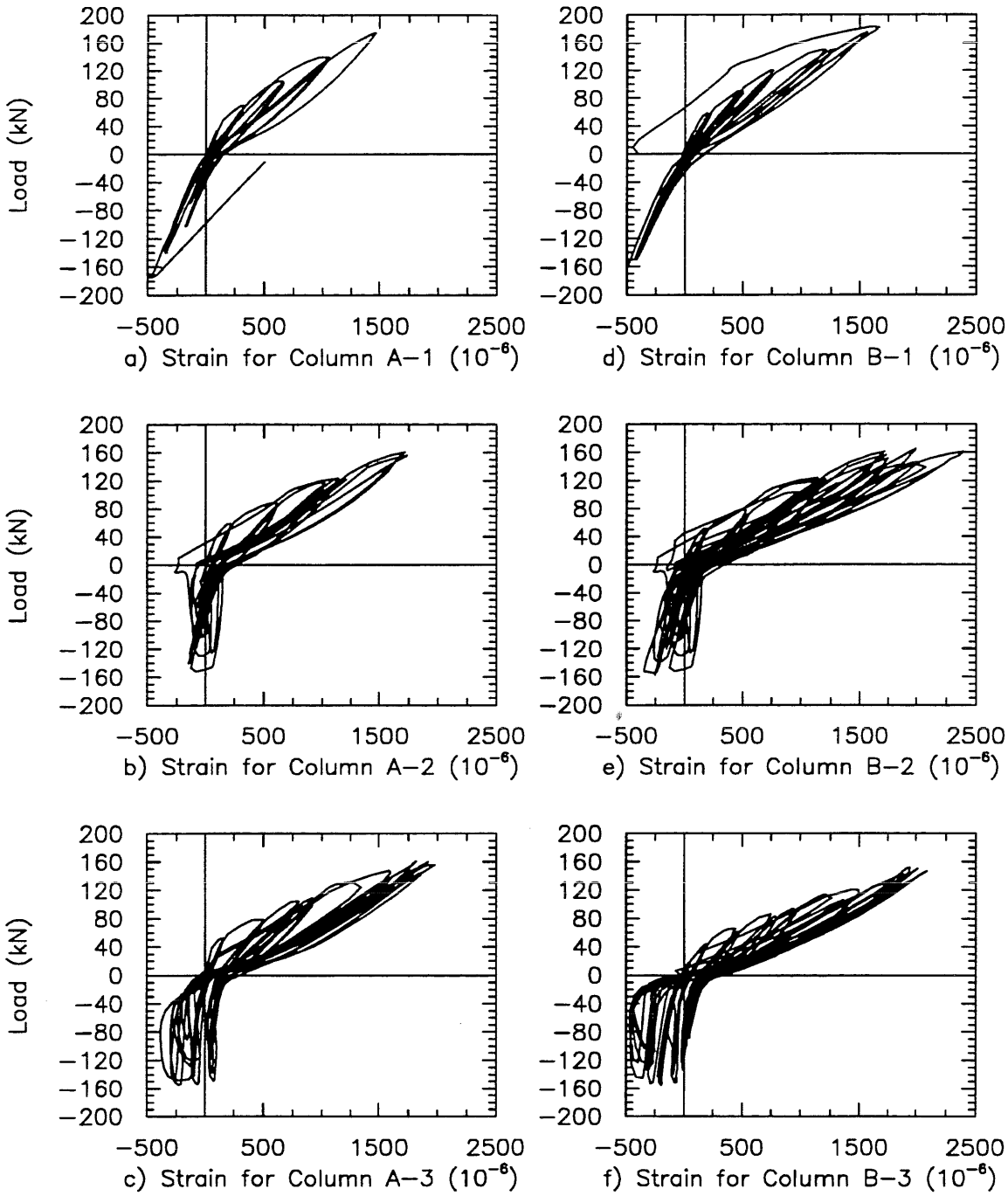

Fig. D2 Load vs. Strain Curve for Gage 2 on Dowel Bar

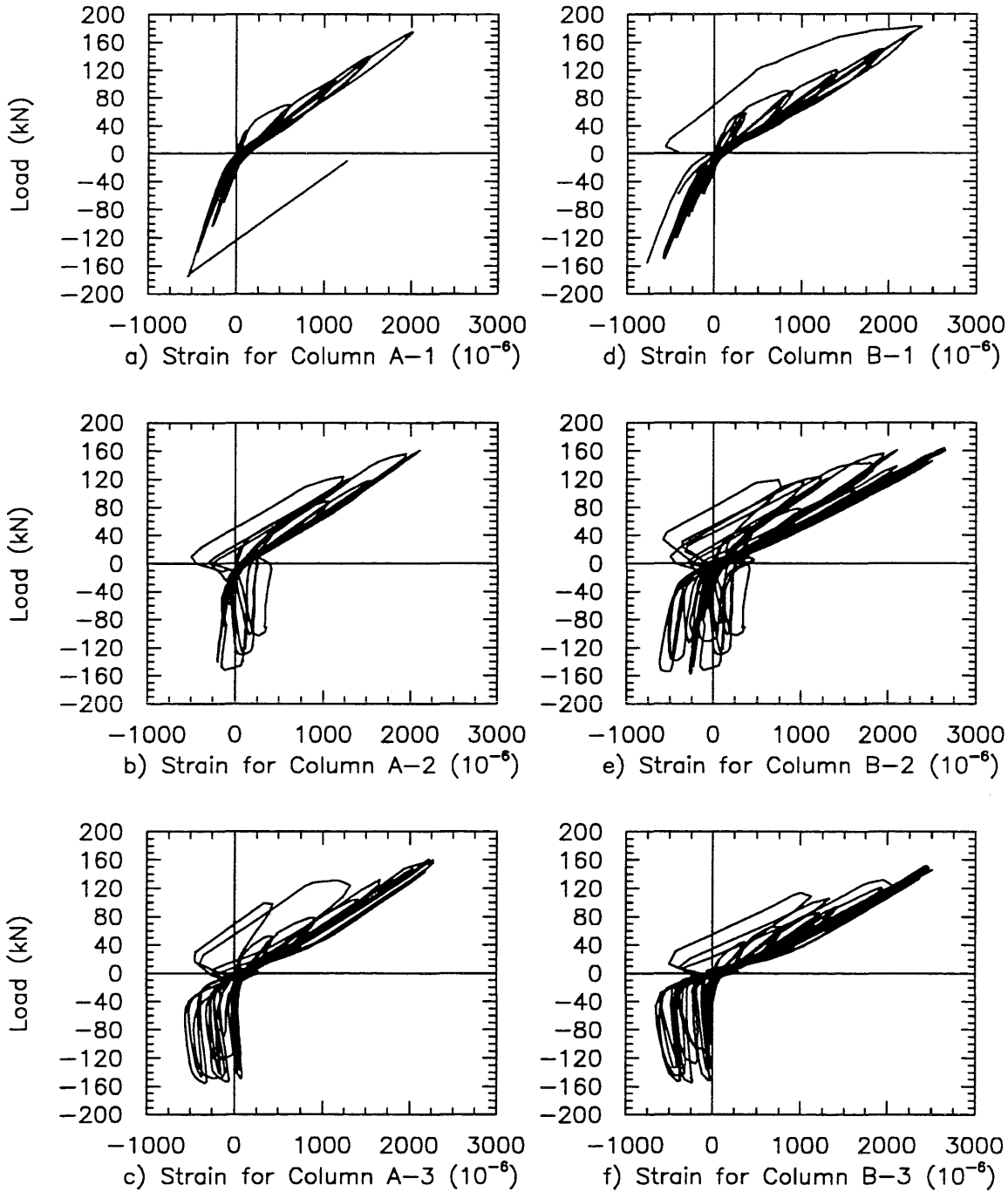

Fig. D3 Load vs. Strain Curve for Gage 3 on Dowel Bar

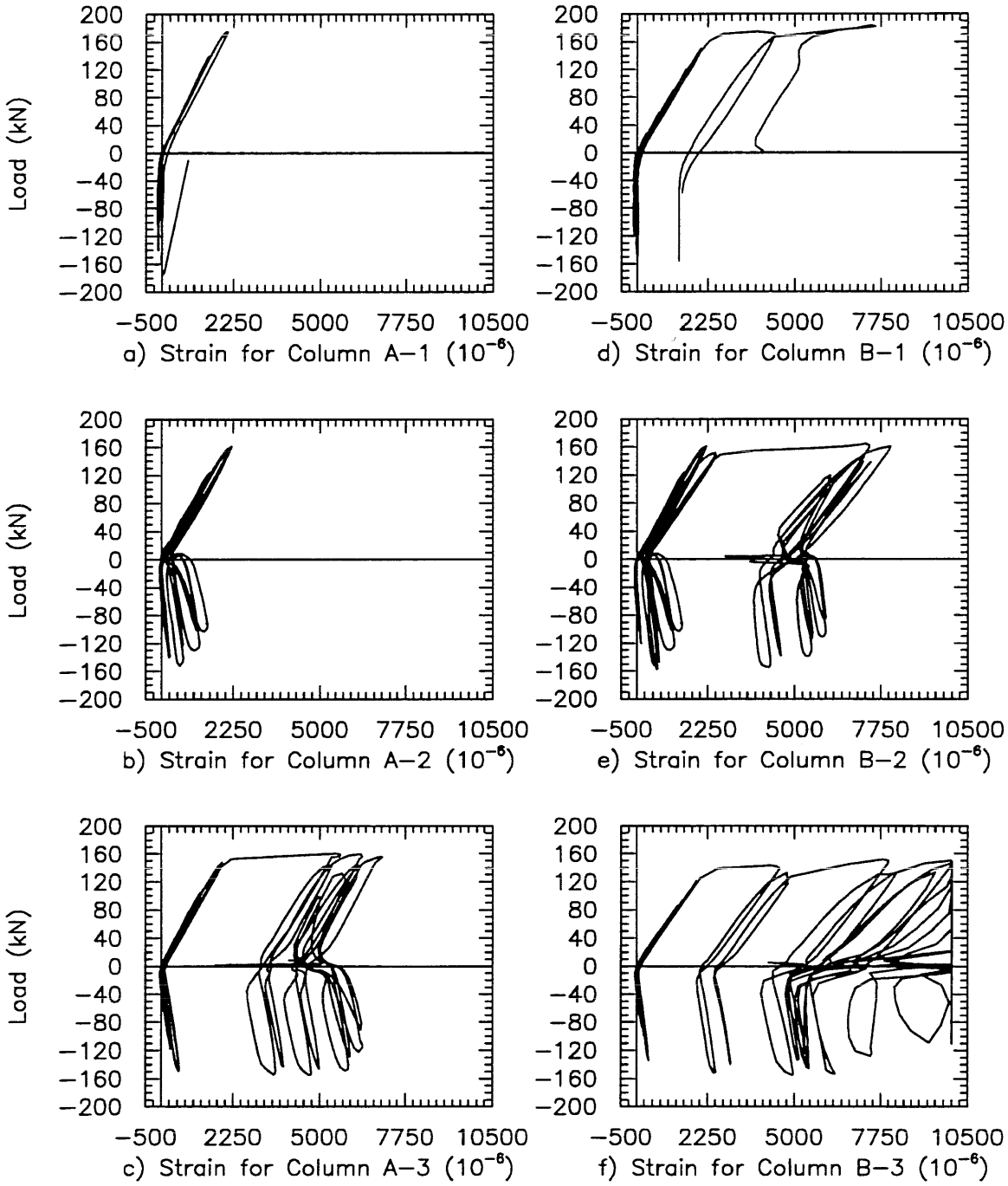

Fig. D4 Load vs. Strain Curve for Gage 4 on Dowel Bar

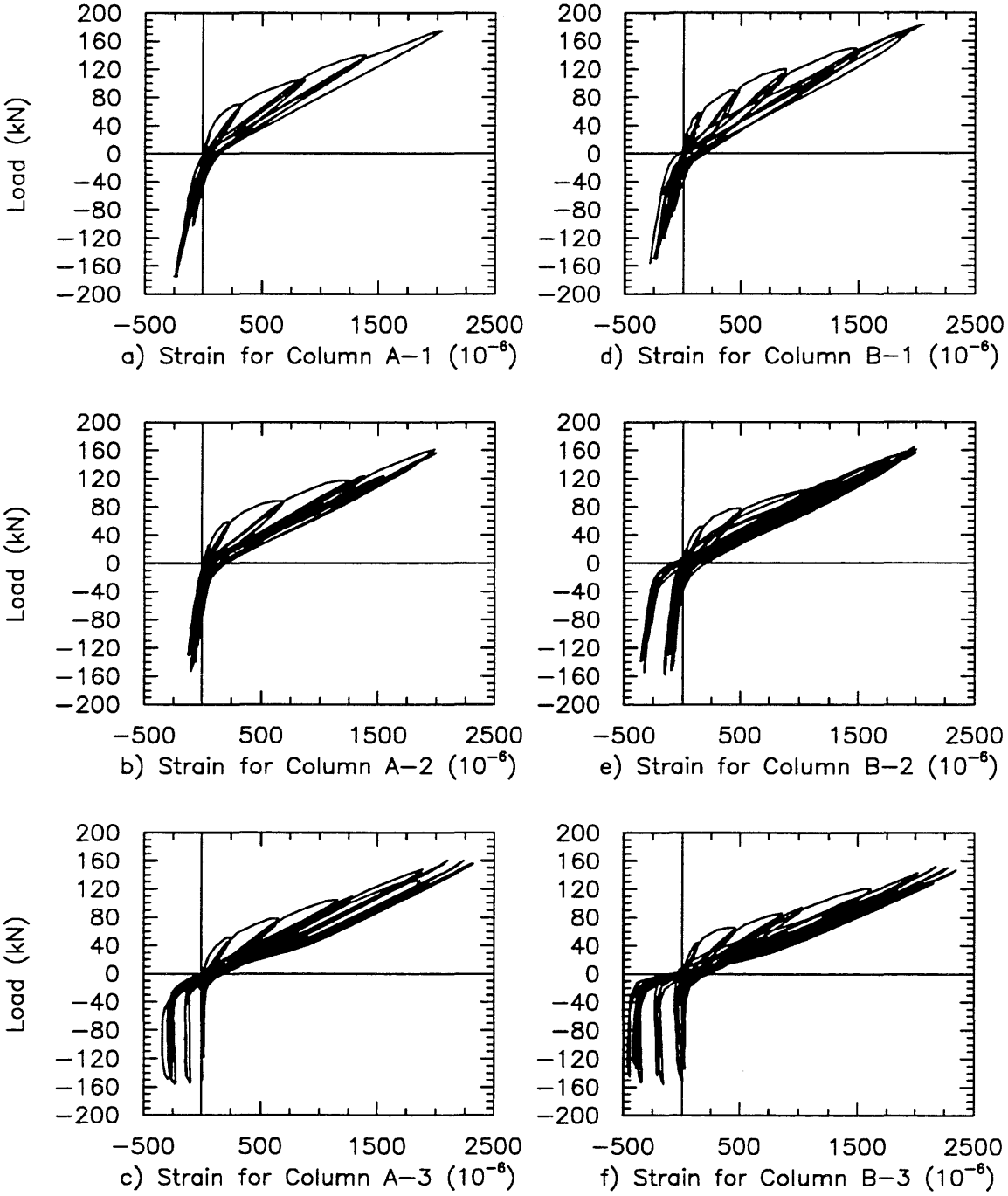

Fig. D5 Load vs. Strain Curve for Gage 5 on Dowel Bar

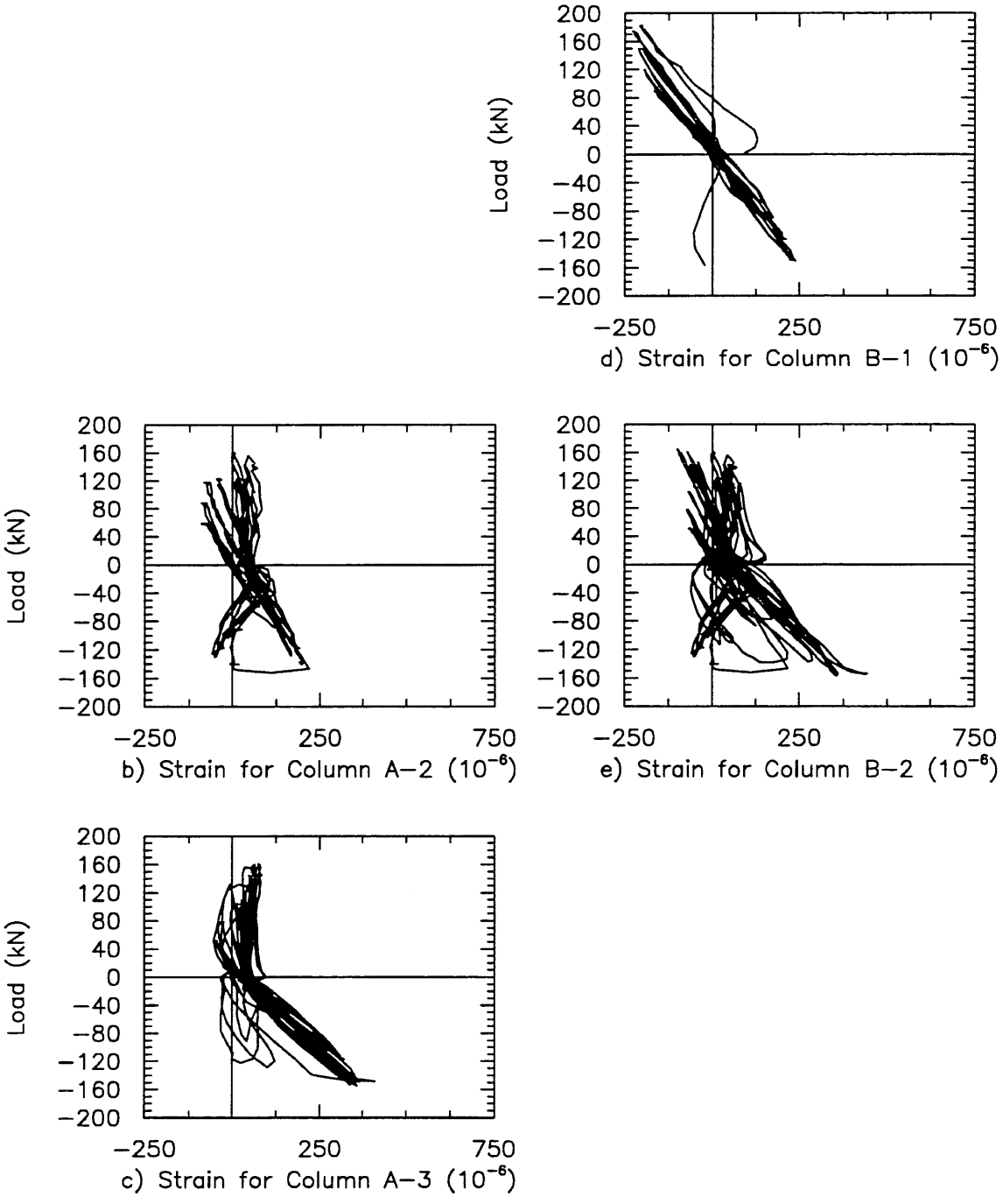

Fig. D6 Load vs. Strain Curve for Gage 6 on Dowel Bar

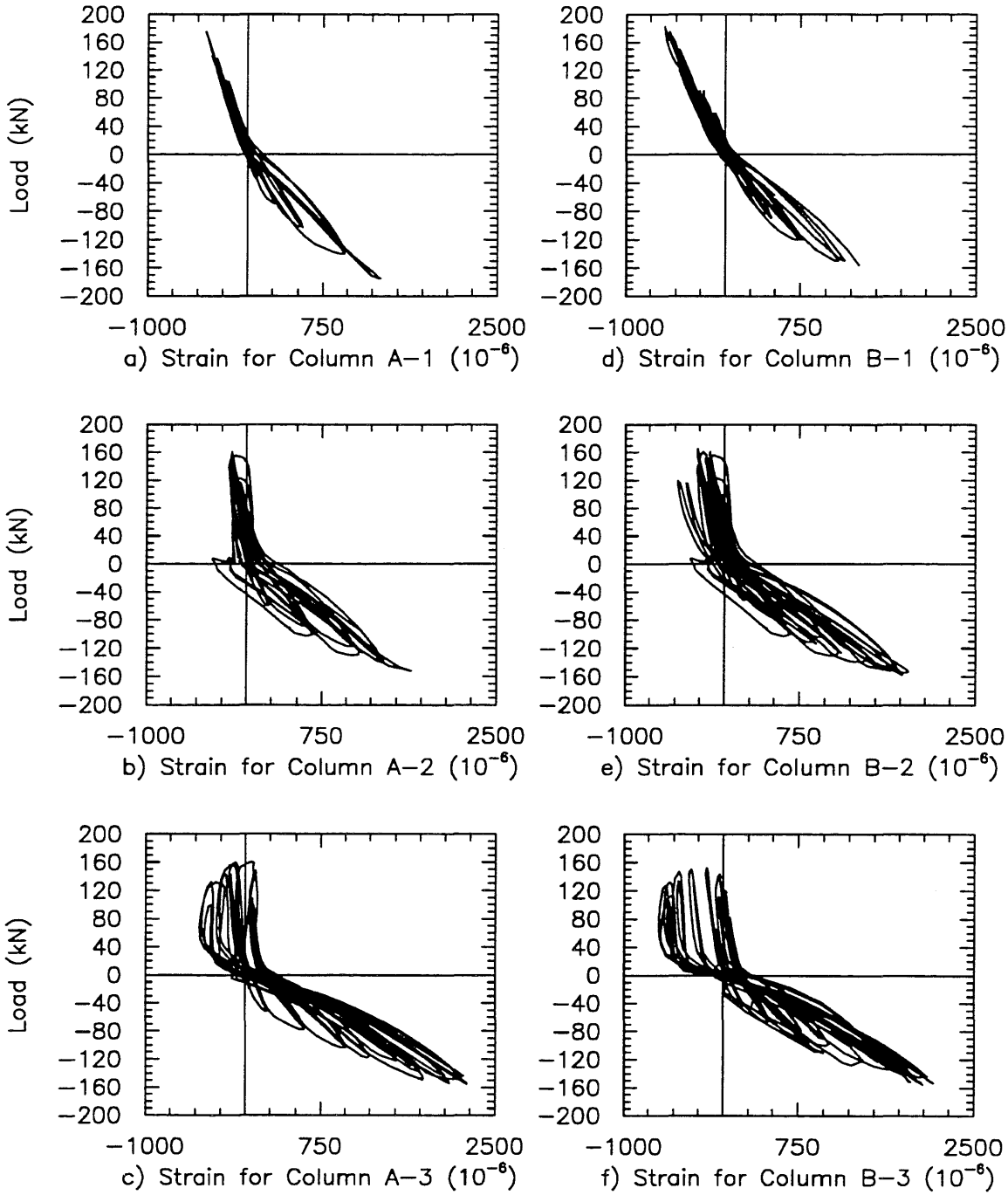

Fig. D7 Load vs. Strain Curve for Gage 7 on Dowel Bar

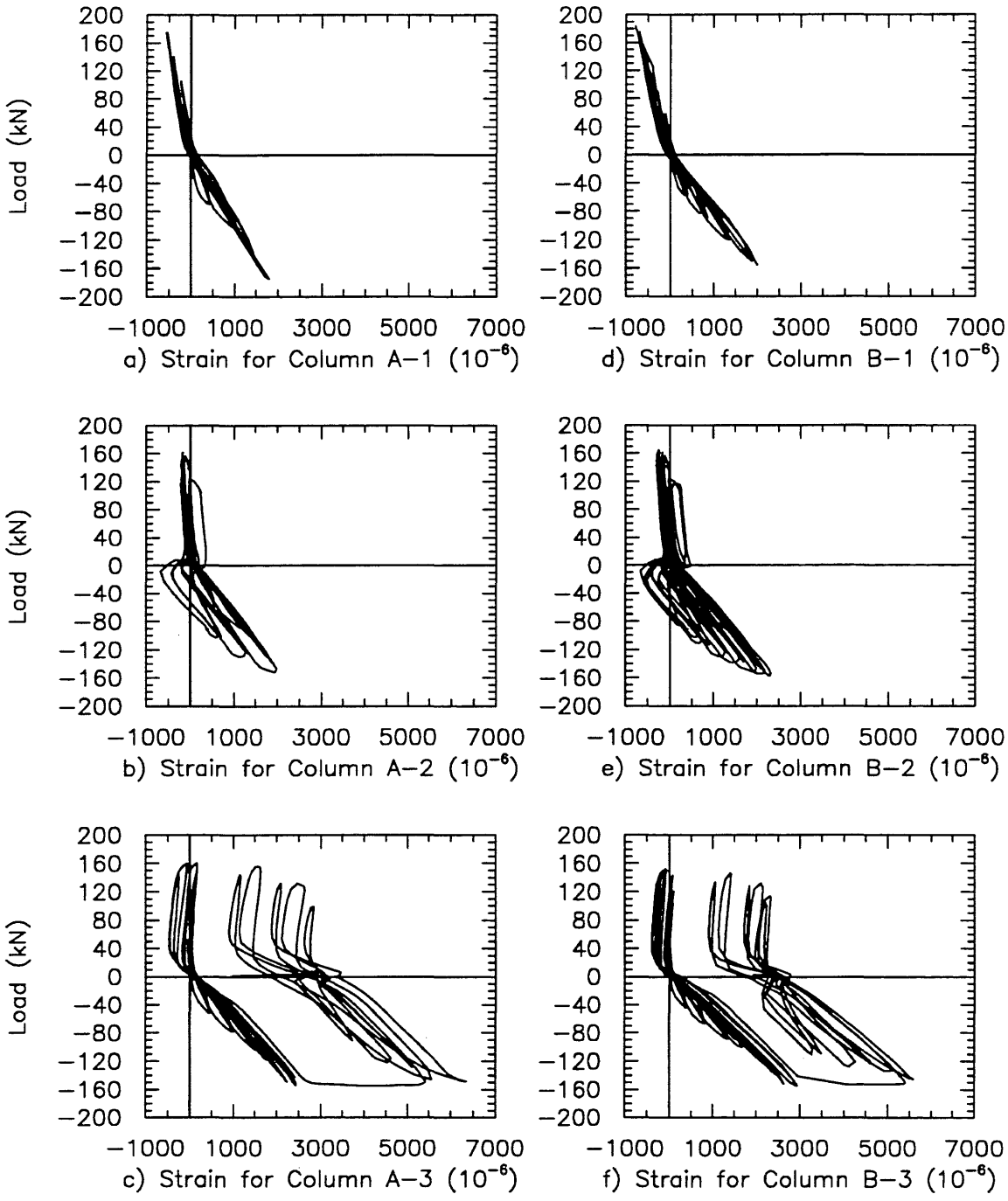

Fig. D8 Load vs. Strain Curve for Gage 8 on Dowel Bar

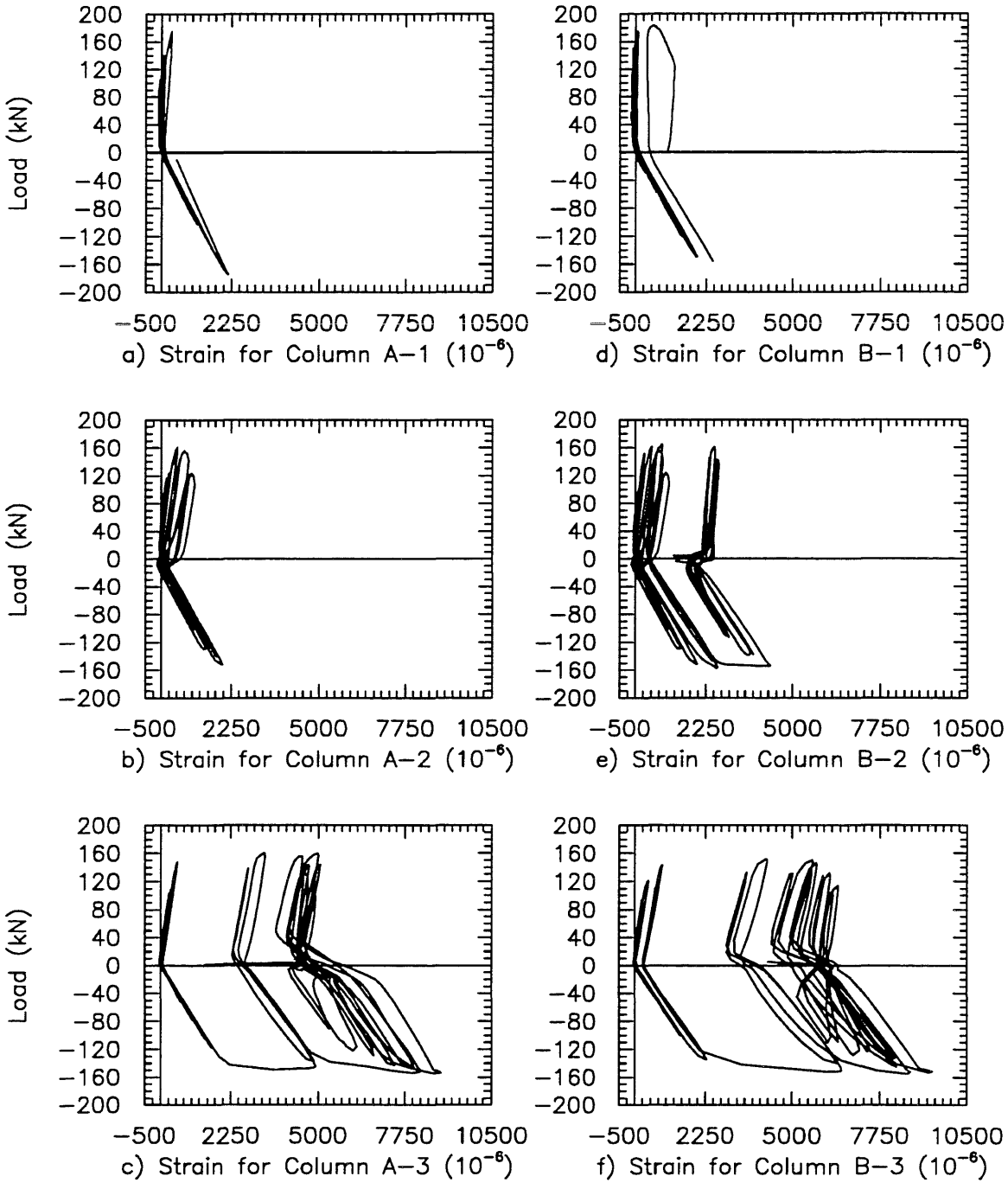

Fig. D9 Load vs. Strain Curve for Gage 9 on Dowel Bar

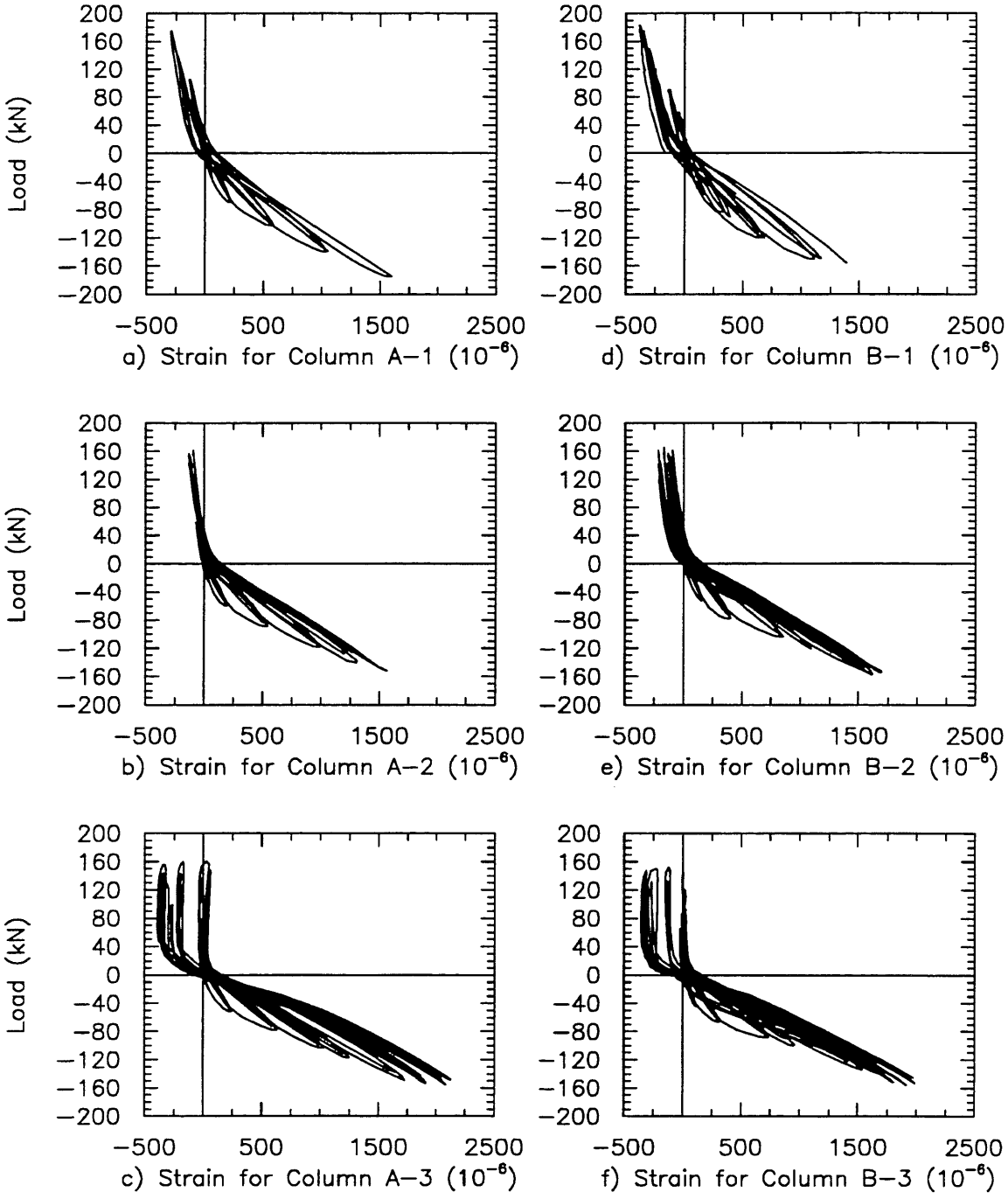

Fig. D10 Load vs. Strain Curve for Gage 10 on Dowel Bar

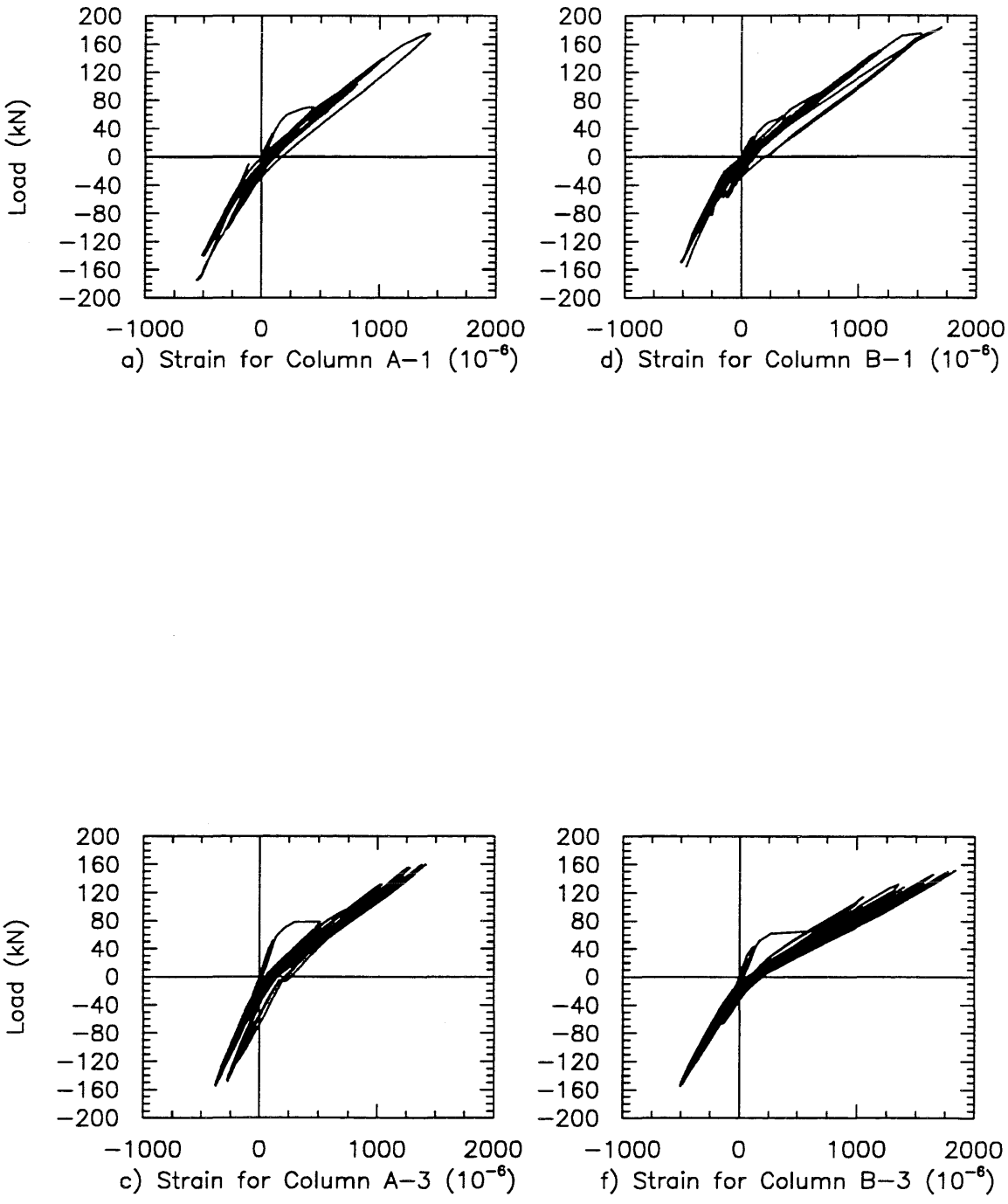

Fig. D11 Load vs. Strain Curve for Gage 11 on Column Bar

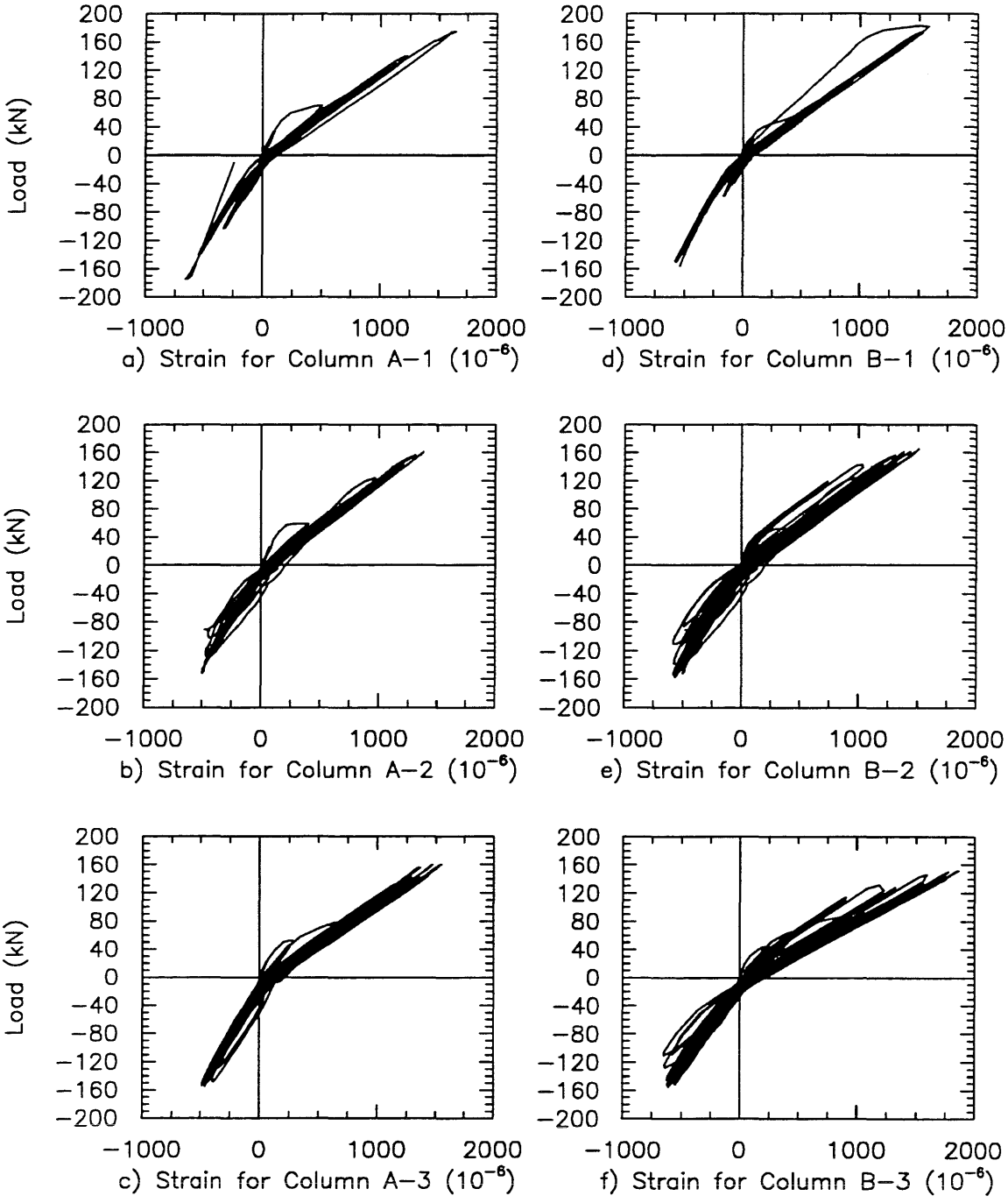

Fig. D12 Load vs. Strain Curve for Gage 12 on Column Bar

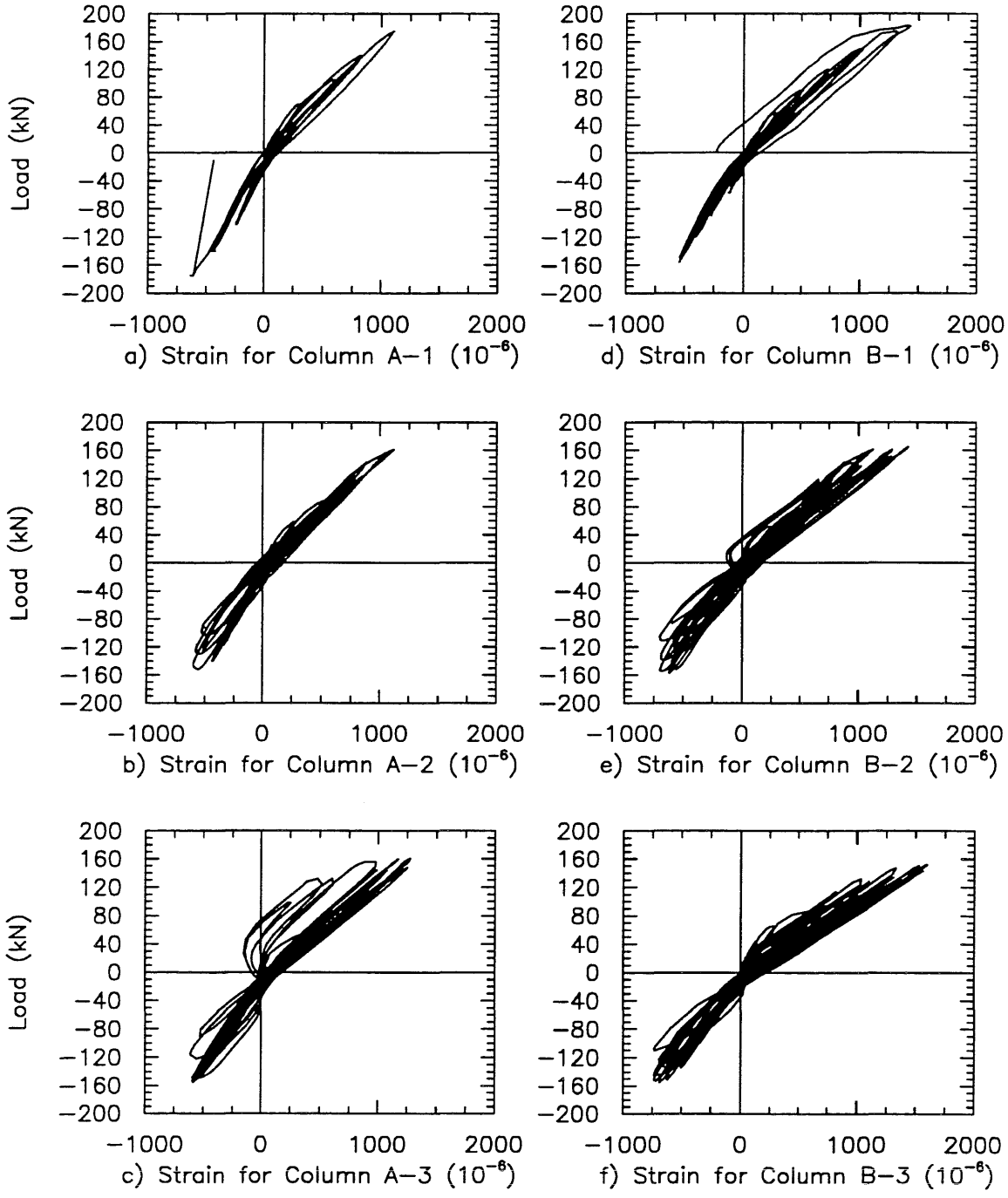

Fig. D13 Load vs. Strain Curve for Gage 13 on Column Bar

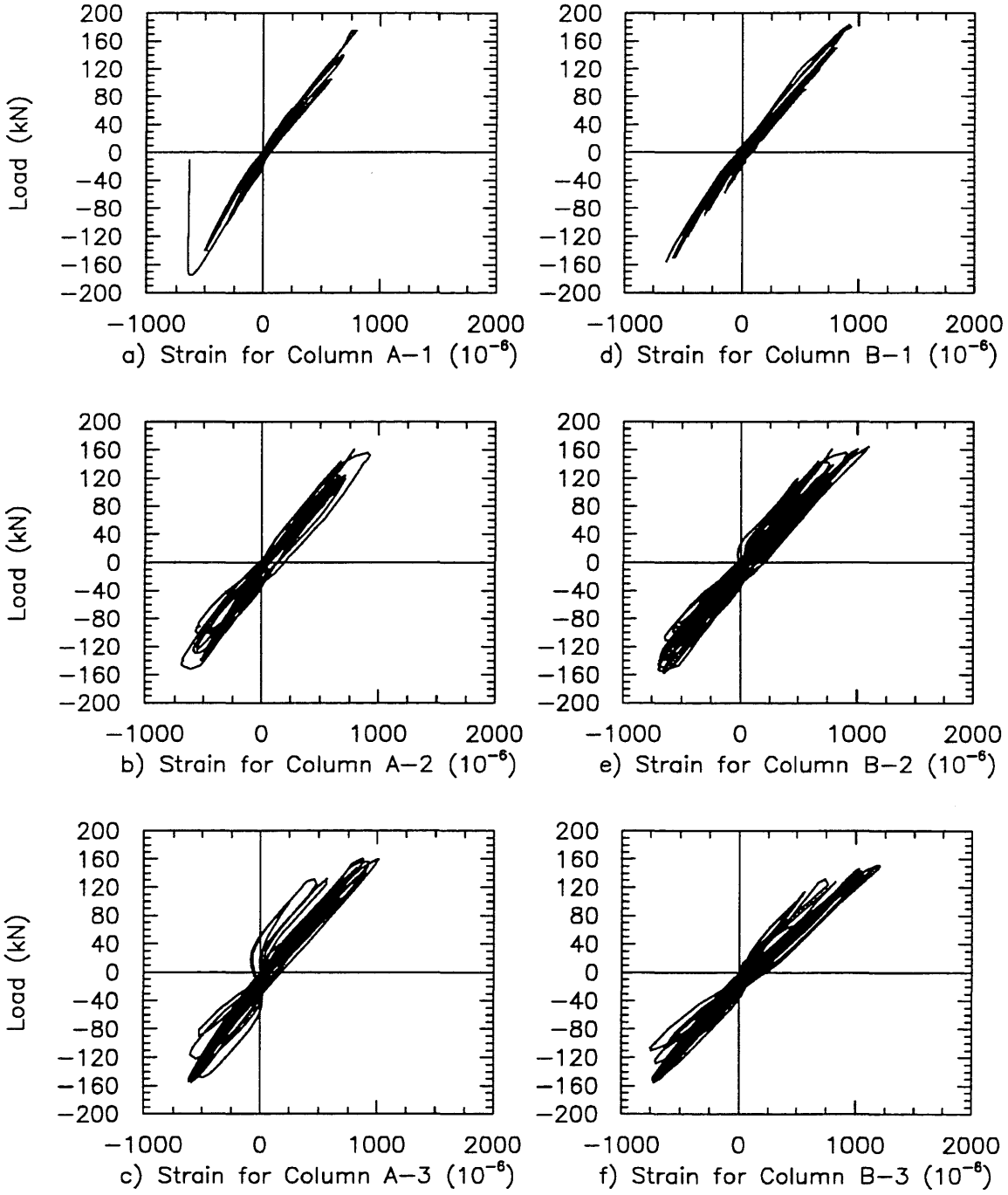

Fig. D14 Load vs. Strain Curve for Gage 14 on Column Bar

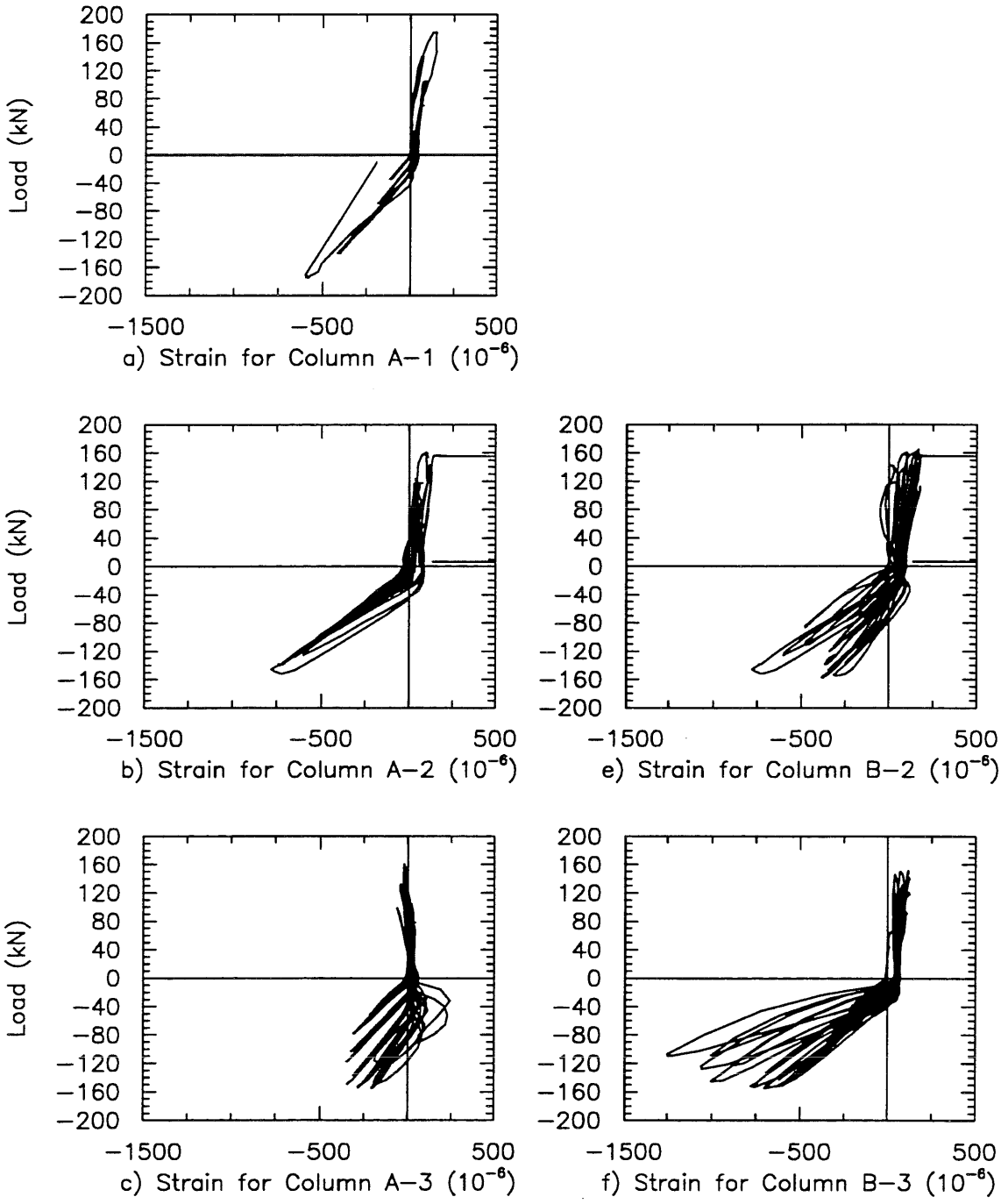

Fig. D15 Load vs. Strain Curve for Gage 15 on Column Bar

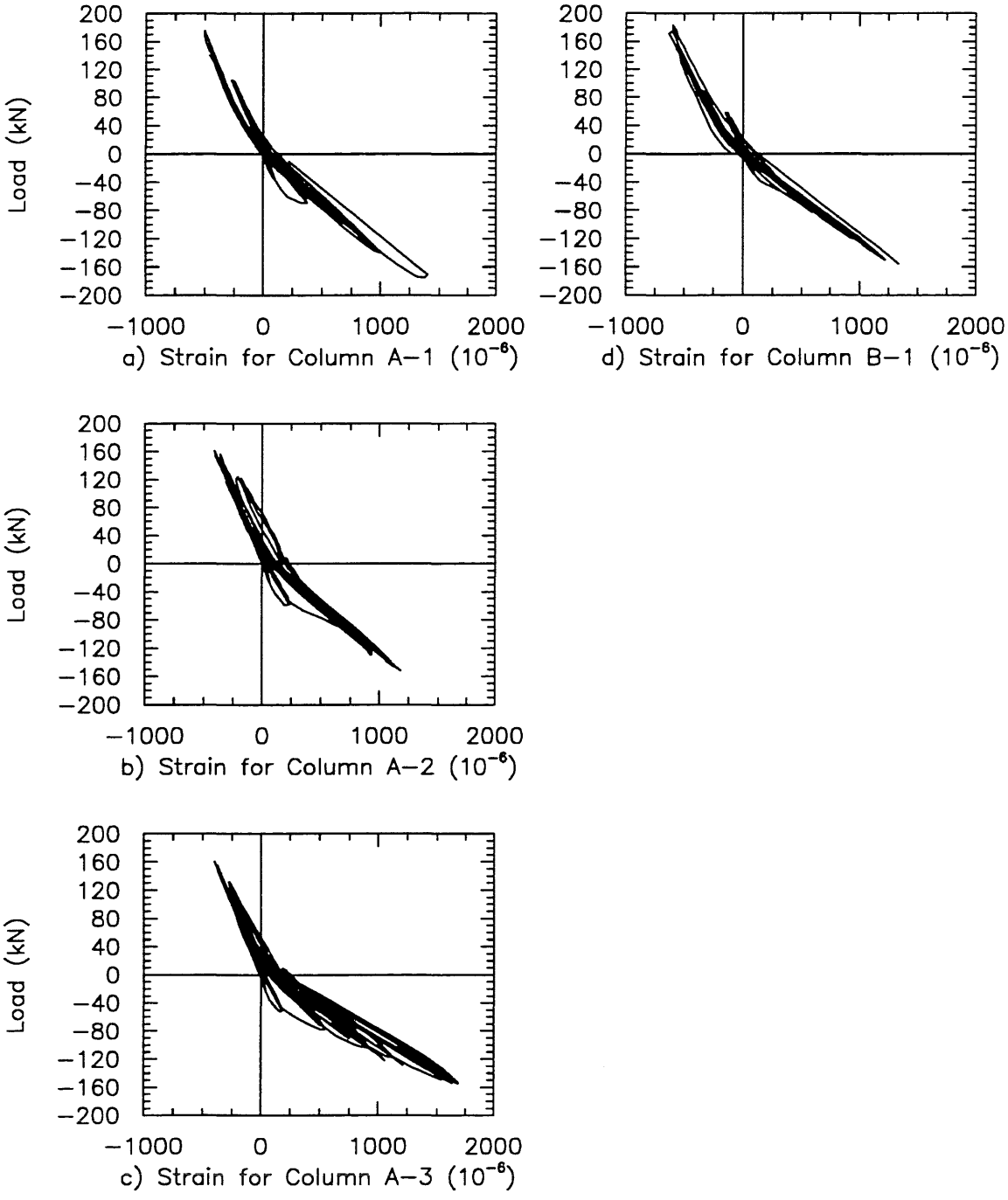

Fig. D16 Load vs. Strain Curve for Gage 16 on Column Bar

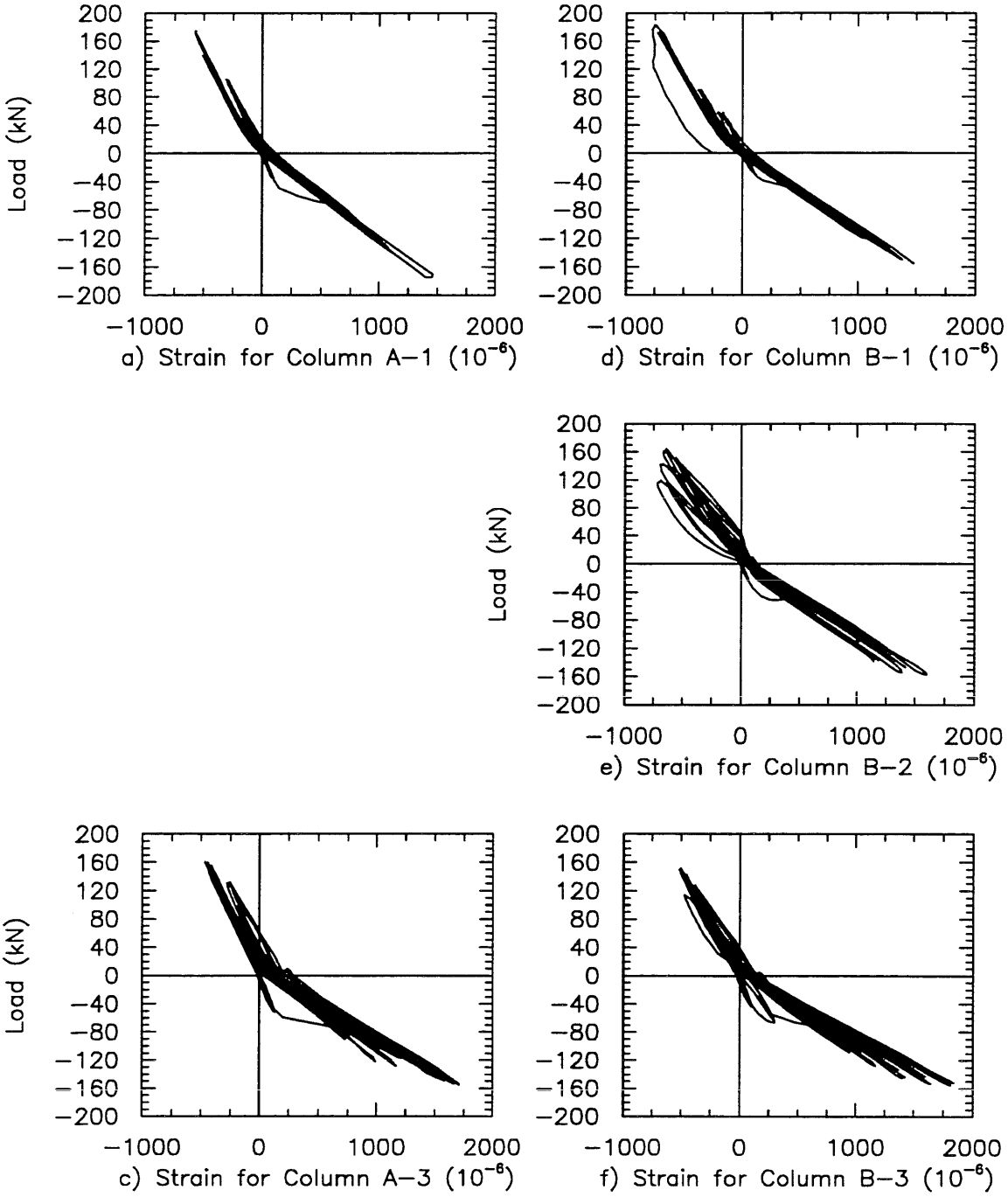

Fig. D17 Load vs. Strain Curve for Gage 17 on Column Bar

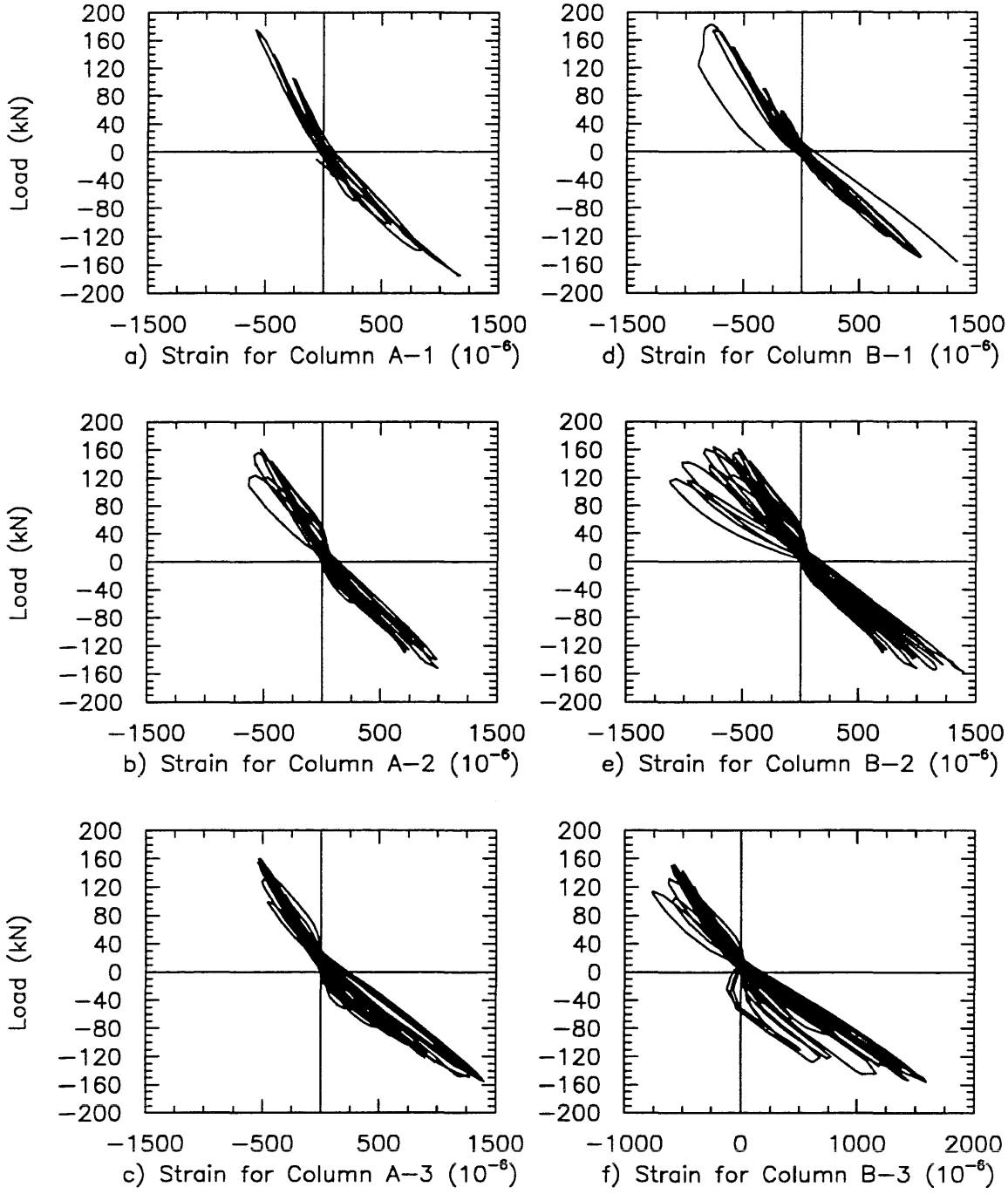

Fig. D18 Load vs. Strain Curve for Gage 18 on Column Bar

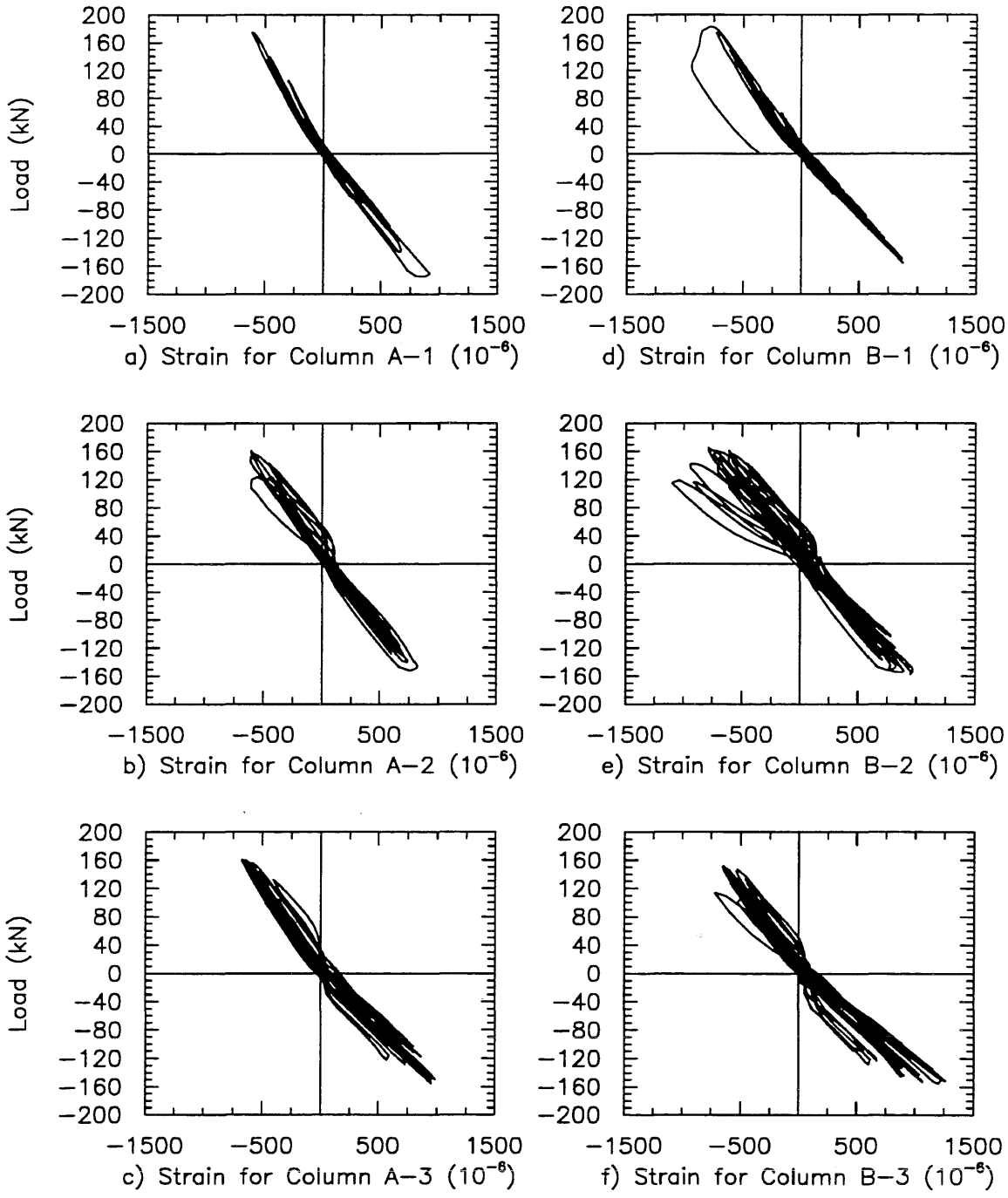

Fig. D19 Load vs. Strain Curve for Gage 19 on Column Bar

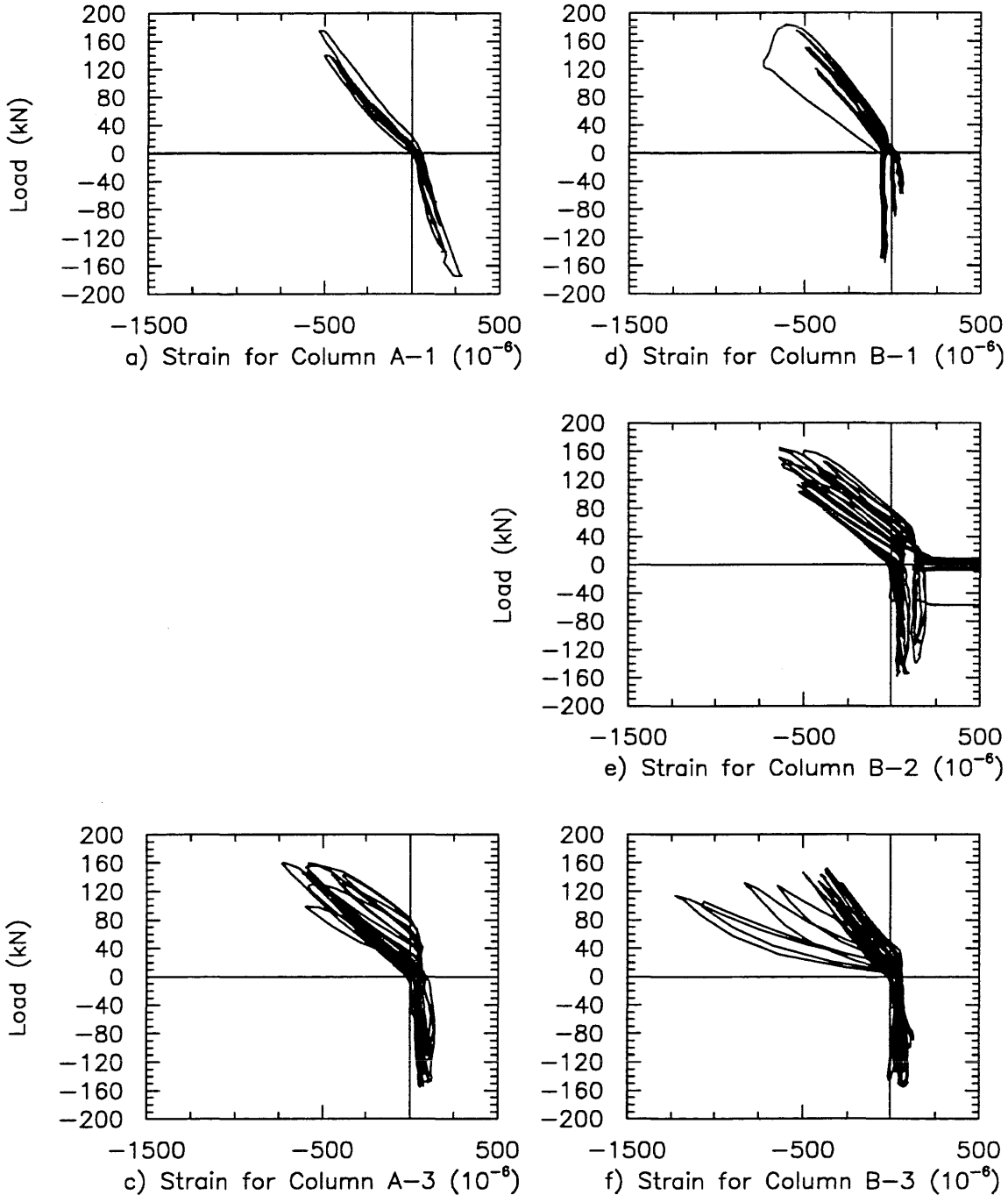

Fig. D20 Load vs. Strain Curve for Gage 20 on Column Bar

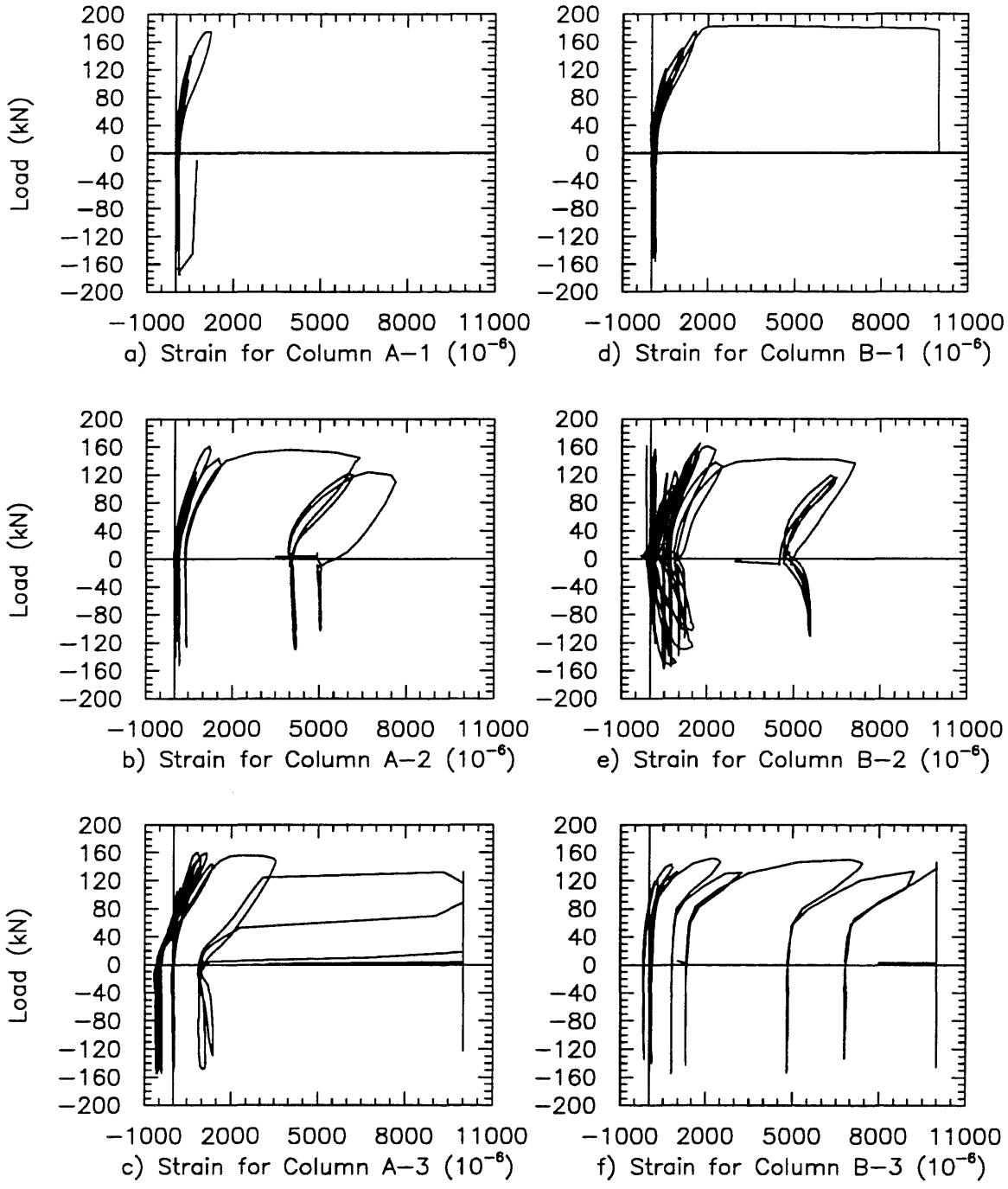

Fig. D21 Load vs. Strain Curve for Gage 21 on Hoop

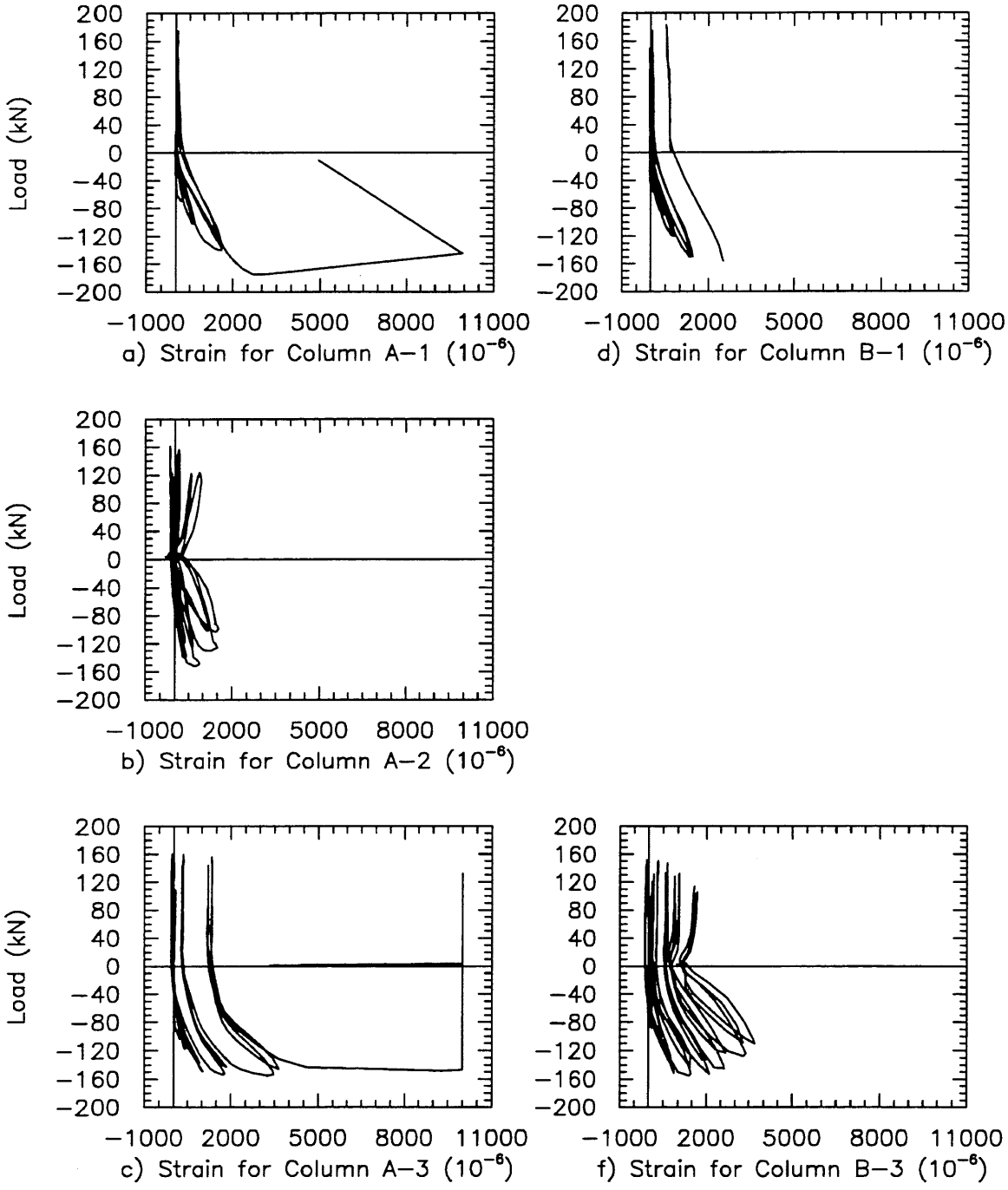

Fig. D22 Load vs. Strain Curve for Gage 22 on Hoop

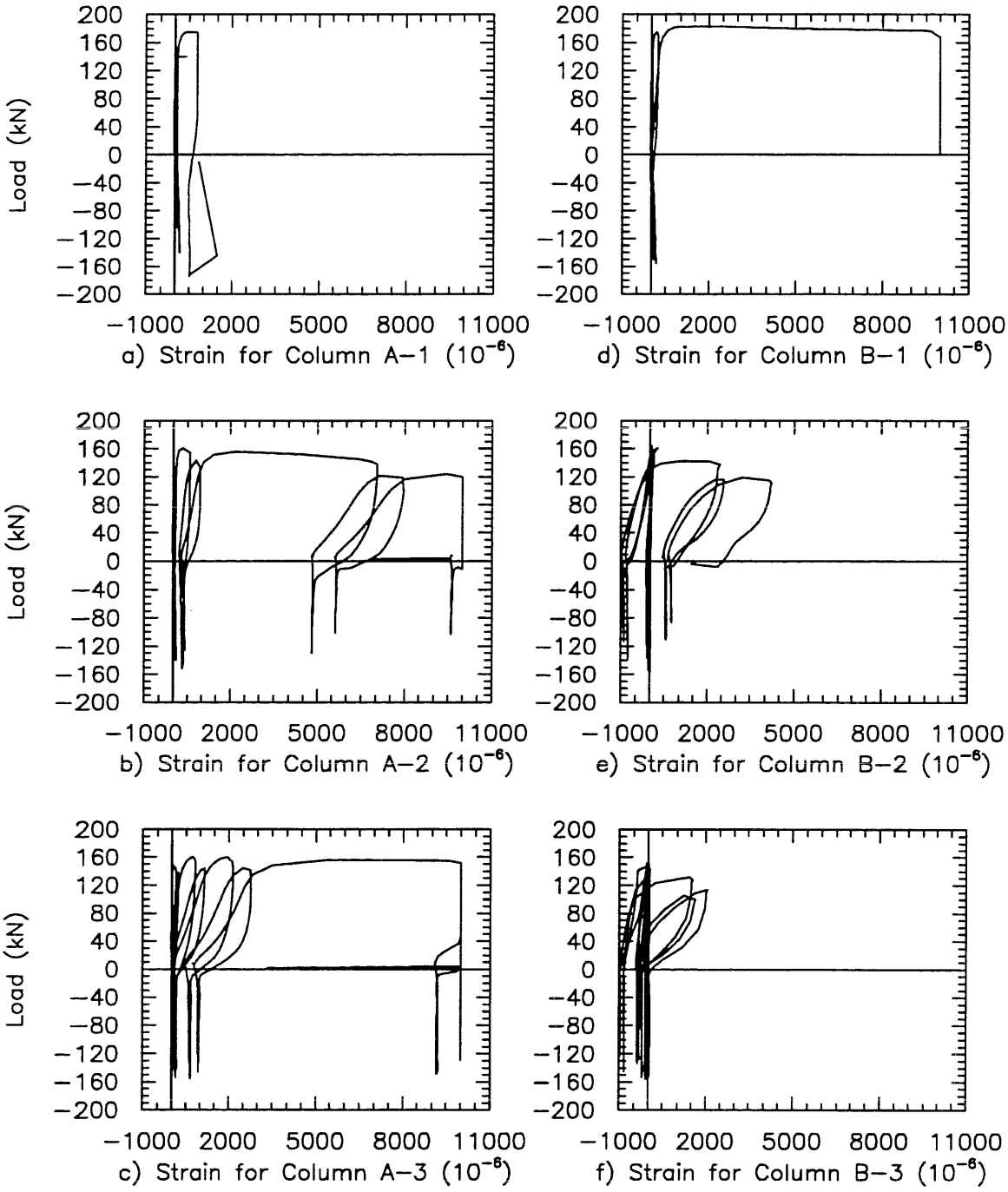

Fig. D23 Load vs. Strain Curve for Gage 23 on Hoop

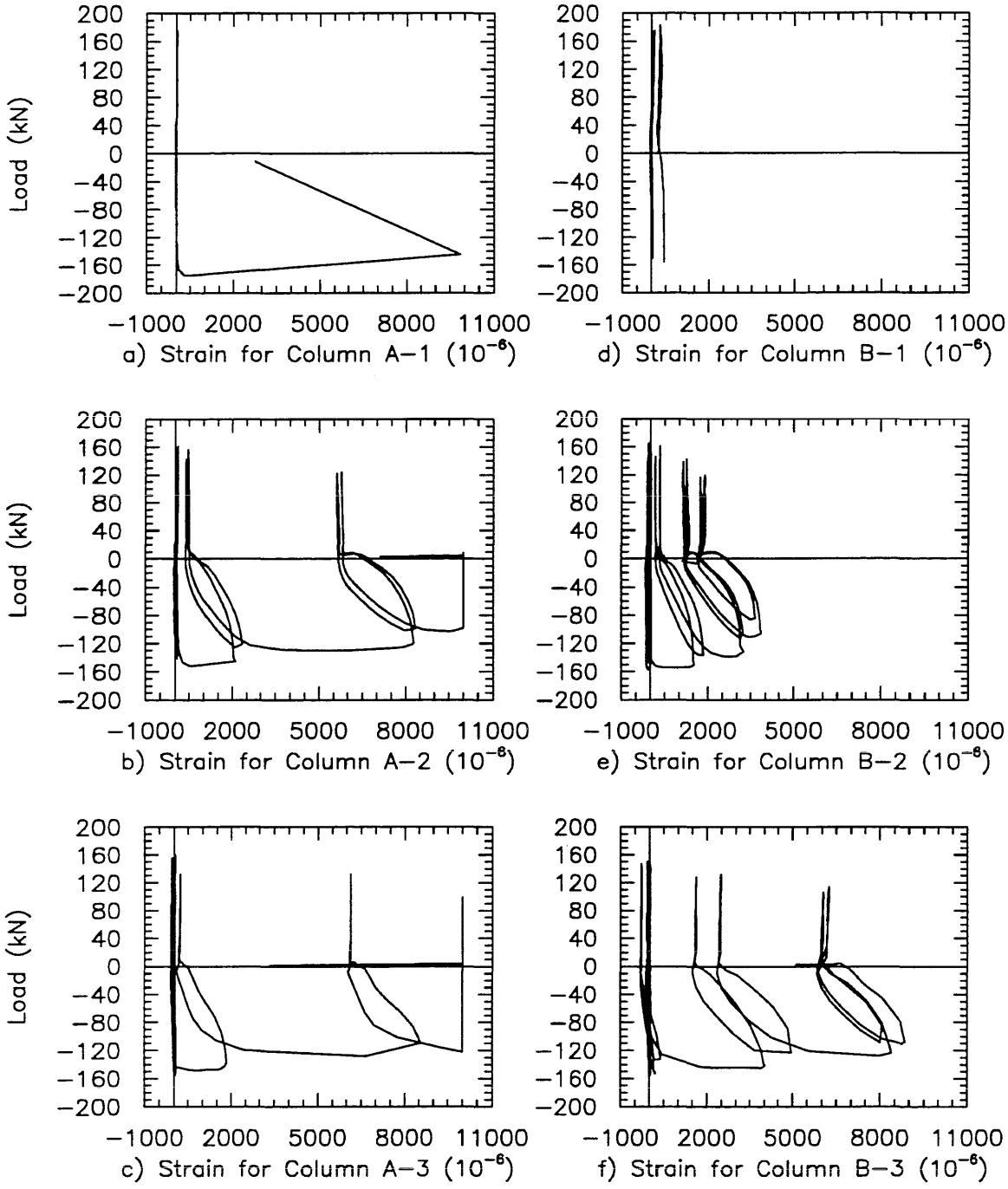

Fig. D24 Load vs. Strain Curve for Gage 24 on Hoop

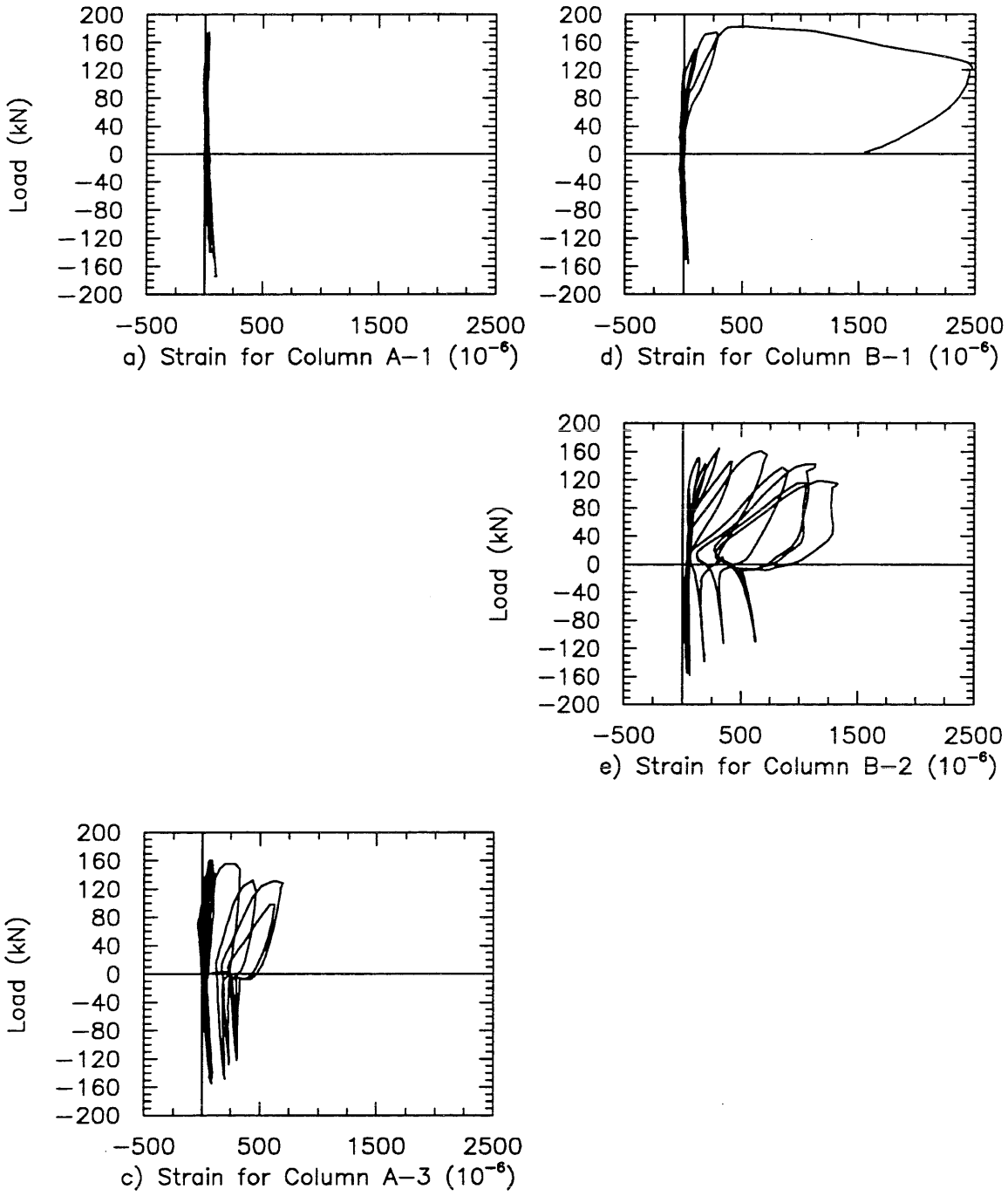

Fig. D25 Load vs. Strain Curve for Gage 25 on Hoop

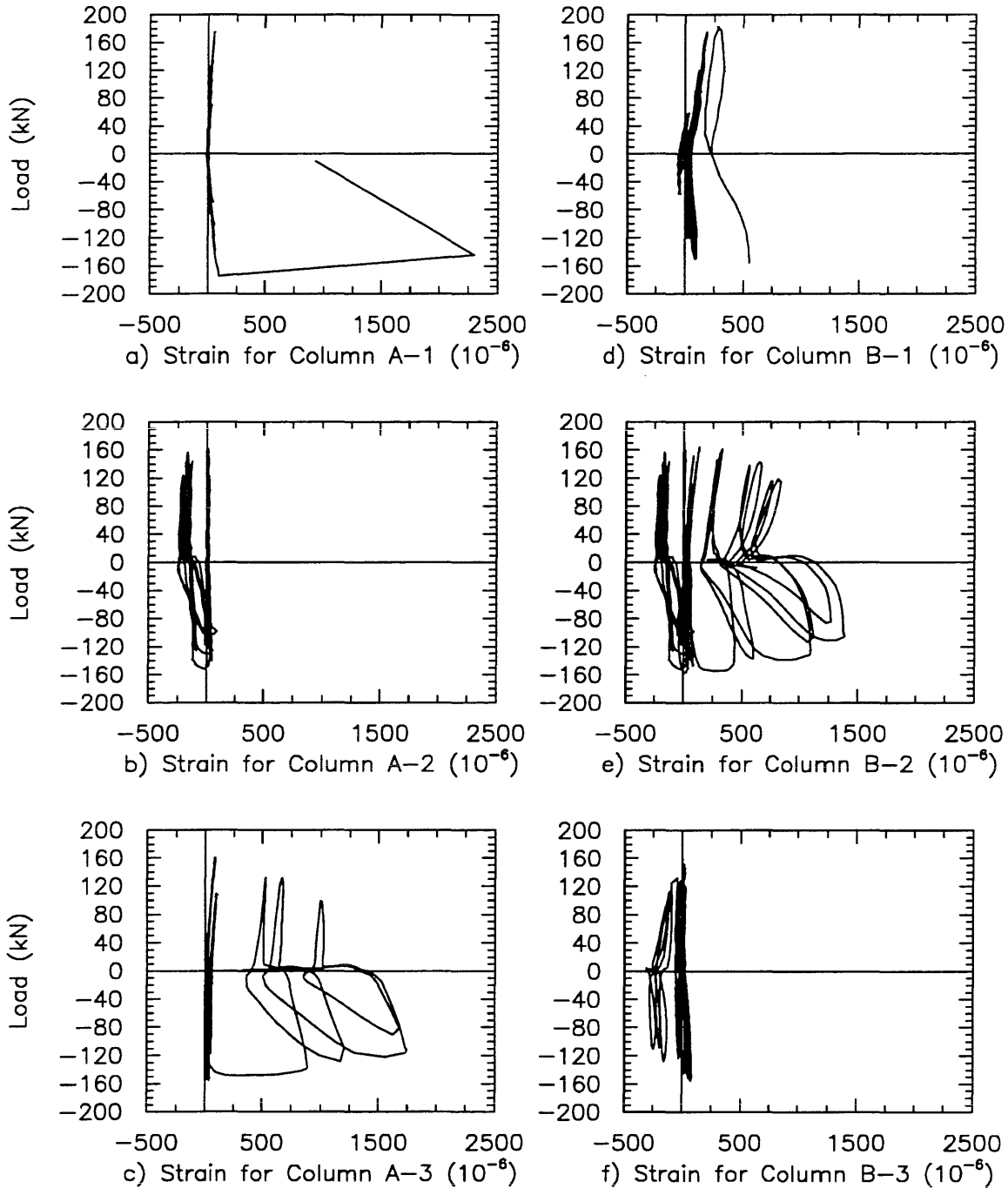

Fig. D26 Load vs. Strain Curve for Gage 26 on Hoop

Appendix E Moment Curvature Relationships

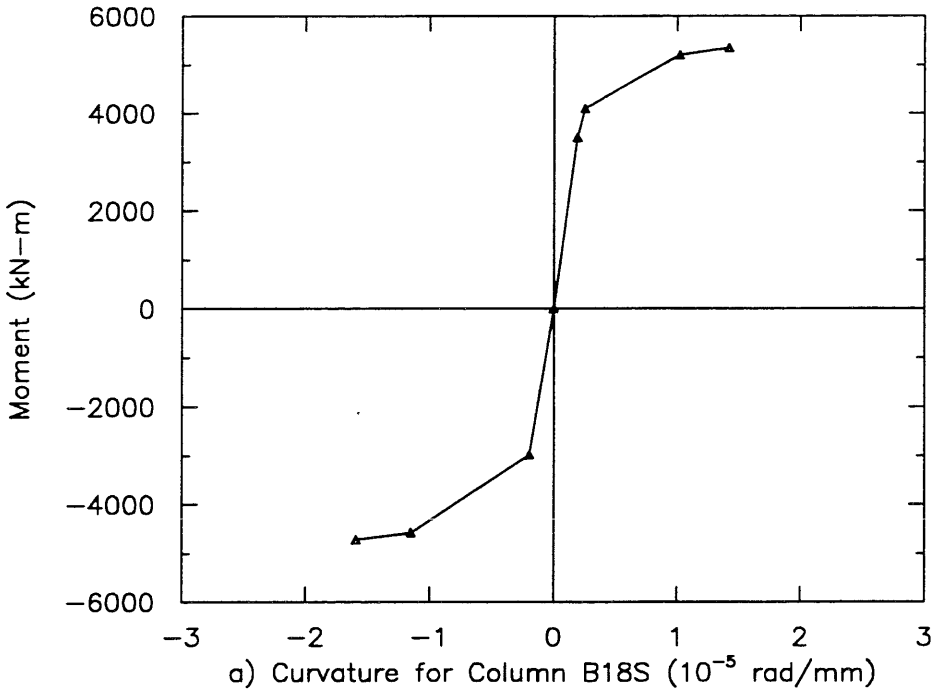

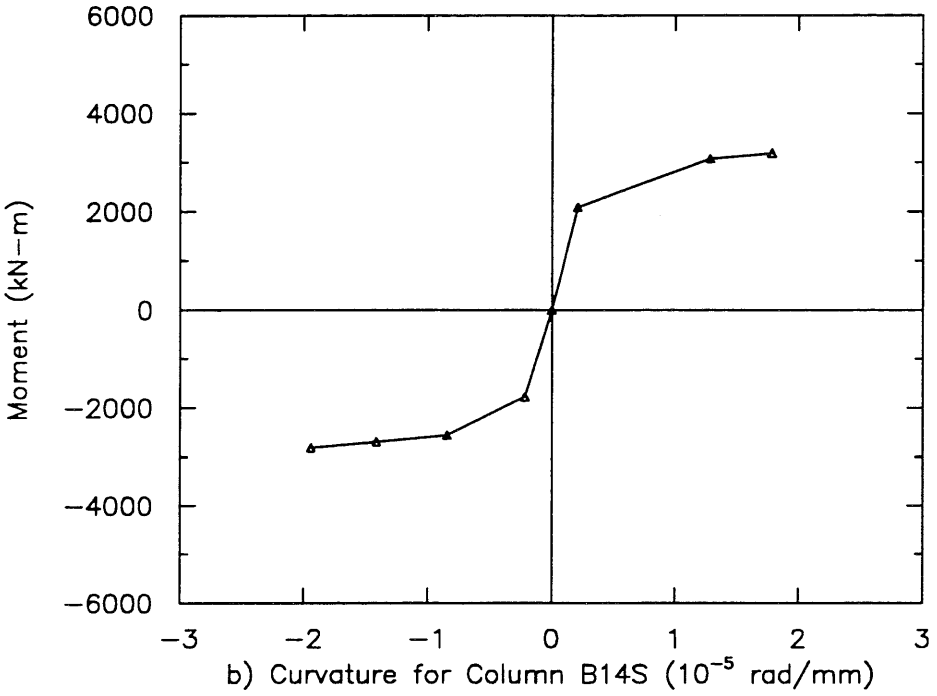

Fig. E1 Moment Curvature Relationships for Field Test Columns

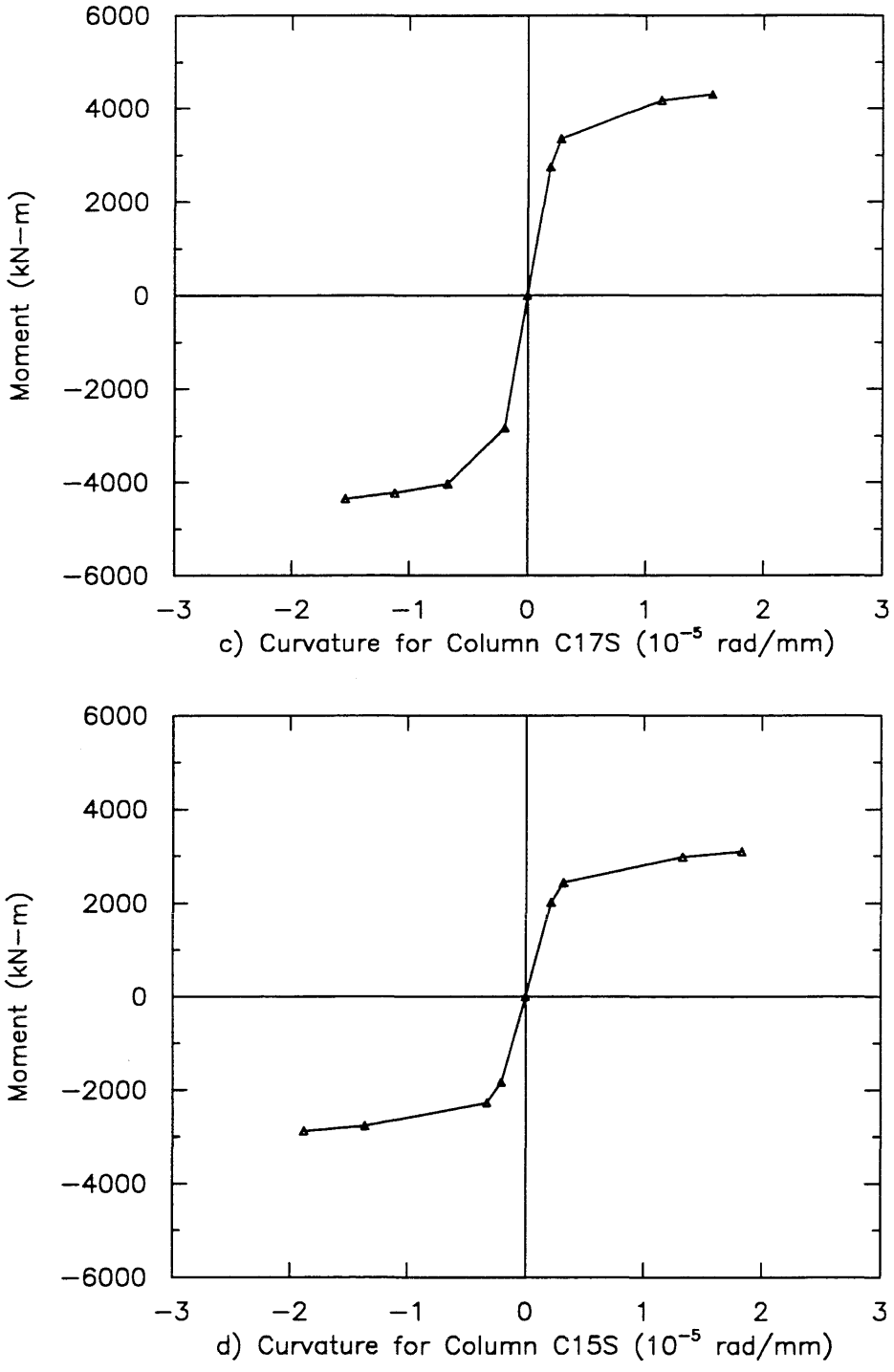

Fig. E1 Moment Curvature Relationships for Field Test Columns (cont.)

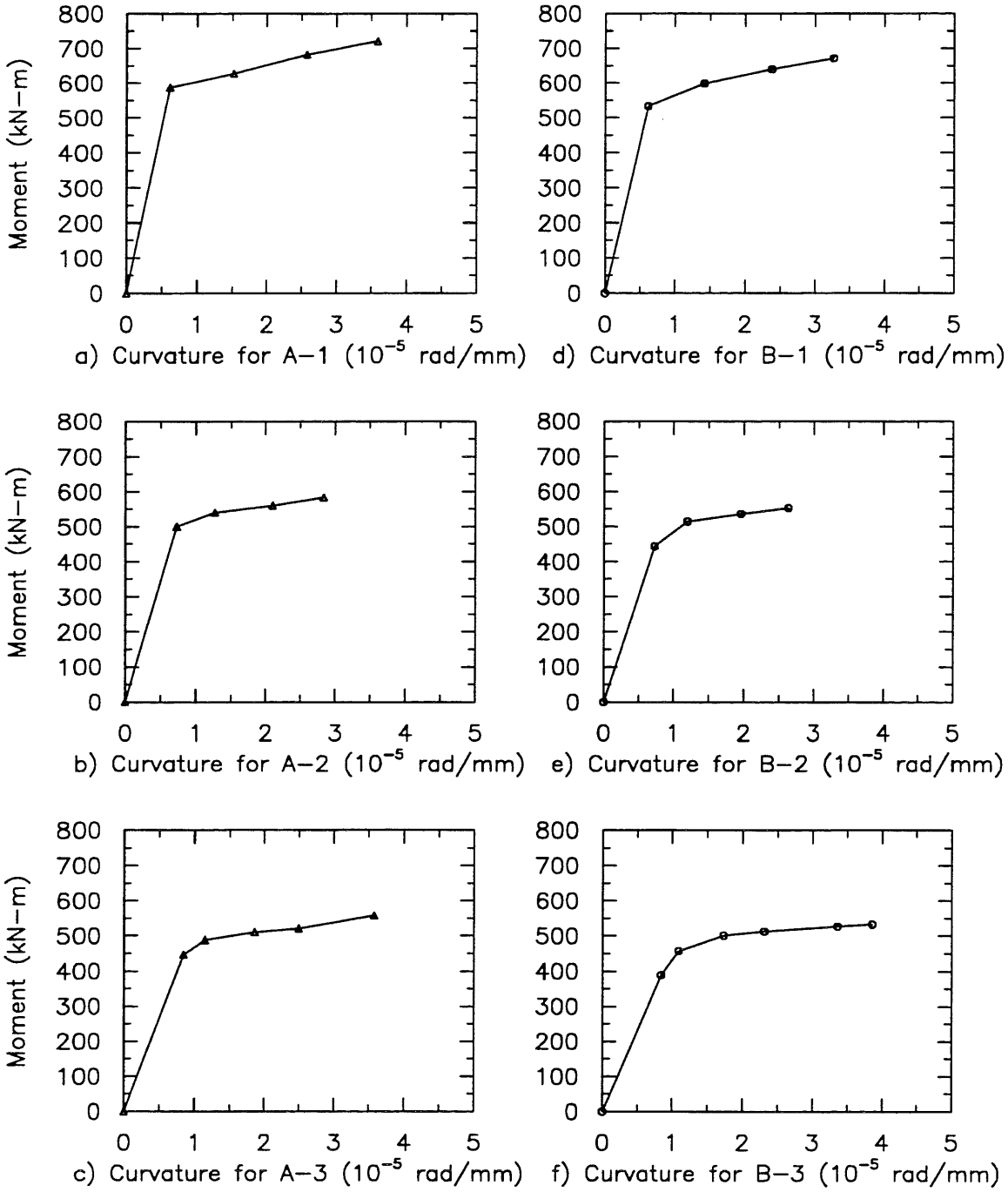

Fig. E2 Moment Curvature Relationships for Laboratory Test Columns